STRUCTURAL AND MAGMATIC HISTORY OF UPPER MANTLE PERIDOTITES IN THE BAY OF ISLANDS COMPLEX, NEWFOUNDLAND

GÜNTER SUHR, Dipl. Geol.

NOTICE

The quality of this microform is heavily dependent upon the quality of the original thesis submitted for microfilming. Every effort has been made to ensure the highest quality of reproduction possible.

If pages are missing, contact the university which granted the degree.

Some pages may have indistinct print especially if the original pages were typed with a poor typewriter ribbon or if the university sent us an inferior photocopy.

Reproduction in full or in part of this microform is governed by the Canadian Copyright Act, R.S.C. 1970, c. C-30, and subsequent amendments.

AVIS

La qualité de cette microforme dépend grandement de la qualité de la thèse soumise au microfilmage. Nous avons tout fait pour assurer une qualité supérieure de reproduction.

S'il manque des pages, veuillez communiquer avec l'université qui a conféré le grade.

La qualité d'impression de certaines pages peut laisser à désirer, surtout si les pages originales ont été dactylographiées à l'aide d'un ruban usé ou si l'université nous a fait parvenir une photocopie de qualité inférieure

La reproduction, même partielle, de cette microforme est soumise à la Loi canadienne sur le droit d'auteur, SRC 1970, c. C-30, et ses amendements subséquents

STRUCTURAL AND MAGMATIC HISTORY OF UPPER MANTLE PERIDOTITES IN THE BAY OF ISLANDS COMPLEX, NEWFOUNDLAND

by

© Günter Suhr, Dipl. Geol.

A thesis submitted to the School of Graduate Studies
in partial fulfilment of the requirements for
the degree of Doctor of Philosophy

Department of Earth Sciences

Memorial University of Newfoundland

May 1991

St. John's Newfoundland

ISBN 0-315-68261-2

ABSTRACT

The Bay of Islands Complex (BOIC) represents a lower Ordovician ophiolite located in western Newfoundland. In the northern part of the BOIC, a 6 km thick mantle section is exposed in the Table Mountain (TM) massif. The structural, microstructural (including olivine lattice data), and geochemical variation within the mantle section were investigated in order to delineate the tectonic and magmatic history of the peridotites.

The field structures indicate the presence of six structural units which are defined by distinct trends of the high temperature mineral stretching lineation of harzburgites, lherzolites, and dunites. On the basis of microstructural evidence, the formation of four of these units is assigned to spreading-related events, the remaining two to detachment tectonics. A high level and a low level zone preserving microstructural evidence for melt infiltration are present. The high level peridotites also show mineral chemical evidence for melt infiltration.

Peridotite microstructures are classified into several 'type microstructures' interpreted to reflect differences in stress, accumulated strain, temperatures of deformation, and presence or absence of melt during deformation. The microstructural behaviour of orthopyroxene and spinel is investigated in more detail. The range of deformation mechanisms inferred from the morphology of orthopyroxene correlates largely with the temperature of deformation. In areas of lower accumulated strain, spinel grains, together with spatially associated phases, appear to preserve morphologies discriminating between different magmatic processes, i.e. spinel formed during partial melting, trapping of melt, and transient melt movement.

The process of melt infiltration into peridotite is further investigated and two end-member processes can conceptionally be distinguished: (i) simple trapping of primitive melt; (ii) extensive flushing of melt through peridotite associated with fractionation of melt and reaction with the host. Mineralogical and geochemical trends associated with both processes are discussed and compared to the TM peridotites.

Relative age relationships between the spreading-related structural units support the plate thickening model for formation of oceanic lithosphere. By applying thermal models for formation of oceanic lithosphere to the TM mantle section, the distance from the ridge axis, at which each unit has been structurally frozen in, can be estimated. The additional use of data concerning the relative sense of shear in the peridotites and the relative position of the ridge axis with respect to the TM massif indicates that the high level, early mantle structures in TM are related to plate driven flow. Later, deeper mantle structures formed during forced flow. The latest spreading-related structures are assigned to an off-axis, diapiric motion of the upper mantle which was stopped at the base of the lithosphere at approximately 50 km from the ridge axis. The lower melt infiltration zone is correlated with this event.

The history of the BOIC can be explained as an evolution during a decreasing spreading rate. The decreasing spreading rate is considered responsible for the emergence of a late, transient, far-reaching forced flow field driven by the buoancy of partially melted peridotite below the ridge during a period of restricted extensional plate movement. As a further consequence of restricted extension, magmatic products ponded at the base of the oceanic crust, resulting in the formation of thick dunite sequences in the late history of the BOIC. This late history is best preserved in the Blow Me Down massif of the BOIC which, based on the preservation of ridge-parallel flow structures up to a depth of several kilometres below the Moho, must have been located close to

the ridge axis when spreading ceased. The presence of lherzolites instead of harzburgites at the base of all four massifs of the BOIC may be explained as the result of slower mantle upwelling prevailing during very slow spreading in the final extensional history of the BOIC. Later, the plates converged, causing detachment of the ophiolite.

The oceanic basin where the BOIC was generated may represent a pull-apart basin (Andaman Sea type) which opened during strike-slip dominated tectonics within an older, arc-type oceanic lithosphere. The boundary between the young lithosphere of the BOIC and the older arc-type lithosphere would correlate with the proposed fracture zone in the Lewis Hills massif.

ACKNOWLEDGEMENTS

Numerous people have helped me in completing this thesis. Dr. Tom Calon introduced me to the structural problems associated with upper mantle rocks and supervised the thesis with much patience during its ups and downs. Dr. Paul Robinson (Dalhousie University) opened the way for me to come to Canada. His help and financial support at Dalhousie is still appreciated but was poorly rewarded. Drs. Adolphe Nicolas and Françoise Boudier (Université de Sciences et Téchnologie du Languedoc, France) provided working facilities in Montpellier to do petrofabric work and taught me many concepts in mantle tectonics. Their help was very important and came at a critical stage of the thesis.

In addition to the people already mentioned, discussions with the following people provided me with important scientific background knowledge. Some of them also critically read thesis material: Drs. Keith Benn, Peter Cawood, and George Ceuleneer, Sherry Dunsworth, Steven Edwards, Jeroen van Gool, Drs. John Malpas, Toby Rivers, H. Seck, and Bob Stevens.

With Stephen Edwards I enjoyed countless, scientifically interesting discussions and entertaining companionship in the field. Jeroen van Gool and David van Everdingen had to endure me also during darker times, but still kept their spirits high. Dr. Peter Cawood gave much support and provided directions to go. To all four, special thanks are extended.

Technical support was essential for this thesis. It was provided by Gert Andrews (major element analysis), Gordon Brown (thin and polished sections at Dalhousie University), Pamela King (REE-analysis), Dr. Henry Longerich (microprobe), Dave MacNeil (Autocad), Wilf Marsh (Photography), Geoff Veinott (microprobe, XRF, XRD),

Dr. Henry Williams (Macintosh-usage), and the "workshop-crew" Foster Thornhill, Lloyd Warford, Rick Soper, and Gerry Ford (thin and polished sections, rock cutting facilities, and things beyond technical support). Special thanks go to Pat Browne who managed somehow to organize everything. Dr. John Malpas generously supported the thesis by providing field vehicles.

In addition to many other people who cannot be mentioned here, I want to thank Drs. Keith Benn and Tony Berger, Sherry Dunsworth and Jamie Meyer, Dr. Brian Fryer, Pat MacLeod and Gisela Westphalen, Dr. Dave Mainprice, Casey Ravenhurst, and Dr. F. Stibane for help and support.

Financial support was received from graduate fellowships of Dalhousie and Memorial University. Field work was supported through various grants awarded to Dr. T. Calon. Generous funding was given for a visit of the Oman Ophiolite Conference by the Dept. of Earth Sciences, the School of Graduate Studies, the Dean of Science, Dr. T. Calon, and the Graduate Student Union.

The most important support, even from far away, came from my father, my mother (until her death), my sister, and my girl friend, Irmgard Kuss. Without them, things wouldn't have worked out.

TABLES OF CONTENTS

LIST OF TABLES

TABLES WITHIN THE TEXT

TABLES IN THE APPENDIX

LIST OF FIGURES

FIGURES WITHIN THE TEXT

FIGURES IN THE APPENDIX

LIST OF ABBREVIATIONS

BFA	-	best-fit axis, i.e. axis of great circle defined by planar elements
BMD	-	Blow Me Down Mountain
BOIC	-	Bay of Islands Complex, excludes western Lewis Hills massif
BOIO	-	Bay of Islands Ophiolite, comprises BOIC and CC
CC	-	Coastal Complex, includes western Lewis Hills massif
cpx	-	clinopyroxene
GBM	-	grain boundary migration
LAB	-	lithosphere - asthenosphere boundary
LH	-	Lewis Hills
LPC	-	Little Port Complex as defined by Williams (1973), excludes western Lewis Hills
MORB	-	mid-ocean ridge basalt
NAM	-	North Arm Mountain
NGBM	-	nucleation and grain boundary migration
opx	-	orthopyroxene
SGR	-	subgrain rotation
σ	-	deviatoric stress
TM	-	Table Mountain
TU	-	Transitional Unit, occurs between structural units 4 and 5

see also the legend to Fig. 5.6 for abbreviations used in section 5.9.

1 INTRODUCTION

1.1 UPPER MANTLE DYNAMICS

1.1.1 Introduction

After twenty years of intense research, there appears to be little doubt that ophiolites represent oceanic lithosphere (e.g. Moores 1982, Coleman 1984, Nicolas 1989). In particular, the similarity of seismic properties of oceanic lithosphere and ophiolites is convincing (Christensen and Salisbury 1979, Christensen 1984). A specific tectonic environment of formation for ophiolites does apparently not exist. Most striking is the absence of an ophiolite which would be generally accepted to have formed within a classic mid-ocean ridge environment (Coleman 1984).

A complete ophiolite sequence consists from base to top of tectonized upper mantle peridotites, layered and isotropic gabbros and minor ultramafic cumulates, a mafic sheeted dyke swarm, mafic volcanics, and minor oceanic sediments. Minor chromitite bodies and felsic intrusives may be present (Anonymous 1972). The sheeted dyke swarm of this assemblage is indicative of extreme extension which is accommodated by formation of oceanic crust. Geodynamically, extensional environments are coupled with upwelling of upper mantle material from depth, either leading to a full ocean formation as in the case of oceanic lithosphere (ophiolites) or to the thinning of continental crust as in rifting environments, e.g. Basin and Range Province. This thesis deals with the deep rooted processes leading to the formation of oceanic lithosphere, i.e. mantle flow, partial melting, and melt migration.

1.1.2 Mantle flow and the formation of oceanic lithosphere: correlation between geophysical models, mid-ocean ridges, and ophiolites

Two end-member models have been suggested by geophysicists for the formation of oceanic lithosphere (Forsyth 1977, Phipps Morgan et al. 1987, Nicolas 1989, p. 30). (i) In the *dyke intrusion model* (McKenzie 1967, Cann 1974), asthenosphere intrudes vertically and in a dyke-like manner into the parting plates and solidifies in a steep flow orientation beneath the ridge. The lithosphere is created in its entire thickness near the spreading centre. Modifications allow for a wedge shaped flow towards the ridge axis. (ii) In the *plate thickening model* (Parker and Oldenburg 1973, Forsyth 1977), the vertical asthenospheric up-flow undergoes an overturn into a subhorizontal return flow directed away from the ridge. The subhorizontally flowing asthenosphere is transformed into lithosphere as the plates cool progressively while they are moving away from the ridge. In this way, the thickness of the lithosphere grows steadily with increasing distance from the spreading centre.

Both models predict surprisingly similar topographic and thermal properties for oceanic lithosphere (Forsyth 1977). Seismic evidence (Raleigh wave data) indicates, however, a thickening of the lithosphere with age in the Pacific and Atlantic ocean (Forsyth 1977). In addition, seismic anisotropy studies in the Pacific ocean support the plate thickening model, as the highest compressional wave velocity - which is parallel to the high temperature olivine slip direction (Francis 1969, Nicolas and Christensen 1987) - is measured perpendicular to the ridge elongation (Christensen 1984, Nicolas and Christensen 1987). The seismic evidence is thus inconsistent with a frozen in, vertical flow pattern as required in the dyke intrusion model.

The large scale models for the formation of oceanic lithosphere are supplemented by more detailed observations from the mid-ocean ridge system. A great effort has been

put into establishing and interpreting the topography across the strike of mid-ocean ridge systems (e.g. Sleep and Rosendahl 1979, Parmentier and Forsyth 1985, Chen and Morgan 1990) and along strike of the spreading axis between transform faults (e.g. Hey et al. 1980, Lonsdale 1983, 1989, Macdonald and Fox 1983, Macdonald et al. 1987, 1988, Sempéré et al. 1990, Karson et al. 1987). The discovery of the along-strike topographic variation ("mid-ocean ridge segmentation") has added a third dimension to models of oceanic lithosphere formation. Lithosphere formation involves topographic highs and lows along the ridge axis, overlapping and propagating spreading centres, and non-overlapping offsets of the spreading ridge. Spreading centres may also migrate into transform domains (Karson 1986). The topography probably correlates with magmatic centres of variable magnitude. The presence of magmatic centres along the strike of a mid-ocean ridge implies a heterogeneous formation of oceanic crust and explains the variation of crustal thickness (e.g. Detrick and Purdy 1980, Mutter et al. 1984) and basalt chemistry (Christie and Sinton 1981, Langmuir and Bender 1984, Klein and Langmuir 1987) observed within a segment of an ocean ridge bounded by transform faults.

The ultimate cause of the topographic and magmatic segmentation must lie within the underlying upper mantle. Several studies favour diapiric (or gravitational) instabilities as cause of mid-ocean ridge segmentation (Whitehead et al. 1984, Schouten et al. 1985, Crane 1985, Lin et al. 1990). The possible existence of these instabilities has been experimentally confirmed (Whitehead 1986). Based primarily on evidence from ophiolite studies, Rabinowicz et al. (1984, 1987) numerically simulated the effect of diapirs on mantle flow. They showed that a forced flow regime near the ridge axis will develop which overrides the regional plate driven flow. In addition, the melt trapped within diapirs reduces the viscosity of the upper mantle and explains the sharp turnover of mantle flow observed in ophiolitic upper mantle.

The presence of diapiric instabilities aligned along the ridge axis implies inhomogeneous lithosphere formation and, as a result, lateral mantle flow develops parallel to the ridge axis. The lateral flow appears directed towards the volcanic centre at depth (Whitehead et al. 1984, Phipps Morgan and Forsyth 1988) but away from the centre towards bounding transform faults at shallow levels (Vogt and Johnson 1975, Parmentier and Forsyth 1985, Nicolas 1989, p. 141).

An important variable for the formation of oceanic lithosphere is the spreading rate. In the plate thickening model, the lithosphere is thicker for slow spreading rates than for fast spreading rates at any given distance from the ridge axis. This means that the lithosphere - asthenosphere boundary (representing an isotherm in the plate thickening model) is progressively more steeply inclined with decreasing spreading rates (Parker and Oldenburg 1973, Sleep 1975, Kusznir and Bott 1976, Sleep and Rosendahl 1979, Chen and Morgan 1990). As a very steeply inclined lithosphere - asthenosphere boundary is typical for the dyke intrusion model, the plate thickening model could converge with that model for slow spreading rates. This would, however, imply that return flow has to break down below a certain spreading rate. Numerical modelling suggests that unsteady return flow will develop with decreasing spreading rates (Scott and Stevenson 1989). Other effects of slow spreading are a reduced thickness of the oceanic crust compared to fast spreading and the possibly complete absence of layer 3 (Sleep 1975, Kuznir and Bott 1976, Reid and Jackson 1981). Features similar to slow spreading are developed in the vicinity of ridge - transform intersections (e.g. Detrick and Purdy 1980, Mutter et al. 1984).

The mode by which melt migrates through the mantle is poorly known. It might occur predominantly by porous flow (Frank 1968, Ahern and Turcotte 1979, McKenzie

1984, Phipps Morgan and Forsyth 1988), within "magmons" (regions of high porosity; Scott and Stevenson 1986, Scott 1988), within diapirs (Whitehead et al. 1984, Whitehead 1986, Crane 1985, Scott 1988), or by veins and dykes (Sleep 1988).

Access to upper mantle rocks within the oceanic ridge system is restricted to large fault scarps. As a result, the study of ophiolitic mantle rocks is extremely important. Structural studies in the mantle section of ophiolites suggest that natural analogues exist to virtually all geometrical accretion models listed above. The *Trinity type* ophiolite (Boudier and Nicolas 1985, Nicolas 1986a, 1989, Boudier et al. 1989) could represent the dyke intrusion model with the reservation that in the Trinity type the inclination of the flow line appears subhorizontal to moderately inclined. The plate thickening model is confirmed in the *Table Mountain type* ophiolites (Prinzhofer et al. 1980, Girardeau and Nicolas 1981, Nicolas and Violette 1982). High spreading rates favour the Table Mountain type mantle structures over the Trinity type structures (Nicolas 1986b). The model of diapiric centres along the ridge axis is exemplified in the Oman ophiolite (Ceuleneer and Nicolas 1985, Ceuleneer et al. 1988, Nicolas 1989). Diapirs and related forced flow may cause shear sense reversals within a given mantle section, as observed in ophiolites (Ceuleneer et al. 1988). The Oman ophiolite demonstrates the transition between the diapiric flow pattern and the return flow pattern (Ceuleneer et al. 1988) as predicted in the plate thickening model. Abundant evidence exists for along-axis mantle flow in ophiolites (Nicolas and Violette 1982, Ceuleneer et al. 1988). Segmentation similar to the mid-ocean ridge system is debated for the Oman ophiolite (Nicolas et al. 1988a, Juteau et al. 1988a,b). Omission of major parts of the plutonic sequence due to slow spreading and rapid cooling appears to be realized in the Xigaze ophiolite (Nicolas et al. 1981, Girardeau et al. 1985). Numerous ophiolites representing fracture zones have been identified (Karson and Dewey 1978, Prinzhofer and Nicolas 1980, Reuber 1984, Murton 1986, Miller and Mogk 1987, Nicolas et al. 1988a).

Studies in ophiolites support three ways of melt migration: by dykes (Nicolas and Jackson 1982, Nicolas 1986a), as diapirs (Nicolas and Violette 1982, Ceuleneer and Nicolas 1985, Ceuleneer et al. 1988), and - possibly restricted to the ophiolitic transition zone - by porous flow (Nicolas and Prinzhofer 1983, Nicolas 1986b).

The fact that ophiolites are preserved in orogenic belts within the continental crust implies that they must have undergone detachment from their oceanic environment. The exact time of detachment is particularly important for ophiolites evolving according to the plate thickening model. Detachment near the ridge locks in the diapiric structures or those with flow parallel to the ridge, whereas later detachment will sample lithosphere with classic return flow structures. These constraints do not apply to the slow spreading ophiolites (dyke intrusion model) as their mantle structures are frozen in at the ridge anyway. This is exemplified by the Trinity ophiolite which preserves a vertical mantle structure, though it was detached 100 my after its formation (le Sueur and Boudier 1986). For the case of the plate thickening model, the Oman ophiolite with its preserved diapiric structures represents the type lithosphere for the early detachment scenario (Boudier et al. 1982, 1988). The Table Mountain massif within the Bay of Islands Ophiolite indicates return flow conditions (Nicolas and Violette 1982) and possibly somewhat later detachment.

1.1.3 Some petrological implications of mantle flow

Within the upwelling region of oceanic environments, mantle rocks will record a continuous decompression history. The temperature history of the peridotites is, however, more complex. For slow ascent rates, the upwelling mantle peridotites are affected by the regional temperature distribution and conductive cooling plays an important role in their thermal history. For high ascent rates, the mantle material will approach adiabatic conditions, i.e. cool only by expansion, but otherwise retain its heat

and temperature due to the relative inefficiency of conductive cooling. As the solidus of dry peridotite drops significantly with decreasing pressure, a fast ascent of mantle peridotite will lead to massive partial melting, the products of which are seen in the oceanic crust (e.g. McKenzie 1984).

The ascent rate of mantle material is proportional to the spreading rate (Nicolas 1986b) though the proportionality factor is debated (Scott and Stevenson 1989). Nicolas (1986b) suggests that for spreading rates > 1cm/y, adiabatic conditions are achieved, melting proceeds to the stage where a harzburgitic residue is left behind, and return flow conditions are initiated. In addition, thick oceanic crust is formed (Reid and Jackson 1981, McKenzie 1984). Slower spreading (and ascent) rates produce only a lherzolitic residue (Boudier and Nicolas 1985). These simplistic rules may be overridden by local factors occurring, for example, within diapirs, near transform faults, at the tip of propagating rifts or by melt impregnation within the mantle.

Very low extension rates are coupled with low ascent rates and will lead to the emplacement of mildly or undepleted upper mantle at variable levels within the lithosphere (Nicolas 1986b). Such weakly extensional environments only rarely lead to full oceanic conditions and the peridotites may freeze within the continental crust as shown by granulitic contacts in the case of some alpine spinel- and plagioclase-lherzolite massifs (Kornprobst 1969, Obata 1980, Kornprobst and Vielzeuf 1984, Nicolas 1986a, 1989). Alternatively, some of the lherzolitic peridotites were formed not by vertical ascent, but along shallow dipping, extensional shear zones (Lemoine et al. 1987, Drury et al. 1990).

Finally, the melt migration mechanism will have a pronounced influence on the state of equilibration of the upper mantle. As the phase relationships of basaltic melts are subject to continuous change with varying PT conditions, melts formed at depth will

have the potential to react with peridotite at lower pressures (e.g. Kelemen 1990). The degree of equilibrium reached will be highest for porous flow and lowest for melt migration within wide dykes.

1.2 PURPOSE OF STUDY

The review of the preceding sections demonstrates the dynamic nature of the upper mantle below oceanic spreading centres and the suitability of ophiolites as analogues to the oceanic lithosphere - asthenosphere system. This thesis investigates the 6 km thick upper mantle section of the Table Mountain Massif in the Bay of Islands Ophiolite. The Table Mountain mantle section has previously been assigned to formation during mantle return flow (Girardeau and Nicolas 1981). It thus offers an ideal location to study the evolution of mantle return flow and the structural and magmatic processes associated with it.

1.3 GEOLOGICAL FRAMEWORK

1.3.1 Tectonic evolution of Newfoundland

Newfoundland is part of the Appalachian-Caledonian orogenic belt which is marked by numerous ophiolite occurrences (Fig. 1.1.; Williams 1984). The orogen formed by opening and closure of the Proto-Atlantic ocean (Iapetus) during the lower Paleozoic (Wilson 1966). Ophiolites preserved in central and western Newfoundland are interpreted as vestiges of the Iapetus or related marginal basins (Stevens 1970, Dewey and Bird 1971).

Newfoundland is conveniently divided into 4 zones (Fig. 1.2; Williams 1979). From east to west the zones are called Avalon, Gander, Dunnage, and Humber. Gander and Dunnage Zone have also been combined into the Central Mobile Belt (Williams 1964, van der Pluijm and van Staal 1988). The Humber Zone represents the autochtho-

Fig. 1.1. General areas of Paleozoic ophiolite occurrences in the Caledonian-Appalachian orogen (from Williams 1984).

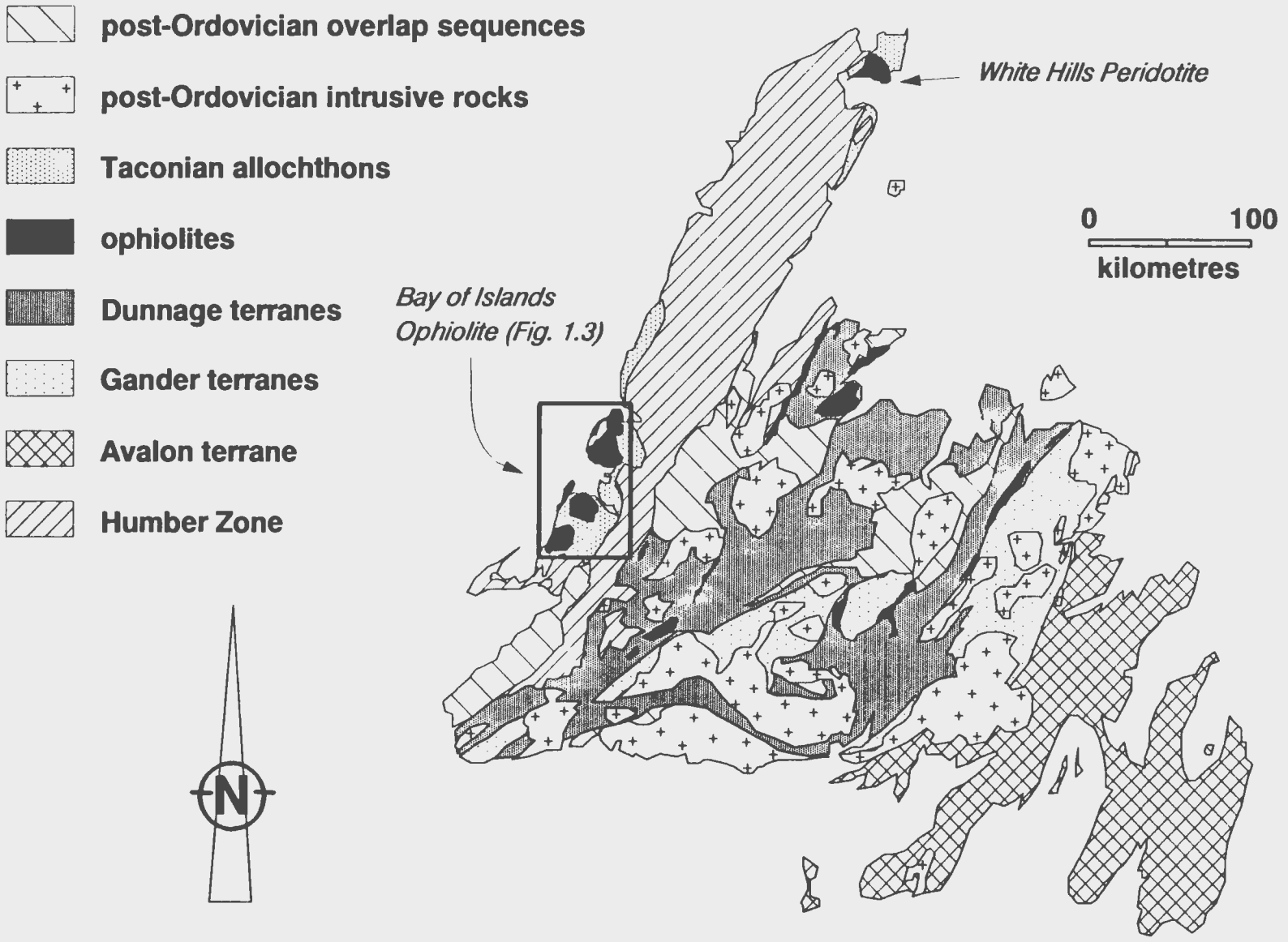

Fig. 1.2. Tectonic framework of Newfoundland (after Colman-Sadd et al. 1990) including ophiolitic occurrences (from Dunning and Chorlton 1985).

nous western continental margin of the Iapetus. The other three zones are considered suspect terranes (Williams and Hatcher 1983). The Dunnage and Gander terranes have been divided into subterranes (Williams et al. 1988).

Overlying the Humber Zone are the Humber Arm and Hare Bay Allochthons. The allochthons can be divided into numerous thrust sheets (Williams 1975). The Bay of Islands Complex (BOIC) represents the highest thrust sheet within the Humber Arm Allochthon. The White Hills Peridotite occurs in a similar tectonic setting in the Hare Bay Allochthon. Together, the BOIC and the White Hills Peridotite are referred to as "western Newfoundland ophiolites". The most likely root-zone for the western Newfoundland ophiolites is the Dunnage terrane. The Dunnage contains numerous ophiolitic occurrences ("central Newfoundland ophiolites") as well as arc-related assemblages (e.g. Williams 1979). It represents an oceanic tract which, according to recent seismic evidence, is entirely allochthonous (Keen et al. 1986, Marillier et al. 1989).

Closure of the Iapetus appears to have taken place during the Taconian orogeny in the early middle Ordovician (Williams 1979), though arguments for a later date exist (van der Pluijm and van Staal 1988, van der Pluijm et al. 1990). During the Taconian event, the Bay of Islands ophiolite was thrust out of the collision zone and emplaced onto the western continental margin. The central Newfoundland ophiolites remained, however, trapped within the collision zone. In addition, they were later affected by the Acadian phase of deformation and are consequently more dismembered than the western Newfoundland ophiolites.

A key element in nearly all plate tectonic models for the Newfoundland Appalachians is an eastward dipping subduction zone between the Humber and Dunnage zones along which an ocean basin was closed during Taconian times (e.g. Williams 1979). Closure coincided with cessation of the early arc magmatism and ophiolite obduction

(Strong 1977). Pre-Taconian, westward dipping subduction zones have also been suggested (Dewey and Bird 1971, Williams 1975, 1979, van der Pluijm et al. 1990). The post-Taconian history of the island is not agreed upon. Two puzzling features are post-Taconian "late arc magmatism" in the Dunnage zone (Strong 1977, Whalen 1989) and the Acadian deformation in the lower Devonian. Some of the more recent models for the post-Taconian history suggest (i) continued eastward subduction of continental mantle after delamination from continental crust (Colman-Sadd 1982, Stockmal et al. 1987); (ii) westward subduction under a Dunnage marginal basin (van der Pluijm and van Staal 1988, van der Pluijm et al. 1990); or (iii) terrane convergence and accretion (Williams et al. 1988).

1.3.2 The Bay of Islands Ophiolite: nomenclature

Within the Humber Arm Allochthon, thrust sheets with igneous and metamorphic rocks overlie thrust stacks of sedimentary rocks (Church and Stevens 1971, Williams 1973). The thrusted sedimentary rocks are collectively referred to as Humber Arm Supergroup and represent pieces of continental margin sequences of Cambrian to Ordovician age. Together with synchronous platformal sediments of the Humber Zone, they record a rift-drift-collapse sequence of the western continental margin of the Iapetus (Williams and Hiscott 1987).

The nomenclature of the igneous and metamorphic assemblages has been subject to several changes (Fig. 1.3). In the original classification, Williams (1973, 1975) distinguished the following slice assemblages: (i) the Skinner Cove Formation, consisting of undeformed alkali basalts with minor sediments. It occurs in scattered exposures along the coast line between Bonne Bay and the Lewis Hills. (ii) The Old Man Cove Formation, characterized by polydeformed greenschists. It is located in thrust slices above the Skinner Cove volcanics. (iii) The Little Port Complex (LPC), which includes

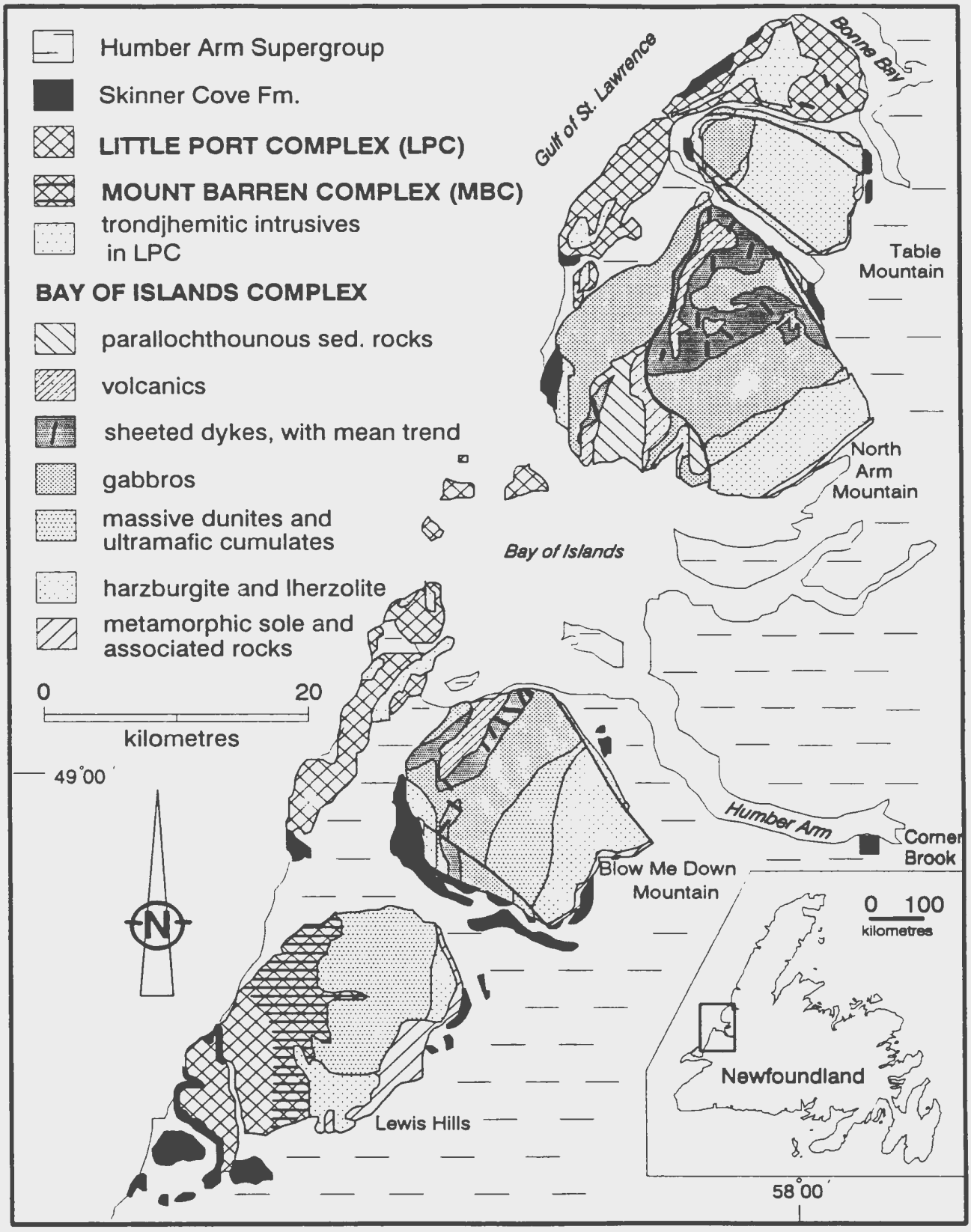

Fig. 1.3. Geologic map of the Bay of Islands Ophiolite. After Williams and Cawood (1989), with minor modifications from Girardeau (1979), Karson (1979), and this work.

amphibolites, gabbros, sheeted dykes and altered lavas, intruded by ultramafic intrusions and large trondjhemite bodies, all cut by later undeformed dykes and overlain unconformably by mafic pillow lavas in the area south of Bonne Bay (Williams 1973, 1975, Karson and Dewey 1978, Karson 1984). The LPC occurs as a belt of NNE-SSW trending, coastal hills to the north of the Lewis Hills (LH) and south of Bonne Bay and structurally overlies the Old Man Cove Formation (Williams 1973 and 1975). The formation of the LPC was related to the development of an island arc (Malpas et al. 1973 and 1979b, Williams 1975, Searle and Stevens 1984, Jenner et al., in press) or to a fracture zone (Karson and Dewey 1978, Karson 1984). (iv) The Bay of Islands Ophiolite. It represents a classical ophiolite. It is exposed in four massifs, which are from north to south Table Mountain (TM), North Arm Mountain (NAM), Blow Me Down Mountain (BMD), and Lewis Hills (LH). Only the two central massifs contain all units of a complete ophiolite succession. The higher units (sheeted dykes and lavas) have been eroded from the TM and the LH massifs.

Karson and Dewey (1978) and Karson (1984) combined the Skinner Cove Formation, Old Man Cove Formation, the LPC and the western LH into the Coastal Complex (CC). They interpreted the CC as a transform fault assemblage and its western extension. The deepest level of the transform fault assemblage is exposed in the western LH. The Bay of Islands Ophiolite, excluding the western LH, was renamed Bay of Islands Complex (BOIC). The BOIC accreted against the CC within the non-transform setting of a fracture zone (Karson and Dewey 1978). Within the LH, the boundary between the CC and the BOIC is preserved as a 3-5 km wide zone (Mount Barren Assemblage) which was assigned to the CC (Karson and Dewey 1978). Later, the term Mount Barren Assemblage was abandoned (Karson 1984, Casey et al. 1985) and the Skinner Cove Formation was considered again a separate thrust sheet representing a seamount clipped during subduction and accreted to the sole of the BOIC (Casey et al.

1985). In a recent compilation, Williams and Cawood (1989) adapted the concept that the LPC extends further to the south into the western LH and reintroduced the Mount Barren Assemblage (now called Mount Barren Complex). They retained the Old Man Cove Formation as a separate thrust slice.

In this thesis, the terms CC and BOIC are used, following the definition of Casey et al. (1985). Whether the CC includes or excludes the Old Man Cove Formation is of no relevance to the thesis. CC and BOIC together are referred to as Bay of Islands Ophiolite (BOIO). The term LPC is used in the definition of Williams (1973, 1975) and Jenner et al. (in press) and excludes the western LH.

1.3.3 The Bay of Islands Ophiolite: previous work

Following the early investigations of Snelgrove et al. (1934), Ingerson (1935), Cooper (1936), and Buddington and Hess (1937), the first comprehensive map of the BOIC was published by Smith (1958). He considered the complex to be a layered intrusion with crystal mush features dominating in the ultramafic part. The allochthonous nature of the BOIC within the Humber Arm Allochthon was first suggested by Stevens (1970). A few years after the introduction of the plate tectonic concept, the Bay of Islands "igneous intrusion" was reinterpreted as an ophiolite and ancient oceanic lithosphere (Stevens 1970, Dewey and Bird 1971, Church and Stevens 1971). Remapping of the BOIO (Williams 1973) was accompanied and followed by detailed petrological work (Irving and Findlay, 1972, Malpas 1976, 1978, Malpas and Strong 1975, Riccio 1976, Church and Riccio 1977). As a result, the residual nature of harzburgites, and the cumulate nature of dunites, layered ultramafic rocks and gabbros was confirmed.

Structural investigation of the mantle tectonites revealed a flow pattern related to mantle return flow and the discovery of shear sense reversals in the mantle section (Gi-

rardeau 1979, Girardeau and Nicolas 1981). The reversals were later explained in a numerical simulation of mantle flow beneath mid-ocean ridges (Rabinowicz et al. 1984).

Detailed work within the massive dunites and overlying layered ultramafic rocks demonstrated their highly deformed nature (Karson 1975, 1977, Berger et al. 1975, Salisbury and Christensen 1978, Thayer 1980, Girardeau and Nicolas 1981, Casey et al. 198.. Moll 1981, Calon 1984, Neyens 1986, Dunsworth et al. 1986). The geological investigation of the LH led to the fracture zone model (Karson 1977, 1984, Karson and Dewey 1978, Karson and Elthon 1987). Mapping of arcuate arrangements of igneous layering in NAM and the LH resulted in a magma chamber model for the BOIC (Casey and Karson 1981). Petrological arguments put forward by Elthon resulted in a more extreme model of a magma chamber with a deep-reaching funnel (Elthon et al. 1982, Casey et al. 1983) which was, however, recently questioned (Elthon 1990). Detailed work in the cumulate section of the BOIC demonstrated the need to invoke open system fractionation involving numerous batches of new magma (Church and Riccio 1977, Elthon et al. 1982 and 1984, Komor et al. 1985a, Casey et al. 1985, Campbell and Turner 1989).

Numerous studies indicated a MORB similarity of the volcanics and sheeted dykes in the BOIC (Coish and Church 1979, Jacobsen and Wasserburg 1979, Suen et al. 1979, Casey et al. 1985). In addition to the main tholeiitic trend, Malpas (1978) found evidence for a mildly alkaline tendency. The mafic volcanics of the CC also showed a MORB affinity (Casey et al. 1985). Within the LH, a generation of diabase dykes occurs which could have formed by low pressure melting of oceanic cumulate rocks (Elthon et al. 1986).

Malpas (1979b) pointed out the difference in character between trondjhemites in the LPC and those of the BOIC. Karson (1984) favoured an origin of the LPC trondjhemites by partial melting of lower oceanic crustal rocks and/or by contamination of a fractionated magma within a spreading centre. Recent trace element and isotopic work (Jenner et al., in press) confirms the genetic difference between trondjhemite occurrences in the CC and the BOIC and suggests (i) a non-MORB nature of the large trondjhemitic intrusions in the LPC, and (ii) possibly a non-MORB nature of the BOIC trondjhemites.

The only thorough structural work in the high level ophiolitic part of the BOIC by Rosenkrantz (1980, 1983) led to the surprising result of a highly variable sheeted dyke orientation in northern North Arm Mountain. The conclusions of Rosenkrantz (op. cit.) about a N-S directed ridge orientation are in contrast to a mean trend developed in other parts of the BOIC (Williams and Malpas 1972, Salisbury and Christensen 1978, Casey et al. 1983) as well as in the northern Coastal Complex (Karson 1984).

The pre-ophiolitic concept of a contact metamorphic aureole in the BOIC (Smith 1958) was revised by Williams and Smyth (1973) and Malpas et al. (1973) in favour of a dynomothermal metamorphic sole. The metamorphic gradient within the sole ranges from granulite occuring next to the upper mantle rocks to subgrrenschist at the base. Internal heat of the ophiolite body and frictional heat generated during ophiolite detachment were considered responsible for development of the very steep thermal gradient. In later studies, Malpas (1979a) demonstrated that frictional heating alone was insufficient to explain the inferred temperatures at the contact. This conclusion was questioned by McCaig (1983) who was impressed by an apparently large difference between the age of formation and the age of obduction of the BOIC (see below). McCaig (1983) presented a model involving thrust stacking on top of the ophiolite prior to formation of the sole in order to account for unexplained high pressures and pro-

grade relations in granulites of the metamorphic sole of the BOIC. Jamieson (1986) suggested that, at least in the White Hills peridotite, the metamorphic sole represents a complex shear zone juxtaposing prograde, low grade metamorphic rocks against retrograde, high grade rocks along a shear zone of intermediate metamorphic grade.

Early age determinations from the BOIC suggested an age of formation of 504 ± 10 Ma (zircons from trondjhemites, Mattinson 1976) and 508 ± 6 and 501 ± 13 Ma (Sm-Nd age of gabbros, Jacobsen and Wasserburg 1979). The minimum age of detachment was placed at 469 ± 5 Ma (K-Ar of amphibolites, new decay constant, Dallmeyer and Williams 1975). The age for the BOIC appeared therefore close that of the CC, determined as 508 ± 5 Ma (zircon age from trondjhemite in the LPC, Mattinson 1975). The latter age has been confirmed (Jenner et al., in press). The age for the BOIC was revised, however, to 486 +2/-1 Ma (Dunning and Krogh 1985, Jenner et al., in press). Various tectonic models suggested for spreading and obduction of the BOIO are discussed in chapter 6.

1.4 ORGANIZATION OF TEXT

The organization of the thesis is as follows. Largely descriptive material is presented in chapter 2 (Field Relationships), chapter 3, and the first parts of chapter 4 (Microstructure) and chapter 5 (Geochemistry). The second half of chapters 4 and 5, and the entire chapter 6 are interpretative. Chapter 6 synthesizes most of the information into a tectonic model for the entire BOIC. Chapters 2 to 5 are preceded by a summary. Stereographic projections of structural data and geochemical data/procedures are listed in the appendices. Two detailed maps showing the structural data and a sample location map can be found in a pocket at the end of the thesis.

1.5 STRUCTURAL WORKING TECHNIQUES

The approach taken in this thesis follows closely the working techniques developed for peridotites (Nicolas et al. 1971, 1972, Nicolas and Poirier 1976, Nicolas 1989). In addition, geochemical data were collected.

In the field, stations were recorded on 1:10,000 colour aerial photographs. Each station contains structural and lithological observations, e.g. rock type, grain size, orientation and strength of the mineral defined foliation and lineation, orientation and type of lithological banding, measurements of fold axes, axial planes and fold asymmetries, dyke lithology and orientation, and boudin elongations. The mineral shape fabric is particularly important as it is closely related to the actual flow plane (Etchecopar 1977, Etchecopar and Vasseur 1987, Nicolas and Poirier 1976, Bouchez et al. 1983). When a shape fabric was not visible in the field, it could usually be retrieved by progressive cutting and bleaching of oriented specimens with dilute HCl in the laboratory (Nicolas and Poirier 1976).

The numerous structural orientations listed within chapter 2 are presented in a dip-direction/dip format for planar elements and plunge-direction/plunge format for linear elements as this is considered the most effective way of communicating orientation data. As an example, a plane striking N40°E and dipping 60° to the northwest is reported as 310/60. A linear element trending N40°E and plunging 60° to the northeast is reported as 40/60.

Microstructural studies were performed using thin sections cut perpendicular to the foliation and parallel to lineation. These sections are considered XZ-cuts*(Bouchez et al. 1983). An exact location of the foliation and lineation is important, as shear sense

---

*XYZ indicate the principal elongations of the finite strain ellipsoid with $X > Y > Z$.

determinations are based on the relation between the foliation trace and the trace of the slip plane in the thin section. The slip plane and direction was determined by olivine petrofabric analysis using a five-axis universal stage. 100 olivine grains were measured in each slide. Orientation data were manipulated using a computer program originally designed by Dr. L. Bouchez (Université de Nantes) and further developed by Dr. D. Mainprice (USTL Montpellier). The petrofabric data nearly always indicated a slip direction parallel to [100] of olivine. Consequently, the shear sense could be determined more rapidly by using the normal to the olivine tilt wall orientation as indicator of the flow plane (Nicolas et. al. 1972). The mean tilt wall orientation (extinction direction) was determined by measuring 50-80 olivine grains. For small grain sizes, a mean extinction direction for several grains was optically determined and taken to represent one measurement. Angles between the foliation and the flow plane of less than 4° were considered insignificant and the shear sense was designated as neutral. Microstructural shear sense determinations presented in section 2.8 are based both on the U-stage and the tilt-wall method.

Analytical procedures for the geochemical work are reported in Appendix B.

2 FIELD RELATIONSHIPS

2.1 SUMMARY

Within the Table Mountain massif upper mantle peridotites and plutonic crustal rocks are folded into an isoclinal synform. A 6 km thick mantle section is developed on the eastern limb of the synform. The mantle section, including massive dunites below the gabbros, has been mapped in detail.

The mantle section is subdivided into six structural units, which are numbered 1 through 6 from the top to the base of section. The units can be defined by changes in the orientation of the high temperature mineral stretching lineation across the unit boundaries.

Unit 1 consists largely of massive dunites with rare (plagioclase-) wehrlitic banding. Dunite bands cut this banding. Gabbro and coarse, layered wehrlite bodies occur within the massive dunites. Orthopyroxenite dykes are only weakly deformed. Stretching lineations plunge moderately to steeply to the westnorthwest and foliations appear sigmoidally arranged on a larger scale.

Within unit 2, lineations trend northnortheast - southsouthwest and foliations dip moderately to steeply to the northwest. A strong aggregate fabric is developed in the fine grained peridotites of the upper part of unit 2. Numerous dunite bands and clinopyroxenite dykes, as well as rare, thin plagioclasites occur in the clinopyroxene-rich harzburgites. Mesoscopic folds are restricted to a few weak flexures of the foliation. On a 100m-scale, the foliation is folded in the southern part of unit 2. The dominant shear sense is dextral. Orthopyroxenite dykes are undeformed to weakly deformed.

Changes from unit 2 to unit 3 are gradational apart from a stretching lineation plunging to the northwest in unit 3. Additional changes near the unit boundary, compared to unit 2 are as follows: (i) the shear sense reverses to sinistral; (ii) dunite bands

are less numerous, but orthopyroxene-rich banding is more abundant; (iii) clinopyroxene is rare in harzburgite; (iv) the orthopyroxene grain size increases; (v) the mineral shape fabric becomes weaker.

Within unit 3, asymmetric folds develop progressively down-section. Their asymmetry is consistent with microstructurally determined, sinistral shear. The distribution pattern of orthopyroxenite dykes suggests progressive transposition during sinistral shear from original steep attitudes perpendicular to the stretching lineation within unit 2 to near foliation-parallel orientations near the base of unit 3.

Unit 4 is defined by a northeast-trending stretching lineation and a heterogeneously distributed, mylonitic fabric within otherwise moderately deformed, clinopyroxene-poor harzburgites. The shear sense is sinistral and most if not all dykes are deformed.

The transition from unit 4 to 5 is marked by changes in most structural and lithological elements and is singled out as a transitional unit (TU). Compared to unit 4, peridotites in unit 5 are: (i) coarser grained and enriched in clinopyroxene, and (ii) their mineral shape fabric is weaker; (iii) the stretching lineation within unit 5 plunges steeply to the westnorthwest; (iv) lithological banding in unit 5 defines a large synformal structure; (v) cross-cutting dykes are virtually absent.

Peridotites of unit 6 are clinopyroxene-rich harzburgites and lherzolites. The mineral shape fabric is strong and orthopyroxene grains are coarse. Several generations of high strain zones overprint each other. No consistent attitude of the stretching lineation is present within the unit. The base of the unit, representing the contact with the metamorphic sole, is marked by a zone of one to several metres thick ultramafic ultramylonite.

The metamorphic sole is divided into two structural subtypes: (i) a thin, continuous belt exposing mainly amphibolites, and (ii) a more "bulky", discontinuous thrust belt consisting of slices of amphibolites, greenschist, and mantle peridotites juxtaposed internally along discrete faults.

2.2 INTRODUCTION

Upper mantle peridotites are exposed in all four massifs of the BOIC. Regional mapping was restricted to the upper mantle section in the Table Mountain massif which is the most accessible massif and preserves the thickest, continuous mantle section in the BOIO. Above upper mantle harzburgites and lherzolites, massive dunites are exposed in TM. Within ophiolites, the dunites are variably assigned to the residual mantle (Sinton 1977, Arai 1980, Nicolas and Prinzhofer 1983, Benn et al. 1988) or to the cumulate section (e.g. Malpas 1978, George 1978, Casey et al. 1981, Lippard et al. 1986). Because of their disputed nature, the massive dunites were included in the field work. Mapping was, however, not extended into the basal layered cumulate sequence, as their field relationships have been recently reported by Girardeau (1979), Girardeau and Nicolas (1981), and Neyens (1986). Where appropriate, data of these authors are taken into consideration.

Field data are presented in three fold-out maps in the back of the thesis: Map I - foliations and lithological banding; Map II - lineations; and Map III - station locations and sample numbers. Summary maps for the different lithologies (Fig. 2.1), mineral stretching lineations (Fig. 2.2), foliations and lithological banding (Fig. 2.3), and microstructurally determined shear senses (Fig. 2.4) are given within the text of this section. They also contain data for the lower crustal section, compiled from Girardeau and Nicolas (1981) for foliations and lineations and from Neyens (1986) for the litholo-

Fig. 2.1 (facing page). Map showing lithological elements in the Table Mountain Massif. Distribution of ultramafic cumulates after Neyens (1986).

LEGEND

———	high angle fault
—▲—▲—▲—▲—	(in coloured areas): low angle fault
—▲—▲—▲—▲—	(in white areas): low angle fault at the base of the Skinner Cove volcanics (from Quinn 1985, Williams and Cawood 1989);
—^—^—^—^—	ductile contact between the metamorphic sole and upper mantle peridotite.
~ ~ ~	zone of relative later, spreading-related high strain,
⌐— ⌐— ⌐—	zone of relative later, detachment-related high strain
. . . . .	structural unit boundary (for units see Fig. 2.2)

The following symbols are used only in areas with dunite, harzburgite and lherzolite

○	plagioclasite vein
+	wehrlitic peridotite
+	plagioclase wehrlite
▲	chromite seam
*	coarse orthopyroxene grains in harzburgite.

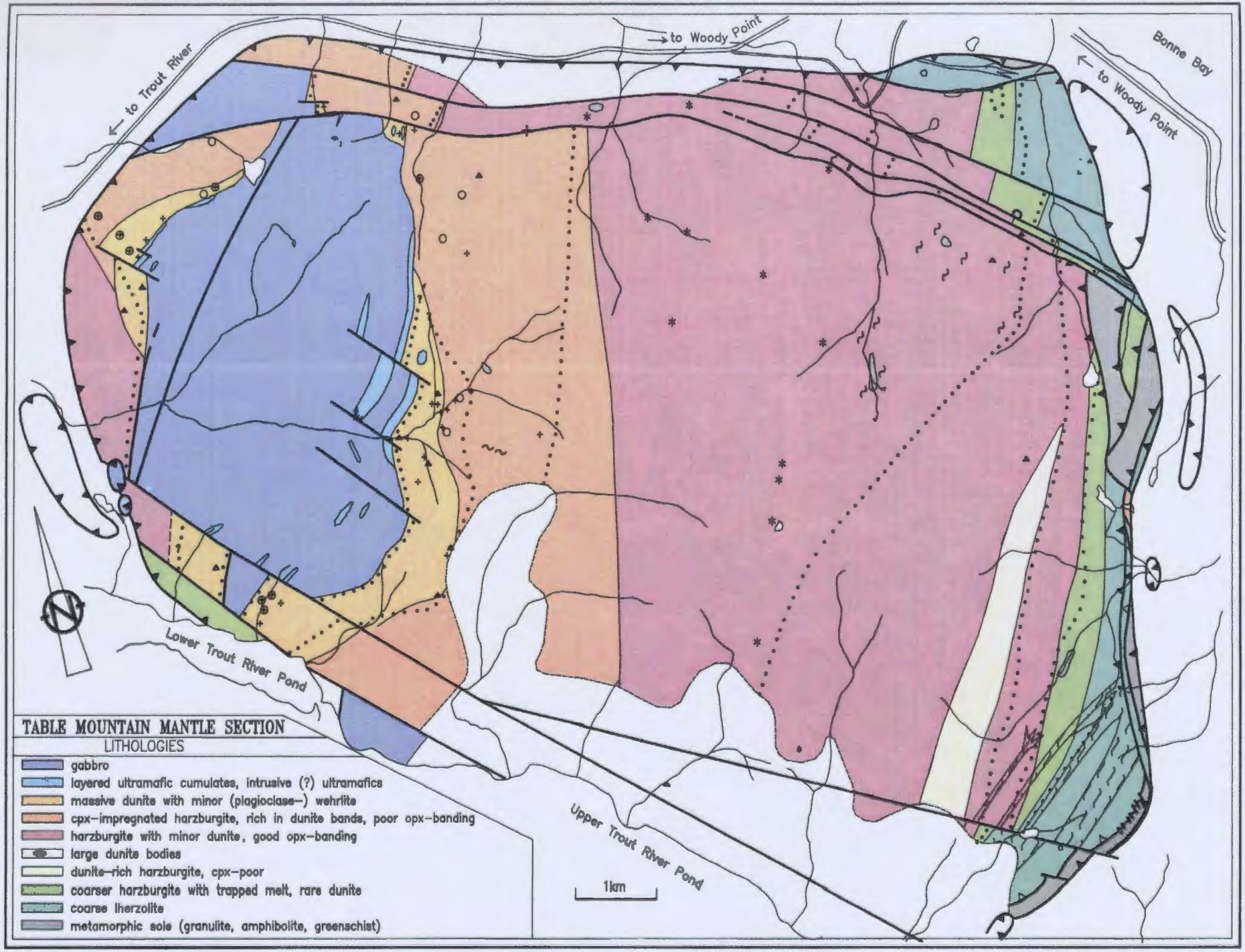
to Trout River
to Woody Point
to Woody Point
Bonne Bay
Lower Trout River Pond
Upper Trout River Pond
1km
TABLE MOUNTAIN MANTLE SECTION
LITHOLOGIES
gabbro
layered ultramafic cumulates, intrusive (?) ultramafics
massive dunite with minor (plagioclase–) wehrlite
cpx–impregnated harzburgite, rich in dunite bands, poor opx–banding
harzburgite with minor dunite, good opx–banding
large dunite bodies
dunite–rich harzburgite, cpx–poor
coarser harzburgite with trapped melt, rare dunite
coarse lherzolite
metamorphic sole (granulite, amphibolite, greenschist)

Fig. 2.2 (facing page). Map showing stretching lineations and structural unit boundaries in the Table Mountain Massif. Data for gabbros and ultramafic cumulates after Girardeau (1979). TU - transition unit; SC - Skinner Cove Formation; MS - metamorphic sole and related lithologies. For legend see Fig. 2.1

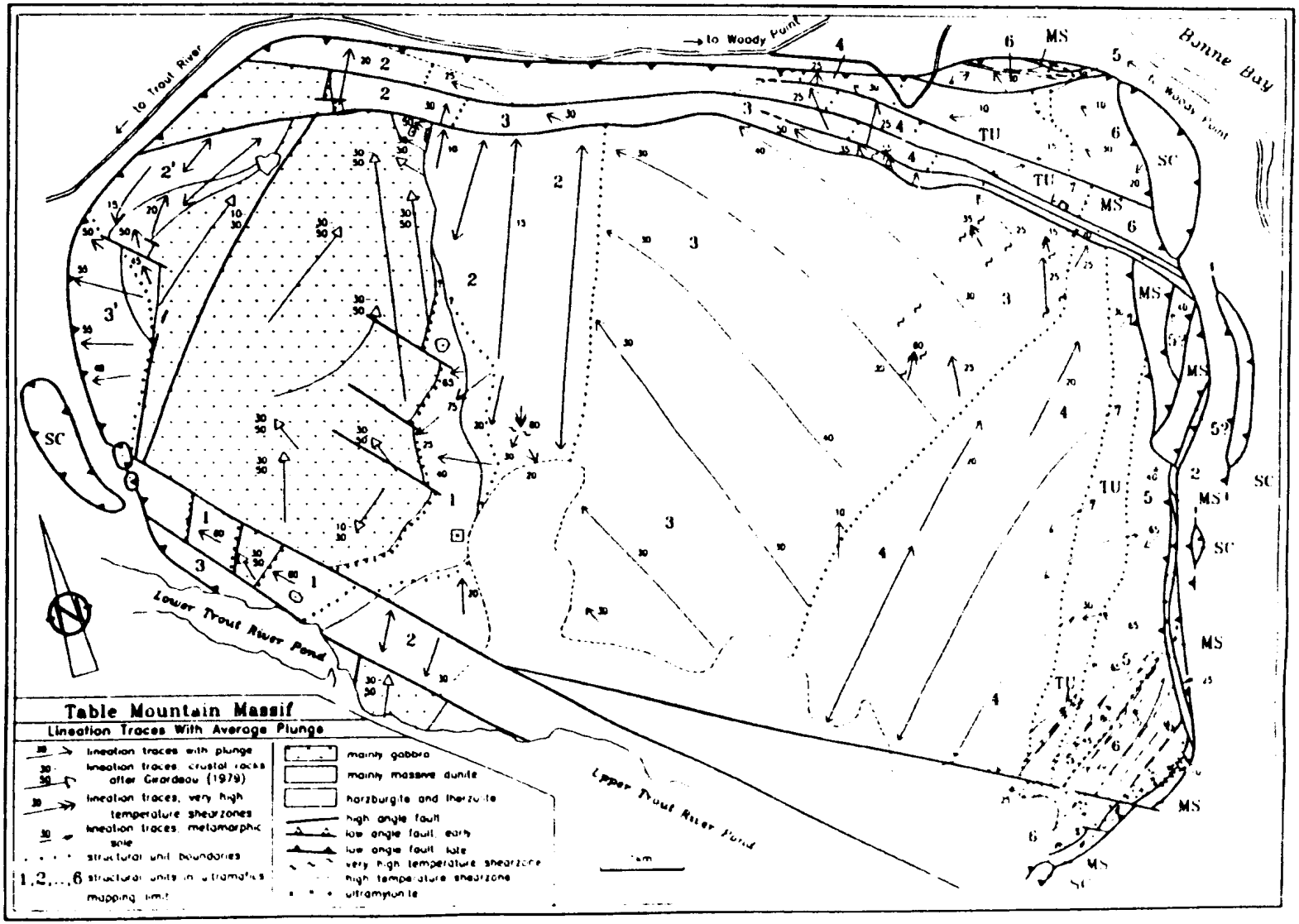
to Trout River
to Woody Point
Bonne Bay
Lower Trout River Pond
Upper Trout River Pond
Table Mountain Massif
Lineation Traces With Average Plunge
lineation traces with plunge
lineation traces, crustal rocks after Geardeau (1979)
lineation traces, very high temperature shearzones
lineation traces, metamorphic sole
structural unit boundaries
1,2,...6 structural units in ultramafics
mapping limit
mainly gabbro
mainly massive dunite
harzburgite and lherzolite
high angle fault
low angle fault, early
low angle fault, late
very high temperature shearzone
high temperature shearzone
ultramylonite
1km

Fig. 2.3 (facing page). Map showing foliations and lithological banding within the Table Mountain Massif. Data for gabbros and ultramafic cumulates after Girardeau (1979). For legend see Fig. 2.1

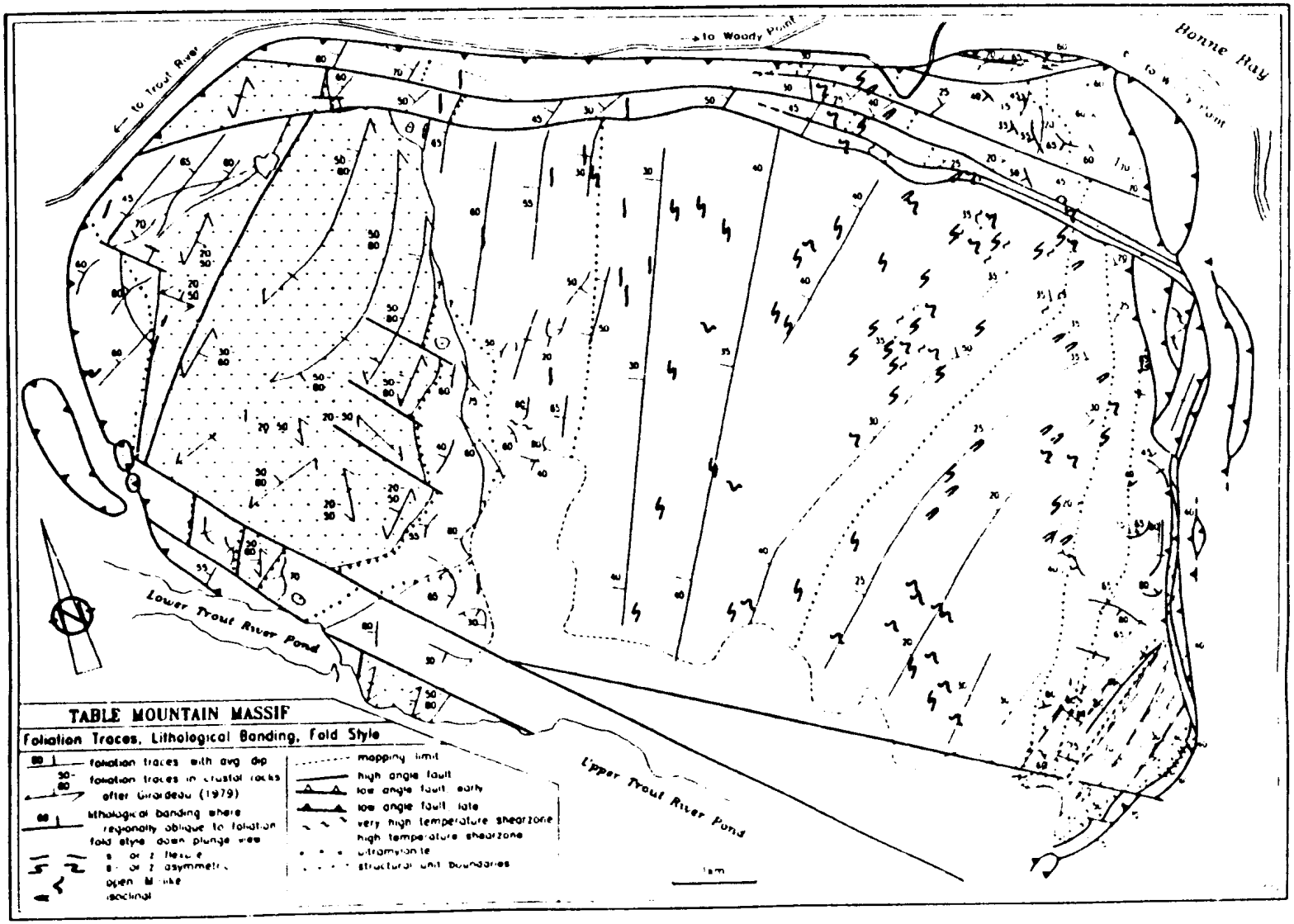
← to Trout River
→ to Woody Point
Bonne Bay
Lower Trout River Pond
Upper Trout River Pond
TABLE MOUNTAIN MASSIF
Foliation Traces, Lithological Banding, Fold Style
foliation traces with avg dip
foliation traces in crustal rocks after Girardeau (1979)
lithological banding where regionally oblique to foliation
fold style down plunge view
S or Z flexure
S or Z asymmetric
open M like
isoclinal
mapping limit
high angle fault
low angle fault, early
low angle fault, late
very high temperature shearzone
high temperature shearzone
ultramafic lens
structural unit boundaries
1km

Fig. 2.4 (facing page). Map showing microstructurally determined shear senses (including those determined with petrofabric data) in the Table Mountain Massif. For legend see Fig. 2.1

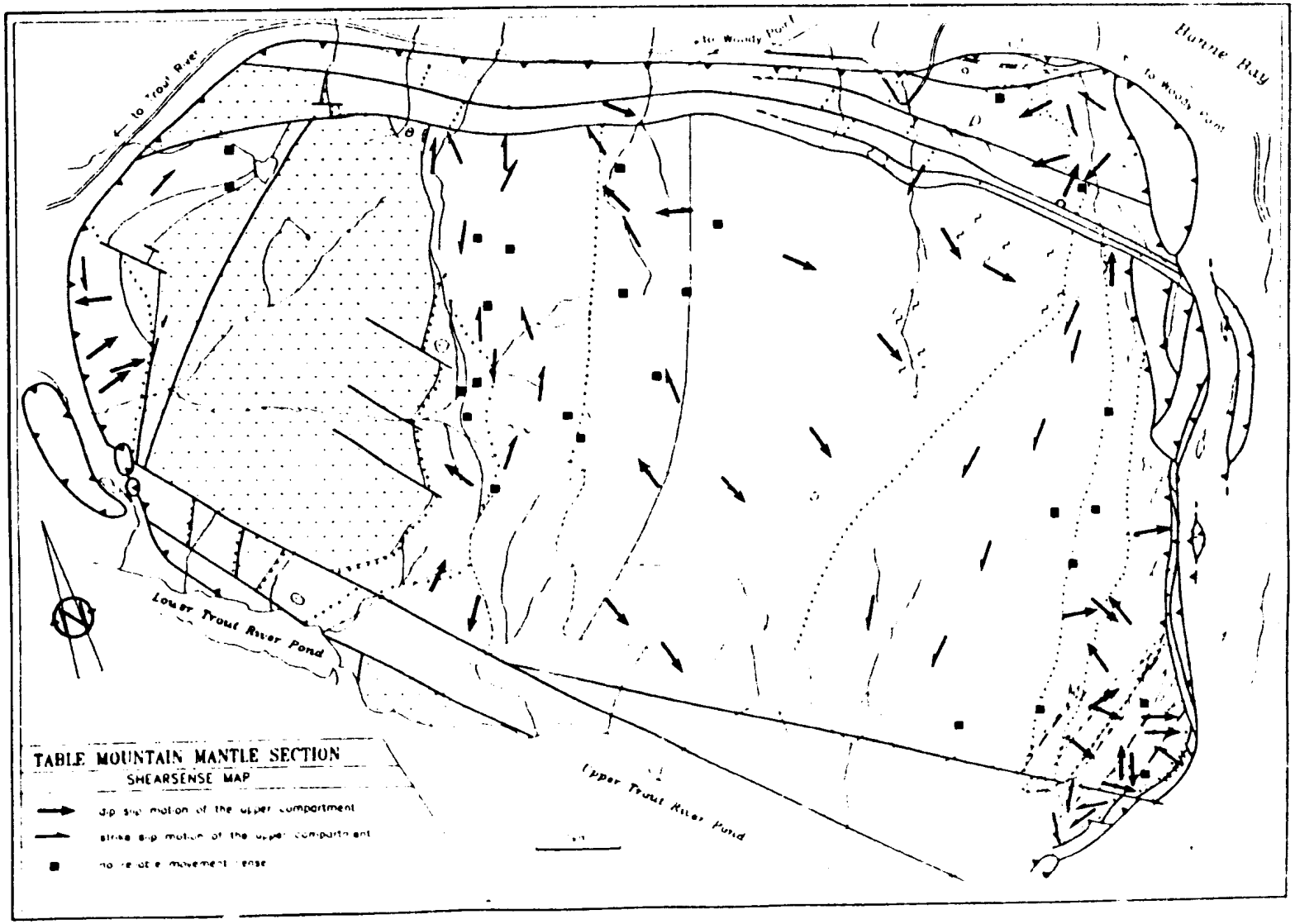
← to Trout River
Lower Trout River Pond
Upper Trout River Pond
Bonne Bay
TABLE MOUNTAIN MANTLE SECTION
SHEARSENSE MAP

gies. Stereographic representations of structural elements for each structural unit are shown in Appendix A (Figs. A2.1-A2.17). The stereographic representations also contain isolated data, e.g. two fold axis measurements within a structural unit. The isolated measurements will not be referred to in the text as they are considered statistically insignificant.

Of particular importance is the lineation map (Map II and Fig. 2.2). It shows that six areas can be distinguished in the peridotites, each separated from the other by a different orientation of the mineral stretching lineation. These six areas are considered to be separate structural units. Starting from the top of the section studied and going down-section, they are numbered 1 through 6 (including one transitional unit, TU, between units 4 and 5). For reference, the structural unit boundaries are also shown on the lithology-, foliation-, and shear sense-maps. All units are defined on the extensive eastern side of the TM masssif. Structures on the western side which correspond to units 2 and 3 on the eastern side are referred to as unit 2' and unit 3'.

The descriptions of the detailed field relationships (sections 2.4.3 to 2.9) report the variation of each structural element or group of elements (e.g. "folds") within the mantle section including the massive dunites. In the description, the division into structural units is used for geographical reference. The term "down-section" will frequently be used. It refers to a direction pointing from the gabbros into the harzburgites to the metamorphic sole. "Up-section" indicates the reverse direction.

2.3 LARGE SCALE FAULTING AND FOLDING

2.3.1 Late faulting

Like the three other massifs of the BOIC, the TM massif represents a gravitational slide and as such is bounded by a shallow detachment fault (Williams 1971 and

1973, Cawood and Williams 1988, Williams and Cawood 1989) which is usually developed as mélange (Williams 1971, Williams and Smyth 1973). Where exposed in the TM massif, the contact of the ophiolite with the country rocks is, however, steep. This is seen in the well-known exposure in the Winterhouse Brook section (Smith 1958, Mercier 1977), as well as in the Shoal Brook section. Other small outcrops along the northern, eastern and southern side of the massif expose shales and sandstones, which are part of the Blow Me Down Brook Formation (Quinn 1985). With the exception of the NAM massif, the shallow detachment model is confirmed by gravity data (Weaver 1967).

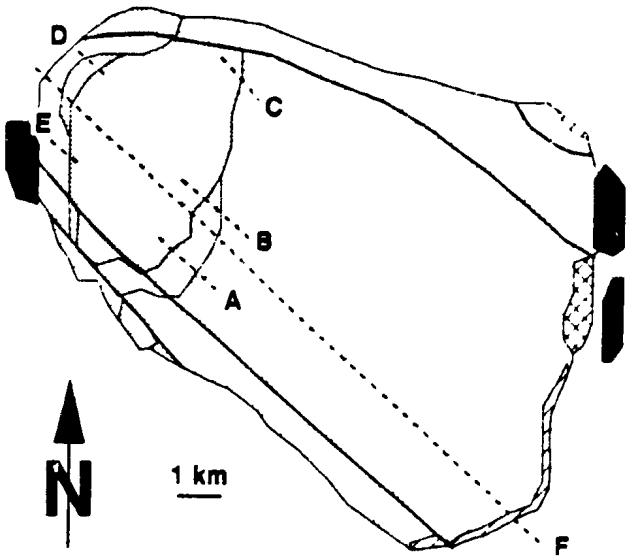

Fig. 2.5. Location of columnar sections through transition zone (A-E, Fig. 2.8) and cross-section (F, Fig. 2.6) in TM massif. For legend see Fig. 1.3.

The northwest-southeast trending, sinistral offset pattern between the four massifs (Fig. 1.3) is duplicated in several, previously unrecognized, apparently sinistral, cross faults along the northern margin of TM. The concentrations of cross faults near the

northern and southern margins of the massif suggests that they are related to the break up of the BOIC into separate massifs. This might have occurred during the final gravitational sliding of the BOIC into its current location.

Deviating from previous studies (Smith 1958, Girardeau 1979, Neyens 1986), gabbroic lithologies within the two fault slivers along the southern margin of the massif are not interpreted as slumps. They are considered as an integral part of the late fault slivers and thus represent the gabbroic core of the TM synform (see 2.3.2). Faulting near the eastern edge of the massif appears to be related to the later history of oceanic detachment of the BOIC (Suhr and Cawood, submitted).

2.3.2 Large scale folding

Regional mapping in the three northern massifs of the BOIC suggests that all three massifs are folded into synforms about a northnorthwest - southsoutheast trending, subhorizontal axis (Williams 1973, Casey and Kidd 1981). Profiles shown in Karson (1979) also indicate folding of the eastern part of the LH massif. Folding of the massifs has not affected the Humber Arm Supergroup and thus must predate the gravitational sliding (Williams 1973, Williams and Cawood 1989).

The synformal nature of the BMD massif has later been questioned (Casey et al. 1979, Salisbury and Christensen 1979). For the TM massif, two models differing from the synform model were suggested. Girardeau and Nicolas (1981) apparently favoured a simple westward tilting of the entire massif, whereas Moll (1981) proposed the presence of a shallow detachment horizon near the geographic top of the TM massif. In her model, a thin mafic section is juxtaposed against the underlying upper mantle sequence along the flat fault.

As the eastern and western harzburgite-dunite transitions are gradational, they are considered primary and unfaulted. Only the presence of a synform can explain the symmetrical arrangement of the sequence harzburgite-dunite to the east and west of the central gabbros in TM. Structural data from within the gabbros of TM are, however, not clearly related to the core of a synform (Fig. 2.3). It is suggested that large parts of the hinge have been suppressed by thrusting of the western limb over the core of the synform (Fig. 2.6). Manipulation of the structural data of the peridotite units 2/2' and 3/3' from both sides of the synform demonstrate that the data can be brought into approximate coincidence if folding has been isoclinal (180° rotation) and occurred about an axis trending N40°E (Fig. 2.7). The isoclinal nature of the synform at TM contrasts with more open folding of the two massifs to the south (e.g. Williams and Cawood 1989).

All major interpretations developed in this study (chap. 6) are based only on the analysis of the extensive and internally unfaulted eastern limb. All stereographic data, including those from the western limb (Figs. A2.3, A2.4) are presented in field orientations, i.e. unrotated.

2.4 LITHOLOGY

2.4.1 Introduction and definition of terms

Four major lithological units can be defined within the TM massif (Fig. 2.1): (i) gabbroic rocks in the core of the synform; (ii) pyroxenites, wehrlites, troctolites and dunites of the "transition zone" (term defined below); (iii) harzburgites and lherzolites of the mantle section; (iv) granulites, amphibolites, and greenschists of the metamorphic sole and associated rock units. Within this study, the emphasis is put on the

formation and deformation of the harzburgites and lherzolites.

Characteristic for the peridotites of the residual mantle is a *lithological banding*, frequently called layering. The term banding is preferred in this study. It describes the modal variation between different phases and superficially resembles the igneous layering of layered intrusions. It lacks, however, any graded bedding and cryptic mineral chemistry variation present in layered intrusions. The modal variation involves mostly olivine and orthopyroxene (opx), but may involve clinopyroxene (cpx) and spinel. The mineral defined foliation is typically to the banding, except in areas of folding where an axial planar fabric may be developed. The origin of the banding has fascinated nearly all workers of alpine peridotites and ophiolites (e.g. Dick and Sinton 1979, Nicolas and Jackson 1982). No single mechanism for the formation of the banding is agreed upon. The term is used here in an entirely descriptive sense.

The petrological Moho (Malpas 1973, George 1978) is located between residual and purely magmatic rocks. While the term is extremely useful, the location of the Moho is practically very difficult to delineate. This has been recognized by Sinton (1977), who used the term *transition zone* for rocks of a mixed residual/magmatic character. Later, Nicolas and Prinzhofer (1983) recognized the universal presence of transition zone rocks in ophiolites.

Typical for the mantle section are cross-cutting dyke lithologies. While the dyke nature of pyroxenites is largely undisputed, the suggestion has been made that dyke-like dunites parallel and oblique to the banding represent the altered wall rocks to magma conduits (Boudier and Nicolas 1972, 1977, Dick 1977b, Kelemen 1990). In this replacement model for dunite formation, all magma has been extracted during closure

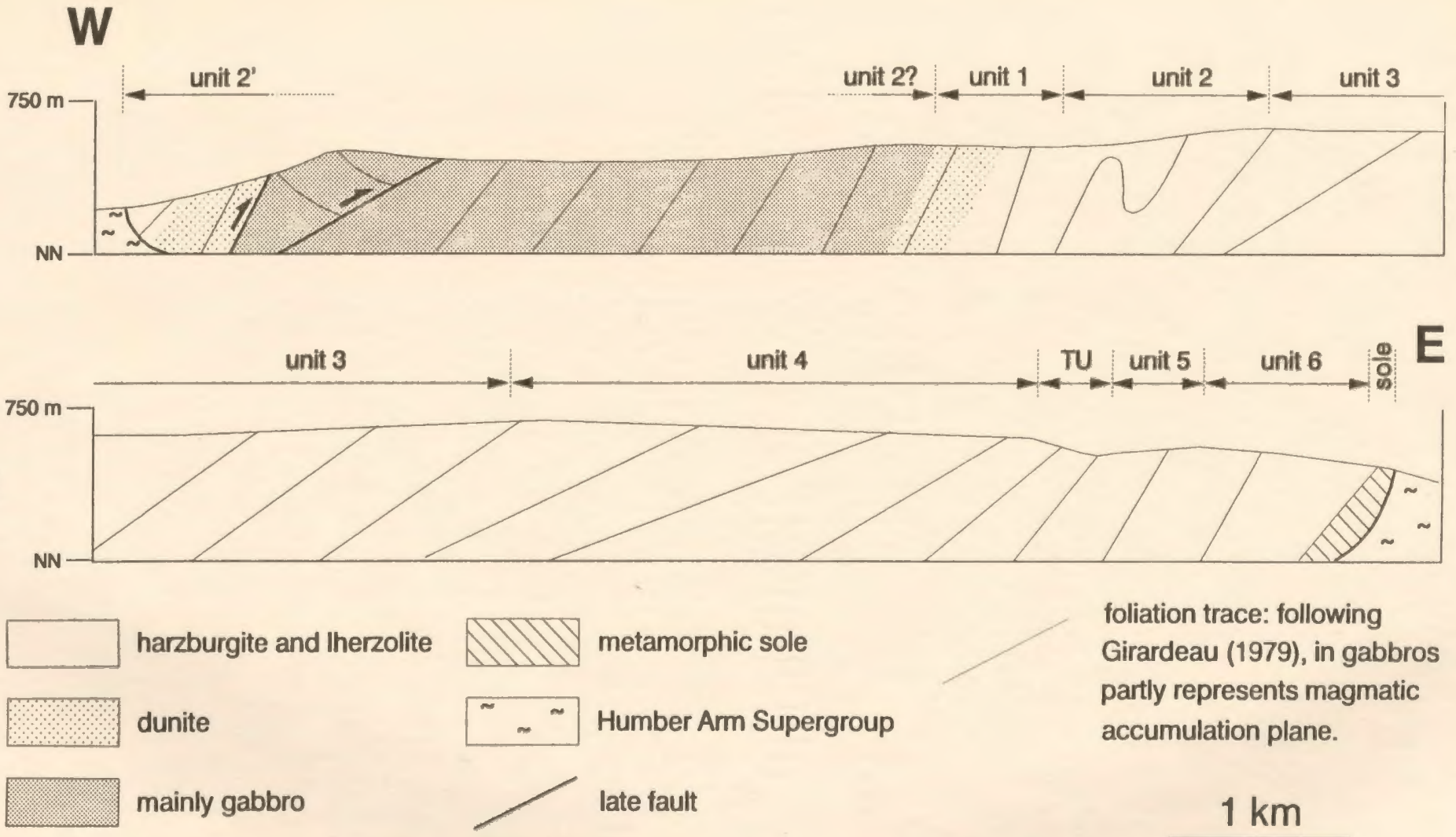

Fig. 2.6. Cross-section through Table Mountain Massif. For location see section 'F' in Fig. 2.5.

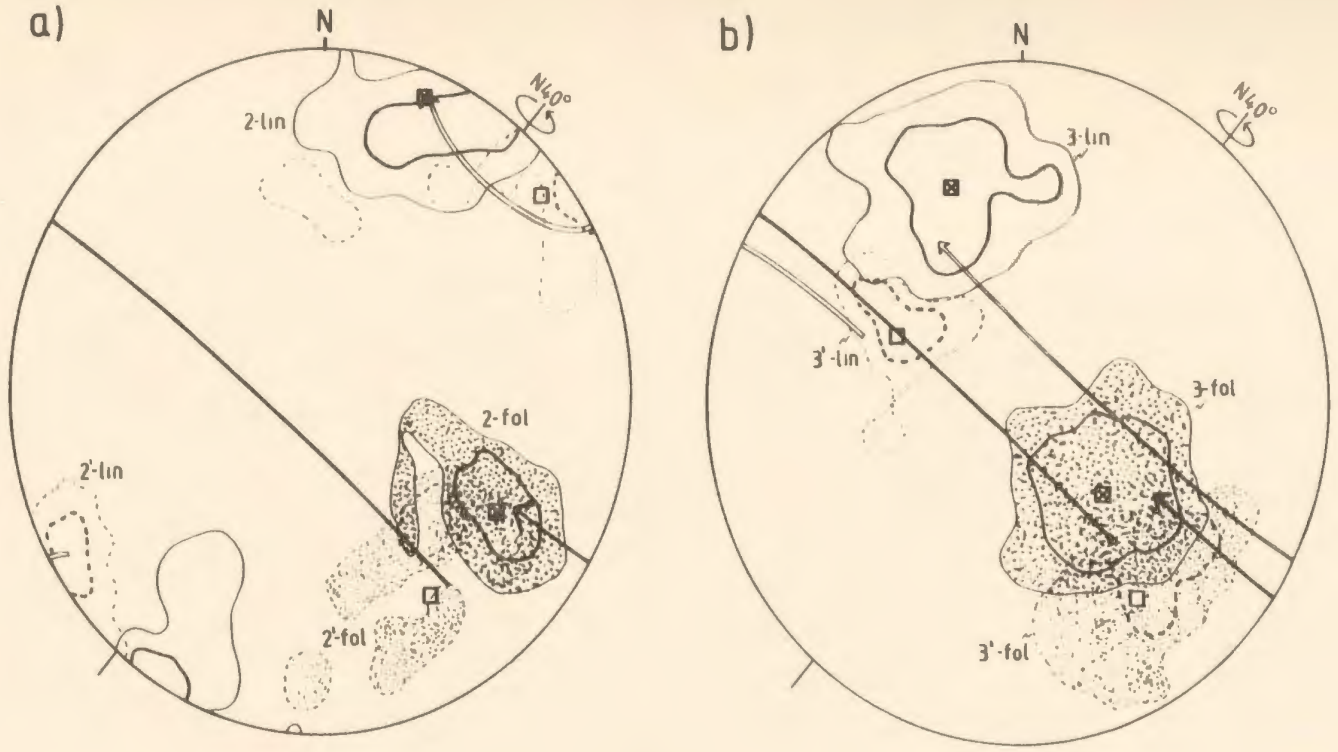

Fig. 2.7. Stereographic projections (equal area) showing the effect of unfolding the structural elements from the western limb of the Table Mountain synform. The 180° rotation is performed about a horizontal axis trending N40°E. Arrows indicate the rotation which should ideally move the maximum density of data from the western limb (open squares) into coincidence with the maximum density of data from the eastern limb (squares with x). The diagrams show that by performing the rotation, the poles to foliations and lineations of the western limb can be brought into approximate coincidence with those of the eastern limb. (a) Rotation with orientation data from unit 2/2'. (b) Rotation with orientation data from unit 3/3'.

Light dotted areas surrounded by dashed lines - foliations of western limb; heavy dotted areas surrounded by continuous lines - foliations of eastern limb; open areas surrounded by dashed line - lineations of western limb ; open areas surrounded by continuous line - lineations of eastern limb. Dashed and continuous lines indicate contours levels in % of 1% area as follows: 2' lin - 5 and 11%; 2' fol - 5 and 11%; 3'lin - 5 and 17%; 3' fol - 3 and 13%; 2 fol - 5 and 9%; 2 lin - 3 and 7%; 3 lin - 3 and 7%; 3 fol - 3 and 9%.

of the conduit. The in-situ formation of dunitic "dykes" can, however, only be demonstrated under special, favourable circumstances (Boudier and Nicolas 1977, Nicolas 1989, p. 227). In order to avoid any genetic connotation, the term *dunite band* will be used for dunites of dyke-like moprphology and an oblique orientation of foliation and the repetitive (pyroxenitic or dunitic) banding.

2.4.2 Transition zone

Lithological sections through the transition zone of TM are shown in Fig. 2.8. The lithologically most diverse sequence is exposed in the central part of the eastern limb of the massif (Fig. 2.8b, Pl. 1a). In this highly deformed section, clinopyroxene-rich harzburgites develop up-section into a lithologically banded sequence of dunite, harzburgite, wehrlite, and plagioclase wehrlite. These peridotites are overlain by massive to poorly banded dunites with minor wehrlitic bands. According to Neyens (1986), a well layered sequence of coarse wehrlites, troctolites, dunites, anorthosites and (olivine-) gabbros follows and grades into layered gabbros. Further up-section, after several hundred metres of layered gabbro, another wedge of ultramafic cumulates appears .

Based on detailed structural work in the area of Fig. 2.8b, Calon and Malpas (1985) and Neyens (1986) proposed the existence of a complex isoclinal fold pattern formed during high temperature plastic deformation. According to Girardeau and Nicolas (1981) the deformation is restricted to the basal ultramafic sequence. Neyens (1986) and Moll (1981) maintained that all gabbros are plastically deformed whereas Mercier (1977) interpreted all deformation as magmatic.

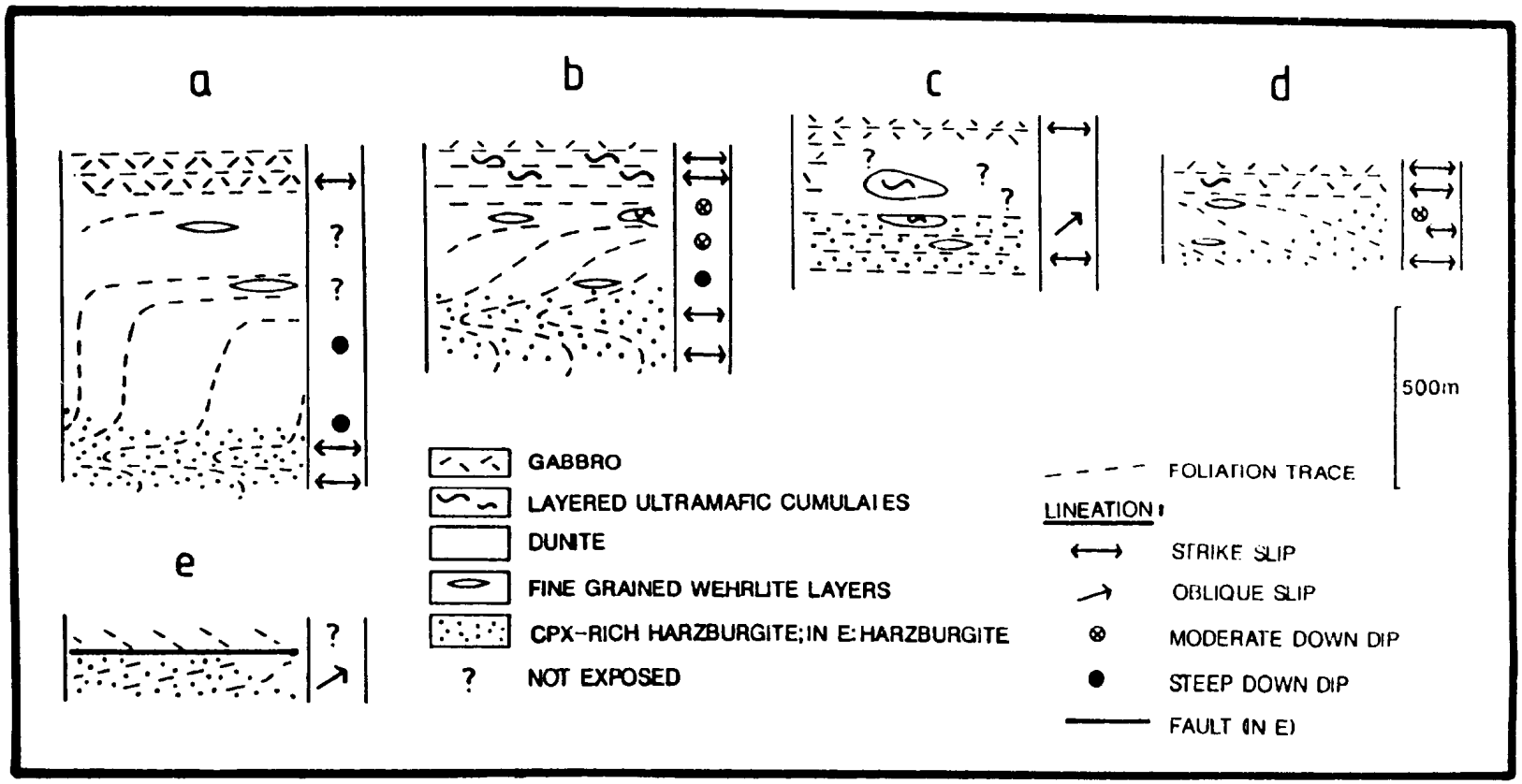

Fig. 2.8. Columnar sections through the transition zone of the Table Mountain massif. For location of sections see Fig. 2.5. Orientation of stretching lineation is given with reference to drawing plane, i.e. strike slip - parallel to drawing plane; down dip - into drawing plane.

The along-strike variation in the lithology of the the transition zone is considerable, as appears typical within and between the other massifs of the BOIC (Casey et al. 1981, Karson et al. 1984, Karson and Elthon 1987) and for other ophiolites, e.g. Oman (Lippard et al. 1986, Nicolas et al. 1988a).

As it is impossible to define a type section through the transition zone, the presence, extent, and age of faults in this area is highly speculative. A conservative approach is thus taken and only in one area is a faulted Moho suggested. In this section on the western side of TM (Fig. 2.8e), mantle harzburgites change along a sharp lithological, structural, and morphological break into unlayered gabbros.

2.4.3 Lithology of host peridotites and foliation-parallel banding

In this section the lithological variation (mineralogy, grain size) of the host peridotites is described. The description includes the, typically repetitive, banding which is parallel to the foliation or, in areas of folding, oblique to it. Cross-cutting pyroxenite dykes and dunite bands oblique to the foliation and lithological banding are described in section 2.9.

(Structural) units 1 and 2. Massive dunites with minor wehrlites occur below crustal gabbros or ultramafic cumulates within structural unit 1 and 2 (Figs. 2.1, 2.8). The dunites contain very fine grained spinels (< 1mm) and rare spinel seams (Pl. 1b) or spinel-rich zones parallel to the foliation. Wehrlites or plagioclase wehrlites occur as rare banding parallel to the foliation (for occurrences see Fig. 2.1). The dunite/wehrlite thickness on the eastern limb varies from approximately 500 m in the south to less than 10 m in the north (Fig. 2.8c); on the western limb, the thickness ranges from 400 m to zero. On the eastern limb, the dunites are largely restricted to structural unit 1. On the western limb, the dunites are affected by the deformation pattern characteristic for unit 2.

In several areas on the eastern limb, gabbroic and layered ultramafic cumulate lenses appear to float within massive dunite. The bodies are typically some tens of metre large and are cut by (cpx-) bearing dunites. These occurrences have previously been interpreted as slumps of ultramafic cumulates (Girardeau and Nicolas 1981, Neyens 1986). Here, they are considered to be an integral part of the dunite sequence.

The transition from massive dunite to mainly harzburgite occurs typically over less than 50 m through a progressive increase in the abundance of the harzburgitic banding (Pl. 1d). On the eastern limb, the transition nearly coincides with the structural transition between unit 1 to unit 2.

Near the dunite/harzburgite transition, discrete, foliation parallel, repetitive, clinopyroxenitic banding is locally observed in dunites and harzburgites (for location, see Fig. 2.1). Locally, the banding is plagioclase-bearing. The typically 1-3 mm, rarely 5 mm wide clinopyroxenitic bands have unusually abrupt contacts compared to the more subtle mineralogical variation between opx-rich and opx-poor banding prevailing further down-section (e.g. Pl. 1g). In one instance, one of several parallel bands was seen to change its orientation and cut across the others (Fig. 2.9a). In another location, the foliation-parallel, clinopyroxenitic bands are terminated by lherzolitic peridotite (Pl. 1e).

Harzburgites below the dunites are typically cpx-rich and may contain very minor wehrlite bands parallel to the foliation. The cpx content decreases gradually down-section within unit 2, a trend which continues into unit 3 and 4. Grain sizes for pyroxenes are 0.5 to 1 mm, i.e. fine grained. Spinel is very fine grained. A few larger crystals of opx reach 1.5 mm. The coarser grain size becomes more common towards the base of the unit. Coarser grained harzburgites also occur in outcrops near the northern slope of the massif.

Fig. 2.9 (facing page). Sketches of field relationships occurring within unit 2.

(a)Repetitive clinopyroxenitic banding in which one of the layers changes its direction and intersects the other layers.

(b)Foliation within lherzolite (dotted lines) which is slightly folded along a cross-cutting orthopyroxenite. The lherzolite contains isoclinally folded clinopyroxenite bands. The preferred interpretation for this relationship involves early dextral shear causing the asymmetric fold in the orthopyroxenite. Later, sinistral shear occurred, using the same flow plane as during dextral shear. As a result, the foliation became slightly folded ("flexure-fold") near the cross-cutting orthopyroxenite.

(c)Complex dyke intersection pattern occurring in harzburgite. Numbers indicate relative age of formation with 1 = early; attitudes are given in parentheses in dip-direction/dip format. [1] - foliation parallel to lithological banding (325/45); [2] - dunite with central, discontinuous websterite (290/76); [3] - orthopyroxenite with narrow, diffuse dunitic margin (70/50); [4] - orthopyroxenite (350/55), which is resorbed and transformed into dunite in the vicinity of [5]. Note that orthopyroxenite is asymmetrically changed into clinopyroxenite (indicated by small circles) next the dunite; [5] late dunite (325/62). Notable is that the angle between the foliation and the dykes does not seem to correlate with the age of the dyke. Such a correlation would be expected during synkinematic dyke formation.

(d)Three generations of dunite occurring within harzburgite. Early dunite (du 1) is part of the lithological banding and parallel to the foliation (dotted line). Intermediate age dunite (du 2) cross-cuts the banding but is itself intersected by an orthopyroxenite dyke (vertically ruled). The latter one is partially resorbed next to the late dunite (du 3).

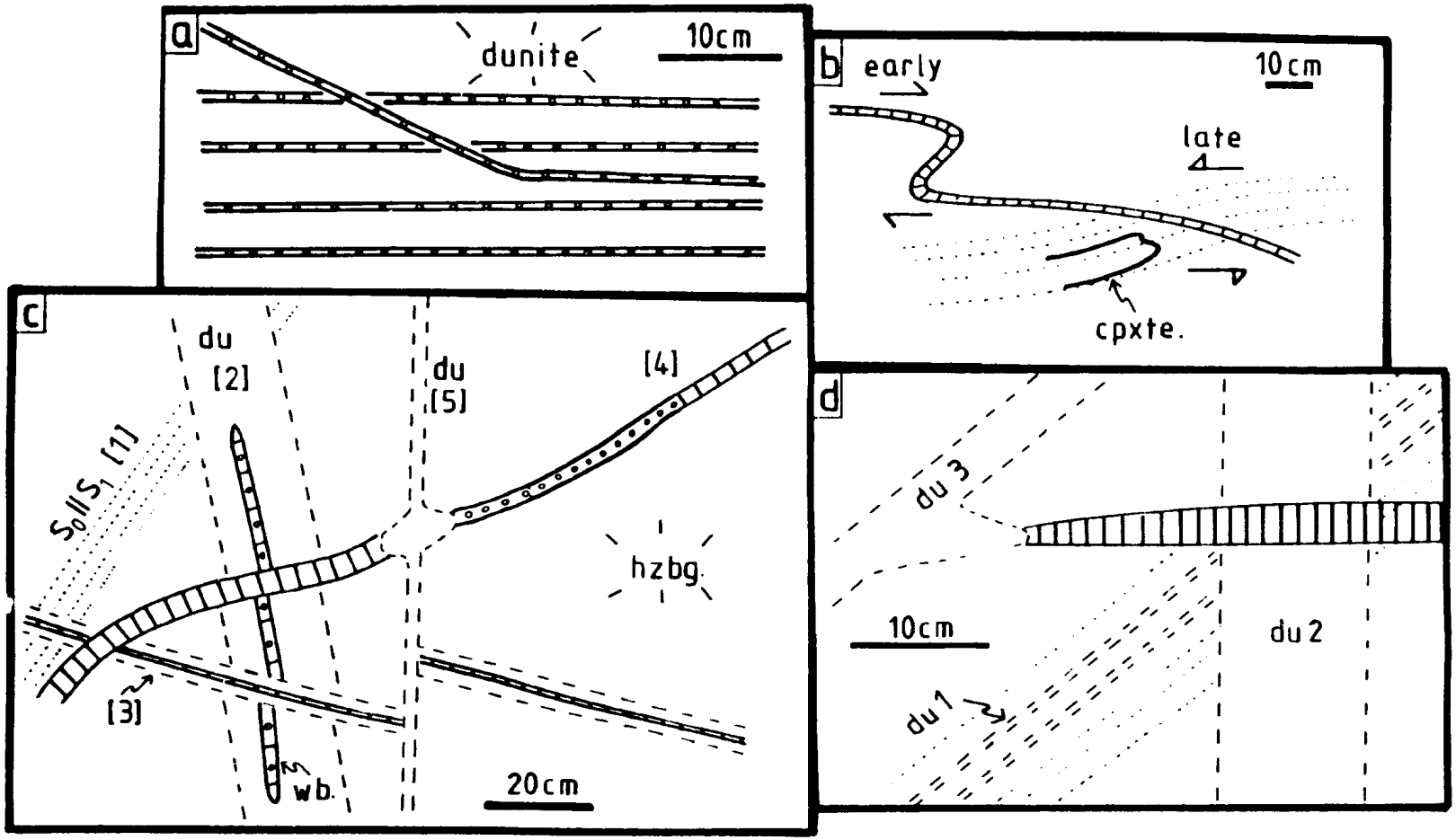
a
dunite
10cm
b
early
10cm
late
cpxte.
c
du
[2]
du
[5]
[4]
$S_0 // S_1$ [1]
hzbg.
[3]
wb.
20cm
d
du 3
10cm
du 2
du 1

Within unit 2, lithological banding is defined by dunite bands (up to 10 cm wide) or by a subtle variation in the pyroxene content of the harzburgites/lherzolites. Duritic banding contains locally cpx grains. Very thin (1 mm wide) clinopyroxenitic bands are also present and occur parallel or oblique to the foliation. Towards the base of the unit, opx-rich banding, typical for unit 3, becomes more abundant than dunitic banding.

Unit 3. The gradual disappearance of cpx continues down-section within unit 3. Most peridotites are harzburgites with only 0-2% cpx. Banding in peridotite is predominantly (olivine-) orthopyroxenitic and ranges from abrupt mineralogical changes reminding strongly to dykes intruded into peridotite (Pl. 1f) to an extremely subtle variation in the opx/olivine ratio (Pl. 1g). Dunite banding is only local importance.

Patchy or flaser-shaped dunitic areas appear where the average modal percentage of opx drops below 15% (Pl. 1h). The grain size of opx ranges from 1-2 mm, spinels reach 1 mm. Scattered outcrops of coarser grained harzburgites (opx grains up to 5 mm in size) seem to occur in a central band within unit 3 (for location see Fig. 2.1). Generally in opx-rich bands, the grain size tends to be coarser. Coarse opx grain sizes are also encountered near the base of unit 3 on the western limb.

Unit 4. The contact between units 3 and 4 is lithologically entirely gradational. Orthopyroxene-poor harzburgites, apparently associated with an increased abundance of dunite bands, are common in the southern, basal part of unit 4 (Fig. 2.1). Orthopyroxene grain sizes are generally in the 1 to 1.5 mm range. Coarser harzburgites (opx < 2.5 mm) appear locally as diffuse zones or bands. Occasionally, opx grain sizes change abruptly along with variations in the modal proportions of opx and olivine. Coarser grained opx is then associated with lower modal amounts of opx. This feature is more common in unit 5. The coarser grained bands are apparently also of higher strain as indicated by a stronger developed opx fabric.

Within the transitional unit (TU), the grain size increases to an average of 1.5 to 2.5 mm. In the north, where the TU is very broad and the *structural* unit 5 is poorly developed, the base of the TU is *lithologically* very similar to unit 5.

Unit 5. Harzburgites of unit 5 are enriched in opx and cpx compared to the overlying unit 4 and TU. The modal volume of pyroxene may be up to 40%. The lithological change is most rapid in the south, where it occurs along a mylonite zone, whereas it is gradational elsewhere. Orthopyroxene is largely unrecrystallized with an average grain size of 2-3 mm, but reaches up to 5 mm. Grain size and cpx content increase down-section. Lithological banding in peridotite is orthopyroxenitic to websteritic and varies from distinct to diffuse (Pl. 2a). Remarkably, following *along the strike of the banding* (Fig. 2.3), the rocks become progressively more depleted in pyroxene from station 1079 -> 757 -> 1143 -> to 1141 (see Map 3 in enclosures for station locations). The depletion trend can also be demonstrated geochemically (section 5.8). The overall appearance of the rocks is homogeneous with a near absence of cross-cutting dykes and lack of dunitic patches; lithological banding in peridotite is, however, common. The appearance of the rocks is darker (see also Riccio 1976) and pyroxenes weather out with positive relief.

Unit 6. Peridotites of unit 6 are mainly lherzolites, minor harzburgites and very rare dunites which appear concentrated in shear zones. Amphibole-bearing ultramafic rocks occur in small scale shear zones and within the basal ultramylonites. Ariegites (= spinel-websterites) described by Church (1972) are located just above the metamorphic sole in the well exposed southeast corner of the massif.

The peridotites are pyroxene-rich. The coarse opx grains (2-7mm) have been variably reduced in size by recrystallization or they are moderately to extremely flattened. Banding in peridotite is clinopyroxenitic, websteritic and orthopyroxenitic.

2.5 FABRIC

2.5.1 Introduction

In this section, the term fabric is restricted to the development, strength, and orientation of the mineral *shape* fabric of the peridotites, i.e. foliation and lineation defined by the constituent mineral grains*. The development of the foliation (S) may be stronger, equal, or weaker than the lineation (L). This is expressed as S > L, S = L, or L > S fabrics, respectively. "Equal" strength of foliation and lineation can be mathematically defined in the *Flinn Diagram* as

$$k = 1 = \frac{(1 + e_2)/(1 + e_3)}{(1 + e_1)/(1 + e_2)}$$

where e_1, e_2, and e_3 are the three principle extensions in the finite strain ellipsoid (cf. Fig. 6.4 for the two-dimensional case) and $k > 1$ indicates L > S fabrics, $k < 1$ indicates S > L fabrics (e.g. Ramsay and Huber 1983). For the purpose of field mapping, the L-S nomenclature is used, however, in a purely qualitative way following a visual estimate of the relative strength of foliation and lineation.

In the field, a distinction was made between *single mineral fabrics* and *aggregate fabrics*. In the case of single mineral fabrics, each grain has a preferred dimensional orientation which is parallel to the overall fabric. For aggregate fabrics, an alignment of several neighbouring grains defines the fabric. As each of the three phases used for the fabric determination (spinel, opx, cpx) behaves differently during high temperature deformation, combinations between single and mineral aggregate fabrics are possible.

---

*A preferred orientation of the crystal lattice of minerals is referred to as *crystallographic* or *lattice* fabric.

Mineral-defined foliations and lineations can be good first approximations of the flow plane and flow line in peridotites (Nicolas and Poirier 1976, Bouchez et al. 1983). The flow-related fabrics are determined microscopically with the preferred crystallographic orientation of olivine as determined by universal stage analysis. As the load-bearing phase in most harzburgites and lherzolites, olivine determines the flow behaviour of the rocks. The derivation of the flow fabric from the mineral shape fabric is, however, not necessarily straightforward in peridotites, particularly because the olivine shape fabric is not visible in the field.

Flow-related mineral shape fabrics in peridotite (i.e. kinematically significant foliations) are difficult to define where an opx pull-apart fabric is developed (Nicolas et al. 1971, Darot and Boudier 1975, Girardeau 1979, Suhr et al., in press). In this case the long axes of single opx grains are oriented at a high angle (typically normal) to the flow plane of the peridotite. However, a second foliation closely related to the flow plane can be defined as (i) the normal to the elongation of the single opx grains; (ii) an aggregate fabric of several pull-apart grains; (iii) the cleavage orientation of opx grains; or (iv) the alignment of single and aggregate spinel and cpx grains. Option (iv) is considered most reliable. Where none of the methods yields a reliable result, olivine petrofabric work can be performed on oriented specimens.

The variation in the lineation attitude found in this study is significantly larger and more domainal than reported previously (Girardeau and Nicolas 1981). The foliation orientation, on the other hand, is quite stable and compares favourably with the data of Girardeau and Nicolas (1981).

2.5.2 Description

Unit 1. The fabric within the massive dunites of unit 1 is a single as well as an aggregate spinel fabric. It changes over a short distance from S > L to L > S. Where present, cpx (weak single fabric, stronger aggregate fabric) and plagioclase (single and aggregate fabric) define planar and linear elements parallel to the spinel fabric.

Foliation and lithological banding are invariably parallel. Foliation attitudes change frequently. In the central part of the unit, they are at high angle to the major lithological contacts and define an overall sigmoidal pattern. Due to poor exposure, the data base for this pattern is somewhat weak (compare Fig. 2.3 with Map I). On the stereonet (Fig. A2.1) a partial great circle could be present with a best fit axis (BFA) of 327/50. This axis lies close to the mean stretching lineation (285/67)(Fig. A2).

Contact relationships with overlying gabbros and ultramafic cumulates are poorly exposed. Particularly in the south of the eastern limb, the gabbroic rocks appear to be internally faulted (Girardeau 1979, Neyens 1986).

Unit 2. Fabrics within unit 2 are moderate to strong, and L > S to L = S. They are typically of aggregate nature. Microscopically, however, spinel defines a good single mineral fabric. Discrete bands or lenses of cpx are common and are parallel or at an oblique angle to the foliation. Apart from one station within unit 2, foliations are invariably parallel to the banding. Along the contact between units 1 and 2 near station 1324 (Map III), the fabric of unit 1 swings through 90° and becomes parallel to that of unit 2.

Whereas the fabric is exceptionally regular in the north of the eastern limb with moderate to steeply westnorthwest dipping foliations (steepening towards the Moho) and shallow lineations, folding on a 100 m-scale can be inferred from the orientation data towards the south (Fig. 2.3). Mesoscopic folds are absent. Lineations (mean

021/08, Fig. A2.2) lie close to the calculated BFA of the foliation distribution (228/19, Fig. A2.1). Folding is not obvious on the western limb (Fig. A2.3). No new, axial planar fabric development is observed in folded areas. Locally, mesoscopic, flexure-like folds of the foliation are observed along crosscutting dykes (Figs. 2.3, 2.9b, Pl. 2e).

Basal gabbros and layered ultramafic cumulates appear to be largely part of structural unit 2, at least in the northern part of the massif (Girardeau and Nicolas 1981, Neyens 1986).

Unit 3. On the eastern limb of the synform, the transition of the fabric from unit 2 into unit 3 is, apart from a change in the lineation trend from 021/08 (unit 2) to a mean of 339/33 (unit 3, Fig. 2.2, A2.2), entirely gradual. On the western limb, however, the change in the orientation of the stretching lineation (Fig. 2.2, Fig. A2.3, A2.4) is accompanied by: (i) a notable increase in the opx grain size; (ii) a weaker fabric aspect; and (iii) a more depleted chemistry of the constituent mineral phases (see chapter 5).

The average strength of the fabric of unit 3 is weaker than that of unit 2 and $S=L$ to $S>L$. It is predominantly of aggregate nature. Spinel fabrics are generally weakly developed. Orthopyroxene pull-apart fabrics are very common, especially where the modal abundance of opx is low ($< 15\%$). Within the western limb, foliation and lineation are best defined as an $S=L$ single mineral spinel fabric. An axial planar fabric is developed where the banding is folded.

The mean foliation attitude of unit 3 (eastern limb) is 313/31 (Fig. A2.1), i.e. dips more gently than in unit 2. In the Winterhouse Brook Canyon area, the strike of the foliation swings 40° clockwise and dips towards 340°. In other areas, particularly above the contact of unit 3 to unit 4 in the northern part of the massif, the macroscopic fabric becomes extremely poorly developed. This occurs typically in areas where the banding and (?) the foliation is folded.

Another aspect of the fabric is the occurrence of opx-stringers with an L>S fabric which occur at an oblique angle to the foliation. They may be isolated or in groups, in which case they are subparallel to each other. Their origin remains enigmatic.

Unit 4. Foliations within unit 4 are L=S and dip gently to the northwest (mean 333/27, Fig. A2.1). The lineation plunges very gently to the northeast (mean 042/11, Fig. A2.2). This orientation is distinct from that of unit 3. The fabric development ranges from poor to mylonitic (Pl. 2b) and is axial planar to folds. Mylonitic fabrics are rare in the south, abundant in the north. The strain distribution is therefore heterogeneous.

The mylonites are zones of high strain which are typically a few metres wide or have poorly defined, diffuse boundaries. They are subparallel to the host fabric and have a sinistral geometry. Characteristic for the mylonites are round, one to several millimetre-wide "knobs" which stand out with high relief and have a somewhat brighter yellow brown colour than the rest of the olivine matrix. Microscopically, they can be identified as aggregates of unserpentinized areas of fine grained olivine. The high strain aspect of the mylonites is locally reflected in stretched dunite lenses. Low strain harzburgites are identical to those of unit 3 and appear in some instances to preserve remnants of the lineation orientation of unit 3. Intermediate strain fabrics are characterized by faint, darker ridges representing accumulations of fine grained opx grains along the foliation planes.

Transitional Unit (TU). In the area between unit 4 and 5 (i.e. the TU), fabrics are moderate to strong and range from L>S to S>L. Planar fabrics dominate. In general, the strength of the fabric can be correlated with the degree of lithological change: high strain prevails in areas of rapid change towards less depleted rocks of unit 5 (in the south of the massif), whereas low strain dominates in the area of very gradual lithological transition (in the central part of the massif). Foliations dip very gently (mean

313/19, Fig. A2.1), lineations trend nearly east-west (mean 249/00, Fig. A2.2). Particularly in the northern part of the massif, the fabric is commonly inclined at 10-50° to the lithological banding, though mesoscopic folds are notably absent.

Unit 5. The fabric within unit 5 ranges from S=L to S>L. It is of average strength in the upper part (comparable to unit 3) and poor in the lower part (Pl 2c). Pyroxene grains are typically equant or show pull-apart structures. Aggregate pyroxene fabrics are weak. The fabric orientation in opx-rich rocks could not always be determined. In the upper part of the unit, spinel is the best indicator for the fabric orientation. The mean foliation has an attitude of 317/67 (Fig. A2.1) and a mean lineation of 298/55 (Fig. A2.2). The fabric orientation is typically oblique to the lithological banding.

Unit 6. The internal structure of unit 6 is complex and can best be studied in the well-exposed southeastern corner of the massif. The following classification is suggested. An *early high strain fabric* is oriented at a high angle between the regional contact of the metamorphic sole and overlying peridotites. This early fabric is transposed into a *later high strain fabric* which is subconcordant to the metamorphic sole. The undisturbed tectonic contact with the metamorphic sole is marked typically by an *ultramylonite*. Local, small scale, *amphibole-bearing shear-zones* (see section 2.7.2) occur in a zone located several hundred metres above the metamorphic sole. Late thrusting along brittle faults led to juxtaposition of various parts of the basal ultramafics (unit 5 and 6) and the metamorphic sole. Due to the superimposition of several generations of ductile shearing events, strain within unit 6 does not increase homogeneously towards the metamorphic sole.

In the early high strain fabric, the foliations and lineations are moderately to strongly developed and S > L. The mean orientation of the foliation is poorly defined (Fig. A2.1 "6_{LS}", where LS stands for relatively *l*ower *s*train), lineations mostly plunge gently to the northwest (Fig. A2.2 "6_{LS}").

In the SE part of the massif, the later high strain zones transpose the early high strain fabric with an apparent component of sinistral shear. Orthopyroxene ribbon grains occur frequently (Pl. 2d). Foliation orientations cluster well around the mean of 345/41, Fig. A2.1 "6_{HS}", where HS stands for *h*igher *s*train)), but lineation trends are not well constrained (Fig. A2.2 "6_{HS}"). The trend of mineral stretching lineations appears to change along strike of the high strain zones.

Ultramylonitic rocks are developed in several sections directly above the metamorphic sole. In several sections through the contact of the peridotites with the metamorphic sole, high strain rocks grading into ultramylonite are deflected sinistrally (in plan view) towards parallelism with the sole. The ultramylonite thickness is less than 3 m. A subtle banding of the ultramylonite defines the fabric. Foliations dip moderately to steeply to the northwest (mean 329/53, Fig. A2.1 "6_{L}"), lineations plunge gently to the northnortheast (mean 025/08, Fig. A2.2 "6_{L}")

Along the northern margin of the massif, a sliver of high strain peridotites is exposed in contact with amphibolites. The high strain peridotites are faulted against lower strain peridotites of the TU and unit 5 to the south. Within the sliver, the high strain peridotites show northwest-dipping foliations which are variably overprinted by steeply dipping, E-W striking high strain zones with dextral shear sense. Because of the faulted nature, the area is presented in separate stereonets (Fig. A2.1 "6_{SL}", A2.2 "6_{SL}").

2.6 FOLDS OF THE LITHOLOGICAL BANDING

2.6.1 Introduction

Within all units, the lithological banding is folded to some extent. The scale, type and origin of these folds vary considerably from unit to unit. Folds which affect both the lithological banding *and* the foliation have already been described in the previous section. Folds associated with shear zones are described in section 2.7.2.

Fold asymmetries of mesoscopic folds of the lithological banding are determined in down-plunge view. Fold axes of *asymmetric* mesoscopic folds generally plunge to the southwest, west, or northwest and are - in contrast to what is common in peridotites (Nicolas and Boudier 1975) - *not* parallel to the stretching lineation.

2.6.2 Description

Mesoscopic folds of the lithological banding develop progressively down-section from unit 2 into unit 3. They are absent in unit 1. The inflection point* of asymmetric folds is typically intersected by pyroxenite dykes, suggesting that the folds formed along the dykes after intrusion of the dykes.

As viewed progressively down-section, the folds develop from rare, weak S-flexures within unit 2 (Pl. 2e) through S-asymmetric (or south verging) folds (Pl. 2f) into open, M-like folds of unit 3 (Pl. 2g). The open folds may tighten locally to become nearly isoclinal. The relationship is interpreted to reflect folding of the peridotites along (rheologically competent) dyke planes during sinistral shear (i.e. the upper block moves southward). Exceptionally, folds are sheared off along the pyroxenite dykes. The fold

*The point where the sense of the curvature changes.

style is generally, parallel but may become weakly similar for tighter folds. Folds associated with high strain zones in the Winterhouse Brook area are nearly isoclinal and of more similar style (section 2.7.2).

Within unit 3, poles to the lithological banding form a good great circle distribution (Fig. A2.5) with a BFA of 279/33. This value corresponds well to directly measured fold axes (mean 283/29, Fig. A2.7). The latter data spread from shallow southwest to shallow northwest plunging. As the mean stretching lineation for unit 3 is 339/33, the data may reflect initial transposition of fold axes formed at high angle to the stretching lineation towards the flow line.

With the exception of the flexure-like folds of unit 2 and the top of unit 3, axial planar foliations are clearly developed with the folds. It appears that the axial planar fabric develops progressively with the intensity of the folding. The shape fabric in the immediate vicinity of the dykes, i.e. in the inflection area of the folds, is often weaker than further away from the dyke. This is probably due to a combined effect of: (i) destruction of the host fabric during reaction with the melt of the dyke at the time of intrusion*; (ii) the abundant development of opx pull-apart fabrics in harzburgites near the dykes.

As expected, the mean orientation of axial planes in unit 3 (Fig. A2.6) is parallel to the foliation. A few, very steep axial planes are restricted to an area where the foliation becomes refolded. This refolding can best be demonstrated from the weak partial girdle distribution of the axial planes about a mean axis of 265/28 (Fig. A2.6).

Within the Winterhouse Brook area, refolding of an early generation of folds by the S-asymmetric folds occurred. The early-generation folds are tight or isoclinal

---

*A reaction between orthopyroxenites and host harzburgites can be chemically demonstrated (see chapter 5).

Z-folds (Pl. 3a,b; see also Fig. 19 in Calon et al. 1988). Their fold axes could only rarely be determined, but they appear to plunge shallowly to the west (Fig. A2.8). The folds shown in Pl. 3b are interpreted as Z-folds formed by dextral shear which were subsequently affected by sinistral shear to cause the rotation of the hinges.

Within unit 4, open folding of the banding is common in the south, whereas tight to isoclinal, similar style folds prevail in the central and northern part (Fig. 2.3). The tightening of the folds appears therefore related to the northward wedging of unit 4. The thinning of unit 4 to the north as seen in the map is, however, exaggerated by a topographic effect.

The banding defines a good great circle distribution with a BFA of 279/27 (Fig. A2.5) parallel to the mean of individually measured fold axes (269/21, Fig. A2.7). Fold axes parallel to the stretching lineation also occur and are associated with isoclinal folds in the central part of unit 4.

Within the TU, the fold style dominating in unit 4 should grade into the one dominating in unit 5 (see below). From the available data, it is not possible to deduce a uniform deflection pattern between both domains (see Map 1). Mesoscopic folds are extremely rare in the northern part of the TU, though the banding is often oblique to the foliation. In the south, where folds are more common, they range from buckle to similar style and open to isoclinal (Pl. 3c,d). The partial girdle distribution of the banding indicates a BFA of 292/25 (Fig. A2.5), consistent with individually measured fold axes (Fig. A2.7).

Unit 5. The map pattern of the lithological banding within unit 5 appears to define a large scale synformal structure (Fig. 2.3). The foliation is typically oblique to the banding. Mesoscopically, the pyroxenitic banding shows abundant buckling (Pl. 3e). The buckling is more pronounced in distinct, rheologically competent banding compared to the more diffuse banding. The small scale buckling of the banding is locally

also present in the TU. The axial planes of the buckle folds appear to be parallel to the foliation. Tight to isoclinal folds with axial planes *parallel* to the regional trend of the banding have also been observed (Pl. 3f).

Within unit 6 no mesoscopic folds of the banding are present. Curvatures of the foliation and banding are interpreted to reflect deflections caused by shear zones (see 2.7.2).

2.7 SHEAR ZONES

2.7.1 Introduction

On a larger scale, most of the units themselves represent some kind of a shear zone. For the purpose of this section, shear zones are defined as zones of high strain, the formation of which outlasted the deformation of the host rocks. Boundaries to the host peridotites are generally well defined. The local shear zones described in this section are identified by a fabric development distinct from the host rocks and/or by the presence of deflection patterns of host fabrics.

2.7.2 Description

Unit 2. In the southern part on the eastern limb, the fabric pattern within unit 2 is complex (Fig. 2.2, 2.3, Maps 1 and 2). Foliations are deflected and lineations plunge very steeply. The pattern could result from a steeply south-dipping shear zone. The situation is difficult to evaluate, as the appearance of the fabric of this zone is indistinguishable from that of the surrounding rocks. This suggests an early, high temperature origin. The early nature of the shear zone is supported by the fact that later cross-cutting dykes (orthopyroxenites and dunite bands) appear unaffected by the suspected shear zone whereas foliation-parallel dunite banding is deflected into the shear zone. Stations from this area are not included in the stereographic projections of unit 2.

Within unit 2 and the upper part of unit 3, isolated occurrences of late shear zones with a flaser-fabric have been observed. The type occurrence is station 1136 (Map III). Microscopically the anastamozing fabric is dominated by amphibole.

The Winterhouse Brook area of unit 3 is the site of diffuse to well-defined, high temperature shear zones. Stations covering these shear zones are singled out as "unit 3_{hs}". The average attitude of the foliation of the shear zones is somewhat steeper than that of the host fabric (mean foliation 334/59, mean lineation 008/48, Fig. A2.1, A2.2). The fabric tends to be L > S. Close to and within the shear zones, tight to isoclinal folds of more similar style are developed (Pl. 3g). In some cases, the presence of shear zones is supported by deflection of orthopyroxenites into the high strain zones (see Fig. 18 of Calon et al. 1988). Outside the shear zones, the orthopyroxenites within unit 3 are boudinaged, but not folded. Fold axes within the shear zones are at various angles to the stretching lineation (Fig. A7). In one location, a very weakly deformed orthopyroxenite occurs as a lens essentially confined to the shear zone, supporting a synkinematic origin of the dyke during the last stages of movement.

Diffuse zones of L > S fabrics occur throughout the Winterhouse Brook area. It appears possible that strain related to these shear zones is more widespread than suggested by the few, well-defined shear zones.

Within the basal unit 6, several generations of shear zones overprint each other. Apart from local, amphibole-bearing shear zones, these have been described previously (section 2.5.2). The amphibole-bearing shear zones are typically only a few centimetre wide and have an anastamozing geometry (Pl. 4a,b). They occur in a zone several hundred metres above the metamorphic sole. One more prominent, 1-2 m wide, amphibole-bearing shear zone strikes more consistently northwest-southeast and contains a northeast-dipping lineation.

2.8 SHEAR SENSES

2.8.1 Introduction

Shear senses can be deduced from field relationships and microstructural studies. The advantage of the microstructural method used in this study (see section 1.5) lies in its applicability to each olivine-rich peridotite sample deformed at high temperatures. The results of the method are consistent with measurements of oblique olivine fabrics (van der Wal et al. 1990) observed within some thin sections. The results from the microstructural determinations are compiled in Fig. 2.4. Field determinations of the sense of shear are restricted to occurrences of asymmetric folds (e.g. Pl. 2f), asymmetric boudins (e.g. Pl. 5a), local or regional deflections of fabrics into shear zones or other structural domains, or rare tension gashes (Pl. 6b). The use of opx porphyroclasts for shear sense determinations (Reuber 1982) is considered unreliable (see section 4.4.4).

2.8.2 Description

Unit 1. Field-based criteria are non-existent. Microstructure-based measurements (5 samples) yield no consistent orientation.

Unit 2. On the eastern limb, weak, S-shaped flexures of the banding along cross-cutting orthopyroxenites indicate a sinistral shear sense. One outcrop relationship of a folded *dyke* indicates early dextral shear followed by later sinistral shear (Fig. 2.9b). The microstructure-based determinations are mainly dextral (upper block to the north). The dextral domains extends into the upper part of structural unit 3. Out of 27 measurements, 14 are dextral, 3 sinistral, and 10 are neutral.

Unit 3. Field evidence from asymmetric folds formed in the vicinity of orthopyroxenites suggests sinistral movement throughout the unit. Sinistral shear is also required to explain the orientation pattern of orthopyroxenites (see next section). In the

complex Winterhouse Brook area, early generation folds of Z-asymmetry (see section 2.6.2) indicate an early dextral shear sense that was overprinted and refolded during sinistral shear. Apart from the top part of the unit, microstructural evidence favours sinistral movement (8 determinations sinistral, 1 neutral, 0 dextral).

Unit 4. Sinistral shear is indicated in the field by changes of the fabric attitude near high strain zones, rotated and attenuated boudins (Pl. 5a) and a few S-asymmetric folds adjacent to orthopyroxenite dykes. The conclusion is supported by microstructural data (8 sinistral determinations, two neutral, 0 dextral).

TU. Field criteria for the dominant sense of shear within the TU are not available. Also no consistent map scale transposition pattern exists. Evidence from the microstructure study is equivocal (2 sinistral, 2 dextral, 6 neutral).

Unit 5. Field criteria are not available. The microstructure-based determinations are not conclusive (two upper block down, three upper block up).

Unit 6. Deflection patterns of markers into shear zones as well as the drag structure of the fabric into the basal ultramylonite indicate a dominant component of sinistral shear in map view. Microstructural evidence is ambiguous, especially considering the unusual spread of movement directions as indicated by the varying trends of the stretching lineation.

2.9 DYKES

2.9.1 Introduction

Lithologies with planar or curviplanar boundaries *oblique* to the foliation and lithological banding are defined as dykes. In areas where folding is suspected and the characteristic lithological banding (i.e. repetitive layering) is absent, dykes cannot conclusively be distinguished from the banding. Banding-parallel dykes are, by this defini-

tion, referred to as banding, not dykes. The orientation patterns of dykes are thus somewhat biased, neglecting dykes which are exactly parallel to the foliation or banding. Although complex areas with such ambiguous relationships exist, most stations allowed the distinction between banding and dykes.

Folding and boudinage of dykes is common and fold-axes and boudin-elongations were determined wherever possible. In an effort to derive the orientation of pyroxenite dykes at the time of their formation, i.e. before they were affected by plastic deformation, apparently undeformed dykes are singled out in separate stereonets. Criteria used to select undeformed to weakly deformed dykes are: (i) an average grain size of >5 mm (Pl. 4c), typically coupled with evidence for primary igneous textures (Pl. 4d) and a lack of recrystallization features; (ii) absence of folding or boudinage; (iii) primary dyke features such as en-échelon arrangement (Pl. 4e); and (iv) high-angle branching of dykes (Pl. 4f).

Dykes occur as orthopyroxenites, clinopyroxenites and websterites, olivine orthopyroxenites and rare olivine clinopyroxenites and gabbroic/anorthositic dykelets, as well as dunite bands.

2.9.2 Orthopyroxenite dykes

Unit 1 hosts the widest orthopyroxenite dykes of the whole massif. They reach up to 3 m in thickness, have sharp margins with the host, locally engulfing host rocks as sheets or lenses, and have crystal sizes up to 10 cm. They cross-cut all lithologies. The near random orientation pattern of *all* orthopyroxenite dykes (Fig. A2.9), similar to the distribution of undeformed dykes (Fig. A2.10), suggest that orthopyroxenites largely postdate the plastic deformation of the host.

Orthopyroxenites within unit 2 occur as several millimetre-, up to 20 cm wide dykes, most commonly in 2-5 cm range. Grain sizes tend to increase with dyke thickness, but thin dykes with large grain sizes have been observed. Also present are orthopyroxenite dykes with a central band of clinopyroxenite.

The vast majority of orthopyroxenites postdates dunites and clinopyroxenites. Many dyke margins of orthopyroxenites are somewhat irregular, which could either be the result of weak deformation-related buckling or could, alternatively, be a primary feature. Comb-textures occur as well, though they are rare (Pl. 4d). Orientation patterns show two maxima, one steep one (mean 340/76, Fig. A2.9) which is clearly oblique to the mean foliation (302/49), and a very shallow one. Undeformed dykes (Fig. A2.10) show a similar orientation pattern to all orthopyroxenite dykes suggesting that the overall effect of transposition on the dyke orientation was small. Where boudinage or buckling was noted, the stretching appears to relate to the shallow maximum, the shortening to the steep one (Fig. A2.9).

In localities where several dyke generations are exposed, no clear relationship exists between the age of the dykes and their relative orientation to the foliation (Fig. 2.9c), supporting a relatively late emplacement age of the dykes with respect to the deformation.

Within the lower part of unit 3, orthopyroxenites are considerably more deformed than within units 1 and 2. Dykes are typically boudinaged, rarely buckled, and the grain-size for the deformed dykes lies between 1-2 mm. Primary features such as en-échelon arrangement (Pl. 4e), branching of dykes (Pl. 4f), or even attenuated dyke tips related to propagation cracks are locally preserved in steeply dipping, undeformed dykes in the upper section of unit 3. The maximum dyke width is approximately 50 cm, 2-5 cm are more typical. Reaction between orthopyroxenite dykes and the host peridotites, particularly any clinopyroxene-rich bands, has been observed (Pl. 4g).

The distribution pattern of the orthopyroxenite dykes shows a point maximum which tails off into a partial great circle with a BFA of 256/25 (Fig. A2.9), i.e. perpendicular to the stretching lineation of the unit and a mean attitude (321/48) near the average foliation plane (313/31), but somewhat steeper (Fig. A2.9). A weak sub-maximum correlates with the orientation of undeformed dykes (mean 159/71, Fig. A2.10). The orientation of undeformed dykes of unit 3 correlates well with those of unit 2. Boudinaged dykes and dykes causing inflections and S-folds of the banding are restricted to orientations close to the foliation (Figs. A2.11, A2.12). Fold axes of buckled dykes show a considerable spread with a mean direction of 250/25 (Fig. A2.13), i.e. perpendicular to the stretching lineation of the unit.

Boudins are lens-shaped and of chocolate-tablet type (Fig. 4h). They tend to be elongated perpendicular to the stretching lineation of the host rock. Orientation data of the elongation of boudins show a maximum normal to the stretching lineation and a tail leading towards the stretching lineation (Fig. A14). This is interpreted to be the result of weak transposition of boudins formed initially at high angle to the movement direction of the peridotite.

The numerous orientation data for orthopyroxenites in unit 3 are consistent with the following model: dykes form in a steep orientation at high angle to the stretching lineation and are then progressively transposed towards the foliation plane during sinistral shear. The shear sense is indicated by the spread of data of all orthopyroxenites which follows a path of progressively more shallow northwest-dipping dykes. Dextral shear, on the other hand, would require the presence of numerous southeast-dipping dykes. The chocolate-tablet type boudins and the S >> L fabric suggest a component of pure flattening during the deformation.

Virtually all orthopyroxenites within unit 4 are deformed and lie close to the foliation plane (Fig. A2.9). Rotated and attenuated boudins (Pl. 5a) indicate high strain during sinistral movement.

Within the TU, orthopyroxenites are similar in character, but less abundant, than in unit 4. The orientation pattern (Fig. A2.9) is more diffuse than for unit 4. Within unit 5 and unit 6 orthopyroxenite dykes are essentially absent.

2.9.3 Clinopyroxenite dykes and gabbroic veinlets

Clinopyroxenite dykes are extremely rare within unit 1. Within unit 2, they occur as one or several millimetre-thick dykelets at small angle to the foliation plane (Fig. A2.16). Note that numerous clinopyroxenites are parallel to the foliation, i.e. constitute banding (see section 2.4.2). In some of the clinopyroxenites, folding can be observed (Pl. 6a) and fold axes are mostly parallel to the lineation (Fig. A2.13). Clinopyroxenites cut the foliation-parallel dunite banding, but appear to be cut by the oblique dunites. Thin gabbroic to anorthositic dykelets are very rare and restricted to regions directly below the gabbros.

Clinopyroxenites are very rare in unit 3, 4, and the TU. Within unit 3, they have been observed as zigzag folded dykes (probably related to dextral shear) and in the centres of boudinaged orthopyroxenites. In the northeastern part of the massif, clinopyroxenites occur in the basal TU. The clinopyroxenites occur as a widely spaced swarm of dykes which crosscuts the banding. Further up-section, banding-parallel clinopyroxenites have been observed.

2.9.4 Olivine orthopyroxenite dykes

Pegmatitic olivine orthopyroxenites occur locally within units 3 and 4, and are most abundant within the TU. In some localities, they are only weakly deformed. The

dykes are typically 10-20 cm wide and in their least deformed state show pegmatitic opx grains (Pl. 5b, see also Fig. 17 in Calon et al. 1988) separated by a matrix of olivine and up to 3 mm large spinel grains. Comb textures appear to have been present before the overprint by plastic deformation occurred. Extreme structural transposition of these dykes would lead to formation of a harzburgitic rock. The orientation pattern is distinct, forming a great circle distribution with a BFA of 204/10 in the TU (Fig. A2.15). Dykes with steeply dipping attitudes tend to be less deformed.

2.9.5 Olivine clinopyroxenite dykes

This dyke type is rare. It has been locally observed as pegmatitic olivine-clinopyroxenite (unit 2) with a similar texture as olivine orthopyroxenite or as buckled dyke in unit 3. Only within the early high strain fabric of unit 6 do olivine clinopyroxenites form a distinct group of folded or boudinaged, up to 40 cm thick, originally pegmatitic dykes.

2.9.6 Dunite pods and bands

Dunites display the widest morphological range of all "dyke" lithologies. They comprise planar and folded bands, elongated or irregular pods with sharp or diffuse margins, as well as patchy occurrences in harzburgite. In addition, massive dunites are present in the transition zone (see section 2.4.3). Unambiguous boudinage or buckling of dunite within harzburgite is very rare and it appears that dunites behaved largely as competent bodies within harzburgite, as is expected from rheological data (e.g., Carter 1976). Orientation patterns of dunites are biased towards more prominent, thick dunites. In most localities, dunite pods and bands predate the orthopyroxenites, as is also observed in the southern LH (Suhr et al., in press).

Unit 1. In locations where cpx-, plagioclase-, or spinel-banding is developed in massive dunites, the banding is commonly intersected by dunite bands. The appearance of the dunite bands is identical to the host dunite so that in the absence of a banding within the massive dunites, cross-cutting dunite bands cannot be identified. In one instance, the melt associated with a dunite band reacted with the host banding to cause a diffuse depletion zone in cpx and plagioclase (Pl. 1c).

Unit 2. Swarms of dunite bands oblique to the banding are common within unit 2. Single dunite bands tend to be not wider than 30 cm, though exceptionally wider bands have been observed. Spinels define a fabric parallel to the host peridotite. The occurrence of dunite banding together with cross-cutting dunite bands results in a pervasive dunite network (Pl. 5d). Cross-cutting dunite bands tend to penetrate into pyroxene-rich banding of the host harzburgite or lherzolite by preferential replacement of the pyroxene (Pl. 5e). It is obvious that some discontinuous dunite banding is formed this way. Using cross-cutting relationships, up to three dunite generations can be deduced in some outcrops (Fig. 2.9d).

As minor amounts of cpx are commonly associated with dunite bands and banding in unit 2, dunites may develop wehrlitic compositional tendencies. Clinopyroxene in dunite occurs as tension gashes (Pl. 6b), scattered grains of cpx, discontinuous cpx-rich zones (Pl. 5f), and as cpx-rich margins of dunite bands and banding (Pl. 6c). Fig. A2.17 suggests that there is a relatively pronounced maximum orientation of dunite bands in unit 2, striking north-south and dipping near vertical.

Unit 3. Dunite bands and pods are less common in unit 3 than unit 2. The shape of dunite pods may be irregular or was partially to fully controlled by pre-existing orthopyroxenitic banding. The margins of dunites range from very diffuse (Pl. 5h) to sharp mineralogical contrasts. Some pods contain equant spinels which are several millimetre-large and show a poor aggregate fabric (Pl. 5h), but in most locations the

spinels are fine-grained and oriented parallel to the host fabric. In the upper part of the Winterhouse Brook Canyon, several large dunite pods are aligned over an area of 400 m in a direction trending N20°E, i.e. at high angle to the foliation trace. The pods are cut by orthopyroxenites. One sulfide-rich dunite body has been found (Station 966, Map 3).

Dunites tend to replace orthopyroxene banding (Pl. 5g). Most dunite bands are folded together with the banding. However, the ability of dunites to form by replacement of orthopyroxene banding makes it difficult to decide whether dunites are actually folded or are just replacing folded opx banding. Both cases appear to exist. The distribution pattern of dunite bands in unit 3 is poorly understood and shows a mean attitude of 234/88 (A2.17).

Unit 4. In the upper part of the unit, the dunites are morphologically similar to unit 3, but generally more deformed. In the lower, southern and central parts of unit 4 and the associated TU, up to several metre-wide dunites cut steeply through the foliation and contribute to the formation of the basal depleted zone (Fig. 2.1). Their margins are diffuse and folded. Microscopically, it can be seen that these dunites contain scattered opx.

Unit 5. Dunites are rare and occur as isolated bands crosscutting the banding and reacting preferentially with the distinct, websteritic banding. Some isolated pods are present as well. Within unit 6, oblique dunites are very rare.

2.10 METAMORPHIC SOLE

2.10.1 Introduction

The metamorphic sole of the BOIC represents crustal material accreted to the base of the ophiolite during detachment (Williams and Smyth 1973, Malpas 1979a, Jamieson 1980, 1986, McCaig 1983). Exposure of the metamorphic sole in TM is generally

limited to 50-100 m below the contact to the mantle rocks, though the preserved thickness of the sole appears to be larger. A notable exception is represented by a thick, bulky thrust belt accreted to the peridotites just to the south of the cross-fault zone. It was first recognized and assigned to the metamorphic sole by Quinn (1985). Within this study the sole was not investigated in the detail necessary to solve the problems of such a complex metamorphic and structural assemblage. The data presented have to be considered as preliminary.

The most complete sequence of the metamorphic sole in the BOIC is described from the Pond Point section in southern North Arm Mountain (Williams and Smyth 1973, Malpas 1979a). In this section, local granulites underlie ultramafic ultramylonite. The granulites grade structurally downwards into (locally garnetiferous) amphibolite, followed by retrogressed amphibolite, greenschist, phyllite and unmetamorphosed sediments (green, grey, black and red shales, sandstones and tuffs). The total thickness of the metamorphosed rocks is less than 300m.

2.10.2 Description

Nowhere in TM is the metamorphic sole as comprehensively exposed as in the Pond Point section. However, in the southeastern part of TM, an unfaulted contact between the peridotites and the metamorphic sole is preserved. In this area, ultramafic ultramylonites lie directly above fine-grained amphibolites and minor garnet-amphibolites and granulites. Ultramafic and mafic rocks are actually interbanded over a thickness of about 2 m (see also Girardeau 1979, McCaig 1983). The interbanding can even be seen on a microscopic scale as trails of opx porphyroclasts in a amphibolite matrix. Directly above this contact, the sequence appears, however, slightly faulted. Exposure ends 100 m below the contact within amphibolites. McCaig (1983) described a lens of coronitic metagabbro from approximately 5 m below the ultramylonites. Foliations in

the contact area between mafics and ultramafics are unusually steep (near vertical). Further north along the metamorphic sole, ultramylonites are still in contact with amphibolites (separated by < 1 m exposure gap), but the sequence is faulted 100 m above the contact and poorly exposed below the contact. Structural data from the continuous belt of amphibolites indicate a mean dip of the foliation of 332/51 and a mean stretching lineation of 047/04 (Figs. A2.1, A2.2). Oblique, small scale shear zones are abundant in the amphibolites.

In the central part, i.e. the section where the Shoal Brook cuts through the sole, high strain ultramafic rocks are underlain by graphitic slates, phyllites and green, grey and red shales. The weakly to unmetamorphosed sediments are interpreted as part of the underlying Humber Arm Supergroup. They could, however, also represent the basal part of the metamorphic sole, as this consists of material derived from the high structural levels of the Humber Arm Supergroup, i.e. the Blow Me Down Brook Formation (Cawood, pers. comm.).

The style of the "metamorphic sole" changes dramatically in the north as is already indicated by the complex morphology of the terrain. In this area, peridotites of unit 5 are faulted against amphibolites. These amphibolites contain spessartine - sillimanite-bearing coticules (metamorphosed manganiferous sediments). Below another faulted contact, 150 m of lower strain ultramafic rocks are exposed. Quinn (1985) described a quartzo-feldspathic gneiss between the amphibolites and the ultramafics. To the east of the harzburgites, folded, retrogressed amphibolites, epidote schists and greenschist are exposed in a prominent morphological ridge (locally called "Pic à Tenerife"). Further to the east, more harzburgites, now heavily serpentinized, occur and are juxtaposed in the east against grey slates. The slates may again be either part of the Humber Arm Supergroup (which is considered more likely) or constitute another tectonic sliver of the thrust belt.

To the north of the cross-faults, exposure ends in the early high strain fabric of unit 6. Rocks exposed on hills to the east were not investigated. They represent volcanics of the Skinner Cove Formation (Quinn 1985).

Near the village of Shoal Brook, in the northeastern-most part of the massif, east-west striking amphibolites are juxtaposed against ultramafic rocks of similar orientation. The original tectonic position of this sliver is not known. In particular, the E-W strike of the fabric is puzzling.

3 MICROSTRUCTURE, PART I: TYPE MICROSTRUCTURES

3.1 SUMMARY

The presence of several structural domains outlined in chapter 2 suggests that the conditions of deformation within the mantle section of the TM massif were not uniform. Previous work in mantle tectonites has shown that microstructures are a sensitive indicator of the conditions of deformation and late magmatic processes. A detailed microstructural analysis is presented to define the conditions of formation of each of the structural units. The terms lithospheric and asthenospheric microstructures are used according to the definition of Ceuleneer et al. (1988).

Microstructures of unit 1 are characterized by strong olivine lattice fabrics produced under asthenospheric conditions. Micron-sized inclusions in olivine are common. Morphological evidence suggests that clinopyroxene, and locally orthopyroxene and amphibole, were introduced by circulating melts at a late stage. Particularly intriguing is a strong opx lattice fabric encountered in one sample. It must have been produced during melt impregnation or partial melting.

Within the upper part of unit 2, asthenospheric olivine microstructures with strong lattice fabrics predominate. Orthopyroxene is highly recrystallized. Scattering of opx and spinel grains indicates high strain. Clinopyroxene and plagioclase occur as phases aligned parallel to the foliation and related to melt impregnation. Some annealing of the impregnations has taken place. Down-section within unit 2, spinel and opx scattering decreases, opx is less recrystallized, and olivine indicates a weak lithospheric overprint. Spinel is more irregular shaped and tends to be associated with opx and cpx.

Peridotites of unit 3 show a weak to moderate lithospheric overprint. Orthopyroxene is moderately recrystallized and pull-apart fabrics of this phase are common. Spinel is intergrown with opx. Up-section, textures transitional to unit 2 occur.

High strain zones of unit 4 display equigranular to porphyroclastic microstructures in high strain zones. Peculiar is the local occurrence of shard-like opx grains with a crystallographic orientation incompatible with activation of the opx slip system (100)[001]. Within the low strain zones of the unit, petrofabric data of one sample may suggest the preservation of a partial, remnant olivine lattice fabric.

Within unit 5, low strain, asthenospheric structures are locally preserved. Opx is coarse and only weakly recrystallized, cpx occurs as melt impregnations as well as larger grains. Spinel is intergrown with smaller opx grains.

Unit 6 displays lithospheric microstructures. Lithospheric overprint varies in intensity from low to very high. The classic development of protomylonitic, mylonitic, into ultramylonitic textures can be observed. Particularly impressive are opx ribbon grains with aspect ratios up to 100:1, as well as large, poikilitic spinel grains interpreted as porphyroblasts.

Dunite bodies in the upper part of the mantle section contain interstitial cpx, whereas those from the lower part preserve isolated opx-spinel intergrowth textures.

Two characteristic upper mantle microstructures occurring in the LH are discussed. The Springers Hill-type contains characteristic large, massive, isolated, subhedral spinel grains. The Eastern LH-type displays delicate and several millimetre-large, cpx-spinel symplectites.

3.2 INTRODUCTION

In the previous chapter it has been shown that the TM mantle section can be subdivided into several structural units. This suggests the presence of several tectonic events. Previous work in mantle peridotites has shown that microstructural studies are well-suited to define the conditions of deformation, i.e. temperature, stress, and accumulated strain (Boullier and Nicolas 1975, Mercier and Nicolas 1975, Nicolas et al.

1980, Mercier 1985, Ceuleneer et al. 1988). A characterization of the conditions of deformation is necessary to locate the geodynamic position of the structural units at the time of formation and thus put important constraints on a general tectonic model presented in chapter 6.

After a short review of the microstructural characteristics of mantle peridotites, *type microstructures* of the TM massif will be described and illustrated for each unit. The type microstructures are end-member microstructures for each unit and as such do not neccesarily represent the most widespread microstructure within a unit. However, they are thought to be characteristic for each unit, i.e. represent material which has suffered a minimal overprint associated with deformation of another unit. The microstructural variations and trends within each unit in addition to the type microstructures are discussed. Two microstructural types encountered only in the LH mantle rocks will be briefly described as a basis for a discussion in chapter 4. Pyroxenite dykes are not described. A detailed study of the pyroxenites in the LH can be found in Edwards (in prep.). Dunite banding and bands are only briefly discussed.

In a second chapter on microstructure (chapter 4), the behaviour of the constituent phases of the peridotites under varying deformational conditions is summarized.

3.3 REVIEW OF MICROSTRUCTURAL CHARACTERISTICS AND DEFORMATION MECHANISMS OF OLIVINE IN UPPER MANTLE PERIDOTITES

The volumetrically dominant phase in mantle peridotites is olivine (60-100%). As such, it is the load-bearing phase and determines the flow behaviour of the peridotites. Numerous olivine petrofabric studies have shown that, with the exception of peridotites displaying the protogranular microstructure and which are restricted to mantle xenoliths (Mercier and Nicolas 1975; see below), mantle peridotites are highly deformed.

The major process responsible for formation of preferred olivine lattice fabrics in upper mantle tectonites appears to be dislocation glide. The olivine slip systems under upper mantle conditions are well studied in synthetic (Raleigh 1968, Carter and Avé Lallemant 1970, Nicolas et al. 1973) and natural peridotite samples (e.g. Nicolas et al. 1971, Boudier 1978, Smewing et al. 1984). In addition, computer simulations present theoretical support for the postulated formation of crystallographic preferred orientations during translation glide of minerals (Etchecopar 1977, Etchecopar and Vasseur 1987).

The results of these studies suggest that, depending on the temperature of deformation, different olivine slip systems are activated (Carter and Avé Lallement 1970, Goetze 1978, Nicolas et al. 1980, Nicolas and Christensen 1987). At high and very high (hypersolidus) temperatures, the olivine slip system (010)[100] is dominant; under moderate and low temperatures, the pencil glide system (0kl)[100] is activated. In addition to the system (010)[100], activation of the system (001)[100] is suggested at very high temperatures (Nicolas and Christensen 1987). It has been reported, for example, by Smewing et al. (1984) from the Oman ophiolite, but also by Mercier (1977) and Girardeau and Mercier (1988) from "lithospheric" (term defined below) peridotites. At low temperatures, the additional activation of the system (010)[001] (Nicolas and Christensen 1987) or (110)[001] (Carter and Avé Lallement 1970) was proposed. Due to high diffusivities at high temperatures, deformation may take place by only one activated slip system (Gueguen and Nicolas 1980). A small obliquity between shape and lattice fabrics is considered as indication of a significant rotational component of strain (Nicolas et al. 1972, Gueguen and Nicolas 1980, Bouchez et al. 1983). Lattice fabrics formed during dislocation glide are related to finite strain (e.g. Nicolas et al. 1973, Toriumi and Karato 1985).

Deformation by dislocation glide is typically accompanied by recrystallization (dynamic recrystallization). Dynamic recrystallization may result in destruction of grains of unfavourable orientation for slip coupled with growth of favourably oriented grains and would thus lead to a strong fabric related to finite strain (Bouchez and Duval 1982, Urai et al. 1986). Recrystallization may occur by subgrain rotation (SGR), grain boundary migration (GBM), or nucleation (typically coupled with GBM).

During recrystallization by SGR, the neoblast orientation is related to the paleoblast orientation and the new grains are at 20-40° to the old grain. After extensive SGR, the olivine lattice fabric is somewhat weakened (Avé Lallement and Carter 1970). Recrystallization by SGR has been demonstrated in peridotites (Poirier and Nicolas 1975, Toriumi and Karato 1985, Girardeau and Mercier 1988).

Nucleation of grains associated with recrystallization has not been convincingly demonstrated for rocks (Poirier and Guillopé 1979). More recently, nucleation was proposed as mechanism operating in (coaxially) deformed peridotites (Toriumi and Karato 1985). According to these authors, the nucleated olivine grains have their [010] axis parallel to the direction of maximum shortening/compression. In the model of Avé Lallement and Carter (1970), recrystallization occurs by nucleation and the nuclei orientations are related to the stress field. In this and later studies (Avé Lallement 1975, Kunze and Avé Lallement 1981), syntectonic recrystallization is thought to represent a major process for the formation of preferred lattice orientations of olivine in the upper mantle.

Lattice preferred orientations of olivine obtained by Karato (1988) indicate that in peridotites deformed during recrystallization through GBM, grains with low dislocation densities *dominate* the lattice fabric as they consume grains with high dislocation densities (deformed grains). The orientation of the low dislocation density grains may be related to the stress field (Karato 1988, 1989b). During conditions favouring GBM as a

recrystallization mechanism, the lattice fabric could thus be related to the stress field and not to finite strain. For $T/T_m < 0.75$ and low deviatoric stresses in dry peridotites (where T - temperature, T_m - solidus, in Kelvin), the lattice preferred orientation of olivine in peridotites may be dominated by GBM (Karato 1989b). Assuming a solidus of 1250°C for the peridotites of the TM section (see section 6.4), recrystallization would occur by SGR for T >870°C. For the TM peridotites, temperatures of deformation appear to be generally above this value (see section 6.3.1).

Diffusional flow of olivine has been reported by Boullier and Gueguen (1975) for fine grained peridotites and more recently by Cooper and Kohlsted (1986) as an added deformation mechanism during hypersolidus flow. Theoretical (George 1977), field (Dick and Sinton 1979), and rheological studies (Goetze 1978, Chopra and Paterson 1981, Chopra 1986, Karato et al. 1986) support a transition from dislocation glide to diffusional flow dependant on the grain size, stress, temperature, and presence of fluid. Specifically, Karato et al. (1986) estimated that the transition to diffusional flow occurs below 0.1 to 1 MPa deviatoric stress for a grain size of 10 mm. The lowest stresses measured in the TM section (by microstructure-based piezometry, see section 3.4) lie in the 10 MPa range. Transitions in deformation mechanisms are predicted in more general terms from deformation mechanism maps (Ashby and Verral 1977).

Application of olivine petrofabric studies in combination with other microstructural observations led to a microstructural classification of peridotites which was based on spinel peridotite mantle xenoliths. Mercier and Nicolas (1975) proposed the distinction of three different microstructure types of peridotites and their cyclic behaviour. In the *protogranular microstructure*, a very weak lattice orientation of olivine is coupled with a unimodal olivine grain size and spinel-opx-cpx clusters. Protogranular peridotites are thought to represent the undeformed upper mantle. Deformation of the protogranular peridotites will yield a *porphyroclastic microstructure* of olivine indicated by a bimodal olivine distribution and strong olivine lattice fabrics. Further deformation produces a

unimodal, fine grained olivine texture consisting only of neoblasts which are either equant (*mosaic equigranular texture*) or flattened (*tabular equigranular texture*). Annealing of the equigranular texture leads to coarsening of the equigranular microstructure which is then similar to the protogranular one. However, spinels, associated with cpx and opx in the true protogranular peridotites, have become scattered during progressive deformation and will not be able to rearrange into this configuration during annealing. The annealed equigranular texture is thus called *protogranular II* and can be recognized by scattered spinel grains in an olivine matrix.

Several other classifications using different textural names have been proposed (Boullier and Nicolas 1975, Pike and Schwartzmann 1977, Harte 1977, Mercier 1985) but nothing significant has been changed in the model apart from the introduction of a rare poikilitic texture (Mercier 1985) and a fluidal textures caused by superplastic flow (Boullier and Gueguen 1975).

Based on, and adapted to, the study of ophiolitic upper mantle, Nicolas et al. (1980) proposed a classification of upper mantle tectonites into coarse equant and coarse porphyroclastic textures, fine porphyroclastic and mylonitic textures. This concept was extended by Nicolas (1986a) and Ceuleneer et al. (1988) to include a classification into *asthenospheric* and *lithospheric* microstructures.

The asthenospheric microstructure is restricted to coarse grained peridotites. It is characterized by a coarse, unimodal (Ceuleneer et al. 1988) or also bimodal (Nicolas 1986a) olivine grain size and an olivine microstructure with well defined, high angle boundaries. In contrast to the protogranular structure, the olivine lattice fabric is exceptionally strong. Features indicative of melt-impregnation are often, though not necessarily always, associated with asthenospheric microstructures. The asthenospheric microstructure is assigned to the spreading period of ophiolitic peridotites.

The lithospheric microstructure is characterized by abundant undulose extinction, tightly spaced tilt walls and low angle grain boundaries. The resulting olivine microstructure is blurred, as grain boundaries are not well defined. Neoblasts and thus a porphyroclastic texture develop from a coarse texture only after an appreciable amount of lithospheric strain (Boudier and Nicolas 1978, Nicolas 1978, Karato et al. 1980, Karato 1984). Peridotites with a low lithospheric overprint may thus still have a coarse, unimodal grain size with, however, a blurred appearance. Significant lithospheric overprint is assigned to detachment tectonics (Nicolas et al. 1980, Nicolas 1986a). The origin of lithospheric and asthenospheric microstructures is further discussed in section 6.4.

3.4 PIEZOMETRY

The size of neoblasts, as well as the subgrain size and dislocation density are proportional to the applied stress and are independent of the ambient temperature (Mercier et al. 1977, Twiss 1977, Nicolas 1978). A slight temperature dependence appears, however, to exist for wet assemblages (Ross et al. 1980). The neoblast size is the most stable stress parameter during a later, weak deformational overprint (Mercier et al. 1977, Nicolas 1978) and is thus preferable for ophiolitic mantle rocks. More than 40% strain is needed to attain a steady state neoblast grain size (Karato et al. 1980). For lower strains, the old fabric is preserved or readjustment is partial and, as a result, meaningless stress values are obtained (Karato 1984). Recent studies concerning the grain growth rate during static as well as dynamic annealing suggest that grain growth is exceedingly fast for olivine, specifically for lower temperature/higher stress conditions, i.e. in peridotites where the stored strain energy is high (Karato 1989a). Unless grain growth is inhibited by impurities, lithospheric microstructures should thus be rapidly overprinted by grain growth and the stress may be underestimated. Cordellier et al. (1981) and Nicolas (1986a) emphasized rapid annealing of olivine microstructures

under wet conditions. Mercier (1985) concluded that olivine microstructures are "inappropriate" to estimate steady state stresses because of rapid microstructural re-equilibration.

Several calibrations for the stress dependence of olivine neoblast sizes have been performed on dry and wet dunites as well as olivine single crystals (Post 1977, Mercier et al. 1977, Mercier 1980a, Ross et al. 1980, Karato et al. 1980). The data for dry assemblages are compiled in Tab. 3.1. They cluster within a factor of three with the exception of Mercier's (1980) relationship. The latter one is empirical and based on an inferred change in the recrystallization mechanism from SGR to nucleation/grain boundary migration (NGBM) in a mantle xenolith profile with increasing temperature. More recently, these data have been reinterpreted by Karato (1984) as reflecting the thermomechanical history of the peridotites and by Avé Lallement (1985) to indicate, contrary to the assumption of Mercier (1980a), an actual change in the stress conditions and not in the recrystallization mechanism. Mercier's (1980) relationship is therefore controversial.

Tab. 3.1: Selected piezometers using the olivine neoblast grain size. The piezometer of Karato et al. (1980) is used in this thesis.

SOURCE	STRESS (σ)/GRAIN SIZE (D) RELATIONSHIP (σ in MPA, D in μm)	EXPERIMENTAL RANGE (MPa)	STRESS CALCULATED FOR 100μm grain
Mercier et. al. 1977	$\sigma = 1020 D^{-0.813}$	30-1000	95 Mpa
Post 1977	$\sigma = 1900 D^{-0.67}$	80-1600	87 MPa
Mercier 1980a	$\sigma = \frac{74500}{D}$	empirical	745 MPa
Ross et al. 1980	$\sigma = 4810 D^{-0.787}$	100-1000	128 Mpa
Karato et al. 1980	$\sigma = 2087 D^{-0.847}$	25-150	42 MPa

A serious problem for piezometers is the extrapolation of data obtained under laboratory conditions to natural deformation conditions. It is only warranted if the mechanism for neoblast formation is the same during the experiment and for the natural assemblages (Nicolas 1978, Poirier and Guillopé 1979). Concerning the olivine neoblast piezometer, it is suspected that for stresses $\sigma > 200$ MPa, the predominant recrystallization mechanism is NGBM as opposed to SGR under low stresses (Nicolas 1978). The calibration of Karato et al. (1980) is preferred as it was performed entirely under conditions of SGR (Tab. 3.1). It tends to yield low deviatoric stress values for a given neoblast size. Stress determinations in the microstructure sections are based on the calibration of Karato et al. (1980).

3.5 MICROSTRUCTURES OF THE TABLE MOUNTAIN MANTLE SECTION

All microstructural observations derive from thin sections which are cut perpendicular to the foliation and parallel to the mineral stretching lineation as seen in the hand-specimen.

3.5.1 Unit 1

3.5.1.1 Introduction

Within this unit, dunites, cpx-dunites, cpx-troctolites, (plagioclase-) wehrlites, and cpx-rich harzburgites/lherzolites occur. Massive dunites occurring within unit 2 are included in this section, as they show no distinct difference from those of unit 1. Due to the wide lithological variation, four type microstructures are introduced and described for unit 1.

3.5.1.2 Type microstructure 1A: clinopyroxene-impregnated troctolite

The sample is taken from a plagioclase-cpx rich layer within the central part of the massive dunites of unit 1. The selected sample (TM 1326, Fig. 3.1) represents a

cpx-bearing troctolite.

The olivine structure is not shown due to a moderate serpentinization, but appears to represent a coarse granular structure with a weak lithospheric overprint. The average grain size is 1.5mm, the lattice fabric appears very strong (gypsum plate test). Inclusion trails in olivine are common.

Spinel occurs as generally small (250μm), moderately elongated grains with an aspect ratio < 3. A few larger grains show serpentinized inclusions. No preferred spatial association with another phase can be recognized for spinel.

Plagioclase occurs as large, elongated, but rather irregular shaped grains. Grain boundaries towards the olivine matrix tend to be concave, indicating an interstitial location with respect to the olivine matrix. Numerous spinel grains and few olivine grains are enclosed in plagioclase. In one case, spinel encloses a plagioclase grain. The internal plagioclase structure is not visible as it is altered to hydrogarnet.

An association of clinopyroxene with plagioclase is common, but cpx occurs also as interstitial grains within the olivine matrix. The interstitial grains may be at high angle to the foliation (Fig. 3.2f). Partial rims or total enclosure of plagioclase by cpx are typical. Characteristically, the morphology of cpx towards the olivine matrix is delicate and suggests an interstitial location. The complex external morphology of cpx excludes an origin of cpx by simple reaction of plagioclase with the olivine-matrix. The face of cpx towards plagioclase is more rounded than the face towards olivine (Figs. 3.1, 3.2e).

The following interpretation is based on the observation that the shape fabric defined by cpx is weak compared to that defined by plagioclase and spinel. Therefore, cpx formed later than plagioclase and spinel. A possible scenerio is that a spinel-bearing dunite containing (interstitial?) plagioclase was deformed and then impregnated with cpx. Spinel-plagioclase relationships indicate that plagioclase largely postdates spinel.

Fig. 3.1. Line drawing of type microstructure 1A, representing a clinopyroxene-impregnated troctolite. For all line drawings the following ornaments apply: black - spinel; heavy outlines with pattern of open circles or heavy dots - clinopyroxene; light outlines with a parallel, dotted line - plagioclase (internal structure not visible due to alteration); heavy outlines with dash pattern - orthopyroxene; light outlines which are internally blank - olivine; dotted lines within olivine - tilt walls; in numerous drawings, olivine grain boundaries are not shown due to alteration; light outlines with hook-pattern - amphibole (only in Fig. 3.2d); lightly dotted areas - serpentinized. With the exception of Fig. 3.7, the foliation is always parallel to the scale bar.

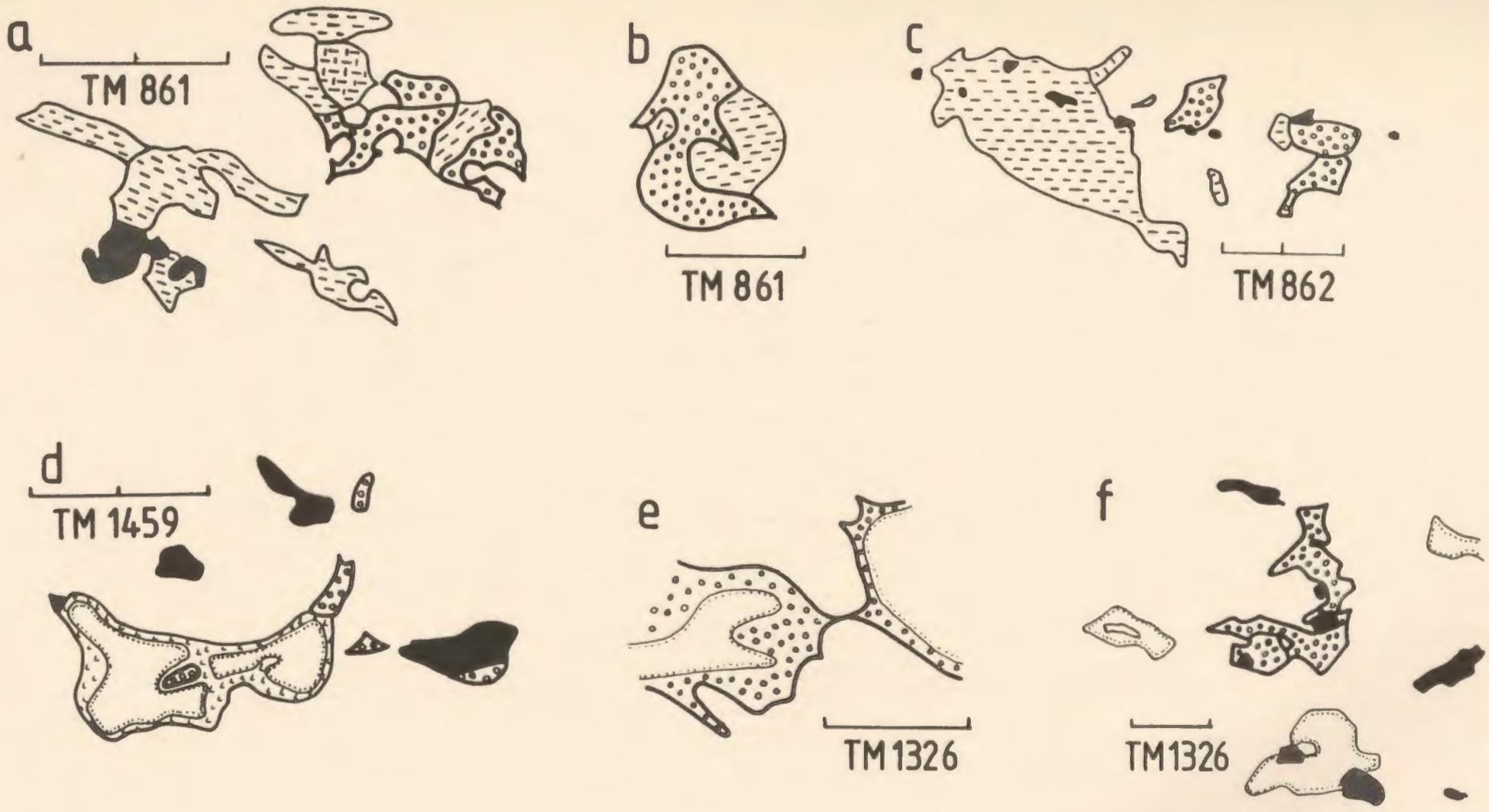

Fig. 3.2. Line drawings showing further microstructural features of unit 1. For ornaments see Fig. 3.1; for details see text. Scale bar has gradation of 0.5mm. a,b,c - harzburgite; d - dunite; e,f - plagioclase wehrlite.

The melt causing the formation of cpx appears to have been located mainly next to plagioclase or, at least, has not been able to be fully extracted from this site. Deformation following the formation of cpx was weak.

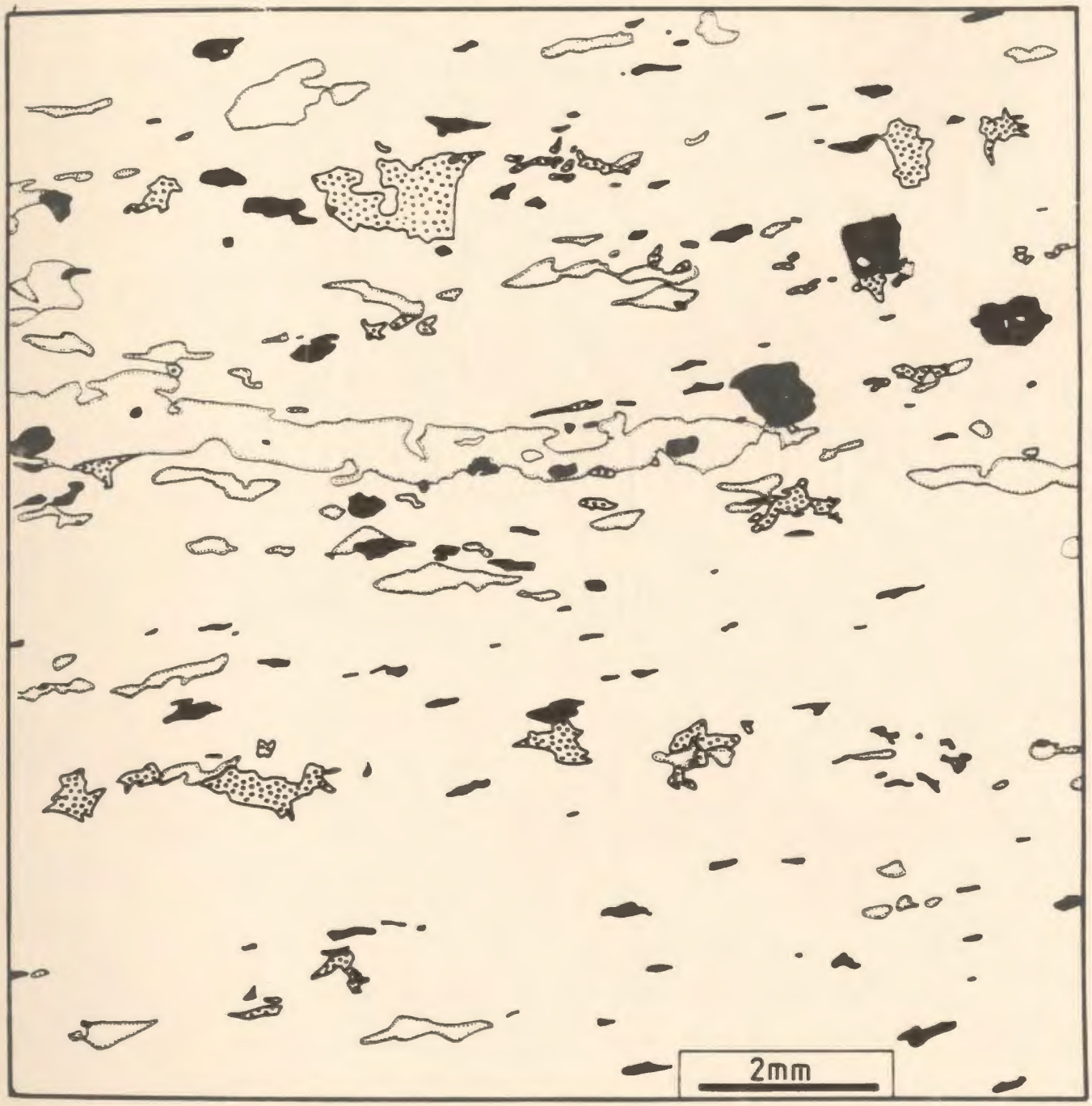

Fig. 3.3. Line drawing showing clinopyroxene-bearing troctolite. For ornaments see Fig. 3.1.

3.5.1.3 Variations of Type 1A

The sample illustrated in Fig. 3.3 shows relationships similar to the type 1A microstructure: (i) deformed spinel and plagioclase; (ii) apparently less deformed cpx; and (iii) preferred association of plagioclase and cpx. Clinopyroxene occurs also as foliation-parallel trails of irregular shaped grains. Notable are three larger, equant spinel grains with numerous inclusions which could represent original, undeformed grains. Judging from rare, less altered patches, plagioclase is internally recrystallized with a neoblast size of approximately 100μm.

In several other samples, a thin, optically continuous rim of amphibole occurs around plagioclase (Fig. 3.2d; see also Himmelberg and Loney 1980). Spinel and cpx do not show amphibole rims. The constant thickness of the rim suggests a reaction involving plagioclase. Malpas (1976) described cpx and hornblende as reaction rims between olivine and plagioclase from the layered cumulates in TM.

3.5.1.4 Type microstructure 1B: asthenospheric dunite with secondary growth

The sample is located in the western part of the massif at the base of the massive dunites. Plagioclase wehrlite layers are present nearby and are cut by another generation of dunites. Structurally, the location is part of unit 2.

This dunite (Fig. 3.4) displays a coarse, well recovered olivine microstructure with high angle grain boundaries, and poor shape fabrics. It represents a typical asthenospheric microstructure. The rare tilt walls are well-defined and straight and grain boundaries are curvilinear. 120° triple point junctions and poikilitic enclosure of spinel by olivine are common. Micron-sized inclusions within olivine are very rare. The deformed state of this sample is suggested by the simultaneous extinction of virtually all olivine grains with the gypsum plate inserted and is demonstrated by the very strong olivine lattice fabric (Fig. 3.5a). The lattice fabric indicates activation of the (0kl)[100]

Fig. 3.4. Line drawing of type microstructure 1B, representing an asthenospheric dunite. For ornaments see Fig. 3.1.

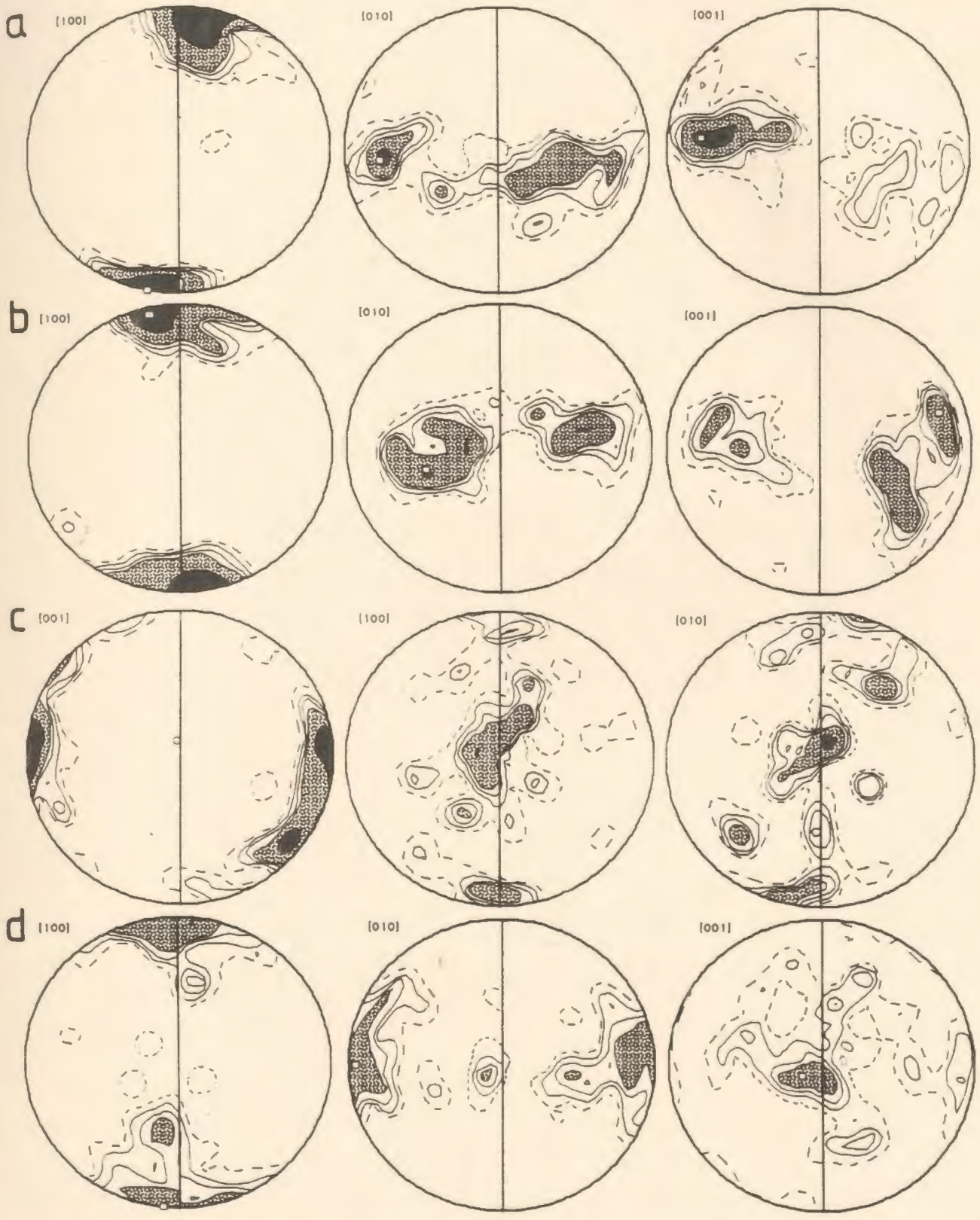

Fig. 3.5. Stereographic projection (equal area, lower hemisphere) of poles to olivine lattice orientations (a,b,d) and orthopyroxene lattice orientation (c). Contours in percent of 1% area, stepped at 1,2,3,4,8, and 16% (where applicable). One percent contour is dashed. Density maximum is indicated by open square. Foliation is oriented vertically north-south (straight line), lineation trends horizontal north-south; 100 measurements each with the exception of (c) which contains 50 data. (a) TM 1331.2; (b) TM 7.1; (c) TM 1315 (opx lattice fabric); (d) TM 862.

slip system. Spinel inclusions in olivine, as well as the rarity of micron-sized inclusion, suggest active GBM. Neoblasts (0.7mm) occur mostly in the vicinity of spinel grains. Therefore they probably do not reflect a steady state grain size (Nicolas et al. 1980).

The brownish spinels are equant to weakly elongated or more rarely irregular shaped. Characteristic are numerous, unidentified, equidimensional inclusions. Tiny clinopyroxene is rare and occurs interstitially in the olivine matrix.

3.5.1.5 Variations of Type 1B

Additional dunite samples from within unit 1 or immediately adjacent to it typically display a somewhat finer grained, porphyroclastic texture with neoblast sizes in the 0.8mm range (corresponding to σ = 7 MPa, Karato et al. 1980). Olivines contain variable, but generally high amounts of inclusion-rich patches and trails. Spinels are fine grained (~ 0.2mm) and elongated with aspect ratios of 2 to 4. Rarely, larger, anhedral spinel grains occur. Clinopyroxene is rare and interstitial. Overall, dunites and (cpx-) troctolites appear to be microstructurally gradational.

Olivine lattice orientations from a porphyroclastic sample (Fig. 3.5b) show strong orientation maxima similar to microstructure Type 1B. The incomplete girdle of [010] may either suggest the activation of a (011)[100] system or, more likely, the 100 grains measured were derived from a few, very large grains by slight misorientation during recrystallization by SGR. In the latter case, the number of grains present before recrystallization within one thin section would not have been statistically significant for the derivation of the slip plane.

3.5.1.6 Type microstructure 1C: orthopyroxene-impregnated dunite ("harzburgite")

This interesting sample (TM 1315) is located exactly in the transition from massive dunites to harzburgites with dunite layers. This zone also constitutes the transition

from structural units 1 to 2.

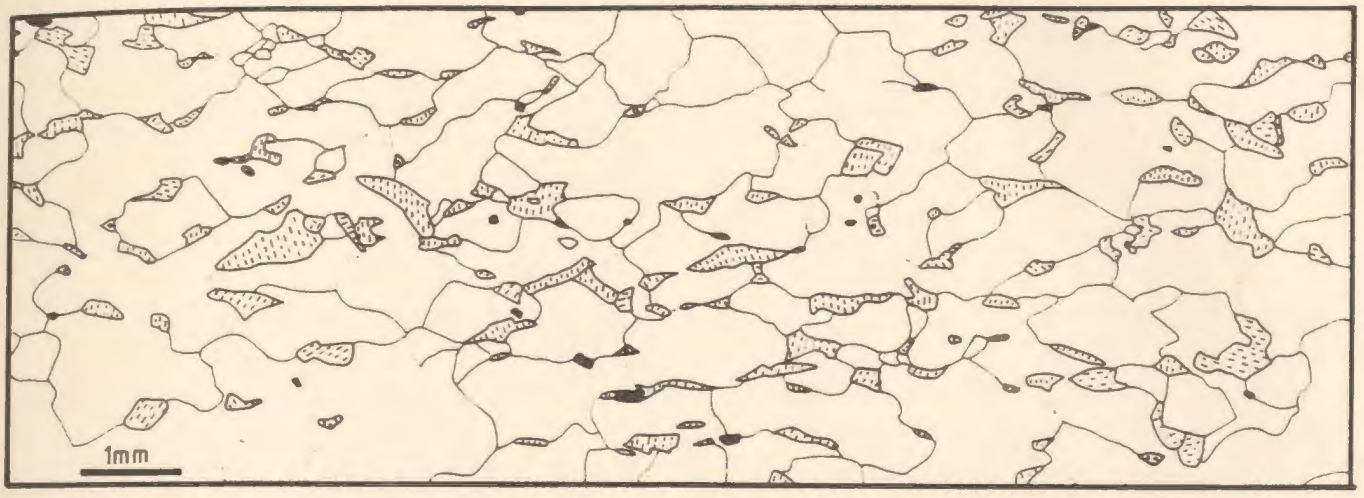

Fig. 3.6. Line drawing of type microstructure 1C, representing an orthopyroxene-impregnated dunite (TM 1315). For ornaments see Fig. 3.1.

In Fig. 3.6, the tabular equigranular microstructure of olivine is shown. The olivine structure is clearly controlled by the distribution of opx grains. In the olivine-richer part of the sample (not shown) the olivine structure is coarse granular and asthenospheric. The preferred optical orientation of olivine appears strong (gypsum plate test). Spinels are very small and sub-to euhedral or weakly elongated. Clinopyroxene occurs as rare interstitial grains in the same habit as opx.

Orthopyroxene forms elongated, attenuated, flaser-like grains. The tips of these grains frequently touch each other or point to each other. Most of the traces of the cleavage (210) and (210) of opx are perpendicular to the foliation. This is peculiar as the opx slip plane (100) lies in zone with this cleavage plane. It would therefore also be oriented at high angle to the foliation in the sample and preclude that opx has undergone a significant overprint by dislocation glide on the well established slip system (100)[001]. An opx lattice fabric analysis (Fig. 3.5c) supports these observations: the [001] slip direction lies perpendicular to the foliation, the potential slip plane (100)

forms a girdle about the [001] direction, i.e. is always perpendicular to the foliation. The preservation of delicate tips of grains and the unrecrystallized nature support a primary orientation of opx.

A formation of opx due to corrosion (i.e. residual grains of opx) during partial melting does not explain the lattice orientation. As the lattice orientation of opx is incompatible with deformation and the shape fabric resembles strongly documented melt impregnation morphologies (e.g. Nicolas and Dupuy 1984), a derivation from trapped melt is favoured. A similar habit of opx has been locally found in harzburgites of unit 2 and 3 (e.g. samples 1340, 873, 900, Fig. 3.10a,f,g; Fig. 4.3), although the characteristic morphology in these samples is restricted to a few of a large number of opx grains.

A shape fabric of single opx grains comparable to the grains in Fig. 3.6 can be seen in a garnet peridotite xenolith shown in Harte et al. (1975, Fig. 8). Recently, Cannat et al. (1990) have shown lattice orientation data from interstitial opx grains of abyssal peridotites of the Garret transform fault which are also incompatible with an origin by deformation. On the basis of platinum group element patterns of harzburgites and orthopyroxenites, Edwards (1990) proposed a melt impregnation origin for some opx grains in harzburgite.

The preferred interpretation of the type microstructure 1C is formation of an opx lattice fabric related to crystallization from a melt. The melt may either be infiltrated or locally (in-situ?) derived. In the latter case, the sample would represent a frozen-in partial melting texture. Shape and lattice fabric could either have been controlled by the stress field or by the shape and lattice fabric of preexisting olivine grains.

3.5.1.7 Type microstructure 1D: layered dunite-wehrlite-olivine clinopyroxenite

The sample (TM 860) was collected near the base of structural unit 1 from a well-layered sequence of dunite with clinopyroxenite layers, harzburgites, and lherzolites. Rare plagioclase layers also occur in the section. The sample consists of alternating bands of dunite, wehrlite, and olivine-clinopyroxenite.

The olivine structure is well preserved only in the dunitic layers (Fig. 3.7). It is coarse granular and clearly asthenospheric. Micron-sized inclusions are moderately abundant. Spinel is poikilitically enclosed by olivine. The lattice fabric is strong (gypsum plate test). In the olivine clinopyroxenitic layer, olivine is more strongly serpentinized and therefore the olivine structure is not shown.

Black spinel occurs only in dunite, cpx-dunite, and wehrlite. It is absent in olivine clinopyroxenite. In dunite, spinel forms moderately elongated (aspect ratio 3:1), small grains indicating a good shape fabric. In the transition to olivine clinopyroxenite, spinel becomes rare and more equant.

Clinopyroxene in dunite is interstitial and encloses spinel. In olivine clinopyroxenite, cpx occurs as large grains enclosing olivine. The shape of these early olivines is elliptical, 0.3 to 0.6mm long and parallel to the foliation. Some cpx displays regularly arranged tablets of tiny spinel-exsolutions.

Only two orthopyroxene grains have been (vaguely) identified.

The sample could either represent an igneous cumulate or massive cpx-impregnation into peridotite. In the latter case, olivine would represent the (compositionally modified) in-situ component of the original peridotite.

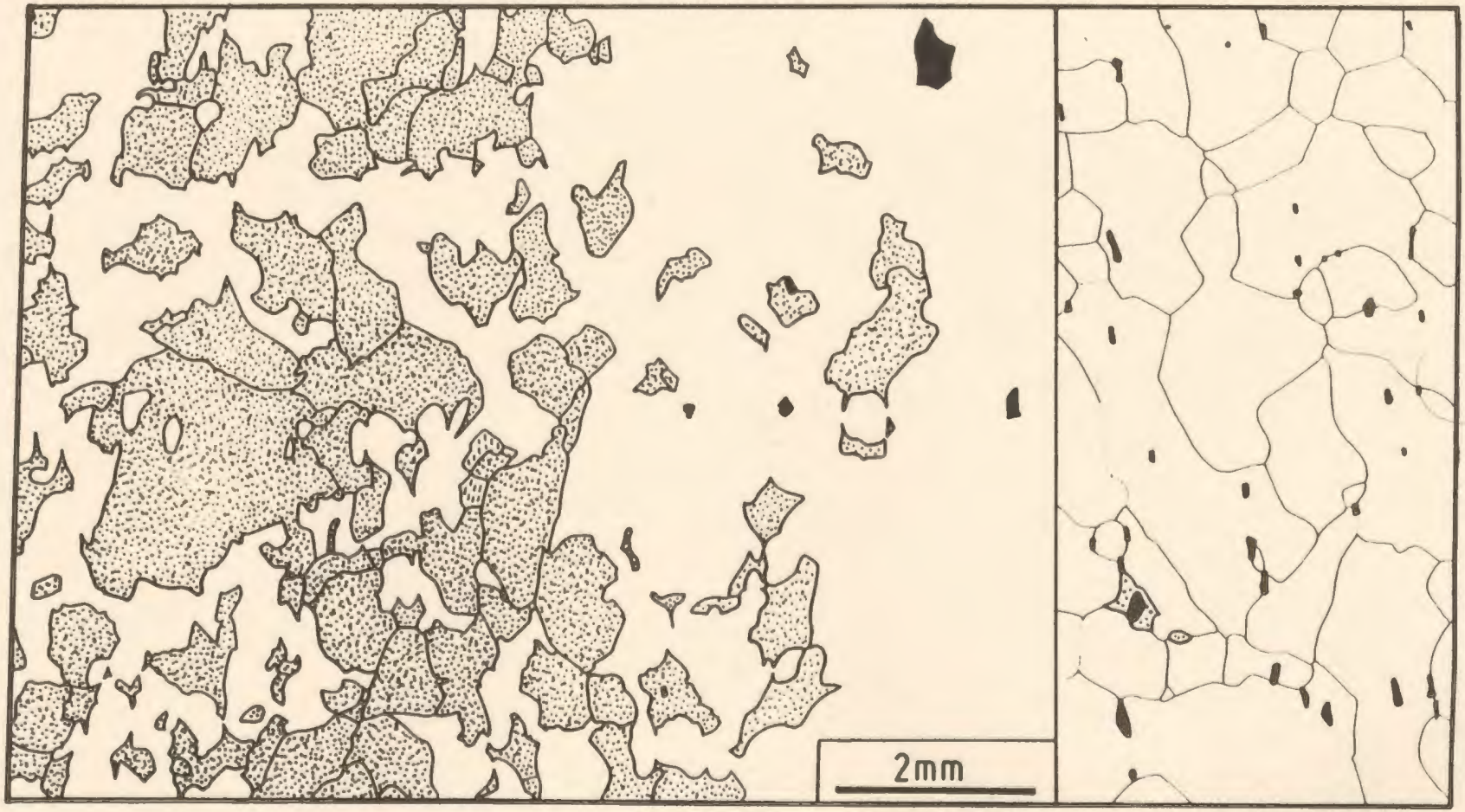

Fig. 3.7. Line drawing of type microstructure 1D, showing details of a layered dunite - wehrlite - clinopyroxenite. Olivine structure not shown in left part of drawing. In the thin section, the dunitic part shown in the right side of the drawing is spatially separated from the olivine-clinopyroxenitic part at the left side of Fig. 3.7. For ornaments see Fig. 3.1. Note that foliation is oriented normal to scale bar. Same scale for both parts of drawing.

3.5.1.8 Further microstructural features of unit 1

Along the base of unit 1, harzburgites and lherzolites occur in addition to the dunites of unit 1. They are moderately serpentinized. The olivine lattice fabric of a harzburgitic sample is very strong and orthorhombic (Fig 3.5d), indicating activation of the high to very high temperature slip system (010)[100]. Spinels within unit 1 tend to be small (varying from 0.1 to 0.3mm) and scattered. Characteristic for harzburgites from unit 1 is an association cpx-opx and sometimes amphibole-opx (Fig. 3.2a,b). Based on their irregular shape within a highly deformed matrix, cpx and amphibole may have an origin by melt impregnation. Fig. 3.3c shows one of the rare instances where an opx grain encloses a spinel trail. This indicates a high grain boundary mobility of opx or opx impregnation.

3.5.2 Unit 2

3.5.2.1 Introduction

The most characteristic microstructure of unit 2 is a high strain, high temperature, cpx-impregnated harzburgite. It occurs only in the uppermost part of the unit, both on the eastern and western side of the gabbros. It has also been located as a small tectonic sliver accreted to the base of the massif (Figs. 2.1, 2.2). The microstructural transition towards unit 3 is gradational and the description will focus on the end-member type of unit 2.

3.5.2.2 Type microstructure 2: asthenospheric, high strain, clinopyroxene-impregnated harzburgite

The type sample TM 884 (Fig. 3.8) displays a banded appearance caused by varying amounts of olivine, opx, and cpx.

The olivine microstructure is weakly porphyroclastic in olivine-rich layers and the average neoblast grain size is 0.4mm, corresponding to σ = 13 MPa. The neoblast abundance is low (10%). The olivine substructure is unblurred and consequently considered to have formed under asthenospheric conditions. This is supported by the presence of syntectonic cpx melt impregnations (see below).

In the opx-rich bands, the olivine microstructure is equigranular (Fig. 3.8). Poikilitic enclosure of opx by olivine is virtually absent, though olivine may partially enclose opx. Petrofabric data (Fig. 3.9a) suggest activation of the (010)[100] and (001)[100] slip systems.

Orthopyroxene occurs as equant grains with slightly convex or straight grain boundaries and an average grain size of 0.6mm. The grains either cluster as aggregates of several grains with well developed triple point junctions or occur in a scattered manner. A bimodal grain-size distribution is not present. All opx grains in this sample are considered neoblasts. Typical pull-apart morphologies are absent. Corroded neoblasts have occasionally been observed. The preferred cleavage orientation appears very weak. The orientation of the cleavage is, however, difficult to recognize in entirely unserpentinized neoblasts. The neoblasts typically lack any cpx exsolution lamellae.

Clinopyroxene is common (up to 5%) and occurs as trails of grains or single grains with a either a highly irregular morphology (upper left in Fig. 3.8) typical for melt impregnation or as equant neoblasts. Some annealing of the impregnations is obvious due to the presence of segments of straight grain boundaries instead of curved grain boundaries (Fig. 3.10b). The average grains size is 0.5mm.

Most cpx occurs within olivine rich zones. Clinopyroxene within opx-rich zones appears more equant and less irregular-shaped (Fig. 3.8). It will be argued that they could have formed by exsolution and recrystallization during high temperature deformation (see section 4.5.2), but an origin by impregnation cannot be excluded, as diopside growth twins of presumably magmatic origin have been found within opx aggregates.

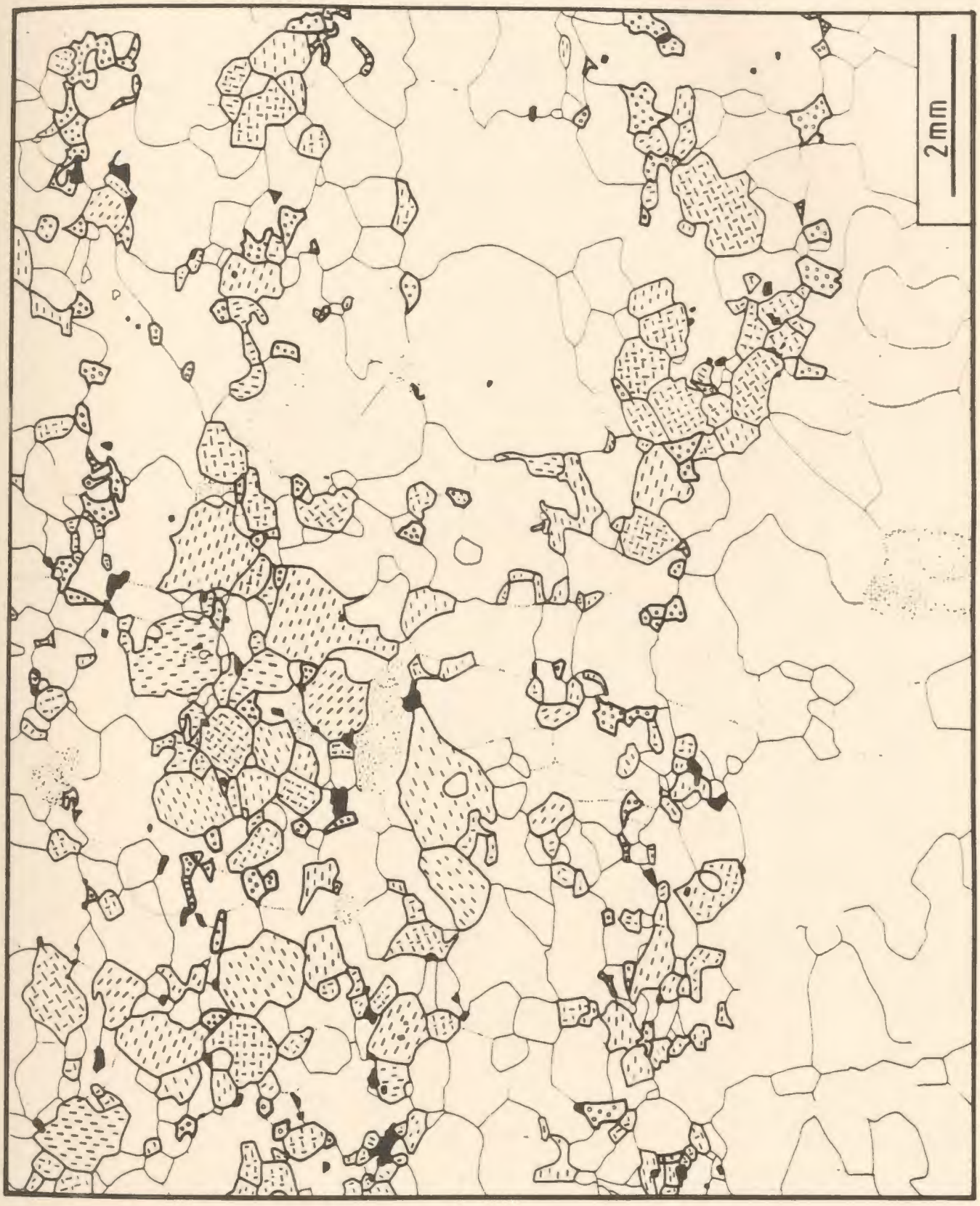

Fig. 3.8. Line drawing of type microstructure 2, representing an asthenospheric, high strain, clinopyroxene-impregnated harzburgite (TM 884). For ornaments see Fig. 3.1.

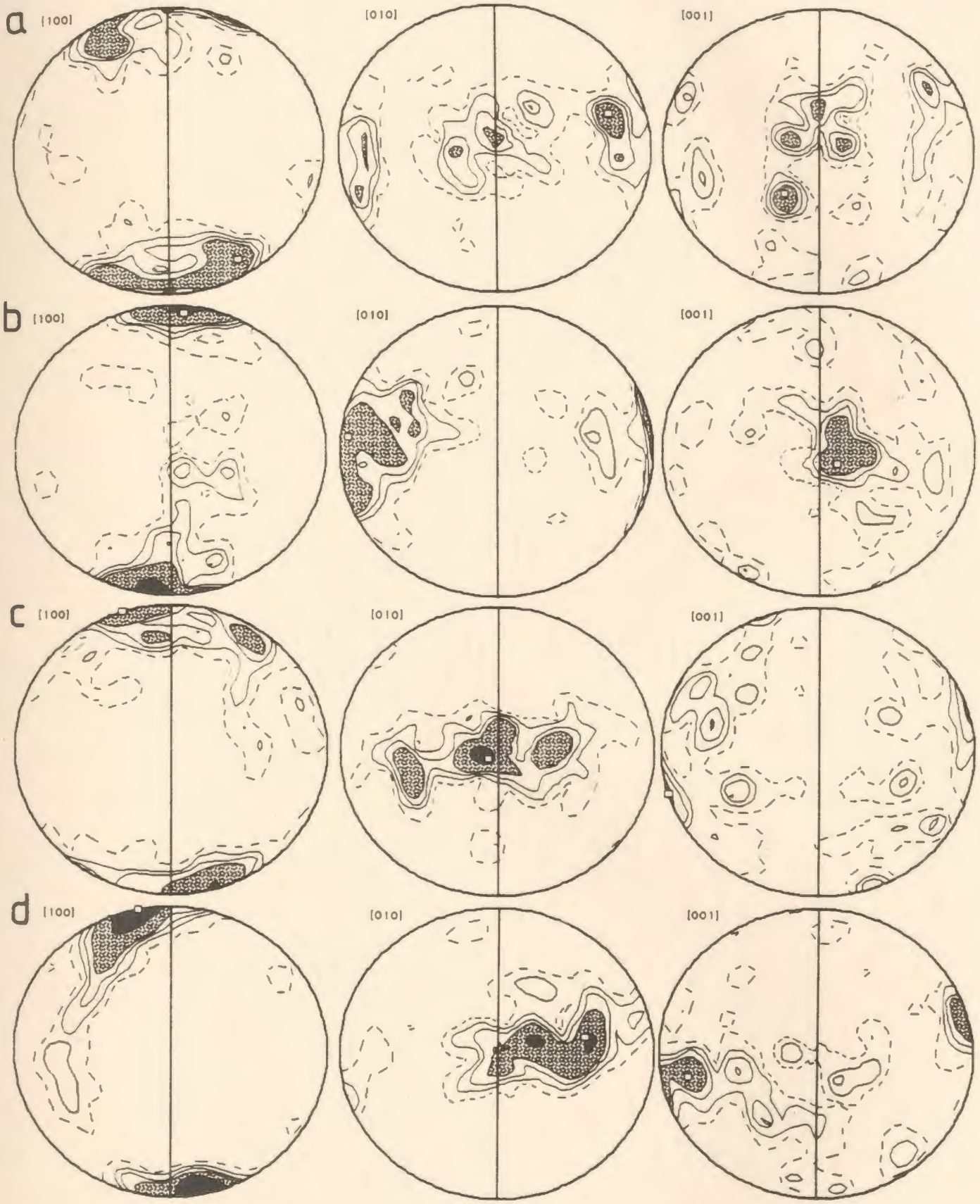

Fig. 3.9. Stereographic projections of olivine lattice orientations for the following samples: (a) TM 884; (b) TM 1428; (c) TM 1232; (d) TM 233.25. For detailed legend see Fig. 3.5.

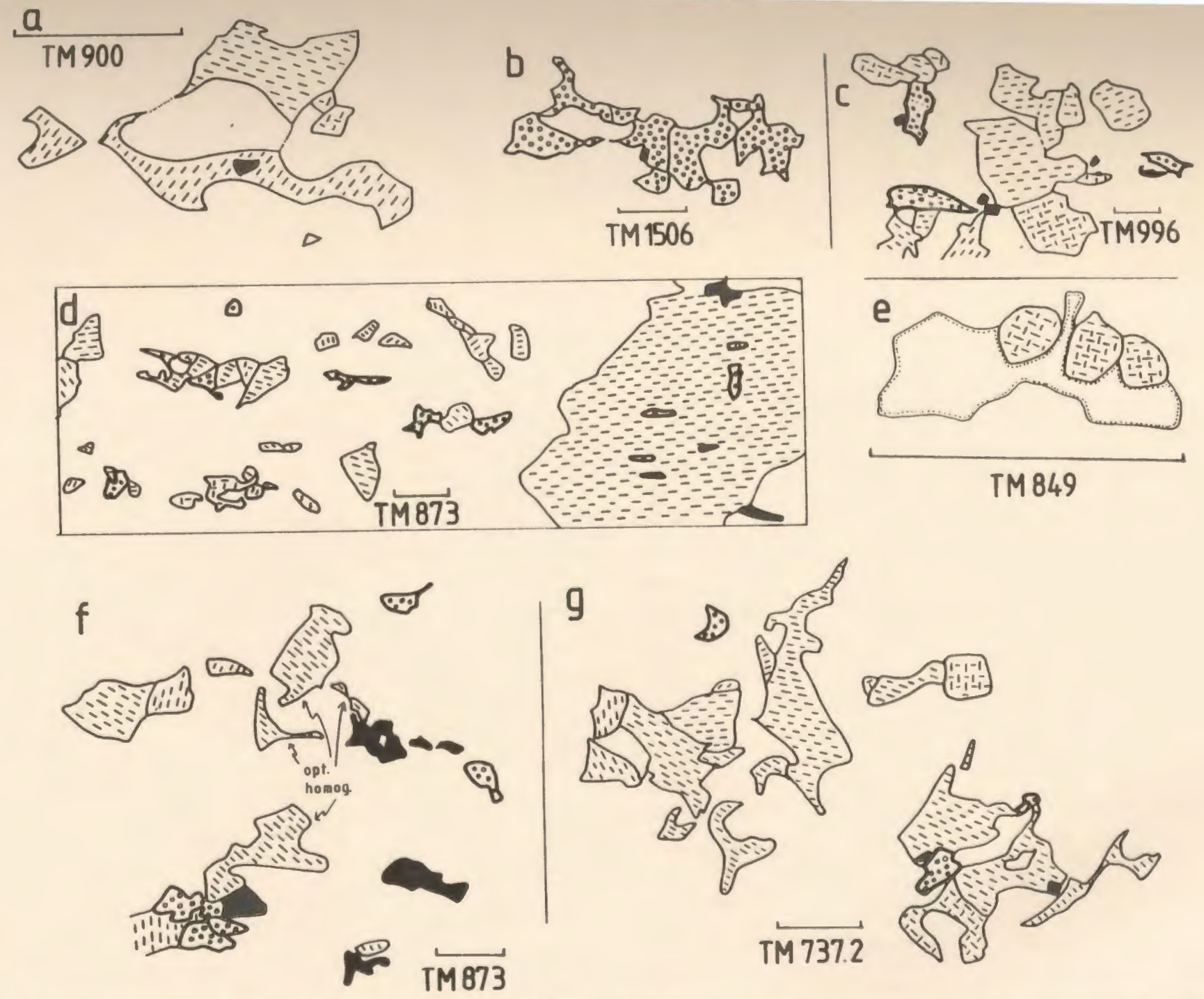

Fig. 3.10. Line drawings showing further microstructural features of unit 2. For ornaments see Fig. 3.1, for details see text. Scale bar has gradation of 0.5mm. b - dunite; all other samples - harzburgites.

Brown-red spinel occurs either as equant, sub- to euhedral grains or weakly elongated grains parallel to the general phase layering in the rock. An intricate intergrowth or association with another phase is uncommon in the type sample but has locally been observed in other similar specimens. Fig. 3.8 shows that spinel occurs preferentially in the opx-rich layers and is rare in the olivine rich layers. Such a relationship is, however, not general and many olivine rich layer have abundant spinel.

3.5.2.3 Variation within unit 2

One of the rare samples of the mantle section containing plagioclase is shown in Fig. 3.11.

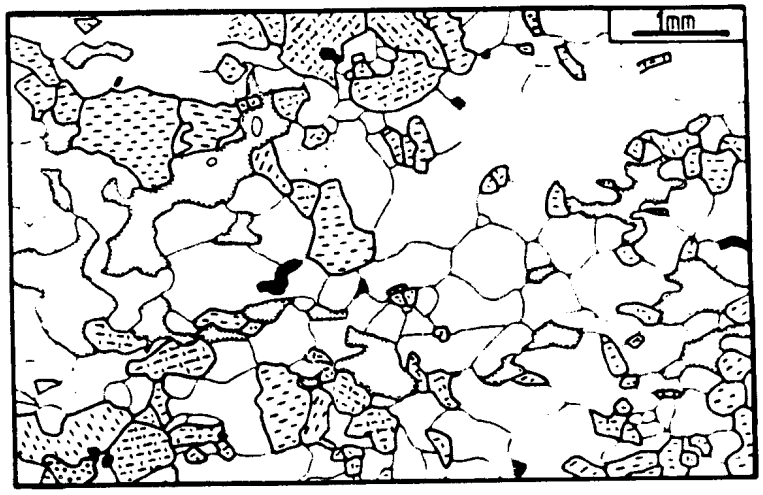

Fig. 3.11. Line drawing of asthenospheric plagioclase harzburgite. For ornaments see Fig. 3.1.

It shares the characteristic features of the type microstructure: (i) mosaic equigranular, asthenospheric olivine microstructure; (ii) highly recrystallized and scattered opx grains (neoblast size 400μm); and (iii), small, scattered spinel grains.

Clinopyroxene is, however, very rare. Plagioclase occurs as lobate grains enriched in bands parallel to the foliation It encloses opx neoblasts (Fig. 3.10e). The internal structure is not known because of an alteration to hydrogarnet.

Possible opx impregnations are restricted to the upper part of unit 2 (Fig. 3.10a,f,g). They are, however, difficult to distinguish from opx grains formed by pull-apart.

A sample from the area in the south of unit 2 (TM 1428), which shows folding of the foliation, was tested for the possible development of a new fabric due to folding. The petrofabric analysis yielded, however, only one coherent, strong olivine lattice fabric related to the measured foliation (Fig 3.9b). The activated slip system was (010)[100].

Down-section within the unit, the following trends develop and continue into unit 3

(i) opx is less recrystallized and less scattered;

(ii) a bimodal opx distribution is preserved (Fig. 3.10b). Orthopyroxene porphyroclasts may contain cpx exsolution lamellae;

(iii)grains within opx aggregates are of more irregular outline;

(iv) spinel may be intergrown with opx ± cpx; it is larger and more irregular shaped;

(v) the olivine structure is somewhat blurred;

(vi) evidence for trapped melt becomes rare.

3.5.3 Unit 3

3.5.3.1 Introduction

As the central part of the mantle section is among the most serpentinized areas of the massif, the microstructure of samples for units 3 and 4 are generally poorly preserved. The choice of the type sample was to some degree influenced by the search for a reasonably preserved olivine structure.

The sample illustrated (TM 747, Fig. 3.12) is located in the central part of unit 3 in the northern slope of the massif. It comes from an area where the lithological banding is oblique to the foliation. The foliation in the hand specimen and on cut and bleached surfaces is indicated by orthopyroxene aggregates and spinel trails and runs E-W in the illustration. Other trails and aggregates occur in orientations oblique to the foliation and the banding and the sample may represent a complex transitional stage of readjustment of passive and active markers during folding or reversals of the sense of shear.

3.5.3.2 Type microstructure 3: weakly lithospheric, lower strain harzburgite

The sample illustrated shows three typical features for the microstructure of unit 3: (i) a weakly lithospheric olivine microstructure; (ii) relatively fine grained opx aggregates in the 1.5 to 2mm range; and (iii) spinel intergrown with opx. The high content of clinopyroxene is, however, not typical for the unit.

The olivine microstructure is lithospheric and consequently difficult to illustrate. Grain boundaries are of low angle nature, undulose extinction and tightly spaced tilt walls are common. The overall appearance is blurred. The tilt wall orientation is highly oblique to the foliation and indicates a flow plane close to the lithological banding. The average neoblast size is 0.25mm which translates into a deviatoric stress of ~ 20 MPa. Fluid or solid inclusions within olivine are absent.

Orthopyroxene displays a porphyroclastic habit with a few larger porphyroclasts (2mm) and variably scattered smaller grains (0.4 to 0.8mm). The grains are less equant than in type microstructure 2. Several grains have their long axes perpendicular to the lithological banding (Fig. 3.12, Pl. 6d). They are considered pull-aparts (Nicolas et al. 1971, Darot and Boudier 1975). Interstitial grains are rare; lobate outlines occur, but are not very common. The preferred cleavage orientation is poor.

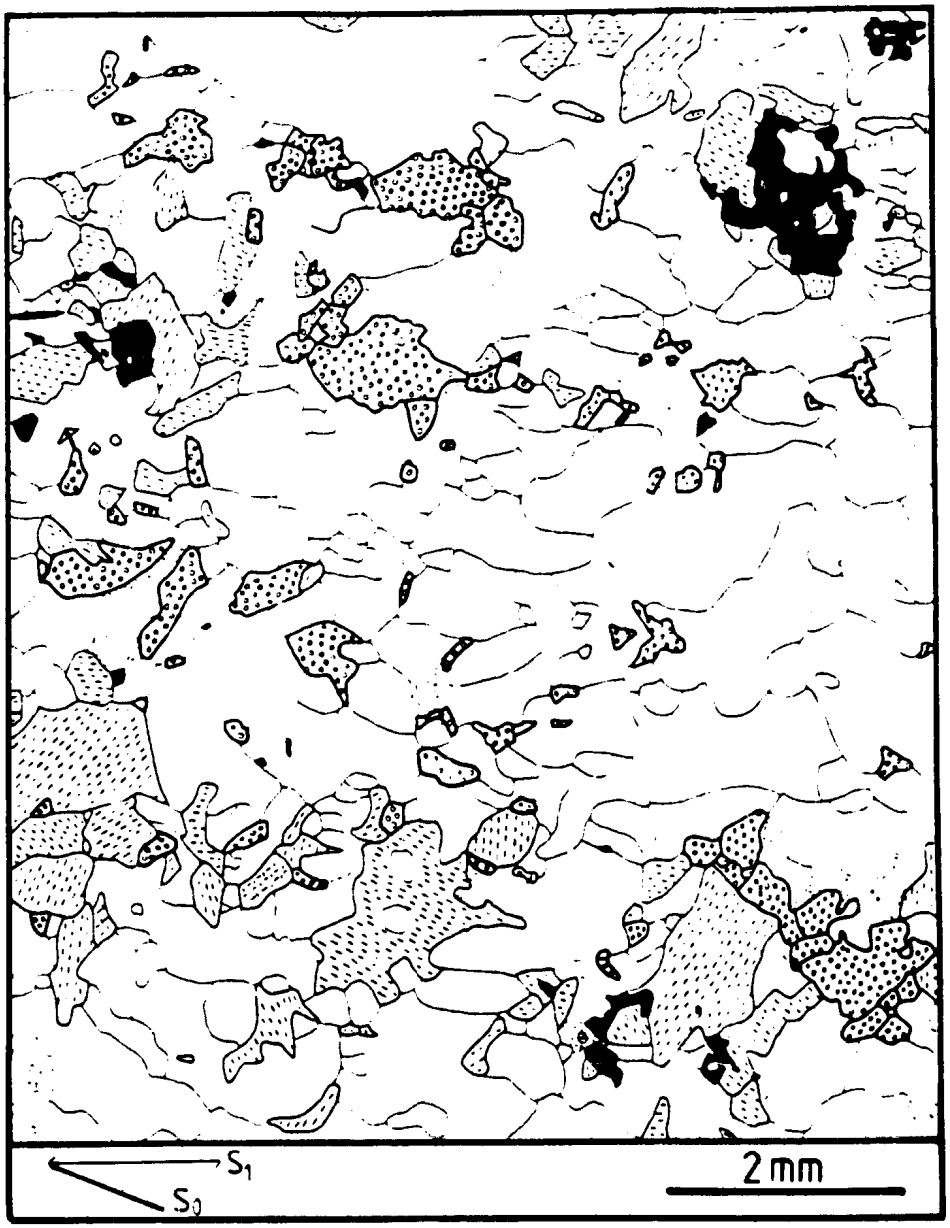

Fig. 3.12. Line drawing of type microstructure 3, representing a weakly lithospheric, lower strain harzburgite (TM 747). For ornaments see Fig. 3.1.

Clinopyroxene ranges from small interstitial grains to large (1.5mm) grains. It occurs mainly in the olivine matrix, but a few grains share faces with opx. The shape of the grains is somewhat irregular. They are variably recrystallized. An alignment parallel to the lithological banding is present. Clinopyroxene is interpreted as an annealed phase related to melt-impregnation, but a primary origin cannot be excluded.

Deep red spinel occurs typically in a fairly intricate intergrowth pattern with opx. Within this intergrowth, spinel may be present as: (i) highly irregular-shaped, large grains (upper right in Fig. 3.12); (ii) as more scattered, smaller, equant grains (upper left and lower right in Fig. 3.12); or (iii) as subhedral grains which may contain inclusions.

3.5.3.3 Variation within unit 3

An olivine lattice fabric was determined from a cpx-poor harzburgite of unit 3 (Fig. 3.9c). The sample represents one of the coarse grained peridotites located within the central part of unit 3 (Fig. 2.1). The petrofabric analysis indicates that deformation took place through the slip systems (001)[100] and (0kl)[100]. Within this specimen, a beautifully corroded orthopyroxene grain is preserved (Pl. 6e). Spinels are coarse grained and associated with opx.

In many samples of unit 3, there seems to be a large range of olivine grain sizes between 0.2 mm and 4 mm and it is difficult to recognize two distinct generations of grains (porhyroclasts and neoblasts). In the upper part of unit 3, the transition towards the microstructures typical for unit 2 sets in (see previous section). Particularly the progressive disintegration of spinel-opx intergrowth textures can be seen (Fig. 3.13). Whereas some of the scattering of opx and spinel occurred by pull-apart (Fig. 3.13, left diagram), other occurrences of the intergrowth texture show an elongation of spinel parallel to the foliation plane as shown in Fig. 3.13, right diagram). They are difficult to explain solely by deformational processes. Peridotites of the lower part of unit 3 gen-

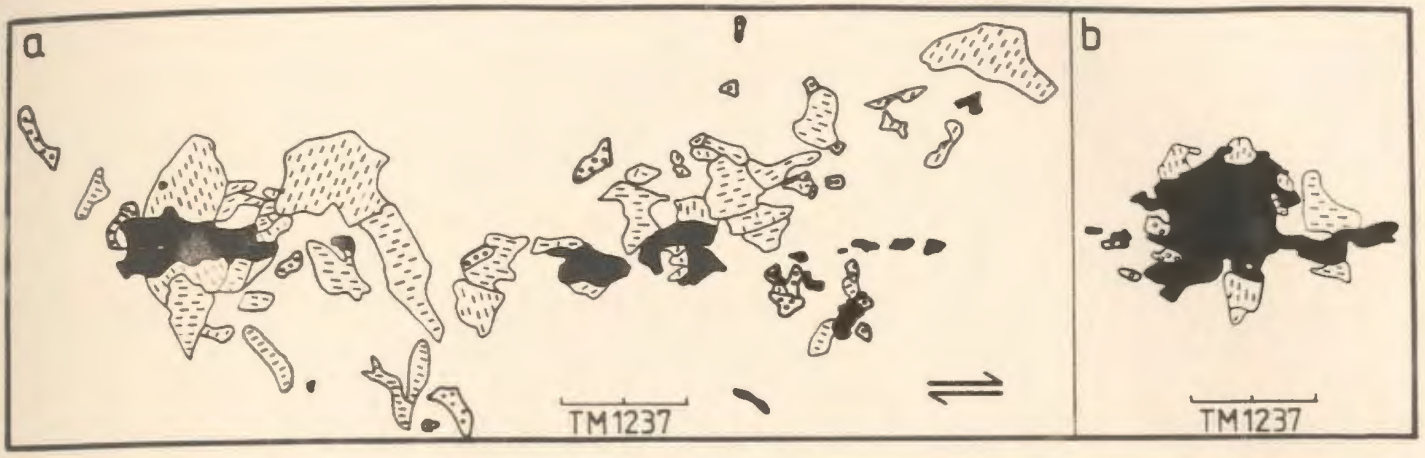

Fig. 3.13. Line drawing showing detail of TM 1237. For ornaments see Fig. 3.1. Gradation on scale bar is 0.5mm. Note scattering of the opx-spinel cluster in left diagram and the asymmetric tail of spinel parallel to the foliation in the line drawing on the right side.

erally show highly scattered opx grains of irregular shape. Pull-apart is very common and contributes to the poor fabric appearance. The olivine lattice fabric of peridotites with the poor shape fabric is, however, strong (Fig. 3.9d). The activation of the slip system (0kl)[100] is suggested. A partial girdle of the (100) plane indicates, however, some interferences. Clinopyroxene occurs in varying, generally low amounts in the olivine matrix in subequant shapes. An association with opx has been observed. The olivine structure is lithospheric. A range of grain-sizes is preserved for olivine, though in many samples a clear bimodal grain-size distribution is difficult to recognize. Spinel scattering varies from strong to weak.

No distinct microstructure was found for the high temperature shear zones occurring at the base of unit 3. This is supported by the olivine petrofabric analysis (Fig. 3.14a) which indicates the presence of the standard, high temperature slip systems (001)[100) and (010)[100]. The predominance of the former system, is, however, somewhat surprising in the light of the prediction that this system is dominant at very high temperatures of deformation (Nicolas and Christensen (1987, see section 3.3).

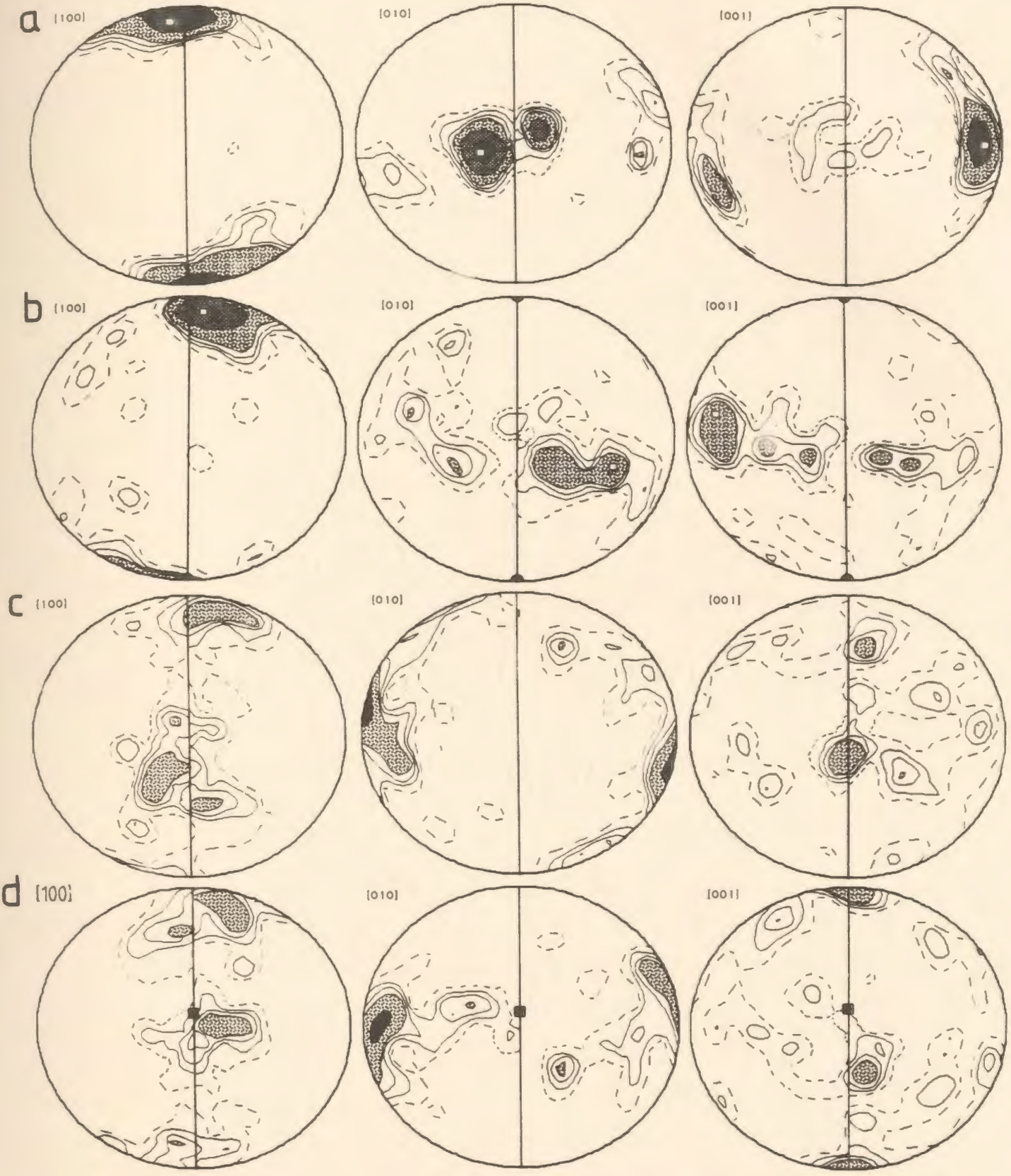

Fig. 3.14. Stereographic projections of olivine lattice orientations for the following samples: (a) TM 233.10; (b) TM 578.3; (c) TM 1100, reference frame corresponds to a field orientation of the stretching lineation of 45/0 determined in the sample; (d) TM 1100; same lattice data as in (c), but reference frame now with respect to a stretching lineation of 305/27 and same foliation as in (c). The rotated lineation of 45/0 from (c) is shown as full square. For detailed legend see Fig. 3.5.

A rare, low temperature shear zone with a flasering foliation within the upper part of unit 3 (TM 772.1) displays a classic porphyroclastic olivine texture with very well developed olivine ribbon grains and porphyroclasts (up to 4mm) and very fine grained neoblast (10-20μm). Spinel either remains unaffected during deformation or shows pull-apart morphologies; opx grains form well-developed, rounded porphyroclasts (i.e. no slipped grains are observed). Clinopyroxene grains are aligned in trails of 0.2mm large, equant grains. The presence or absence of cpx and opx in the matrix is difficult to determine. Anastamozing bands of colourless amphibole, subparallel to the foliation, consist of equant to weakly elongated, 50μm large grains (tremolite?). The shear sense can readily be deduced using S-C relationships (Lister and Snoke 1984). Rarely, similar shear zones occur within unit 2.

On the western limb of the TM synform, unit 3 reaches up to the (faulted?) Moho. In its uppermost part, delicate, irregular-shaped opx and cpx grains have been observed (cf. Fig. 4.3). They are very rare further down-section. Additional details, specifically about the spinel-pyroxene relationships, are discussed in section 4.6.

3.5.4 Unit 4

3.5.4.1 Introduction

The sample selected as type microstructure represents one of the numerous mylonitic high strain zones within unit 4. The lower strain rocks of unit 4 are microstructurally similar to the lower part of unit 3 and are not discussed in detail. Of interest is, however, a more complex olivine lattice fabric in these rocks.

3.5.4.2 Type microstructure 4: mylonitic, depleted harzburgite

Due to the fine grain size and lithospheric olivine microstructure, an illustration by photomicrographs and detailed sketches is more effective than a complete microstructure drawing.

The olivine microstructure is porphyroclastic in opx-poor areas and tabular equigranular in opx-rich areas (Pl. 6f). Lithospheric overprint is strong, the neoblast abundance high. The olivine neoblast size is ~ 100μm (corresponds to 42 MPa). porphyroclasts are often ribbon-shaped with aspect ratios of 3:1 to 5:1. Micron-sized inclusions can locally be observed in porphyroclasts. The lattice fabric (Fig 3.14b) shows a very strong maximum concentration of the (100) plane (20.9% per 1% area), slightly oblique to the lineation. The activated slip system was (0kl)[100].

Orthopyroxene aggregates are rare. Most larger opx grains occur as unrecrystallized, 0.5-2mm large, rounded porphyroclasts (Pl. 6f, Fig. 3.15a). Very rarely, these grains can be seen to have undergone moderate slip (aspect ratios < 2:1). Part or all of the margin of opx porphyroclasts may be recrystallized into a fine grained mosaic of olivine and opx (average grain size 50-100μm).

Characteristic for the high strain samples are shard-like orthopyroxene grains, elongated parallel to the foliation and with the (210) or (210) cleavage perpendicular to the foliation and elongation (Figs. 3.15a-d, Pl. 6g). This implies an orientation incompatible with activation of the opx slip system (100)[001](see section 3.5.1.6). The average size of the shards is 150x60μm. These grains occur locally in discontinuous bands or as tails to opx porphyroclasts, or, as in the type sample, the grains are dispersed throughout the olivine matrix. Where the shards are associated with porphyroclasts (Fig. 3.15a,b), they taper out within a short distance of the porphyroclasts, suggesting a genetic relationship with the porphyroclast. The grains are characterized by sharp tips which sometimes meet up with the tip of a neighbouring grain. Rarely, the shards partially enclose olivine grains (Fig. 3.15c) or are optically continuous across separating olivine grains (Fig. 3.15b). The shards remain in their "hard" orientation for activation of glide even if the associated opx porphyroclast is in "easy glide" orientation (Fig. 3.15a). Their origin is puzzling (see section 4.4.3).

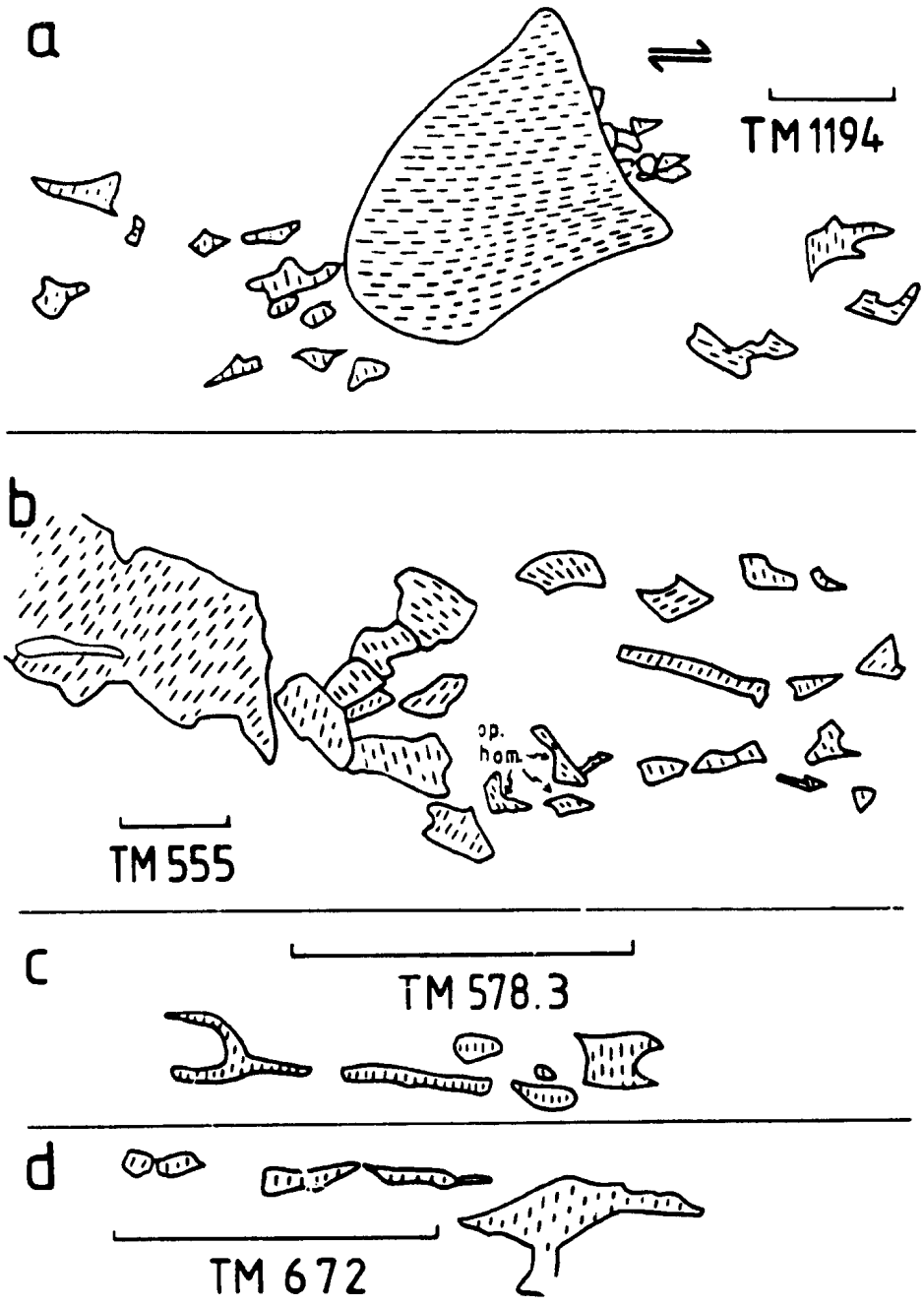

Fig. 13.15. Line drawings of microstructural features of unit 4. For ornaments see Fig. 3.1; op. hom. - optically homogeneous extinction. Gradation on scale bar is 0.5mm.

Black or red spinel shows no preferred association with another phase and occurs as scattered, anhedral to euhedral, 15μm large grains. Porphyroclasts up to 1mm are, however, locally present (Pl. 6f).

Clinopyroxene is very rare It occurs as tiny (50-100μm), elongated, interstitial grains in the olivine matrix parallel to the foliation. It can occur in a habit similar to the opx shards.

3.5.4.3 Variation within unit 4

Host peridotites to the high strain zones in unit 4 are highly serpentinized and appear to contain little new microstructural information.

Olivine shows a weakly porphyroclastic texture with low to moderate lithospheric overprint. The neoblast size appears to be in the 0.4mn. range. In higher strain rocks, the proportion of neoblasts and the amount of lithospheric overprint increases and ribbon grains are occassionally developed. In several more highly strained samples, good oblique olivine shape fabrics are developed (van der Wal et al. 1990). In such fabrics, the shape preferred orientation of olivine is oblique to the foliation defined by spinel and pyroxene grains (see Pl. 7e). They indicate a sinistral sense of shear.

A lattice fabric analysis for a low to moderately strained sample indicates a maximum of (010) near the foliation plane and thus slip mainly on (010) (Fig. 3.14c). In addition, the poles to (010)-planes form, however, a partial girdle about an axis at high angle to the stretching lineation. The [100] axis, usually a reliable indicator of the slip direction, forms a peculiar double maximum, one lying close to the lineation, the other at high angle to it. Using the [100] maximum close to the lineation, part of the data set can be explained with activation of the slip system (010)[100] during flow parallel to the measured stretching lineation of N45°W. It is suggested that the second sub-maximum of the (100) plane could represent olivine orientations related to another movement direction using the same flow plane. Rotation of the data indicates that such a flow

line, related to the second sub-maximum of [100], would be oriented towards a field orientation of the stretching lineation of N55°W, i.e. close to the stretching lineation within unit 3 (Fig. 3.14d). The petrofabric analysis may thus lend some support to the field evidence which suggests that mylonitic high strain zones of unit 4 overprinted unit 3 fabrics. In low strain domains of unit 4, however, the overprint was incomplete and a remnant olivine lattice fabric of unit 3 may be preserved.

Related to this model, the second submaximum of (100) planes may represent a generation of grains with an unfavourable orientation for slip. Such a bimodal behavior of grains during deformation has been modelled (Etchecopar 1977) and observed in experimentally deformed ice (Bouchez and Duval 1982). Alternatively, the fabric could represent deformation during mainly pure shear using the slip system (010)[100]. Such conditions produce a [100] girdle in the foliation plane (Nicolas et al. 1973, Etchecopar and Vasseur 1987). The slight asymmetry of the lattice fabric with respect to the foliation argues, however, against this model.

Orthopyroxene occurs as variably recrystallized clusters or scattered, 0.5 to 3mm large grains. There is a general tendency for large grains to show evidence for slip more frequently than small grains - a feature which is poorly understood. Possibly, strain within the ductile olivine matrix could be partitioned relatively easily around smaller opx grains whereas larger opx grains offered such a resistance to flow that they started to slip. In higher strain rocks, the opx clusters become strung out and a mosaic texture of olivine and opx develops between opx porphyroclasts.

In low strain samples, the spinel microstructure is relatively coarse (1mm). An association with opx is present only for a minority of the grains within one thin section. Grain size decreases in the higher strain rocks. Elongated grains are rare and pull-apart of spinel dominates.

Clinopyroxene is very rare and occurs as interstitial or near equant grains in the olivine matrix.

Peridotites in the south and near the base of the unit show a lower lithospheric overprint than elsewhere in unit 4, confirming the field evidence (see sections 2.5 and 2.6).

3.5.5 Transitional unit (TU)

No distinct microstructures are preserved within this transitional unit. Microstructures are similar to the moderately (lithospherically) strained samples of unit 4, though the opx grain size tends to be somewhat larger than in this unit. A detailed description is not included.

Coarser peridotites from the base of the TU to the north of the cross-fault zone have, apart from a few samples (TM 1037, TM 258, TM 259), a strong lithospheric overprint of the olivine structure. Otherwise they are similar to unit 5. This suggests that in this area the TU overprints peridotites which in the rest of the TM massif occur within unit 5.

3.5.6 Unit 5

3.5.6.1 Introduction

The most characteristic microstructures are preserved near the base of unit 5. They display a very poor shape fabric of all constituent phases. In particular, the definition of the shape fabric using the spinel orientation is not possible even in bleached hand specimens due to a lack of any spinel preferred orientation (Fig. 3.16). A spinel shape fabric is, however, present in the upper part of the unit.

3.5.6.2 Type microstructure 5: coarse, low strain, asthenospheric, clinopyroxene-impregnated harzburgite

The olivine microstructure of sample TM 1181 is weakly porphyroclastic (Fig. 3.16). The unblurred nature suggests only very weak lithospheric overprint. The neo-

blast grain size ranges between 0.5 and 1mm, corresponding to σ = 11-6 MPa. The proportion of neoblasts is low to moderate. The olivine lattice fabric is only moderately strong and suggests slip on (010) and (001) in the [100] direction (Fig. 3.17a). The (100) planes form, however, also a partial girdle subparallel to the foliation.

Orthopyroxene is volumetrically abundant. It occurs in clusters which are coarser (2-5mm) than in other units (apart from unit 6) of the massif. The degree of recrystallization varies but is generally low. Neoblasts in the clusters are irregularly shaped. Scattering of opx is moderate and pull-apart occurs frequently. Highly lobate, corroded grains are locally preserved. An intricate intergrowth of smaller grains of opx with spinel is common. Interstitial opx is rare. Locally, it is associated with cpx and spinel.

The clinopyroxene morphology is more fully discussed in section 4.5.2. Briefly, cpx occurs in three modes:

(i) as rare neoblasts (0.3mm) within the opx clusters (Fig. 3.16);

(ii) as isolated, larger grains or larger grains occurring together with opx in grain aggregates (Fig. 3.18);

(iii) most commonly as interstitial grains to olivine (Fig. 3.16, Pl. 6h), variably associated with spinel and rarely with small amounts of opx. Sometimes, micron-thin layers of cpx are preserved between olivine (Pl. 7a). In thin section, spatially separated grains of cpx may show simultaneous optical extinction, suggesting that the grains are connected in three dimensions. The interstitial cpx occurs commonly as trails between larger opx grains, aligned parallel to the foliation (cf. Fig. 4.5). They may then grade into more massive grains. Diopside growth twins have been observed. The trapped melt origin of the cpx grains described under (iii) appears well substantiated.

Fig. 3.16. Line drawing of type microstructure 5, representing an asthenospheric, low strain, clinopyroxene-impregnated harzburgite (TM 1181). For ornaments see Fig. 3.1.

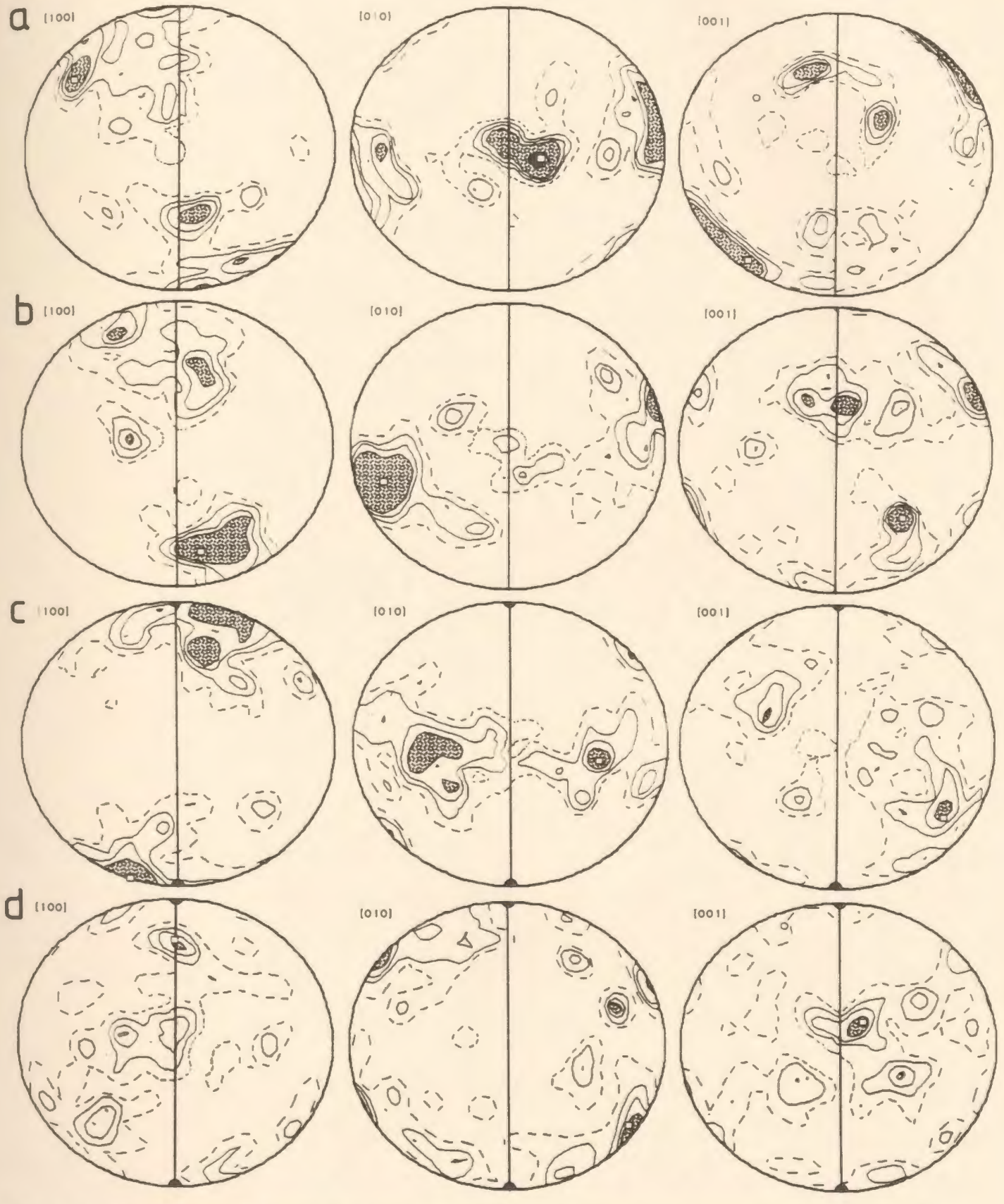

Fig. 3.17. Stereographic projections of olivine lattice orientations for the following samples: (a) TM 1181; (b) TM 1145; (c) TM 1062; (d) TM 1225. For detailed legend see Fig. 3.5.

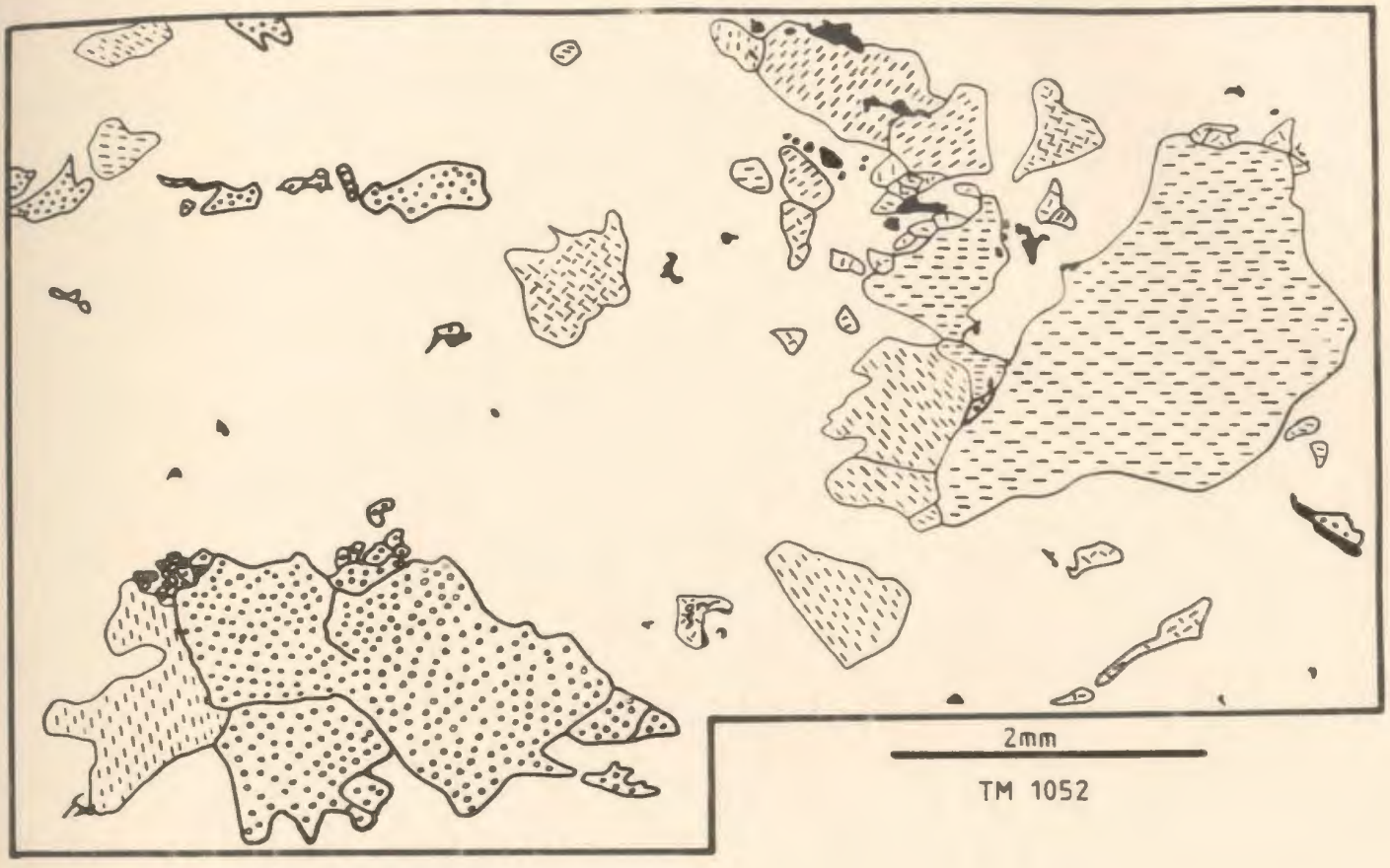

Fig. 3.18. Microstructural detail of sample TM 1052 in unit 5. Note large cpx grain aggregate in lower left and cpx trail in upper left.

Spinel occurs invariably as small (0.1-0.4mm), vermicular grains, mostly intergrown with cpx and/or opx. The characteristic association sp-cpx/opx within unit 5 will be discussed in detail in section 4.6. Recrystallized opx grains typically contain some vermicular spinel grains between the neoblasts.

3.5.6.3 Variation within unit 5

Further up-section within unit 5, the microstructures become more lithospheric and similar to those of unit 3. Specifically, spinel occurs as larger grains intergrown with opx and minor cpx or alternatively as wormy grains also associated with pyroxenes and defining a moderately strong fabric. Up-section, the opx abundance and grain size diminishes and cpx occurs as scattered grains within the olivine matrix; the grains

are less delicate than in the type microstructure. Olivine lattice fabric data from a sample in the upper part of the unit indicate no change in the slip system: (0kl)[100] with predominance of the (010) slip plane (Fig. 3.17b).

3.5.7 Unit 6

3.5.7.1 Introduction

The peridotites of unit 6 . . all affected by a variably strong, lithospheric overprint. The type microstructure is represented by a sample from the *later high strain zones* (see section 2.5) in the southeastern part of the massif.

3.5.7.2 Type microstructure 6: coarse, high strain, mylonitic lherzolite

The sample (TM 1056) constitutes one of the more extreme opx ribbon mylonites (Fig. 3.19) of the late high strain fabric. The olivine (-opx?) matrix of the sample is not shown in the line drawing because of its fine grained nature.

The olivine microstructure is tabular equigranular (aspect ratio 3:1) and has a 100x30μm average neoblast size (Pl. 7e), indicating $\sigma \sim$ 60MPa (for 65μm). The neoblast grain size changes in certain layers and lenses parallel to the foliation, indicating partitioning of strain into certain layers. Adjacent to opx porphyroclasts, the grain size can be as low as 30x10μm. The modal volume of olivine porphyroclasts is low and they show abundant tilt walls. The maximum size of olivine porphyroclasts is 1mm, the aspect ratio is <5. Inclusions are absent. As opx and cpx neoblasts in the olivine matrix cannot be distinguished with certainty from olivine neoblasts, petrofabric data were collected from an intermediate strain sample (TM 1062) having a slightly coarser neoblast size. The activated slip system is (0kl)[100] (Fig. 3.17c).

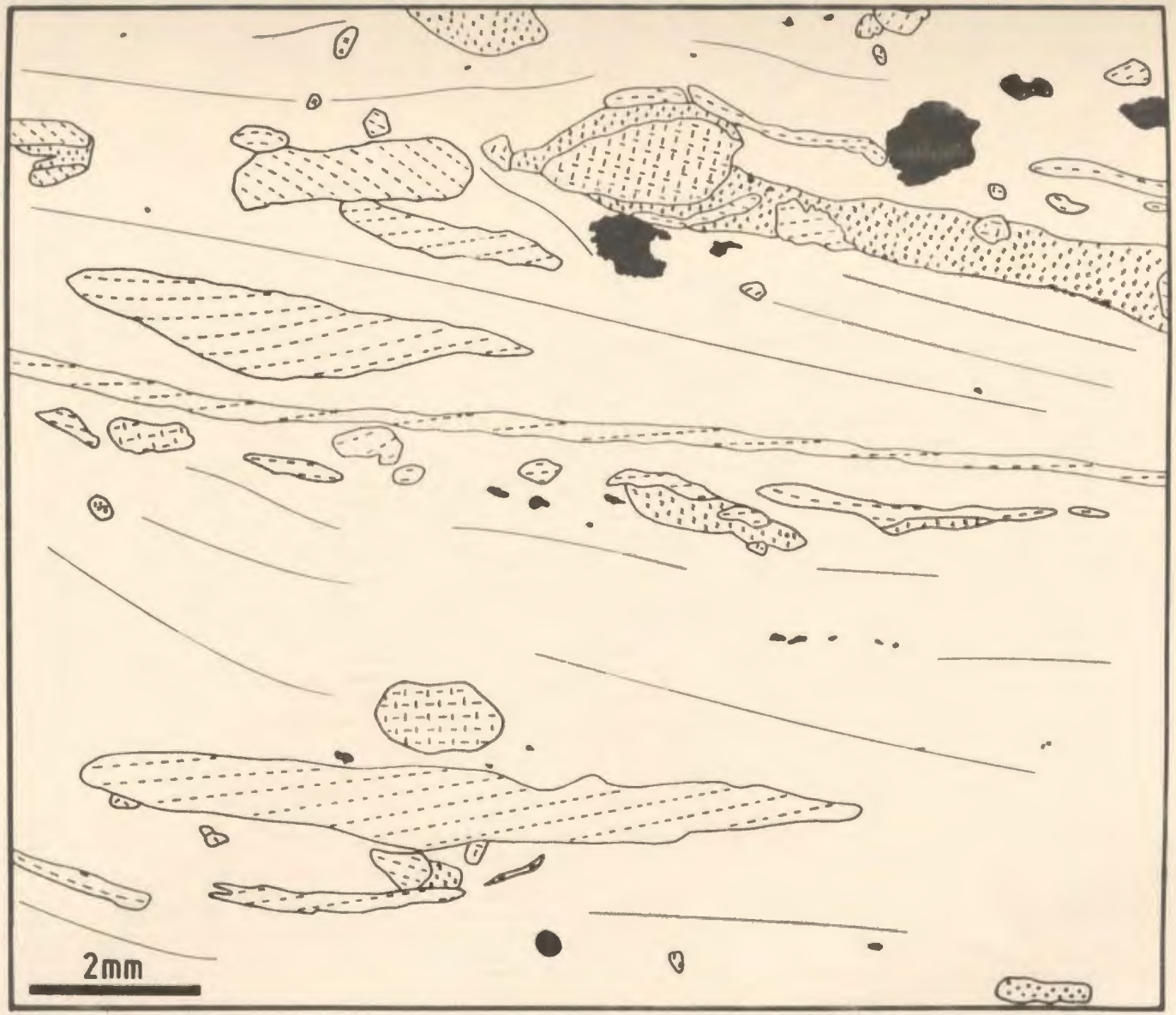

Fig. 3.19. Line drawing of type microstructure 6, representing a lithospheric, high strain lherzolite (TM 1056). The fine grained, lithospheric olivine microstructure is not shown. Instead, thin lines indicate the foliation of the olivine matrix. For ornaments see Fig. 3.1.

Three types of orthopyroxene grains can be distinguished (Fig. 3.19). These are:

(i) ribbon grains. They have an average aspect ratio of 10:1, which may, however, reach 100:1. Within the ribbon grains, the trace of cpx exsolution lamellae and the opx cleavage are invariably subparallel to the elongation of the grains and the foliation. As exsolutions of high Ca-pyroxenes from enstatite occur along the (100) plane of enstatite (e.g. Deer et al. 1966), activation of the well documented slip system (100)[001] of opx is suggested.

(ii) porphyroclasts with low aspect ratios. They have well rounded outlines and were apparently microstructurally stiff, as opx ribbon grains are bent around them. As indicated by the two visible, perpendicular cleavage traces in thin section, these grains are in a unfavourable orientation for slip and have consequently "locked up" during deformation (Etchecopar 1977, Etchecopar and Vasseur 1987);

(iii) opx neoblasts. They are in the 50μm-range and are abundant as tails to "hard" opx porphyroclasts described under (ii)), but also occur as scattered grains in the matrix.

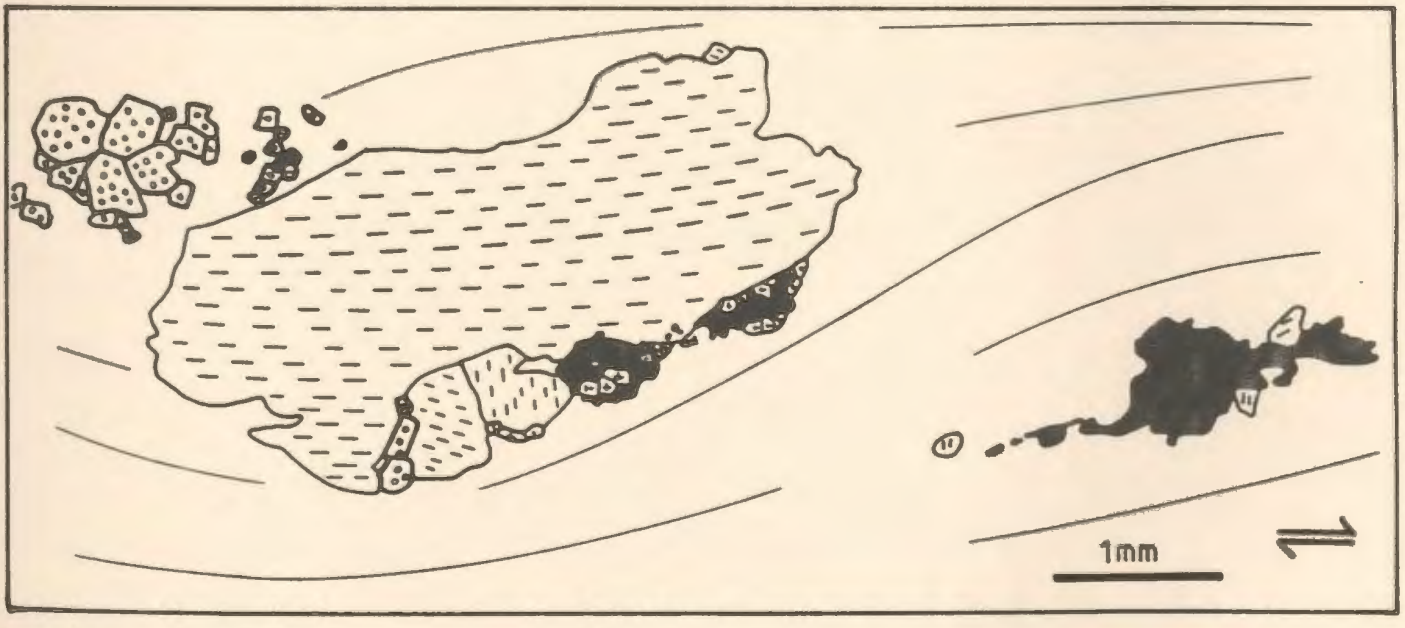

Fig. 3.20. Large spinel grain with asymmetric "wings"; sample TM 1062, unit 6. For ornaments see Figs. 3.1 and 3.19

Clinopyroxene occurs as rare porphyroclasts (up to 0.5mm). It is probably abundant as a matrix mineral, but is difficult to distinguish from olivine.

Spinel is present as tiny (20μm), wormy grains in the olivine-opx matrix. It is absent in opx porphyroclasts (Pl. 7g). In addition, it occurs as large grains (up to 1mm, in other samples up to 3mm, Fig. 7f) which partly or totally enclose olivine and opx. Several of the large grains are sometimes aligned in foliation-parallel layers. Intermediate-sized spinel grains occur as well. They are typically elongated or have (asymmetric) tails (Fig. 3.20).

3.5.7.3 Variation of type 6

Within unit 6, the low strain peridotites of unit 5 are progressively deformed into protomylonitic and then mylonitic peridotites. These two groups correspond roughly to the *early high strain fabric* and the *late high strain fabric* peridotites defined in chapter 2. A very similar microstructural sequence is beautifully illustrated by Boudier (1978, Fig. 5) for peridotites from the Lanzo massif. Characteristic is the progressively increasing proportion of olivine neoblasts (see also Boudier and Nicolas 1978).

In samples showing intermediate strain, olivine shape fabrics, oriented slightly oblique to the foliation (defined by opx), allow a rapid determination of the shear sense. Within all samples studied from unit 6, the mean neoblast size of olivine varied between 150 μm for the lowest strain samples (i.e. the samples with the weakest mineral shape fabric) and 20 μm for the highest strain samples. In specific layers of the highest strain samples, the neoblast size may be as low as 2x5μm. Even the fine grained neoblasts are elongated and the lattice fabric is very strong (gypsum plate test), so that superplastic flow as a deformation mechanism can be excluded. Stress values derived for the 150 to 20 μm range vary from 30 MPa to 165 MPa. Particularly in the lower stress samples, a second generation of olivine neoblasts with a much finer grain size seems to be present.

Within the same sequence of increasing strain, orthopyroxenes grade from large, unrecrystallized grains or aggregates of grains into the three types described for the type microstructure. In the intermediate strain facies, opx grains may be sliced up by trails of opx neoblasts. In the highest strain microstructures, all but a few small, roundish porphyroclasts have disappeared. The shard-type opx typical for unit 4 is not well developed.

In the lowest strain rocks of unit 6, clinopyroxene occurs as (i) interstitial grains in the olivine matrix located in the foliation-parallel extension of large opx porphyroclasts (Pl. 7d); (ii) as larger grains within opx aggregates, or (iii) as typical porphyroclast-neoblast association. Rarely, the simple growth twin has been observed in association with spinel (Pl. 7b, 7c). Rare clinopyroxene ribbon grains (Pl. 7f) occur in intermediate strain peridotites.

In the low strain samples of unit 6, spinel occurs as small vermicular grains or in intergrowth with pyroxenes. Large, partly poikilitic grains are only present in the higher strain samples. Characteristic is further an association of spinel with recrystallized opx $\pm$ cpx. Spinel-pyroxene relations will be discussed in section 4.6.

3.5.7.4 Further microstructural features of unit 6

In the *small scale shear zones* (see section 2.7.2), synkinematic, colourless amphibole is enriched in specific bands. In these bands, cpx is replaced by amphibole. In the type sample, which represents the widest of these shear zones encountered, opx has also been replaced. The shear zone consists of a regular amphibole-olivine banding (Pl. 8e) and pyroxenes are absent. The synkinematic amphiboles have a good preferred cleavage orientation and are 0.3-0.6mm long. Olivine neoblasts are in the 80μm range. Spinel is associated with amphibole as small (40μm), subhedral grains.

Porphyroclasts are virtually absent in ultramafic ultramylonites from the basal contact to the metamorphic sole. The average grain size is rather even for all phases present, but varies from sample to sample between 20 and 100μm. Amphibole is present in most of the ultramylonites in bands replacing cpx. Spinel tends to be brown-red, but green spinel occurs locally. It may alternate within a single thin section in bands with red spinel.

In the immediate contact area between peridotite with the metamorphic sole, interbanding of amphibolite/granulite with peridotite is observed. This interbanding is present even on the thin section scale: in sample TM 1728.3 layers of cpx + plagioclase + garnet alternate with layers of olivine + opx + amphibole + spinel, as well as with pure amphibole layers. Green spinel in this sample is granoblastic (cf. Fig. 4.13g). In adjacent samples of amphibolite, trails of serpentinized opx porphyroclasts have been observed.

An olivine lattice fabric analysis was performed for one of the coarser grained ultramylonite specimen (Fig. 3.17d). The stretching lineation direction was determined in thin section using the spinel elongation in the foliation plane. The pattern is difficult to interpret. The activation of several different slip systems is suggested. Olivine lattice fabrics are typically weaker for basal ophiolitic peridotites deformed at lower temperatures (Nicolas et al. 1980, Gueguen and Nicolas 1980, Boudier et al. 1988).

The basal peridotites from TM and Trout River have been petrologically investigated by Church (1972). He reports several exotic mineral assemblages: (i) amphibole + phlogopite; (ii) amphibole + cpx + garnet + green spinel; (iii) olivine + amphibole + opx + cpx + green spinel. Amphiboles are kaersutitic; spinel was determined as ceylonite. Malpas (1979a) argued against the interpretation of these rocks as high pressure crystallization products (Church 1972), as they are restricted to the basal mylonitic zone. McCaig (1981, 1983) reinvestigated the contact area and defined the following

assemblages: Ti-pargasite + Ti-phlogopite + ilmenite interbanded with lherzolite; (ii) pargasite + opx + cpx + olivine + spinel; (iii) relatively undeformed websterite: cpx + Ti-pargasite + opx + spinel +/- olivine +/- plagioclase. McCaig (1981) interpreted the Ti-rich peridotite as a metasomatized peridotite and the Ti-poor peridotite as an isochemically recrystallized lherzolite. The websterite could represent a "mafic" inclusion of metamorphic sole rocks (McCaig 1981).

3.5.8 Cross-cutting dunites

No systematic study was performed on the numerous dunite bodies within the harzburgites and lherzolites. There is, however, one obvious difference between cross-cutting dunites occurring within the upper part of the mantle section (units 1,2, and 3) and those within the lower part of the mantle section (unit 4, TU, and 5). The former units contain dunites with isolated, interstitial cpx, the latter ones may contain dunites with isolated opx. Whereas in the upper dunites, micron-sized inclusions in olivine are common, they are rare further down-section. Orthopyroxene from the lower dunites is intergrown with irregular-shaped spinel grains . Numerous dunites, however, contain neither cpx nor opx.

3.5.9 Postkinematic alteration

For the purpose of this study, the postkinematic alteration of minerals is of little significance and it is dealt with here only briefly.

Olivine alters readily to serpentine. Near faults and at the base of the massif, the alteration is most intense and produces a dark variety of serpentine (caused by fine grained magnetite?) which leaves opx and cpx essentially intact. In the central part of the massif (units 3,4) serpentinization is accompanied by a red-brown surface colour due to oxidation). It thus appears that serpentinization near faults and in the basal part of the TM massif was accompanied by more reducing fluids than in the central part.

Orthopyroxene is retrogressed to tremolite, talc, or, most commonly to serpentine. Chlorite formation occurred locally. Clinopyroxene is generally well preserved. A brownish oxidation, apart from the high relief, helps in its identification. Spinel may alter marginally to serpentine. Near the base (unit 5,6) and generally near late faults, a magnetite rim is typically developed. Late, postkinematic amphibole (tremolite?) occurs in patches and stringers in apparently randomly distributed samples and is then not clearly formed after a specific phase.

X-ray diffraction analysis of 12 powdered samples showed the presence of chrysotile and lizardite, but failed to detect any antigorite. The dark basal serpentine appears not to be distinct from the more greyish serpentine further up section. As an additional phase, brucite was present in most samples studied. Within the transition zone of NAM, Komor et al. (1985b) found the association chrysotile, lizardite, brucite and accessory magnetite as products of serpentinization of dunites and wehrlites. The main reaction forming serpentine seems to have involved only olivine:

$$2 \text{ olivine} + 3H_2O \rightarrow 1 \text{ serpentine} + 1 \text{ brucite.}$$

3.6 SELECTED MICROSTRUCTURES OF THE LEWIS HILLS MANTLE SECTION

3.6.1 Introduction

In addition to the microstructure types of the TM massif presented in the preceding section 3.5, two distinct microstructures of mantle peridotites have been observed in separate areas of the LH massif. Within this section 3.6, the microstructural *assemblage* of the LH occurrences is described. It provides the background for a discussion of the spinel microstructures in peridotites of the BOIC, which also includes the LH examples.

3.6.2 Springers Hill area

The geology of the Springers Hill area has been discussed elsewhere in detail (Karson 1977, Dahl and Watkinson 1986, Dunsworth et al. 1986, Edwards 1990, Suhr et al., in press). The area represents harzburgites located beneath the ophiolitic transition zone and which are intersected by numerous ultramafic dyke generations (Suhr et al., in press).

The type microstructure is illustrated in Fig. 3.21. Olivine displays a coarse granular to weakly porphyroclastic microstructure with a weak lithospheric overprint. Orthopyroxene occurs as large grain-aggregates which are highly recrystallized into subequant neoblasts with abundant tripie point junctions. The grain aggregates are not dispersed (cf. type microstructure 2). Clinopyroxene is very rare. One occurrence in the upper left of the drawing is interstitial to olivine and intergrown with minor opx. It may have formed by melt-impregnation. Alternatively, cpx is located within the opx aggregates as small grains. Spinel occurs as characteristic large, isolated, massive grains with anhedral to subhedral habit. A few grains contain some inclusions. A preferred association with another phase is not obvious.

Variations of the microstructure include mainly a stronger lithospheric overprint which results also in disintegration by pull-apart of the opx aggregates. Clinopyroxene may be associated with opx (and amphibole?) within the olivine matrix. Spinel may be associated with opx. More details are presented elsewhere (Suhr et al., in press).

3.6.3 Eastern Lewis Hills

The sampled area is a small peridotite sliver accreted to the base of the main LH upper mantle sequence during the early detachment history (Suhr and Cawood, submitted). It is exposed in the easternmost LH massif. The harzburgites of the sliver are heterogeneously overprinted by lithospheric high strain zones. The sample described represents the harzburgite with the lowest lithospheric overprint.

Fig. 3.21. Line drawing of the Springers Hill type-microstructure, representing an asthenospheric, low strain, depleted harzburgite (LH 63)(from Suhr et al., in press). Foliation is oriented parallel to long side of drawing. For ornaments see Fig. 3.1.

The olivine microstructure is coarse to weakly porphyroclastic. Olivine grains reach up to 15mm diameter, with an average of 2-5mm. They may enclose small opx grains. Localized lithospheric bands and patches are present.

Orthopyroxene occurs in clusters of grains and rare isolated grains. The average grain size of aggregates is 10mm, even single grains are coarse (2.5mm). Corrosion features can be seen in concave outward and lobate curvatures. In particular smaller grains, but also some larger ones, tend to be smoothly rounded, i.e. give an impression of resorption. Scattering of grains occuring in grain aggregates is low.

Clinopyroxene occurs in two highly characteristic modes:

(i) it surrounds smaller opx grains as an optically continuous corona (Fig. 4.5i), and larger opx grains as a partial rim. In one case a "double corona" has been observed, each corona representing an optically homogeneous rim. Whereas the shape of opx towads cpx is well rounded, the external shape of the corona appears more interstitial. Clinopyroxene occurs also as partial rim between olivine inclusions and the opx grain which hosts the inclusion. External shape and variable width of the cpx coronas exclude an origin by simple reaction between olivine and opx. At least in one occurrence, the partial rim around a large opx grain represents amphibole. Rarely, cpx occurs also as interstitial grain within the olivine matrix.

(ii) Clinopyroxene occurs as a symplectic intergrowth with spinel. The external shapes of the symplectites range from spherical (Fig. 4.12b) to irregular (Pl. 8a). The intergrowth patterns tend to be radially arranged. A spinel layer occurs commonly between cpx and the olivine matrix. The modal percentage of spinel in the symplectites averages 30% (in plane polarized light). Observations in reflected light suggest that it is actually lower. The simple growth twin typical for magmatic diopside can be seen in one occurrence (Pl. 8a). Spinel-cpx symplectites appear to be commonly located at the long edge of unequant opx clusters/grains.

Spinel occurs (i) in the symplectites described above; they may then extend as spinel tails into the olivine matrix or connect two symplectites (Pl. 8a); (ii) as large (up to 2mm) grains associated with opx; and (iii) as isolated spinel grains in the olivine matrix. The isolated spinel grains tend to be subhedral with somewhat rounded edges, but may have tails extending into the olivine matrix (Fig. 4.7f).

4 MICROSTRUCTURE, PART 2: MICROSTRUCTURAL PROCESSES AND IMPLICATIONS FOR THE FORMATION OF UPPER MANTLE PERIDOTITE

4.1 SUMMARY

The microstructural behaviour of orthopyroxene, clinopyroxene, and spinel under varying upper mantle conditions in harzburgites, lherzolites, and dunites of the TM and LH mantle section is discussed. A first estimate of the conditions of deformation can be obtained using the known microstructural behaviour of olivine.

The microstructural behaviour of orthopyroxene can be correlated with the temperature of deformation. Slip and pull-apart are the preferred responses to moderate and high temperatures of deformation, respectively. During very high temperatures of deformation, opx is observed to recrystallize, or undergo corrosion and have an origin by melt impregnation. Ambiguous opx microstructures are, however, common.

Evidence for an origin of clinopyroxene by melt-impregnation is abundant. Interesting melt-related morphologies of cpx include the location in pressure shadows of opx and spinel grains, trails of cpx grains parallel to the flow plane, and (partial) coronas of optically homogeneous cpx around opx. Apparently, the TM peridotites have been re-enriched by formation of cpx during melt infiltration.

The spinel microstructures are divided into 7 different morphological/genetic types. The types are classified by considering the total mineral assemblage and inferred pre-exsolution assemblages. During high melt flux a progressive reconstitution of the microstructure occurs. Spinel grains are located in the olivine matrix as large, massive grains which contain numerous inclusions (F-type). Chemically, a magmatic system is approached. The I-type spinels (impregnation-origin) occur as small, interstitial grains associated with cpx. They relate to entrapment of melt. However, complex processes

occuring before, during, and after entrapment make it unlikely that the spinel-clinopyroxene assemblage represents pristine melt. Residual spinel (R-type) forms due to melting of pyroxenes and is morphologically identified as spinel intergrown with large opx aggregates.

Metamorphic spinels are present as exsolutions from pyroxenes (E-type) and large, poikilitic porphyroblasts (P-type). They develop preferentially during lower temperature overprint and high degrees of recrystallization in lherzolites. Deformation may overprint each of the above spinel types. It leads to scattering, pulling apart, asymmetric porphyroclasts, and elongated grains (D-types). Magmatic spinels (M-type) have not been studied in detail.

Numerous problematic pyroxene-spinel symplectites are probably the result of spinel exsolution from pyroxenes. The precursor grains to the symplectites, i.e. the grains before spinel exsolution, are thought to be melt-related. The microstructural spinel types can be brought into a genetic scheme developed with the help of mineral chemistry data (chapter 5). It distinguishes three principal magmatic processes during peridotite formation: progressive partial melting, melt-flushing, and entrapment of melt.

4.2 INTRODUCTION

The microstructural variation within the TM and LH massifs (see chapter 3) offers, together with the available field control, an excellent opportunity to study the response of the constituent phases of the peridotites to changing physical and chemical deformational parameters. Current concepts of upper mantle dynamics (sections 1.1.2 and 1.1.3) suggest that mainly four parameters will dominate a microstructural pattern in mantle peridotite:

- plastic deformation under asthenospheric or lithospheric conditions;

- partial melting due to overstepping of the solidus;
- melt migration resulting in reaction of melt with host rocks and trapping of melts;
- exsolution and reaction due to re-equilibration to changing PT conditions.

It will be shown that the four phases in the mantle peridotites have a variable record for each of these components. Olivine, for example, shows little morphological evidence for partial melting and melt migration, although the variation in the forsterite-content (chapter 5) suggests that the phase is undergoing modification during partial melting or reaction with melt. Olivine is, however, well suited to characterize conditions of deformation as it is the load-bearing phase in the peridotite.

Spinel, on the other hand, shows a wide range of morphologies which are difficult to reconcile with an origin by deformation. As spinels appear rheologically hard (e.g. Christiansen 1986) and spinel is commonly intergrown with rheologically stiff pyroxenes, strain does not readily overprint morphologies of spinel-pyroxene intergrowth textures. As indicated by the extreme range in chemical compositions within mantle peridotites (e.g. Malpas and Strong 1975, Dick and Bullen 1984), spinel is chemically, and - as I will try to show - also a morphologically active phase during hypersolidus conditions and a potentially powerful indicator of hypersolidus processes.

The main problem in the interpretation of spinel morphologies is the distinction between hypersolidus and subsolidus (metamorphic) processes. In order to circumvent this problem, the emphasis in the interpretation of spinel morphologies is put on the *assemblage* of spinel with other phases, not on the detailed morphology of spinel itself. For example, melt might conceivably crystallize as cpx-plagioclase clusters within residual peridotite and subsequently reequilibrate to a cpx-opx-spinel cluster due to chemical re-equilibration with host peridotites. As a result of re-equilibration, spinel within the cluster may be chemically identical to spinel occurring outside the cluster in a different assemblage. However, the *assemblage* cpx-opx-spinel still preserves evidence of an early phase of trapping of melt.

McKenzie (1984) has shown that during oceanic spreading, peridotites may lie above their solidus during the entire ascent in the upper mantle until the base of the Moho is reached. In order to understand ophiolitic peridotite microstructures, a knowledge of the equilibrium distribution of basaltic melt in peridotite is therefore required. Waff and Bulau (1979) were able to demonstrate that basaltic melt is distributed along all corners and edges of olivine grain boundaries in dunite, thus allowing an excellent melt connectivity and rapid melt extraction. The melt morphology under hydrostatic conditions is geometrically defined as concave outward towards olivine, the curvature being constant. In later experiments, the influence of pyroxenes in peridotite on this equilibrium distribution was tested. These studies are controversial as they suggest either that melt is absent in olivine-olivine-opx edges (Toramaru and Fujii 1986) or stable (Fujii et al. 1986). The presence of water allows the wetting even of opx-opx-opx *edges*, but all opx grain *faces* will remain dry (Fujii et al. 1986). The presence or absence of melt in edges containing opx has important implications for the connectivity in harzburgites and the efficiency of melt extraction. In any case, the smaller dihedral angle of olivine with respect to pyroxenes will result in better connectivity of dunites compared to harzburgites (Toramaru and Fujii 1986). The results of these studies can be used to identify trapped melt in natural peridotites. Recently, experiments have been performed under non-hydrostatic stress conditions. They have shown that rapid grain boundary migration during hypersolidus conditions may stabilize melt along *all* grain boundaries (Bussod and Christie 1984, Green and Borch 1990). The melt appears to form an an anisotropic network oriented at 30° to the principal compressive stress direction (Bussod 1990).

4.3 MICROSTRUCTURAL BEHAVIOUR OF OLIVINE

The well known microstructural behaviour of olivine has been reviewed in section 3.3. Some problematical aspects concerning the olivine microstructures will be dis-

cussed in this section. The classification of olivine microstructures into lithospheric and astnenospheric is evaluated in section 6.4. Other critical elements of the microstructural behaviour of olivine (e.g. during hypersolidus flow) are not well enough understood to warrant a discussion.

As expected, the dominant slip system in olivine of the TM peridotites was (0kl)[100]. Little evidence was found for the notion of Nicolas and Christensen (1987) that (001) becomes the preferred slip plane during very high temperatures of deformation (hypersolidus conditions). On the contrary, the (001) slip plane appears to dominate even under some lower temperature conditions (e.g. Fig. 3.14a), as suggested also by Girardeau and Mercier's (1988) data. A clearly different lattice fabric was only obtained for an ultramafic ultramylonite, but the fabric is poorly understood.

The large majority of olivine lattice fabrics determined are monoclinic and support the concept that deformation within the TM upper mantle section occured with a significant component of non-coaxial strain. Shear sense determinations using the tilt walls of olivine (section 1.5) are rapid and consistent with petrofabric and field evidence. The tilt wall method seems less reliable during the special circumstances in which a shear sense reversal has occurred, but the shear plane has remained constant (see discussion in section 6.12.2). It also appears that for an area preserving hypersolidus microstructures, consistent shear senses are more difficult to obtain. The reason is not yet fully understood.

Possible evidence for remnant olivine lattice fabrics within sample TM 1100 have already been discussed (section 3.5.4.3). This evidence must, however, remain speculative, particularly because of a problem affecting all olivine lattice data. This problem concerns the number of *independent* olivine grains measured within one thin section. The term "independent" refers to large grains which are not part of a cluster of optically related smaller grains. Such olivine grain-clusters could easily form by minor recrystallization of a formerly larger host grain. Consequently, the measurement of 100

grains within one thin section may relate to only 10 or 20 "original" grains - a number which is statistically doubtful. Several of the olivine lattice diagrams represent a peculiar preference of a particular slip plane, e.g. (011) in TM 1331.2 and TM 7.1 (Fig. 3.5a,b) instead of the expected girdle distribution. Only the spatial distribution of optical axes within a thin section could clarify this problem.

The amount of magmatic versus residual olivine in mantle peridotites is not known and is a matter of debate (e.g. Nicolas and Prinzhofer 1983). Whereas cpx has been found to occur in morphologies typical for melt trapped within peridotite (section 4.5.2), such morphological analogues of olivine have not been detected in the TM peridotites. The high grain boundary mobility of olivine (Karato 1989a) and the easy serpentinization of olivine grain boundaries may be two reasons for the apparent scarcity.

4.4 MICROSTRUCTURAL BEHAVIOUR OF ORTHOPYROXENE

4.4.1 Introduction and review

Orthopyroxene typically constitutes 15-25 vol% in the peridotites of the TM section. Therefore, it does not constitute the load-bearing phase during deformation. Its microstructural behaviour is not only influenced by the ambient conditions of deformation, but also by the viscosity contrast to the surrounding olivine matrix. The relative difference in viscosity between olivine and opx may vary as a function of temperature, stress, and strain-rate. This represents a problem in studying the opx microstructures in olivine-rich peridotites over a wide range of natural deformational conditions, as the opx behaviour is dependent to some degree on the (changing) viscosity contrast with the olivine matrix. Note, for example, how the temperature - strain rate curves for websterite and dunite intersect each other (Fig. 6.3a). The advantage of studying "disseminated" opx lies, however, in the possibility of calibrating the

deformation conditions of opx with the microstructural features of the olivine matrix. The microstructure of orthopyroxenite dykes (Etheridge 1975) in the mantle section has not been studied in detail (see, however, Edwards, in prep.).

Experimental studies have demonstrated that opx is rheologically harder than olivine (Kohlsted and Vander Sande 1973, Carter 1976, Ross and Nielsen 1978), as well as more resistant to recrystallization (Kohlsted and Vander Sande 1973, Carter 1976, Mercier 1985). Recrystallization under upper mantle conditions occurs only at very high temperatures (Nazé et al. 1987). The orientations of neoblasts lie close to the paleoblast orientation (Basu 1977), probably at an angle of about 30° (George 1975, Mercier 1985). The rheological hardness is microstructurally seen in pull-apart behaviour (Nicolas et al. 1971, Darot and Boudier 1975, Etchecopar 1977, Basu 1977, Suhr et al., in press) and bodily rotation of grains (Etchecopar 1977, Mercier 1985) and in the field as boudinage of orthopyroxene-rich dykes. According to Mercier (1985), it may be extremely difficult for pyroxenes to recrystallize within a rheologically weak olivine matrix under normal upper mantle conditions.

Slip on the "easy" glide system (100)[001] is frequently observed (Etheridge 1975, Gueguen and Boullier 1975, Carter 1976, Nicolas and Poirier 1976, Basu 1977). Other reported slip systems are (010)[001] and (100)[010] (Nazé et al. 1987, Ross and Nielsen 1978) but their conditions of formation are poorly constrained. Under special circumstances superplastic behaviour has been demonstrated (Gueguen and Boullier 1975). The long debated orthoenstatite - clinoenstatite conversion occurs only under low T/high σ conditions which are rarely realized in nature (Raleigh and Kirby 1971). During the transformation, dramatic softening of opx can occur (Nazé et al. 1987). In accordance with the hard nature of opx, lattice fabric data for high temperature mantle conditions are generally weak and stronger lattice fabrics tend to occur only at lower T, high σ conditions (Nicolas et al. 1980, Mercier 1985).

Using the evidence from protogranular mantle xenoliths, where opx-cpx-spinel clusters are interpreted as the most primitive grain configuration (Mercier and Nicolas 1975), opx aggregates of similar size in the TM section are considered as relatively primitive associations. The reduced amount or absence of cpx in the TM clusters is probably the result of partial melting (Nicolas 1986a).

The microstructural behaviour of opx will be discussed as a function of the temperature of deformation. The latter one is estimated, together with other deformational parameters, for the entire TM section in section 6.3 (see Fig. 6.2). Higher temperature features will be emphasized in the following discussion. Lower temperature microstructures are discussed in more detail by Etheridge (1975) and Basu (1977).

4.4.2 Response to low temperatures of deformation

Low temperature plastic deformation is seen in rare shear zones in the lower and upper part of units 2 and 3, respectively (see section 3.5.3.3). The shear zones contain anastomozing bands with syntectonic, very fine grained amphibole. Orthopyroxene grains are sharply folded or kinked and show no recovery or neoblast formation in the hinges (Fig. 4.1-LT). Only minor grain elongation by slip seems to have occurred. The opx grains are scattered and appear to have been rigidly rotated as deduced from deflection patterns of the neighbouring olivine matrix. Orthopyroxene grains tend to be well rounded.

4.4.3 Response to moderate temperatures of deformation

Based on a strong lithospheric olivine structure, deformation in the basal unit 6 occurred between 800-1000°C (Nicolas 1989). Within unit 6, opx grains deformed by dislocation glide and formed ribbon grains with aspect ratios up to 100:1 (Fig. 4.1-MT1; see also section 3.5.7.2). Minor bending occurred without the development

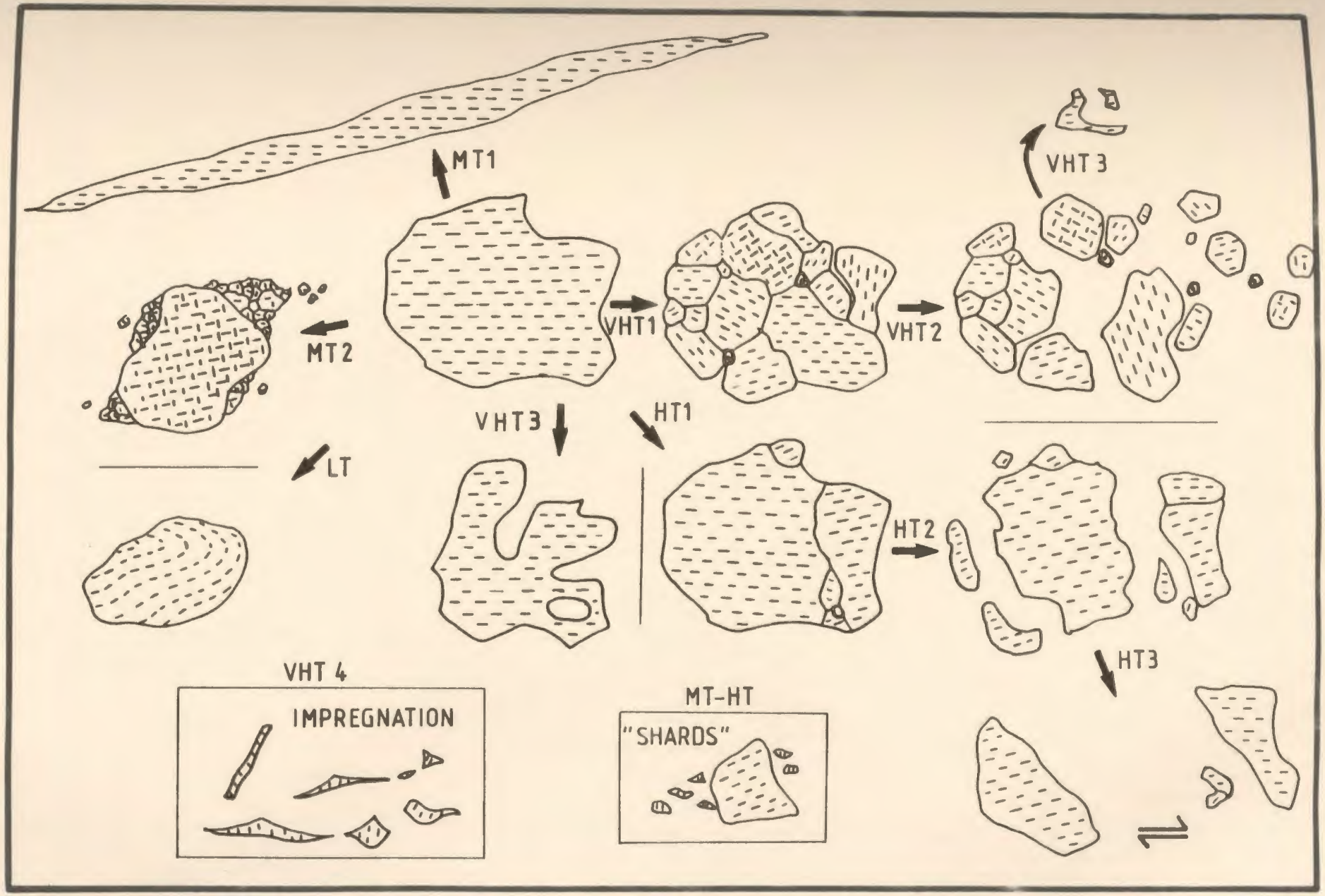

Fig. 4.1. Microstructural behavior of orthopyroxene as a function of the temperature of deformation. LT - low temperature (<900°C); MT - moderate temperature (800-1000°C); HT - high temperature (1000-1200°C); VHT - very high temperature (>1200°C). For details see text.

of recovery features. Recrystallization occurred where higher strains are accumulated, i.e. in tights bends, sheared grains, and especially at grain margins of rigid porphyroclasts (Fig. 4.1-MT2). Porphyroclasts remained rigid where the grains had an orientation unsuitable for slip on the system (100)[001]. During high accumulated strain, the amount of neoblasts increased progressively and the neoblasts formed tails to porphyroclasts or represent entirely recrystallized bands subparallel to the foliation. Under extreme strain, the neoblasts are scattered within the olivine matrix.

Deformation within high strain zones of unit 4 is considered to have occurred during moderate to high temperatures of deformation, i.e. at about 1000°C (section 6.3). This would also represent the conditions of formation for the problematical opx "shards" (see section 3.5.4.2; Fig. 4.1-MT-HT). The orientation of these grains, inferred from a predominantly steeply oriented cleavage trace with respect to the foliation, must be $(001)_{opx}$ parallel to the foliation, i.e. would involve slip on predominantly (001). No such slip system is known (Nazé et al. 1987). Tentatively, it is suggested that the shards may represent tabular neoblasts of unfavourable orientation for slip. The sharp tips of the shards must represent the subsequent mutual adjustment of grain boundaries between opx and olivine. Recently, it has been shown that the formation of tabular-shaped (olivine) neoblasts is favoured by deformation during wet conditions (Drury and van Roermund 1989). While wet conditions would favour grain boundary mobility, little positive evidence for the presence of fluid (e.g. amphibole) has been found within unit 4.

4.4.4 Response to high temperatures of deformation

This temperature regime (1000 – 1200°C) is correlated with weakly lithospheric conditions present in the lower part of unit 2, in unit 3, and most of unit 5.

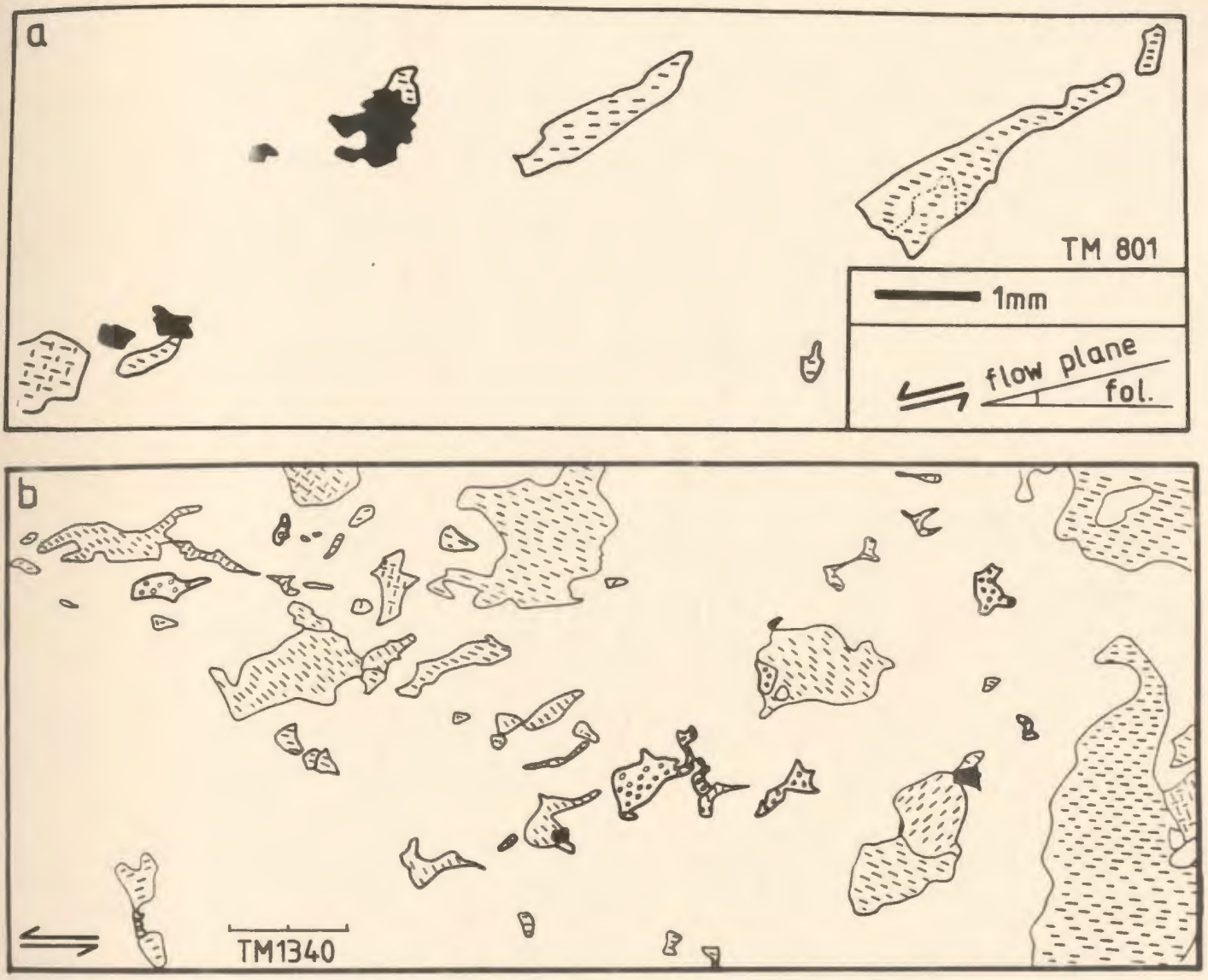

Fig. 4.2. (a) Pull-apart origin of orthopyroxene grains. Note that the asymmetry with respect to the foliation cannot be explained by slip of orthopyroxene. (b) Probable pull-apart origin of orthopyroxene grains in central part of drawing. Note erratic shapes of small opx grains in upper left. Their origin is not fully understood. For legend see Fig. 3.1. Gradation on scale bar is 0.5mm. Shear sense based on olivine microstructure is shown by arrows.

In the high temperature microstructures, pyroxenes occur mainly as grain aggregates which are variably recrystallized into several smaller grains. The neoblasts are relatively irregular-shaped and grain boundaries tend to be ragged and curved (Fig. 4.1-HT1). During recrystallization of larger opx grains with cpx exsolution lamellae, the lamellae appear to migrate out of their opx hosts to form discrete, small cpx neo-

blasts located interstitially between the opx neoblasts (see also Girardeau and Mercier 1988). For grains which underwent slip parallel to (100), aspect ratios < 3 have been observed (cf. Fig. 4.5g). Slip is, however, rare and recrystallization by subgrain rotation or pull-apart prevails.

Pull-apart occurs either along the internal boundaries of the grain aggregates or by fracturing of entire grains (Fig. 4.1-HT2). Pull-apart is common, even where an orientation suitable for easy glide appears to exist. The pulled apart grains have their longest axis at high angle to the foliation (tabular grains, Darot and Boudier 1975) or may be very irregular-shaped. Some pulled apart grains have the appearance of slipped grains (Fig. 4.1-HT3). However, their sense of asymmetry is inconsistent with an orientation acquired during slip. This can be shown by comparing the asymmetry of opx grains with the shear sense derived from the olivine microstructure determination (Fig. 4.2). The orientation of these grains may reflect a nearly primary orientation produced by pull-apart during simple shear deformation.

Subsequent rigid body rotation of the tabular shaped pull-apart grains may or may not occur. While the grains in Pl. 6d appear to be quite stable in their orientation normal to the foliation, antithetic rigid rotation of the pull-aparts of Figs. 4.2 may have contributed to their oblique orientation (< 45°) with respect to the flow plane. Antithetic shear could have been promoted by a pure shear component of the deformation. On the other hand, Suhr et al. (in press) suggest that in the Springers Hill area of the LH, the orientation pattern of an opx shape fabric can be explained by various degrees of synthetic rotation of opx pull-apart grains and grain aggregates during (simple shear) strain following pull-apart.

4.4.5 Response to very high temperatures of deformation

In this category, features acquired near or during hypersolidus conditions are listed. The ambient temperature was > 1200° C (Nicolas 1986a). These conditions are preserved locally in unit 1, the upper part of unit 2, and near the base of unit 5.

Recrystallization affecting opx aggregates has experimentally been simulated at approximately 1300°C (Nazé et al. 1987). It is only observed in the upper part of unit 2 where a polygonal arrangement of opx neoblasts is present (Fig. 4.1-VHT1, Fig. 3.8). The neoblasts are more even-sized (0.4 to 0.6mm) than during deformation in the high temperature category (section 4.4.4) and have nearly straight grain boundaries and well developed triple point junctions. During progressive deformation, the recrystallized aggregates have been pulled apart along the neoblast boundaries, resulting in scattered, apparently rigid, equant opx neoblasts in the olivine matrix (Fig. 4.1-VHT2, Fig. 3.11).

Another response of opx to hypersolidus temperatures is (incongruent?) melting (Dick 1977a,b, Nicolas et al. 1980). It is seen as highly irregular, corroded grains with lobate contacts to olivine (Fig. 4.1 - VHT3, Pl. 6e). Associations of opx with spinel, interpreted as residues of partial melting, are discussed in section 4.6.5.

An origin of opx due to melt impregnation is suspected in some samples of units 1 and 2 (Fig. 4.1 - VHT4). Morphology and lattice orientation of the type section as well as the preferred mode of formation have been discussed previously (section 3.5.1.6).

The distinction between opx morphologies formed by pull-apart, corrosion, and melt impregnation is difficult. In addition, for the shard-like opx grains, an origin of tabular neoblasts modified by grain boundary adjustment between olivine and opx is conceivable. As a result, four possible modes of formation of opx grains with irregular morphology and/or pointed tips are suggested (pull-apart, corrosion, impregnation, grain boundary adjustment). In addition, for small grains, the effect of serpentinization on the morphology is difficult to evaluate. For some microstructures, it is not possible

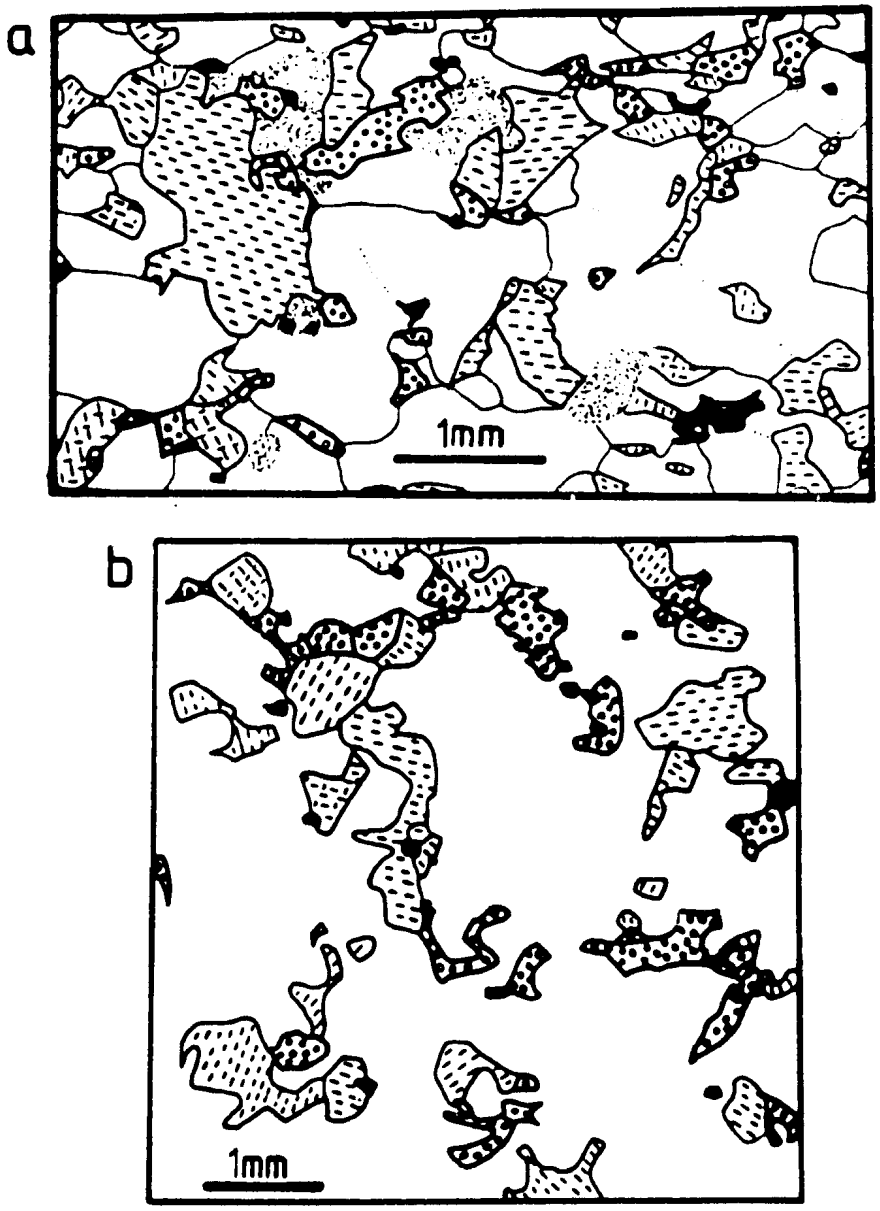

Fig. 4.3a (TM 873) and Fig. 4.3b (TM 1340). Isotropic shape fabric developed in mantle tectonites of unit 2. The origin of orthopyroxene by either pull-apart, corrosion, melt impregnation, or olivine-orthopyroxene grain boundary adjustment cannot be clarified. Clinopyroxene is most likely related to melt impregnation. Note numerous face-face contacts between orthopyroxene and (melt-related!) clinopyroxene grains. Olivine structure is not shown in (b). For legend see Fig. 3.1.

to assign a specific origin to opx: in Fig. 4.3, attenuated, tabular opx grains occur at high angle to the foliation in a superficially entirely isotropic microstructure. Only the olivine lattice fabric and a faint aggregate fabric in hand specimen indicate the deformed nature of the rock. Clinopyroxene has a similar morphology to tabular opx.

The mutual grain boundary mobility between opx and olivine is essentially unknown. The best evidence for a high mobility of opx surfaces is seen in extremely rare cases where opx encloses spinel trails (Fig. 3.3c).

4.4.6 Deformation during hydrous conditions

Available peridotite samples from the BOIC which have been clearly deformed during hydrous conditions are very rare. The best example comes from an orthopyroxene ribbon mylonite within the Springers Hill area (Dunsworth et al. 1986, Suhr and Calon 1987, Suhr et al., in press). Hydrous conditions are indicated by anastamozing bands of synkinematic amphibole. Orthopyroxene of the ribbons is recrystallized into a fine grained, equigranular to slightly tabular equigranular matrix (30-150μm). It appears, that recrystallization of opx was enhanced during hydrous deformation.

Near the base of the ophiolite, hydrous deformation of peridotites (ultramylonites and small scale shear zones of unit 6) led to the breakdown of opx and formation of amphibole.

4.4.7 Discussion

In summary, opx grains, if favourably oriented for slip, take actively part in the deformation of peridotite during lower temperature - high stress conditions ($<$ 1000°C). This is confirmed by the presence of strong lattice fabrics of opx during lithospheric deformation (Nicolas et al. 1980, Mercier 1985, Girardeau and Mercier 1988). During moderate to high temperatures of deformation, rigid pull-apart appears to be the preferred microstructural response, indicating that most strain is accommo-

dated by the olivine matrix. In relation to olivine, opx appears to become more rigid during high temperatures of deformation - a feature consistent with rheological data (Fig. 6.3). During hypersolidus/low stress conditions, however, recrystallization of opx is again more common, showing that opx less resistent to deformation under these conditions than at temperatures between 1000-1200°C. Even given these guidelines for the microstructural behaviour of opx, the deformational behaviour of this phase remains poorly understood and to a certain degree unpredictable. In addition, the microstructural response of disseminated opx grains might also be influenced by their grain size (see section 3.5.4.3).

4.5 MICROSTRUCTURAL BEHAVIOUR OF CLINOPYROXENE

4.5.1 Introduction and review

At lower temperatures, cpx deforms by mechanical twinning on (100)[001]. At higher temperatures, deformation is accommodated by translation gliding on the same system (Raleigh 1965, Raleigh and Talbot 1967, Carter 1976, Kirby and Kronenberg 1984) or relatively non-selective gliding (Avé Lallement 1978). Cataclastic behaviour is present at low temperatures (600°C) and low pressures (Kirby and Kronenberg 1984). Rheological weakening occurs by deformation under wet conditions (Boland and Tullis 1986). Under upper mantle conditions, translation gliding should prevail (Avé Lallement 1978, Gueguen and Nicolas 1980).

Growth twins along (100) are common in the igneous environment and consist of only "one or two subindividuals in a grain" (Raleigh and Talbot 1967; see also Nicolas and Poirier 1976). Like orthopyroxene, clinopyroxene is rheologically hard but weakens relative to olivine so that at depths < 20-60km, websterite may be rheologically weaker than dunite (Avé Lallement 1978). Petrofabric studies on natural websterites of the Lanzo massif suggest that they remained extremely rigid and preserved a magmatic flow structure (Boudier 1978).

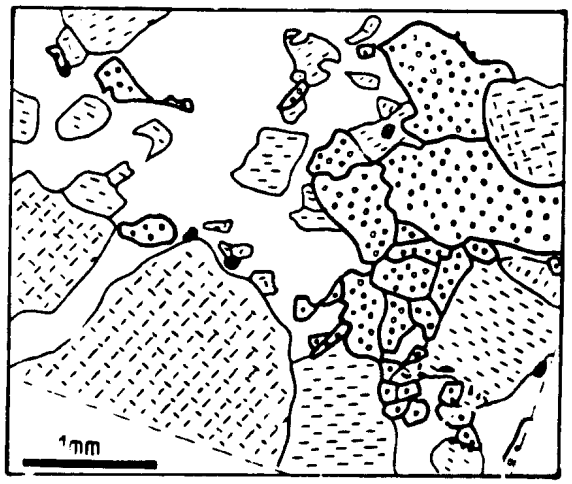

Fig. 4.4. Recrystallized clinopyroxene-orthopyroxene aggregate within sample TM 1079.2. Note the lack of spinel in the aggregate. For legend see Fig. 3.1.

The low modal abundance of cpx in the TM peridotites makes it inadvisable to derive more general conclusions about the deformation behaviour of cpx. Common cpx microstructures include porphyroclast/neoblast relationships of larger cpx aggregates (Fig. 4.4) and ribbon grains involving slip parallel to exsolution lamellae of opx (i.e. parallel to (100)(Pl. 7f). Pull-apart features similar to opx have not been observed.

4.5.2 Melt-related morphologies

The behaviour of cpx during partial melting is difficult to deduce as low strain, residual lherzolites are rare. Grains with a morphology similar to corroded opx (Pl. 6e) have not been identified with certainty. There is some evidence for spinel-cpx intergrowth textures (Fig. 4.9d) which could, in analogy to similar spinel-opx intergrowth textures (section 4.6.5) be interpreted as residual morphologies produced during a partial melting episode. However, the number of observations is statistically not significant.

The most interesting and common morphologies of cpx can be related to melt impregnation in harzburgites and cpx-bearing dunites. Clinopyroxene approaches the characteristic surface equilibrium textures for the basalt (melt) - peridotite system (Waff and Bulau 1979) and occurs in a matrix of deformed olivine. The contrast in the state of deformation of the matrix and cpx excludes any simple, single stage history. Specifically, cpx occurs:

(i) as isolated grains of interstitial morphology (Fig. 4.5a, Pl. 6h). The cpx grains show various stages of annealing (Fig. 3.10b) and may be at high angle to the foliation (Fig. 3.2f). In rare cases, a micron-thin, optically continuous layer of cpx was observed in the olivine matrix (Pl. 7a);

(ii) as trails of interstitial grains parallel to the flow plane (Fig 4.5b). The parallelism to the flow plane indicates the synkinematic nature of melt movement;

(iii) in pull-aparts of opx grains (Fig 4.5c). Clinopyroxene is interpreted as melt-related. The occurrence of cpx or amphibole in pull aparts of chromite deposits is well known (Ceuleneer and Nicolas 1985);

(iv) as trails or accumulation of interstitial grains in pressure shadows of spinel (Fig. 4.5e) or opx (Fig. 4.5d, Pl. 7d). The interstitial morphology suggests that melt (now cpx) formed in space created by unsticking of the ductile olivine matrix from rigid opx and spinel grains;

(v) the cpx trails of (iv) may grade into massive layers of cpx which show little indication of a melt origin in their centre. However, one or both ends of the massive grains can taper out into very "pointed" morphologies (Fig. 4.5f). The occurrence of large cpx grains is therefore not necessarily an indication of residual or primary cpx. As in the case of opx, it remains unclear, how much of a concave outward morphology of cpx may be produced by grain boundary adjustment between cpx and olivine in the solid state.

(vi) Clinopyroxene may also occur as partial corona to opx grains (Fig. 4.5g,h). The

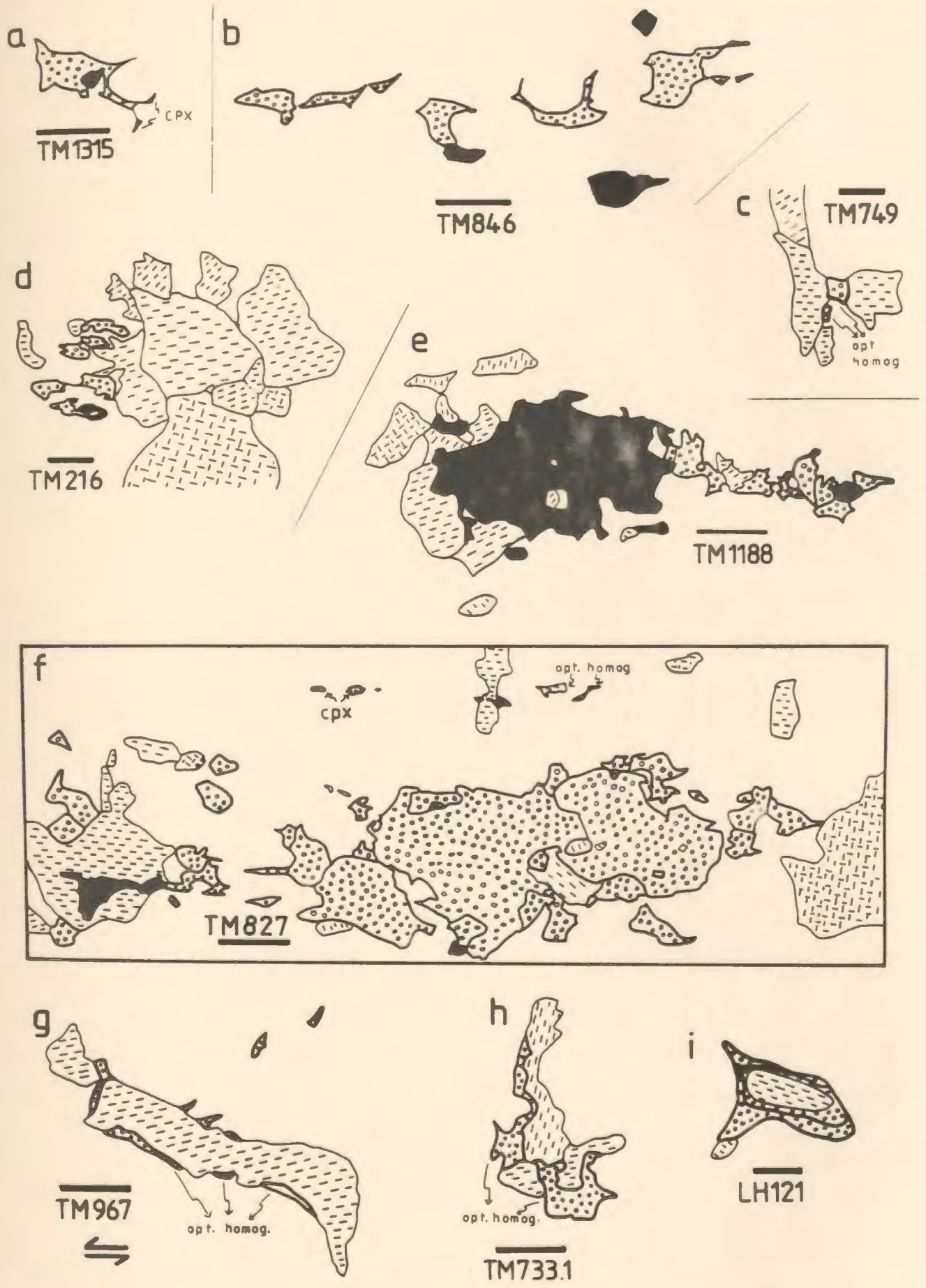

Fig. 4.5. Possible hypersolidus microstructures involving clinopyroxene. For details, see text. For legend, see Fig. 3.1. Black bar = 0.5mm.

different segments of the corona have an identical optical extinction. In the eastern LH mantle peridotites, opx is well-rounded and appears corroded where it is enclosed by cpx coronas. The external shape of cpx is, however, concave outward (Fig. 4.5i).

(vii) Simple growth twins of cpx appear to be present in several locations of unit 1,2,5 and the eastern LH and indicate a magmatic origin (Plates 7b,c, 8a).

(viii) Finally, cpx growth twins have also been observed in thin (several mm to cm), foliation parallel bands of clinopyroxenite or wehrlite (Pl. 8b). Alternatively, these bands show cpx which encloses olivine poikilitically (Fig. 3.7). In both cases spinel is absent in cpx-rich zones. The melt-related origin of these bands is beyond doubt. The question remains, whether they represent dykes which intruded close to the foliation or melt segregation features as suggested by Boudier and Nicolas (1977) and Nicolas and Jackson (1982). The latter model is preferred for thin clinopyroxenites.

In summary, the common occurrence of interstitial cpx in the TM peridotites suggests that, with the exception of unit 6, a large amount of cpx has an origin by melt-impregnation. Particularly in the central part of the mantle section, cpx has an interstitial location in the olivine matrix, and an annealed morphology. This clinopyroxene could represent annealed cpx related to melt impregnation or may have formed by the scattering of opx aggregates containing cpx. A third possibility is the transposition of cpx-bearing dykes and bands. Additional cpx was "introduced" during subsolidus deformation by exsolution from opx and subsequent recrystallization and formation of cpx neoblasts. It appears that most harzburgites in TM must have reached or stepped beyond the "cpx-out" barrier (Dick and Bullen 1984) at some stage of the partial melting history. Later, the peridotites became re-enriched in cpx by incomplete melt-extraction, melt impregnation or exsolution processes.

In several samples, cpx in a melt morphology has been observed to share rational grain boundaries with opx (Fig. 3.10c, 4.3). This wetting of grain faces could be the result of non-hydrostatic, deviatoric stress conditions during melt-infiltration (Green and Borch 1990, Bussod 1990).

4.6 MICROSTRUCTURAL BEHAVIOUR OF SPINEL

4.6.1 Introduction and review

Among the four main phases in ophiolitic peridotite, spinel shows the widest compositional as well as morphological range. Therefore, it should contain valuable information about the processes shaping the peridotites. While the chemical classification of spinel is straightforward and has been succesfully applied to mantle peridotites (e.g. Dick and Bullen 1984), several attempts have been made to classify the disseminated spinels in mantle peridotites morphologically and assign a specific origin to them (Mercier and Nicolas 1975, Talkington and Malpas 1980, Boudier et al. 1984, Christiansen 1985). However, specifically for the numerous spinel-pyroxene intergrowth textures (Talkington and Malpas 1980, Leblanc et al. 1980, Cassard 1980), known also from mantle xenoliths (Talbot et al. 1963, Dawson and Smith 1975, Basu and MacGregor 1975, Smith 1977, Neumann 1991), no interpretation is agreed upon. One of the major problems appears to be that the intergrowth textures are chemically not distinct from other generations of spinels within the same thin section (Dawson and Smith 1975, Wallace 1975), a feature which also holds true for the TM mantle section.

The following four processes governing the spinel morphology in mantle peridotites have frequently been invoked (chromite ores and schlieren are excluded):

(i) exsolution during decreasing PT conditions from pyroxene (Talkington and Malpas 1980, 1984, Mercier and Nicolas 1975), olivine (Leblanc et al. 1980, Arai 1978), or garnet (Smith 1977, Green and Burnley 1988). The exsolutions occur as symplectic or myrmekitic spinel-pyroxene intergrowth (Talkington and Malpas 1980,

Mercier and Nicolas 1975, Leblanc 1980), as well-ordered tablets in opx (Basu and MacGregor 1975) or olivine (Arai, 1978), or may even be ideoblastic (Leblanc 1980);

(ii) formation of residual spinel during incongruent melting of pyroxene in harzburgite. This results in "porphyroclastic spinel" (term used specifically by Talkington and Malpas 1984), isolated spinel in the olivine matrix and spinel associated with pyroxene (Dick 1977a), and spinel-opx symplectites and massive spinels occurring in the vicinity of dunite bands (Leblanc et al. 1980).

(iii) deformation structures as seen in

- pull-apart spinels caused by rigid behaviour during stretching (Doukhan et al. 1984, Christiansen 1986)
- plastically deformed grains related to translation glide and grain boundary migration (Basu 1977, Leblanc 1980, Doukhan et al. 1984, Christiansen 1986) or as "irregular shaped, interstitial clusters" caused by recrystallization (Talkington and Malpas 1980, 1984).
- elongated anhedral grains caused by diffusional flow (Christiansen 1986) coupled with strong chemical zoning (Ozawa 1989).

(iv) formation by trapped melt. Dick (1977a) viewed euhedral spinel in peridotite as "precipitates from pockets of melt". Nicolas et al. (1987) reinterpreted spinel opx-cpx clusters described by Mercier and Nicolas (1975) as in-situ precipitation of trapped melt formed at the site of former garnet.

The frequently used term "holly-leaf spinel" (Mercier and Nicolas 1975) is descriptive and relates to spinel with irregular, typically concave outward directed morphologies.

In this section a new morphological classification scheme is proposed and preferred modes of origin are discussed. The scheme is consistent with mineral chemical

data presented in the next chapter. It is re-emphasized that the proposed origin concerns the spinel-pyroxene assemblage *as a whole* and considers also the total microstructure within a thin section. The following spinel types are distinguished:

- M-type; it represents purely magmatic spinel.
- F-type; it is produced by the action of intense melt percolation in peridotite (high melt flux).
- I-type; it is related to melt impregnation and fractionation in peridotite.
- R-type; spinel represents the residue of partial melting.
- E-type; it is the result of exsolution due to decreasing PT conditions.
- P-type; it represents porphyroblast growth. E- and P-type are considered to be metamorphic in origin
- D-type; its morphology is governed by deformational processes and it may be derived from any of the preceding spinel types.
- Spinels of dubious origin are treated under a "Problematica"-section. They appear largely related to processes associated with melt infiltration.

4.6.2 Type M: magmatic spinel

The M-type spinel forms by purely magmatic processes. It is encountered in the layered cumulate pile and in pyroxenitic dykes in the mantle section. In the few samples collected from these lithologies, the most common spinels are small (0.1-0.4mm), black, euhedral to subhedral grains or deformed equivalents. More interstitial or larger, typically massive sub- to anhedral types occur as well and are similar to the F-type described below. The true range of magmatic spinels has certainly not been encountered, due to the restriction of this study to the mantle section and massive dunites. The interested reader is referred to Malpas (1976), Talkington and Malpas

(1980), and Edwards (in prep.) for a more detailed account of the magmatic spinel morphology in ophiolitic peridotites. The wide morphological range of spinels from ophiolitic podiform chromite ores is described, for example, by Thayer (1969).

4.6.3 Type F: spinel formed by high melt flux

Structural and petrological work has demonstrated that the transition zone is an area of particularly high melt flux (Nicolas and Prinzhofer 1983, Gregory 1984, Rabinowicz et al. 1987, Nicolas 1989). Spinels formed in this environment could thus be the result of interaction between melts and infiltrated host rocks. The Springers Hill area in the LH, as well as structural unit 1 and the top of unit 2 in TM, are located within or just below the transition zone.

A particular spinel type occurs in harzburgites of the Springers Hill area (Fig. 3.21, Suhr et al., in press): this type is large (often 1mm), euhedral to anhedral, usually with rounded edges and has numerous inclusions (Fig. 4.6e-g). An association with a specific other phase is not obvious. In less characteristic subtypes, the inclusions are rare to absent and an association with opx occurs. Typical is a. uneven spatial distribution of spinels on the thin section scale with sometimes just one or two large spinels (up to 4x2mm large) occurring in one slide.

Independent microstructural and chemical evidence suggests that the Springers Hill area has undergone melt infiltration. The evidence includes (i) reverse spinel zoning with increasing Cr# towards the rim in 50% of the samples analyzed (see chapter 5). Such zoning could indicate equilibration with refractory melts (i.e. melts in equilibrium with high Cr/Cr+Al ratios in spinel). However, the Cr-Al zoning in spinels is not well understood (see section 5.5); (ii) $Cr\#_{sp} > 60$ suggesting partial melting beyond the cpx-out barrier (Dick and Fisher 1984, Dick and Bullen 1984), but consistent occurrence of some cpx or amphibole grains within the samples. Some of the cpx grains show a clear impregnation morphology (Fig. 3.21). (iii) platinum group

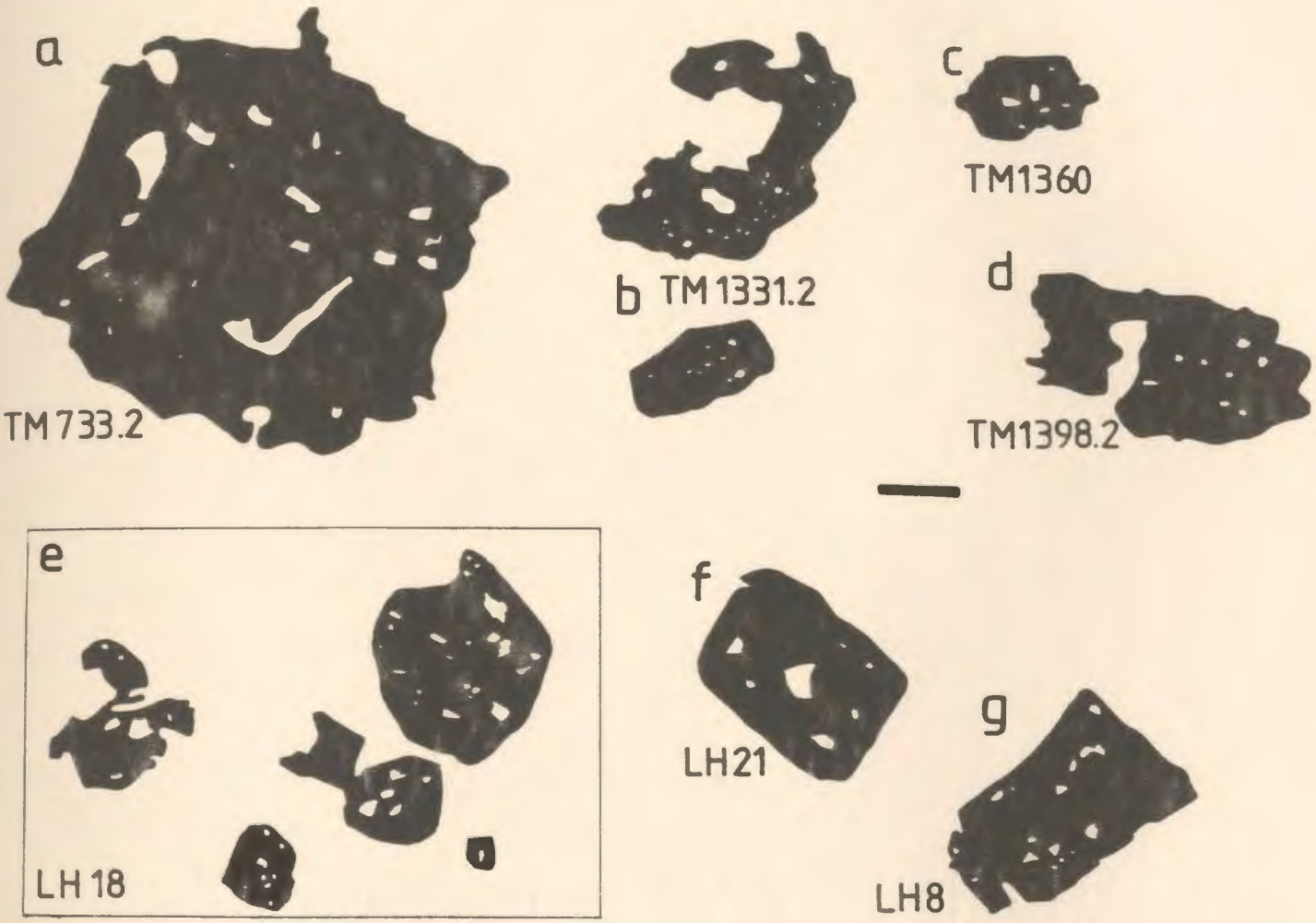

Fig. 4.6. Spinel morphologies classified as F-type. They are thought to have formed in peridotites which have undergone intense melt percolation. Spinels are located within the olivine matrix and are not associated with pyroxene. For details, see text. For legend, see Fig. 3.1. Black bar = 0.5mm.

element patterns from a nearby area incompatible with residual harzburgite but compatible with impregnation by an orthopyroxenite component (Edwards 1990). (iv) High melt flux indicated by the abundance of dunite bands and pyroxenite dykes (Suhr et al., in press).

Spinels similar to the Springers Hill area occur in certain dunitic and wehrlitic areas in the transition zone of TM (Fig. 4.6b-d). These spinels are identical to spinels from dunite bodies in the Oman ophiolite (Christiansen 1985). In the case of TM, a

melt impregnation event is inferred from the difference in the state of strain of the olivine matrix and cpx. However, a residual component within the dunites has not been identified with certainty so that melt impregnation may alternatively have affected cumulate rocks. Interestingly, the largest spinel grains of the morphology of Fig. 4.6 were found in a rare occurrence of dunite with wehrlite bands (occurrence shown in Pl. 4g) within harzburgites of the central part of unit 3 (Fig. 4.6a). This area is considered as one of the two low strain windows in the TM mantle section (section 6.3).

The morphological similarity between the Springers Hill and TM spinels is striking. The spinel grains shown approach the morphology of some magmatic spinels and the spinels are thought to have formed due to reaction of a host with transient melt causing major microstructural rearrangements (*F-type*). Inclusions preserved within the spinel grains would have been trapped during growth associated with the microstructural rearrangement. The ability of spinel to morphologically rearrange in the presence of interstitial melt associated with trapping of inclusions has been shown by Hulbert and von Gruenewaldt (1985) for the critical zone of the Bushveld complex.

4.6.4 Type I: spinel related to melt-impregnation

As shown in section 4.5.2, the equilibrium morphology of basaltic melt in peridotite is approached by interstitital cpx grains. It is good evidence for a melt-derived origin of cpx. Identical morphologies for spinel grains have not been observed, though a few spinel "specimens" (Fig. 4.7f, and the "bridging", interstitital spinel in Fig. 4.12a) are reminiscent to such a morphology.

In numerous cases, however, spinel is associated with cpx and *both together* are located interstitially within the olivine matrix or close to larger opx grains (Fig. 4.7). Minor amounts of opx may also be present (Fig. 4.7c,g,h,i). The small cpx-spinel symplectites may also occur as trails next to large opx porphyroclasts (Fig. 4.8), similar to the postulated segregation of melt (cpx) in pressure shadows of opx and spinel. In rare

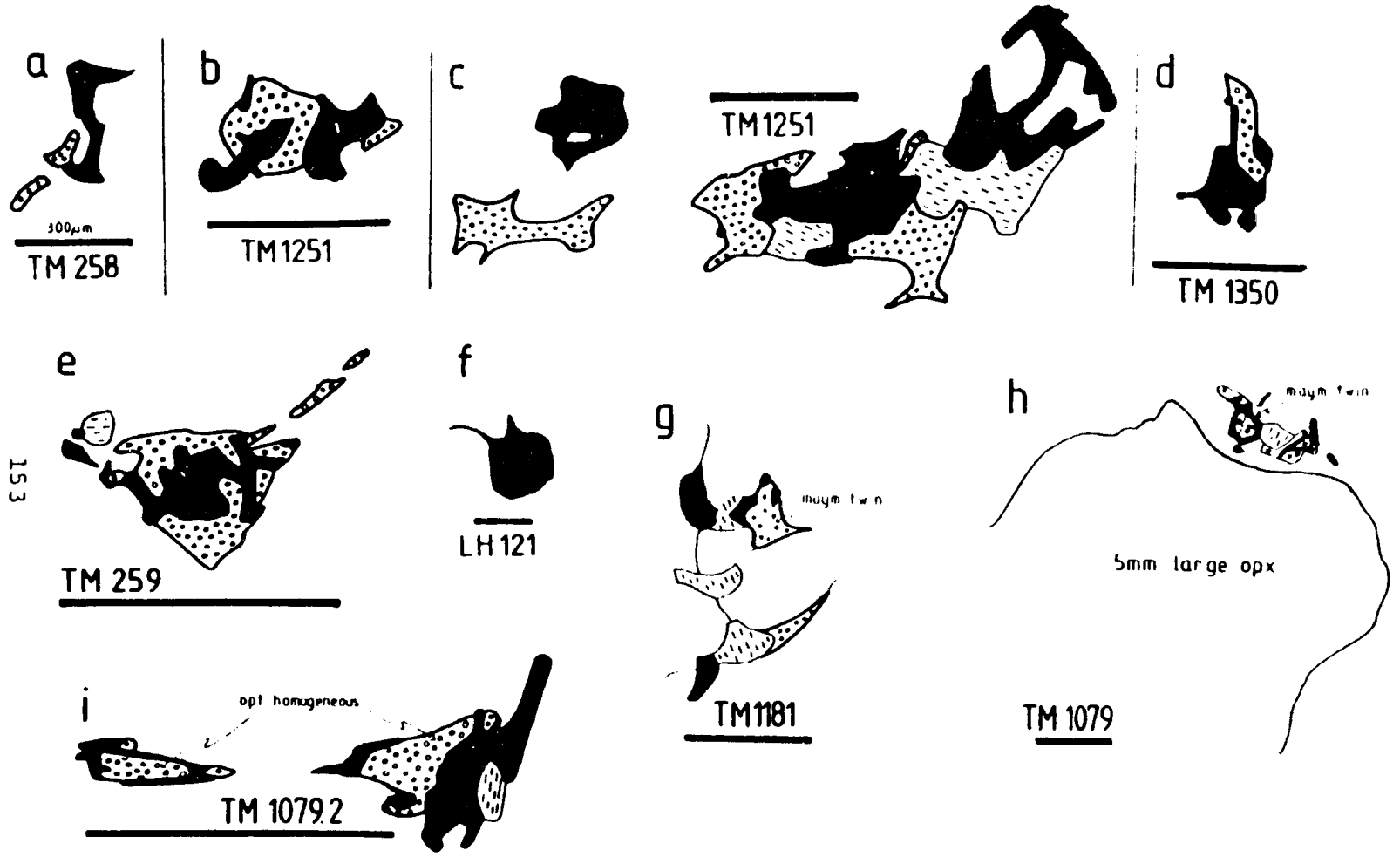

Fig. 4.7. Spinel morphologies classified as I-type. They are thought to have formed in peridotite in which melt-impregnation and fractionation occurred. For details, see text. For legend, see Fig. 3.1. Black bar = 0.5mm.

examples, the simple cpx growth twin appears associated with the cpx-spinel association (Fig. 4.7h, Pl. 7b,c). Characteristic for all occurrences is that the cpx-spinel association forms discrete, small grains in the 500-1000μm range.

All occurrences illustrated in Fig. 4.7 are thought to have been derived from migrating and trapped melt. The mineralogical assemblage, its location and morphology, and the presence of cpx growth twins favour such an interpretation. As discussed in section 4.7, the exact process of formation is, however, complex and difficult to define.

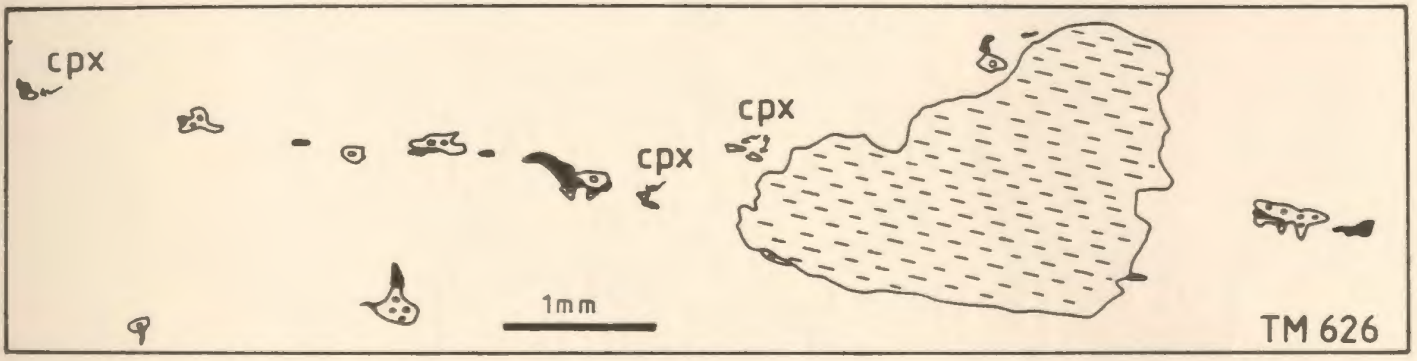

Fig. 4.8. Trail of cpx-spinel clusters aligned subparallel to foliation (horizontal) and in potential pressure shadow location of opx porphyroclast. For legend see Fig. 3.1.

4.6.5 Type R: spinel formed as residual phase

Characteristic for this morphological type are relatively coarse spinel-pyroxene intergrowth textures (Fig. 4.9). The intergrowth pattern tends to be less intricate than for spinels separated out in a Problematica section (section 4.6.6). Whereas the intergrowth does affect the largest opx aggregates (Fig. 4.9b), there is a preference for medium-sized opx aggregates or grains (<2mm) to be associated with spinel while the largest grains are spinel-barren.

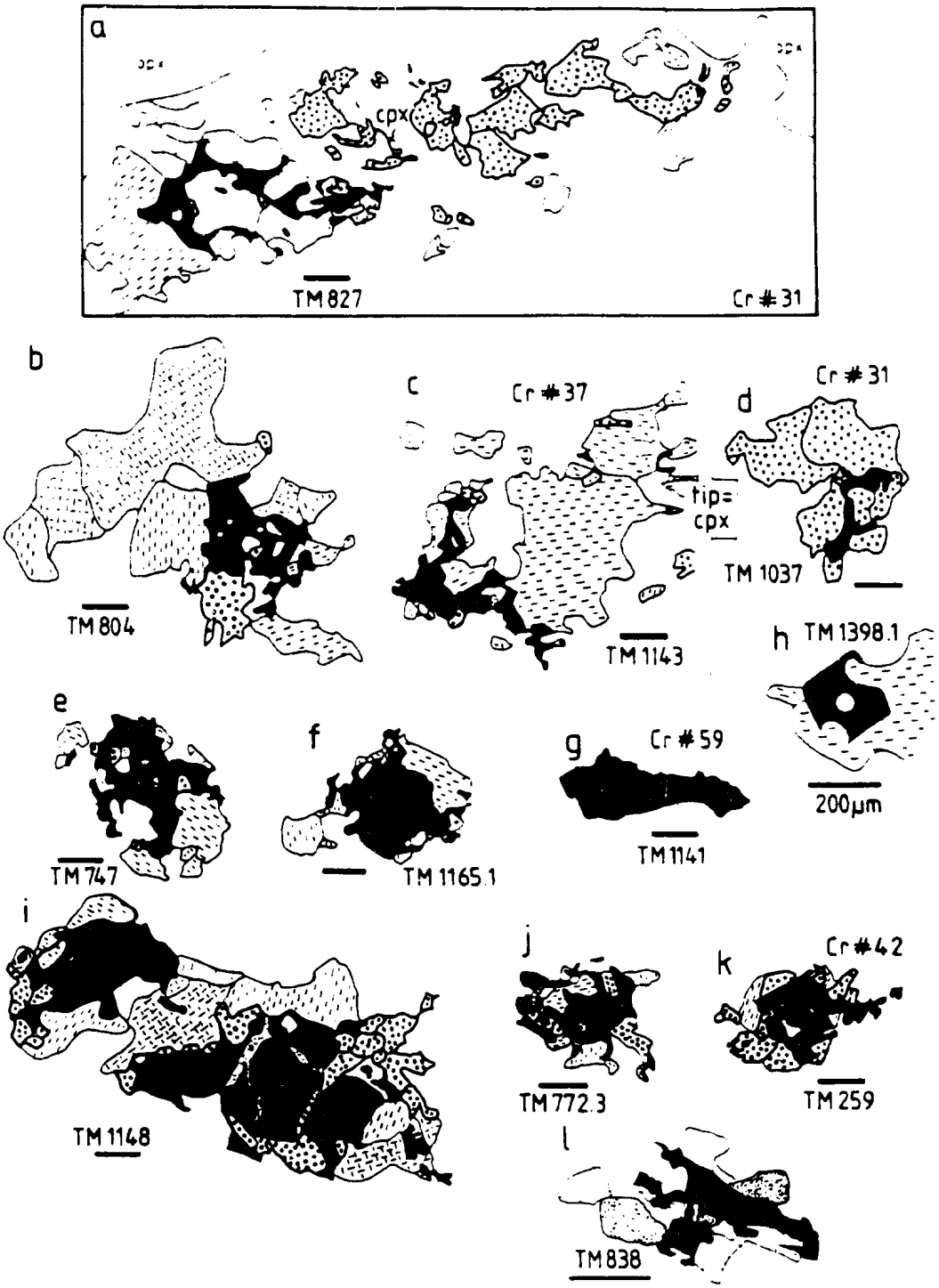

Fig. 4.9. Spinel morphologies classified as R-type. They are thought to have formed as residues of partial melting. For details, see text. Cr# indicates 100Cr/Cr+Al ratio in spinel, where available. For legend, see Fig. 3.1. Black bar = 0.5mm.

Orthopyroxene is far more abundant than clinopyroxene in the intergrowths with spinel. In less depleted peridotites*, however, the association cpx-spinel is more common (Fig. 4.9d,l). In addition, spinel tends to be morphologically less massive in less depleted peridotites (Fig. 4.9a). There is a crude correlation between the Cr# of spinels and the volume ratio of spinel/pyroxene in as far as low Cr#'s are associated with relative low abundances of spinel. Possibly, this correlation culminates in massive spinel without any associated pyroxene during high degrees of depletion (Fig. 4.9g) and the observed absence of R-type spinels in samples with Cr# < 30.

Spinel tends to be located in the central part of the intergrowth as rather massive grains with radially extending arms (Fig. 4.9f,i,k). This is particularly common where spinel forms a high percentage of the intergrowth. A characteristic feature is that numerous large opx clusters within a single thin section occur without any associated spinel, whereas some contain the intergrowth pattern. There is a small possibility that this is a cutting effect. Some specimens (Fig. 4.9j,k) converge morphologically with those in the next section.

The R-type is interpreted as partial melting of opx and cpx with generation of residual spinel. This interpretation is supported by the chemical trends which are consistent with progressive melting of peridotite (Dick 1977a, Jaques and Green 1980, Dick and Bullen 1984, Talkington and Malpas 1984, Duncan and Green 1987). The spinels are spatially associated with opx aggregates which will progressively melt out during increasing degrees of melting (Dick and Fisher 1984). Thus, the occurrence of spinel at the site of the melting phase (opx) and its chemistry is consistent with a residual origin.

---

*The degree of depletion can be evaluated with the Cr# of spinel and the amount of Al in pyroxene, as well as the modal percentage of pyroxene (see Dick and Fisher 1984 and chapter 5). The colour of spinel in plane polarized light can also provide information about the spinel composition.

An anomaly among the intergrowth textures is shown in Fig. 4.9i. While it shares all morphological features of the R-type, it is much larger, restricted to unit 5, and occurs as trails of up to 8 such grains parallel or slightly oblique to the foliation. Their origin is puzzling and they are tentatively interpreted as remelted, small pyroxenite dykes.

4.6.6 Problematica

In this section, problematic morphological types from unit 5 in TM and from harzburgites of the eastern LH are discussed.

The following features are considered characteristic for the TM occurrence (Fig. 4.10):

(i) symplectic intergrowth of spinel-opx, spinel-cpx, or spinel-cpx-opx;
(ii) size between 0.5 and 1mm;
(iii) occurrence as discrete, interstitial grains
(iv) subequant shape;
(v) possibly the presence of cpx growth twins within the symplectite (Fig. 4.10f; identification not certain);
(vi) local protrusion of spinel into the olivine matrix (Fig. 4.10b).

In addition, within TM, spinel-opx (-cpx) symplectites occur as partial rims of, or adjacent to, larger opx grains (Fig. 4.11a-d). Typically, opx is optically continuous from the large grain into the symplectite. Characteristic is that the symplectites do not form a continuous rim around opx and their size is restricted to < 1mm.

In the basal LH, droplet-like cpx-spinel symplectites (Fig. 4.12b) are obviously related to the larger cpx-spinel symplectites (Fig. 4.12a, see also Pl. 8a). The melt origin of the large cpx-spinel symplectites is indicated by the cpx growth twin within the symplectite (Fig. 4.12a, Pl. 8a) and is supported by the poikilitic habit and spinel

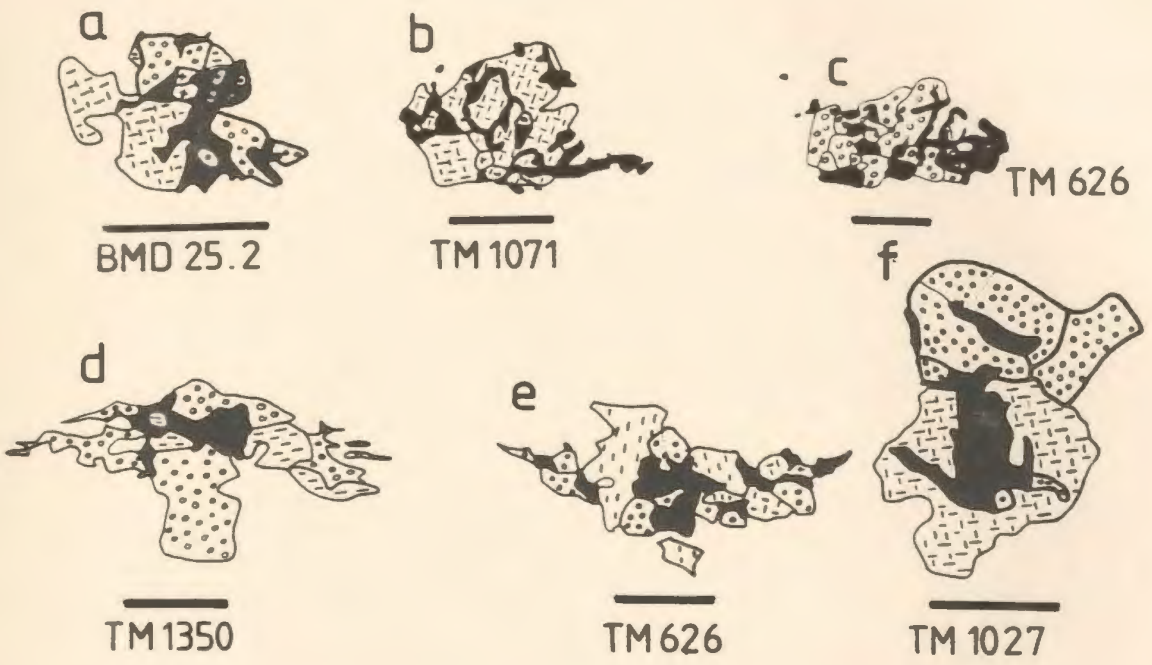

Fig. 4.10. Problematical spinel-pyroxene symplectites located within the olivine matrix (Table Mountain mantle section). For details, see text. For legend, see Fig. 3.1. Scale bar = 0.5mm.

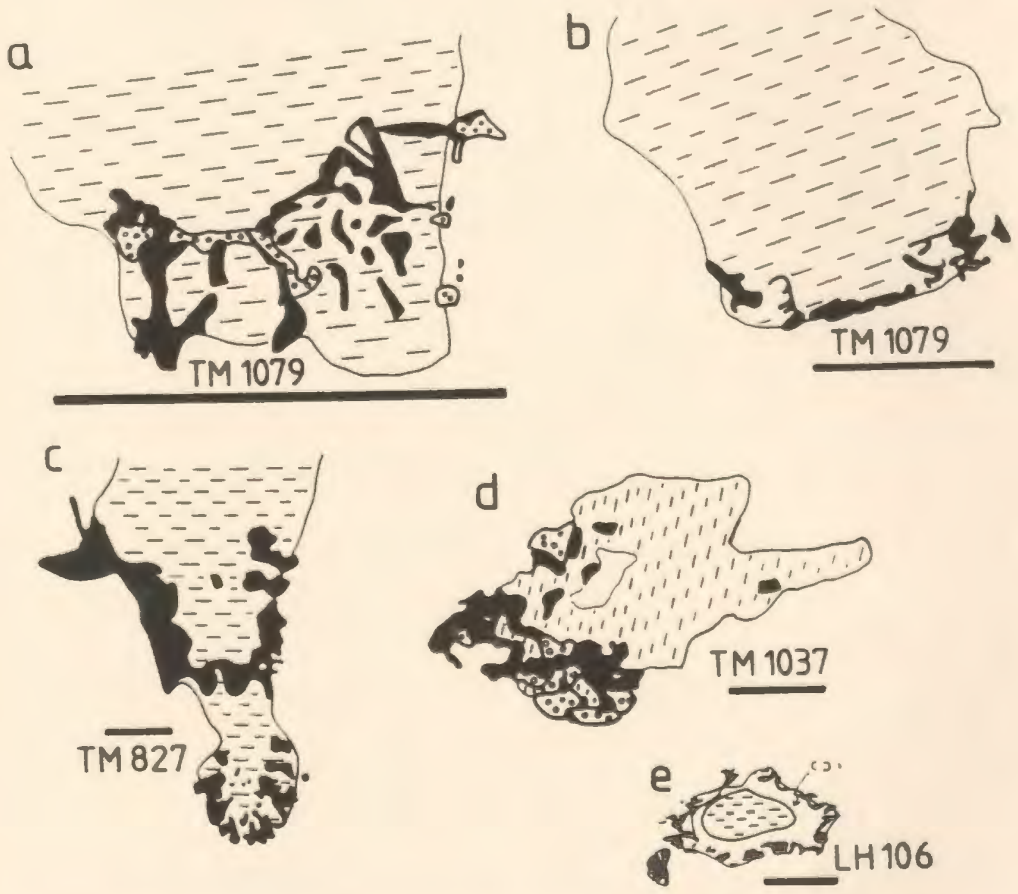

Fig. 4.11. Problematical spinel-pyroxene symplectites located marginally to larger opx grains. For details, see text. For legend, see Fig. 3.1. Black bar = 0.5mm.

"bridges" connecting two symplectites. The morphological similarity between the large symplectites, droplet-like symplectites and the TM occurrences suggest a genetic relation.

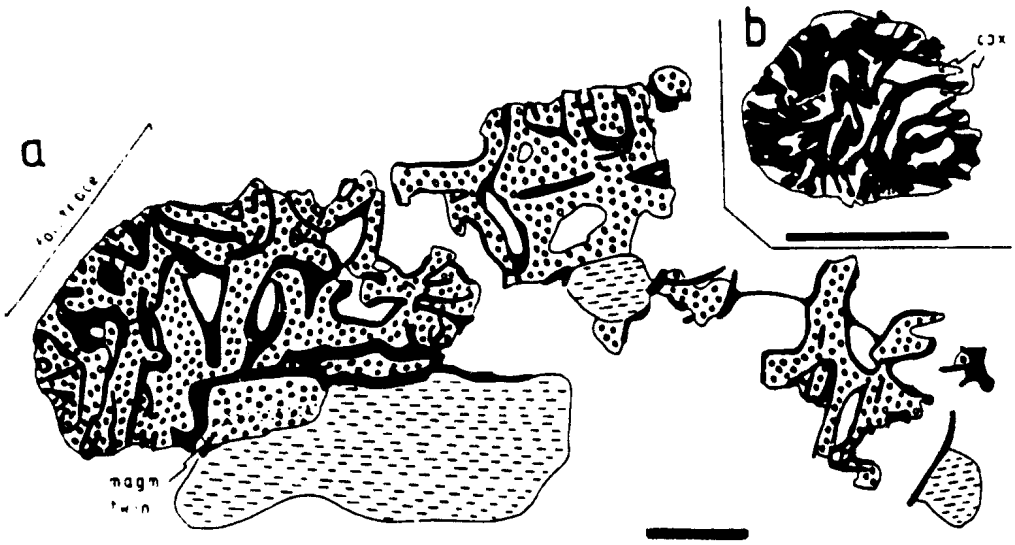

Fig. 4.12. Intricate spinel-clinopyroxene (-orthopyroxene) symplectites from the eastern Lewis Hills mantle section; sample LH 121. For details see text. For legend, see Fig. 3.1. Scale bar = 0.5mm.

Spinel-opx-symplectites which are virtually identical to the LH occurrence are described from mantle xenoliths (Wallace 1975) and ophiolites (Cassard 1980). The description from Dawson and Smith (1975) coincides very closely in virtually all parameters with the TM occurrences, i.e. size, mineral association (additional spinel-amphibole and spinel-olivine symplectites reported), often radial spinel arrangement. Dawson and Smith (1975) report a marginal position of the symplectites with respect to a larger and optically continuous pyroxene grain or an interstitial occurrence. As was pointed out by Dawson and Smith (1975) and is true for other symplectite occurrences including those of TM: "It is the texture of the intergrowth minerals that is different, not their chemistry,". Similar symplectites are reported by Talbot et al. (1963), Rodgers (1973),

Basu and MacGregor (1975), Talkington and Malpas (1980), Cassard (1980) and even from chromite ores by Hock and Friedrich (1985). Basu and MacGregor (1975) also emphasize that the grains are interstitial or marginal to larger opx grains.

Symplectites described from protogranular xenoliths by Mercier and Nicolas (1975), Smith (1977), and Nicolas et al. (1987) are similar to the TM occurrences with the important exception that the TM symplectites are smaller by a factor of 5-10. Until recently, magmatic diopside had not been described from any of the occurrences listed above. It is now, however, documented from a mantle xenolith suite (Neumann 1991). From these symplectites, melt inclusions are also reported.

The symplectites have been the subject of various interpretations:

- exsolutions from high Al-enstatite (Mercier and Nicolas 1975, Leblanc 1980, Talkington and Malpas 1980 and 1984), or contemporaneous exsolution of silicates and spinel from opx during subsolidus conditions and migration of the components into an interstitial or marginal location (Basu and MacGregor 1975). This model is rejected by Smith (1977), as it requires what he considers to be unrealistically high Al-contents in pyroxene;
- solid state re-equilibration from garnets (Aoki and Shiba 1973, Wallace 1975, Smith 1977, Green and Burnley 1988);
- in-situ melting of garnets (Nicolas et al. 1987);
- eutectic crystallization (Hock and Friedrich 1985).

Chemically, the symplectic spinels in TM have aluminous compositions. They are compositionally not distinct from other spinel types within the same thin section. The Lewis Hill symplectites are moderately chromitiferous and again have very similar compositions to massive spinel grains located within opx clusters of the same sample.

4.6.7 Type E and P: spinel formed by "exsolution" and porphyroblast growth

These two spinel-forming processes are considered to occur mainly under subsolidus conditions, i.e. are metamorphic. Exsolution could also occur under hypersolidus conditions, but is probably kinetically too slow compared to hypersolidus processes to be significant.

The E-type (exsolved spinel) is most obvious in lherzolitic rocks overprinted by lower temperature deformation (high strain peridotites in unit 6). The "exsolutions" occur as small, vermicular grains outside large, unrecrystallized opx porphyroclasts (Fig. 4.13a) and within the olivine matrix (Pl. 7g). In their study of the White Hills Peridotite, Talkington and Malpas (1984) list the following reaction to explain the occurrence of similar spinels:

$$xMgAl_2O_4 + (1+x)MgSiO_3 = MgSiO_3xAl_2O_3 + xMg_2SiO_4$$

spinel — enstatite — Al-enstatite — forsterite

While Talkington amd Malpas (1984) use the term "exsolution", reaction would probably be a better term. The use of olivine in the retrograde reaction explains the absence of spinel inside opx porphyroclasts (Pl. 7g), i.e. in locations where no reaction-surface exists between pyroxene and olivine. Accordingly, well-ordered exsolution tablets within opx grains (Fig. 4.13c) must be explained differently (probably by real exsolution). The abundance of the E-type spinels within lherzolites is explained by the aluminous nature of the pyroxenes in these peridotites (up to 6% Al_2O_3). Aluminum is needed for the exsolution of significant quantities of aluminous spinels in the lherzolites. The reaction is obviously enhanced by recrystallization (Fig. 4.13a). The E-type spinels are thus abundant in highly strained rocks deformed during

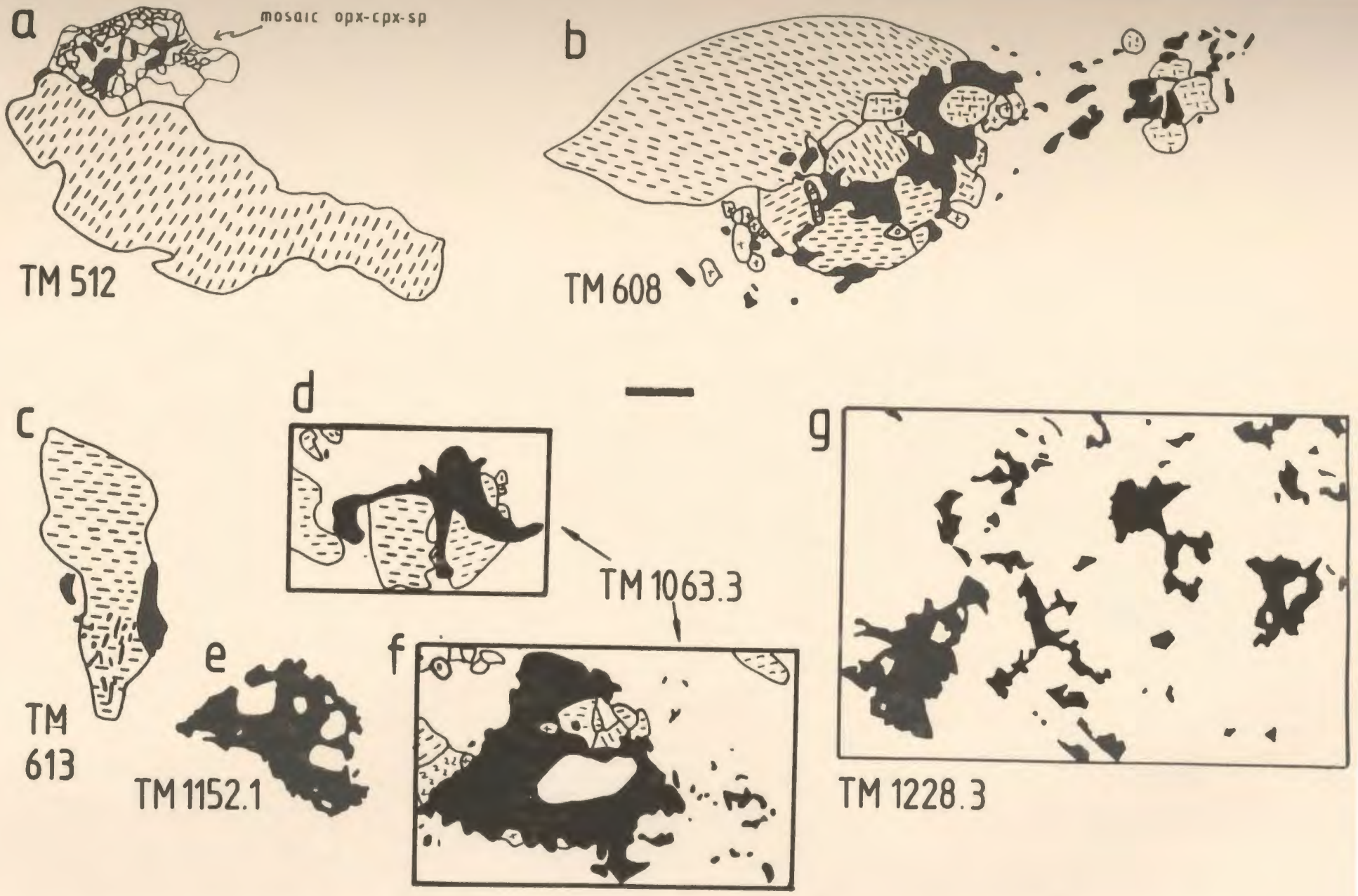

Fig. 4.13. (a,c) Spinel morphologies assigned to the E-type which are thought to be caused by subsolidus exsolution from Al-rich pyroxenes. (b, d-f) Spinel morphologies assigned to the P-type. They are thought to represent spinel porphyroblasts growing in Al-rich peridotites. (g) Granoblastic spinel within a metasomatized sample from the immediate contact area of peridotites and the metamorphic sole (amphibolites). Silicate matrix is not shown in this drawing. For details, see text. For legend, see Fig. 3.1. Black bar = 0.5mm.

low temperature conditions. The exsolution model is supported by lower Al-abundances in rims of opx grains and opx neoblasts compared to opx porphyroclasts (see data in Tab. B-5).

The P-type occurs within the same lherzolites as the E-type and develops from the spinel exsolutions into large poikilitic grains (Fig. 4.13b,d-f). An alignment in specific foliation-parallel layers has been observed. Porphyroblasts have not been observed in lower strain lherzolites at the base of unit 5 and the top of unit 6. It is suggested that high strain peridotites supply the necessary diffusive pathways for porphyroblast growth. In addition, strain will lead to recrystallization and therefore liberalization of the potential spinel component locked up in the core of large porphyroclasts.

Finally, spinel occurs also as granoblastic phase with overall interstitial character in a metasomatized peridotite from the contact of peridotites and amphibolites. Its origin was not further investigated (Fig. 4.13g).

4.6.8 Type D: spinel morphologies dominated by deformation

Little is known precisely about the dominant deformation mechanism of spinels under upper mantle conditions. Given the wide compositional range of spinels, the deformation mechanism is most likely compositionally dependent. Higher diffusivities of aluminous spinels compared to chromitiferous spinels are suspected (Basu 1977, Ozawa 1989). High diffusivities would support plastic behaviour of aluminous spinels over rigid to brittle behaviour of chromitiferous spinels (Basu 1977). No particular effort has been made to solve this problem.

Plastic deformation and recrystallization is supported by asymmetric porphyroclasts shown in Fig. 3.20. Pull-apart is observed frequently as trails of irregular shaped grains with sharp edges. The typically small, weakly elongated spinels of unit 2 may

form in a variety of ways, including pull-apart, diffusion creep (Ozawa 1989), or translation glide. Alternatively, they could even form through reaction with melts along certain flow planes and be not deformation-related at all.

4.7 DISCUSSION OF HYPERSOLIDUS MICROSTRUCTURES

A full appreciation of the morphological spinel types is only possible after evaluation of chemical trends presented in chapter 5. The scheme developed on the basis of the spinel classification and the chemical data suggests the presence of three magmatic processes affecting the BOIC peridotites: (i) progressive partial melting; (ii) progressive flushing with melt; and (iii) trapping of melt.

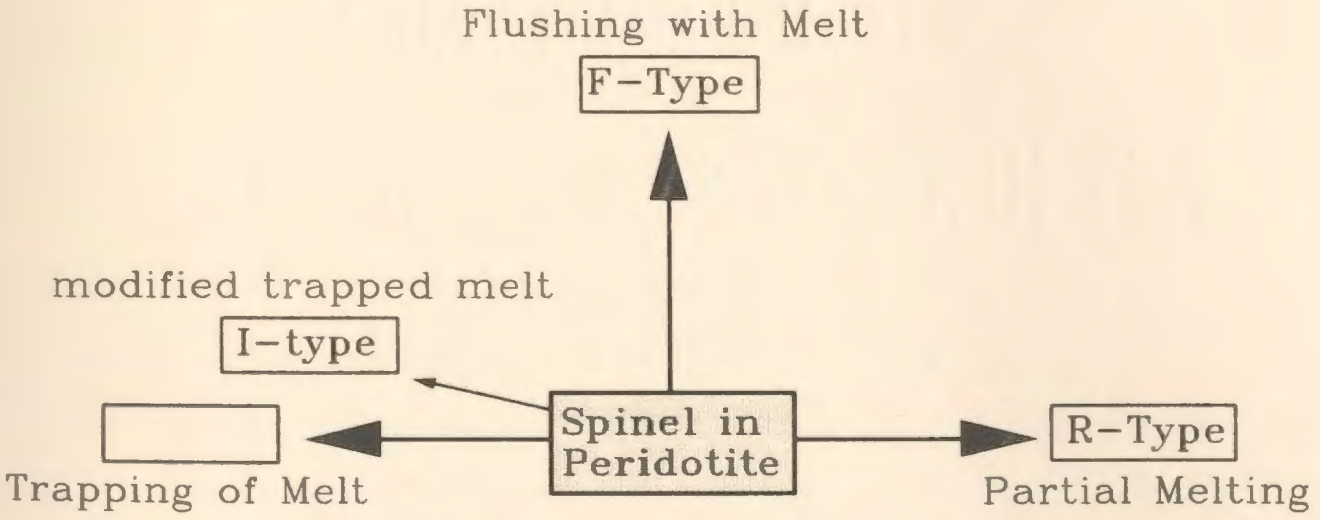

Fig. 4.14. Processes associated with the morphological classification of spinel in the Bay of Islands mantle peridotites. The pristine trapped melt field is probably not realized and phases identified microstructurally as trapped melt have been chemically modified. See also section 5.12.

Fig. 4.14 shows how the morphological spinel types could fit into this classification. The R-type represents the progressive partial melting trend in which melt is extracted and spinel stays behind as a residual phase. The F-type represents flushing with melt, i.e. forms in an open system which, for high melt:rock ratios, approaches a

magmatic system. In the end-member, the spinel and peridotite composition has been drastically changed due to a very high melt:rock ratio. The preferred model for the I-type spinel suggests that it crystallized from trapped melt.

The critical question is whether the I-type spinels, together with the associated phases, represent pristine melt. This would allow calculation of melt compositions from the mineral chemistry of trapped melt phases, as was done by Dick (1989) for oceanic peridotites.

The ophiolitic mantle rocks of the BOIC occur within a continuous lithological section reaching from the oceanic crust into the upper mantle. Even for the deepest peridotites in the section, the current depth below the oceanic Moho is not more than 6 km. No obvious break in lithology or structure was discovered in the mantle section so that the later removal of parts of the section appears unlikely. The contact to the oceanic Moho is of high temperature, ductile flow nature. Synkinematic evidence for melt infiltration and partial melting is locally preserved. It is concluded that the current depth of the peridotites below the Moho does not deviate significantly from the depth at the time of late ductile deformation and partial melting within the mantle section. Both processes must have taken place at low pressures and the depth of equilibration of the mantle rocks must be shallow (<5-6 kbar). Equilibration pressures of 18-20 kbar calculated for the BOIC mantle rocks (Malpas 1978) are probably erroneous. It is thus expected that any melt present at the time of deformation would crystallize in the plagioclase stability field (e.g. Jaques and Green 1980). Trapped basaltic melt should therefore be represented by (olivine-) plagioclase - cpx clusters. However, such clusters are consistently absent in the BOIC mantle rocks.

Within the BOIC, "trapped melt" occurs as single grains of cpx (Fig. 4.5), possibly single grains of opx (Fig. 3.6), or cpx-spinel clusters which may contain minor amounts of opx (Fig. 4.7). As is shown in the mineral chemistry section, the

composition of these phases is unlike that of pristine melt. For example, the TiO_2-content of the interstitial clinopyroxenes within sample TM 1181 (Fig. 3.16) is only 0.05 wt.% (Tab. B-4a) and is similar to other cpx grains within the same thin section. In basaltic rocks from the NAM volcanic section, the TiO_2-content ranges between 0.5 and 2 wt.% (Siroky et al. 1985). While the basaltic rocks may be somewhat evolved, their primary TiO_2-content was certainly higher than 0.05 wt%. Either the composition of the melt forming the impregnations has been changed before melt entrapment or it was altered afterwards during subsolidus conditions.

The morphologically delicate nature of many grains related to melt impregnation, particularly cpx grains (e.g. Pl. 7a), suggests to the author that they can have undergone very little alteration with the exception of a cryptic change in the mineral chemistry. In other words, it appears unlikely that what is now a delicate, concave outward directed cpx morphology, could have originally represented a more complex cpx-plagioclase cluster. Therefore at least some of the interstitial cpx grains represent primary, melt-related *microstructural* features.

The experiments of Jaques and Green (1980) demonstrated that during low pressure melting, plagioclase will rapidly disappear from the residue even at low degrees of partial melting. Consequently, peridotites having undergone higher degrees of partial melting will be undersaturated with respect to plagioclase. They could potentially "resorb" a high amount of plagioclase component from a percolating melt. Note that with rare exceptions in the uppermost TM mantle section, plagioclase is absent and the mantle rocks of TM are moderately to highly depleted (cf. Fig. 5.6). Kelemen (1990) showed that during migration of tholeiitic melt through harzburgite, plagioclase, if on the liquidus, will disappear from it, whereas cpx and olivine remain a liquidus phase after reaction with harzburgite.

Consequently, the crystallization of plagioclase will be suppressed during percolation and trapping of melt in the mantle section. The large potential of harzburgite to react with transient melt (e.g. Kelemen 1990, Kelemen et al. 1990) also casts severe doubts on the existence of any primary, pristine nature of melt impregnations occurring within a peridotite network. After all, within the grain boundary network of peridotites, abundant reaction surface exists during migration of melt.

Subsequent to crystallization of melt in peridotite, subsolidus re-equilibration will homogenize any mineral chemical difference which would still exist between phases crystallized from melt and residual phases within the harzburgite (e.g. Nicolas 1989). This could explain why microstructurally distinct types of cpx or spinel cannot be distinguished from each other by mineral chemistry. The usage of the term "trapped melt" for microstructurally visibly, melt-related mineral phases in peridotites is thus chemically probably not correct. It is suggested that melt trapped within a peridotite network and its crystallization products have been changed prior, during and subsequent to the entrapment.

A harzburgite sample from the eastern LH section supports the notion that reaction does take place between peridotite and melt (Fig. 4.11e). In this sample, rounded opx is enclosed by cpx, the latter showing marginal spinel exsolution features. The preferred interpretation is that reaction of interstitial melt with opx led to corrosion of opx and marginal transformation into cpx, so that cpx would approach equilibrium with the melt. During a later stage, spinel was exsolved by a reaction involving olivine. Therefore, the symplectite is restricted to the cpx-olivine interface. Note the morphological similarity to Fig. 4.5i. There, however, cpx acquired a concave outward morphology suggesting a melt-peridotite surface equilibrium and direct precipitation from a melt.

The origin of most grains listed in the Problematica section could be related to a complex combination of melt-infiltration, reaction and entrapment in a peridotite, followed by subsolidus annealing and chemical equilibration. The involvement of magmatic processes is strongly suggested by the local preservation of diopside growth twins. While the external morphology is not compatible with current ideas about the shape of basaltic melt in equilibrium with peridotite, it could be a result of annealing or indicate that the dihedral angle between melt and peridotite was $>60°$. The latter situation would lead to more spherical grains and severe problems of extracting melts. The large size of cpx-spinel symplectites from the LH may actually indicate that such problems were present.

In summary, morphologically identified trapped melt does not appear to represent pristine melt. There is good evidence to suggest that prior and during entrapment of the melt, as well as after crystallization of the melt, chemical exchange took place between the melt, any crystallization products, and the host. The detailed processes associated with trapping of melt are not well understood.

5 GEOCHEMISTRY

5.1 SUMMARY

Peridotites of the TM mantle section show a large range in Cr/Cr+Al ratios in spinel. The spinel data correlate with changes in the mineral chemistry of other phases. The origin of the chemical variation is investigated using mineral chemistry variation diagrams and the spatial distribution of the data.

The regional spatial distribution of the chemical data indicates the presence of a depleted, intermediate stratigraphic horizon (structural units 3,4, TU). At its base, it is juxtaposed along a steep chemical gradient against less depleted basal peridotites (units 5,6). Both together define a chemical evolution indicative of progressive partial melting. The intermediate zone grades up-section into less depleted peridotites which have the chemical signature of melt infiltrated peridotite (unit 2). At the base of unit 1, a wedge of harzburgites occurs with low Al-pyroxenes and spinels. They may be related to another phase of melt infiltration. The top of the section studied is formed by massive dunites with aluminous spinels (units 1,2). Their chemical signature is intermediate between melt infiltrated peridotite and the mineral chemistry of layered cumulate rocks from North Arm Mountain determined by Elthon et al. (1984) and Komor et al. (1985a).

A conceptual model is proposed which defines the chemical make-up of mantle peridotites in the BOIC as a result of three end-member processes: (i) progressive partial melting, leading from lherzolites to harzburgites and ultimately dunites; (ii) trapping of melt which is mixing-dominated and adds gabbroic tendencies to mantle peridotites (presence of plagioclase and clinopyroxene); (iii) melt flushing, in which melt infiltrating the peridotite undergoes fractionation and reacts with peridotite. It tends to add dunitic to wehrlitic tendencies to peridotites and, at high rock/melt ratios, would lead to cumulate-like rocks.

5.2 INTRODUCTION

In the upper mantle beneath oceanic spreading centres, mantle flow and partial melting are intimately connected, as the upward flow of mantle material allows for the decompression melting of peridotite (e.g. Bottinga and Allègre 1978, McKenzie 1984). There exists virtually no doubt that the monotonous harzburgite and lherzolite sections in ophiolites represent the residues of this decompression melting (Irvine and Findlay 1972, Menzies and Allen 1974, Dick 1977a, Malpas, 1978).

The question of the exact amount of partial melting that the peridotites have undergone (e.g. Malpas 1978) has developed into more process-oriented studies about the genesis of mantle peridotites. Recent studies have investigated

- whether melting occurred by batch, fractional, or continuous melting (Langmuir et al. 1977, Frey et al. 1985, Bodinier 1988, Johnson et al. 1990), by equilibrium or disequilibrium processes (Prinzhofer and Allègre 1985), and the depth of partial melting (Frey et al. 1985, Prinzhofer and Allègre 1985, Bodinier 1988, Bodinier et al. 1988);

- the role of melt percolation during partial melting and associated mineralogical changes (Nicolas and Prinzhofer 1983, Gregory 1984, Berger and Vannier 1984, Lorand 1987, Bodinier et al. 1988, Navon and Stolper 1989, Kelemen 1990, Kelemen et al. 1990);

- the amount of trapped melt in the peridotites (Dick 1977, Sinton 1977, Nicolas and Prinzhofer 1983, Nicolas and Dupuy 1984, Frey et al. 1985, Evans 1985, Dick 1989);

- the presence and origin of larger scale chemical and mineralogical variation within the mantle sequence (Malpas 1978, Harkins et al. 1980, Obata 1980, Obata and Nagahara 1987, Ozawa 1983, 1988, Quick 1981b, Bodinier 1988);

- chemical changes in the vicinity of cross-cutting dykes (e.g. Podvin et al. 1985, Evans 1985, Bodinier et al. 1990);

- and the influence of thermal re-equilibration on the mineral chemistry (Sinton 1977, Arai 1980, Dick and Bullen 1984, Komor et al. 1985a).

As a result of the multitude of processes which may influence the peridotite composition, it becomes virtually impossible to determine the exact amount of partial melting a peridotite has undergone.

The purpose of this chapter is: (i) to chemically characterize the TM mantle section and the scale of any chemical heterogeneities; and (ii) to evaluate which processes were dominant in defining the chemical pattern of the mantle section.

5.3 DATABASE AND CLASSIFICATION

The basis of this chapter is provided by a large number of mineral analyses collected regionally over the entire TM mantle section, including the massive dunites, as well as a smaller number of samples analyzed from the LH.

In TM, 170 samples (with approximately 1050 analyses) were analyzed for spinel, 107 samples (550 analyses) for cpx, 100 samples (500 analyses) for olivine, 70 samples (375 analyses) for opx, as well as a smaller number of samples for amphibole, plagioclase, and garnet. From the LH mantle section, 350 analyses from 22 samples are reported, most of them from the Springers Hill area. In the appendix, the following data are presented: analytical procedures (section B.2); estimated precision and accuracy for each phase (Tab. B-2); analytical data for each spot analyzed, separated for different phases (Tabs. B-3 to B-7); selected, representative analyses (Tab. B-8); and averages and standard deviations for each phase within a structural unit (Tab. B-9). Analytical data presented in the following sections are *averages of all spots analyzed* in

one thin section, i.e. typically several analyses of core and rim compositions. Orthopyroxene and sometimes clinopyroxene have been analyzed with a defocused beam in order to integrate the small-scale exsolution lamellae.

A small number of samples have been analyzed for their whole rock major and trace element chemistry by AAS and XRF. Analytical procedures and data are given in the appendix (B.1, Tab. B-1).

Apart from the exceptions listed below, the classification of the peridotites into structural units (chapter 2) is retained. The structural unit concept allows for a rapid recognition of correlations between large scale structure and chemistry. For each structural unit, dunites and wehrlites, i.e. opx-free lithologies, are separated from harzburgites and lherzolites because of the different mineral equilibria and possibly genesis involved. The transitional unit TU between unit 4 and 5 is combined with unit 4 for clarity in the diagrams. Cross-cutting dunites within the mantle section are *not* included in the graphical representations of section 5.8, and 5.9. The cross-cutting dunites are specifically dealt with in section 5.10 and Tab. B-9.

Mineral chemical data are given in atomic proportions. Mineral names in brackets following an element or ratio always refer to the element or ratio within this mineral, e.g. atomic proportion of Al in clinopyroxene = Al (cpx); the 100Cr/Cr+Al ratio is abbreviated Cr#, and the 100Mg/Mg+Fe^{tot} ratio is abbreviated Mg#.

5.4 WHOLE ROCK CHEMISTRY

Whole rock chemistry parameters show good correlations with whole rock Al_2O_3 (Fig. 5.1). The latter is considered an indicator of the degree of depletion in peridotites (e.g. Ringwood 1975, Palme and Nickel 1985). The trends for SiO_2, MgO, CaO, NiO, and TiO_2 (Fig. 5.1a,c,d,e,g) show the expected co-variations with progressive

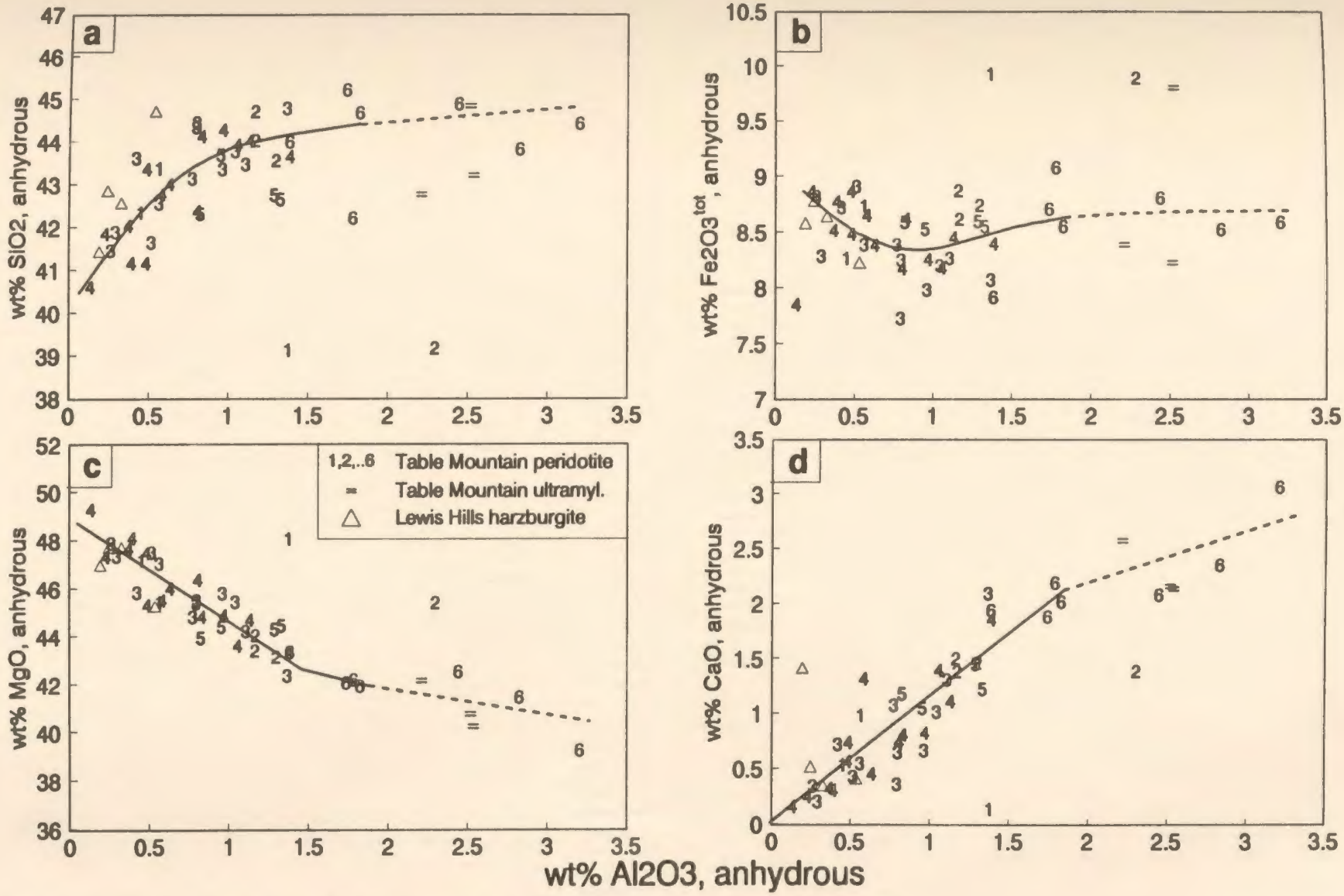

Fig. 5.1. Whole rock chemistry variation diagrams. Numbers refer to structural units of samples. For other symbols see legend in (c).

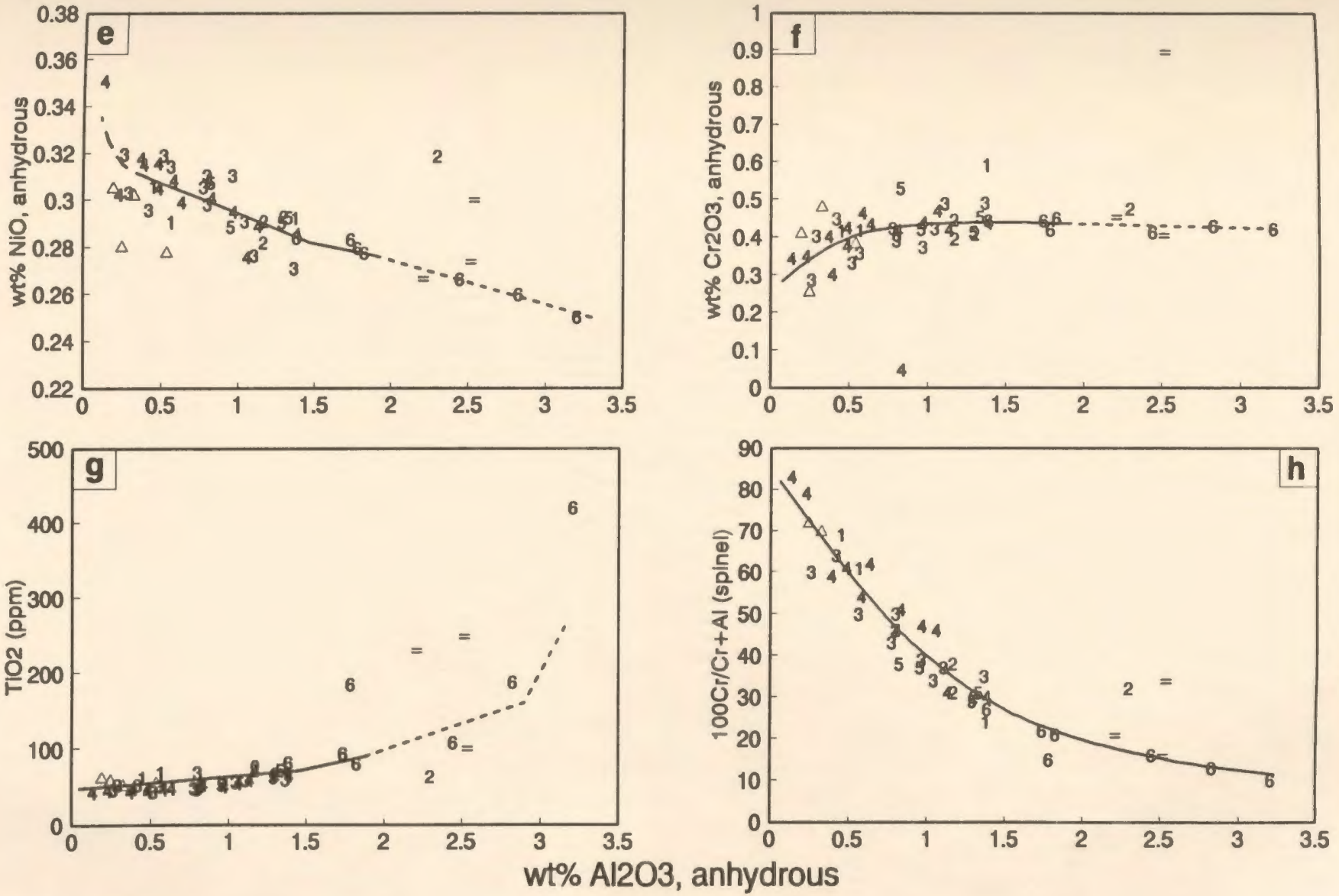

Fig. 5.1. (continued)

depletion. Such trends are weak for Fe_2O_3* and Cr_2O_3 (Fig. 5.1b,f). Cr_2O_3 indicates incompatible behaviour at *high* degrees of partial melting, as suggested previously (Dick and Fisher 1984, Dick and Bullen 1984, Dick 1989; see also discussion in Frey et al. 1985). The partial melting trends are dashed at $Al_2O_3 > 2$ wt.%, as samples with high Al_2O_3 are rare. In addition, the samples with $Al_2O_3 > 2$ wt% are restricted to the base of the peridotite sequence (unit 6) where a local overprint by later metasomatism cannot be ruled out (Suen et al. 1979).

SiO_2 shows a more pronounced decrease at $Al_2O_3 < 1$wt.% which is probably related to a more important partitioning of opx (relative to other silicates) into the melt compared to lower degrees of partial melting. Most elements trend towards the abundance in olivine if extrapolated to 0 wt.% Al_2O_3. Exceptions are Cr and Ti which reside in residual spinel in highly depleted rocks.

TiO_2 concentrations are extremely low for a given Al_2O_3 value if compared to other peridotites (Frey et al. 1985, Bodinier 1988, Bodinier et al. 1988). This implies a more efficient method of incompatible element extraction in the Bay of Islands peridotites than in other peridotite massifs. It could have been accomplished by fractional melting as postulated for abyssal peridotites (Johnson et al. 1990) compared to batch melting in the Ronda and the Pyrenéen peridotites (Frey et al. 1985, Bodinier et al. 1988) or continuous melting in the Lanzo massif (Bodinier 1988).

The two samples containing no opx fall consistently out of the general trends. They are a dunite with aluminous spinels from the massive dunites of the transition zone (unit 1, TM 1316), and a plagioclase wehrlite at the boundary between harzburgites and massive dunites (unit 2, TM 1331.1).

Compared to TM, the Springers Hill samples are highly depleted. At their low Al_2O_3, they are relatively depleted in NiO (Fig. 5.1e) and enriched in SiO_2 (Fig. 5.1a)

compared to TM. This could be the result of a higher opx to olivine ratio in the Springers Hill samples compared to TM. Lower NiO could, however, also be evidence for equilibration with transient melt (see sections 5.9.4, 5.12).

Fig. 5.1h illustrates the good correlation between whole rock aluminum and the Cr/Cr+Al ratio in spinel (e.g. Dick 1977. Dick and Bullen 1984, Talkington and Malpas 1984). The shallowing of the dip of the curve at bulk $Al_2O_3 > 1.5$ wt% reflects the onset of saturation of spinel with Al (see also Fig. 5.6). The Cr# (spinel) is, however, considered the best available mineral chemical indicator of the degree of depletion and for the chemical range represented by the TM and LH peridotites. It has been shown experimentally that the Cr# (spinel) increases with the degree of partial melting (Mysen and Kushiro 1977, Jaques and Green 1980, Duncan and Green 1987). With the exception of spinel-poor wehrlites (Komor et al. 1985a), the Cr# (spinel) is believed not to be significantly affected by lower temperature re-equilibration in peridotites (Arai 1980, Dick and Bullen 1984).

Other potentially useful chemical indicators in minerals for the degree of depletion of the peridotites are either much more prone to changes during subsolidus re-equilibration (e.g. Ca (opx)), see section 5.5) or the microprobe data are below the limit of detection for the bulk of the peridotites studied, as in the case of Ti (cpx).

Eleven peridotite samples from different positions within the massif were analyzed for their REE content according to the method of Jenner et al. (1990) and Longerich et al. (1990). Several analytical problems were encountered, particularly due to the low REE abundance. The most serious problem was preferential loss of HREE during separation in ion exchange columns. The data quality is considered too low for publication standard, but the patterns are available from the author, upon request, for informative purposes only.

5.5 MINERAL CHEMISTRY: ZONING PATTERNS

Core and rim compositions of opx, cpx, and spinel were routinely determined during microprobe analysis. Olivine zoning was not tested, as it is usually not reported from mantle peridotites except for occurrences adjacent to spinel (e.g. Quick 1981a, Conquéré and Fabriès 1984). The following analysis of zoning patterns is qualitative and preliminary, as different domains and lithologies are not distinguished. At this stage, only the *major trends* are of interest. The scatter in the diagrams indicates that other processes may locally override those which are responsible for generation of the more general trends.

Tab. 5.1. Summary of general trends in chemical zoning patterns observed during the microprobe analysis of the TM and Lewis Hills Peridotites. Trends are indicated as variation from *core to rim* in a given grain.

Oxide or ratio	spinel	clinopyroxene	orthopyroxene
Cr_2O_3	decrease	decrease	decrease
Al_2O_3	increase	decrease	decrease
MgO	decrease	poorly defined	increase
FeO	increase	decrease	increase
CaO		increase	decrease
Cr#	decrease	poorly defined	decrease
Mg#	decrease	increase	weak decrease

The results are presented graphically in Figs. A5.3 to A5.5 (in the appendix) as core/rim ratios plotted against the degree of depletion (Cr# in spinels). The general trends are summarized in Tab. 5.1. For Al and Cr in spinels from the Springers Hill harzburgites, a reverse trend to the general zoning trend is frequently observed (Fig. A5.3a,b).

Numerous studies have shown that zoning patterns in minerals from peridotites are a first order function of subsolidus cooling (e.g. Sinton 1977, Quick 1981a, Conquéré and Fabriès 1984). Consequently, it will be tested as to how far the above trends

can be explained by re-equilibration to lower temperatures in a closed system. While the total number of possible reactions occurring during cooling between the four phases olivine, spinel, cpx, and opx, is certainly very high, an attempt is made to explain the zoning trends with a few, well-known reactions.

The Fe-Mg exchange between spinel and olivine has been well studied (e.g. Irvine 1965, Jackson 1969, Evans and Frost 1975, Fabries 1979, Ozawa 1984). During decreasing temperatures, Mg/Fe exchange between spinel and olivine will result in Mg-depletion and Fe-enrichment in spinel rims. These trends are observed in the BOI peridotites (Tab. 5.1). Fe-Mg exchange between spinel and pyroxenes may enhance this spinel zoning (Medaris 1975, Hatton and von Gruenewaldt 1985).

Olivine may contain minor amounts of Cr and Al (Arai 1978, Berger and Vannier 1984, Agee and Walker 1990), which could exchange with Cr and Al of spinel. It is, however, generally accepted that spinel-olivine re-equilibration cannot account for the Cr-Al variation in spinel (Dick and Bullen 1984, Hatton and von Gruenewaldt 1985, Agata 1988).

The amount of solid solution of enstatite in diopside and diopside in enstatite decreases with decreasing temperature (e.g. Boyd and Schairer 1964, Davis and Boyd 1966, Mori and Green 1975, Wells 1977, Herzberg 1978, Kretz 1982). As a result of the increasing miscibility gap, exsolution lamellae develop in pyroxenes. These have been observed in unrecrystallized pyroxenes (chapter 3). They are rare in neoblasts. For cpx, the chemical effect of opx exsolution is an increase in the Ca-content and the Mg#, and a decrease in the Fe and Mg content, whereas the opposite is true for cpx exsolution from opx. These trends are largely realized in the rims of cpx and opx (Tab. 5.1).

In order to account for the simultaneous decrease of Cr *and* Al in opx as well as cpx, a reaction involving the Tschermak-molecule (TS) has probably taken place in the

pyroxenes. The appropriate TS molecules are MgTS in opx ($MgAl_2SiO_6$) and CaTS in cpx ($CaAl_2SiO_6$). In pyroxenes, chromium substitutes for Al in the octahedral site (e.g. Ernst 1978, Mercier 1980b, Nagata et al. 1983). Considering the low Na-content of cpx and opx, the significance of jadeite ($Na(Cr,Al,Fe)Si_2O_6$) as carrier of Al and Cr is low in the investigated peridotites. In peridotites or appropriate simplified analogue chemical systems, the decrease of Al in pyroxenes with decreasing temperature is well known (e.g. Obata, 1976, Herzberg, 1978, Gasparick 1984). The reaction

$$En_{opx} + Sp \; <--> \; TS_{opx} + Fo_{ol} \text{ (e.g. Obata 1976)}$$

can explain the Al and Cr zoning trends in opx where Fo stands for forsterite, ol for olivine, En for enstatite, and Sp for spinel ($MgAl_2O_4$). A similar reaction involving CaTS in cpx can account for the Cr-Al zoning in cpx. The reaction has been reviewed by Talkington and Malpas (1984). It accounts for the microstructurally observed formation of spinel at the margins of pyroxene grains and within recrystallized pyroxene grains (see section 4.6.7).

Mysen (1976) has shown that during cooling of peridotite, Cr-Al exchange takes place between opx and cpx. In this exchange, Al is enriched and Cr depleted in opx with decreasing temperature. As a result, the Cr# of opx decreases, as observed in the TM samples. The reverse trend for cpx is, however, poorly defined.

The remaining problem concerns why Cr decreases in opx, cpx, *and* spinel and the Cr# decreases in opx as well as spinel. The reverse zoning behaviour of Al and Cr in spinel would suggest that the Cr/Al behaviour in spinel is governed by an exchange reaction. Due to the high modal abundance of opx compared to cpx, the Cr/Al exchange of spinel with opx would have been more significant than with cpx. However, Cr and the Cr# decrease both in opx and spinel, so that it cannot be demonstrated that such an exchange reaction took place.

The "Cr-problem" in peridotites has already been noted by Sinton (1977). He concluded that bulk Cr-loss occurred, carried away by transient melts. His interpretation remains a viable solution. It is, however, difficult to estimate the effects of the relative importance of all reactions.

In summary, four reactions can account for nearly all of the observed zoning trends in the peridotites:

(1) Fe-Mg exchange between olivine and spinel, which leads to decreasing Mg and Mg# and increasing Fe in spinel-rims compared to cores. This reaction may be enhanced by Fe-Mg exchange between pyroxenes and spinel.
(2) Al-Cr exchange between opx and cpx could account for the decreasing Cr# of opx rims.
(3) Reaction of Cr-bearing CaTS component in cpx and Cr-bearing MgTS in opx with olivine. Such a reaction explains the decreasing Al and Cr in rims of pyroxenes and the presence of metamorphic spinel near olivine-pyroxene interfaces.
(4) Exsolution of enstatite from cpx and diopside from opx, accounting for rims in cpx which are high in Ca and Mg# and low in Fe, and rims in opx high in Fe and Mg and low in Ca.

The behaviour of Cr and the Cr# of spinel are, however, not easily explained within a closed system.

Judging from the strength of the zoning patterns, the values for Al, Cr, and Fe in cpx and Al, Cr, Ca, and the Cr# in opx have been significantly changed during subsolidus re-equilibration. The very useful Cr/Cr+Al ratio (spinel), however, is rather insensitive to these changes. Due to the large abundance of olivine, the Mg# of olivine is not expected to change dramatically during subsolidus re-equilibration either (e.g. Dick and Bullen 1984, Komor et al. 1985a).

5.6 DEPENDENCE OF PARTITION COEFFICIENTS BETWEEN PYROXENE AND SPINEL ON THE CR/AL RATIO IN SPINEL

In Fig. 5.2a the Cr-content in clinopyroxene is plotted against that of corresponding spinels for the analyzed peridotites. Data points are replaced by the Cr# (spinel) in the sample. The partition coefficient of Cr between cpx and spinel is strongly dependent on the Cr# (spinel) and varies by a factor of 20. The same holds true for orthopyroxene-spinel relations (Fig. 5.2b). Re-equilibration trends for Cr can be inferred from the zoning patterns (Tab. 5.1) and are shown in Fig. 5.2 as an arrow called "REQ". The REQ arrow in Fig. 5.2a,b is oriented at an acute angle to lines of constant distribution coefficients and cannot explain the large variation of distribution coefficients observed. The partition coefficient D=Ti(cpx)/Ti(spinel) varies even by a factor of 40 as a function of the spinel composition (Fig. 5.2c). This means that Cr and Ti reside mainly in pyroxenes in more fertile rocks whereas they partition relatively more into spinel in more depleted rocks.

A similar plot for D=Al(cpx)/Al(spinel) shows that D varies by a factor of three for aluminum as a function of the Cr# (spinel)(Fig. 5.2d). The pattern could be governed by solid state re-equilibration if the depleted rocks had generally cooled to lower temperatures than the more fertile peridotites. This may be supported by the data of Ben Jamaa and Mercier (1987) who calculated higher equilibration temperatures for the lowermost peridotites in TM. These peridotites are also the least depleted ones (cf. Pl. 8f). The core-rim behaviour of clinopyroxenes (Fig. A5.4a) does, however, not allow a similar conclusion.

Peridotites from the Xigaze ophiolite (Girardeau and Mercier 1988) behave in a similar way to the TM rocks. The dependence of D=Cr(opx)/Cr(spinel) on the the Cr# (spinel) is obvious (Fig. 5.3b), whereas for D=Al(opx)/Al(spinel), such a dependence

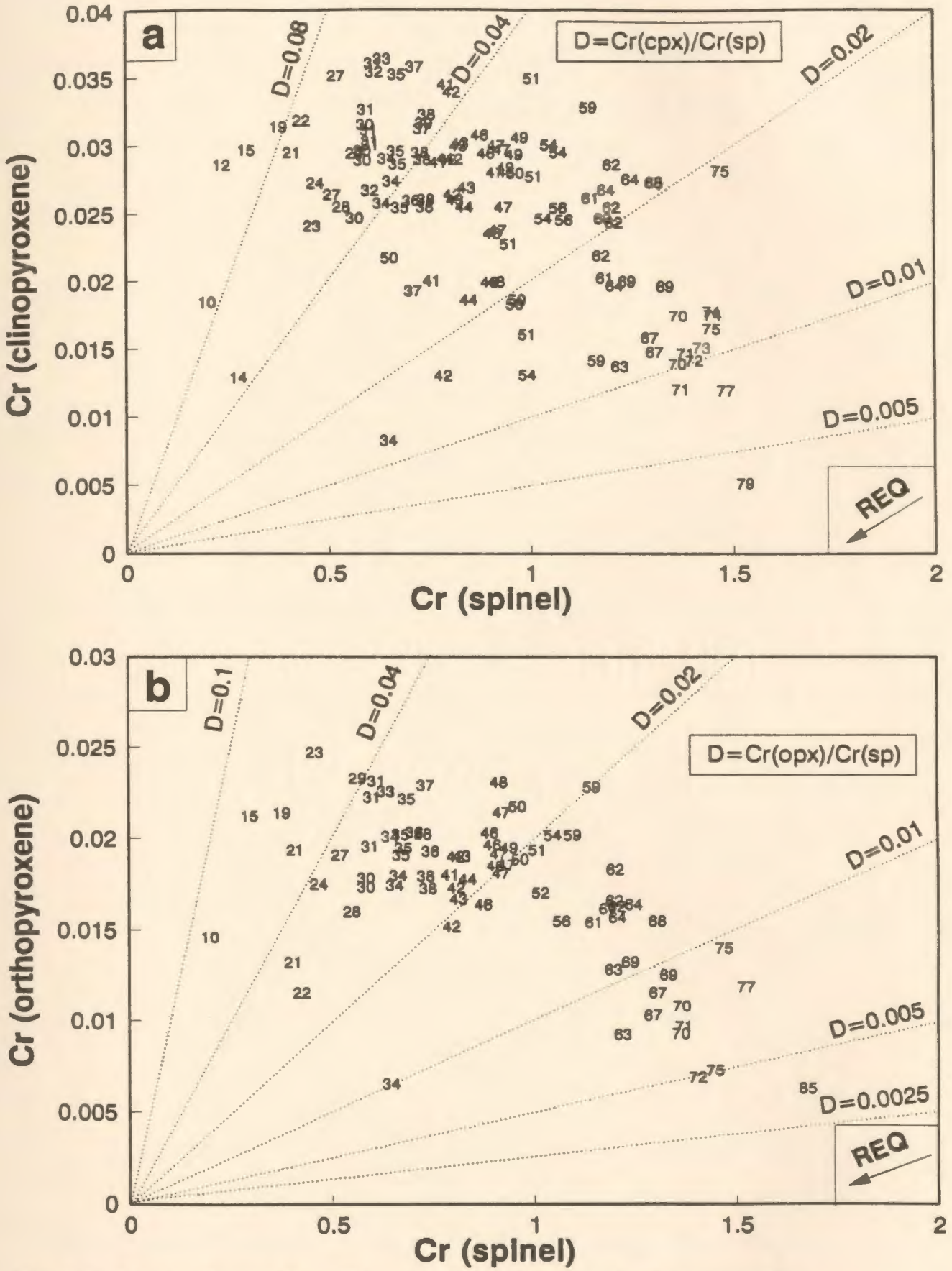

Fig. 5.2. Dependence of partition coefficient D on spinel composition. Numbers indicate the Cr# of spinel in the sample. The Cr# is a good indicator of the degree of depletion of the peridotite. REQ - subsolidus reequilibration trend.

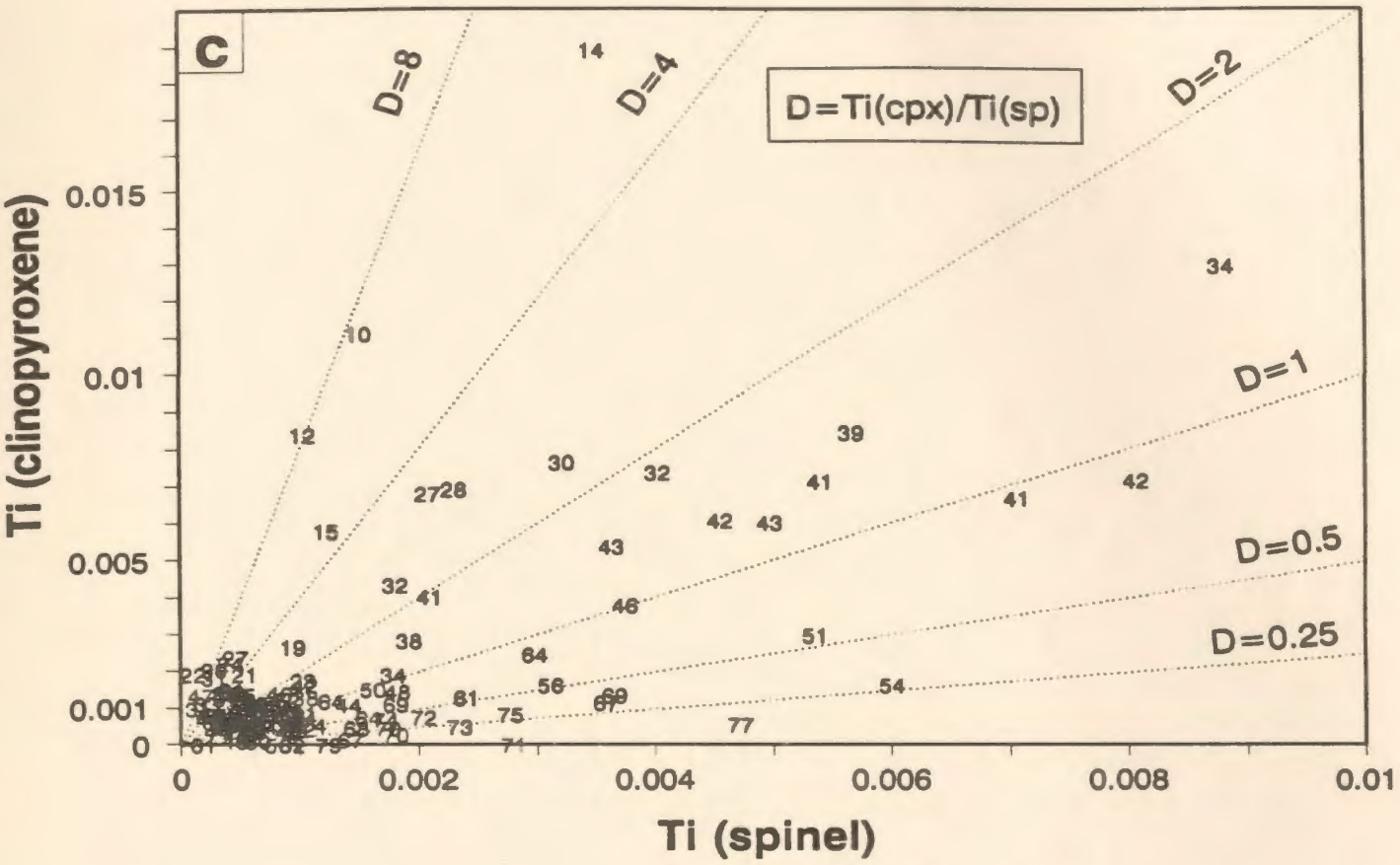

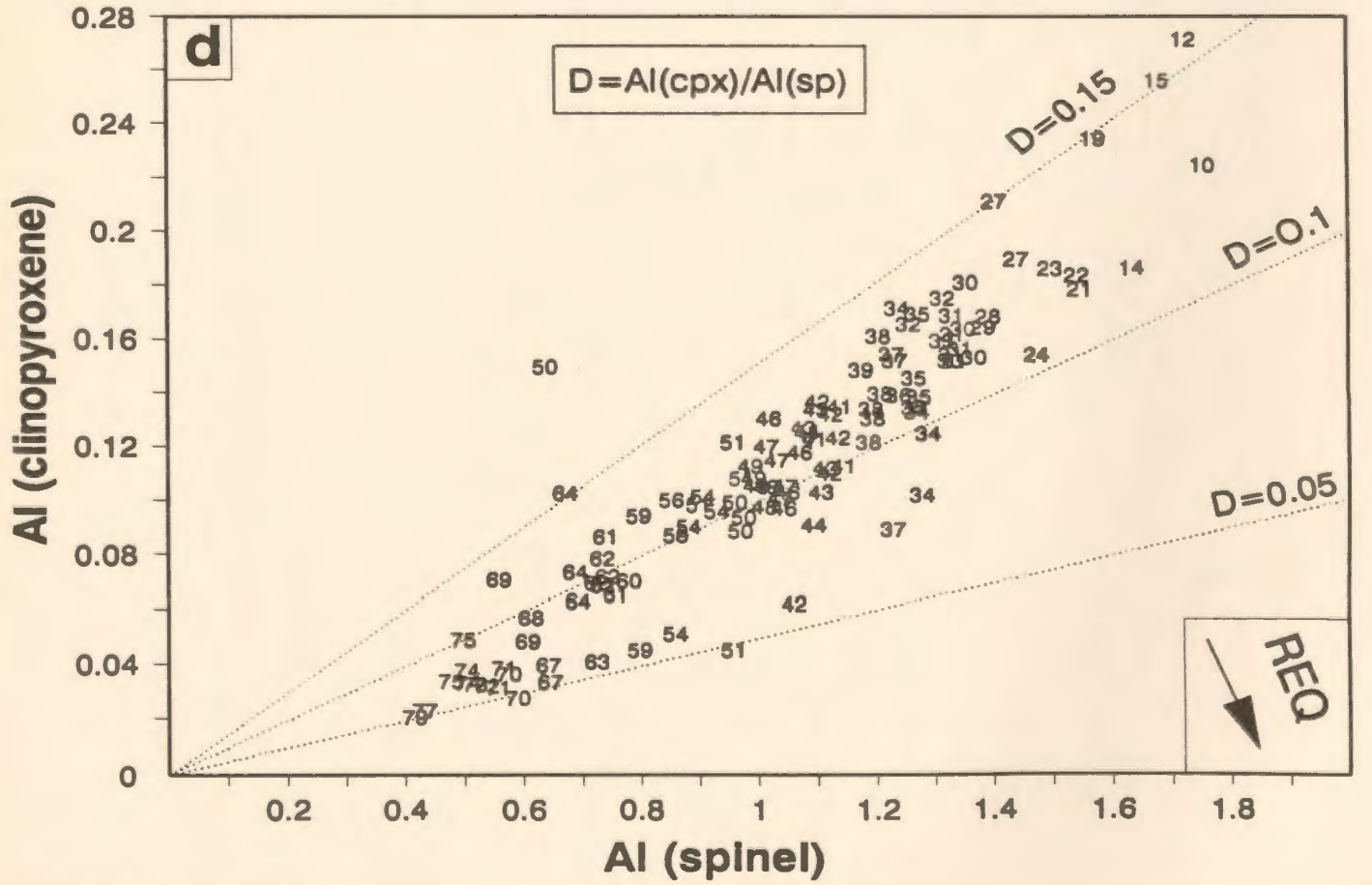

Fig. 5.2 (continued).

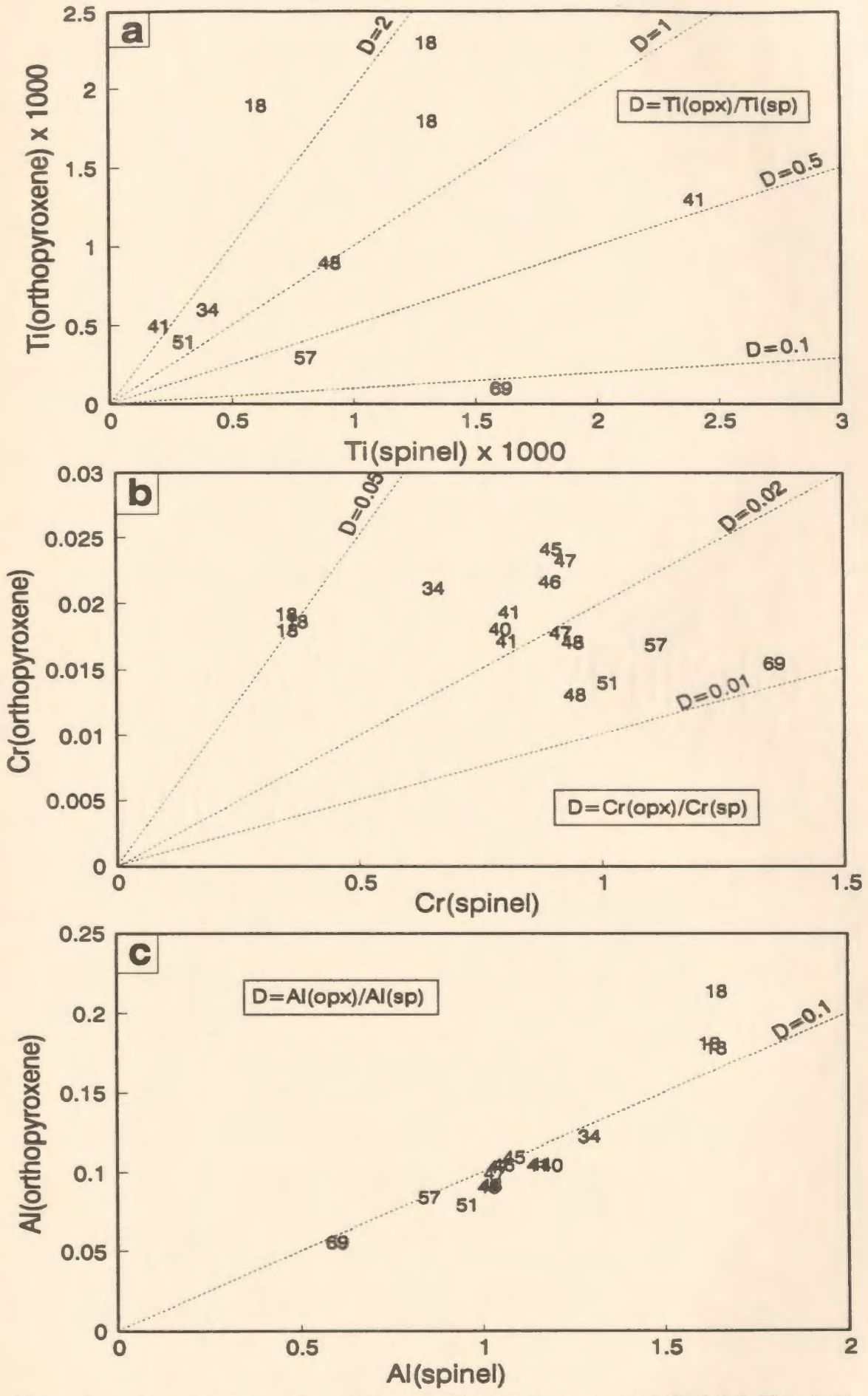

Fig. 5.3. Dependence of partition coefficient D on spinel Cr# (cf. Fig. 5.2). Data from Girardeau and Mercier (1988).

is only vaguely present (Fig. 5.3c). For Ti, a similar trend to TM exists if the unreliable values of low abundance (Ti < 0.0001) are excluded (Fig. 5.3a). A dependence of partition coefficients from the Cr/Cr+Al ratio is known also from other peridotite sequences (Sachtleben and Seck 1981, Stosch 1982, Bodinier et al. 1987).

The complex partitioning behaviour of Ti illustrates the difficulty of interpreting, particularly incomplete, mineral chemistry data. For example, the same concentration level of Ti (spinel) for peridotites with low and high Cr# (spinel) does not indicate the same whole rock Ti for both samples, as for low Cr#'s, significant amounts of Ti are locked up in clinopyroxene.

The dependence of the partition coefficients of Cr, Ti, and possibly Al between pyroxenes and spinels on bulk composition indicates that non-ideal mixing exists in these phases (e.g. Carroll Webb and Wood 1986). Failure to apply appropriate mixing models will result in consistent overestimation of equilibration temperatures for Cr-rich peridotites (e.g. Medaris 1975, Sachtleben and Seck 1981, Conquéré and Fabriès 1984, Witt and Seck, in press).

5.7 FREQUENCY DISTRIBUTION OF SELECTED MINERAL CHEMICAL PARAMETERS

Fig. 5.4 illustrates the frequency distribution of selected mineral chemical parameters as a function of their lithology. Lithologies are divided into dunites and wehrlites of the transition zone, harzburgites and minor lherzolites with the exception of unit 5 and 6, basal peridotites (cpx-harzburgites and lherzolites of unit 5 and 6), ultramylonites of unit 6, and crosscutting dunites in the mantle sequence. For the Mg# (olivine) only, harzburgites of the Springers Hill area are shown as well.

Cr#'s of spinels range from 10-80 with a few more extreme values in cross-cutting dunites (Fig. 5.4a). Compared to the mean composition, spinels in basal peridotites

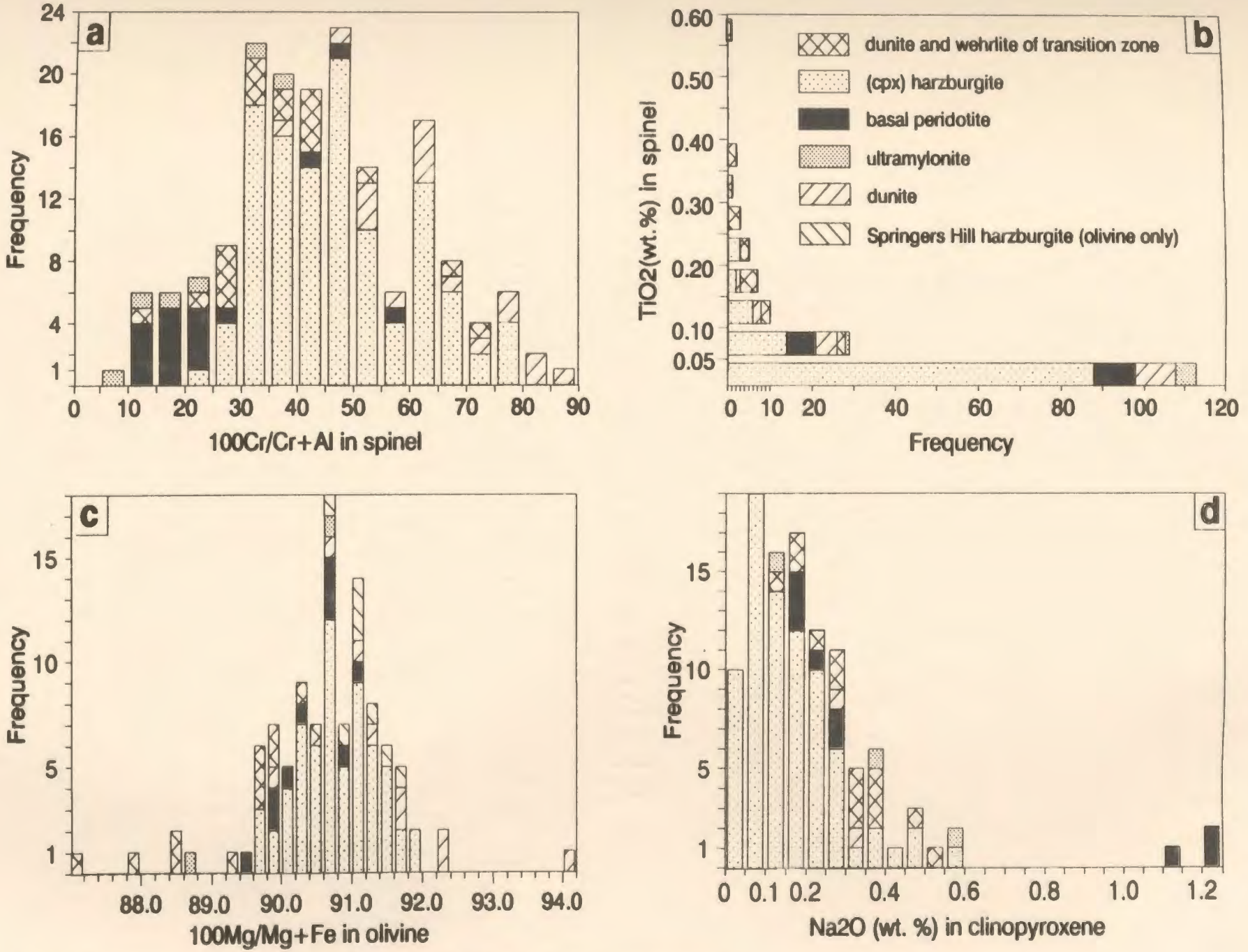

Fig. 5.4. Frequency distribution of selected mineral chemistry parametres.

and transition zone dunites and wehrlites are more aluminous, dunites from within the harzburgites are more chromitiferous, and ultramylonites from the base of the massif show a wide range of generally aluminous spinels.

In terms of the TiO_2 (spinel) content (Fig. 5.4b) and Mg# (olivine)(Fig. 5.4c), the basal peridotites are less clearly distinguished from the bulk of the harzburgites than with the Cr# (spinel). They contain, however, higher Na_2O values which are bimodally distributed (Fig. 5.4d). Transition zone rocks are higher in TiO_2 (spinel) and Na_2O (cpx) and lower in the Mg# (olivine) than the harzburgites Cross-cutting dunites have high Mg# (olivine) but are not depleted in TiO_2 with respect to the harzburgites.

5.8 SPATIAL DISTRIBUTION OF MINERAL CHEMISTRY DATA

The spatial distribution of the most important mineral chemical parameters is shown in the maps of Pl. 8f and Fig. A5.6. Data from cross-cutting dunites are *not* included. All maps indicate that, apart from the top and the base, the mantle section consists of spinels with intermediate Cr#'s and low Ti and ferric iron values, and cpx with low Ti and Na contents.

The Cr# (spinel) distribution (Pl. 8f) shows the very steep chemical gradient near the base of the mantle harzburgites and lherzolites. The pattern towards low Cr#'s at the base is offset along with the major fault system in the north of the massif. The changeover to less depleted rocks at the base correlates with the unit 4/TU boundary. A wedge-shaped area containing more abundant dunites (Fig. 2.1) may correlate with a more depleted phase chemistry.

Near the base of the gabbros, more complex trends are recognized in the Cr# (spinel) pattern (Pl. 8f). They are best illustrated in the chemical profiles (Fig. 5.5): in the southern profile, below thick dunites, a wedge with highly chromitiferous spinels is developed in harzburgites just below the dunites. The dunites themselves contain alumi-

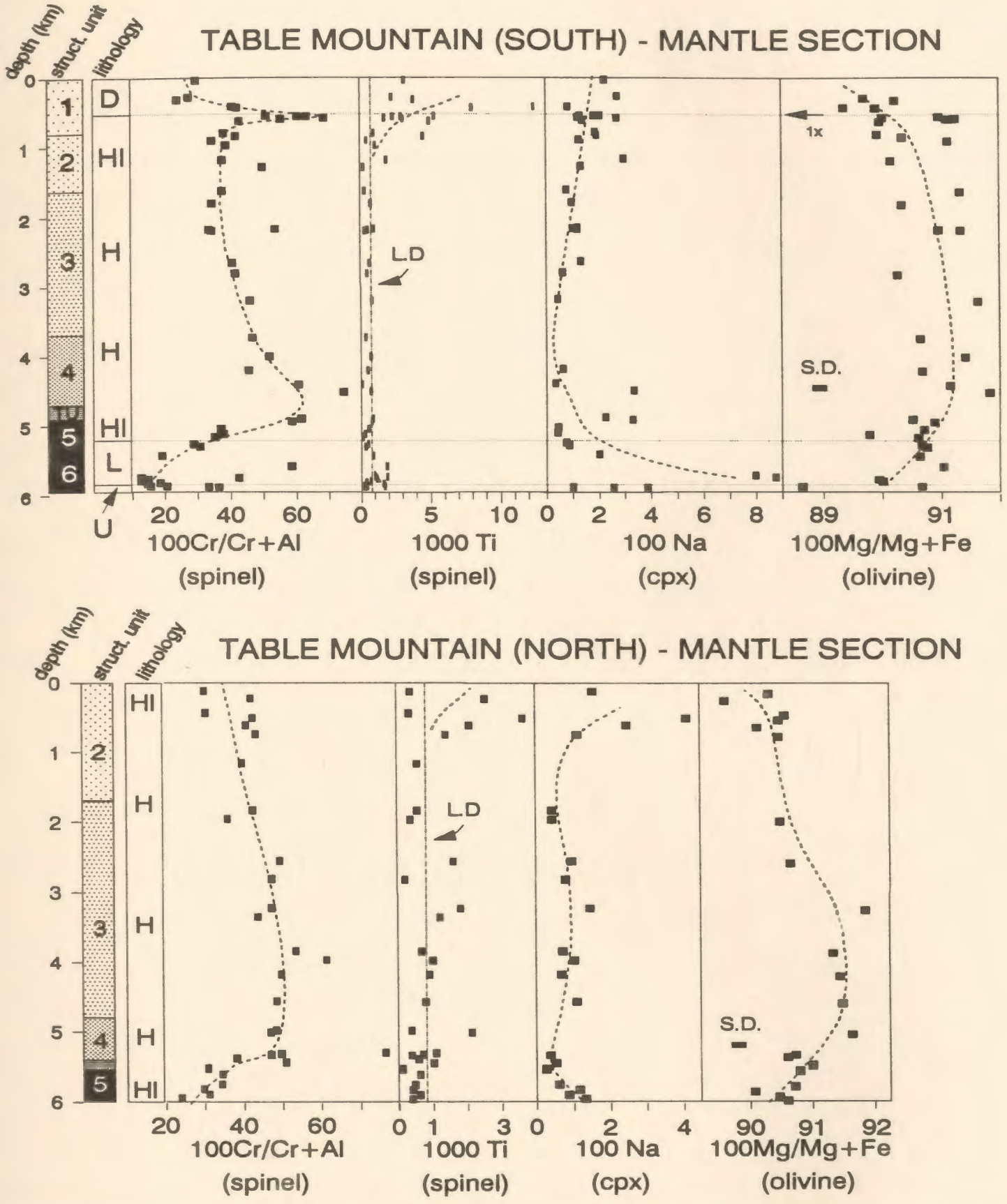

D	- dunite	L	- lherzolite
H	- harzburgite	U	- ultramylonite
HI	- harzburgite, melt infiltrated	L.D.	- limit of detection
		S.D.	- standard deviation

Fig. 5.5. Mineral chemical profiles through the Table Mountain mantle section.

nous spinels. The change from harzburgites with chromitiferous spinels to underlying harzburgites with aluminous spinels coincides with the boundary of the structural units 1 and 2. A similar, though broader, high Cr#-wedge is developed in the corresponding western side of the syncline (Pl. 8f). There, it is developed in structural unit 3. In the northern part of the massif, where the dunites are thin or absent, little of the chemical variation from the south is seen towards the Moho.

Other parameters show similar trends: Ti (spinel) is enriched mainly below the gabbros (Fig. A5.6a), Ti (cpx) and Na (cpx), as well as the probably less reliable ferric iron values in spinels, show enrichments both towards the Moho and near the base of the massif (Figs. A5.6b,c,d). The forsterite content of olivine is more difficult to evaluate because of higher scatter, but appears to indicate again trends to lower values near the base and top of the mantle section (Fig. 5.5).

5.9 CHEMICAL CHARACTERIZATION OF PROGRESSIVE PARTIAL MELTING, MELT INFILTRATION, AND CUMULATE TRENDS IN THE PERIDOTITES.

5.9.1 Introduction

In this section, several graphs are discussed, each representing a different combination of mineral chemical parameters. The most important trends can be seen in Fig. 5.6. Six further variation diagrams are located in the appendix (Fig. A5.7). The graphs contain data from the TM as well as LH massifs with the exception of cross-cutting dunites. The data obtained in this study are plotted as symbols representing the structural unit in which they occur. The upper diagram of each graph shows the data of this thesis as well as the fields for cumulate rocks from North Arm Mountain and peridotite intrusives from the LH taken from the literature. The literature data are included to define ultramafic cumulate trends and thus allow a comparison of the ultramafic cumulate data with the controversial massive dunites of the TM massif.

The LH Intrusives (LHI) in Figs. 5.6 and A5.7 represent a suite of poorly layered, intrusive peridotites, mainly wehrlites, occurring in the central and western LH (Smith and Elthon 1988); "93" represents dunites and wehrlites from a very detailed study of a 8 m thick, layered cumulate section (NA93), located 50 m above the top of the residual harzburgites in NAM (Komor et al. 1985a); fields "49D and "49W" represent dunites and mainly wehrlites, respectively from a 136 m thick layered dunite - wehrlite - clinopyroxenite sequence in NAM. The traverse (NA49-50) lies 700 m above the top of the residual mantle and was studied by Elthon et al. (1984).

5.9.2 Progressive partial melting trends (PPM)

The peridotite samples, excluding those of units 1, 2 and the transition zone, (MT-field) are stretched out along a wide range of Cr# (spinel) or Al (cpx) in Figs. 5.6 and A5.7. Such an array is typical for mantle peridotites and most likely reflects varying degrees of depletion (Dick 1977a, Dick and Bullen 1984, Michael and Bonatti 1985). In the inset to Figs. 5.6 and A5.7, this trend is referred to as progressive partial melting (PPM). A similar array appears to be defined by ferric iron in spinel (Fig. A5.7f) but the data quality is here low (see Tab. B-2a). For other parameters, e.g. Ti in spinel (Fig. A5.7c,f), Mg# in olivine (Fig. A5.7d) and Ni in olivine (Fig. A5.7d,e) the peridotites of the MT-field do not define a large data array. Na (cpx) is a problem as three data points with very high Na are isolated from the main trend (Fig. A5.7b). It is not clear whether these samples (TM 1029.11, TM 932, TM 1063.3) are metasomatically influenced or represent truly more primitive mantle. In the latter case, Na (cpx) would represent a valuable discriminator for the group of less depleted peridotites (cf. Kornprobst et al. 1981).

Na (cpx) and Ti (spinel) increase slightly in the lowest Cr# (spinel) range, reflecting relatively more fertile compositions (Figs. A5.7b,c). It is notable that somewhat higher Na (cpx) and Ti (spinel) concentrations were also measured for highly depleted

Fig. 5.6. Mineral chemical variation diagram with data from Table Mountain and the Lewis Hills (facing page).

LEGEND

UPPER DIAGRAMS

1,2,..6 - harzburgite or lherzolite from Table Mountain massif, number indicates structural unit

x - massive dunite or wehrlite from Table Mountain transition zone

= - ultramafic ultramylonite from base of Table Mountain peridotites

c - layered cumulate rocks from Table Mountain

△ - Springers Hill harzburgites

* - harzburgites from eastern Lewis Hills mantle section

+ - harzburgite from sliver accreted to base of eastern Lewis Hills mantle section

93 - layered ultramafic cumulates from profile NA 93 in North Arm Mountain (Komor et al. 1985)

49W - mainly wehrlites of layered ultramafic cumulate profile NA 49-50 (Elthon et al. 1984)

49D - dunites from layered ultramafic cumulate profile NA 49-50 (Elthon et al. 1984)

LHI - intrusive peridotites from the Lewis Hills massif (Smith and Elthon 1988)

LOWER DIAGRAMS

MT - main trend of Table Mountain mantle peridotites. Excludes samples from unit 1,2, transition zone, and ultramylonites as well as isolated data points

U1,2 - range defined by samples from unit 1 and 2 , excluding TZ

TZ - range defined by samples from transition zone (opx-free peridotites, marked x)

UMC - range defined by fields 93, 49W, 49D, i.e. layered ultramafic cumulates

INSETS

PPM - progressive partial melting trend, inferred from MT-field

ACT - apparent cumulate trend, inferred from UMC-field

INF - melt infiltration trend, inferred from U1,2-field

suggested or apparent trends

REQ - subsolidus reequilibration trend, inferred from core-rim relationships

C+M 88 - progressive partial melting trend from Cabanes and Mercier (1988)

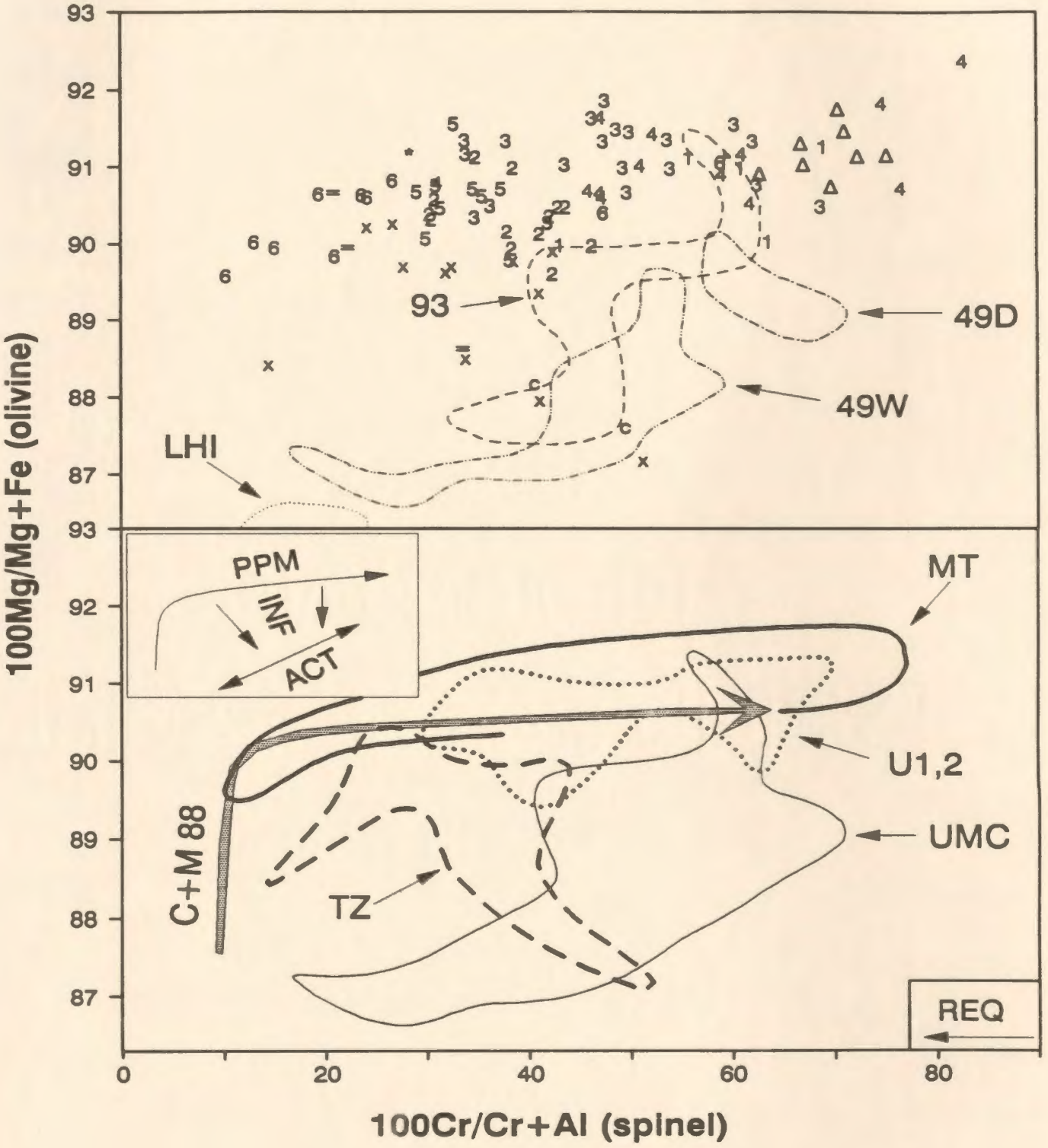
100Mg/Mg+Fe (olivine)
100Cr/Cr+Al (spinel)
93
92
91
90
89
88
87
0
20
40
60
80
93
49D
49W
LHI
PPM
INF
ACT
MT
U1,2
UMC
TZ
C+M 88
REQ

rocks compared to peridotites with an intermediate Cr# (spinel). This is particularly clear for Ti (spinel) in the Springers Hill samples (Fig. A5.7c, 'SH'-field). Possibly, this Ti-trend is a reflection of the progressive partitioning of Ti from pyroxenes to spinel in more depleted rocks (section 5.6). The whole rock data do not necessarily indicate an elevated total TiO_2 content in the Springers Hill samples (Fig. 5.1g). However, higher Fe(III) in spinel (Fig. A5.7f) and lower NiO in olivine (Fig. A5.7d), reflecting a lower whole rock NiO (Fig. 5.1e), as well as the frequently observed reverse Cr-Al zoning pattern in spinels support a special character of the Springers Hill samples (see section 5.12).

The most suitable diagram to classify the partial melting history with mineral chemical parameters is the Mg# (olivine) - Cr# (spinel) plane (Fig. 5.6), e.g. Dick and Bullen (1984), Ozawa (1988). This diagram tracks the early partial melting history with a progressively changing forsterite content of olivine and nearly constant Cr# (spinel). The more extreme partial melting history is monitored by a strong variation in the Cr# (spinel) and only subtly increasing Mg# in olivine (Cabanes and Mercier 1988). In this "olivine-spinel array" (Arai 1990) melting at different pressures and oxygen fugacities can potentially be distinguished (Cabanes and Mercier 1988). Cabanes and Mercier (1988), using mantle xenolith data, suggest that the primitive mantle plots at a forsterite value of approximately 87.5 and a Cr# of 10.

In Fig. 5.7, compositional data of experimentally melted, dry Tinaquillo lherzolite (Jaques and Green 1980) are plotted in the olivine-spinel array. Plagioclase is not stable with liquid in the PT-conditions shown, as it disappears very rapidly from the residue with inititation of partial melting even at low pressures. The higher pressure data below 20% partial melting fit quite nicely into the TM trend whereas progressive partial melting at 5 and 2 kbar yields residues with very high forsterite contents not realized in the TM harzburgites. Cr# < 20 were not measured in the experiments, neither in the depleted Tinaquillo lherzolite nor in experiments with primitive pyrolite. The data dem-

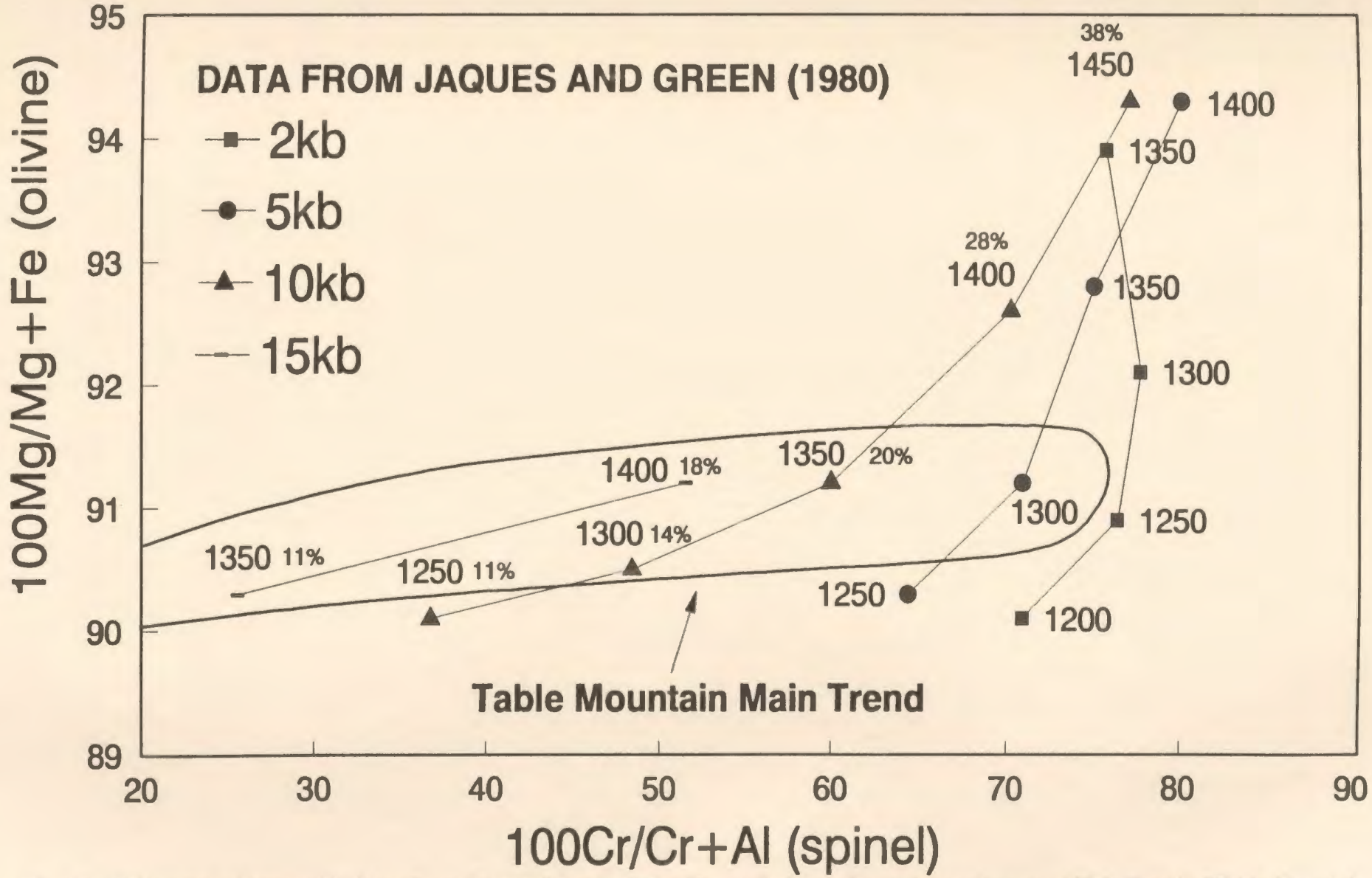

Fig. 5.7. Olivine-spinel array with data of experimentally melted, dry Tinaquillo lherzolite and superimposed Main Trend of Table Mountain mantle rocks. Large numbers indicate temperatures in degrees Celcius. Small numbers give degree of melting in percent.

onstrate that the TM peridotite trend cannot be produced by equilibrium partial melting at very low pressures (2, 5 kbar): neither are the high forsterite values of the experiments present in TM, nor can low pressure melting, restricted to the plagioclase stability field, explain the wide range of Cr# (spinel) observed in the BOIC. Melting must have been initiated at greater depth (> 10 kbar), implying also a long flow and strain history.

High forsterite values at high degrees of melting may, however, also be caused by iron loss in the experiments. This is suppo' 'd by the increase of the Mg# of spinels during progressive melting in the experimental runs of Jaques and Green (1980), a feature inconsistent with natural partial melting trends (e.g. Dick and Bullen 1984). In general terms, dry melting will produce higher forsterite contents in the residue than wet melting (Mysen and Kushiro 1977, Jaques and Green 1980, Dick and Fisher 1984, Cabanes and Mercier 1988).

As suggested in section 5.4, partial melting in the TM mantle section probably took place by fractional melting. Fractional melting was already demonstrated to have occured in abyssal peridotites (Johnsen et al. 1990). During this mode of melting, mantle peridotites suffered first high and then low pressure melting during their progressive, adiabatic ascent - a feature consistent with the microstructural evidence for low pressure, syntectonic melting in the uppermost peridotites (see type microstructure 2 and discussion in section 4.7). Mixing of magma batches produced at different pressures below the ridge is then likely. It may have occurred along magma conduits (Nicolas 1986b), within magma chambers, or possibly within the melt-charged uppermost mantle peridotites below the petrological Moho. Mixing would tend to homogenize melts produced from relatively fertile peridotites at depth and depleted peridotites at shallow oceanic levels (e.g. Klein and Langmuir 1987, Falloon and Green 1988).

5.9.3 Ultramafic cumulate trends (ACT)

Compared to the TM mantle rocks, the ultramafic cumulates of NAM have a lower forsterite content, higher Ti and lower Mg# in spinel, and lower NiO in olivine for a given Cr# (spinel)(Figs. 5.6, A5.7). These relative trends are similar to those from other ophiolites (Ozawa 1988, Hébert et al. 1989). There appears to be not much difference in the amount of Na (cpx) between residual rocks and NAM ultramafic cumulate rocks. The range of Al (cpx) and Cr# (spinel) from NAM is somewhat more restricted than in the TM residual rocks, but still extensive. An evolutionary trend (apparent cumulate trend, ACT) is typically present in the data range defined by the cumulate rocks. According to Elthon et al. (1984) and Komor et al. (1985a), the ACT can be explained by repeated injection of small batches of melt followed by fractionation of up to 20 % of the melt reservoir at high pressures. In a different model, the injection of new magma batches is restricted to the base of the magma chamber due to the high density of injected primitive magma and a small width of the feeder dykes (Campbell and Turner 1989). Bédard (1991) has interpreted the ultramafic cumulate sequence of NAM as a multistage intrusive history, so that the ACT could result from the superimposition of different magmatic suites.

Spinels from the NAM layered cumulates with more than 20 wt% Al_2O_3 are considered to be the result of subsolidus re-equilibration with cpx due to a very low modal ratio of spinel/cpx (Komor et al. 1985a). Clinopyroxene-free dunites including spinel-rich dunites in the transition zone of TM (e.g. TM 1316, 1316.2) show up to 50 wt% Al_2O_3 in spinel (see Tab. B-3). They must be of *primary* origin as subsolidus equilibration with cpx cannot have taken place.

The mineral chemistry of the LHI (high Al and Na in cpx, high Al and Fe(III) in spinel, and low forsterite contents) is distinct from the layered cumulates in nearly all

diagrams and supports the interpretations of Karson and Dewey (1978), Karson et al. (1983), and Dunsworth et al. (1986) about the distinct geological and structural make-up of these bodies.

The ACT indicated in the insets of Figs. 5.6 and A5.7 is purely descriptive and is not meant to imply any specific process. However, the well layered nature and, even the rather poorly developed, cryptic units suggest a magmatic origin (Irvine and Findlay 1972, Malpas 1978, Elthon et al. 1982 and 1984, Komor et al. 1985a). It should be noted that layered ultramafic rocks above the massive dunites have also been interpreted to represent dyke and sill injection and melt infiltration into mantle peridotites (Nicolas and Prinzhofer 1983, Benn et al. 1988).

Most important in the context of this thesis is whether the massive dunites with minor wehrlites (TZ) are chemically more akin to residual rocks (MT), ultramafic cumulate rocks (UMC) or the intrusive, unlayered peridotites (LHI). The mineral chemistry variation diagrams suggest no obvious similarity of TZ-peridotites from TM to the residual rocks, i.e. a progressive partial melting trend.

Melt percolation of a LHI-type magma through the residual peridotites cannot entirely be ruled out to explain the TZ peridotite trends. It would result in a chemical signature intermediate between the LHI (the magmatic component) and the MT peridotites (the replaced/assimilated lithology). This interpretation would be favoured by Nicolas and Prinzhofer (1983), Benn et al. (1988) and Nicolas (1989).

The evolutionary trend of the TZ peridotites is matched best by the layered cumulates (UMC). In contrast to the UMC, peridotites with low Al (spinel) have not been sampled in TM. A further difference to the layered cumulate rocks from NAM is the high Ni (olivine) values in the TZ peridotites.

In summary, with the limited amount of data, only an entirely residual origin of the TZ peridotites can be excluded. Both a fully magmatic origin as well as the melt percolation model (in-situ dunite formation) of Nicolas and Prinzhofer (1983) appear feasible.

5.9.4 Melt infiltration trends (INF)

The fields of harzburgites and lherzolites of unit 1 and 2 (U1,2) are typically offset from the MT towards higher Ti (spinel), higher Na (cpx), lower Mg# (spinel, olivine), and lower Ni (olivine)(Figs. 5.6, A5.7). Cumulate rocks from NAM show similar trends compared to the residual rocks, though the trends are much more pronounced. The chemical difference is interpreted as the result of a melt-infiltration component in residual harzburgites. Abundant evidence for melt impregnation is present microstructurally (chapters 3,4). Studies of the sulfide mineralogy of the uppermost harzburgites of the BOIC support this interpretation (Lorand 1987). Nearly identical trends are found in melt-infiltrated peridotites near a gabbro vein in the Zambales ophiolite mantle section (Evans 1985) and other melt-infiltrated peridotites (Dick and Bullen 1984, Evans and Hawkins 1989, Cannat et al. 1990).

5.10 CROSS-CUTTING DUNITES

In Fig. 5.8, some mineral chemical parameters from cross-cutting dunites, including foliation-parallel dunites, of the TM mantle section are compared to the fields defined by peridotites as established in the previous section. The harzburgite-hosted dunites extend the main trend from TM into the very high Cr# (spinel) range (Fig. 5.8a-c) and they contain more Mg-rich spinels and olivines (Figs. 5.8a,b). Ti contents of spinels are often elevated compared to the MT (Fig. 5.8c,d), as appears typical for dunites in ophiolitic mantle rocks (Dick 1977a). Ferric iron contents in spinel cover a

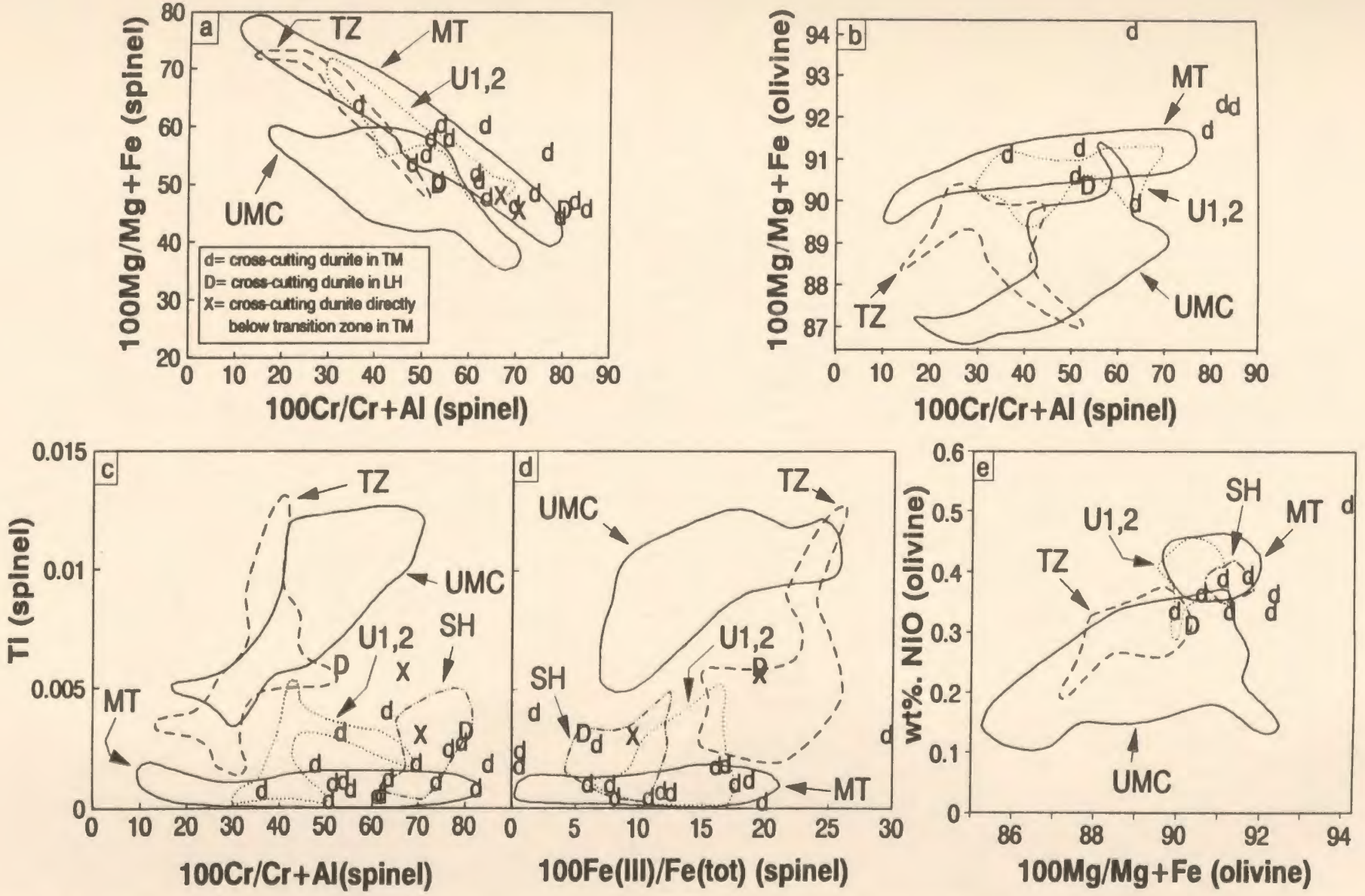

Fig. 5.8. Mineral chemistry variation diagrams for cross-cutting dunites. Fields for different lithological units of host peridotites are shown. For legend see inset in (a) and Fig. 5.6.

wide range (Fig. 5.8d). NiO data of olivines are generally lower than for the MT (Fig. 5.8e). The field 'TZ' which represents massive dunites and wehrlitic rocks from the transition zone hardly overlaps with the cross-cutting dunites.

Compared to their average host rock, cross-cutting dunites within unit 2 appear to have more aluminous spinels, whereas in units 3,4, and TU the spinels are more chromitiferous than in their host (Tab. B-9). The change from host rock to dunite within unit 2 is, however, often subtle to non-existent, particularly for narrow dunite bands (e.g. TM 873, Tab. B-3a). Dunites have higher average concentrations of Ti (spinel) than their average host rocks.

The cross-cutting dunites are interpreted as wall rock to melt conduits (Boudier and Nicolas 1972 and 1977, Dick 1977b, Quick 1981b, Bodinier 1988, Kelemen 1990). The formation of dunitic wall-rock could have occurred either by further melting due to heat introduced with the magma conduit (thermal disequilibrium) or by a reaction/diffusional gradient between magma and host (chemical disequilibrium). The data set is insufficient to discriminate between both options.

5.11 SCALE OF CHEMICAL HETEROGENEITIES

The spatial distribution of the mineral chemical data (section 5.8) shows that major changes of the chemistry occur in the transition zone area and near the base of the peridotites. Apart from these regional changes, heterogeneities have been encountered in four more local settings:

- near orthopyroxenites
- near the very base in the ultramylonites
- in high strain zones
- near cross-cutting dunites

5.11.1 Local heterogeneities

Orthopyroxenites

Local changes of peridotite wall rock near cross-cutting gabbroic or pyroxenitic dykes are well known (e.g. Podvin et al. 1985, Evans 1985, Bodinier et al. 1990), though they have been more extensively studied in mantle xenoliths than peridotite massifs. Generally, the affected wall rock has an intermediate composition between dyke and unaffected host rock. Based mainly on field evidence, the mineralogical changes reported here near orthopyroxenites appear to be limited to less than 1 m distance from the dyke margin. Where not strongly overprinted by subsequent deformation, the alteration effect can be seen in the field as a more random fabric and reduced pyroxene content in harzburgites occurring adjacent to the dykes.

Two occurrences have been investigated by studying a sample taken directly adjacent to the orthopyroxenite (samples TM901.1, and TM1189.1) and one several metres away from it (TM 901.3, TM 1189.2). In both cases, compared to the more distant host rocks, the samples taken adjacent to the dykes display a decrease in the Mg# (olivine), as well as decreasing Al (opx, cpx, and spinel), and possibly an increase of Ti (spinel) (Tabs. B-3 to B-6). Notable is also a reverse spinel zoning for Al in the sample taken directly adjacent to the dyke (TM 1189.1, Tab. B-8a, #37,38).

Ultramylonites

Ultramafic ultramylonites occur immediately above the metamorphic sole. Their chemistry does not fit into the homogeneous gradient towards lower Cr# (spinel) observed in the peridotites above the base of the mantle sequence. The ultramylonites show a wider range of mineral chemistries than overlying peridotites. This is interpreted as local, lower temperature metasomatism during thrusting (see section 3.5.7.4). The ultramylonite assemblage is of disequilibrium nature, as seen in large ranges of chemical parameters within one thin section (compare different spot-analyses in Tabs.

B-3 to B-7). In addition to their hydrous nature involving typically pargasitic hornblende (Tab. B-7), the ultramylonites tend to be low in Ni (olivine)(Fig. A5.7d), high in ferric iron of spinel (Fig. A5.7f), and low in Ca (opx) and Cr (opx)(not shown in figures).

Shear zones

In two cases, the mineral chemistry of high strain samples from the centre of shear zones has been compared to that of their host rocks (TM 723, TM 1063). In both cases, the highest strain samples are the most chromitiferous ones (Tab. B-3). The preferred interpretation is that these trends are not the result of chemical changes associated with shearing, but that they reflect originally more depleted regions. As olivine-rich peridotites are more ductile than pyroxene-rich peridotites, strain will preferentially partition into those zones. A further chemical change is hydration seen in some late high strain zones near the sole (TM 934.1, TM 922, Tab. B-7).

Heterogeneous Harzburgite

In a 20x20 m large area at the base of unit 4, three samples with different pyroxene contents have been analyzed for their spinel chemistry. The data (TM 835.1, TM 835.2, TM 835.3, Tab. B-3a) indicate a large range in Cr#'s (spinel) from 36 to 75. While the map-scale pattern of the Cr# distribution suggests a km-scale homogenization, the example of station TM 835 indicates that local heterogeneities may be preserved. In TM 835, this heterogeneity may be coupled to a poorly exposed cross-cutting dunite (-network), i.e. a zone of melt (or fluid) movement.

5.11.2 Regional heterogeneities

On a regional scale, three different heterogeneities have to be dealt with. The dramatic and consistent decrease of Cr# (spinel) and other parameters near the base is coupled with a change in the structural style (chapter 2), a distinct microstructure

development (chapter 3), and with the disappearance of cross-cutting orthopyroxenites and the presence of only rare dunites (chapter 2). This change is apparently related to a mantle flow pattern and will be discussed in the final chapter (section 6.12.1).

The subtle changes to more aluminous chemistries near the top of the mantle sequence, near the boundary of unit 3 to 2, correlate with microstructural evidence for melt impregnation. The mineral chemistry often deviates from a progressive partial melting trend (e.g. Fig. 5.6). These data are best interpreted to reflect a regional melt infiltration event concentrated below the Moho (section 5.9.4).

On a smaller scale, the narrow region of distinct harzburgites situated below the massive dunites has to be explained. They have chromitiferous spinels with elevated Ti (spinel) contents (harzburgites of unit 1). A model of local melt infiltration of a more refractory nature is preferred. Local melt infiltration is best explained by feeder dykes loosing their propagation force and expelling the melt into the surrounding matrix (Nicolas 1986b).

5.12 MODEL

In section 5.9 the mineral chemistry of the TM peridotites has been interpreted in terms of varying degrees of partial melting and melt infiltration tendencies and compared to ultramafic cumulate rocks from North Arm Mountain. An attempt is now made to synthesize the data into a conceptual model by distinguishing three *end-member* processes: a partial melting trend, a trend reflecting trapping of pristine melt, and a melt flushing trend involving melt-host reaction and fractionation (Fig. 5.9a).

The partial melting trend is caused by progressive out-melting due to adiabatic ascent of peridotite, lowering of the solidus by fluid, or introduction of heat through dyke emplacement. Melt is effectively extracted after a given increment of melting. In the end-member, no melt enters the system and all melt is extracted. The typical litho-

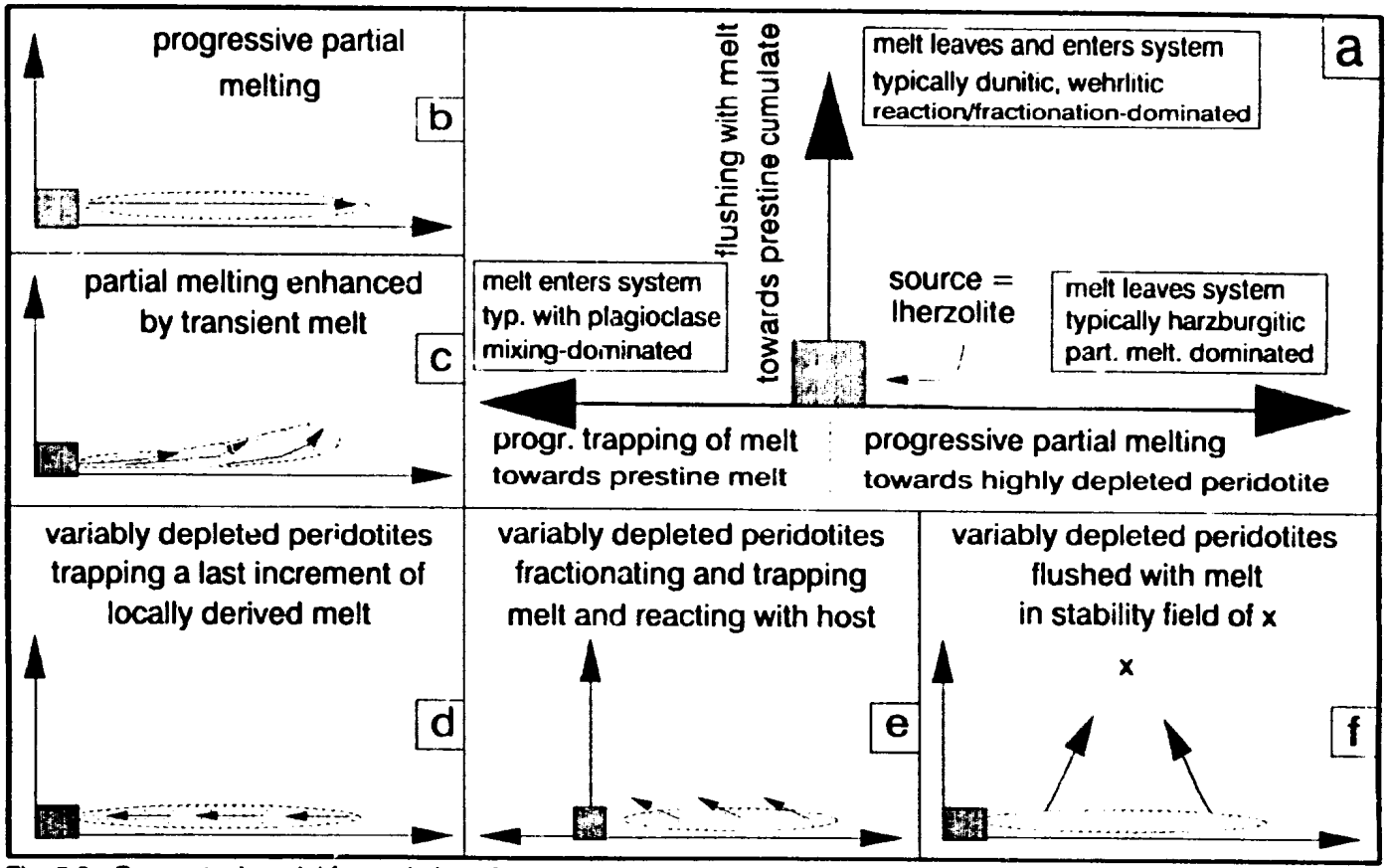

Fig. 5.9. Conceptual model for evolution of mantle peridotites in the Bay of Islands Ophiolite. In (a), the three theoretical endmembers are defined. (b) - (f) represent five specific cases. For details see text.

logical trend is from lherzolite towards harzburgite. The extreme end-member is a dunite. This is the dominant process accounting for the mineral chemical variation in the TM mantle section (field MT and trend PPM in Figs. 5.6, A5.7). It leads to high Cr# (spinel), low Al in pyroxenes, high Ni (olivine), and low Ti, Na (pyroxenes). Microstructurally, the R-type spinels are associated with this process.

Trapped melt is relatively easy to identify microstructurally. The critical question is whether the microstructurally identified, melt-related phase (e.g. cpx) represents primitive melt or melt modified during the entrapment process. In the trapped melt end-member, it has to represent pristine melt. Therefore, *by definition*, in the end-member, the melt-infiltrated peridotite is simply the result of *addition* of melt to residual peridotite (mixing). In contrast to the melt-flushing type discussed below, reaction between melt and peridotite does *not* take place and in-situ fractionation has not occurred. In the model, the infiltrating melt remained above its solidus, became enclosed (trapped), and then solidified. Melt-solid distribution coefficients (K_d) are *irrelevant*. Only in such a system is it possible to calculate the composition of the infiltrating melt from the trapped melt phases. Characteristic for the system is a positive mass balance as more melt is going in than out, i.e. the opposite to the partial melting trend. A progressively higher amount of trapped melt would lead towards pristine melt. However, amounts of trapped melt are typically small as connectivity is reached at small amounts of melt (Waff and Bulau 1979) in the peridotite system. Exceptions seem to exist during the stage of overturn from vertical to horizontal flow beneath a spreading centre (Rabinowicz et al. 1987) and in olivine-depleted peridotites (Toramaru and Fujii 1986, Nicolas et al. 1987).

The predominance of basaltic volcanics within the BOIC extrusive sequence (see references in section 1.3.3) suggests that the trapped melt in the mantle peridotites was basaltic. Therefore, (olivine-) plagioclase-clinopyroxene clusters are expected in a harzburgite or lherzolite under low pressure conditions. Dick (1989) has calculated the melt

composition from the phases representing the trapped melt. The strict limitations required for such a calculation (listed above) were, however, not discussed. Olivine has not yet been reported as a trapped melt phase. Probably, this is the result of the destruction of morphological evidence for melt impregnation due to the rapid grain boundary migration involving olivine under hypersolidus conditions. The rarity of even cpx-plagioclase clusters suggests that melt which was trapped, generally suffered a more complex history. This probably included, fractionation, melt-host reaction and subsolidus re-equilibration (section 4.7). Conditions which favour pure mixing are local derivation of melt (as then melts are more likely to be in chemical equilibrium with their host) and "low" temperatures as this will limit reactions between host and melt and enhance instant freezing. It is, however, difficult to inject melt into peridotite under such conditions. Microstructurally, the I-type spinels are connected with melt-entrapment.

The third type of process is melt-host reaction and fractionation involved in percolation of melt through peridotite. The existence of rocks in mantle peridotite massifs which have undergone reactions with percolating melts has been proposed by Sinton (1977), Nicolas and Prinzhofer (1983), Gregory (1984), Bodinier et al. 1988, Nicolas (1989), Fabriès et al. (1989). In this category, melt percolates through a peridotite network. When the temperature drops below the liquidus, fractionation of phases will take place, most likely olivine, spinel, clinopyroxene and plagioclase. In addition, under lower pressure conditions, the opx-bearing peridotite reacts with a basaltic melt (derived from some depth). An important reaction is the resorption of orthopyroxene (e.g. Sinton 1977, Stolper 1980, Fisk 1986). Kelemen (1990) showed that under such conditions, plagioclase of tholeiitic melts, if on the liquidus, disappears from it, whereas cpx and olivine remain liquidus phases after reaction with harzburgite. The modal trends in the system are thus the disappearance of opx (from the host rock) and plagioclase (from the melt) and an enhanced stability of cpx, i.e. a wehrlitic tendency is

to be expected. Under extreme percolation (flushing), the stability conditions of the crystal-melt system under the ambient PT conditions will be approached, i.e. pseudo-cumulate rocks are expected. This involves the total resorption of opx and adjustment of all peridotite phases to compositions in equilibrium with the melt. Very high melt:rock ratios are required for this process.

During melt-host reaction, the mass-balance may be positive or negative, depending on how much melt was generated by melt-host reaction. After the reaction, melt and peridotite compositions are changed. The process is an in-situ replacement of pre-existing rock and is governed by solid-liquid distribution coefficient. Tholeiitic liquids which have undergone reactions with host harzburgites will be depleted in Ti and Zr (Kelemen et al. 1990), implying an enrichment of both elements in the residual harzburgite. On the other hand, if highly refractory melts (i.e. melts in equilibrium with highly depleted peridotites), percolate through a relatively fertile peridotite, they will cause depletion of incompatible trace elements in the host. Microstructurally, it is suggested that the F-type spinel is associated with this process.

The important distinction between mixing- and reaction-dominated peridotites has previously been made by Bodinier et al. (1988). Bodinier et al. (1988) used the term "equilibrated". They discussed the different geochemical trends between both processes and showed the effect of melt flushing on certain trace elements in the peridotite as a function of the stable phases in the system. An extreme end-member is represented by plagioclase-cpx dunites in Lanzo which are residual rocks containing cumulate plagioclase and cpx derived from N-type MORB (Bodinier 1988). Nicolas (1989) showed the effect of partial equilibration of melt with harzburgite and its potential significance for the formation of massive dunites. Fabriès et al. (1989) calculated trace element concentrations in peridotites in equilibrium with percolating alkali basaltic melts. Compared to

mixing with melt, the flushing will typically lead to lower concentrations of incompatible elements in harzburgite. For low melt-fluxes, both processes are, however, difficult to distinguish.

In Fig. 5.9b-f, five specific cases of this model are shown. In 5.9b, simple progressive partial melting takes place and leaves variably depleted peridotites behind. The lithological development is from lherzolite to harzburgite to dunite. The trend marked MT in Fig. A5.7 (PPM in the inset) corresponds to this situation and is represented by peridotites from the Bay of Islands excluding those from near the transition zone (unit 1,2).

In Fig. 5.9c, it can be seen that partial melting is enhanced by the presence of a transient melt. This process is a combination of a strong component of partial melting with a small contribution of the reaction/fractionation component. For example, within a diapir decompression melting takes place and reflects the partial melting component. However, melt derived from greater depths may enter the diapir via dykes. The injected melt is in disequilibrium with the residual peridotite and may start to fractionate olivine or any other phase on the liquidus. In addition, it carries additional heat into the melting zone. As a result, melting will be enhanced by reaction between the injected melt and the residual peridotite and the additional heat brought in with the melt. Trapping and crystallization of melt is very unlikely at this, essentially overheated, stage.

Chemical evidence suggests that the Springers Hill samples may belong to this category. They are highly depleted but have relatively high Ti (spinel) and low Ni (olivine and whole rock) contents compared to depleted harzburgites of the same, or even lower, Cr# (spinel). Transient melt evidence comes also from the F-type spinels identified together with R-type spinels in the Springers Hill harzburgites. Abundant dunites in Springers Hill may represent the magmatic feeders. An alternative mechanism to explain the Springers Hill harzburgites would be to retain and subsequently

re-equilibrate a small amount of melt after each increment of partial melting. This would lead to a higher concentration of incompatible trace elements compared to strictly fractional melting (Langmuir et al. 1977, Frey et al. 1985, Johnson et al. 1990).

Fig. 5.9d represents a special case where strictly *fractional* melting occurs. A last increment of this, now refractory melt (perhaps 1-2%) is not extracted but retained in the rock. It simply re-enriches the peridotite towards a slightly less depleted character. Chemically, not much evidence for melt impregnation is expected, though it would be seen microstructurally.

Fig. 5.9e represents a more general and realistic case of melt infiltration. Melt infiltration is accompanied by reaction of melt with the host peridotites and fractionation of phases unless the infiltrating melt is above its liquidus. Both processes, reaction and fractionation, drive the system towards the cumulate direction. When the melt is squeezed off, some melt remains trapped in the peridotite. This trapped melt represents a contribution of pristine or even evolved melt. It drives the composition to the left in the diagram (Fig. 5.9e). Most rocks of the uppermost peridotites (unit 1,2), as well as unit 5 peridotites with evidence for trapped melt, are probably part of this category.

A mass balance can clarify this point. Samples TM 1181, TM 599, TM 884 show evidence for several modal percent of impregnation-related clinopyroxene. Aphyric basalts from the NAM massif contain 0.5 to 2 wt.% TiO_2 (Siroky et al. 1985). Even only 2% (modal) of added, pristine trapped melt with 1.0% TiO_2 would result in a contribution of 200 ppm of TiO_2 to the whole rock titanium. Given that most TiO_2 contents of the TM samples are between 50-70ppm, values in the order of 250 ppm would be expected for the samples mentioned. The TiO_2 of the samples mentioned is, however, only very weakly elevated compared to other samples showing no evidence for trapped melt (Tab. B-1). This means that the trapped melt phases in the samples do not simply represent prestine melt. The melt which was trapped within the peridotite network must

already have been modified prior to enclosure or the trapped melt phases represent a fractionation product of the transient melt. Clinopyroxenes fractionated in an open system will contain much lower TiO_2 contents than cpx formed in a closed system. Note, for example, low TiO_2 contents in ultramafic cumulates from the NAM massif (Elthon et al. 1984, Komor et al. 1985).

Finally, in Fig. 5.9f, the speculative effect of flushing, i.e. percolation with high melt:rock ratios, is shown. Variably depleted peridotites would be driven towards the composition and stability conditions of a melt under certain PT conditions. The system reaches the equilibrium of the melt-system or nearly so. Accordingly, the host chemistry is entirely changed. The effect is a large scale homogenization of the peridotite suite. This has clearly *not* taken place for the entire TM mantle section, as is shown by the wide range of mineral chemistries preserved. Some high level, massive dunites with aluminous spinels and minor cpx could fit, however, into this category. Consistent with this interpretation, their geochemical trend is towards known cumulates from the BOIC. Their distinction from true cumulates or adcumulates remains, however, to be demonstrated.

5.13 CONCLUSIONS

The chemical variation within the TM mantle section is seen as the result of a multitude of processes. The dominant process is progressive partial melting due to decompression melting. This probably led to a fairly homogeneous harzburgite sequence now still preserved at an intermediate level of the TM mantle section. As suggested in chapter 6, underplating of an off-axis diapir below this sequence could be responsible for the strong chemical gradient at the base of the massif, as it would bring up more fertile mantle having undergone a limited amount of melting. Both intermediate and low structural levels together define a mineral chemistry field called Main Trend reflecting various degrees of partial melting. The top of the mantle sequence,

once probably similar to the intermediate sequence, was subsequently melt-infiltrated. On theoretical grounds, melt infiltration may occur by simply adding pristine melt to the host peridotite or by complex processes involving reaction and fractionation. Both processes (mixing vs. reaction/fractionation) lead to very different end-member compositions (pristine melt vs. cumulate composition, respectively), which are, however, in their subtle expression in natural rocks not easy to distinguish.

The mineral chemistry of the high-level mantle sequence in TM is probably the result of a large component of the residual end-member and small components of the trapped melt and reaction/fractionation component.

6 DISCUSSION

6.1 INTRODUCTION

Structural, microstructural, and geochemical evidence presented in the preceding chapters demonstrates the heterogeneous nature of the mantle section within the TM massif. This heterogeneity is not random but shows a well defined spatial distribution. The regional variation of the structure (i.e. the six structural units) correlates with certain microstructural and geochemical features. The most important results relevant for this chapter are listed below (see also Fig. 6.1):

- presence of relatively homogeneous, largely Moho-parallel foliations, but kilometre-sized domains of distinct lineations;
- a shear sense reversal in the upper part of the mantle section and presence of neutral shear sense domains;
- progressive deformation of orthopyroxenite dykes from unit 2 into unit 3 and absence of the dykes in unit 5;
- apparently synformal structure of the lithological banding in unit 5;
- domains of asthenospheric, weakly to moderately lithospheric, and highly lithospheric microstructures;
- a steep partial melting gradient at the base of the massif ("basal lherzolites");
- presence of two melt-impregnation zones, one below the Moho, another one within unit 5.

This evidence, together with the inferred relative ages of the structural units (section 6.2), the distribution of stress, strain, and temperature of deformation (section 6.3), the spreading or detachment-related origin of the units (sections 6.4, 6.5), the relative position of the mantle section with respect to the ridge (section 6.6), must be incorporated into a model whereby oceanic spreading is followed shortly afterwards by detachment of the oceanic lithosphere and final emplacement onto the continental mar-

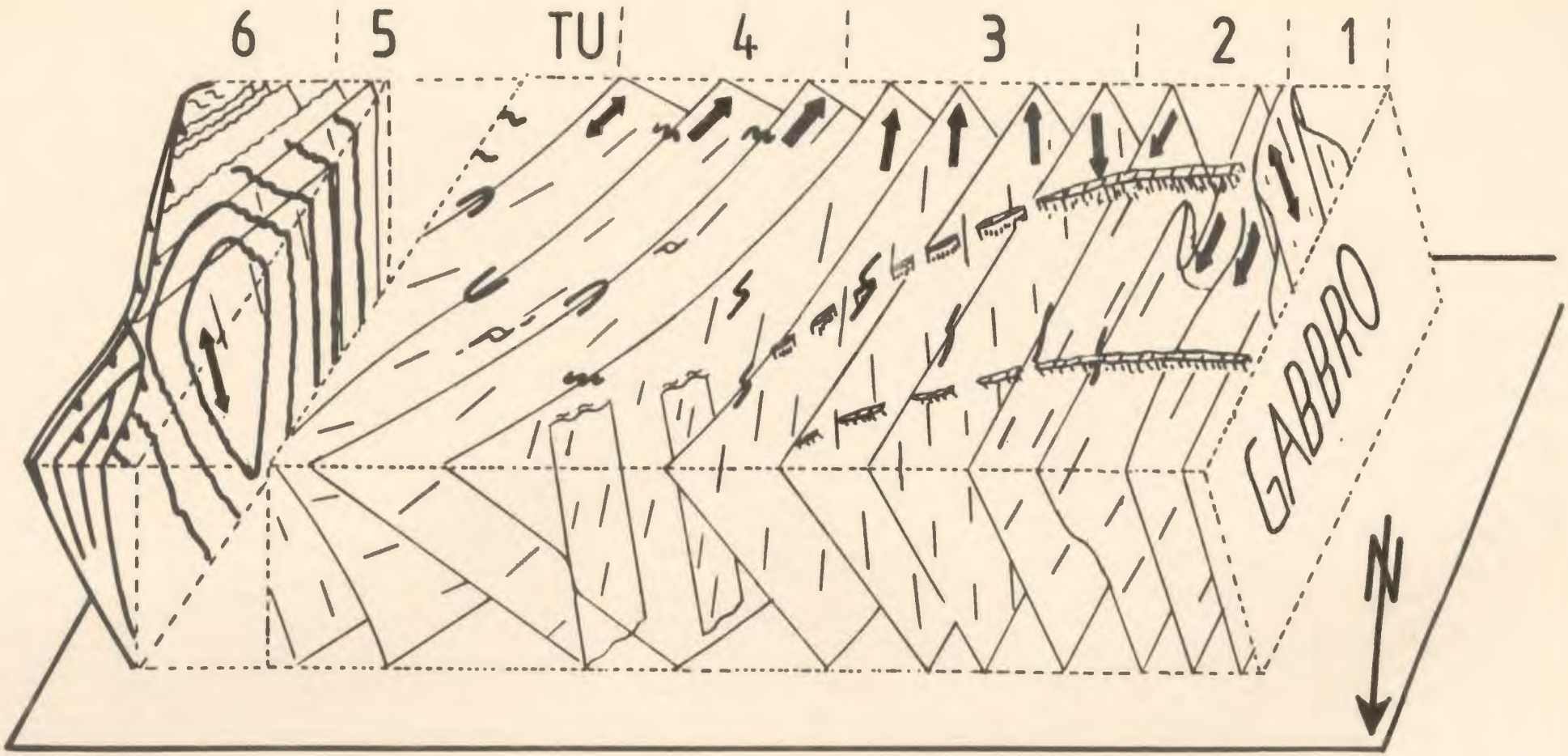

Fig. 6.1. Three dimensional, simplified structure of the eastern Table Mountain mantle section. View from the north. (Curved) surfaces with lines - foliation planes with stretching lineations; heavy lines - lithological banding; heavy lines with black triangles on one side - late thrust planes; lenses and sheets with ruled pattern - orthopyroxenite dykes; arrows - movement direction of upper block;

gin (see section 1.3.3). The tectonic model (sections 6.7, 6.10) should be consistent with structural and petrological evidence presented previously in the numerous studies of the Bay of Islands Complex and Coastal Complex as well as with geophysical models for formation of the oceanic lithosphere.

6.2 RELATIVE AGE OF STRUCTURAL UNITS

The relative structural age of the units is determined using overprinting criteria, the assumption that lower temperature fabrics relate to relatively later events, as well as other microstructural considerations. On the basis of the deflection of the flow pattern of unit 1 into unit 2, unit 2 appears to structurally postdate unit 1. However, if it is assumed that unit 1 relates to a late, forced intrusion of melt-charged peridotite (section 6.7.2), the relative age relationship between both units *could* also be reverse. The undeformed nature of orthopyroxenites in unit 1 as opposed to unit 3 supports an early tectonic freezing of unit 1.

As foliations are parallel between units 2 and 3 (and between units 3 and 4), the foliation data cannot be used to evaluate the relative age relationships between these units. However, three arguments favour a relatively later structural age for unit 3 compared to unit 2:

(1) orthopyroxenite dykes are deformed by sinistral shear within unit 3 (section 2.9.2), whereas they are only weakly deformed within the dextrally sheared unit 2.

(2) in the lower part of unit 3, early folds related to dextral shear are overprinted by later folds indicating sinistral shear (section 2.6.2). This suggests that dextral shear, typical for unit 2, once also affected unit 3, but was later overprinted by sinistral shear.

(3) subtle, local flexures of the foliation along cross-cutting orthopyroxenites within

unit 2 indicate a sinistral shear sense in unit 2. This is interpreted as the highest level expression of the later sinistral shear (dominant within unit 3) overprinting early dextral shear in unit 2.

Unit 4 is in many respects similar to unit 3, but shows a different stretching lineation. In high strain zones, however, moderately to highly lithospheric microstructures are developed and orthopyroxenites may be extremely deformed (Pl. 5a). It is inferred that peridotites typical of unit 3 were heterogeneously overprinted within unit 4. Even in lower strain areas of unit 4 strain was, however, generally large enough to imprint a stretching lineation trending N45°E within the peridotites.

Structural overprinting between units 4 and 5 is complex and is concentrated within the TU. No consistent style of transposition appears to be present within the TU. The homogeneous sinistral shear sense from unit 3 and 4 is lost. Microstructures of unit 5 are locally asthenospheric and strain is low (see section 6.3), contrasting with lithospheric microstructures of unit 4. Unit 5 is considered more primitive (earlier) than unit 4.

Unit 6 shows lower temperature microstructures and more heterogeneous strain than unit 5. In lower strain areas of unit 6, microstructures typical for unit 5 can still be recognized. Unit 6 thus postdates and overprints unit 5.

As a result, the deformational sequence begins with formation of unit 1 and 2. Unit 2 probably once extended into what is now unit 3. Then the strain characteristic for unit 3 developed. It probably reached at least as far as the base of the current unit 4. It was followed by accretion of unit 5. Finally, the moderately to strongly lithospheric structures formed, affecting the hanging wall of unit 5 (unit 4) and the base of the ophiolite (unit 6).

6.3 EVOLUTION OF DEFORMATIONAL PARAMETERS AS A FUNCTION OF DEPTH

6.3.1 Temperatures of deformation

A first order estimate of the temperatures of deformation can be obtained using the classification of peridotites as being either asthenospherically or lithospherically deformed according to the definitions given in section 3.3.

The highest temperatures of deformation are thus preserved within the top of unit 2, and at the base of unit 5 and locally within unit 1 (Fig. 6.2). The morphological identification of trapped melt, formed late-synkinematically in these peridotites, is an important criterion for hypersolidus flow. Nicolas (1986a) estimates 1300°C for such microstructures. Here a temperature between 1200-1250°C is chosen which represents the solidus of depleted peridotite under low pressures (Jaques and Green 1980).

The rest of the peridotites shows weakly lithospheric microstructures (base of unit 2, unit 3, top of unit 5, lower strain areas of units 4 and 6) or a moderate to strong lithospheric overprint (units 4, 6). The strongly lithospheric microstructures are estimated to have formed between 900 and 1000°C (Nicolas 1986a, Nicolas 1989, p. 29). As basal ultramylonites show diffuse olivine lattice fabrics different to those of the rest of unit 6, the value of not more than 900°C might apply to the ultramylonite, a temperature of 900-1000°C to the bulk of unit 6. A relatively lower temperature origin for the ultramylonite is corroborated by the occurrence of syntectonic amphibole which is restricted to the ultramylonites and to local, small scale shear zones within unit 6. For the weakly lithospheric microstructures, the temperatures of deformation probably were between 1000-1200°C.

Strictly seen, the argument that weak and strong lithospheric microstructures translate into higher and lower temperatures of deformation, respectively, is difficult to substantiate. Alternatively, both formed at the same temperature but the weakly lithos-

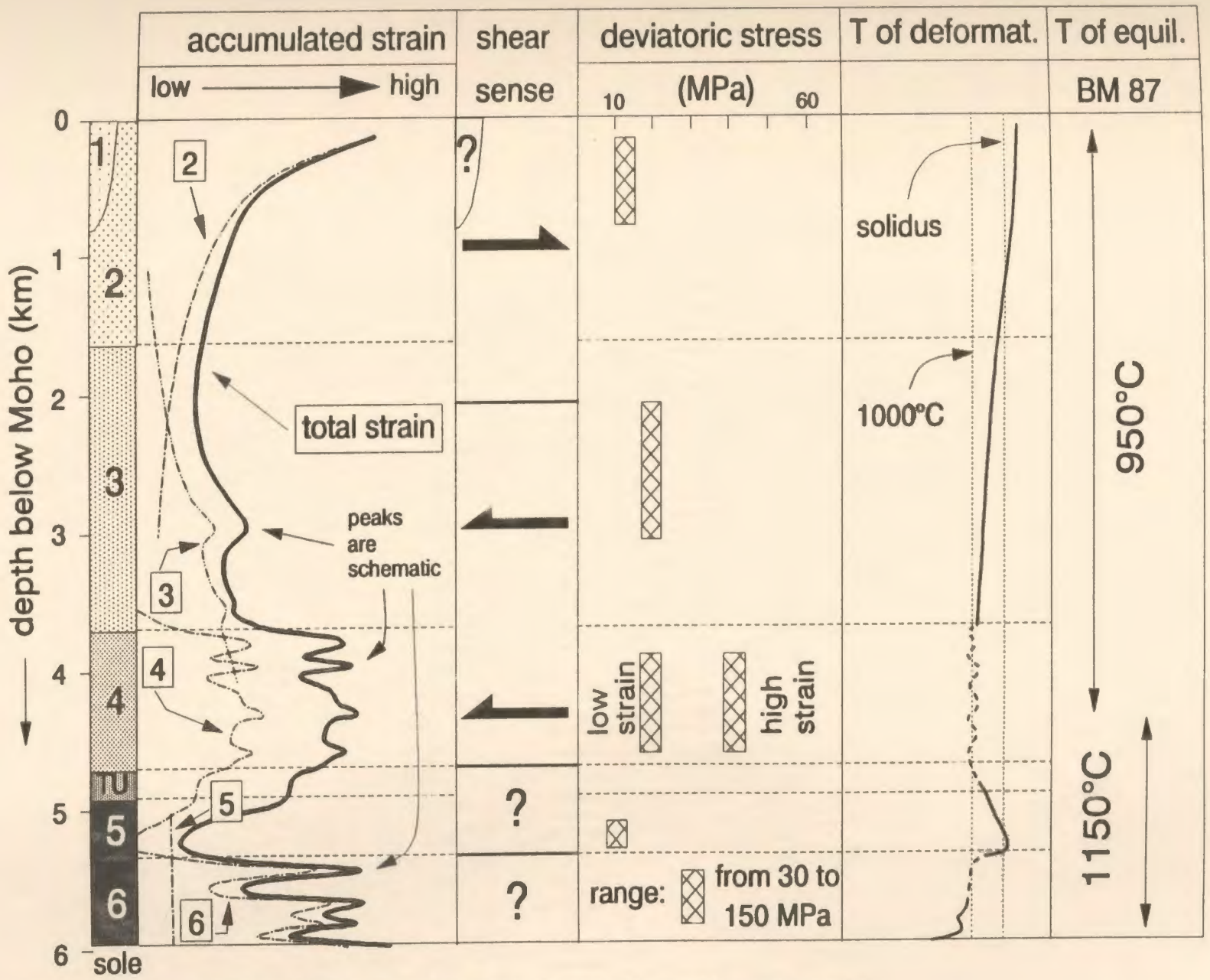

Fig. 6.2. Variation of deformational parameters within the Table Mountain mantle section.
BM 87 - Ben Jamaa and Mercier (1987). For discussion of data see text.

pheric microstructures relates to low accumulated, lithospheric strain. Compared to weakly lithospheric microstructures, strongly lithospheric microstructures develop moderately elongated olivine grains, oblique olivine fabrics, and clear strain partitioning in the field. All three features are probably related to strain induced rheological hardening typically associated with decreasing temperatures of deformation (transition from dislocation climb to dislocation glide). In addition, the neoblast size is smaller in the strongly lithospheric microstructures. Therefore an actual temperature difference between both microstructures types is preferred.

Asthenospheric, weakly lithospheric, and strongly lithospheric microstructures could not be clearly related to the activation of specific slip systems. The only exception is represented by the ultramylonite. The equilibration temperatures determined by Ben Jamaa and Mercier (1987) for the TM mantle section do not correlate with the deduced temperatures of deformation (Fig. 6.2).

6.3.2 Stress

Stress levels can be estimated using the neoblast size of olivine (section 3.4, Tab. 3.1). Stresses in the TM mantle section are lower where temperatures of deformation are estimated to be higher (Fig. 6.2). This is to be expected as peridotites are rheologically weaker at higher temperatures and then will be unable to support high stresses (cf. Fig. 6.3).

Given the wide range of neoblast sizes within unit 6 (see section 3.5.7.3), it is probably not appropriate to use an *average* stress value for detachment. Most likely, the microstructures of unit 6 recording low deviatoric stresses of about 30 MPa have formed close to the time when detachment was initiated. Higher stress microstructures, up to at least 150 MPa, formed by progressive overprinting of the early detachment structures. Such an overprinting model is supported by the observation that even within

a single thin section, a wide range of neoblast sizes exists. From the microstructure study it appears that the different neoblast sizes may either be intermixed on a grain scale or be separated into foliation parallel layers (see section 3.5.7.3).

6.3.3 Relative amounts of accumulated strain

Estimation of accumulated strain in peridotites is difficult. Possible methods are the elongation of spinel grains and chromite nodules (Girardeau 1979, Ceuleneer and Nicolas 1985), the obliquity between shape and lattice fabric (Ceuleneer et al. 1988), the strength of the lattice fabric of olivine (Etchechopar and Vasseur 1987), the porphyroclast to neoblast ratio (Boudier and Nicolas 1978, Kirby and Green 1980), and several methods using the deformation of dykes and development of boudins (e.g. Talbot 1970). A problem with using dykes is that they can enter the strain path at any time. For the orthopyroxenite dykes in TM, it is assumed that systematic differences in the ages of intrusion do not exist between the different units.

A basic observation is that the majority of the orthopyroxenite dykes are deformed within unit 3 but, are weakly to undeformed within unit 2. From the stereonet distribution of the dykes it could be inferred that deformation of the orthopyroxenites was related to sinistral shear, consistent with the shear sense derived for unit 3 from asymmetric folds and microstructural criteria. Folds are progressively building up down-section within unit 3 in locations where the lithological banding is intersected by orthopyroxenite dykes. It is concluded that strain increased down-section within unit 3 and was related to sinistral shear occurring under weakly lithospheric conditions. During deformation of orthopyroxenites of unit 3, unit 2 was, from a deformational point of view, essentially frozen in.

Microstructurally, a striking feature within the upper part of unit 2 is the absence of any spinel-orthopyroxene clusters, otherwise typical for unit 3. Going up-section from unit 3 to unit 2, the clusters are progressively pulled apart and spinel forms more

pronounced trails parallel to the foliation (Fig. 3.13). It is concluded that strain, increasing up-section from unit 3 to unit 2, was responsible for disintegration of the spinel-orthopyroxene clusters.

Increasing strain up-section must be related to dextral shear observed within unit 2. It has to predate the intrusion of the majority of orthopyroxenites into unit 2 and also the sinistral shear within unit 3. There are no means to determine how high the accumulated strain was within the top of unit 2. In keeping with what is known from deformation near the crust-mantle boundary (Nicolas and Prinzhofer 1983), (asthenospheric) strain within the top of unit 2 is considered very high. The same is inferred for unit 1, though little hard evidence can be presented apart from the scattered and small, elongated spinel grains typical for this unit.

As asthenospheric strain decreases down-section within unit 2 and the weakly lithospheric strain decreases up-section within unit 3, a low strain area results in the upper part of unit 3. It might be related to the outcrops of coarse-grained harzburgites (orthopyroxene grain size 3-5 mm) at this level (Fig. 2.1).

In unit 4, peridotites with an appearance and microstructure similar to unit 3, contain northeast-trending mineral stretching lineations. Strain within unit 4 culminates in high strain zones which show mylonitic microstructures, high neoblast to porphyroclast ratios in the olivine matrix, and attenuated orthopyroxenite boudins. It is inferred that peridotites which were lithologically (and structurally?) similar to those in unit 3, have been structurally overprinted within unit 4. As a result, a new stretching lineation developed in the peridotites. For unit 4, an early structural history related to that of unit 3 could be indicated by remnant olivine lattice fabrics and locally present lineation trends similar to those still preserved in unit 3. Strain within the high strain zones was clearly significant. If the overprinting model is correct, accumulated strain within unit 4 was also *regionally* higher than within unit 3. The strain distribution shown in Fig. 6.2

is based on the overprinting model.

Peridotites of unit 5 are characterized by the absence of any markers of high strain, particularly at their base. Specifically, trapped melt textures are undeformed, showing that lithospheric overprint was weak. This is in striking contrast to the high lithospheric strain within the overlying unit 4. In order to evaluate the amount of strain during the asthenospheric history, the microstructure of unit 5 is compared to the high strain asthenospheric microstructure of unit 2. Within unit 5, the strength of the mineral-defined foliation and lineation is weak (moderate to strong in unit 2), lattice fabrics are only moderately strong (strong in unit 2), spinels are closely associated with pyroxenes (not the case in unit 2), the pyroxenes are pulled apart but poorly recrystallized (highly recrystallized and scattered in unit 2), pyroxenitic lithological banding can have sharply defined boundaries and is boudinaged or buckled (very vaguely present in unit 2). Unfortunately, cross-cutting orthopyroxenites are not present as strain markers. The base of unit 5 is considered a low to moderate strain asthenospheric, low strain lithospheric microstructure. Towards the top of unit 5 and within the TU, lithospheric strain increases.

The most prominent features within unit 6 are orthopyroxene ribbon grains reaching aspect ratios in XZ sections up to 100:1 and a highly recrystallized olivine matrix. This indicates very high strain. Using these criteria, it can be deduced that lithospheric strain increases heterogeneously towards the base of the peridotite section. Ultramylonites located at the base are entirely recrystallized, suggesting again very high strain. Recrystallization may, however, have been enhanced by the presence of fluid.

In summary, the total strain variation can be explained by superimposing several structural events, each of which is correlated with a structural unit. The total strain variation consists of two low strain zones (top part of unit 3, and base of unit 5), and three high strain zones (Fig. 6.2).

6.4 EVALUATION OF PERIDOTITE MICROSTRUCTURES

6.4.1 Are the deformational parameters calculated from peridotite microstructures geologically realistic?

The term asthenospheric microstructure is used in this thesis where high temperature, low stress, well recovered olivine microstructures are preserved. In TM, asthenospheric microstructures are typically associated with evidence for hypersolidus flow in the form of undeformed to weakly deformed melt impregnation textures within a deformed olivine matrix. The term thus refers to temperatures of deformation near the solidus of depleted upper mantle under the low pressure conditions preserved in ophiolites, i.e. at least 1200-1250 °C (Jaques and Green 1980). Such high temperatures of deformation are also required by models which simulate the heat required to generate the oceanic crustal thickness present in the BOIC (5-7 km) by decompression melting of peridotite (McKenzie 1984). Flow stresses calculated with the relationship of Karato et al. (1980) for asthenospheric microstructures of unit 2 lie in the range of 10 MPa.

A number of olivine and dunite flow law data are plotted in Fig. 6.3a. Compared to the dry deformation conditions illustrated in Fig. 6.3a, olivine and dunite are rheologically weaker during deformation under wet conditions (Post 1977, Chopra and Paterson 1984, Karato et al. 1986) and in the presence of melt (Bussod 1983, 1990, Bussod and Christie 1984, Cooper and Kohlstedt 1986, Green and Borch 1990). Due to the discrepancies between different flow laws, the strain rates indicated for the asthenospheric microstructure (1200°C, 10 MPa stress) vary between 10^{-10} and 10^{-13} s^{-1}. For a primitive detachment microstructure of unit 6 (1000°C and 30 MPa), the inferred strain rates vary from 2.1×10^{-12} to 2.7×10^{-15} s^{-1}. Application of the flow law of Karato et al. (1982) yields intermediate strain rates of 7×10^{-12} s^{-1} and 2.5×10^{-13} s^{-1} for the asthenospheric and detachment microstructure, respectively (Figs. 6.3a,b). The flow law of Karato et al. (1982) corresponds well with more recently published olivine flow laws of

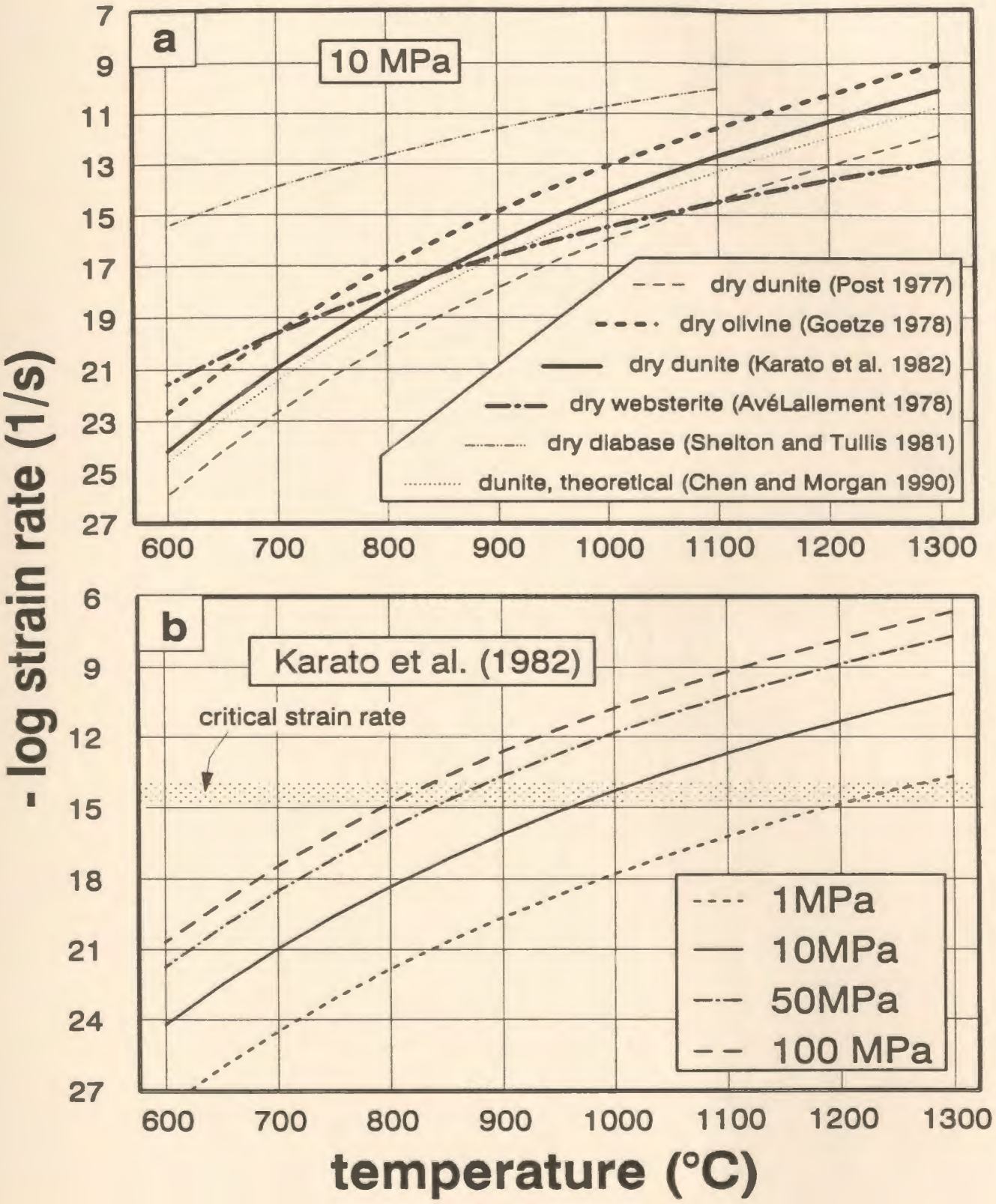

Fig. 6.3. (a) Temperature - strain rate relationships for different lithologies at 10 MPa deviatoric stress. In (b), strain rates are shown for different levels of deviatoric stress using the flow law of Karato et al. (1982). Shaded area in (b) marks the "critical strain rate" below which deformation is geologically irrelevant.

Chopra and Paterson (1984) and Chen and Morgan (1990).

These strain rates can be evaluated in very simplified tectonic scenarios: it is assumed that detachment occurred by converging plates having oppositely directed velocities of 3 cm/y each. The relative velocity along the detachment plane was therefore 6 cm/y. Unit 6, which is related to detachment, has a width of 500 m. It may represent the half-width of the shear zone along which detachment took place by simple shear. In a further simplification it is assumed that the strain distribution along the 1000 m wide shear zone was homogeneous. The shear strain rate γ can then be calculated. It is related to the extensional strain rate (e_1) by $\gamma = 2e_1 = -2e_3$ (e.g. Ramsay 1980, see Fig. 6.4). For e_1 a value of 9.5×10^{-13} s^{-1} is obtained. The strain rate is an average value as within shear zones, strain is inhomogeneous and increases towards its centre.

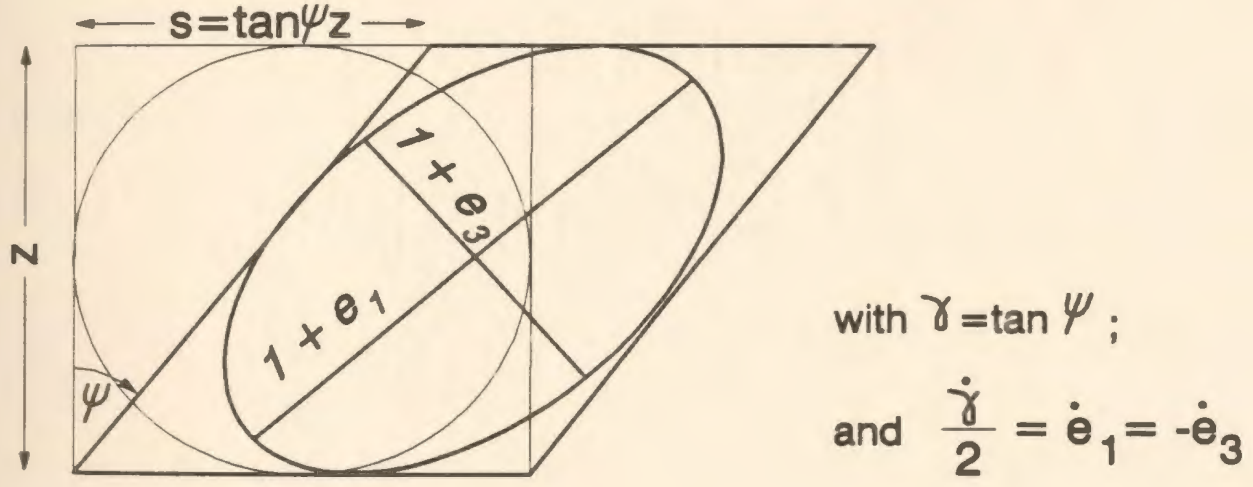

Fig. 6.4. Relationships between angular shear strain ψ, shear strain γ, shear strain rate $\dot{\gamma}$ and the extensional strain rate e (e.g. Ramsay 1980).

In case of the asthenospheric microstructures, a slightly different scenario may be visualized in which a rigid plate (the lithosphere) is moving with a velocity of 5 cm/y over the weaker asthenosphere. Strain is spread homogeneously over 1 km width below the lithosphere. The resulting strain rate is very similar to the detachment case (7.9×10^{-13} s^{-1}). Alternatively, it could be considered that strain is concentrated within the

uppermost 100 m of the asthenosphere. This is not entirely unrealistic, as the uppermost asthenosphere beneath spreading centres was possibly rheologically weakened by the presence of melt (Kohlsted and Cooper 1986, Nicolas 1989, Green and Borch 1990) or water. The resulting strain rate is an order of magnitude higher ($7.9x10^{-12}$ s^{-1}). Both estimates are similar to a strain rate of 10^{-13} s^{-1} predicted by numerical modelling for deformation of peridotites in a melt-charged, forced flow regime (Ceuleneer et al. 1988). Typical geological strain rates (within the *lithosphere*) lie between 10^{-11} and 10^{-15} s^{-1}, but may be higher in mylonite zones (Pfiffner and Ramsay 1982). Given the evidence for high accumulated strain within unit 2 and 6 (see section 6.3), both units are considered zones of strain concentration.

Overall, the microstructurally derived strain rates appear not to be unrealistic. Strain rates for the asthenospheric microstructure may be somewhat high, particularly because the chosen temperature (1200°) represents a minimum value. Within unit 6, samples recording very high stresses are common. For example, olivine neoblasts of the type microstructure of unit 6 indicate 60 MPa deviatoric stress. If this peridotite equilibrated at 1000°C, a strain rate of $2.9x10^{-12}$ s^{-1} is indicated. Assuming the same equilibration temperature, samples containing 20 μm small neoblasts (150 MPa) would imply a strain rate of $7.1x10^{-11}$ s^{-1}. Particularly in the case where the 20 μm small neoblasts appear to represent a second generation of neoblasts, it seems likely that the microstructure does not represent equilibrium conditions on a thin section scale and the inferred high strain rates should not be used.

The strain rates discussed within this section are compiled in Tab. 6.1. This table contains also strain rate values based on the assumption that neoblasts could record a lower temperature then the one estimated for the bulk of a peridotite microstructures within one thin section. As a result, calculated strain rates would be lower.

Tab. 6.1. Summary of strain rate estimates based on microstructural evidence and on simplified tectonic scenarios. The piezometer of Karato et al. (1980) and the dunite flow law of Karato et al. (1982) have been used for the microstructural determinations; n.a. - not applicable; "width" refers to the zone in which the deformation is concentrated. For details see text.

SPREADING						
method	half-spreading rate	stress (MPa)	temperature (°C)	width	strain rate	remarks
microstructure	n.a.	10	1200	n.a.	$7x10^{-12}$	upper unit 2
theoretical	5 cm/y	n.a.	n.a.	1 km	$7.9x10^{-13}$	homogeneous strain
theoretical	5 cm/y	n.a.	n.a.	0.1 km	$7.9x10^{-12}$	homogeneous strain

DETACHMENT						
method	rate of convergence	stress (MPa)	temperature (°C)	width	strain rate	remarks
microstructure	n.a.	30	1000	n.a.	$2.5x10^{-13}$	unit 6, primitive
microstructure	n.a.	60	1000	n.a.	$2.9x10^{-12}$	unit 6, high strain zone
microstructure	n.a.	150	1000	n.a.	$7.1x10^{-11}$	occurs in thin bands or scattered neoblasts
microstructure	n.a.	150	900	n.a.	$1x10^{-12}$	same, but lower T assumed for formation of neoblasts
theoretical	6 cm/y	n.a.	n.a.	1 km	$9.5x10^{-13}$	homogeneous strain

Piezometers calibrated for deformation in the presence of melt have not yet been published. Due to the possibility that part of the deformation is accomodated by diffusional flow (Cooper and Kohlsted 1986), they may deviate from previous relationships. The flow laws for olivine under such conditions, as yet incomplete, indicate significant rheological weakening (Cooper and Kohlsted 1986, Green and Borch 1990, Bussod 1990). However, dislocation glide still seems to be the rate-limiting factor (Bussod 1990).

Finally, peridotite microstructures together with olivine flow laws can be used to evaluate the location of the lithosphere - asthenosphere boundary (LAB). The asthenosphere should be characterized by the ability to undergo a significant amount of deformation when low stresses (< 10 MPa; Goetze et al. 1978, Nicolas 1978) are applied. Strain rates $> 10^{-15}$ s^{-1} are considered significant over geological time scales (e.g. Pfiffner and Ramsay 1982, Kusznir and Park 1987). Using the flow law of Karato et al. (1982), a strain rate of 10^{-15} s^{-1} can be reached during a 10 MPa deviatoric stress at 950°C (Fig. 6.3b). Consequently, the rheological asthenosphere may coincide with an isotherm as low as 950°C and be thus clearly subsolidus.

6.4.2 Where do lithospheric microstructures form?

Another important aspect is whether microstructures termed lithospheric always refer to an overprint during detachment (Nicolas 1986a) or whether they may also be connected with the spreading history (Girardeau and Mevel 1982, Girardeau and Mercier 1988).

Goetze (1978) and Nicolas (1978) proposed that stress values between 1 and 10 MPa are characteristic for the asthenosphere. Higher stress microstructures, i.e. the lithospheric ones, would not represent true deformation within the asthenosphere.

Accepting this definition, lithospheric microstructures may form either near thermal boundaries of the asthenosphere, i.e. in marginal locations, or entirely within the lithosphere. For the case of the marginal locations, three tectonic situations appear most relevant for ophiolitic rocks:

(i) in the dying stages of asthenospheric return flow;
(ii) during shear of mantle rocks along a cold wall, e.g. next to transform faults;
(iii) during reactivation of rigid, colder lithosphere by intrusion of hot mantle material.

Whether lithospheric strain within an ophiolitic mantle sequence is ultimately related to spreading or detachment tectonics can only be concluded from the regional context. In general, in the vicinity of a spreading centre, steep geothermal and therefore rheological gradients exist. The rheological stratification will require that special circumstances existed in order to allow partitioning of the deformation from the weak asthenosphere into the rigid lithosphere during spreading. While minor lithospheric microstructures (e.g. a local shear zone) may always be somehow related to spreading, the *abundant* development of spreading-related, lithospheric microstructures within an ophiolitic mantle sequence does probably imply a special tectonic scenario.

The author has only a limited experience of the microstructural characteristics of mantle xenoliths. It appears, however, that the *weakly* lithospheric microstructure of the TM massif (e.g. peridotites of unit 3) is distinguished from the porphyroclastic olivine microstructure of mantle xenoliths by the presence of low angle grain boundaries (blurred appearance) and a less well-developed bimodal grain size distribution. Considering their original position and mode of sampling, the xenolith microstructures most likely preserve steady state conditions within the upper mantle before their entrainment into the magma. Such conditions would allow the formation of the well-recovered, well-equilibrated olivine structure in xenoliths. The abundant undulose extinction and poorly developed bimodal grain size distribution of the weakly lithospheric microstruc-

tures in TM point to kinetic problems. The kinetic problems could be related to a late, lower temperature overprint of low strain magnitude. Such a low strain overprint during retrograde conditions may not be able to fully reorganize a preexisting microstructure.

6.4.3 Why are asthenospheric microstructures preserved within ophiolites?

Even given the range of uncertainties in the stress determinations and experimentally determined flow laws, it appears that microstructures indicating high temperature, low stress, and high strain rates are preserved at least in the uppermost TM mantle section. This is somewhat surprising as virtually all conceivable particle paths in ophiolitic mantle tectonics are retrograde (see also the mineral chemistry zoning patterns, section 5.5). As a result of the retrograde path, a low temperature overprint of high temperature microstructures is expected, and seems also preserved within the mildly lithospheric microstructures. In order to preserve the more primitive, asthenospheric microstructures, a given region undergoing *intense* deformation (note the high strain rates!) within the mantle section must have been rapidly abandoned, i.e. strain must have partitioned elsewhere.

During oceanic lithosphere extension, a downward migration of the deformation front is predicted by the geophysical models of oceanic lithosphere formation (Parker and Oldenburg 1973). Such a tectonic scenario offers an excellent way to partition deformation elsewhere (down-section) and avoid a lower temperature overprint of high temperature microstructures. A special case exists for the deformation along the gabbro/harzburgite boundary. The modelling of Chen and Morgan (1990) showed that rheologically weak mafic rocks of the oceanic crust may deform much more rapidly compared to the underlying peridotites (see weak rheology of diabase in Fig 6.3a). For deformation along the gabbro/harzburgite boundary, deformation may thus even partition up-section from the harzburgites. In summary, during extension, for a region in the

upper mantle under a spreading centre, deformation can be effectively partitioned out of the region of active deformation into other regions. In this way, a significant low temperature overprint can be avoided.

It is more difficult to avoid a low temperature - high stress overprint during detachment, as thrust planes will climb into the colder, "lithospheric" regions. One efficient way to circumvent this is footwall collapse and forward propagation of the thrust plane. This will result in a slicing of the peridotite sequence, a feature rarely observed in ophiolites. More importantly, however, Hacker (1990) has shown that when the basal, climbing thrust plane intersects the lower boundary of the mafic oceanic crust, deformation will rapidly partition into the rheologically weaker mafic lithologies. In this unique event during detachment, the high temperature, high strain rate microstructures of unit 6 may be rapidly frozen in, leaving the rest of the peridotite sequence largely unsliced.

6.5 SPREADING OR DETACHMENT RELATED ORIGIN OF STRUCTURAL UNITS

Given its position near the base of the ophiolite, unit 6 is, in accordance with all previous workers, considered detachment-related. Hypersolidus deformation structures in unit 1 and 2, and 5 make those units spreading-related. Units 3 and 4 are more difficult to interpret. They are mildly (unit 3) to moderately (unit 4) lithospheric.

Local evidence for syntectonic partial melting and melt emplacement occurs within unit 3 (Plates 1h, 6e). In addition, microstructures of unit 3 are entirely gradational to unit 2. A spreading-related origin is favoured for unit 3.

The high stress nature (40 MPa) of the high strain zones in unit 4 and the development of (another!) new flow direction favour a detachment-related origin of the mylonites. As the lower strain areas have the same stretching lineation direction as the high

strain zones, they, too, and therefore the whole unit, would be detachment related. While unit 4 will subsequently be treated as related to detachment tectonics, it is emphasized that no entirely reliable criteria for its origin exist. Previously, it was assigned to spreading events (Girardeau and Nicolas 1981).

6.6 PALEOGEOGRAPHIC ORIENTATION OF THE TABLE MOUNTAIN MASSIF

Due to the allochthonous setting of the BOIO, its present orientation cannot be assumed to correspond to that in the oceanic environment. For example, the steep dip of the Moho in the TM massif is not primary but thought to result from later folding during obduction (Williams 1973). A proper palinspastic reconstruction of the BOIO is, however, essential in order to assign a tectonic meaning to the structures mapped in the mantle section. Based on models for the structure of a mid-ocean ridge system (see chapter 1 and for example Sleep 1975, Dewey and Kidd 1977, Juteau et al. 1977), the paleogeographic orientation of ophiolites can be established (Juteau et al. 1977, Nicolas and Violette 1982, Nicolas 1989). The following points have to be addressed:

(1) paleogeographic upright position
(2) trend of the paleo-ridge axis
(3) relative position with respect to the ridge axis
(4) relative position with respect to a transform/fracture zone

Points (1) through (4) can potentially be solved using the internal geometry of the BOIC and the CC. In this thesis, the paleogeographic reconstruction of Karson and Dewey (1978) and Casey et al. (1983) for the BOIC (Fig. 6.5a) is critically evaluated and accepted with some modifications (Fig. 6.5d).

In order to bring the major lithological unit boundaries (i.e. the boundaries between lavas, sheeted dykes, gabbros, and ultramafics) back to a presumed paleohori-

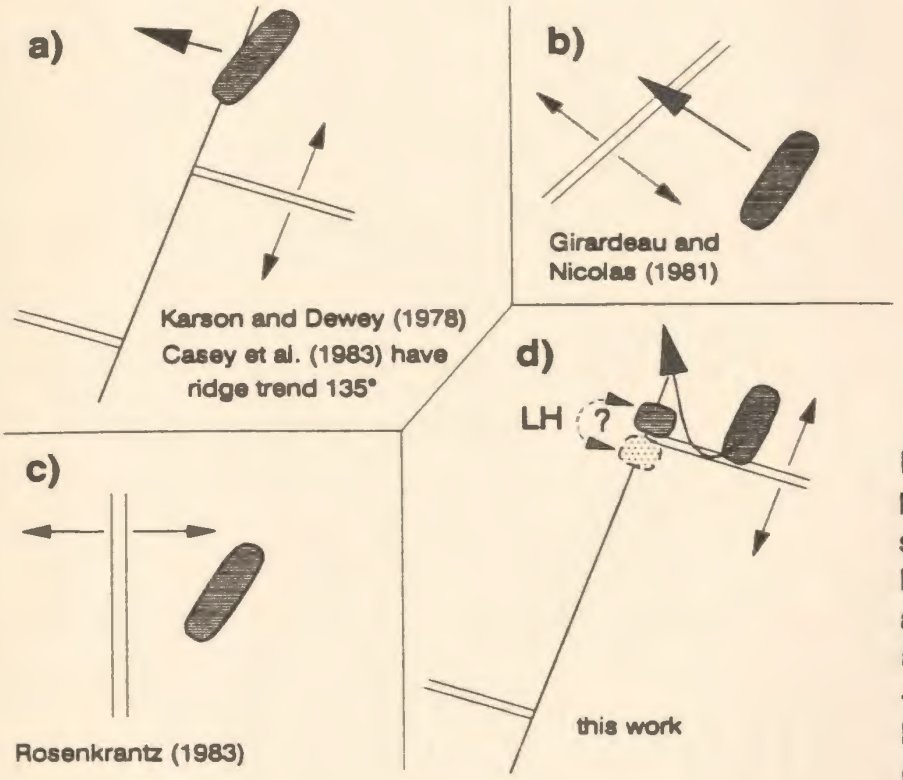

Fig. 6.5. Paleogeographic setting of the Bay of Islands ophiolite according to different authors. Small arrows - spreading direction; large arrows - detachment direction

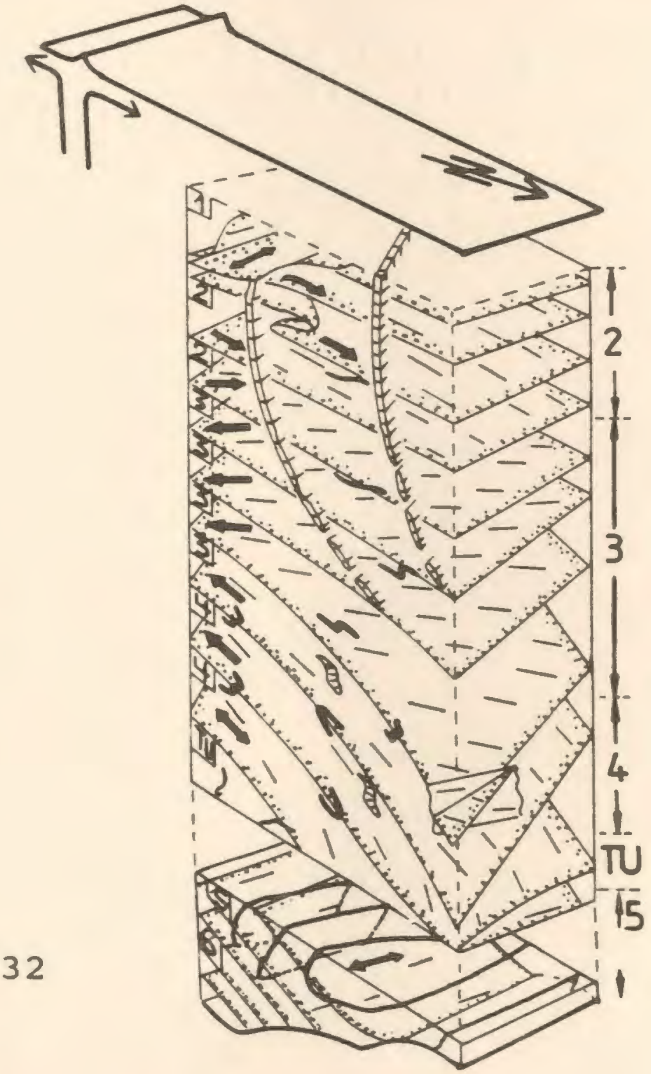

Fig. 6.6. Table Mountain mantle section, rotated back to a paleohorizontal gabbro - harzburgite boundary and into the most likely orientation with respect to the ridge axis. For legend see Fig. 6.1. For discussion, see text.

zontal orientation, the TM massif has to be unfolded. For the eastern limb of the syncline, this involves a 60° rotation to the east about a N40°E oriented, subhorizontal axis (section 2.3.2).

From the mean orientation of the sheeted dyke swarm in the BOIC, Casey et al. (1983) infered a northwest-southeast orientation of the ridge trend. This implies a late, 45° anti-clockwise rotation of the LH about a vertical axis. In this thesis, the fracture zone orientation of Karson and Dewey (1978) is used as the major controlling element for the palinspastic reconstruction. Karson and Dewey's (1978) orientation is parallel to the Little Port Complex (strike of N25°E) and implies only a 25° anti-clockwise rotation of the LH. If the mean sheeted dyke orientation of Casey et al. (1983) is used together with the fracture zone orientation of Karson and Dewey (1978), the spreading axis would have been oriented 20° off the normal to the trend of the fracture zone. While the geometry of plate movements does not strictly constrain this angle to normality, there is a tendency for ridges to align in such a way that transform fault segments are shortened (Atwater and Macdonald 1977, Fujita and Sleep 1978). A N135°E trend of the ridge axis and a N25°E trend of the fracture zone would, however, imply a lengthening of the connecting transform segment (cf. Fig. 6.5a). The spreading axis assumed in this thesis trends N115E, i.e. is normal to the fracture zone but at a 20° angle to the mean sheeted dyke trend. Given the overall variation of the sheeted dyke swarm in the BOIC (e.g. Rosenkrantz 1983), this appears to be within the limits of the statistical variation of the dyke data.

As discussed in Casey et al. (1983), the relative position of the BOIC with respect to the ridge is based on the following criteria:

(1) the magma chamber geometry in NAM. It is, however, model dependent. Using, for example the magma chamber model of Nicolas et al. (1988b), a reverse position with respect to the ridge would be inferred using the same

field evidence;

(2) one way chilling statistics of sheeted dykes in NAM. The bias between west- and eastward chilled dykes is low (10.9%) (Rosenkrantz 1983);

(3) the evidence of (1) and (2) is consistent with the growth direction of dendritic crystals at magma chamber walls in NAM and the sense of shear along the suspected fracture zone.

The inferred position of the BOIC is to the north of the ridge. While none of the above arguments is particularly strong, there is little good evidence to make a case for an opposite position either. Two lines of arguments based on evidence from this thesis support, with minor modifications, the conclusions of Casey et al. (1983). They concern (i) the relative orientation of the flow plane of mantle rocks with respect to the orientation of the gabbro-harzburgite boundary; and (ii) the trend of flow lines in the BMD massif compared to those in the TM massif. Both points will be discussed further below.

With respect to the fracture zone, the BOIC may either be located in the transform or non-transform segment. Based on the different states of deformation between the CC and the BOIC, a non-transform origin was favoured for the LH and the BOIC (Karson and Dewey 1978, Karson 1984). Suhr et al. (in press) reviewed the evidence and concluded that the evidence from the LH massif alone is inconclusive as to its position next to a transform or non-transform segment.

Reconstructions for the paleogeography of the BOIC from other studies are not accepted as they put too much emphasis on the dyke orientation within one small area of the BOIO (Rosenkrantz 1983, Fig. 6.5c) or because they are uniquely based on mantle flow lineations within one massif (Girardeau and Nicolas 1981, Fig. 6.5b).

The most important feature predicted by the reconstruction of Karson and Dewey (1978) and Casey et al. (1983) is the alignment of the four massifs of the BOIC in an

orientation nearly perpendicular to the ridge axis. Together, the four massifs of the BOIC thus would offer a cross-sectional view of an oceanic ridge system and the BOIC would be ideally suited to study the evolution of mantle return flow with time. The Oman ophiolite, on the other hand, preserves a longitudinal section along the ridge axis (Nicolas et al. 1988a). While the LH massif is located on the fracture zone contact, no such evidence is found in the three other massifs (Karson and Elthon 1987). Karson and Elthon (1987) thus infer a slightly oblique arrangement of the massifs of the BOIC with respect to the trend of the fracture zone. As discussed below, in the preferred interpretation of this thesis the LH massif is split off from the rest of the BOIC (Fig. 6.5d). The discussion about mantle return flow is restricted to the three northern massifs.

The palinspastic orientation of the BOIC within the framework of a spreading ridge is shown in Fig. 6.6. The most striking feature is the overall subhorizontal attitude of the foliation, a typical feature for mantle frozen in during return flow.

Within structural unit 1 of the TM mantle section, mineral stretching lineations are nearly parallel to the ridge axis and foliations vary from steeply south-dipping to paleohorizontal. Foliations of unit 2 are paleohorizontal, and its stretching lineation is oriented at 90° to the ridge axis. The shear sense for unit 2 implies passive spreading (lithosphere pulls underlying asthenosphere). By taking account of the relative sense of shear, the flow plane of unit 2 dips slightly away from the ridge located to the south, as is expected during progressive accretion of the asthenosphere to the base of the lithosphere upon cooling (Nicolas and Violette 1982).

Within unit 3, the stretching lineations are oriented obliquely to the ridge axis and the shear sense indicates active spreading. Further down-section within unit 3, the foliations dip away from the spreading centre. Due to the sinistral shear sense, the flow plane is tilted away from the ridge axis in a less pronounced way than the foliation planes.

Foliations within unit 4 develop a peculiar, paleogeographic northeast-dip. Shear sense and stretching lineation indicate that the upper part moved, relative to the lower part, nearly orthogonally towards the ridge axis. The mineral shape fabrics of unit 5 indicate a similar orientation to unit 3, but the shear sense is undetermined. The synformal structure of the lithological banding has a paleo-subhorizontal "fold axis" trending nearly parallel to the paleo-ridge axis. Planar fabrics within the basal unit 6 are dipping gently away from the ridge. Stretching lineations and shear senses are equivocal.

6.7 EXTENSIONAL HISTORY OF THE TABLE MOUNTAIN MASSIF

6.7.1 Plate tectonic forces

Numerous studies from ophiolitic mantle sections have demonstrated the spreading-related origin of a large part of the structures preserved. The driving force for oceanic spreading, and thus the structures in ophiolites, must lie in the plate tectonic forces. This is supported by the similarity of numerical models of mantle flow and the large scale structures seen in ophiolites (see chapter 1). In order to evaluate the significance of plate tectonic forces for the formation of the structural units in the TM mantle section, these forces are briefly reviewed (e.g. Chapple and Tullis 1977, Carlson 1983, Bott and Kusznir 1984).

During passive spreading, the lithosphere drives the underlying asthenosphere. Forces causing passive spreading are: (i) slab pull due to the high density of old, cold, down-going lithosphere; (ii) ridge push due to the gravitational force from topographic elevation of ocean ridges and hot spots; and (iii) the somewhat enigmatic trench suction force. Trench suction is probably best explained by the oceanward migration of the trench line of steeply dipping, dense slabs (Chase 1978, Molnar and Atwater 1978, Uyeda and Kanamori 1979). Global plate interaction may also cause the passive opening of small basins to accommodate divergent motions between the plates (pull-apart basins; e.g. Taylor and Karner 1983).

During active spreading, asthenosphere drives the lithosphere. Active spreading forces are: (i) forced flow, due to the buoyancy of melt charged peridotite under ridges (Rabinowicz et al. 1984); and (ii) induced flow, present only in marginal basins and caused by coupling of the down-going slab with the overlying mantle wedge (Toksöz and Hsui 1978, Jurdy and Stefanick 1983, Taylor and Karner 1983, Uyeda 1986, Bott et al. 1989).

Forced or buoyancy driven flow enhances the focusing of magmatism to the immediate ridge vicinity and is modelled either as diapirically ascending melt (Rabinowicz et al. 1987) or due to the feedback between intense melt percolation and mantle upwelling (Scott and Stevenson 1989, Buck and Su 1989). Forced flow may be very fast, but is restricted to the ridge vicinity (Rabinowicz et al. 1984, Ceuleneer et al. 1988). Near the spreading centre, decoupling of the crust and mantle may occur due to melt-charged mantle flow (Rabinowicz et al. 1987, Ceuleneer et al. 1988). Near the Moho, the direction of forced flow ideally diverges radially from a point source, but will be directed progressively normal to the ridge with increasing distance from the ridge due to the damming effect of transform faults (Vogt and Johnson 1975, Nicolas and Violette 1982, Ceuleneer et al. 1988). At depth, flow appears to converge towards the point source (Whitehead et al. 1984).

6.7.2 Spreading history

The relative age relationships of the structural units (section 6.2) suggest that the highest level peridotites were frozen in earlier than more basal peridotites. This feature is independent confirmation of the geophysical (Parker and Oldenburg 1973) and structural (Ceuleneer et al. 1988) models which predict that oceanic lithosphere grows with time while it is carried away from the ridge. The "Parker and Oldenburg model" allows

the calculation of the approximate distance from the ridge axis at which asthenosphere was converted into lithosphere, i.e. significant deformation ceased in the mantle section. Some limitations of this calculation are discussed by Ceuleneer et al. (1988).

In order to calculate the distances from the ridge at which each structural unit formed, the following parameters are chosen:

(1) the lithosphere - asthenosphere boundary (LAB) is taken to be 1000°C during spreading. Microstructural evidence suggests that the bulk of the deformation occurred at a somewhat higher temperature, so that the chosen LAB represents a *minimum* temperature. Rheological constraints would allow the LAB to be as low as 950°C (section 6.4.1). Using the same conceptual model but different values for the parameters, Tapponier and Francheteau (1978) chose 1050°C as LAB. Nicolas (1989) used temperatures between 1000 and 1100°C. A value of 600°C selected by Phipps Morgan et al. (1987) for the LAB is rheologically unrealistic (Fig. 6.3). Chen and Morgan (1990) proposed a value of 750°C as it corresponds to the lower boundary of oceanic intra-plate seismicity.

(2) The half-spreading rate is 5 cm/y. The well developed plutonic crustal section (Casey and Karson 1981) justifies the high spreading rate (Sleep 1975, Kusznir and Bott 1976, Kusznir 1980).

(3) The mean thickness of the oceanic crust in the BOIC is estimated as 6 km (Karson et al. 1984, Karson and Elthon 1987). Purely geophysical constraints would favour a higher crustal thickness for a spreading rate of 5cm/y if 2% melt or less are retained in the mantle (Reid and Jackson 1981), but the geological information is preferred.

The basic assumption for this calculation is that deformation has ceased once the peridotites intersected the 1000°C isotherm. As is discussed below, the detailed model assumes minor reactivation of the lithosphere. Distances derived from the thermal

model are therefore only first-order guidelines. The calculated distances would *decrease* with slower spreading rates (see Tab. 6.2), higher temperatures of the LAB, and a thinner oceanic crust. The distances for different thermal models are compiled in Tab. 6.2. The model of Parker and Oldenburg (1973) did not yet consider cooling of the upper crust by seawater penetration. It yields a very thin lithosphere even by using the 1200°C isotherm as LAB. The model of Boudier et al. (1988) is chosen.

Tab. 6.2. Estimates of distance from ridge axis (in km) for a given thickness of the lithosphere and different thermal models of lithosphere formation. LAB = lithosphere - asthenosphere boundary.

Reference	spreading rate	Base Moho	Base unit 2	Base TU	base unit 6	temperature of LAB
Parker and Oldenburg 1973	5cm/y	20	34	68	81	1200°C
Parker and Oldenburg 1973	1cm/y	4	7	14	16	1200°C
Kusznir and Bott 1976	3cm/y	13	17	38		1000°C
Boudier et al. 1988	5cm/y	9	17	46	56	1000°C

According to these parameters, the base of the crust in the BOIC was transformed into lithosphere at 9 km from the centre of the ridge axis (Fig. 6.7). This locates also the beginning of accretion (= freezing of flow) of units 1 and 2. Flow parallel to the ridge, as observed in unit 1, is most likely related to forced flow to which dunites with interstitial melt and minor harzburgites (unit 1) were subjected. The geometry of flow, particularly the zonal arrangement of the foliations around the lineation, is typical for flow parallel to the ridge (Nicolas 1989, p. 77). Alternatively, the peridotites of unit 1 were sucked into passively parting plates at the ridge. Mantle flow parallel to the ridge

is a well known feature from ophiolitic mantle sections (Nicolas and Violette 1982, Ceuleneer et al. 1988) and is needed to explain the deepening of the median valley of slow spreading ridges towards fracture zones (Parmentier and Forsyth 1985).

Shear sense information from unit 2 indicates that during formation of this unit, the plates moved apart passively. Consistently, lineations of unit 2 are parallel to the spreading direction, the latter being parallel to the trend of the fracture zone. At the time of freezing, peridotites of unit 2 still contained abundant melt, implying hypersolidus deformation. The base of the lithosphere was situated approximately 17 km off the ridge axis when accretion of unit 3 commenced. If minor reactivation of the lithosphere is assumed at this stage (see below), the changeover to unit 3 occurred initially at a slightly larger distance.

The critical relationship in TM is the overprint of a passive spreading force (unit 2) by an active spreading force (unit 3) which is coupled with a change of the flow direction by 40°. Movement was then directed oblique to the fracture zone and spreading direction.

A possible explanation is that, at this stage, the TM mantle section came under the influence of the forced flow field of an emerging diapir. The *sharp* lineation change from unit 2 to unit 3 suggests that the lithosphere was slightly reactivated at this stage. Otherwise, a more gradual change of the lineation would be expected during the time when passive and active spreading forces were superimposed. Indications for such a reactivation may be seen on the western limb of TM, where stretching lineations of unit 3 truncate those of unit 2. The area is, however, affected by late faulting so that the relationship remains questionable.

Prior to or during the transition from plate driven flow to forced flow, most of the orthopyroxenites intruded. Further down-section on the eastern limb within unit 3, the increasing angle between the foliation and the Moho (Fig. 6.6) may suggest that the

Fig. 6.7 (facing page). History of accretion of upper mantle peridotites to the base of the oceanic crust within the Table Mountain section. Section is located parallel to trend of the fracture zone. Unit 2 formed during passive spreading, unit 3 solidified during forced flow, and unit 5 represents an off-axis diapir. During formation of unit 3 and 5, the lithosphere was slightly reactivated. Unit 1 not shown. During detachment, unit 4 overprinted peridotites of unit 3, and unit 6 those of unit 5. Subsolidus asthenosphere represents the region where hypersolidus flow structures are overprinted by spreading-related, subsolidus deformation. Where the particle path through this region is short, high temperature microstructures are preserved. Thermal structure from Boudier et al. (1988). For more details see text.

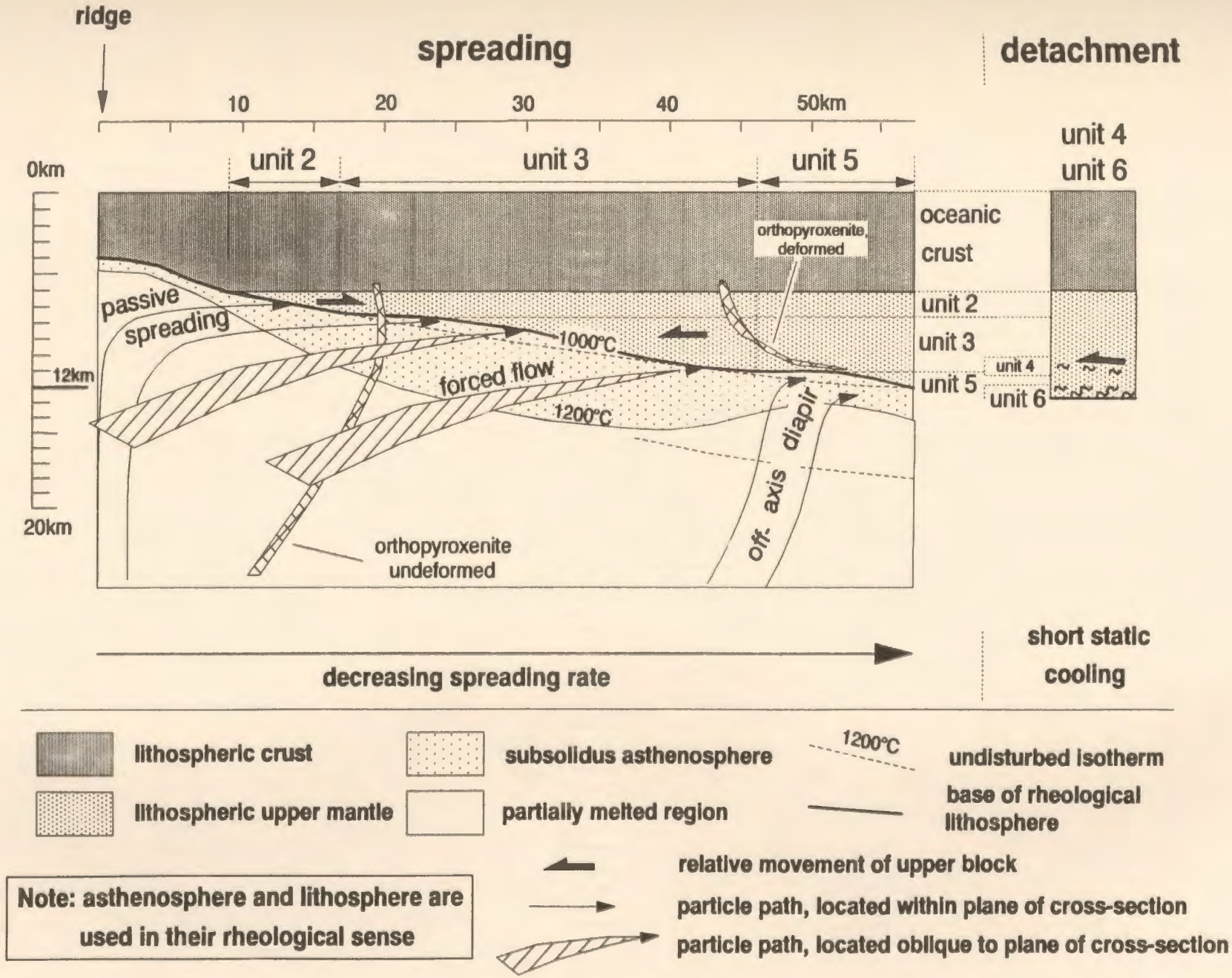
ridge
spreading
detachment
10
20
30
40
50km
unit 2
unit 3
unit 5
unit 4
unit 6
0km
oceanic
crust
orthopyroxenite,
deformed
passive
spreading
1000°C
unit 2
unit 3
12km
forced flow
unit 4
unit 5
unit 6
1200°C
diapir
off- axis
20km
orthopyroxenite
undeformed
short static
cooling
decreasing spreading rate
lithospheric crust
subsolidus asthenosphere
1200°C
undisturbed isotherm
lithospheric upper mantle
partially melted region
base of rheological
lithosphere
relative movement of upper block
particle path, located within plane of cross-section
particle path, located oblique to plane of cross-section
Note: asthenosphere and lithosphere are
used in their rheological sense

LAB steepened due to a decrease of the spreading rate (Parker and Oldenburg 1973, Sleep 1975, Kusznir and Bott 1976). A slight change of the stretching lineation of unit 3 to more northerly trends with increasing depth might record the progressive damming of flow by transforms with increasing distance from the ridge (cf. Fig. 6.9b, section 6.9).

The more lithospheric structures of unit 3 compared to unit 2 suggest that deformation during forced flow occurred or at least continued during subsolidus conditions. It is assumed that peridotites of unit 4 and the TU were subjected to the same deformation as unit 3 and then solidified to form the base of the lithosphere against which unit 5 accreted at about 46 km distance from the ridge axis (Tab. 6.2).

As explained in more detail in section 6.12.1, the structural and petrological association of unit 5 supports an interpretation that unit 5 represents the structurally modified roof of an off-axis diapir. Again a slight reactivation of the lithosphere is assumed (Fig. 6.7). The diapir ponded fairly deep in the mantle, possibly at a stage where extension was fairly restricted due to the decreasing spreading rate inferred from the basal structures of unit 3. Lherzolites at the base of TM may have been brought up together with the diapiric motion. The ascent within the off-axis diapir was, however, non-adiabatic so that melting was more limited, resulting in lherzolitic instead of harzburgitic residues (McKenzie 1984, Nicolas 1986b).

Based on the rolling mill model of Rabinowicz et al. (1984, 1987), Mercier et al. (1984) suggested that the basal lherzolites of the BOIC formed where the "off-axis" branch of mantle flow meets the diverging part of the on-axis branch. The numerical modelling predicts, however, that both branches meet at a depth of approximately 20 km below the Moho, much deeper than the observed location of basal lherzolites in TM.

As evidence for detachment structures from the TM section is equivocal, the data from this massif alone are insufficient to develop a model for obduction. The detachment history (i.e. the origin of units 4 and 6) will be discussed below after considering the data from the other massifs of the BOIC (Girardeau and Nicolas 1981, Suhr and Cawood, submitted) and constraints from the tectonic model for the extensional period.

Fig. 6.7. also gives an explanation for the preservation of hypersolidus rather than subsolidus microstructures in the TM mantle section. The region between the solidus of the peridotites and the base of the lithosphere may be called "subsolidus asthenosphere". The particle paths for a given unit within the subsolidus asthenosphere are of different lengths. The shorter the path, the less intense will be the subsolidus overprint of hypersolidus microstructures. As seen in Fig. 6.7, the path is shortest where the highest temperature microstructures are preserved, i.e. in unit 2 and unit 5. In addition, at the boundary between mafic and ultramafic rocks near the Moho, deformation of the uppermost ultramafics will tend to partition into the mafic crust due to rheological constraints (see section 6.4.3). This would enhance the preservation of highest temperature microstructures in the uppermost mantle.

If a position of the paleo-ridge to the north of the BOIC had been inferred (see, however, the evidence in section 6.6), a scenario involving active spreading (unit 2) followed by passive spreading (unit 3) would be implied. This is the normal case inferred for ophiolites. In the Oman ophiolite, forced flow is restricted to approximately 20 km measured normal to the ridge and is then replaced by the regional plate driven flow (Ceuleneer et al. 1988). The changeover occurs at about 500 m below the Moho in Oman, 6-700 m below the dunites (or 11-1200 m below the gabbros) in New Caledonia (Prinzhofer et al. 1980). Numerical modelling puts it at 2.5 km depth (Nicolas and Rabinowicz 1984). The model of passive spreading for unit 3 would imply that spreading occurred obliquely across the fracture zone orientation suggested by Karson and

Dewey (1978). Consequently, either the trend of the fracture zone or the flow direction would have to be incorrect as movement of the plate at 40° across the fracture zone implies that the fracture zone is not stable.

6.8 CONSISTENCY OF INTERPRETATION WITH OTHER MASSIFS FROM THE BAY OF ISLANDS COMPLEX

If passive spreading of unit 2 was replaced by active spreading of unit 3, then lithosphere which formed later than that in the TM massif would record less or nothing of the passive spreading structures. Such lithosphere may be preserved in mantle rocks of the southern massifs of the BOIC (Fig. 6.8).

Data for the mantle section of NAM are very limited. Casey (1980) indicated that a change in the trend of the stretching lineation occurs in the upper part of the mantle section of NAM. It could relate to the unit 2/3 change. The trend of the lineations in the uppermost harzburgites and plastically deformed transition zone is compatible with those of unit 2 (see also Dunsworth et al. 1986). A foliation pattern mapped by T. Calon in the uppermost harzburgites of NAM (unpubl. data, pattern shown in Neyens 1986) is consistent with dextral shear.

In the BMD massif, neither stretching lineations nor a shear sense comparable to unit 2 are present (Girardeau and Nicolas 1981). Lineations plunge to the northwest, the shear sense is sinistral apart from a narrow section of ill-defined movement directions below the gabbros. The bulk of the mantle section in the BMD massif appears thus related to unit 3 in TM.

Structures and lithologies in the LH massif are difficult to evaluate as they could be influenced by the proximity to a fracture zone (Karson and Dewey 1978, Karson and Elthon 1987, Suhr et al., in press) and possible rotations of the entire massif associated

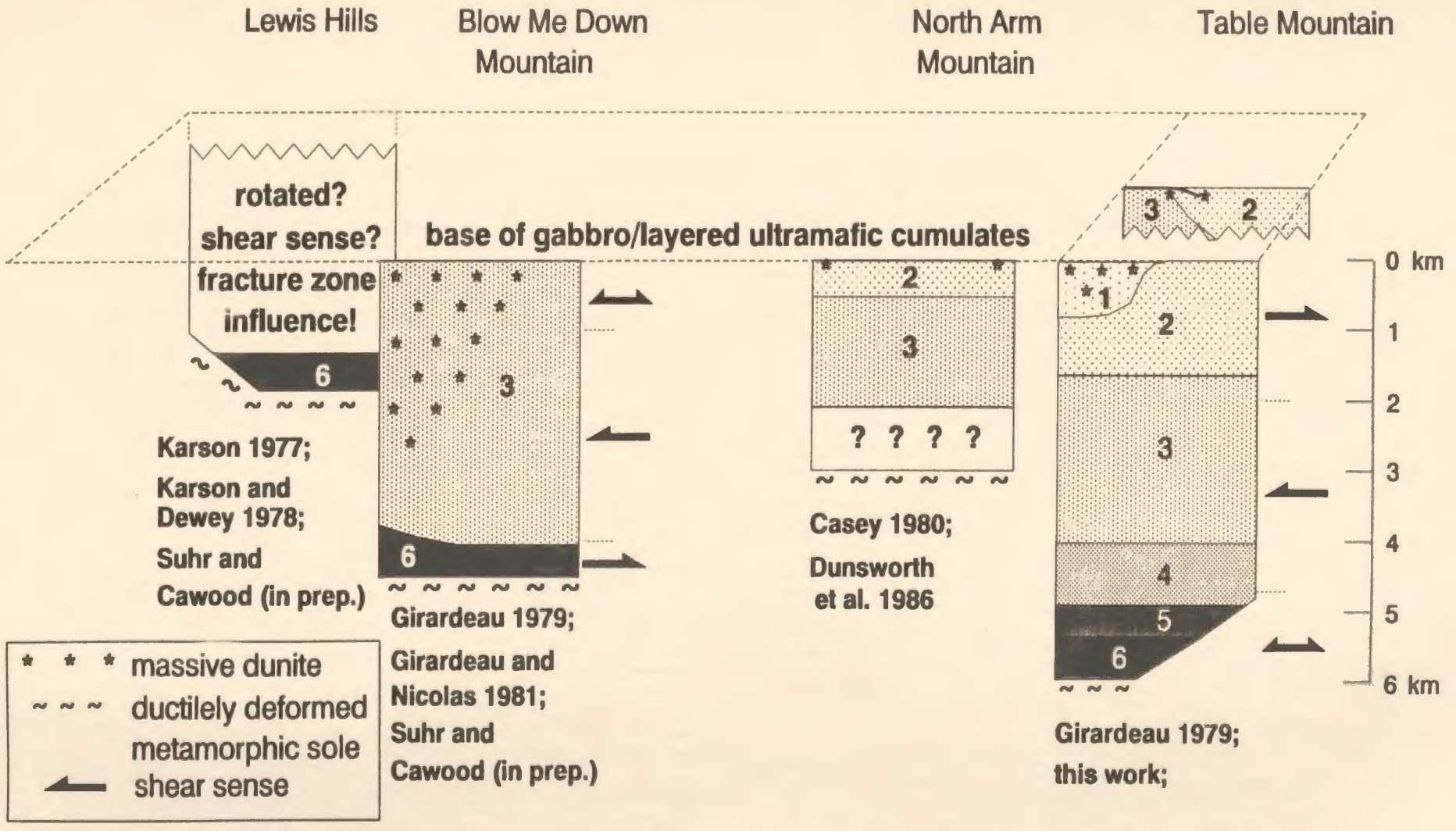

Fig. 6.8. Possible correlation of structural units established in the Table Mountain section with the other massifs of the Bay of Islands Ophiolite. View from the east. Details in text.

with the final emplacement (Williams and Malpas 1972, Karson and Dewey 1978, Casey et al. 1983). Crustal structures (Karson and Dewey 1978, Karson 1977, 1979) as well as at least the mantle structures in the southern LH (Dunsworth et al. 1986, Suhr et al., in press) are very peculiar and unlike those of the three other massifs. The LH massif will therefore not be considered here.

Evidence for basal lherzolites or at least significantly coarser grained, cpx-bearing harzburgites exists also from the base of the three other massifs of the BOIC (Church and Riccio 1977, also pers. observ.).

Data of the detachment-related structures in the BMD massif indicate a uniformly northward directed thrusting (Girardeau and Nicolas 1981, Suhr and Cawood, submitted). For NAM, no data for the basal sections are published. In the eastern LH, stretching lineations related to detachment trend 350° (Suhr and Cawood, submitted), i.e. are parallel to the direction of the fracture zone within the same massif. No shear senses were determined.

6.9 POSITION OF THE MASSIFS AT THE TIME OF DETACHMENT AND GEOMETRY OF FORCED FLOW FIELD

In section 6.7.2 it was argued at what distances from the ridge axis different units of the TM mantle section were accreted to the base of the lithosphere. If the temperature at the basal décollement plane during initiation of detachment is known, the distance of the TM massif from the ridge at the time of *detachment* can also be estimated.

Microstructural evidence supports 1000°C for initiation of detachment, but not more than 900°C for freezing of the most basal peridotites (i.e. the ultramylonites). The temperatures recorded by mineral equilibria in the metamorphic sole are as high as 850°C (Malpas 1979a, McCaig 1983). This implies that temperatures of the overlying peridotites were lying at least at around 1000°C, even accounting for frictional heat

added during thrusting (Malpas 1979a).

Pavlis (1986) evaluated the significance of frictional heating during the formation of megathrusts. For olivine-dominated rheologies and *independent of the initial temperatures*, frictional heating will result in temperatures of 900-950°C within a broad region around the décollment horizon as long as strain rates are above 4 cm/y. In contrast to the calculations of Malpas (1979a), time is not considered a critical constraint for the maximum temperatures reached at the décollment plane! Consequently, it could be argued that detachment may have been initiated at *any* temperature, only to reach 900-950°C due to frictional heating. However, initial detachment at lower temperatures, say 750°C, would imply a prograde history for the basal peridotites. Prograde relationships are not known from the mineral zoning patterns of the peridotites (Malpas 1979, McCaig 1983, section 5.5). Overall, the frictional heating argument needs further evaluation.

Casey and Dewey (1984) suggested that original detachment horizons for ophiolites lay at a deeper level than the location of currently observed detachment structures. In their model, detachment was initiated along the hangingwall of a subduction zone. In the course of detachment, wedges of mantle became expelled as the dip of the subduction zone progressively shallowed due to attempted underplating of continental lithosphere. Given the rigidity of oceanic lithosphere, it appears highly unlikely that mantle wedges can simply be expelled: there is very little evidence for intra-plate deformation of oceanic lithosphere (Park 1988, p. 47). No lithological or structural discontinuities have been found within the TM mantle section. In addition, Nicolas (1989) showed that a subduction zone environment is too cold to represent anything similar to a metamorphic sole.

In summary, evidence from microstructure and geothermometry indicates that temperatures during detachment were lying between 900 and 1000°C. These tempera-

tures closely coincide with the LAB at the time of spreading. It is intuitively favourable to detach oceanic lithosphere along a rheological boundary (Boudier 1982, 1988, Spray 1984). The temperatures, however, also coincide with those which would be reached during frictional heating in olivine-dominated lithologies (Pavlis 1986). The temperatures at *initiation* of detachment can therefore not safely be evaluated. As a consequence, it is also difficult to make a statement about the time difference between cessation of spreading and initiation of detachment with thermal arguments alone. Isotopic evidence reviewed in section 1.3.3 suggests that this time difference was 17 my, or at least 10 my by accounting for the error range of the age determinations (Dunning and Krogh 1985). Evidence from the sedimentary record of the Humber Arm Allochthon and the Humber Zone was reviewed by Dunning and Krogh (1985). It indicates that obduction of oceanic lithosphere must have occurred very shortly after formation of the BOIC. However, it is not possible to determine whether it was the BOIC itself which was obducted at this time.

Spreading-related mineral stretching lineations within the BMD massif are trending northwest-southeast (Girardeau and Nicolas 1981), i.e. are nearly parallel to the trend of the ridge axis. Using this orientation, the distance of the massifs during cessation of spreading can be reconstructed as follows.

Flow parallel to the ridge is common within ophiolites but is restricted to the vicinity of the ridge (Nicolas and Violette 1982, Ceuleneer et al. 1988). Preservation of a singular, spreading-related flow structure parallel to the ridge requires that the BMD massif has been frozen in at the ridge. Otherwise, the flow structures would have been overprinted by return flow structures directed away from the ridge (as seen in the TM massif) when the massif was carried away from the ridge axis during continued spreading. In other words, in any other position than near the ridge axis, stretching lineations from further down-section in the mantle sequence would have to show a component of flow orthogonal to the ridge due to the transform damming effect. In addition, flow

parallel to the ridge requires that the BMD massif was not located adjacent to the CC. The CC would have acted as a barrier for such flow and caused a deflection of flow parallel to the CC as observed in the LH massif (Suhr et al. in press). Only the LH massif was thus positioned next to the CC (Karson and Elthon 1987).

If the BMD massif was located very close to the ridge axis at the time of detachment, the current distance between the BMD and TM massifs (70 km) represents also the distance of the TM massif from the ridge axis at the time of detachment. Using this distance it can be evaluated whether a model suggesting a temperature of detachment between 900 and 1000°C without any input from frictional heating is realistic at all. In other words, the question is whether such a high temperature would still be present in the oceanic lithosphere at a distance of 70 km from the ridge axis at the detachment level observed within the TM mantle section. The base of unit 6 in TM is located at a lithospheric thickness of 12 km. By using the thermal model of Boudier et al. (1988), the TM massif would have been located 56 km (for 1000°C) or 80 km (for 900°C) away from the ridge. The distance would increase to 70 km (for 1000°C) if the thermal model of Chen and Morgan (1990) is used. The residual-heat-only model is thus thermally feasible.

The distances calculated from the thermal models would decrease if the spreading rate continuously decreased from 5 cm/y to 0 cm/y in the final stages of spreading. It is likely that the spreading rate has slowed down in the final extensional history of an oceanic basin as plates will not instantly stop moving.

In summary, the TM massif shows well developed return flow structures and transform damming effects and thus was located at a considerable distance from the ridge axis when spreading ceased. The BMD masssif was located next to the ridge axis and away from a thermal boundary which would have deflected ridge-parallel flow. The LH massif, however, shows evidence for a location next to a mechanical boundary.

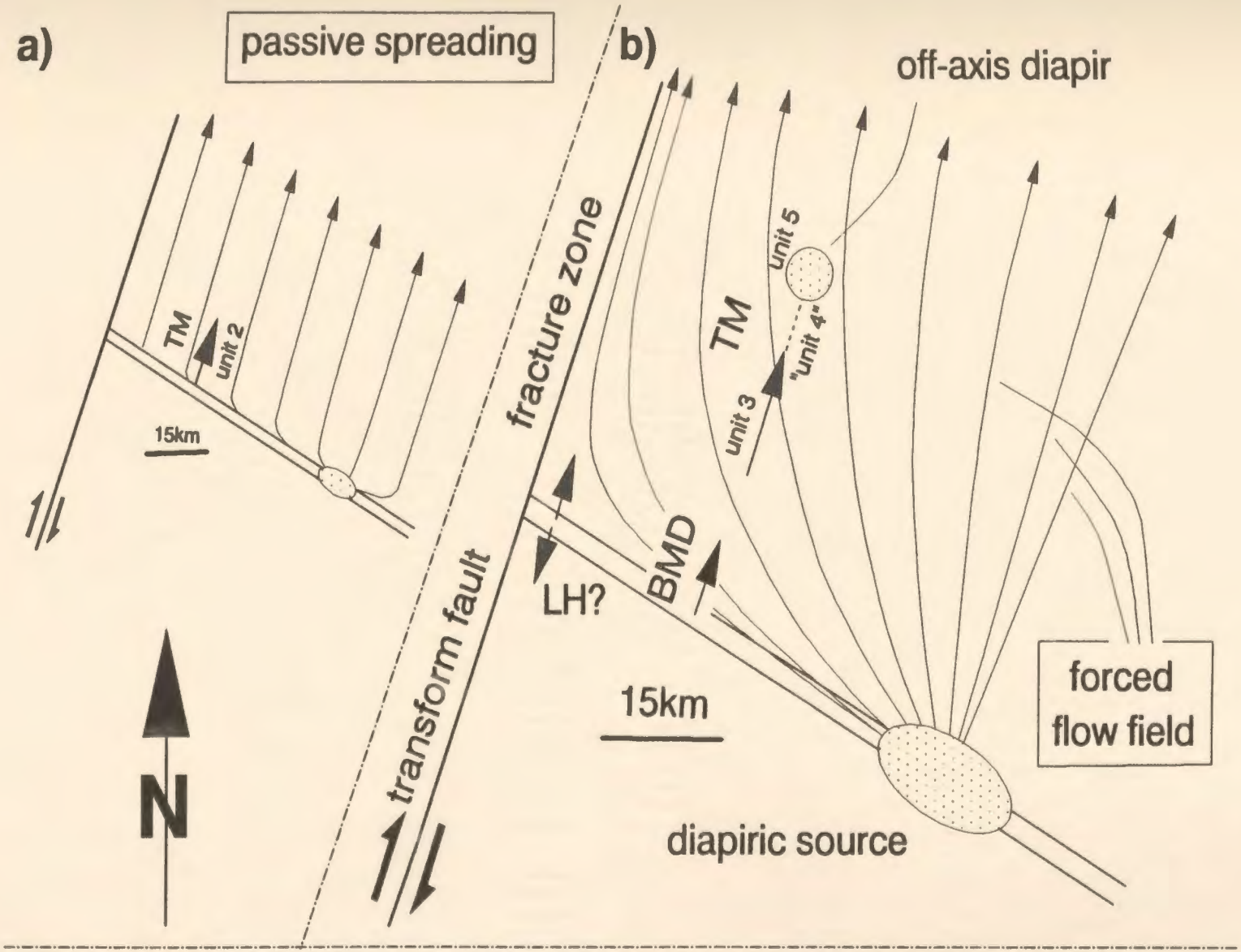

Fig. 6.9. Flow fields inferred for the upper mantle of the Bay of Islands Complex during (a) passive and (b) active spreading. During (b), a forced flow field did build up. The lithosphere, against which the asthenosphere was accreted, was weakly reactivated at this stage. Structures within the Lewis Hills do not conclusively allow a positioning of the massif to either the north or the south of the ridge axis. TM - Table Mountain; BMD - Blow Me Down Mountain; LH - Lewis Hills.

Fig. 6.9 summarizes the information. The early structures in TM (unit 2) are related to the predominance of passive spreading (Fig. 6.9a). Passive spreading was responsible for initially carring the TM massif away from the ridge axis before the BMD massif was formed. Subsequently, a forced flow field began to build up. It is related to an emerging diapir and its geometry can be derived from the flow lines of the BMD massif and unit 3 in TM (Fig. 6.9b). Down-section within unit 3, the slightly changing stretching lineations are a result of the transform damming effect. Further down-section, the relationships in TM have been obscured by the structural overprint of unit 4 during detachment. The BMD massif froze in at the ridge and therefore does not record the transform damming effect. Fig. 6.9b also shows the position of the suspected off-axis diapir in TM. Fig. 6.9b would represent the massif configuration during cessation of spreading and initiation of detachment (Fig. 6.9), though the time span between both events is difficult to evaluate.

According to earlier interpretations (Karson and Dewey 1978, Casey et al. 1983, 1985, Karson and Elthon 1987), the four massifs of the BOIC are gradational in structure and were linearly aligned in the oceanic environment. Structure and petrology of the LH and BMD massifs are, however, different enough to justify the separation of both massifs as shown in Fig. 6.9. The difference in structure even includes the later history of synclinal folding which is only developed in the three northern massifs but not in the LH massif (Karson 1979). The alignment of the three northern massifs together with the LH into their current position might thus be a very late feature.

6.10 TECTONIC MODEL

Due to the highly allochthonous setting of ophiolites, tectonic models concerning their environment of formation generally involve a large amount of speculation. Some boundary conditions are listed below:

(1) the BOIC is approximately 20 my younger than the LPC (Dunning and Krogh 1985, Jenner et al., in press), and, according to the tectonic interpretation of Karson and Dewey (1978), also postdates the western LH by the same age difference.

(2) The contact between the western and eastern LH is undoubtedly of high temperature nature (Karson 1977) and thus relates to the oceanic history of the LH massif. It is here accepted that the contact constitutes a fracture zone or its aseismic extension so that its orientation is parallel to the spreading direction.

(3) The Little Port Complex has island arc affinities not reflected in isotope and geochemical data for the BOIC (Malpas 1979b, Jenner et al., in press). The proximity of igneous rocks with arc and MORB signature is atypical for mid-ocean ridge systems. A formation of the BOIC within an older oceanic terrane with arc affinities is therefore preferred.

The overall tectonic setting visualized for the BOIC is a pull-apart basin which opened during dextral strike-slip deformation in an older oceanic lithosphere with arc affinities (the CC)(Fig. 6.10a). The setting proposed is similar to that of Karson and Dewey (1978). A modern analogue is the Andaman Sea where subduction of the Indian Plate produced a marginal ocean basin. Strike-slip tectonics dominate at the subduction site as well as within the marginal basin (Curray et al. 1979).

The pull-apart basin model allows for:

(1) rapid, passive opening and closing of an ocean;

(2) presence of abundant, long fracture zone segments due to strike-slip dominated tectonics, connected by short segments of spreading ridges;

(3) a high angle relationship between the trend of the ridge axis within the marginal basin and the associated subduction zone. In most back arc basin sett-

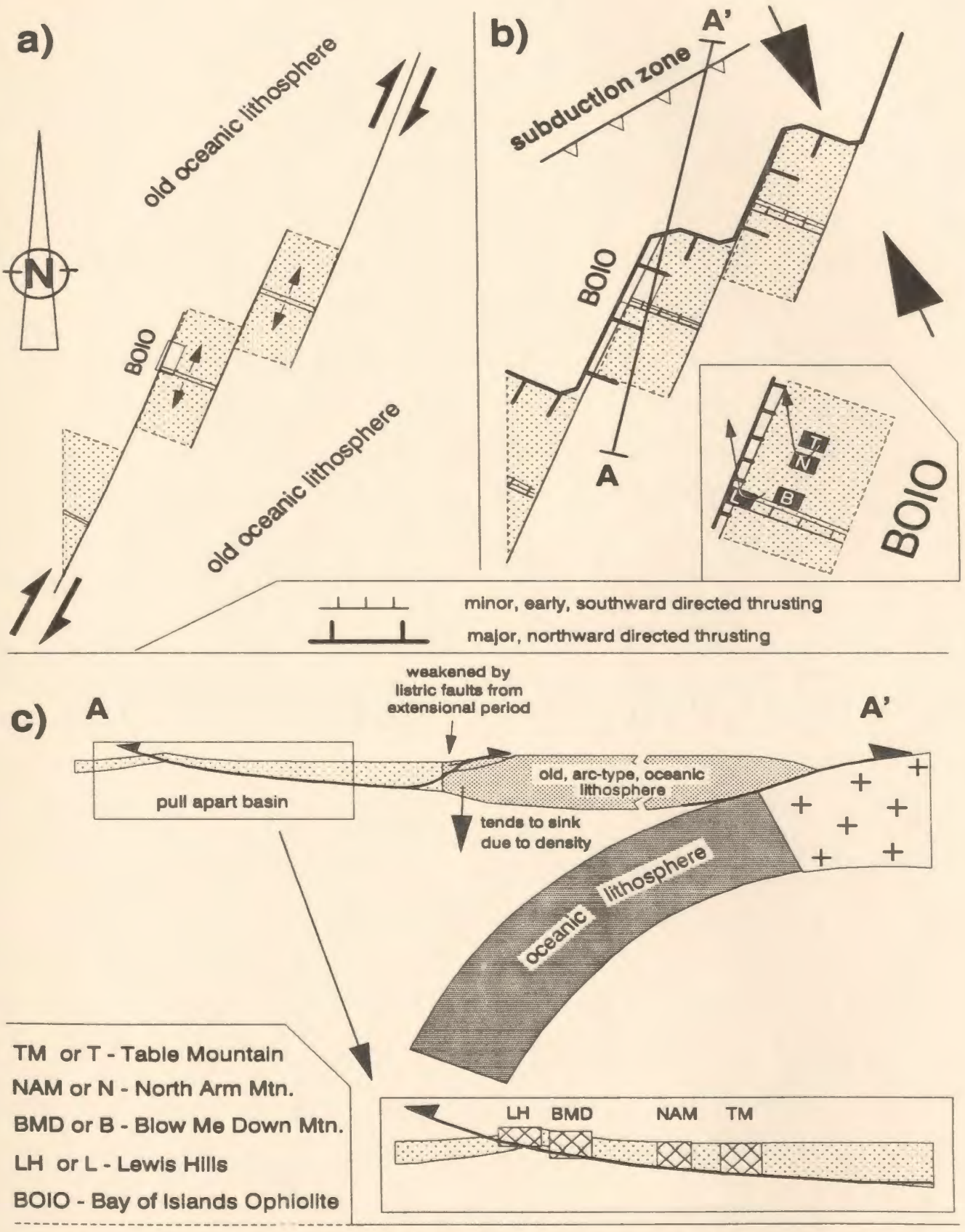

Fig. 6.10. Tectonic setting of the Bay of Islands Complex during (a) oceanic spreading and (b) detachment. Inset in (b) shows movement of ophiolite during detachment (from Suhr and Cawood, in prep.). (c) Cross-section along line shown in (b). Note that within inset of (c), massifs are projected into plane of profile. Lewis Hills may also be located to north of ridge axis, aligned with BMD massif. For details, see text.

ings, both tectonic elements are parallel (e.g. Weissel 1981).

(4) juxtaposition of young oceanic lithosphere (the BOIC) against older, essentially unrelated lithosphere (the CC) along one of the long fracture zone segments. This interpretation contrasts with those of Karson and Dewey (1978) and Casey et al. (1981, 1983, 1985) who see the lithosphere of the CC as produced within the same tectonic setting as the BOIC lithosphere.

In the model, dextral transcurrent faulting above a subduction zone led to passive opening of a small oceanic pull-apart basin. The pull-apart basin was contained within approximately 20 my old, oceanic lithosphere with arc affinities. The transcurrent faulting within the marginal basin was probably favoured by oblique subduction (Jarrard 1986). Later, due to changes in the plate configuration outside the basin, the opening rate decreased. Given the tectonic models of Newfoundland (e.g. Williams 1979), the subduction zone may have been located in the northeast of the marginal basin (Fig. 6.10b). Attempted subduction of continental lithosphere (the North American craton) led to basin-closure and detachment.

6.11 DETACHMENT HISTORY

The detachment history of the BOIC has recently been addressed by Suhr and Cawood (submitted). Their considerations are summarized below. In order to detach oceanic lithosphere from the oceanic environment, the oceanic lithosphere must be broken along three sides in addition to a basal décollement horizon. The three sides represent a frontal and two lateral ramps. Four tectonic settings are considered likely to act as lateral or frontal ramps to break the lithosphere:

(1) the spreading ridge (Boudier et al. 1982, 1988);

(2) transform faults (Karson and Dewey 1978, Casey and Dewey 1984, Dewey and Shackelton 1984);

(3) the contact between marginal basin and surrounding older lithosphere (Karig 1982);

(4) the seaward side of subduction zones, where shear fractures due to bending of the lithosphere might assume thrust geometries and cause obduction (Nicolas and LePichon 1980).

The inferred proximity of the BOIC to the ridge and a transform fault/fracture zone environment suggest that both may have played a major role during detachment. Karson and Dewey (1978) and Casey and Dewey (1984) suggested that detachment occurred by west- to northwest-directed movement of the BOIC which led to thrusting of the BOIC on top of the CC along the fracture zone.

The structurally most simple, and therefore most reliable detachment structures exist at the base of the BMD massif. Data from this massif indicate that detachment occurred by northward directed thrusting (Girardeau and Nicolas 1981, Suhr and Cawood, submitted). The northward movement implies that the fracture zone acted largely as a later ramp to obduction. In addition to this major movement, several other, detachment-related structures have to be explained: (i) structural complexities encountered in the basal section of the TM massif; (ii) southwestward movement of unit 4 in TM; (iii) unusually abundant and complex lithospheric structures at high levels of the oceanic crust (transition zone) in the southern LH massif (Suhr and Cawood, submitted).

Suhr and Cawood (submitted) thus infer a short, early motion towards the ridge, indicated in the southwest-directed thrusting of unit 4 in TM as well as structures in the southeastern LH (Fig. 6.10b,c). Only in unit 4 of TM was this motion protected from later overprint due to its higher level position. The initial detachment motion used the weakness of the plate boundary along the ridge to break the lithosphere (Fig. 6.10c). At this stage, the LH massif, which was either positioned immediately to the south (as shown in Fig. 6.10c) or north of the ridge, constituted the leading edge of obduction. This movement was, however, rapidly blocked by the upward movement along the

northward-dipping detachment plane (which could have been the LAB). Similarly, in the Oman ophiolite, initially west-directed thrusting moving towards the ridge was deflected into north-south trending, strike-slip movements due to the elevation of the LAB near the ridge. However, in Oman, the ridge was later overridden (Boudier et al. 1988).

In the BOIC, however, the detachment direction changed and was directed towards 350° as indicated regionally in the Blow Me Down massif. Complex movement patterns expected at the turn-around stage are seen in unit 6 of TM as well as in the southern LH. At the turn-around stage or during the northward thrusting, the ophiolite was moved onto the CC. Evidence for this can be seen in ductilely accreted slivers of CC-type lithosphere to the base of the ophiolite in the LH during early detachment (Suhr and Cawood, submitted). During northward movement, the lithosphere to the north of the BOIC must have been broken. Possibly, the boundary between the pull-apart basin (young, buoyant oceanic lithosphere) and the 20 my older surrounding oceanic lithosphere (dense, thick oceanic lithosphere) was used (Fig. 6.10c). Breakage and subsequent thrusting might have been facilitated by the presence of listric, extensional faults in the older oceanic lithosphere dating from the extensional period.

Fig. 6.10b also shows the different obduction paths taken by the LH massif and the three other massifs due to their varying distance to the "cold wall" of the CC. Suhr and Cawood (submitted) show that this is reflected in different styles of accretion at the base of the ophiolite during detachment.

6.12 FURTHER ASPECTS

6.12.1 Model for the formation of unit 5 and basal lherzolites

The structural change from unit 4 to unit 5 is characterized by the following trends:

- the foliation becomes steeper and the stretching lineation changes;
- progressively down-section within unit 5, the mineral shape fabric becomes weaker and melt impregnations are present and undeformed;
- the uniform shear sense within unit 4 is lost in the TU;
- lithological banding is multiply deformed and defines an apparent synformal structure which is not clearly related to the foliation;
- the grain size becomes coarser, clinopyroxene more abundant and geochemically the peridotites of unit 5 are less depleted than those of unit 4;
- orthopyroxenite dykes are nearly absent in unit 5, cross-cutting dunites are very rare.

All changes are gradational. They are interpreted in a model of underplating of a diapir at the base of the lithosphere (Fig. 6.11). The lithological banding relates to flow structures of the diapiric roof modified by detachment-related strain of units 4 and 6. The foliation in unit 5 is a relatively late, high temperature feature associated with underplating. The TU is the zone where remnant structures typical for unit 5 are preserved but overprinted by higher strain in the diapiric roof or, alternatively, associated with detachment.

The off-axis nature of the diapir is derived from the palinspastic reconstruction which indicates that during accretion of unit 5, the mantle sequence must have been positioned ~ 50 km off the ridge axis (Fig. 6.11b). Unless a *component of vertical (diapiric) motion* is invoked, it is extremely difficult to explain the preservation of pristine melt impregnation features during extended return flow. During simple return flow, the particle paths intersects progressively cooler isotherms and indicates cooling under constant pressure, not fusion.

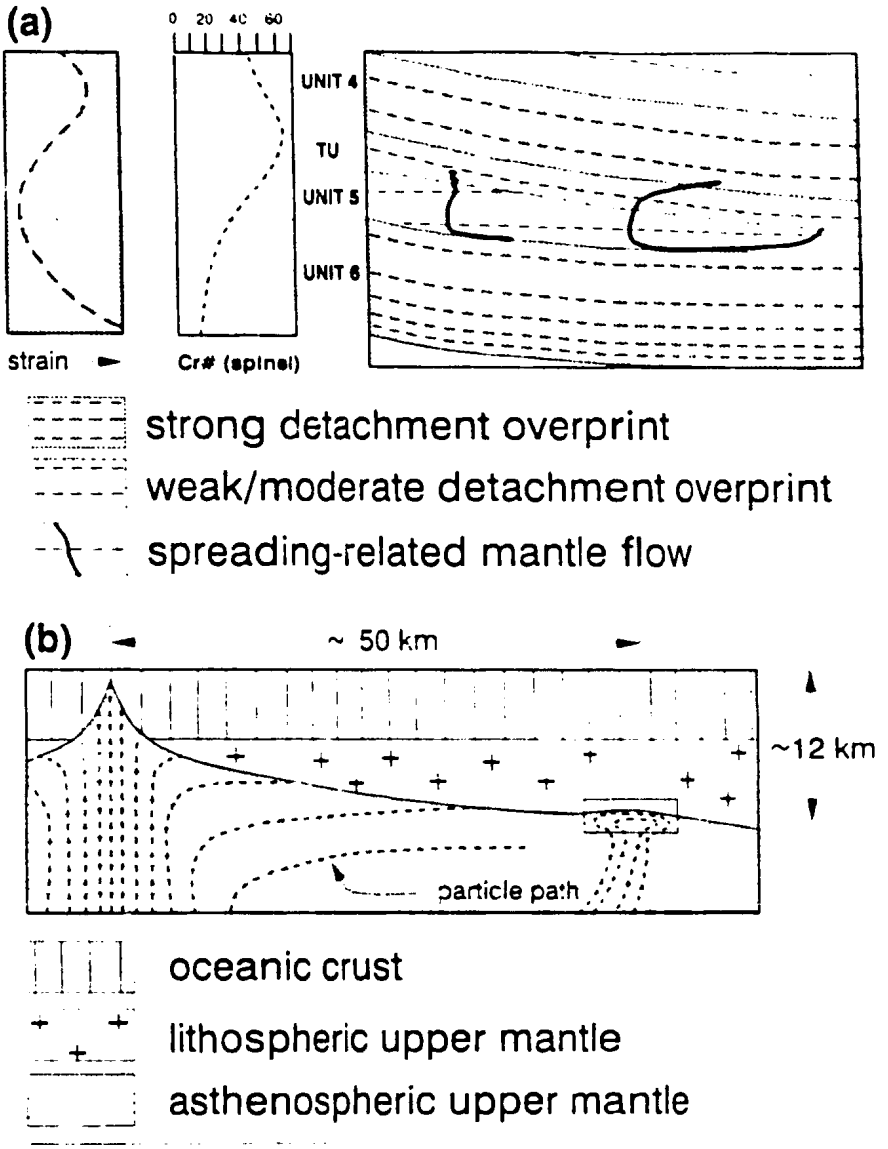

Fig. 6.11. (a) Schematic geological profile through the base of the Table Mountain mantle section. Heavy line represents lithological banding, the orientation of which appears only weakly modified by detachment strain. (b) Tectonic situation associated with formation of unit 5. Isotherms (not shown) are parallel to lithosphere - asthenosphere boundary. As a result, particle paths along the main mantle upwelling are retrograde. They cannot explain in-situ melt impregnation features preserved in unit 5. Consequently, a steep particle path (diapiric) is suggested for unit 5. The ponding of a diapir at the base of the lithosphere may also explain the orientation of the banding shown in (a).

The less depleted chemistry of units 5 and 6 is explained in this model as due to non-adiabatic ascent of the mantle associated with the diapir. The strong chemical gradient between units 4, 5 and 6 is thus the result of juxtaposition of two mantle sequences having experienced a different partial melting history.

The absence of orthopyroxenite dykes is consistent with this interpretation, as it was inferred that orthopyroxenite dykes intruded largely in the time interval between the accretion of units 2 and 3. At the time of the major period of intrusion of the dykes, the mantle section of unit 5 was spatially separated from the region of orthopyroxenite dyke emplacement (Fig. 6.7).

Low strain of unit 5 results from the shorter strain path of the peridotites. Unit 5 might not have been affected by detachment strain of unit 4, as the former is rheologically harder due to higher amounts of orthopyroxene compared to the more depleted unit 4.

More lherzolitic rocks also occur at the base of the three southern massifs of the BOIC. It is difficult to make a single diapir responsible for all these more lherzolitic rocks. As the basal lherzolites are the last material to be accreted to the lithosphere before detachment occurred, they must reflect conditions of very limited extension, i.e. very low spreading rates. It is suggested that the basal lherzolites in the other massifs of the BOIC are the result of non-adiabatic mantle upwelling prevailing during the dying stages of an ocean ridge system (see 6.13).

6.12.2 Model to explain the spatial discrepancy between unit 2/3 boundary and shear sense reversal

The change of the stretching lineation from unit 2 to unit 3 has so far been equated with the shear sense reversal from dextral to sinistral. However, the boundaries between the two domains of different stretching lineations and different shear senses do

not spatially coincide precisely. The following model is proposed to explain the spatial discrepancy.

During dextral shearing of unit 2, the foliation will be at a small angle to the actual flow plane indicated by the olivine lattice fabric (Fig. 6.12a). The structural data and the model suggest that the dextrally sheared peridotites with a stretching lineation trending N20°E were overprinted by sinistral shear *using a very similar flow plane* with a stretching lineation trending N20°W. The arrangement between foliation and flow plane needed to record a sinistral shear sense in a microstructure ... e shown on the right side of Fig. 6.12a.

During the reversal shown in Fig. 6.12, the shear plane remains the same (or nearly so). Therefore, it *instantly represents the stable flow plane* also after the reversal. In order to determine the shear sense, the "proper" foliation orientation is needed. The foliation is determined using spinel and orthopyroxene grains. Fig. 6.12b demonstrates that these two phases may react to the shear sense reversal either by synthetic or antithetic shear using their preferred mode of deformation (slip, rigid translation, etc.). Synthetic shear requires very large strains. Antithetic shear movement, which is probably preferred (Etchecopar 1977), needs only very low strain. It would be facilitated by a pure shear component during deformation. It also requires, however, that pyroxene or spinel grains rotate *through* the plane of finite extensional strain in order for a dextral shear sense to be recorded. This is not possible.

Only increasing strain during sinistral shear, recorded down-section within unit 3, will allow the microstructure to reorganize sufficiently to adapt in such a way to the dominant movement sense that the proper shear sense can be determined also microstructurally. The strain required for this reorganization is probably higher than that necessary to reorient the stretching lineation by 40°. The stretching lineation thus tracks the new deformational event after a relative small amount of strain, whereas the shear

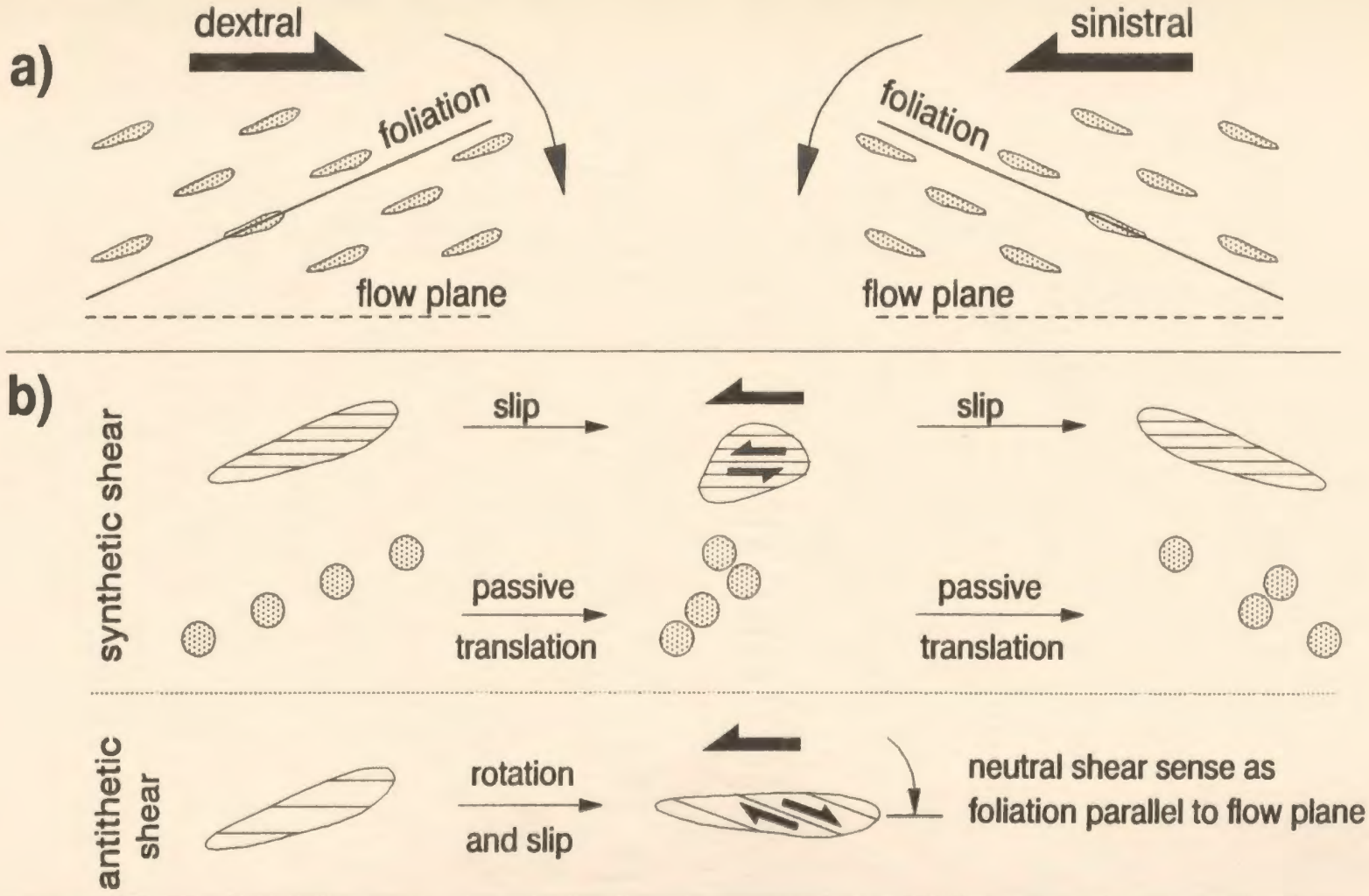

Fig. 6.12. Model explaining the sluggish behaviour of the microstructural shear sense method used in this work to adjust to a shear sense reversal. During the reversal, the flow plane is kept constant. (a) Relative orientation of the foliation to the flow plane indicates the shear sense. The foliation is indicated by orthopyroxene or spinel grains shown as dotted grains or grains with horizontal ruling. The flow plane is determined with olivine petrofabrics and olivine dislocation walls. In (b) it is shown, that the foliation may adjust either by synthetic or antithetic shear to a shear sense reversal. Details of (b) are explained in text.

sense still records the old event.

Consistent with this interpretation, neutral shear senses have frequently been measured in the area of the dextral-sinistral inversion. Flexure-type mesoscopic folds of the banding indicating sinistral shear are present within the dextral microstructure domain, demonstrating the sluggishness of the microstructural shear sense method to adapt to the new conditions.

In summary, it is suggested that under certain circumstances the microstructural method to determine movement senses used in this thesis may have a high amount of memory for a shear sense dating from an early phase of deformation.

6.13 CONCLUSIONS

Conventionally, ophiolite formation has been seen as a two stage history involving a fully extensional phase of oceanic spreading which was followed by a compressional obduction event. Age constraints from the ophiolitic rocks of the BOIC (Dunning and Krogh 1985, Jenner et al., in press) and the associated metamorphic sole (Williams and Dallmeyer 1975), the high temperature nature of the metamorphic sole (Williams and Smyth 1973, Malpas 1979a, McCaig 1983), and the nature and age of sedimentary rocks within the Humber Arm Allochthon (reviewed in Dunning and Krogh 1985) are consistent with the model that both events must have followed each other rapidly. Due to the difficulty in evaluating the amount of strain heating during detachment, it is not possible to argue whether detachment followed immediately after spreading or whether both events were separated by a few million years.

The orientation of spreading-related mineral stretching lineations in the BMD massif strongly suggests that the BMD massif was located at the site of the ridge during cessation of spreading and therefore also during initiation of detachment. At the time of detachment, the TM massif was less than 100 km from the ridge axis. The BOIC must

record the last accretionary stages of the spreading history of an ocean basin. It can be shown that lithology and structure of the mantle section of the BOIC is consistent with formation during a decreasing spreading. This would also set the required tectonic scene for detachment. Four stages can be distinguished in the evolutionary history of the BOIC.

Stage 1: high spreading rate, adiabatic upwelling

Fully extensional conditions are realized during plate driven flow of unit 2 in TM. Microstructures record low stresses which militate against any significant stress concentrations during passive spreading. Possibly enhanced by the lack of stress concentrations, harzburgites are apparently able to retain a considerable amount of trapped melt which results in a distinct geochemical signature.

Stage 2: decreasing spreading rate, adiabatic upwelling

Forced flow from an emerging diapir is considered responsible for the structure of unit 3. The far-reaching forced flow field of this diapir (35-50km from the ridge) compared to the Oman ophiolite (20 km, Ceuleneer et al. 1988) as well as the steeper LAB in the basal part of unit 3, may be the result of a decreasing spreading rate coupled with continued mantle upwelling (see below). Harzburgites (i.e. not lherzolites) did form synchronously at the ridge axis (peridotites of the BMD massif) and suggest that mantle upwelling was still adiabatic (Boudier and Nicolas 1985, Nicolas 1986b).

It is suggested that the decreasing spreading rate was imposed onto the BOIC spreading centre due to external plate reorganizations. However, the rate of mantle upwelling did not react immediately to changes in the passive spreading rate. This sluggish behaviour was caused by a melt column of several tens of kilometres height which existed at the time below the ridge (McKenzie 1984). It exerted an additional force to drive mantle upwelling (Rabinowicz et al. 1984, 1987, Scott and Stevenson 1989) and active spreading.

The more lithospheric microstructures of unit 3 compared to unit 2 may indicate that stress concentrations are more likely to occur during forced flow conditions than during the more laminar flow of passive spreading. Higher stresses during tectonic freezing of unit 3 might also have been responsible for the efficient melt removal and therefore more depleted geochemical signature of unit 3 compared to unit 2.

Stage 3: slow spreading rate, non-adiabatic upwelling

More restricted spreading conditions are seen in the lherzolitic base of the BOIC. These peridotites represent the products of non-adiabatic ascent of upper mantle. In addition, the off-axis diapirism of unit 5 in TM may have been caused by diffuse mantle upwelling during restricted passive extension. It is currently not clear whether a decreasing spreading rate leads to increased (Girardeau and Mercier 1988, Scott and Stevenson 1989) or decreased (Nicolas and Rabinowicz 1984, Chen and Morgan 1990) channeling of mantle up-flow beneath a ridge.

Thick dunite sequences are developed in the BMD and LH massifs, i.e. in the massifs inferred to have been located near or at the ridge. The dunites may reflect the restricted extension. Dunites are related to either intense melt percolation (replacement model of dunites) or fractionation (magmatic model) at the base of the Moho. Both features will be enhanced if spreading is insufficient to accommodate melt production so that melt ponds at the base of the crust instead of entering the crust or erupting at the seafloor.

Stage 4: Negative spreading rate, no upwelling

This configuration is characteristic for detachment. Detachment tectonics are complex and appear to have involved a short southward movement before the major northward-directed thrusting. Blockage of the initial southward movement might have occurred by the elevated LAB near the ridge (Boudier et al. 1988), enhanced by a surplus of melt production with respect to the associated spreading rate in the final accretionary stages of the spreading centre.

In the introduction to this thesis, the impressive correlation between mid-ocean ridge systems, geophysical models for oceanic lithosphere formation, and ophiolites was emphasized. Within this chapter, however, it is concluded that the Bay of Islands Complex may differ from ocean ridges in one important aspect. Whereas mid-ocean ridges are characterized by constant spreading rates over a long period of time, the Bay of Island Complex may represent a very transient spreading regime. It is characterized by a decreasing spreading rate and associated deviations from adiabatic upwelling. While numerical modelling of mantle flow is based on constant spreading rates or constant extensional forces, a model involving decreasing spreading rates may be more realistic for certain ophiolitic mantle sequences.

Recently some of the crustal signatures of the Oman ophiolite have been interpreted to reflect the dying stages of a spreading system (Ernewein et al. 1988, Reuber et al. 1988).

The suggested tectonic setting of the BOIC is a pull-apart basin formed during dextral strike-slip movements within older oceanic lithosphere with arc signature. This setting is very similar to the one suggested by Karson and Dewey 13 years ago. Contrary to the interpretation of Karson and Dewey, however, the LH and the BMD massifs are here both located very close to the ridge axis, detachment is thought to have occurred mainly northward and not westward and the fracture zone appears to have juxtaposed the BOIC against genetically *unrelated* oceanic lithosphere of the CC.

BIBLIOGRAPHY

Agata, T., 1988. Chrome spinels from the Oura layered igneous complex, central Japan. Lithos, 21: 97-108.

Agee, C.B., and Walker, D., 1990. Aluminum partitioning between olivine and ultrabasic silicate liquid to 6 GPa. Contrib. Mineral. Petrol., 105: 243-254.

Ahern, J.L., and Turcotte, D.L., 1979. Magma migration beneath an ocean ridge. Earth Planet. Sci. Lett., 45: 115-122.

Anonymous, 1972. Ophiolites. Geotimes, 17: 24-25.

Aoki, K.-I., and Shiba, I., 1973. Pyroxenes from lherzolite inclusions of Itinome-gata, Japan. Lithos, 6: 41-51.

Arai, S., 1978. Chromian spinel lamellae in olivine from the Iwanai-Dake peridotite mass, Hikkaido, Japan. Earth Planet. Sci. Lett., 39: 267-273.

Arai, S., 1980. Dunite-harzburgite-chromite complexes as refractory residue in the Sangun-Yamaguchi zone, western Japan. J. Petrol., 21: 141-165.

Arai, S., 1990 (abstract). Characterization of spinel peridotites in terms of olivine-spinel mantle array. Terra Abstr., 2: 125.

Ashby, M.F., and Verrall, R.A., 1977. Micromechanisms of flow and fracture, and their relevance to the rheology of the upper mantle. Phil. Trans. R. Soc. Lond., A 288: 59-95.

Atwater, T., and MacDonald, K.C., 1977. Are spreading centers perpendicular to their transform faults? Nature, 270: 715-719.

Avé Lallement, H.G., 1975. Mechanisms of preferred orientations of olivine in tectonite peridotite. Geology, 3: 653-656.

Avé Lallement, H.G., 1978. Experimental deformation of diopside and websterite. Tectonophysics, 48: 1-27.

Avé Lallement, H.G., 1985. Subgrain rotation and dynamic recrystallization of olivine, upper mantle diapirism, and extension of the Basin and Range province. Tectonophysics, 119: 89-117.

Avé Lallement, H.G., and Carter, N.L., 1970. Syntectonic recrystallization of olivine and modes of flow in the upper mantle. Geol. Soc. Am. Bull., 81: 2203-2220.

Basu, A.R., 1977. Textures, microstructures and deformation of ultramafic xenoliths from San Quinton, Baja California. Tectonophysics, 43: 213-246.

Basu, A.R., and MacGregor, I.D., 1975. Chromite spinels from ultramafic xenoliths. Geochim. Cosmochim. Acta, 39: 937-945.

Bédard, J.H., 1991. Cumulate recycling and crustal evolution in the Bay of Islands Ophiolite. J. Geol., 99: 225-249.

Ben Jamaa, N., and Mercier, J.-C.C., 1987 (abstract). Major element phase chemistry of ophiolitic harzburgites from western Newfoundland. Terra Cognita, 7: 355.

Benn, K., Nicolas, A., and Reuber, I., 1988. Mantle-crust transition zone and origin of wehrlitic magmas: evidence from the Oman ophiolite. Tectonophysics, 151: 75-85.

Berger, A.R., Dewey, J.F., and Karson, J., 1975. Polyphase-deformed cumulate wehrlite/gabbro mega-lenses in the dunite/harzburgite metamorphic ultramafic rocks of the Lewis Hills ophiolite complex, southwest Newfoundland. Geol. Soc. Am., Abstr. Progr.: 25.

Berger, E.T., and Vannier, M., 1984. Les dunites en enclaves dans les basaltes alcalins des îles océaniques: approche pétrologique. Bull. Minéral., 107: 649-663.

Bodinier, J.L., 1988. Geochemistry and petrogenesis of the Lanzo peridotite body, western Alps. Tectonophysics, 149: 67-88.

Bodinier, J.L., Dupuy, C., Dostal, J., and Merlet, C., 1987. Distribution of trace transition elements in olivine and pyroxenes from ultramafic xenoliths: application of microprobe analysis. Am. Mineral., 72: 902-913.

Bodinier, J.L., Dupuy, C., and Dostal, J., 1988. Geochemistry and petrogenesis of Eastern Pyrenean peridotites. Geochim. Cosmochim. Acta, 52: 2891-2907.

Bodinier, J.L., Vasseur, G., Vernieres, J., Dupuy, C., and Fabries, J., 1990. Mechanisms of mantle metasomatism: geochemical evidence from the Lherz orogenic peridotite. J. Petrol., 31: 597- 628.

Boland, J.N., and Tullis, T.E., 1986. Deformation behavior of wet and dry clinopyroxenite in the brittle to ductile transition region. *IN*: Hobbs, B.E., and Heard, H.C., (eds.), Mineral and Rock Deformation: Labratory Studies. Am. Geophys. Union Mon., 36: 35-49.

Bott, M.H. P., and Kusznir, N.J., 1984. The origin of tectonic stress in the lithosphere. Tectonophysics, 105: 1-13.

Bott, M.H. P., Waghorn, G.D., and Whittaker, A., 1989. Plate boundary forces at subduction zones and trench-arc compression. Tectonophysics, 170: 1-15.

Bottinga, Y., and Allègre, C.J., 1978. Partial melting under spreading ridges. Phil. Trans. R. Soc. Lond., A288: 501-525.

Bouchez, J.L., and Duval, P., 1982. The fabric of polycrystalline ice deformed in simple shear: experiments in torsion, natural deformation and geometrical interpretation. Textures and Microstructures, 5: 171-190.

Bouchez, J.-L., Lister, G.S., and Nicolas, A., 1983. Fabric asymmetry and shear sense in movement zones. Geol. Rdsch., 72: 401-419.

Boudier, F., 1978. Structure and petrology of the Lanzo peridotite massif (Piedmont Alps). Geol. Soc. Am. Bull., 89: 1574-1591.

Boudier, F., and Nicolas, A., 1972. Fusion partielle gabbroique dans la lherzolite de Lanzo. Bull. Suisse Minéral. Pétrol., 52: 39-56.

Boudier, F., and Nicolas, A., 1977. Structural controls on partial melting in the Lanzo Peridotite. *IN*: Dick, H.J. B., (ed.), Magma Genesis, Dept. Geol. Miner. Ind. Oregon, 96: 63- 78.

Boudier, F., and Nicolas, A., 1978. Stress and strain estimates in the Lanzo peridotite massif (western Alps). Coll. Int. CNRS, 272: 221-228.

Boudier, F., Nicolas, A., and Bouchez, J.L., 1982. Kinematics of oceanic thrusting and subduction from basal sections of ophiolites. Nature, 296: 825-828.

Boudier, F., Jackson, M., and Nicolas, A., 1984. Structural study of the Balmuccia massif (western Alps): a transition from mantle to lower crust. Geol. Mijnbouw, 63: 179-188.

Boudier, F., and Nicolas, A., 1985. Harzburgite and lherzolite subtypes in ophiolitic and oceanic environments. Earth Planet. Sci. Lett., 76: 84-92.

Boudier, F., Ceuleneer, G., and Nicolas, A., 1988. Shear zones, thrusts and related magmatism in the Oman ophiolite: initiation of thrusting on an oceanic ridge. Tectonophysics, 151: 275-296.

Boudier, F., Le Sueur, E., and Nicolas, A., 1989. Structure of an atypical ophiolite: the Trinity complex, eastern Klamath Mountains, California. Geol. Soc. Am. Bull., 101: 820-833.

Boullier, A.M., and Gueguen, Y., 1975. SP-mylonites: origin of some mylonites by superplastic flow. Contrib. Mineral. Petrol., 50: 93-104.

Boullier, A.M., and Nicolas, A., 1975. Classification of textures and fabrics of peridotite xenoliths from South African kimberlites. Phys. Chem. Earth, 9: 467-475.

Boyd, F.R., and Schairer, J.F., 1964. The system $MgSiO_3$- $CaMgSiO_2O_6$. J. Petrol., 5: 275-309.

Buck, W.R., and Su, W., 1989. Focused mantle upwelling below mid-ocean ridges due to feedback between viscosity and melting. Geophys. Res. Lett., 16: 641-644.

Buddington, A.F., and Hess, H.H., 1937. Layered peridotite laccoliths in the Trout River area, Newfoundland. Am. J. Sci., 33: 380-388.

Bussod, G.Y. (abstract), 1983. The effect of partial melting on the mechanical properties of spinel lherzolite. EOS, 64: 849.

Bussod, G., and Christie, J. (abstract), 1984. Experimental deformation of partially-melted spinel lherzolite. EOS, 65: 1097.

Bussod, G.Y. (abstract), 1990. The effect of a deviatoric stress regime on melt segregation: inferences from experimentally deformed lherzolites. EOS, 71: 1566

Cabanes, N., and Mercier, J.-C.C., 1988. Insight into the upper mantle beneath an active extensional zone: the spinel-peridotite xenoliths from San Quintin (Baja California, Mexico). Contrib. Mineral. Petrol., 100: 374-382.

Calon, T., 1984 (abstract). Patterns of high-temperature, plastic deformation in the plutonic sections of ophiolites. Geol. Assoc. Can., Mineral. Assoc. Can., Progr. Abstr., 9: 50.

Calon, T.J., and Malpas, J.G., 1985 (abstract). Role of deformation in the evolution of the plutonic complex, Bay of Islands Ophiolite. Geol. Assoc. Can., Mineral. Assoc. Can., Progr. Abstr., 10: A8.

Calon, T., Dunsworth, S.M., and Suhr, G., 1988. The Bay of Islands ophiolite. Field trip guidebook B8. Geol. Assoc. Can., Mineral. Assoc. Can., St. John's.

Campbell, I.H., and Turner, J.S., 1989. Fountains in magma chambers. J. Petrol., 30: 885-923.

Cann, J.R., 1974. A model for oceanic crustal structure developed. Geophys. J. R. astr. Soc., 39: 169-187.

Cannat, M., Bideau, D., and Hébert, R., 1990. Plastic deformation and magmatic impregnation in serpentinized ultramafic rocks from the Garret transform fault. Earth Planet. Sci. Lett., 101: 216-232.

Carlson, R.L., 1983. Plate motions, boundary forces, and horizontal temperature gradients: implications for the driving mechanism. Tectonophysics, 99: 149-164.

Carroll Webb, S.A., and Wood, B.J., 1986. Spinel-pyroxene-garnet relationships and their dependence on Cr/Al ratio. Contrib. Mineral. Petrol., 92: 471-480.

Carter, N.L., 1976. Steady state flow of rocks. Rev. Geophys. Sp. Phys., 14: 301-360.

Carter, N.L., and Avé Lallement, H.G., 1970. High temperature flow of dunite and peridotite. Geol. Soc. Am. Bull., 81: 2181-2202.

Casey, J.F., 1980. The geology of the southern part of the North Arm Mountain massif, Bay of Islands ophiolite complex, western Newfoundland with application to ophiolite obduction and the genesis of the plutonic portions of oceanic crust and upper mantle. Ph.D. thesis, State Universtiy of New York, Albany, 620p.

Casey, J.F., Karson, J., O'Connell, S., and Rosencrantz, E., 1979. Comment on 'The seismic velocity structure of a traverse through the Bay of Islands ophiolite complex, Newfoundland, an exposure of oceanic crust and upper mantle' by M. Salisbury and N. Christensen. J. Geophys. Res., 84: 6299-6230.

Casey, J.F., and Karson, J.A., 1981. Magma chamber profiles from the Bay of Islands ophiolite complex. Nature, 292: 295-301.

Casey, J.F., and Kidd, W.S. F., 1981. A parallochthonous group of sedimentary rocks unconformably overlying the Bay of Islands ophiolite complex, North Arm Mountain, Newfoundland. Can. J. Earth Sci., 18: 1035-1050.

Casey, J.F., Dewey, J.F., Fox, P.J., Karson, J.A., and Rosencrantz, E., 1981. Heterogeneous nature of oceanic crust and upper mantle: a perspective from the Bay of Islands ophiolite complex. *IN*: Emiliani, C., (ed.), The Sea, vol. 7. Wiley Interscience, New York, pp. 305-338.

Casey, J.F., Karson, A., Elthon, D., Rosencrantz, E., and Titus, M., 1983. Reconstruction of the geometry of accretion during formation of the Bay of Islands ophiolite complex. Tectonics, 2: 509-528.

Casey, J.F., and Dewey, J.F., 1984. Initiation of subduction zones along transform and accreting plate boundaries, triple-junction evolution, and forearc spreading centres - implications for ophiolitic geology and obduction. *IN*: Gass, I.G., Lippard, S.J., and Shelton, A.W., (eds.), Ophiolites and Oceanic Lithosphere, Geol. Soc. Spec. Publ., 13: 269-280.

Casey, J.F., Elthon, D.L., Siroky, F.X., Karson, J.A., and Sullivan, J., 1985. Geochemical and geological evidence bearing on the origin of the Bay of Islands and Coastal Complex ophiolites of western Newfoundland. Tectonophysics, 116: 1-40.

Cassard, D., 1980. Structure et origine des gisements de chromite du Massif Du Sud (ophiolites de Nouvelle-Calédonie), thèse troisième cycle, Université de Nantes, 240p.

Cawood, P.A., and Williams, H., 1988. Acadian basement thrusting, crustal delamination, and structural styles in and around the Humber Arm allochthon, western Newfoundland. Geology, 16: 370-373.

Ceuleneer, G., and Nicolas, A., 1985. Structures in podiform chromite from the Maqsad district (Sumail ophiolite, Oman). Mineral. Deposita, 20: 177-185.

Ceuleneer, C., Nicolas, A., and Boudier, F., 1988. Mantle flow patterns at an oceanic spreading centre: the Oman peridotites record. Tectonophysics, 151: 1-26.

Chapple, W.M., and Tullis, T.E., 1977. Evaluation of the forces that drive the plates. J. Geophys. Res., 82: 1967-1984.

Chase, C.G., 1978. Extension behind island arcs and motions relative to hot spots. J. Geophys. Res., 83: 5385-5387.

Chen, Y., and Morgan, W.J., 1990. A nonlinear rheology model for mid-ocean ridge axis topography. J. Geophys. Res., 95: 17583- 17604.

Chopra, P.N., 1986. The plasticity of some fine-grained aggegates of olivine at high pressure and temperature. *IN*: Hobbs, B.E., and Heard, H.C., (eds.), Mineral and Rock Deformation: Laboratory Studies, Geophys. Monograph 36, pp. 25-33. Am. Geophys. Union, Washington D.C.

Chopra, P.N., and Paterson, M.S., 1981. The experimental deformation of dunite. Tectonophysics, 78: 153-173.

Chopra, P.N., and Paterson, M.S., 1984. The role of water in the deformation of dunite. J. Geophys. Res., 78: 7861-7876.

Christensen, N.I., 1984. The magnitude symmetry and origin of upper mantle anisotropy based on fabric analyses of ultramafic tectonites. Geophys. J. R. astr. Soc., 76: 89-111.

Christensen, N.I., and Salisbury, M.H., 1979. Seismic anisotropy in the oceanic upper mantle: evidence from the Bay of Islands ophiolite complex. J. Geophys. Res., 84: 4601-4610.

Christie, D.M., and Sinton, J.M., 1981. Evolution of abyssal lavas along propagating segments of the Galapagos spreading center. Earth Planet. Sci. Lett., 56: 321-335.

Christiansen, F.G., 1985. Deformation fabric and microstructures in ophiolitic chromitites and host ultramafics, Sultanate of Oman. Geol. Rdsch., 74: 61-76.

Christiansen, F.G., 1986. Deformation of chromite: S. E. M. investigations. Tectonophysics, 121: 175-196.

Church, W.R., 1972. Ophiolite: its definition, origin as oceanic crust, and mode of emplacement in orogenic belts, with special reference to the Appalachians. Dept. Energy, Mines, Res., Spec. Publ., 42: 71-85.

Church, W.R., and Stevens, R.K., 1971. Early paleozoic ophiolite complexes of the Newfoundland Appalachians as mantle-oceanic crust sequences. J. Geophys. Res., 76: 1460-1466.

Church, W.R., and Riccio, L., 1977. Fractionation trends in the Bay of Islands ophiolite of Newfoundland: polycyclic cumulate sequence in ophiolites and their classification. Can. J. Earth Sci., 14: 1156-1165.

Coish, R.A., and Church, W.R., 1979. Igneous geochemistry of mafic rocks in the Betts Cove ophiolite, Newfoundland. Contrib. Mineral. Petrol., 70: 29-39.

Coleman, R.G., 1984. The diversity of ophiolites. Geol. Mijnbouw, 63: 141-150.

Colman-Sadd, S.P., 1982. Two stage continental collision and plate driving forces. Tectonophysics, 90: 263-282.

Colman-Sadd, S.P., Hayes, J.P., and Knight, I., 1990. Geology of the island of Newfoundland; Map 90-01, Newfoundland Dept. Mines Energy, St. John's.

Conquéré, F., and Fabriès, J., 1984. Chemical disequilibrium and its thermal significance in spinel-peridotites from the Lherz and Freychinède ultramafic bodies (Ariège, French Pyrenées). *IN*: Komprobst, J., (ed.), Kimberlites II. The Mantle and Crust-Mantle Relationships, Elsevier, Amsterdam, pp. 319-332.

Cooper, J.R., 1936. Geology of the southern half of the Bay of Islands Igneous Complex. Newfoundland Dept. Nat. Res., Geol. Sec., Bull., 4: 62p.

Cooper, R.F., and Kohlstedt, D.L., 1986. Rheology and structure of olivine-basalt partial melts. J. Geophys. Res., 91: 9315-9323.

Cordellier, F., Boudier, F., and Boullier, A.M., 1981. Structural study of the Almklovdalen peridotite massif (southern Norway). Tectonophysics, 77: 257-281.

Crane, K., 1985. The spacing of rift axis highs: dependence upon diapiric processes in the underlying asthenosphere? Earth Planet. Sci. Lett., 72: 405-414.

Curray, J.R., Moore, D.G., Lawver, L., Emmel, F., Raitt, R.W., and Henry, M., 1979. Tectonics of the Andaman Sea and Burma. Amer. Assoc. Petrol. Geol. Mem., 29: 189-198.

Dahl, R., and Watkinson, D.H., 1986. Structural control of podiform chromitite in Bay of Islands ophiolite, Springer Hill area, Newfoundland. Current Res., Part B, Geol. Surv. Can., 86- 1B: 757-766.

Dallmeyer, R.D., and Williams, H., 1975. $^{40}Ar/^{39}Ar$ ages for the Bay of Islands metamorphic aureole: their bearing on the timing of Ordovician ophiolite obduction. Can. J. Earth Sci., 12: 1685- 1690.

Darot, M., and Boudier, F., 1975. Mineral lineations in deformed peridotites: kinematic meaning. Pétrologie, 1: 225-236.

Davis, B.T. C., and Boyd, F.R., 1966. The join $Mg_2Si_2O_6$-$CaMgSi_2O_6$ at 30 kilobars pressure and its application to pyroxenes from kimberlites. J. Geophys. Res., 3567-3576:

Deer, W.A., Howie, R.A., and Zussman, J., 1966. An introduction to the rock forming minerals, Longman Group Ltd., Harlow, 528p.

Dawson, J.B., and Smith, J.V., 1975. Chromite-silicate intergrowths in upper mantle peridotites. Phys. Chem. Earth, 9: 339-350.

Detrick, R.S., and Purdy, G.M., 1980. The crustal structure of the Kane fracture zone from seismic refraction studies. J. Geophys. Res., 85: 3759-3777.

Dewey, J.F., and Bird, J.M., 1971. Origin and emplacement of the ophiolite suite: Appalachian ophiolites in Newfoundland. J. Geophys. Res., 76: 3179-3206.

Dewey, J.F., and Kidd, W.S. F., 1977. Geometry of plate accretion. Geol. Soc. Am. Bull., 88: 960-968.

Dewey, J.F., and Shackleton, R.M., 1984. A model for the evolution of the Grampian tract in the early Caledonides and Appalachians. Nature, 312: 115-121.

Dick, H.J.B., 1977a. Partial melting in the Josephine peridotite. I. The effect on mineral composition and its consequence for geobarometry and geothermometry. Am. J. Sci., 277: 801-832.

Dick, H.J.B., 1977b. Evidence of partial melting in the Josephine peridotite. *IN*: Dick, H.J. B., (ed.), Magma Genesis, Dept. Geol. Min. Ind. Oregon, Bulletin 96: 59-62.

Dick, H.J.B., 1989. Abyssal peridotites, very slow spreading ridges and ocean ridge magmatism. *IN*: Saunders, A.D., and Norry, M.J., (eds.), Magmatism in the Ocean Basins, Geol. Soc. London Spec. Publ., 42: 71-105.

Dick, H.J.B., and Sinton, J.M., 1979. Compositional layering in alpine peridotites: evidence for pressure solution creep in the mantle. J. Geol., 87: 403-416.

Dick, H.J.B., and Bullen, T., 1984. Chromian spinel as a petrogenetic indicator in abyssal and alpine-type peridotites and spatially associated lavas. Contrib. Mineral. Petrol., 86: 54-76.

Dick, H.J.B., and Fisher, R.L., 1984. Mineralogical studies of the residues of mantle melting: abyssal and alpine-type peridotites. *IN*: Kornprobst, J., Kimberlite. II. The mantle and crust-mantle relationships, Elsevier, Amsterdam, pp. 295-308.

Doukhan, N., Doukhan, J.-C., Nicolas, A., and Secher, D., 1984. Transmission electron microscope analysis of the deformation of chromites from ophiolites. Bull. Minéral., 107: 777-793.

Drury, M.R., and Urai, J., 1990. Deformation-related recrystallization processes. Tectonophysics, 172: 235-253.

Drury, M.R., Hoogerduijn Strating, E.H., and Vissers, R.L.M., 1990. Shear zone structures and microstructures in mantle peridotites from the Voltri massif, Ligurian Alps, N.W. Italy. Geologie en Mijnbouw, 69: 3-17.

Duncan, R.A., and Green, D.H., 1987. The genesis of refractory melts in the formation of oceanic crust. Contrib. Mineral. Petrol., 96: 326-342.

Dunning, G.R., and Chorlton, L.B., 1985. The Annieopsquotch ophiolite belt of southwest Newfoundland: geology and tectonic significance. Geol. Soc. Am. Bull., 96: 1466-1476.

Dunning, G.R., and Krogh, T.E., 1985. Geochronology of ophiolites of the Newfoundland Appalachians. Can. J. Earth Sci., 22: 1659- 1670.

Dunsworth, S., Calon, T., and Malpas, J., 1986. Structural and magmatic controls on the internal geometry of the plutonic complex and its chromite occurrences in the Bay of Islands ophiolite, Newfoundland. Current Research, Part A, Geological Survey of Canada, 86-1B: 471-482.

Edwards, S.J., 1990. Harzburgites and refractory melts in the Lewis Hills Massif, Bay of Islands Ophiolite Complex: the base-metals and precious-metals story. Can. Mineral., 28: 537-552.

Elthon, D., 1990 (abstract). Ion probe microanalysis of cumulate clinopyroxenes from the Bay of Islands ophiolite, Newfoundland. Symposium on ophiolite genesis and evolution of oceanic lithosphere, Muscat, Oman.

Elthon, D., Casey, J.F., and Komor, S., 1982. Mineral chemistry of ultramafic cumulates from the North Arm Mountain massif of the Bay of Islands ophiolite: evidence for high-pressure crystal fractionation of oceanic basalts. J. Geophys. Res., 87: 8717- 8734.

Elthon, D., Casey, J.F., and Komor, S., 1984. Cryptic mineral-chemistry variations in a detailed traverse through the cumulate ultramafic rocks of the North Arm Mountain massif of the Bay of Islands ophiolite, Newfoundland. *IN*: Gass, I.G., Lippard, S.J., and Shelton, A.W., (eds.), Ophiolites and Oceanic Lithosphere, Geol. Soc. Spec. Publ., 13: 83-97.

Elthon, D., Karson, J.A., Casey, J.F., Sullivan, J., and Siroky, F.X., 1986. Geochemistry of diabase dikes from the Lewis Hills massif, Bay of Islands ophiolite: evidence for partial melting of oceanic crust in transform faults. Earth Planet. Sci. Lett., 78: 89-103.

Ernewein, M., Pflumio, C., and Whitechurch, H., 1988. The death of an accretion zone as evidenced by the magmatic history of the Sumail ophiolite (Oman). Tectonophysics, 151: 247-274.

Ernst, W.G., 1978. Petrochemical study of lherzolitic rocks from the Western Alps. J. Petrol., 19: 341-392.

Etchecopar, A., 1977. A plane kinematic model of progressive deformation in a polycrystalline aggregate. Tectonophysics, 39: 121-139.

Etchecopar, A., and Vasseur, G., 1987. A 3-D kinematic model of fabric development in polycrystalline aggregates: comparisons with experimental and natural examples. J. Struct. Geol, 9: 705- 717.

Etheridge, M.A., 1975. Deformation and recrystallisation of orthopyroxene from the Giles complex, central Australia. Tectonophysics, 25: 87-114.

Evans, B.W., and Frost, B.R., 1975. Chrome-spinel in progressive metamorphism - a preliminary analysis. Geochim. Cosmochim. Acta, 39: 959-972.

Evans, C.A., 1985. Magmatic 'metasomatism' in peridotites from the Zambales ophiolite. Geology, 13: 166-169.

Evans, C.A., and Hawkins, J.W., 1989. Compositional heterogeneities in upper mantle peridotites from the Zambales Range Ophiolite, Luzon, Philippines. Tectonophysics, 168: 23-41.

Fabriès, J., 1979. Spinel-olivine geothermometry in peridotites from ultrmafic complexes. Contrib. Mineral. Petrol., 69: 329-336.

Fabriès, J., Bodinier, J.-L., Dupuy, C., Lorand, J.-P., and Benkerrou, C., 1989. Evidence for modal metasomatism in the orogenic spinel lherzolite body from Caussou (northeastern Pyrenees, France). J. Petrol., 30: 199-228.

Falloon, T.J., Green, D.H., Hatton, C.J., and Harris, K.L., 1988. Anhydrous partial melting of a fertile and depleted peridotite from 2 to 30kb and application to basalt petrogenesis. J. Petrol., 29: 1257-1282.

Fisk, M.R., 1986. Basalt magma interaction with harzburgite and the formation of high magnesium andesites. Geophys. Res. Lett., 13: 467-470.

Forsyth, D.W., 1977. The evolution of the upper mantle beneath mid-ocean ridges. Tectonophysics, 38: 89-118.

Francis, T.J. G., 1969. Generation of seismic anisotropy in the upper antle along the mid-ocean ridges. Nature, 221: 162-165.

Frank, F.C., 1968. Two-component flow model for convection in the Earth's upper mantle. Nature, 220: 350-352.

Frey, F.A., Suen, C.J., and Stockman, H.W., 1985. The Ronda high temperature peridotite: geochemistry and petrogenesis. Geochim. Cosmochim. Acta, 49: 2469-2491.

Fujii, N., Osamura, K., and Takahashi, E., 1986. Effect of water saturation on the distribution of partial melt in the olivine-plagioclase system. J. Geophys. Res., 91: 9253-9259.

Fujita, K., and Sleep, N.H., 1978. Membrane stresses near mid-ocean ridge - transform intersections. Tectonophysics, 50: 207-221.

Gasparik, T., 1984. Two-pyroxene thermobarometry with new experimental data in the system CaO-MgO-Al_2O_3-SiO_2. Contrib. Mineral. Petrol., 87: 87-97.

George, R.P., 1975. The internal structure of the Troodos ultramafic complex, Cyprus. Ph.D. thesis, State University of New York, Stony Brook, 223p.

George, R.P., 1977. Subsolidus deformation mechansims and hypersolidus creep of peridotite. *IN*: Dick, H.J.B. (ed.), Magma Genesis. Dept. Geol. Miner. Ind. Oregon, 96: 233-262.

George, R.P., 1978. Structural petrology of the Olympus ultramafic complex in the Troodos ophiolite, Cyprus. Geol. Soc. Am. Bull., 89: 845-865.

Girardeau, J., 1979. Structure des ophiolites de l'ouest de Terre Neuve et modèle de croute océanique, thèse troisième cycle, Université de Nantes, 146p.

Girardeau, J., and Nicolas, A., 1981. The structures of two ophiolite massifs, Bay of Islands, Newfoundland: a model for the oceanic crust and upper mantle. Tectonophysics, 77: 1-34.

Girardeau, J., and Mevel, D., 1982. Amphibolitized sheared gabbros from ophiolites as indicators of the evolution of the oceanic crust: Bay of Islands, Newfoundland. Earth Planet. Sci. Lett., 61: 151-165.

Girardeau, J., Mercier, J.-C. C., and Yougong, Z., 1985. Origin of the Xigaze ophiolite, Yarlung Zagbo suture zone, southern Tibet. Tectonophysics, 119: 407-433.

Girardeau, J., and Mercier, J.-C.C., 1988. Petrology and texture of the ultramafic rocks of the Xigaze ophiolite (Tibet): constraints for mantle structure beneath slow-spreading ridges. Tectonophysics, 147: 33-58.

Goetze, C., 1978. The mechanisms of creep in olivine. Phil. Trans. R. Soc. Lond., A 288: 99-109.

Govindaraju, K., 1989. 1989 compilation of working values and sample description for 270 geostandards. Geost. Newslet., 13: 1- 113.

Green II, H.W., and Burnley, P.C., 1988 (abstract). Pyroxene-spinel symplectites: origin by decomposition of garnet confirmed. EOS, 69: 514.

Green II, H.W., and Borch, R.S., 1990 (abstract). The rheology and microstructure of partially molten lherzolite experimentally deformed under upper mantle pressures and temperatures. Terra Abstracts, 2: 132.

Gregory, R.T., 1984. Melt percolation beneath a spreading ridge: evidence from the Semail peridotite, Oman. *IN*: Lippard, S.J., Shelton, A.W., and Gass, I.G., (eds.), Ophiolites and Oceanic Lithosphere, Geol. Soc. Lond. Spec. Publ., 13: 55-62.

Gueguen, Y., and Boullier, A.M., 1975. Evidence of superplasticity in mantle peridotites. *IN*: Strens, R.G. J., (ed.), Physics and Chemistry of Minerals and Rocks, John Wiley and Sons, New York, pp. 19-33.

Gueguen, Y., and Nicolas, A., 1980. Deformation of mantle rocks. Ann. Rev. Earth Planet. Sci., 8: 119-144.

Hacker, B.R., 1990. Simulation of the metamorphic and deformational history of the metamorphic sole of the Oman Ophiolite. J. Geophys. Res., 95: 4895-4907.

Harkins, M.E., Green, H.W., and Moores, E.H., 1980. Multiple intrusive events documented from the Vourinos ophiolite complex, northern Greece. Am. J. Sci., 280-A: 284-295.

Harte, B., 1977. Rock nomenclature with particular relation to deformation and recrystallisation textures in olivine-bearing xenoliths. J. Geol., 85: 279-288.

Harte, B., Cox, K.G., and Gurney, J.J., 1975. Petrography and geological history of upper mantle xenoliths from the Matsoku kimberlite pipe. Phys. Chem. Earth, 9: 477-506.

Hatton, C.J., and von Gruenewaldt, G., 1985. Chromite from the Swartkop chrome mine - an estimate of the effects of subsolidus reequilibration. Econ. Geol., 80: 911-924.

Hébert, R., Serri, G., and Hékinian, R., 1989. Mineral chemistry of ultramafic tectonites and ultramafic to gabbroic cumulates from the major oceanic basins and Northern Apennine ophiolites (Italy) - A comparison. Chem. Geol., 77: 183-207.

Herzberg, C.T., 1978. Pyroxene geothermometry and geobarometry: experimental and thermodynamic evaluation of some subsolidus phase relations involving pyroxenes in the system CaO-MgO-Al_2O_3-SiO_2. Geochim. Cosmochim. Acta, 42: 945-957.

Hey, R., Duennebier, K., and Morgan, W.J., 1980. Propagating rifts on midocean ridges. J. Geophys. Res., 85: 3647-3658.

Himmelberg, G.R., and Loney, R.A., 1980. Petrology of ultramafic and gabbroic rocks of the Canyon Mountain ophiolite, Oregon. Am. J. Sci., 280-A: 232-268.

Hock, M., and Friedrich, G., 1985. Structural features of ophiolitic chromitites in the Zambales Range, Luzon, Philippines. Mineral. Deposita, 20: 290-301.

Hulbert, L.J., and von Gruenewaldt, G., 1985. Textural and compositional features of chromite in the lower and critical zones of the Bushveld complex south of Potgietersrus. Econ. Geol., 80: 872-895.

Ingerson, E., 1935. Layered peridotitic laccoliths in the Trout River area, Newfoundland. Am. J. Sci., 29: 422-440.

Irvine, T.N., 1965. Chromian spinel as a petrogenetic indicator. Part 1. Theory. Can. J. Earth Sci., 2: 648-672.

Irvine, T.N., and Findlay, T.C., 1972. Alpine-type peridotite with particular reference to the Bay of Islands igneous complex. Can. Dept. Energy, Mines, Res., Spec. Publ. 42: 77-128.

Jackson, E.D., 1969. Chemical variation in co-existing chromite and olivine in chromite zones of the Stillwater complex. In: Wilson, H.D.B., (ed.), Magmatic Ore Deposits, Econ. Geol. Mon., 4: 41-71.

Jackson, E.D., Green II, H.W., and Moores, E.M., 1975. The Vourinos ophiolite, Greece: cyclic units of lineated cumulates overlying harzburgite tectonite. Geol. Soc. Am. Bull., 86: 390-398.

Jacobsen, S.B., and Wasserburg, G.J., 1979. Nd and Sr isotopic study of the Bay of Islands ophiolite complex and the evolution of the source of midocean ridge basalts. J. Geophys. Res., 84: 7429-7445.

Jamieson, R.A., 1980. Formation of metamorphic aureoles beneath ophiolites - evidence from the St. Anthony complex, Newfoundland. Geology, 8: 150-154.

Jamieson, R.A., 1986. P-T path from high temperature shear zones beneath ophiolites. J. Metam. Geol., 4: 3-22.

Jaques, A.L., and Green, D.H., 1980. Anhydrous melting of peridotite at 0-15kb pressure and the genesis of tholeiitic basalts. Contrib. Mineral. Petrol., 73: 287-310.

Jarrard, R.D., 1986. Terrane motion by strike-slip faulting of forearc slivers. Geology, 14: 780-783.

Jenner, G.A., Longerich, H.P., Jackson, S.E., and Fryer, B.J., 1990. ICP-MS - A powerful tool for high-precision trace-element analysis in Earth sciences: evidence from analysis of selected U.S.G.S. reference samples. Chem. Geol., 83: 133-148.

Jenner, G.A., Dunning, G.R., Malpas, J., Brown, M., and Brace, T., in press. Bay of Islands and Little Port Complexes, revisited: age, geochemical and isotopic evidence confirm supra-subduction zone origin. Can. J. Earth Sci.

Johan, Z., and Augé, T., 1985. Ophiolitic mantle sequences and their evolution: mineral chemistry constraints. *IN*: Gallagher, M.J., Ixer, R.A., Neary, C.R., and Prichard, H.M., (eds.), Metallogeny of basic and ultrabasic rocks, pp. 305-318. The Institute of Mining and Metallurgy.

Johnson, K.T., Dick, H.J.B., and Shimizu, N., 1990. Melting in the oceanic upper mantle: an ion microprobe study of diopsides in abyssal peridotites. J. Geophys. Res., 95: 2661-2678.

Jurdy, D.M., and Stefanick, M., 1983. Flow models for back-arc spreading. Tectonophysics, 99: 191-206.

Juteau, T., Nicolas, A., Dubessy, J., Fruchard, J.C., and Bouchez, J.L., 1977. Structural relationships in the Antalya ophiolite complex, Turkey: possible model for an oceanic ridge. Geol. Soc. Am. Bull., 88: 1740-1748.

Juteau, T., Beurrier, M., Dahl, R., and Nehlig, P., 1988a. Segmentation at a fossil spreading axis: the plutonic sequence of the Wadi Haymiliyah area (Haylayn block, Sumail nappe, Oman). Tectonophysics, 151: 167-197.

Juteau, T., Ernewein, M., Reuber, I., Whitechurch, H., and Dahl, R., 1988b. Duality of magmatism in the plutonic sequence of the Sumail nappe, Oman. Tectonophysics, 151: 107-135.

Karato, S., 1984. Grain-size distribution and rheology of the upper mantle. Tectonophysics, 104: 155-176.

Karato, S., 1988. The role of recrystallization in the preferred orientation of olivine. Physics Earth Planet. Int., 51: 107-122.

Karato, S., 1989a. Grain growth kinetics in olivine aggregates. Tectonophysics, 168: 255-273.

Karato, S., 1989b. Seismic anisotropy: mechanisms and tectonic implications. *IN*: Karato, S., and Toriumi, M., (eds.), Rheology of Solids and the Earth, pp. 393-422. Oxford Univ. Press, Oxford.

Karato, S., Toriumi, M., and Fujii, T., 1980. Dynamic recrystallization of olivine single crystals during high-temperature creep. Geophys. Res. Lett., 7: 649-652.

Karato, S., Toriumi, M., and Fujii, T., 1982. Dynamic recrystallization and high-temperature rheology of olivine. *IN*: Akimoto, S., and Manghnani, M.H., (eds.), High pressure research in geophysics. Adv. Earth Planet. Sci., vol. 12, pp. 171-189. Center for Academic Publications Japan, Tokyo.

Karato, S., Paterson, M.S., and FitzGerald, J.D., 1986. Rheology of synthetic olivine aggregates: influence of grain size and water. J. Geophys. Res., 91: 8151-8176.

Karig, D.E., 1982. Initiation of subduction zones: implications for arc evolution and ophiolite development. *IN*: Leggett, J.K., (ed.), Trench-forearc geology: sedimentation and tectonics on modern and ancient active plate margins, Geol. Soc. Spec. Publ., pp. 563-576.

Karson, J.A., 1975. Structural studies in the mafic and ultramafic rocks of the Lewis Hills, western Newfoundland. M.S. thesis, State University of New York, Albany, 125p.

Karson, J.A., 1977. The geology of the northern Lewis Hills, western Newfoundland. Ph.D. dissertation, State University of New York, Albany, 474p.

Karson, J.A., 1979. Geological map and descriptive notes of Lewis Hills massif, western Newfoundland. Dept. Energy, Mines, Resources, Can.; open file 628, Ottawa.

Karson, J.A., 1984. Variations in structure and petrology in the Coastal Complex, Newfoundland: anatomy of an oceanic fracture zone. *IN*: Lippard, S.J., Shelton, A.W., and Gass, I.G., (eds.), Ophiolites and Oceanic Lithosphere, Geol. Soc. Spec. Publ., 13: 131-144.

Karson, J.A., 1986. Lithosphere age, depth and structural complications resulting from migrating transform faults. J. Geol. Soc. Lond., 143: 785-788.

Karson, J.A., and Dewey, J.F., 1978. Coastal Complex, western Newfoundland: an early Ordovician oceanic fracture zone. Geol. Soc. Am. Bull., 89: 1037-1049.

Karson, J., Elthon, D., and DeLong, S.E., 1983. Ultramafic intrusions in the Lewis Hills Massif, Bay of Islands Ophiolite Complex, Newfoundland: implications for igneous processes at oceanic fracture zones. Geol. Soc. Am. Bull., 94: 15-29.

Karson, J.A., Collins, J.A., and Casey, J.F., 1984. Geologic and seismic velocity structure of the crust/mantle transition in the Bay of Island ophiolite complex. J. Geophys. Res., 89: 6126-6138.

Karson, J.A., and Elthon, D., 1987. Evidence for variations in magma production along oceanic spreading centers: a critical appraisal. Geology, 15: 127-131.

Karson, J.A., Thompson, G., Humphris, S.E., Edmond, J.M., Bryan, W.B., Brown, J.R., Winters, A.T., Pockalny, R.A., Casey, J.F., Campbell, A.C., Konkhammer, G., Palmer, M.R., Kinzler, R.J., and Sulanowska, M.M., 1987. Along-axis variations in seafloor spreading in the MARK area. Nature, 328: 681-685.

Keen, C.E., Keen, M.J., Nichols, B., Reid, I., Stockmal, G.S., Colman-Sadd, S.P., O'Brien, S.J., Miller, H., Quinlan, G., Williams, H., and Wright, J., 1986. Deep seismic reflection profile across the northern Appalachians. Geology, 14: 141-145.

Kelemen, P.B., 1990. Reaction between ultramafic rock and fractionating basaltic magma I. Phase relations, the origin of calc-alkaline magma series, and the formation of discordant dunite. J. Petrol., 31: 51-98.

Kelemen, P.B., Johnson, K.T.M., Kinzler, R.J., and Irving, A.J., 1990. High-field strength element depletions in arc basalts due to mantle-magma interaction. Nature, 345: 521-524.

Kirby, S.H., and Green II, H.W., 1980. Dunite xenoliths from Hualalai volcano: evidence for mantle diapiric flow beneath the island of Hawaii. Am. J. Sci., 280A: 550-575.

Kirby, S.H., and Kronenberg, A.K., 1984. Deformation of clinopyroxenite: evidence for a transition in flow mechanisms and semi-brittle behavior. J. Geophys. Res., 89: 3177-3193.

Klein, E.M., and Langmuir, C.H., 1987. Global correlations of ocean ridge basalt chemistry with axial depth and crustal thickness. J. Geophys. Res., 92: 8089-8115.

Kohlstedt, D.L., and Vander Sande, J.B., 1973. Transmission electron microscopy investigation of the defect microstructure of four natural orthopyroxenes. Contrib. Mineral. Petrol., 42: 169-180.

Komor, S.C., Elthon, D., and Casey, J.F., 1985a. Mineralogic variation in a layered ultramafic cumulate sequence at the North Arm Mountain Massif, Bay of Islands ophiolite, Newfoundland. J. Geophys. Res., 90: 7705-7736.

Komor, S.C., Elthon, D., and Casey, J.F., 1985b. Serpentinization of cumulate ultramafic rocks from the North Arm Mountain massif of the Bay of Islands ophiolite. Geochim. Cosmochim. Acta, 49: 2331-2338.

Kornprobst, J., 1969. Le massif ultrabasique des Beni Bouchera (Rif Interne, Maroc): Etude des péridotites de haute température et de haute pression, et des pyroxénolites, à grenat ou sans grenat, qui leur sont associées. Contrib. Mineral. Petrol., 23: 283-322.

Kornprobst, J., Ohnenstetter, D., and Ohnenstetter, M., 1981. Na and Cr contents in clinopyroxenes from peridotites: a possible discriminant between "sub-contiental" and "sub-oceanic" mantle. Earth Planet. Sci. Lett., 53: 241-254.

Kornprobst, J., and Vielzeuf, D., 1984. Transcurrent crustal thinning: a mechanism for the uplift of deep continental crust upper mantle. *IN*: Kornporobst, J. (ed.), Kimberlite. II. The mantle and crust-mantle relationship, pp. 347-360, Elsevier, Amsterdam.

Kretz, R., 1982. Transfer and exchange equilibria in a portion of the pyroxene quadrilateral as deduced from natural and experimental data. Geochim. Cosmochim. Acta, 46: 411-421.

Kunze, F.R., and Avé Lallement, H.G., 1981. Non-coaxial experimental deformation of olivine. Tectonophysics, 74: T1-T13.

Kusznir, N.J., 1980. Thermal evolution of the oceanic crust; its dependence on spreading rate and effect on crustal structure. Geophys. J. R. astr. Soc., 61: 167-181.

Kusznir, N.J., and Bott, M.H. P., 1976. A thermal study of the formation of oceanic crust. Geophys. J. R. astr. Soc., 47: 83-95.

Kusznir, N.J., and Park, R.G., 1987. The extensional strength of the continental lithosphere: its dependence on geothermal gradient, and crustal composition and thickness. *IN*: Coward, M.P., Dewey, J.F., and Hancock, P.L., (eds.), Continental Extensional Tectonics, Geol. Soc. Spec. Publ., 28: 35-52.

Langmuir, C.H., Bender, J.F., Bence, A.E., and Hanson, G.N., 1977. Petrogenesis of basalts from the famous area: mid-Atlantic ridge. Earth Planet. Sci. Lett., 36: 133-156.

Langmuir, C.H., and Bender, J.F., 1984. The geochemistry of oceanic basalts in the vicinity of transform faults: observations and implications. Earth Planet. Sci. Lett., 69: 107-127.

Leblanc, M., 1980. Chromite growth, dissolution and deformation from a morphological view point: SEM investigations. Mineral. Deposita, 15: 201-210.

Leblanc, M., Dupuy, C., Cassard, D., Moutte, J., Nicolas, A., Prinzhofer, A., and and Rabinovicz, M., 1980. Essai sur la genèse des corps podiformes de chromitite dans les péridotites ophiolitiques de Noevelle-Calédonie et de Méditerranée orientale. Ophiolites. Proceedings International Ophiolite Symposium, Geol. Surv. Dept. Cyprus, Nicosia, pp. 691-701.

Lemoine, M., Tricart, P., and Boillot, G., 1987. Ultramafic and gabbroic ocean floor of the Ligurian Tethys (Alps, Corsica, Apennines): in search of a genetic model. Geology, 15: 622-625.

Le Sueur, E., and Boudier, F., 1986. Structures du complexe basique et ultrabasique de Trinity, Californie: genèse d'une ophiolite atypique. Bull. Soc. Géol. France, 6: 1007-1014.

Lin, J., Purdy, G.M., Schouten, H., Sempere, J.-C., and Zervas, C., 1990. Evidence from gravity data for focused magmatic accretion along the Mid-Atlantic Ridge. Nature, 344: 627-632.

Lippard, S.J., Shelton, A.W., and Gass, I.G., 1986. The ophiolite of northern Oman, Geol. Soc. London Mem., 11, 178 pp.

Lister, G.S., and Snoke, A.W., 1984. S-C mylonites. J. Struct. Geol., 6: 617-638.

Longerich, H.P., Jenner, G.A., Fryer, B.J., and Jackson, S.E., 1990. Inductively coupled plasma-mass spectrometric analysis of geological samples: a critical evaluation based on case studies. Chem. Geol., 83: 105-118.

Lonsdale, P., 1983. Overlapping rift zones at the 5.5°S offset of the East Pacific rise. J. Geophys. Res., 88: 9393-9406.

Lonsdale, P., 1989. Segmentation of the Pacific-Nazca Spreading Center, 1°N-20°S. J. Geophys. Res., 94: 12197-12225.

Lorand, J.P., 1987. Cu-Fe-Ni-S mineral assemblages in upper-mantle peridotites from the Table Mountain and Blow-Me-Down Mountain ophiolite massifs (Bay of Islands area, Newfoundland): their relationships with fluids and silicate melts. Lithos, 20: 59-76.

Macdonald, K.C., and Fox, P.J., 1983. Overlapping spreading centers: new accretion geometry on the East Pacific Rise. Nature, 302: 55-57.

Macdonald, K.C., Fox, P.J., Perram, L.J., Eisen, M.F., Haymon, R.M., Miller, S.P., Carbotte, S.M., Cormier, M.-H., and Shor, A.N., 1988. A new view of the mid-ocean ridge from the behaviour of ridge-axis discontinuities. Nature, 335: 217-225.

Malpas, J., 1973 (abstract). A restored section of oceanic-crust and mantle in western Newfoundland. Geol. Soc. Am., Abstr. Progr., 5: 191.

Malpas, J., 1976. The petrology and petrogenesis of the Bay of Islands ophiolite suite, western Newfoundland. Ph.D. thesis, Memorial Universty of Newfoundland, St. John's, 430p.

Malpas, J., 1978. Magma generation in the upper mantle, field evidence from ophiolite suites, and application to the generation of oceanic lithosphere. Phil. Trans. R. Soc. Lond., 288A: 527- 545.

Malpas, J., 1979a. The dynamothermal aureole of the Bay of Islands ophiolite suite. Can. J. Earth Sci., 16: 2086-2101.

Malpas, J., 1979b. Two contrasting trondhjemite associations from transported ophiolites in western Newfoundland: initial report. *IN*: Barker, F., (ed.), Trondhjemites, dacites, and related rocks, pp. 465-487. Elsevier, Amsterdam.

Malpas, J., Stevens, R.K., and Strong, D.F., 1973. Amphibolite associated with Newfoundland ophiolite: its classification and tectonic significance. Geology, 1: 45-47.

Malpas, J., and Strong, D.F., 1975. A comparison of chrome-spinels in ophiolites and mantle diapirs of Newfoundland. Geochim. Cosmochim. Acta, 39: 1045-1060.

Marillier, F., Keen, C.E., Stockmal, G.S., Quinlan, G., Williams, H., Colman, S.P., and O'Brien, S.J., 1989. Crustal structure and surface zonation of the Canadian Appalachians: implications of deep seismic reflection data. Can. J. Earth Sci., 26: 305-321.

Mattinson, J.M., 1975. Early Paleozoic ophiolite complexes of Newfoundland: isotopic ages of zircons. Geology, 3: 181-183.

Mattinson, J.M., 1976. Age of zircons from the Bay of Islands Ophiolite Complex, western Newfoundland. Geology, 4: 393-394.

McCaig, A.M., 1981 (abstract). Metasomatic and isochemical metamorphic changes in the basal peridotite of the Bay of Islands Complex during ophiolite emplacement. J. Struct. Geol. 3: 337.

McCaig, A.M., 1983. P-T conditions during emplacement of the Bay of Islands ophiolite complex. Earth Planet. Sci. Lett., 63: 459- 473.

McKenzie, D., 1967. Some remarks on heat flow and gravity anomalies. J. Geophys. Res.. 72: 6261-6273.

McKenzie, D., 1984. The generation and compaction of partially molten rock. J. Petrol., 25: 713-765.

Medaris Jr., L.G., 1975. Coexisting spinel and silicates in alpine peridotites of the granulite facies. Geochim. Cosmochim. Acta, 39: 947-958.

Mengel, F.C., 1987. Thermotectonic evolution of the Proterozoic-Archaean boundary in the Saglek area, northern Labrador. Ph.D. thesis, Memorial University, St. John's, 379p.

Menzies, M., and Allen, C., 1974. Plagioclase lherzolite - residual mantle relationships within two eastern Mediterranean ophiolites. Contrib. Mineral. Petrol., 45: 197-213.

Mercier, J.-C.C., 1977. Natural peridotites: chemical and rheological heterogeneity of the upper mantle. Ph.D. thesis, State University New York, Stony Brook, 668p.

Mercier, J.-C.C., 1980a. Magnitude of the continental lithospheric stresses inferred from rheomorphic petrology. J. Geophys. Res., 85: 6293-6303.

Mercier, J.-C.C., 1980b. Single pyroxene thermobarometry. Tectonophysics, 70: 1-37.

Mercier, J.-C.C., 1985. Olivine and Pyroxenes. *IN*: Wenk, H.-R., (ed.), Preferred orientation in deformed metals and rocks, pp. 407-430, Academic Press, Inc., Orlando.

Mercier, J.-C.C., and Nicolas, A., 1975. Textures and fabrics of upper mantle peridotites as illustrated by xenoliths from basalts. J. Petrol., 16: 454-487.

Mercier, J.-C.C., Anderson, D.A., and Carter, N.L., 1977. Stress in the lithosphere: inferences from steady state state flow of rocks. Pure Appl. Geophys., 115: 199-226.

Mercier, J.-C.C., Benoit, V., and Girardeau, J., 1984. Equilibrium state of diopside-bearing harzburgites from ophiolites: geobarometric and geodynamic implications. Contrib. Mineral. Petrol., 85: 391-403.

Michael, P.J., and Bonatti, E., 1985. Peridotite composition from the North Atlantic: regional and tectonic variations and implications for partial melting. Earth Planet. Sci. Lett., 73: 91-104.

Miller, R.B., and Mogk, D.W., 1987. Ultramafic rocks of a fracture-zone ophiolite, North Cascades, Washington. Tectonophysics, 142: 261-289.

Moll, N.E., 1981. The structure and petrology of the gabbro unit and the mafic-ultramafic contact, Table Mountain, Bay of Islands complex, Newfoundland. Ph.D. thesis, University of Washington, Seattle, 158p.

Molnar, P., and Atwater, T., 1978. Interarc spreading and Cordilleran tectonics as alternates related to the age of subducted oceanic lithosphere. Earth Planet. Sci. Lett., 41: 330-340.

Moores, E.M., 1982. Origin and emplacement of ophiolites. Rev. Geophys. Sp. Phys., 20: 735-760.

Mori, T., and Green, D.H., 1975. Pyroxenes in the system $Mg_2Si_2O_6$-$CaMgSi_2O_6$. Earth Planet. Sci. Lett., 26: 277-286.

Murton, B.J., 1986. Anomalous oceanic lithosphere formed in a leaky transform fault: evidence from the western Limassol Forest complex, Cyprus. J. Geol. Soc. Lond., 143: 845-854.

Mutter, J.C., Detrick, R.S., and North Atlantic Transect Study Group, 1984. Multichannel seismic evidence for anomalously thin crust at Blake Spur fracture zone. Geology, 12: 534-537.

Mysen, B.O., 1976. Experimental determination of some geochemical parameters relating to conditions of equilibration of peridotite in the upper mantle. Am. Mineral., 61: 677-683.

Mysen, B.O., and Kushiro, I., 1977. Compositional variations of coexisting phases with degree of melting of peridotite in the upper mantle. Am. Mineral., 62: 843-865.

Nagata, J., Goto, A., and Obata, M., 1983. The parabolic pattern of chromium partitioning observed between pyroxenes and spinel from ultramafic rocks and its petrologic significance. Contrib. Mineral. Petrol., 82: 42-51.

Navon, O., and Stolper, E., 1987. Geochemical consequences of melt percolation: the upper mantle as a chromatographic column. J. Geol., 95: 285-307.

Nazé, L., Doukhan, N., Doukhan, J.-C., and Latrous, K., 1987. A TEM study of lattice defects in naturally and experimentally deformed orthopyroxenes. Bull. Minéral., 110: 497-512.

Neumann, E.-R., 1991. Ultramafic and mafic xenoliths from Hierro, Canary Islands: evidence for melt infiltration in the upper mantle. Contrib. Mineral. Petrol., 106: 236-252.

Neyens, M., 1986. Deformation at the crust-mantle interface, Table Mountain ophiolite massif, Newfoundland. M.Sc. thesis, University of Utrecht, 87p.

Nicolas, A., 1978. Stress estimates from structural studies in some mantle peridotites. Phil. Trans. R. Soc. Lond., A 288: 49-57.

Nicolas, A., 1986a. Structure and petrology of peridotites: clues to their geodynamic environment. Rev. Geophys., 24: 875-895.

Nicolas, A., 1986b. A melt extraction model based on structural studies in mantle peridotites. J. Petrol., 27: 999-1022.

Nicolas, A., 1989. Structures of ophiolites and dynamics of oceanic lithosphere. Kluwer Publ., 367 p.

Nicolas, A., Bouchez, J.L., Boudier, F., and Mercier, J.C., 1971. Textures, structures and fabrics due to solid state flow in some European lherzolites. Tectonophysics, 12: 55-86.

Nicolas, A., Bouchez, J.L., and Boudier, F., 1972. Interprétation cinématique des déformations plastique dans le massif de lherzolite de Lanzo (Alpes Piémontaises) - comparaison avec d'autres massifs. Tectonophysics, 14: 143-171.

Nicolas, A., Boudier, F., and Boullier, A.M., 1973. Mechanisms of flow in naturally and experimentally deformed peridotites. Am. J. Sci., 273: 853-876.

Nicolas, A., and Boudier, F., 1975. Kinematic interpretation of folds in alpine-type peridotites. Tectonophysics, 25: 233-260.

Nicolas, A., and Poirier, J.P., 1976. Crystalline Plasticity and Solid State Flow in Metamorphic Rocks. John Wiley & Sons, London, 444p.

Nicolas, A., and LePichon, X., 1980. Thrusting of young lithosphere in subduction zones with special reference to structures in ophiolitic peridotites. Earth Planet. Sci. Lett., 46: 397-406.

Nicolas, A., Boudier, F., and Bouchez, J.-L., 1980. Interpretation of peridotite structures from ophiolitic and oceanic environments. Am. J. Sci., 280-A: 192-201.

Nicolas, A., Girardeau, J., Marcoux, J., Dupre, B., Xibin, W., Yougong, C., Haixiang, Z., and Xuchang, X., 1981. The Xigaze ophiolite (Tibet): a peculiar oceanic lithosphere. Nature, 294: 414-417.

Nicolas, A., and Jackson, M., 1982. High temperature dikes in peridotites: origin by hydraulic fracturing. J. Petrol., 23: 568-582.

Nicolas, A., and Violette, J.F., 1982. Mantle flow at oceanic spreading centers: models derived from ophiolites. Tectonophysics, 81: 319-339.

Nicolas, A., and Prinzhofer, A., 1983. Cumulative or residual origin for the transition zone in ophiolites: structural evidence. J. Petrol., 24: 188-206.

Nicolas, A., and Dupuy, C., 1984 Origin of opl. olitic and oceanic lherzolites. Tectonophysics, 110: 177-187.

Nicolas, A., and Rabinowicz, M., 1984. Mantle flow pattern at oceanic spreading centres: relation with ophiolitic and oceanic structures. *IN*: Gass, I.G., Lippard, S.J., and Shelton, A.W., (eds.), Ophiolites and Oceanic Lithosphere, Geol. Soc. Lond. Spec. Publ., 13: 147-151.

Nicolas, A., and Christensen, N.I., 1987. Formation of anisotropy in upper mantle peridotites: a review. *IN*: Fuchs, K., and Froidevaux, C. (eds.), The composition, structure and dynamics of the lithosphere-asthenosphere system, Am. Geophys. Union, Geodyn. Ser., 16, 111-123.

Nicolas, A., Lucazeau, F., and Bayer, R., 1987. Peridotite xenoliths in Massif Central basalts, France: textural and geophysical evidence for asthenospheric diapirism. *IN*: Nixon, P.H., (ed.), Mantle Xenoliths, J. Wiley & Sons Ltd., 563-574.

Nicolas, A., Ceuleneer, G., Boudier, F., and Misseri, M., 1988a. Structural mapping in the Oman ophiolites: mantle diapirism along an oceanic ridge. Tectonophysics, 151: 27-56.

Nicolas, A., Reuber, I., and Benn, K., 1988b. A new magma chamber model based on structural studies in the Oman ophiolite. Tectonophysics, 151: 87-105.

Obata, M., 1976. The solubility of Al_2O_3 in orthopyroxenes in spinel and plagioclase peridotites and spinel pyroxenite. Am. Mineral., 61: 804-816.

Obata, M., 1980. The Ronda Peridotite: garnet-, spinel-, and plagioclase-lherzolite facies and the P-T trajectories of a high temperature mantle intrusion. J. Petrol., 21: 533-572.

Obata, M., and Nagahara, N., 1987. Layering of Alpine-Type peridotite and the segregation of partial melt in the Upper Mantle. J. Geophys. Res., 92: 3467-347.

Ozawa, K., 1983. Relationships between tectonite and cumulate in ophiolites: the Miyamori ultramafic complex, Kitakami Mountains, northeast Japan. Lithos, 16: 1-16.

Ozawa, K., 1984. Olivine-spinel geospeedometry: analysis of diffusion-controlled Mg-Fe²⁺ exchange. Geochim. Cosmochim. Acta, 48: 2597-2611.

Ozawa, K., 1988. Ultramafic tectonite of the Miyamori ophiolitic complex in the Kitakami Mountains, northeast Japan: hydrous upper mantle in an island arc. Contrib. Mineral. Petrol., 99: 159-175.

Ozawa, K., 1989. Stress-induced Al-Cr zoning of spinel in deformed peridotites. Nature, 338: 141-144.

Palme, H., and Nickel, K.G., 1985. Ca/Al ratio and composition of the Earth's upper mantle. Geochim. Cosmochim. Acta, 49: 2123-2132.

Park, R.G. 1987. Geological structures and moving plates. Blackie & Son Ltd, Glasgow, 337p.

Parker, R.L., and Oldenburg, D.W., 1973. Thermal model of ocean ridges. Nature, 242: 137-139.

Parmentier, E.M., and Forsyth, D.W., 1985. Three-dimensional flow beneath a slow spreading ridge axis: a dynamic contribution to the deepenir of the median valley toward fracture zones. J. Geophys. Res., 90: 678-684.

Pavlis, T.L., 1986. The role of strain heating in the evolution of megathrusts. J. Geophys. Res., 91: 12407-12422.

Pfiffner, O.A., and Ramsay, J.G., 1982. Constraints on geological strain rates: arguments from finite strain states of naturally deformed rocks. J. Geophys. Res., 87: 311-321.

Phipps Morgan, J., Parmentier, E.M., and Lin, J., 1987. Mechanisms for the origin of mid-ocean ridge axial topography: implications for the thermal and mechanical structure of accreting plate boundaries. J. Geophys. Res., 92: 12823-12836.

Phipps Morgan, J., and Forsyth, D.W., 1988. Three dimensional flow and temperature perturbations due to a transform offset: effects on oceanic crustal and upper mantle structure. J. Geophys. Res., 93: 2955-2966.

Pike, J.E., and Schwarzman, E.C., 1977. Classification of textures in ultramafic xenoliths. J. Geol., 85: 49-61.

Podvin, P., Berger, E.T., and Vannier, M., 1985. Interactions géochimiques liées à la mise en place de dikes pyroxénitiques et gabbroïques dans des harzburgites ophiolitiques. Bull. Minéral. 108: 45-62.

Poirier, J.-P., and Nicolas, A., 1975. Deformation-induced recrystallization due to progressive misorientation of subgrains, with special referencce to mantle peridotites. J. Geol., 83: 707- 720.

Poirier, J.-P., and Guillopé, M., 1979. Deformation induced recrystallization of minerals. Bull. Minéral., 102: 67-71.

Post, R.L., 1977. High temperature creep of Mt. Burnet dunite. Tectonophysics, 42: 75-100.

Prinzhofer, A., and Nicolas, A., 1980. The Bogota peninsula, New Caledonia: a possible oceanic transform fault. J. Geol., 88: 387- 398.

Prinzhofer, A., Nicolas, A., Cassard, D., Moutte, J., Leblanc, M., Paris, J.P., and Rabinovicz, M., 1980. Structures in the New Caledonia peridotites-gabbros: implications for oceanic mantle and crust. Tectonophysics, 69: 85-112.

Prinzhofer, A., and Allègre, C.J., 1985. Residual peridotites and the mechanisms of partial melting. Earth Planet. Sci. Lett., 74: 251-265.

Quick, J.E., 1981a. Petrology and petrogenesis of the Trinity peridotite, an upper mantle diapir in the eastern Klamath Mountains, northern California. J. Geophys. Res., 86: 11837- 11863.

Quick, J.E., 1981b. The origin and significance of large, tabular dunite bodies in the Trinity peridotite, Northern California. Contrib. Mineral. Petrol., 78: 413-422.

Quinn, L., 1985. The Humber Arm allochthon at South Arm, Bonne Bay, with extension in the Lomond area, west Newfoundland. M.Sc. thesis, Memorial University of Newfoundland, St. John's, 188p.

Rabinowicz, M., Nicolas, A., and Vigneresse, J.L., 1984. A rolling mill effect in asthenosphere beneath oceanic spreading centers. Earth Planet. Sci. Lett., 67: 97-108.

Rabinowicz, M., Ceuleneer, G., and Nicolas, A., 1987. Melt segregation and flow in mantle diapirs below spreading centers: evidence from the Oman ophiolite. J. Geophys. Res, 92: 3475-3486.

Raleigh, C.B., 1965. Glide mechanisms in experimentally deformed minerals. Science, 150: 739-741.

Raleigh, C.B., 1968. Mechanisms of plastic deformation of olivine. J. Geophys. Res., 73: 5391-5406.

Raleigh, C.B., and Talbot, J.L., 1967. Mechanical twinning in naturally and experimentally deformed diopside. Am. J. Sci., 265: 151-165.

Raleigh, C.B., and Kirby, S.H., 1971. Slip and the clinoenstatite transformation as competing rate processes in enstatite. J. Geophys. Res., 76: 4011-4022.

Ramsay, J.G., 1980. Shear zone geometry: a review. J. Struct. Geol., 2: 83-99.

Ramsay, J.G., and Huber, M.I., 1983. The techniques of modern structural geology, volume 1. Strain Analysis. Academic Press, Inc., London, 307p.

Reid, I., and Jackson, H.R., 1981. Oceanic spreading rates and crustal thickness. Mar. Geophys. Res., 5: 165-172.

Reuber, I., 1984. Mylonitic ductile shear zones within tectonites and cumulates as evidence for an oceanic transform fault in the Antalya ophiolite, S.W. Turkey. *IN*: Dixon, J.E., and Robertson, A.H. F., (eds.), The Geological Evolution of the Eastern Mediterranean, Geological Society Lond. Spec. Publ., 17: 319-334.

Reuber, I., 1988. Complexity of the crustal sequence in the northern Oman ophiolite (Fizh and southern Aswad blocks): the effect of early slicing? Tectonophysics, 151: 137-165.

Reuber, I., Michard, A., Chalouan, A., Juteau, T., and Jermoumi, B., 1982. Structure and emplacement of the alpine-type peridotites from Beni Bousera, Rif, Morocco: a polyphase tectonic interpretation. Tectonophysics, 82: 231- 251.

Riccio, L., 1976. Stratigraphy and petrology of the peridotite-gabbro component of the western Newfoundland ophiolites. Ph.D. thesis, University of Western Ontario, London.

Ringwood, A.E., 1975. Composition and Petrology of the Earth`s mantle, McGraw Hill, New York.

Rodgers, K.A., 1973. Chrome-spinels from the Massif du Sud, southern New Caledonia. Mineral. Mag., 39: 326-339.

Rosencrantz, E.J., 1980. The geology of the northern part of North Arm Massif, Bay of Islands ophiolite complex, Newfoundland: with application to upper oceanic crust lithology, structure, and genesis. Ph.D. thesis, State University of New York, Albany, 318p.

Rosencrantz, E.J., 1983. The structure of sheeted dikes and associated rocks in North Arm massif, Bay of Islands ophiolite complex, and the intrusive process at oceanic spreading centers. Can. J. Earth Sci., 20: 787-801.

Ross, J.V., Avé Lallement, H.G., and Carter, N.L., 1980. Stress dependence of recrystallized-grain and subgrain size in olivine. Tectonophysics, 70: 39-61.

Ross, J.V., and Nielsen, K.C., 1978. High-temperature flow of wet polycrystalline enstatite. Tectonophysics, 44: 233-261.

Sachtleben, Th, and Seck, H.A., 1981. Chemical control of Al-solubilty in orthopyroxene and its implications on pyroxene geothermomentry. Contrib. Mineral. Petrol., 78: 157-165.

Salisbury, M.H., and Christensen, N.I., 1978. The seismic velocity structure of a traverse through the Bay of Islands ophiolite complex, Newfoundland, an exposure of oceanic crust and upper mantle. J. Geophys. Res., 83: 805-817.

Salisbury, M.H., and Christensen, N.I., 1979. Reply to comment on 'The seismic velocity structure of a traverse through the Bay of Islands Ophiolite Complex, Newfoundland, an exposure of oceanic crust and upper mantle, J. Geophys. Res., 84: 6301-6302.

Schouten, H., Klitgord, K.D., and Whitehead, J.A., 1985. Segmentaton of mid-ocean ridges. Nature, 317: 225-229.

Scott, D.R., 1988. The competition between percolation and circulation in a deformable porous medium. J. Geophys. Res., 93: 5451-6462.

Scott, D.R., and Stevenson, D.J., 1986. Magma ascent by porous flow. J. Geophys. Res., 91: 9283-9296.

Scott, D.R., and Stevenson, D.J., 1989. A self-consistent model of melting, magma migration and buoyancy-driven circulation beneath mid-ocean ridges. J. Geophys. Res., 94: 2971-2988.

Searle, M.P., and Stevens, R.K., 1984. Obduction processes in ancient, modern and future ophiolites. *IN*: Gass, I.G., Lippard, S.J., and Shelton, A.W., (eds.), Ophiolites and Oceanic Lithosphere, Geol. Soc. Lond. Spec. Publ., 13: 303-315.

Sempéré, J.-C., Purdy, G.M., and Schouten, H., 1990. Segmentation of the Mid-Atlantic Ridge between 24°N and 30°40'N. Nature, 344: 427-431.

Shelton, G., and Tullis, J.A. (abstract), 1981. Experimental flow laws for crustal rocks. EOS Trans., Am. Geophys. Union, 62: 396.

Sinton, J., 1977. Equilibration history of the basal Alpine-type peridotite, Red mountain, New Zealand. J. Petrol., 18: 216-246.

Sleep, N.H., 1975. Formation of oceanic crust: some thermal constraints. J. Geophys. Res., 80: 4037-4042.

Sleep, N.H., 1988. Tapping of melt by veins and dikes. J. Geophys. Res., 93: 10255-10272.

Sleep, N.H., and Rosendahl, B.R., 1979. Topography and tectonics of mid-ocean ridge axes. J. Geophys. Res., 84: 6831-6839.

Smewing, J.D., Christensen, N.I., Bartholomew, I.D., and Browning, P., 1984. The structure of the oceanic upper mantle and lower crust as deduced from the northern section of the Oman ophiolite. *IN*: Gass, I.G., Lippard, S.J., and Shelton, A.W., Ophiolites and Oceanic Lithosphere, Geol. Soc. Lond. Spec. Publ., 13: 41-54.

Smith, C.H., 1958. Bay of Islands Igneous Complex, western Newfoundland. Geological Survey of Canada, Memoir 290, 129p.

Smith, D., 1977. The origin and interpretation of spinel-pyroxene clusters in peridotite. J. Geology, 85: 476-482.

Smith, S.E., and Elthon, D., 1988. Mineral compositions of plutonic rocks from the Lewis Hills massif, Bay of Islands ophiolite. J. Geophys. Res., 93: 3450-3468.

Snelgrove, A.K., Roebling III, F.W., and Kammara, J.L.J., 1934. The Blow-Me-Down intrusive complex. Am. Mineral., 19: 21-23.

Spray, J.G., 1984. Upper mantle decoupling and ophiolite displacement. *IN*: Gass, I.G., Lippard, S.J., and Shelton, A.W., (editors), Ophiolites and Oceanic Lithosphere. Geol. Soc. Spec. Publ., 13: 255-268.

Stevens, R.K., 1970. Cambro-Ordovician flysch sedimentation and tectonics in west Newfoundland and their possible bearing on a Proto-Atlantic ocean. Geol. Assoc. Can. Sp. Pap., 7: 165-177.

Stockmal, G.S., Colman-Sadd, S.P., Keen, C.E., O'Brien, S.J., and Quinlan, G., 1987. Collision along an irregular margin: a regional plate tectonic interpretation of the Canadian Appalachians. Can. J. Earth Sci., 24: 1098-1107.

Stolper, E., 1980. A phase diagram for mid-ocean ridge basalts: preliminary results and implications for petrogenesis. Contrib. Mineral. Petrol., 74: 13-27.

Stosch, H.-G., 1981. Sc, Cr, Co, Ni partitioning between minerals from spinel peridotite xenoliths. Contrib. Mineral. Petrol., 78: 166-174.

Strong, D.F., 1977. Volcanic regimes of the Newfoundland Appalachians. *IN*: Baragar, W.R.A., Coleman, L.C., and Hall, J.M., (eds.), Volcanic Regimes in Canada, Geol. Ass. Can., Spec. Pap. 16: 61-90.

Suen, C.J., Frey, F.A., and Malpas, J., 1979. Bay of Islands ophiolite suite, Newfoundland: petrologic and geochemical characteristics with emphasis on rare earth element geochemistry. Earth Planet. Sci. Lett., 45: 337-348.

Suhr, G., and Calon, T., 1987. A structural and microstructural study of mantle tectonites in the Springers Hill area (Bay of Islands Ophiolite, Newfoundland). Unpubl. rpt. Geol. Surv. Can., contract # 23233-6-0697/01ST, 60p.

Suhr, G., Calon, T., and Dunsworth, S.M., in press. Origin of complex upper mantle structures in the southern Lewis Hills (Bay of Islands Ophiolite, Newfoundland). Can. J. Earth Sci.,

Suhr, G., and Cawood, P.A. (submitted). Structural history of ophiolite obduction, Bay of Islands, Newfoundland. Geol. Soc. Am. Bull.

Talbot, C.J., 1970. The minimum strain ellipsoid using deformed quartz veins. Tectonophysics, 9: 47-76.

Talbot, J.L., Hobbs, B.E., Wilshire, H.G., and Sweatman, T.R., 1963. Xenoliths and xenocrysts from lavas of the Kerguelen archipelago. Am. Mineral., 48: 159-179.

Talkington, R.W., and Malpas, J., 1980. Spinel phases of the White Hills peridotite, St. Anthony Complex, Newfoundland: part I, occurrence and chemistry. Ophiolites. Proceedings International Ophiolite Symposium, Geol. Surv. Dept. Cyprus, Nicosia, pp. 607-619.

Talkington, R.W., and Malpas, J., 1984. The formation of spinel phases of the White Hills peridotite, St. Anthony Complex, Newfoundland. N. Jb. Miner. Abh., 149: 65-90.

Tapponnier, P., and Francheteau, J., 1978. Necking of the lithosphere and the mechanics of slowly accreting plate boundaries. J. Geophys. Res., 83: 3955-3970.

Taylor, B., and Karner, G.D., 1983. On the evolution of marginal basins. Rev. Geophys., 21: 1727-1741.

Thayer, T.P., 1969. Gravity differentiation and magmatic re-emplacement of podiform chromite deposits. *IN*: Wilson, H.D.B., (ed.), Magmatic ore deposits, a symposium, Econ. Geol. Mon., 4: 132-146.

Thayer, T.P., 1980. Syncrystallization and subsolidus deformation in ophiolitic peridotite and gabbro. Am. J. Sci., 280-A: 269-283.

Toksöz, M.N., and Hsui, A.T., 1978. Numerical studies of back-arc convection and the formation of marginal basins. Tectonophysics, 50: 177-196.

Toramaru, A., and Fujii, N., 1986. Connectivity of melt phase in a partially molten peridotite. J. Geophys. Res., 91: 9239-9252.

Toriumi, M., and Karato, S., 1985. Preferred orientation development of dynamically recrystallized olivine during high temperature creep. J. Geol., 93: 407-417.

Twiss, R.J., 1977. Theory and applicability of a recrystallized grain size paleopiezometer. Pure Appl. Geophys., 115: 227-244.

Urai, J.L., Means, W.D., and Lister, G.S., 1986. Dynamic recrystallization of minerals. *IN*: Hobbs, B.E., and Heard, H.C., (eds.), Mineral and Rock Deformation: Labratory Studies (Paterson Volume), Am. Geophys. Union Mon., 36: 161-199.

Uyeda, S., 1986. Facts, ideas and open problems on trench-arc-backarc systems. *IN*: Wezel, F.-C., (ed.), The Origin of Arcs, pp. 435-461, Elsevier, Amsterdam.

Uyeda, S., and Kanamori, H., 1979. Back-arc opening and the mode of subduction. J. Geophys. Res., 84: 1049-1061.

van der Pluijm, B.A., Johnson, R.J.E., and van der Voo, R., 1990. Early Paleozoic paleogeography and accretionary history of the Newfoundland Appalachians. Geology, 18: 898-901.

van der Pluijm, B.A., and van Staal, C.R., 1988. Characteristics and evolution of the central mobile belt, Canadian Appalachians. J. Geol., 96: 535-547.

van der Wal, D., Drury, M.R., Vissers, R.L.M., and Hoogerduijn Strating, E.H., 1990. Oblique fabrics in alpine-type peridotite tectonites. Terra Abstr., 2: 144.

Vogt, P.R., and Johnson, G.L., 1975. Transform faults and longitudinal flow below the midocean ridge. J. Geophys. Res., 80: 1399-1428.

Waff, H.S., and Bulau, J.R., 1979. Equilibrium fluid distribution in an ultramafic partial melt under hydrostatic stress conditions. J. Geophys. Res., 84: 6109-6114.

Wallace, R.C., 1975. Mineralogy and petrology of xenoliths in a diatreme from South Westland, New Zealand. Contrib. Mineral. Petrol., 49: 191-199.

Weaver, D.F., 1967. A geological interpretation of the Bouguer anomaly field of Newfoundland. Dominion Observatory, 35: 233-251.

Weissel, J.K., 1981. Magnetic lineations in marginal basins of the western Pacific. Phil. Trans. R. Soc. Lond., A 300: 223-247.

Wells, P.R. A., 1977. Pyroxene thermometry in simple and complex systems. Contrib. Mineral. Petrol., 62: 129-139.

Whalen, J.B., 1989. The Topsail's igneous suite, western Newfoundland: an Early Silurian subduction-related magmatic suite? Can. J. Earth Sci., 26: 2421-2434.

Whitehead, Jr., J.A., 1986. Buoyancy-driven instabilities of low-viscosity zones as models of magma-rich zones. J. Geophys. Res., 91: 9303-9314.

Whitehead, Jr., J.A., Dick, H.J.B., and Schouten, H., 1984. A mechanism for magmatic accretion under spreading centres. Nature, 312: 146-148.

Williams, H., 1964. The Appalachians in northeastern Newfoundland - a two-sided symmetrical system. Am. J. Sci., 262: 1137-1158.

Williams, H., 1971. Mafic-ultramafic complexes in western Newfoundland Appalachians and the evidence for their transportation: a review and interim report. Geol. Ass. Can. Proc., 24: 9-25.

Williams, H., 1973. Bay of Islands map area, Newfoundland (12G). Geol. Surv. Can., Pap. 72-34, (includes Map 1355A).

Williams, H., 1975. Structural succession, nomenclature, and interpretation of transported rocks in western Newfoundland. Can. J. Earth Sci., 12: 1874-1894.

Williams, H., 1979. Appalachian Orogen in Canada. Can. J. Earth Sci., 16: 792-807.

Williams, H., 1984. Miogeoclines and suspect terranes of the Caledonian-Appalachian Orogen: tectonic patterns in the North Atlantic region. Can. J. Earth Sci., 21: 887-901.

Williams, H., and Malpas, J., 1972. Sheeted dikes and brecciated dike rocks within transported igneous complexes, Bay of Islands, western Newfoundland. Can. J. Earth Sci , 9: 1216-1229.

Williams, H., and Smyth, W.R., 1973. Metamorphic aureoles beneath ophiolite suites and alpine peridotites: tectonic implications with west Newfoundland examples. Am. J. Sci., 273: 594-621.

Williams, H., and Hatcher, R.D., 1983. Appalachian suspect terranes. *IN*: Hatcher, R.D., Williams, H., and Zietz, I., (eds.), Contributions to the tectonics and geophysics of mountain chains, Geol. Soc. Am., Mem. 158: 33-53.

Williams, H., and Hiscott, R.N., 1987. Definition of the Iapetus rift-drift transition in western Newfoundland. Geology, 15: 1044-1047.

Williams, H., Colman-Sadd, S.P., and Swinden, H.S., 1988. Tectonic-stratigraphic subdivisions of central Newfoundland. Current Research, Part B, Geol. Surv. Can., 88-1B: 91-98.

Williams, H., and Cawood, P.A., 1989. Geology, Humber Arm Allochthon, Newfoundland. Geol. Surv. Can., Map 1678A, scale 1: 250000.

Wilson, J.T., 1966. Did the Atlantic close and then re-open? Nature, 211: 676-681.

Witt-Eickschen, G., and Seck, H.A., in press. Solubility of Ca and Al in orthopyroxene from spinel peridotite: an improved version of an empirical geothermometer. Contrib. Mineral. Petrol.

APPENDIX A: PAGE-INTENSIVE FIGURES.

In the following 27 pages, figures related to main body of text are presented. The figures have, however, been moved to the Appendix, as they contain information not crucial for the understanding of the text. On the other hand, by retaining them in the text, chapters 2 and 5 would have become highly disintegrated.

Figs. A2.1 - A2.17 (following pages). Stereographic projections (equal area, lower hemisphere) of data from structural elements of the Table Mountain Massif, listed according to structural units. A constant counting circle was used for contouring. Therefore, density values are *not* comparable between data sets containing different number of measurements. Only the *location* of the density maxima is used for interpretations in this thesis.

Unit designations are as follows: 1 - unit 1; 2 - unit 2; 3 - unit 3; 3_{HS} - unit 3, high temperature shear zones; 4 - unit 4; TU - transition unit; 5 - unit 5; 6_{LS} - unit 6, early high strain fabric; 6_{HS} - unit 6, later high strain fabric; 6_{UL} - unit 6, ultramylonite; 6_{NF} - unit 6, faulted sliver in northeastern part of massif; AMP - amphibolites in continuous belt of metamorphic sole.

Symbols within stereonets have the following meaning: open square - location of maximum density of data; circle with cross - pole to best fit great circle; black triangle (within Fig. A2.7) - mean stretching lineation of the same unit; black circle (within Fig. A2.9) - mean foliation of the same unit. For fold axes of dykes (Fig. A2.13): crosses - orthopyroxenites dykes; dots - clinopyroxenite dykes.

Number of measurements is indicated in lower left corner of each diagram. All contours are in % of 1% area. Contour levels are at 2% intervals starting at 1%, i.e. 1,3,5,7% etc.. *Exceptions are listed below:*

Fig. A2.1 Foliations. Unit 5 - contours at 3,5,9,13%; unit 6_{NF} - contours at 3,5,9,11%; Amp - contours at 3,7,11,15,19%.

Fig. A2.2 Mineral Lineations. Unit 3_{HS} - contours at 5,9,15,19,25%; unit 5 - contours at 3,7,11,15,19%; unit 6_{LS} - contours at 3,7,11,13,17%; unit 6_{HS} - contours at 1,5,7,9,11%.

Fig. A2.3 Data of Unit 2'. Foliations - contours at 3,5,7,11,13,17,19,21,25%; mineral lineations - contours at 3,5,9,11,15,17%.

Fig. A2.4 Data of unit 3'. Foliations - contours at 3,7,9,13,17,19%; mineral lineations - contours at 5,9,13,17,23,27,31%.

Fig. A2.6 Axial Planes. Unit 3_{HS} - contours at 5,11,17,21,27,33%; unit 4 - contours at 3,7,13,17,21,25,29,33,37%.

Fig. A2.9 Orthopyroxenite dykes. Unit 1 - contours at 3,7,9,13%.

Fig. A2.12 "Inflection dykes". Unit 3 - contours at 3,9,13,17,21,25%.

Fig. A2.14 Boudin-elongations. Unit 3 - contours at 3,5,7,11,13,17,21%.

Fig. A2.17 Dunite bands. Unit 3 - contours at 3,5,7,11,13,15%.

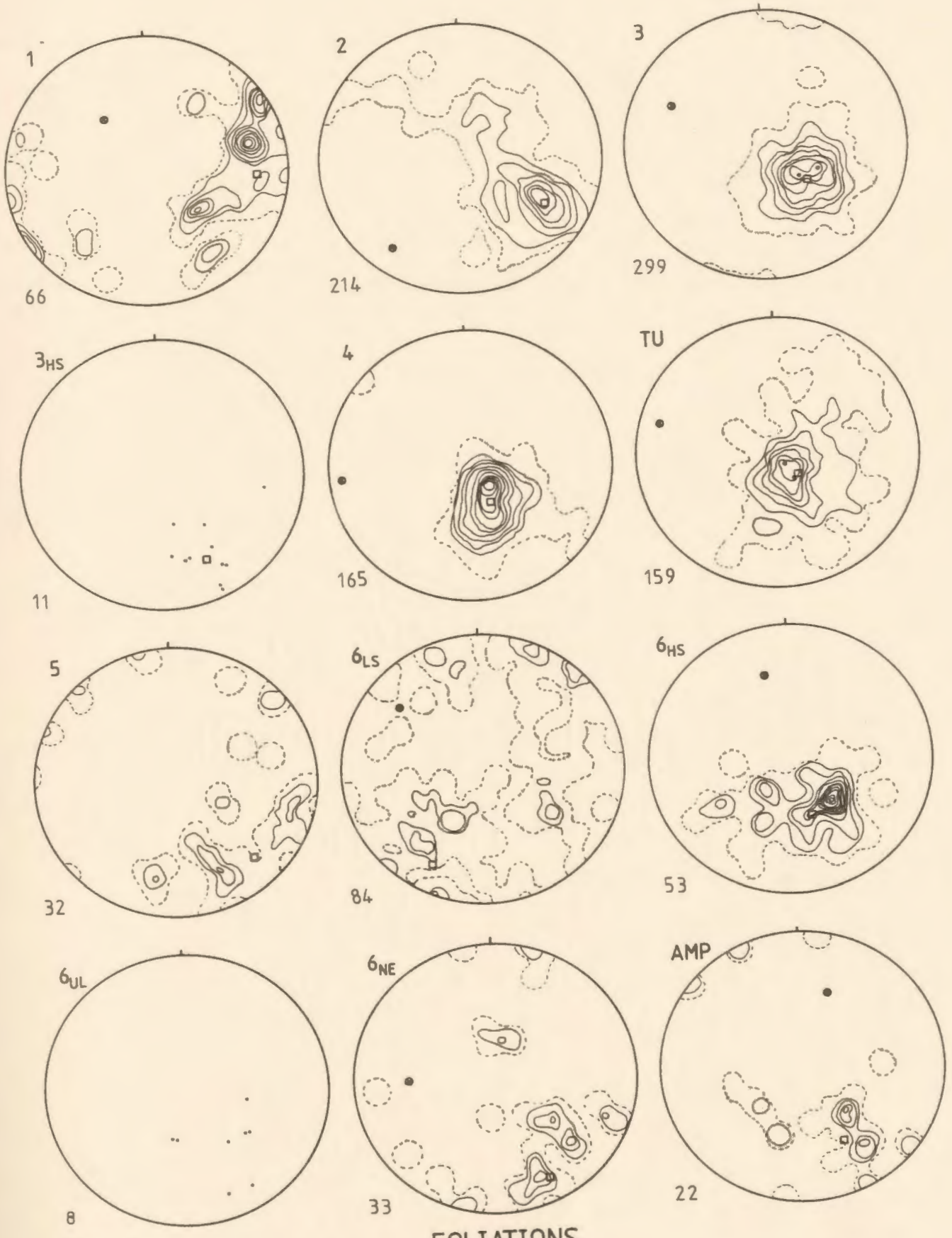

FIG. A 2.1

FOLIATIONS

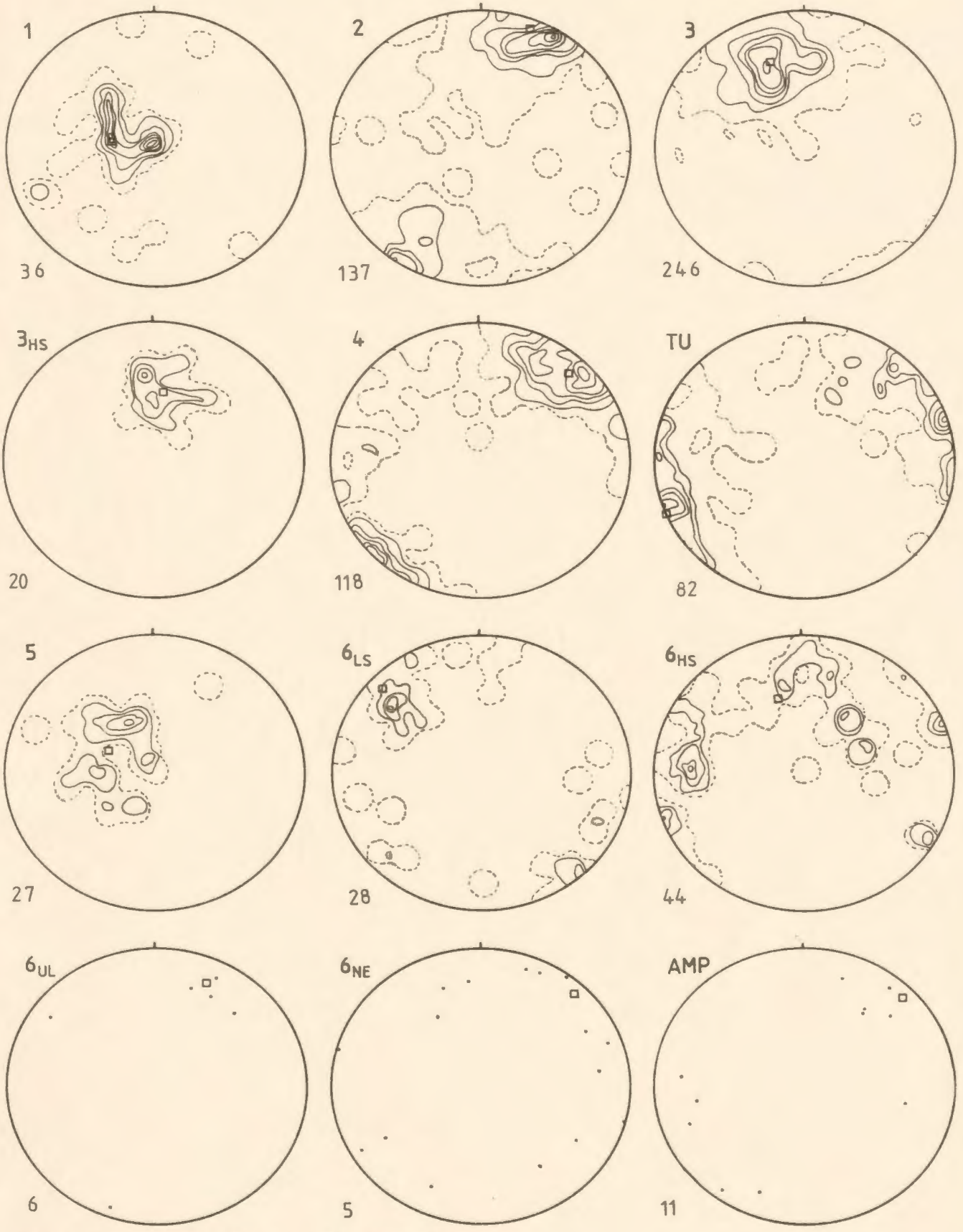

FIG. A2.2. MINERAL LINEATIONS

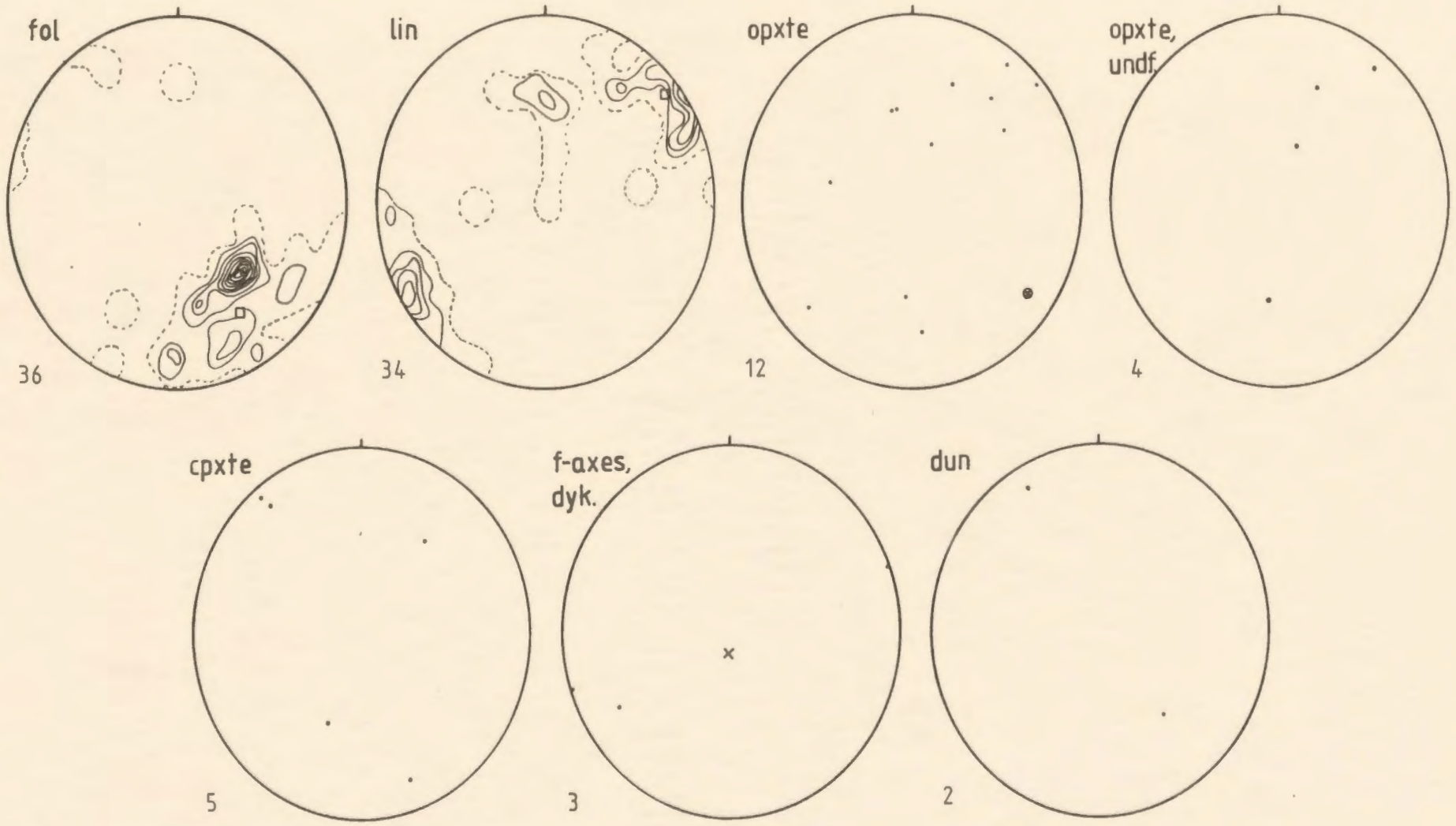

FIG. A2.3 UNIT 2'

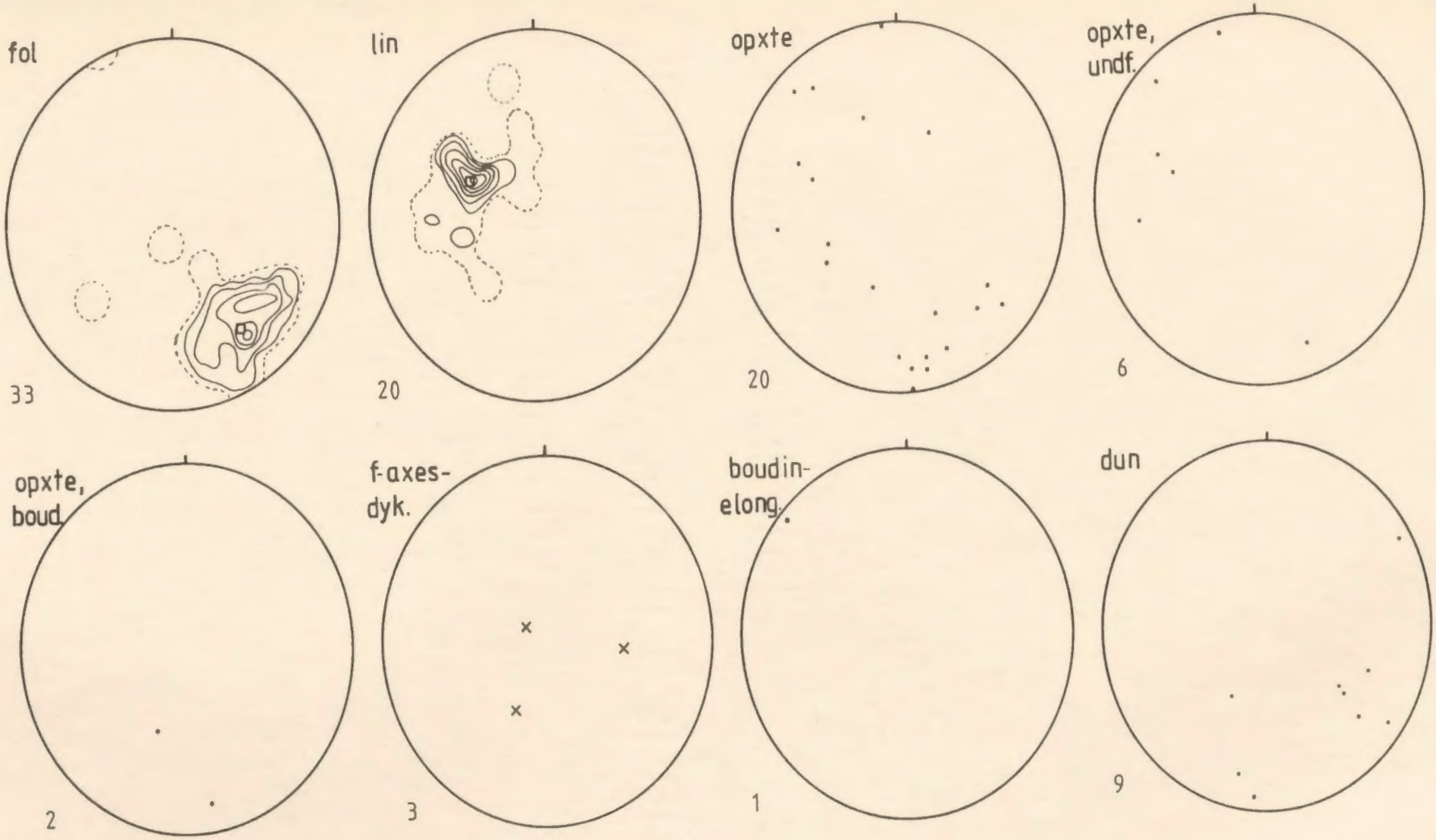

FIG. A2.4

UNIT 3'

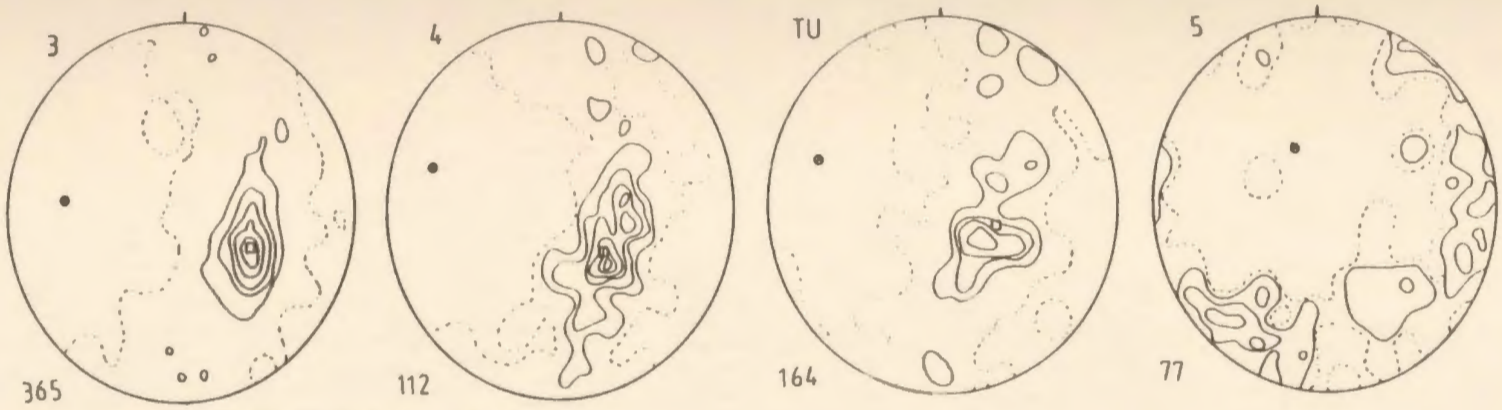

FIG. A2.5 LITHOLOGICAL BANDING

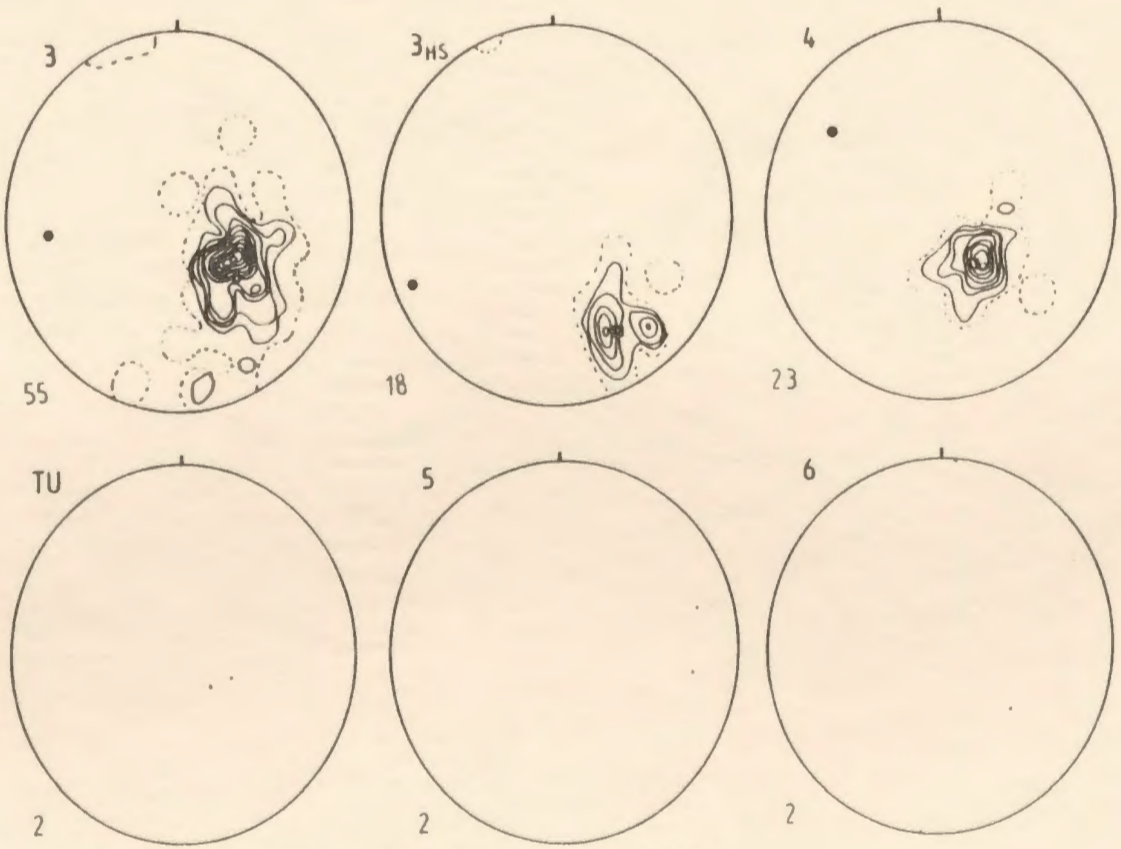

FIG. A2.6. AXIAL PLANES OF LITHOLOGICAL BANDING

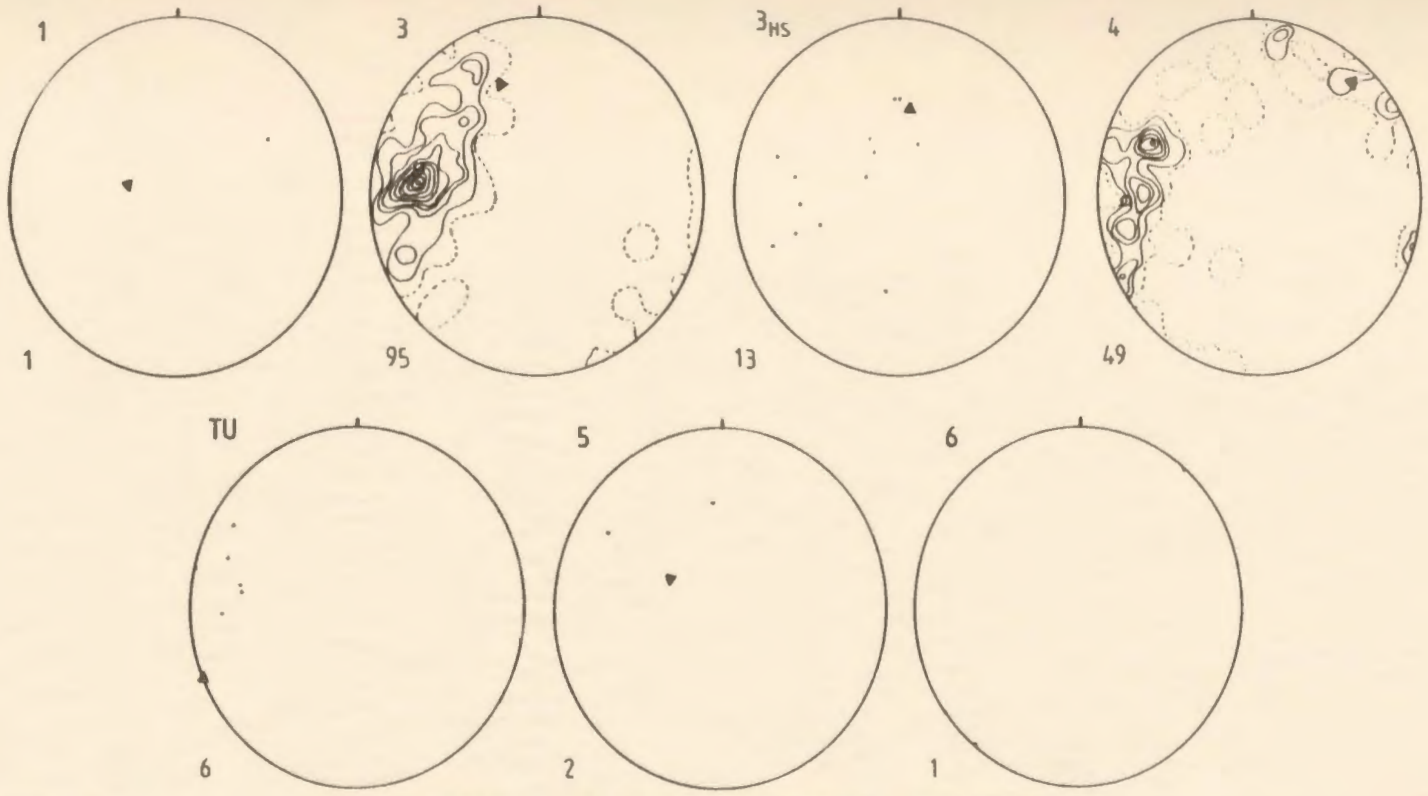

FIG. A2.7 FOLD AXES OF LITHOLOGICAL BANDING

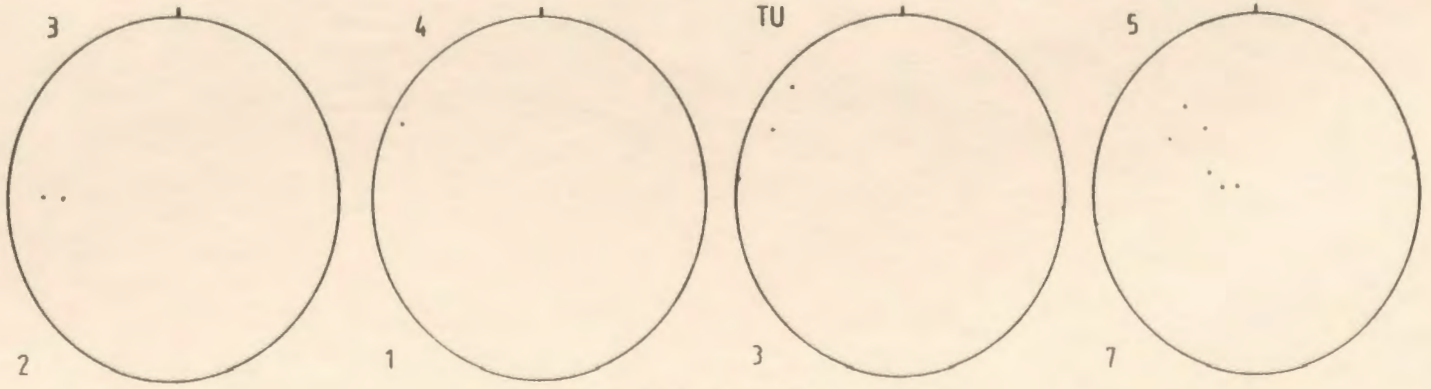

FIG. A2.8 EARLY FOLD AXES

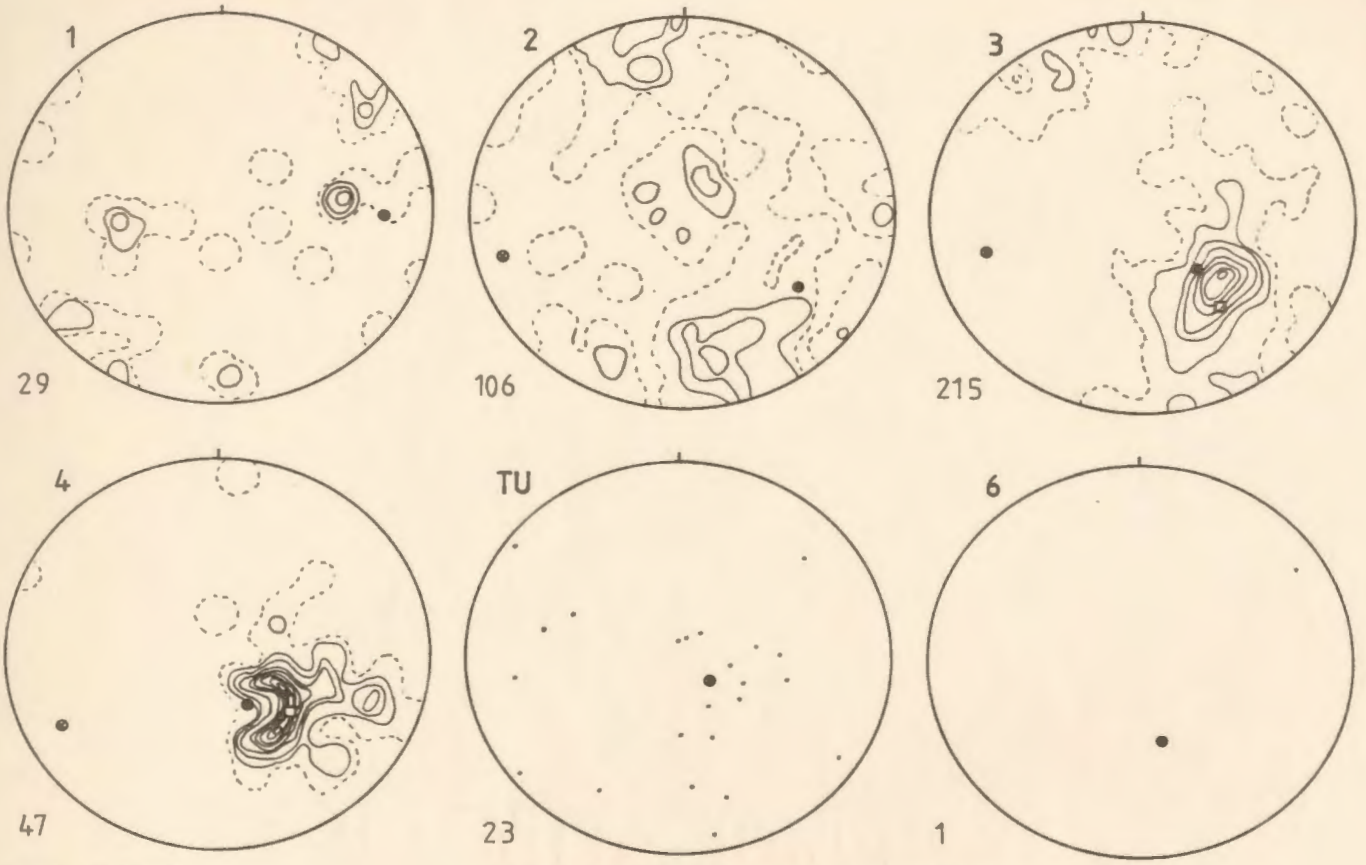

FIG. A2.9 ORTHOPYROXENITE DYKES

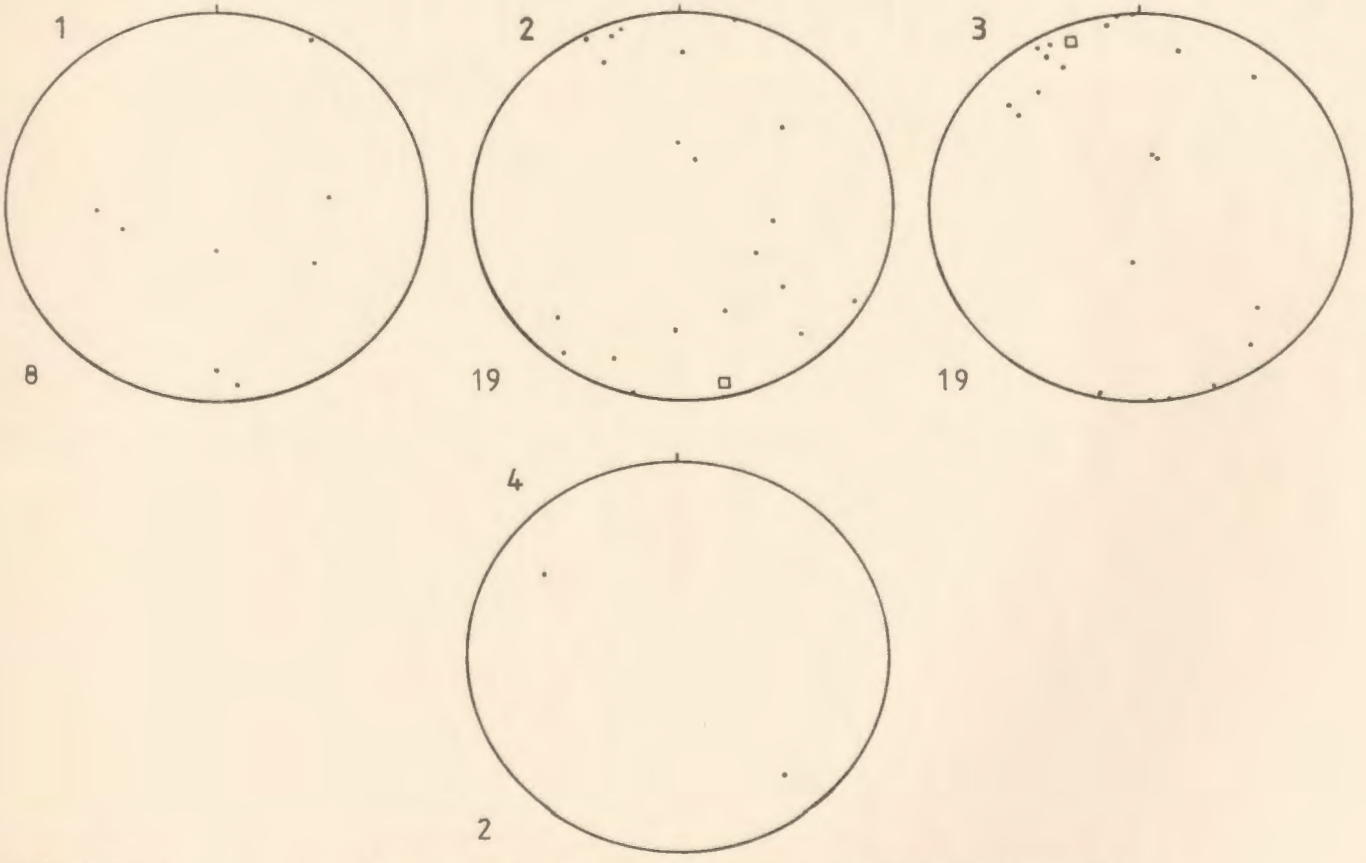

FIG. A2.10 UNDEFORMED ORTHOPYROXENITE DYKES

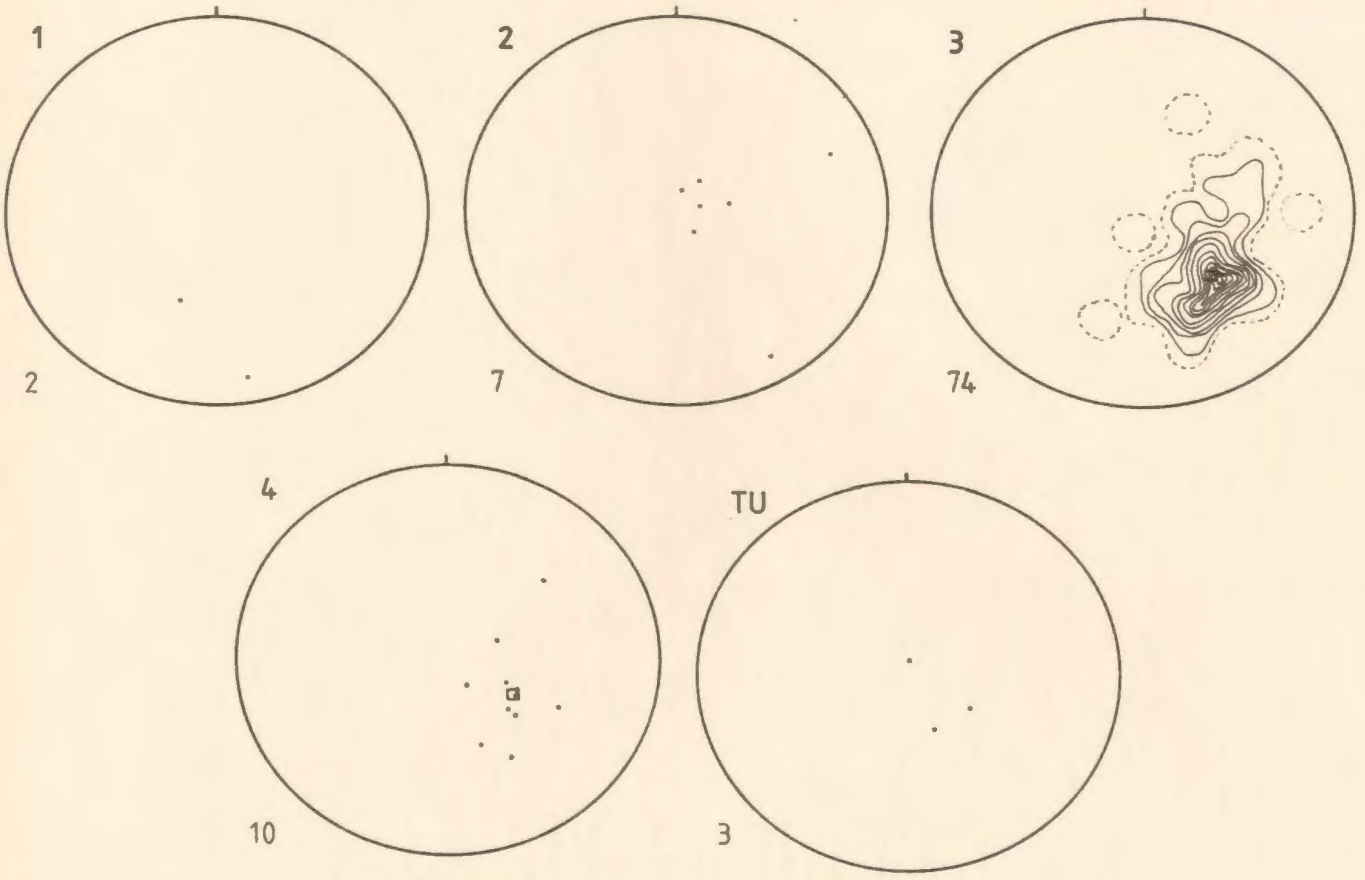

FIG. A2.11 BOUDINAGED DYKES

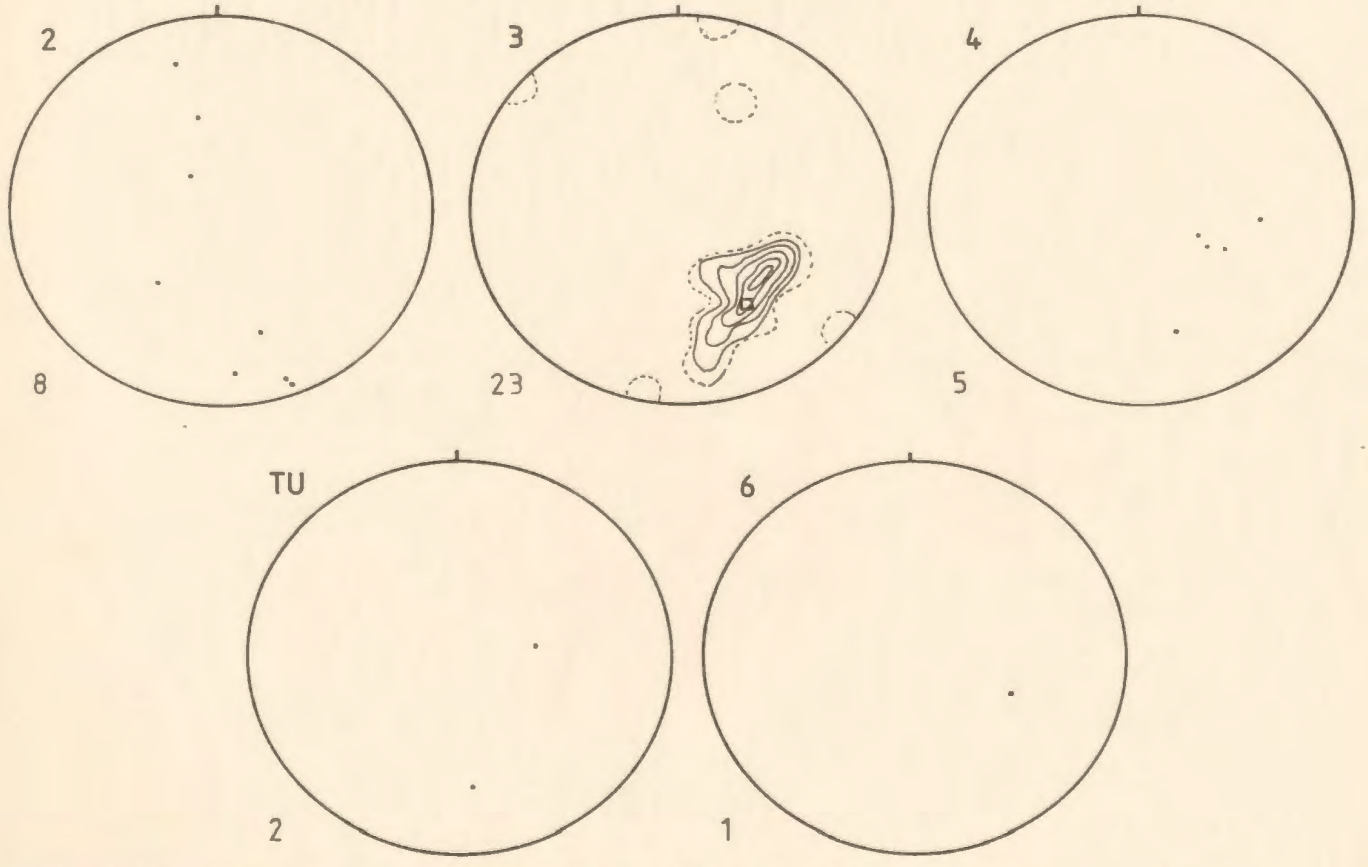

FIG. A 2.12 "INFLECTION" DYKES

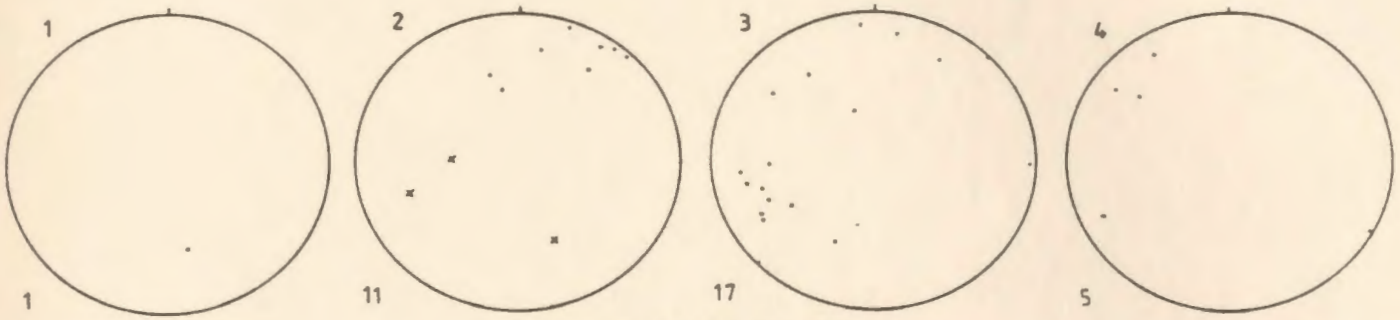

FIG. A 2.13 FOLD AXES OF DYKES

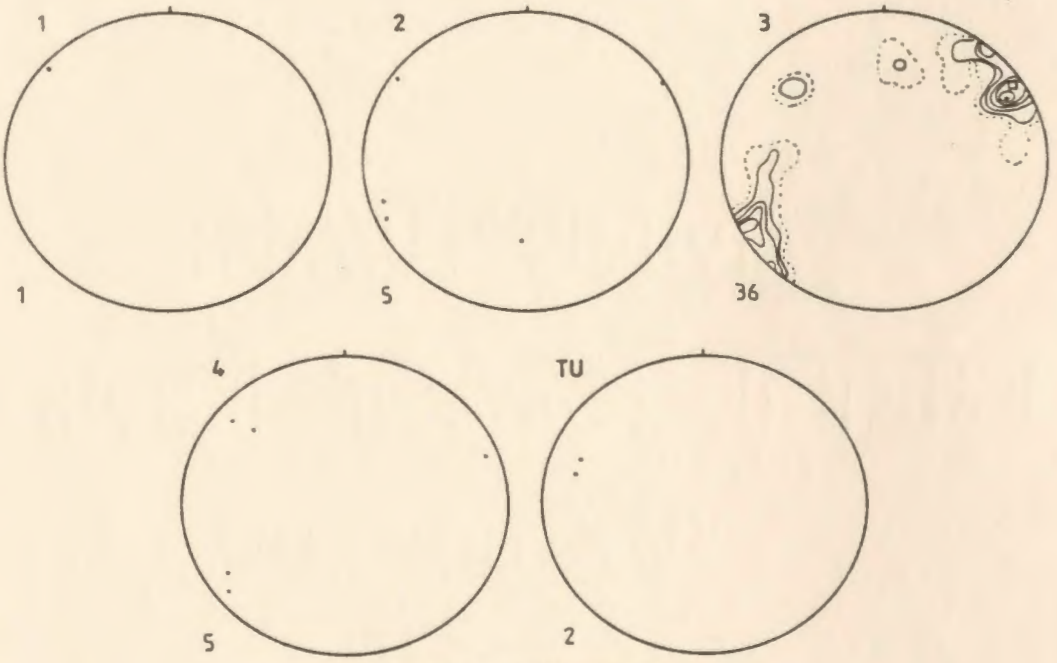

FIG. A2.14 BOUDIN ELONGATIONS

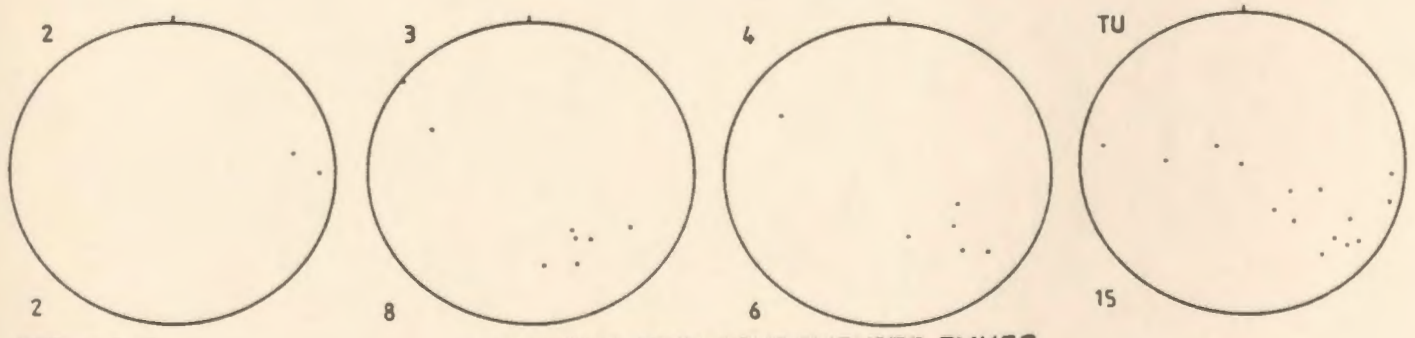

FIG. A2.15 OLIVINE ORTHOPYROXENITE DYKES

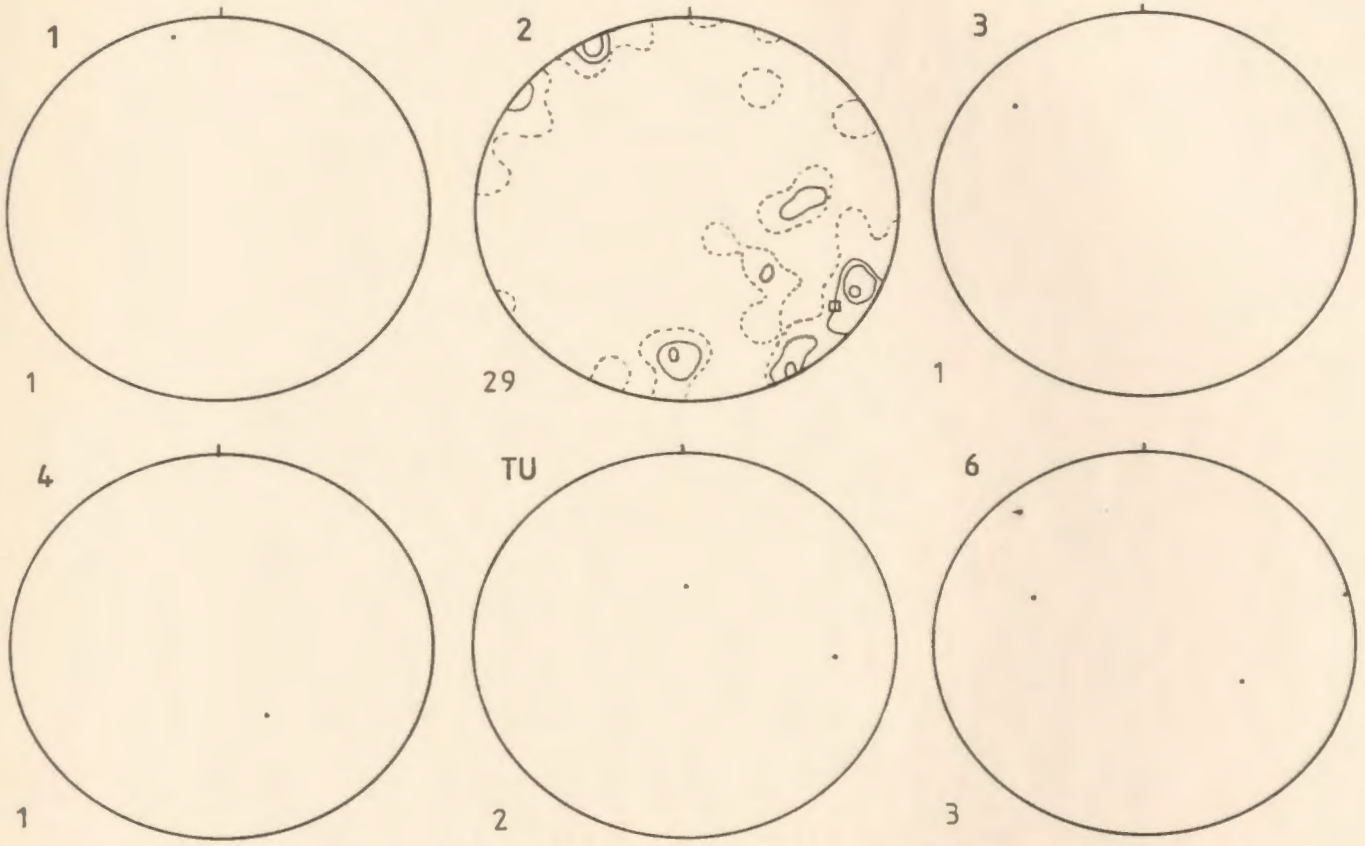

FIG. A2.16 CLINOPYROXENITE DYKES

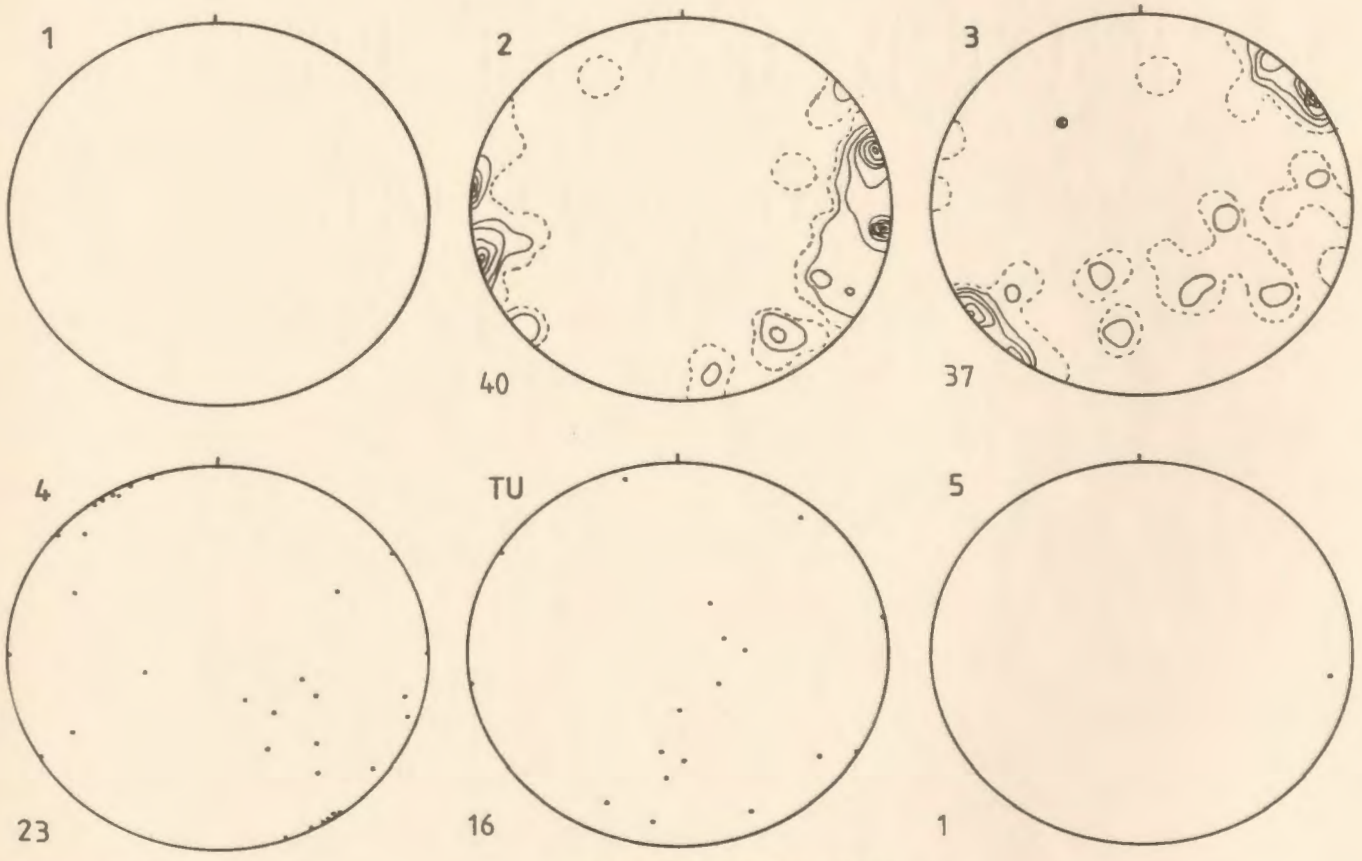

FIG. A2.17 DUNITE BANDS

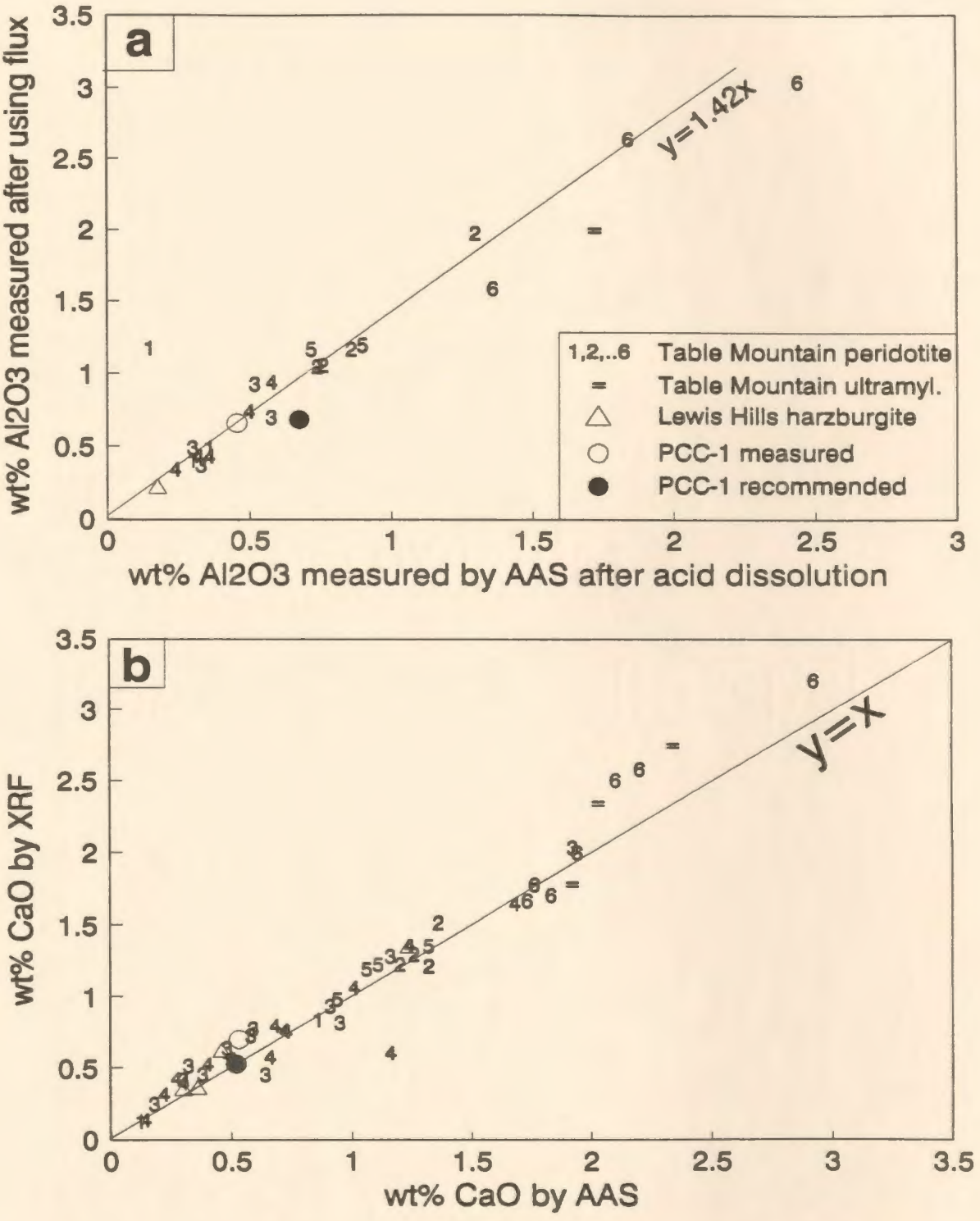

Fig. A5.1. (a) Comparison of Al2O3 determinations of peridotite after acid dissolution and dissolution by flux.
(b) Comparison of CaO determinations in peridotite using atomic absorption spectroscopy and X-ray fluoresence.

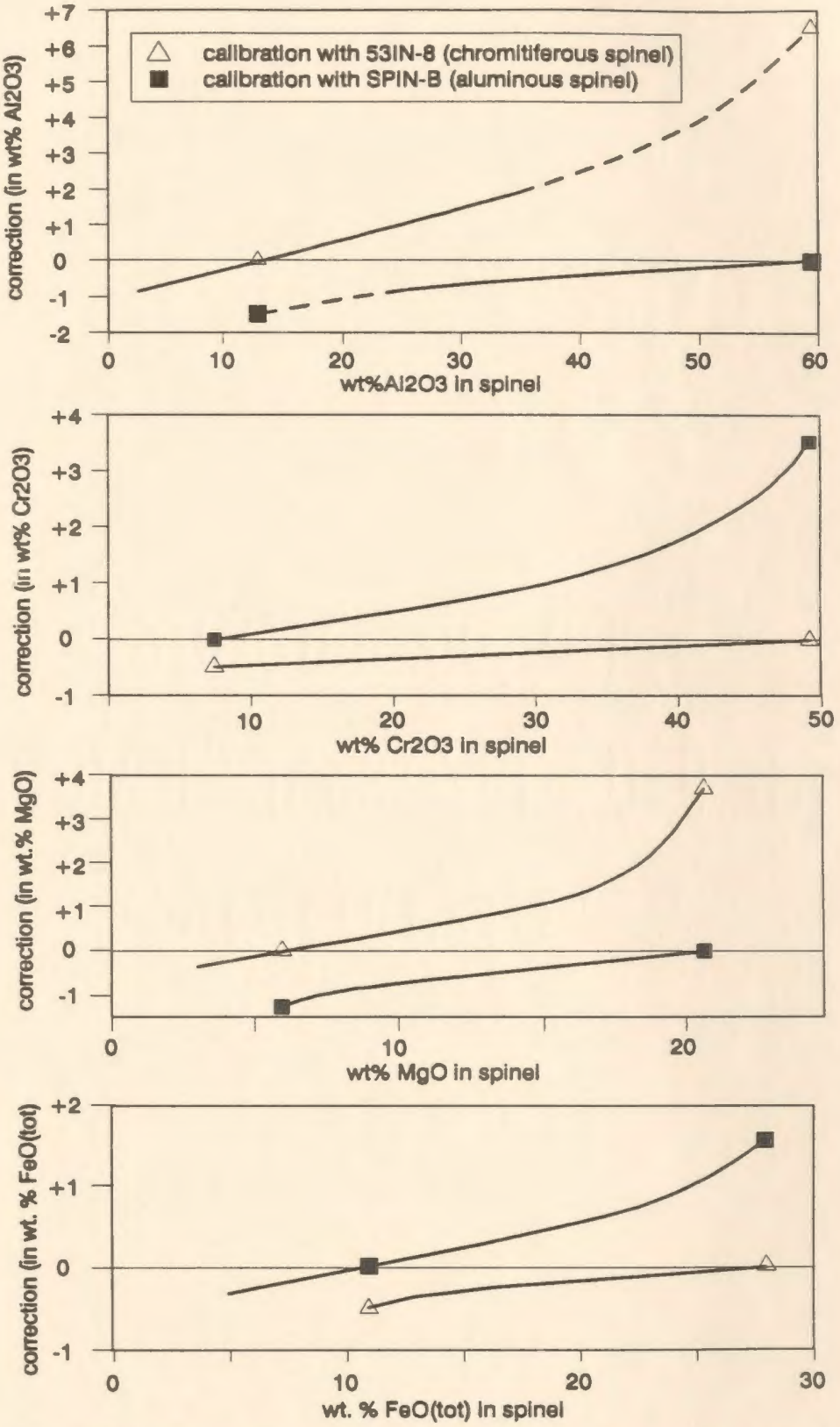

Fig. A5.2. Correction scheme for spinel microprobe data. See text for details.

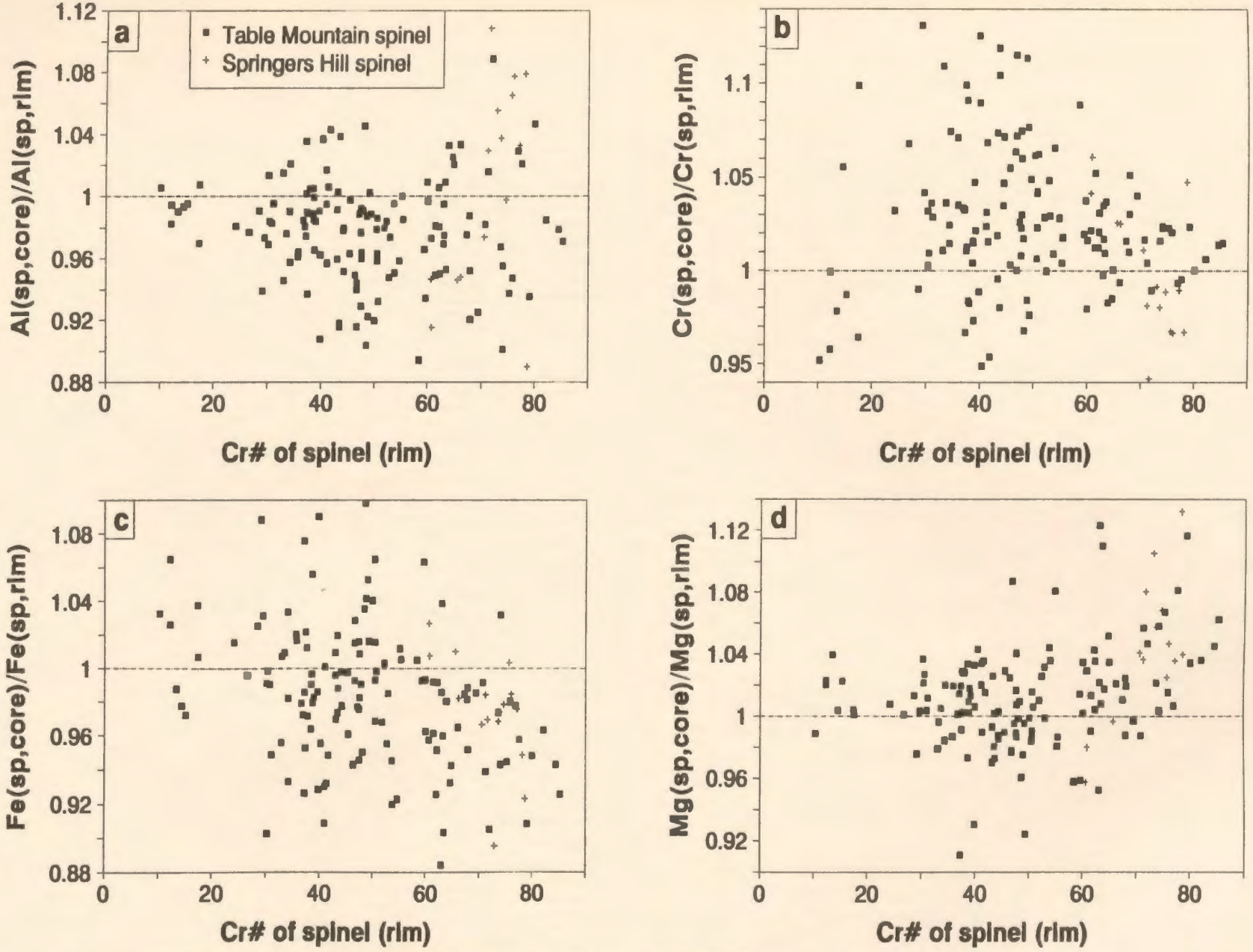

Fig. A5.3. Core-rim ratios of various mineral chemical parameters in spinel.

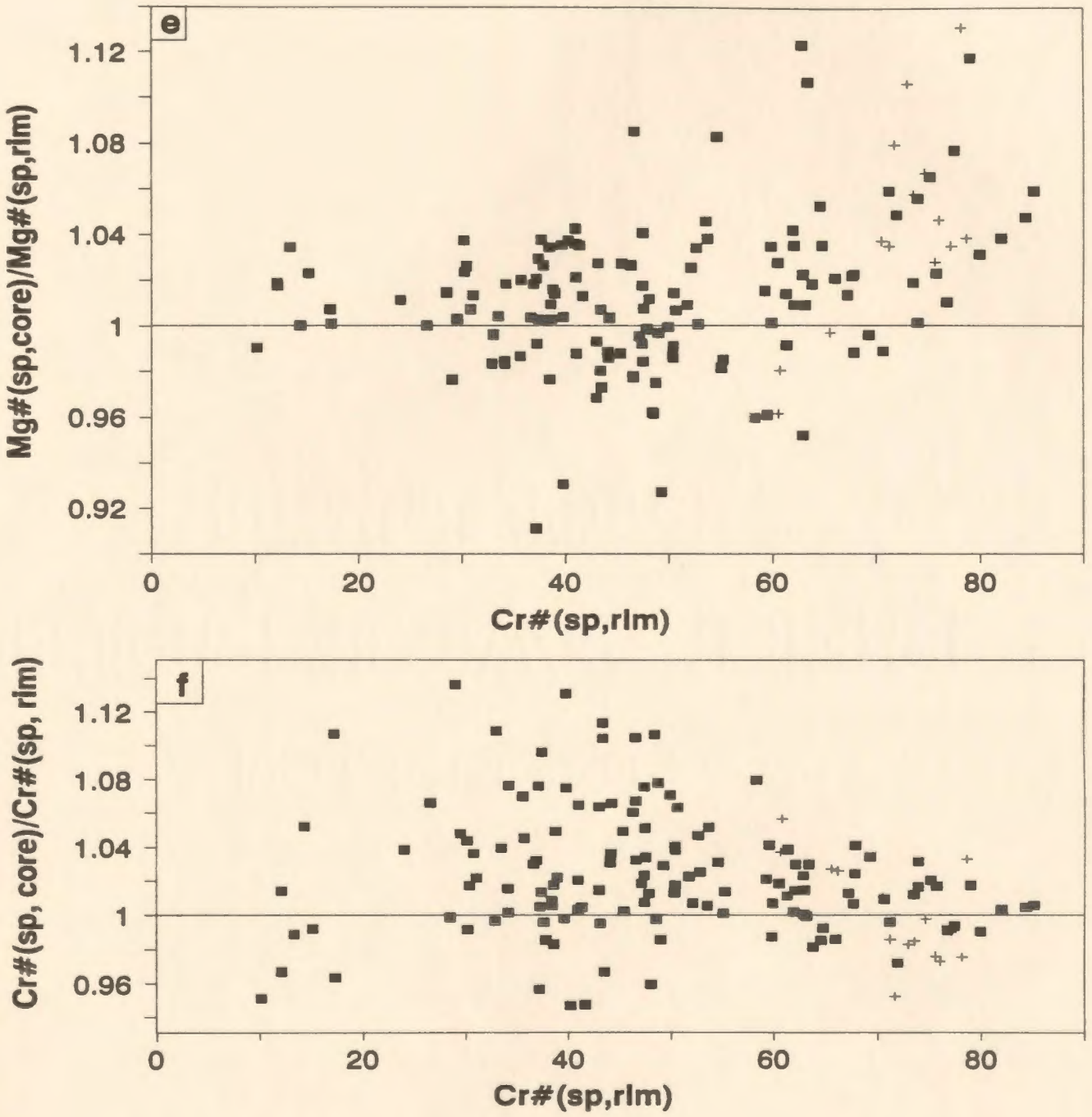

Fig. A5.3. (continued)

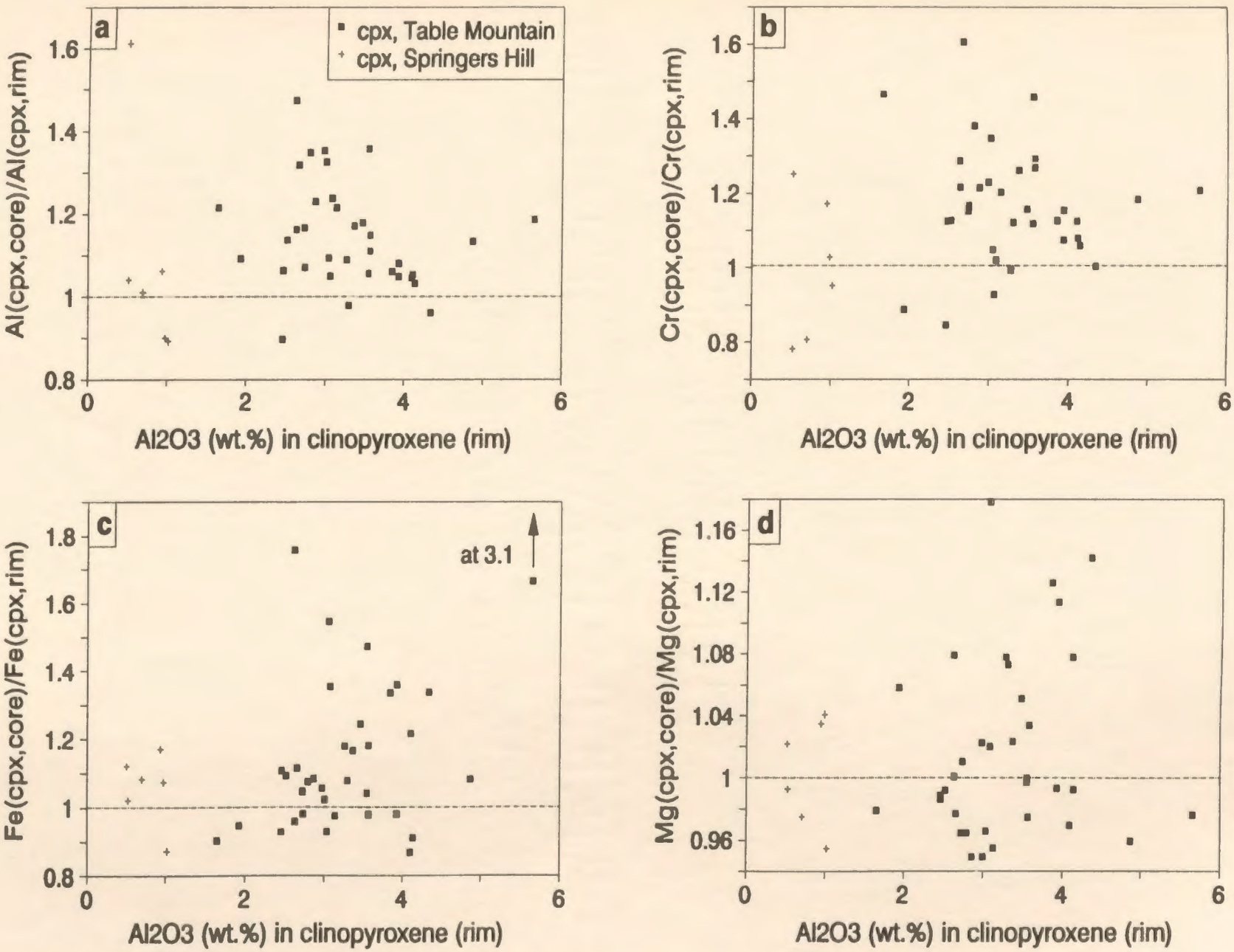

Fig. A5.4. Core-rim ratios of various mineral chemical parameters in clinopyroxene.

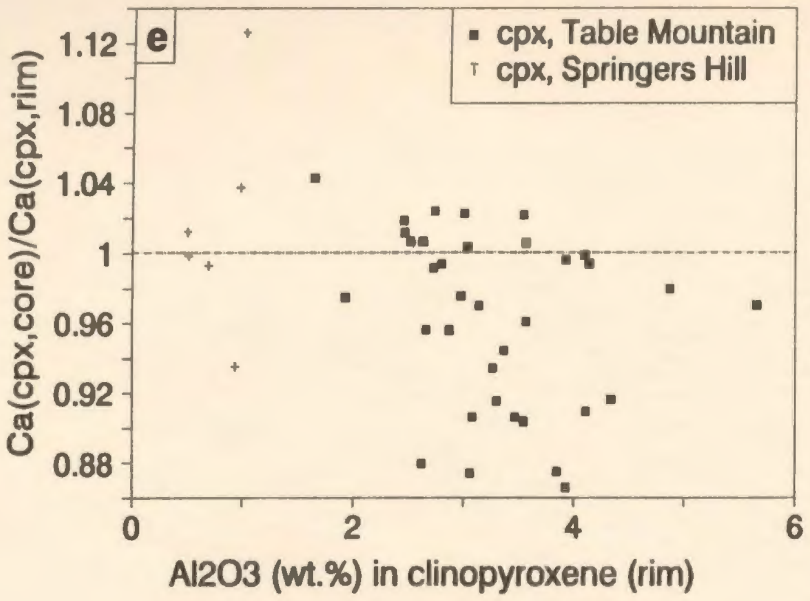

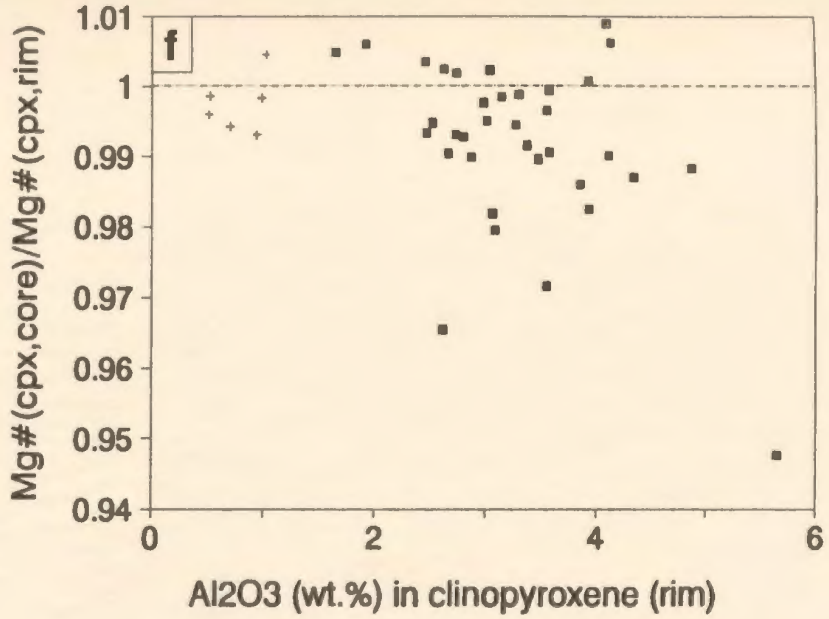

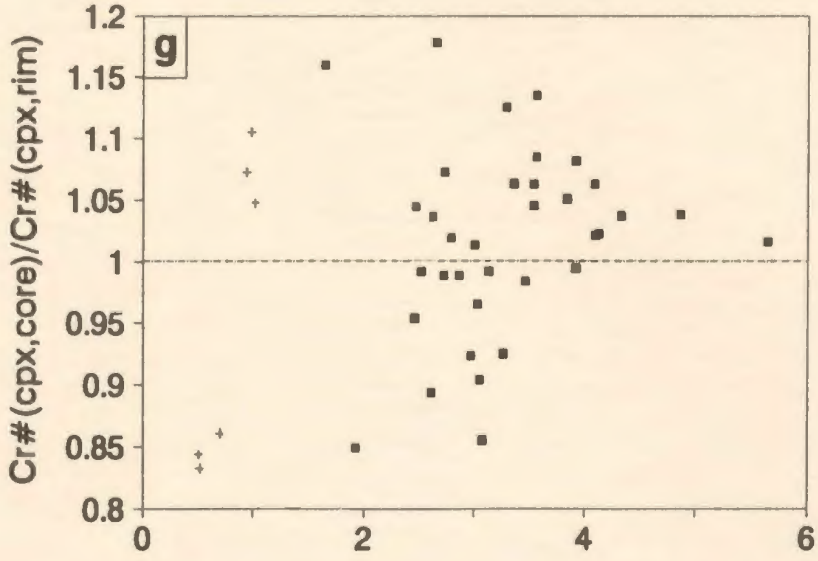

Fig. A5.4. (continued)

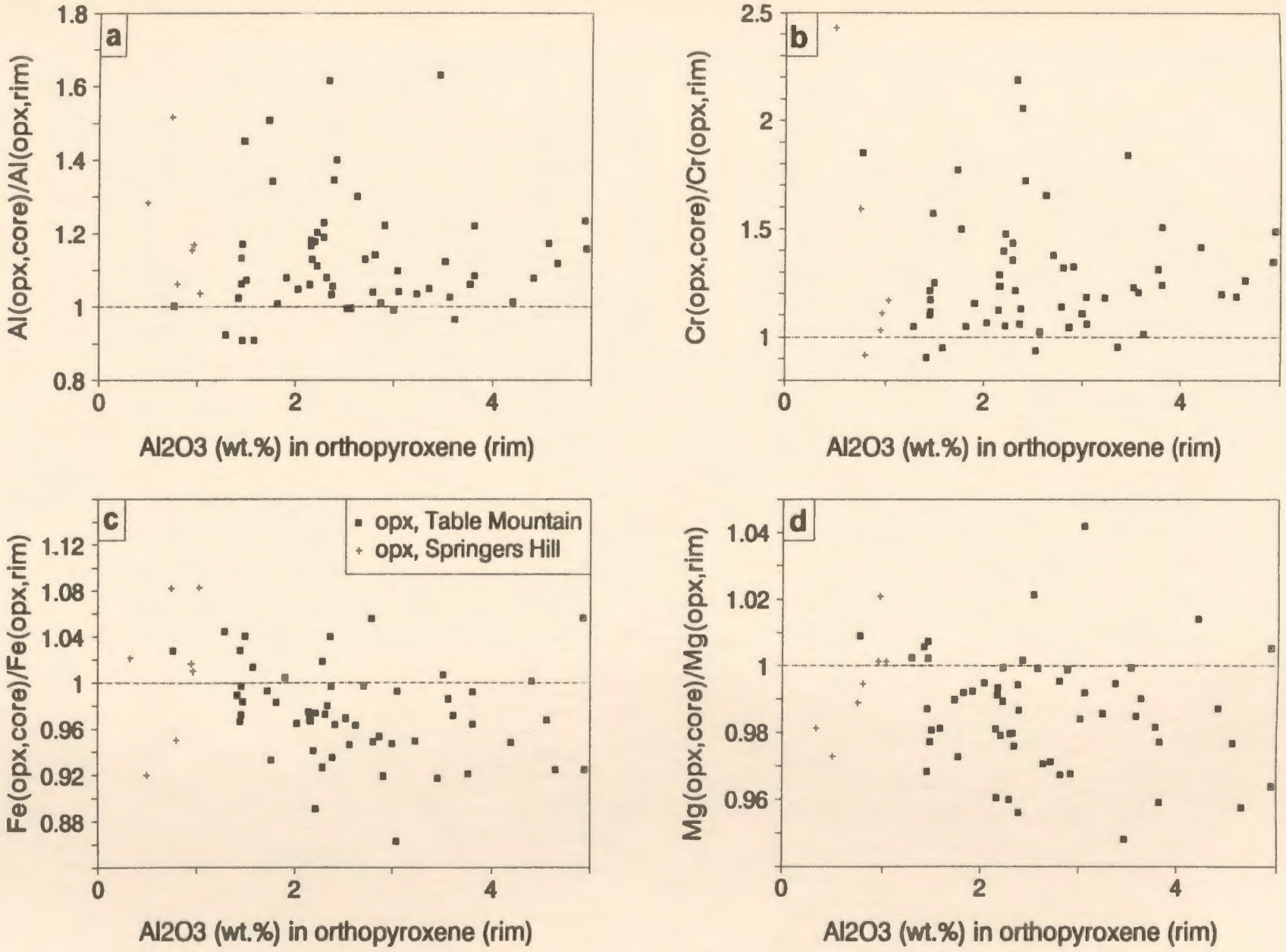

Fig. A5.5. Core-rim ratios of various mineral chemical parameters in orthopyroxene.

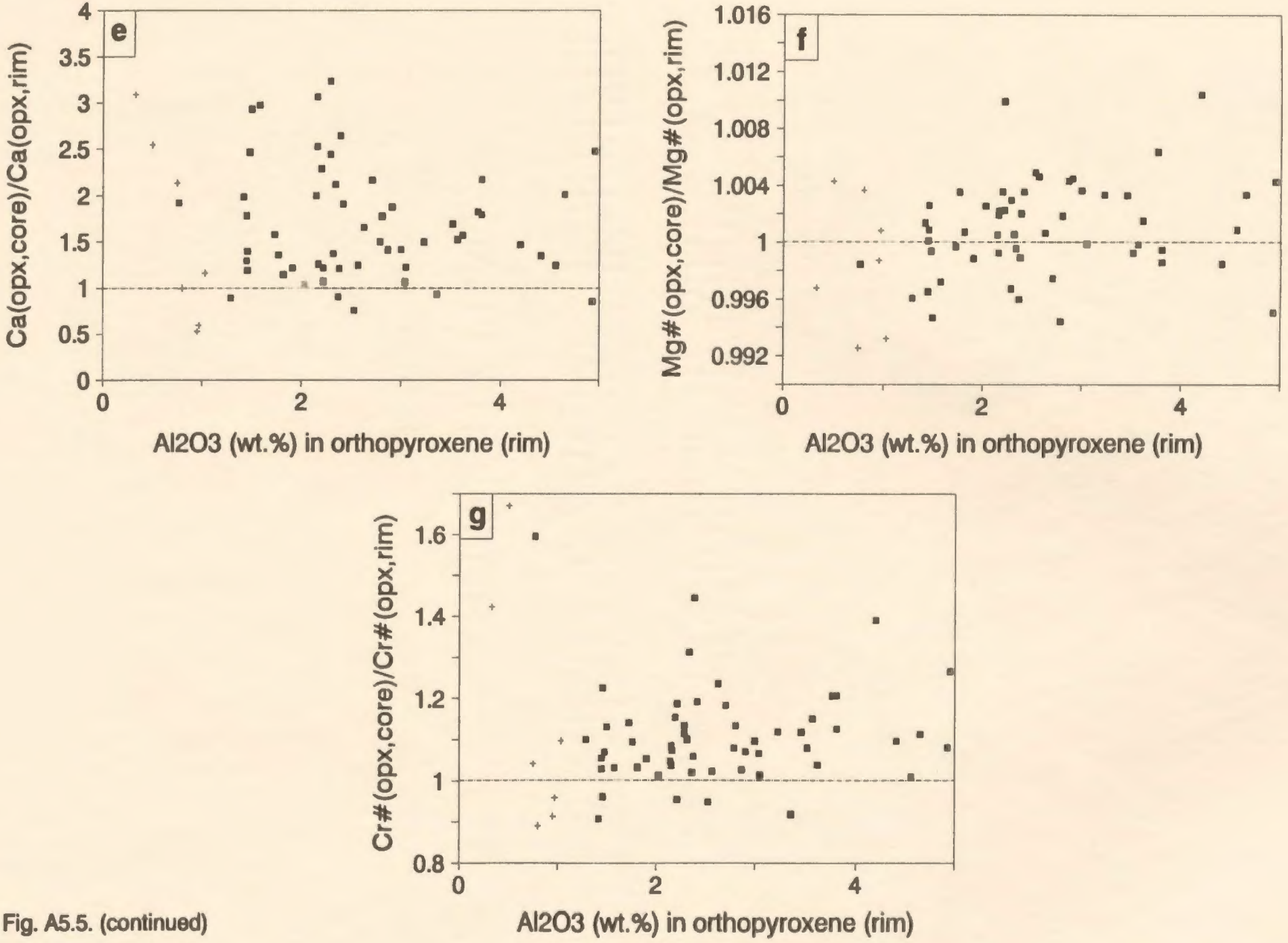

Fig. A5.5. (continued)

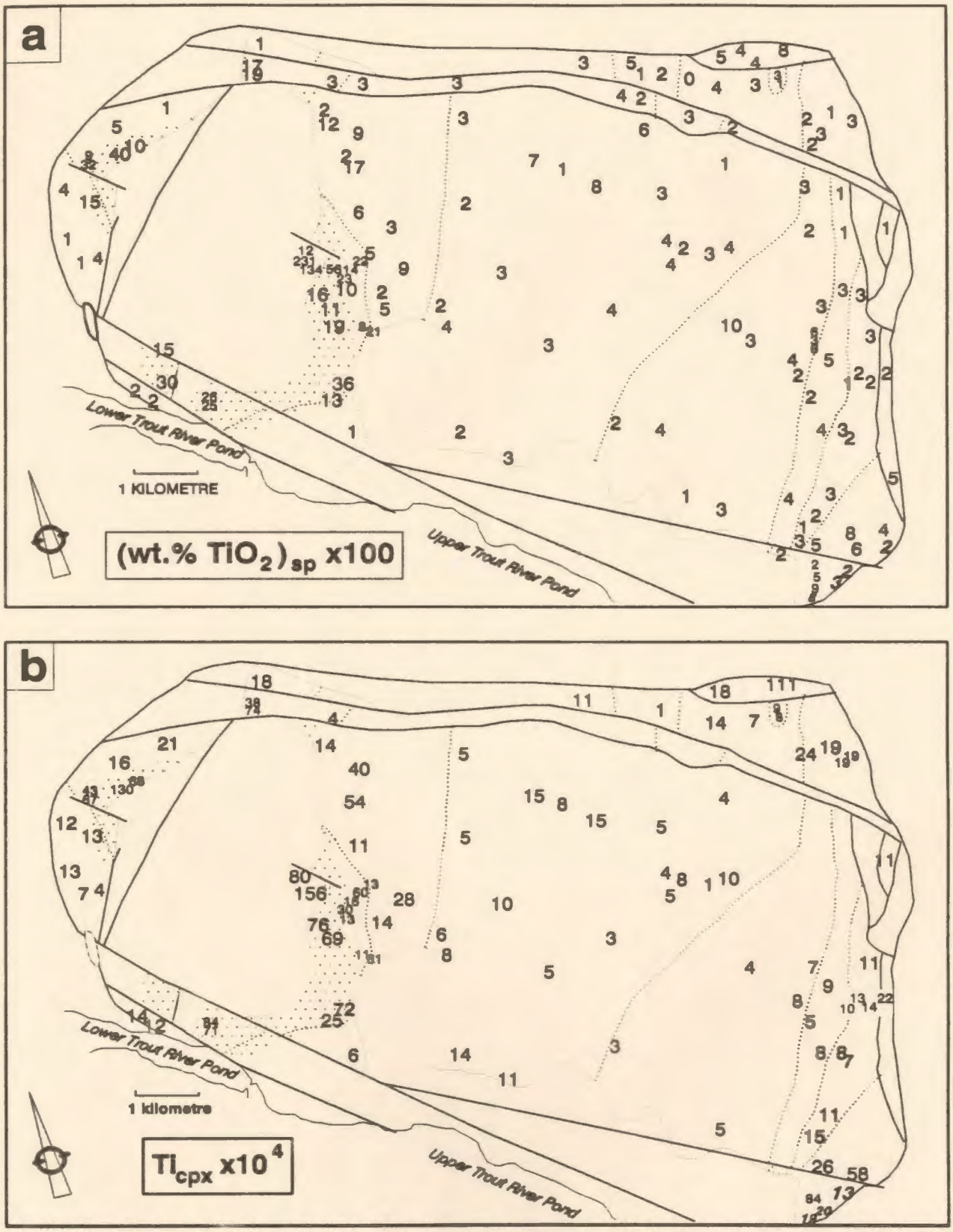

Fig. A5.6. Spatial distribution of selected mineral chemical parameters. Dotted line - structural unit boundaries; shaded area - massive dunites; numbers in italics - ultramylonite; heavy lines - brittle faults.

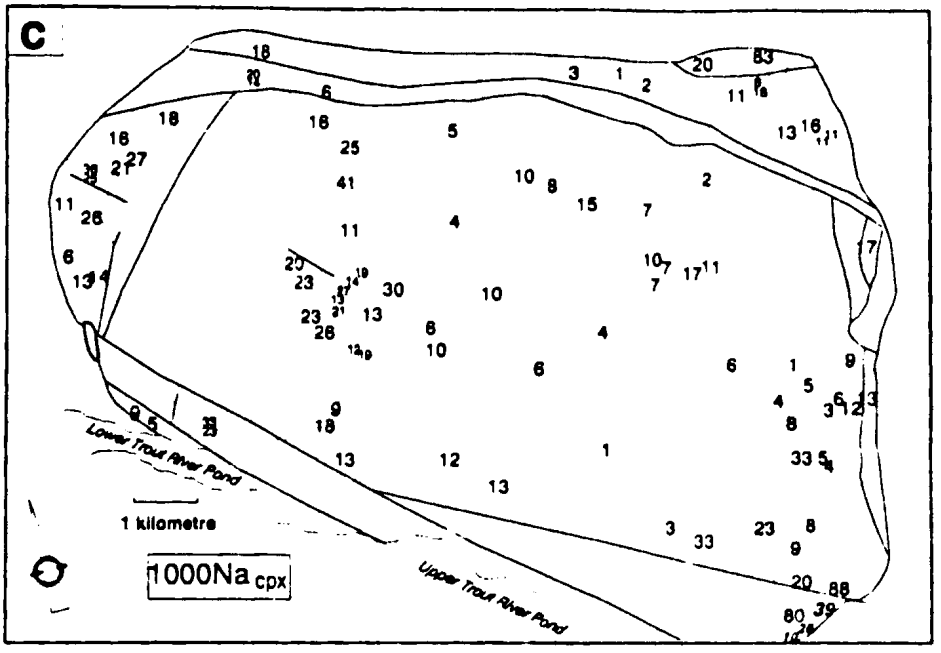

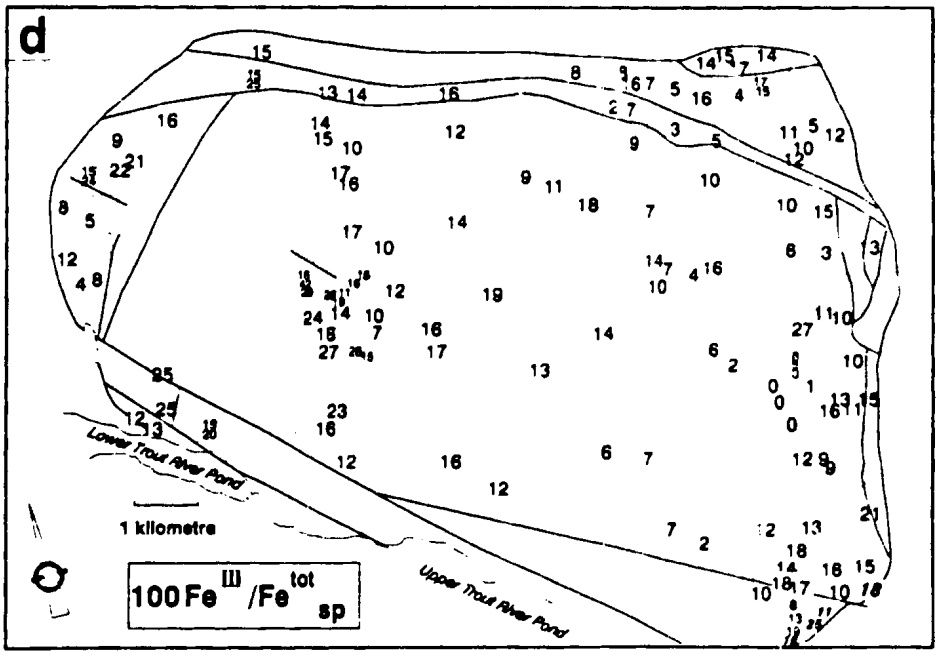

Fig. A5.6. (continued)

Fig. A5.7. Mineral chemistry variation diagrams (following pages).

LEGEND

UPPER DIAGRAMS

- 1,2,..6 - harzburgite or lherzolite from Table Mountain massif, number indicates structural unit
- x - massive dunite or wehrlite from Table Mountain transition zone
- = - ultramafic ultramylonite from base of Table Mountain peridotites
- c - layered cumulate rocks from Table Mountain
- . - Springers Hill harzburgites
- * - harzburgites from eastern Lewis Hills mantle section
- + - harzburgite from sliver accreted to base of eastern Lewis Hills mantle section
- 93 - layered ultramafic cumulates from profile NA 93 in North Arm Mountain (Komor et al. 1985)
- 49W - mainly wehrlites of layered ultramafic cumulate profile NA 49-50 (Elthon et al. 1984)
- 49D - dunites from layered ultramafic cumulate profile NA 49-50 (Elthon et al. 1984)
- LHI - intrusive peridotites from the Lewis Hills massif (Smith and Elthon 1988)

LOWER DIAGRAMS

- MT - main trend of Table Mountain mantle peridotites. Excludes samples from unit 1,2, transition zone, and ultramylonites as well as isolated data points
- U1,2 - range defined by samples from unit 1 and 2 , excluding TZ
- TZ - range defined by samples from transition zone (opx-free peridotites, marked x)
- SH - range defined by samples from Springers Hill (only where distinct)
- UMC - range defined by fields 93, 49W, 49D, i.e. layered ultramafic cumulates

INSETS

- PPM - progressive partial melting trend, inferred from MT-field
- ACT - apparent cumulate trend, inferred from UMC-field
- INF - melt infiltration trend, inferred from U1,2-field
- OL-F - olivine fractionation trend
- MIX - possible melt-mixing trend

(PPM, ACT, INF, OL-F, MIX: suggested or apparent trends)

- REQ - subsolidus reequilibration trend, inferred from core-rim relationships

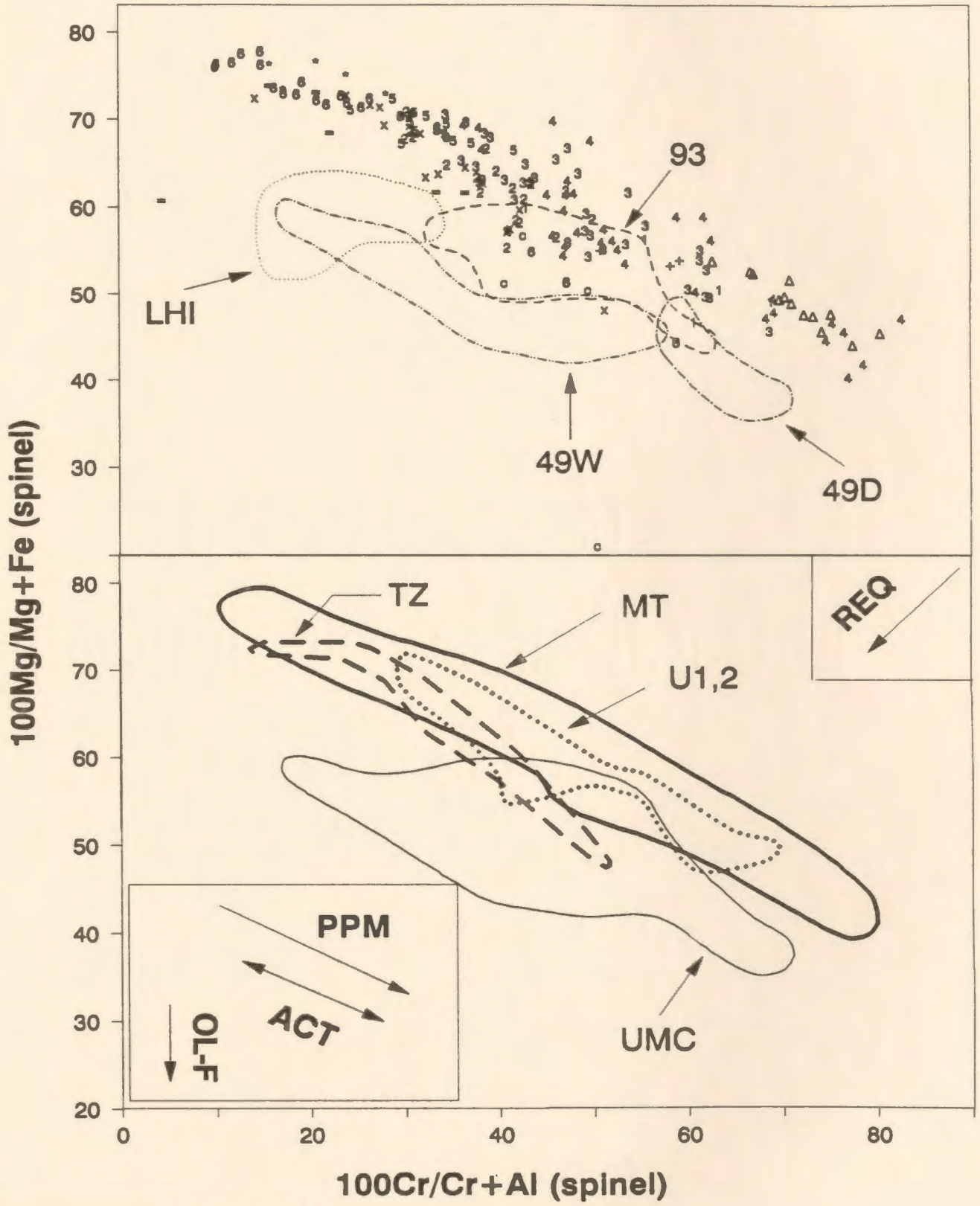

Fig. A5.7a. For legend see first page of figure.

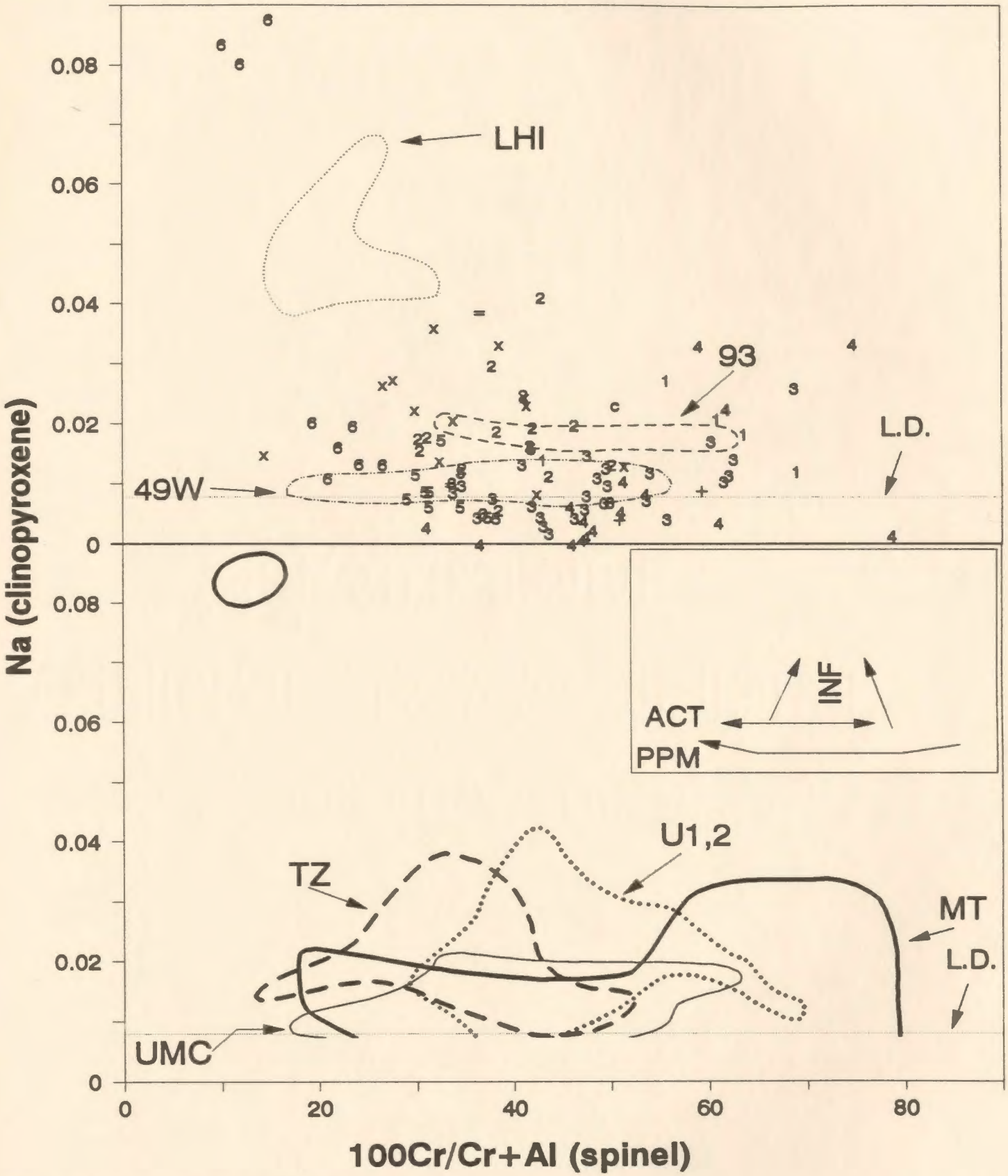

Fig. A5.7b. For legend see first page of figure.

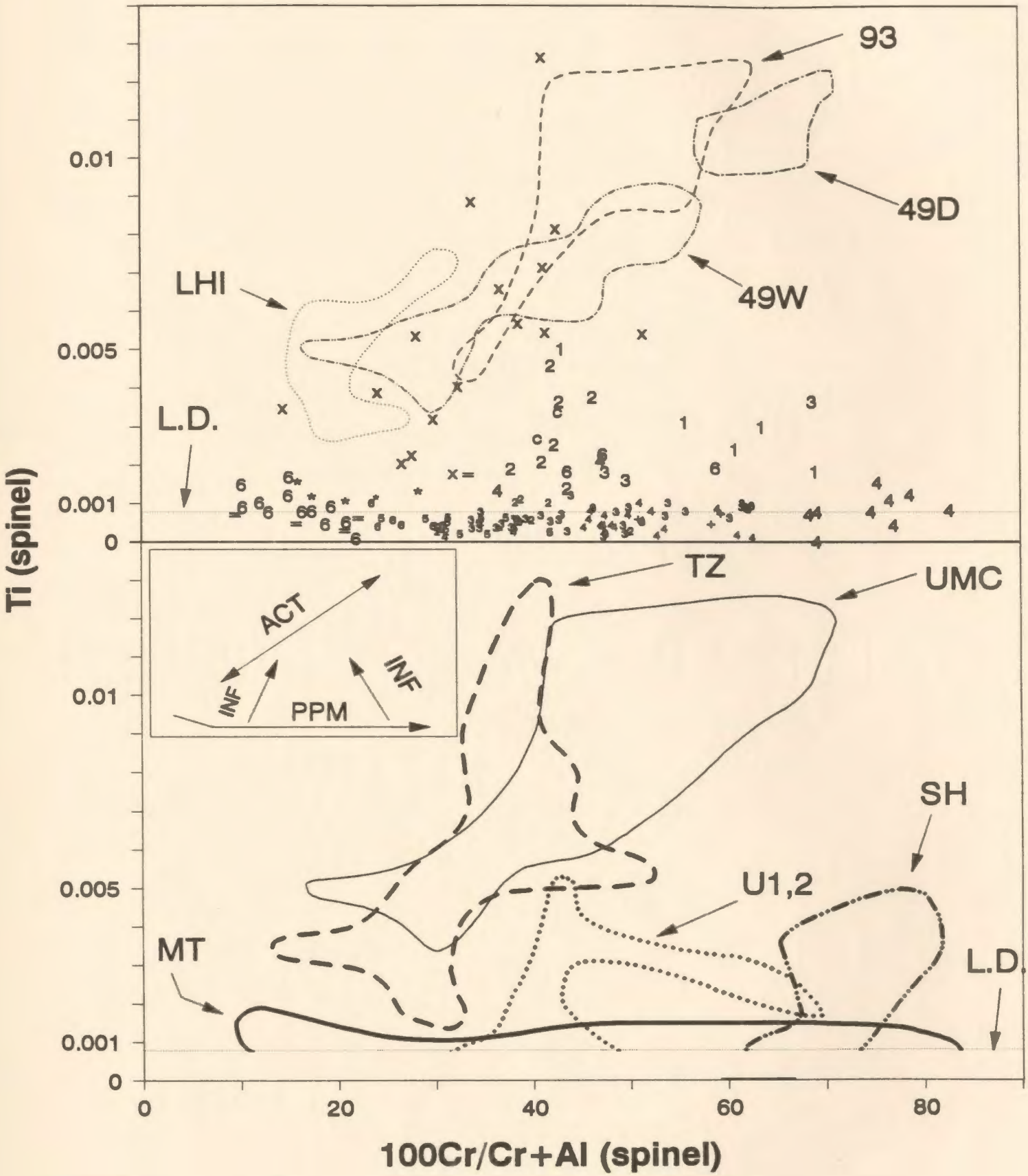

Fig. A5.7c. L.D. (in upper diagram) - limit of detection.
For legend see first page of figure.

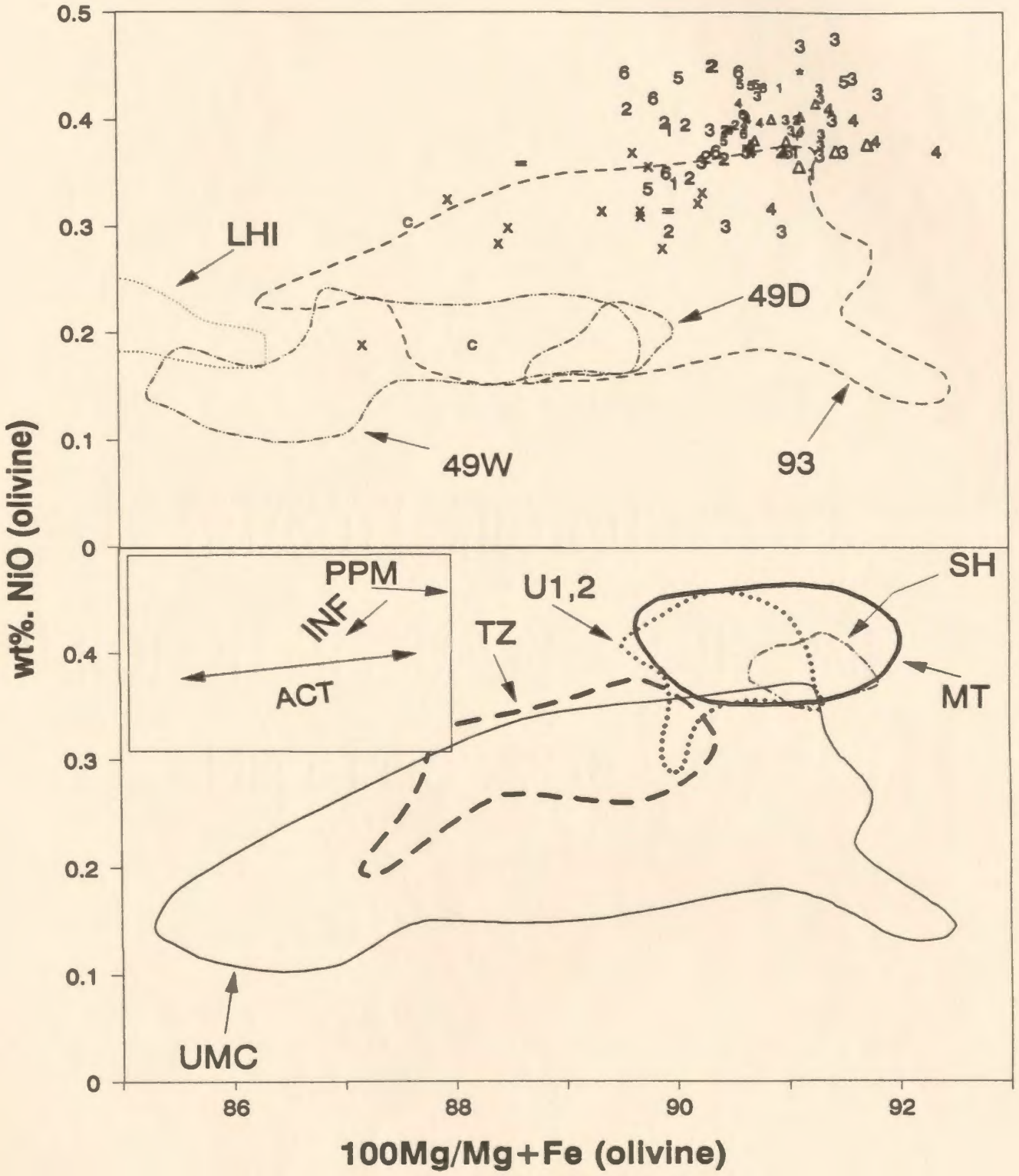

Fig. A5.7d. For legend see first page of figure.

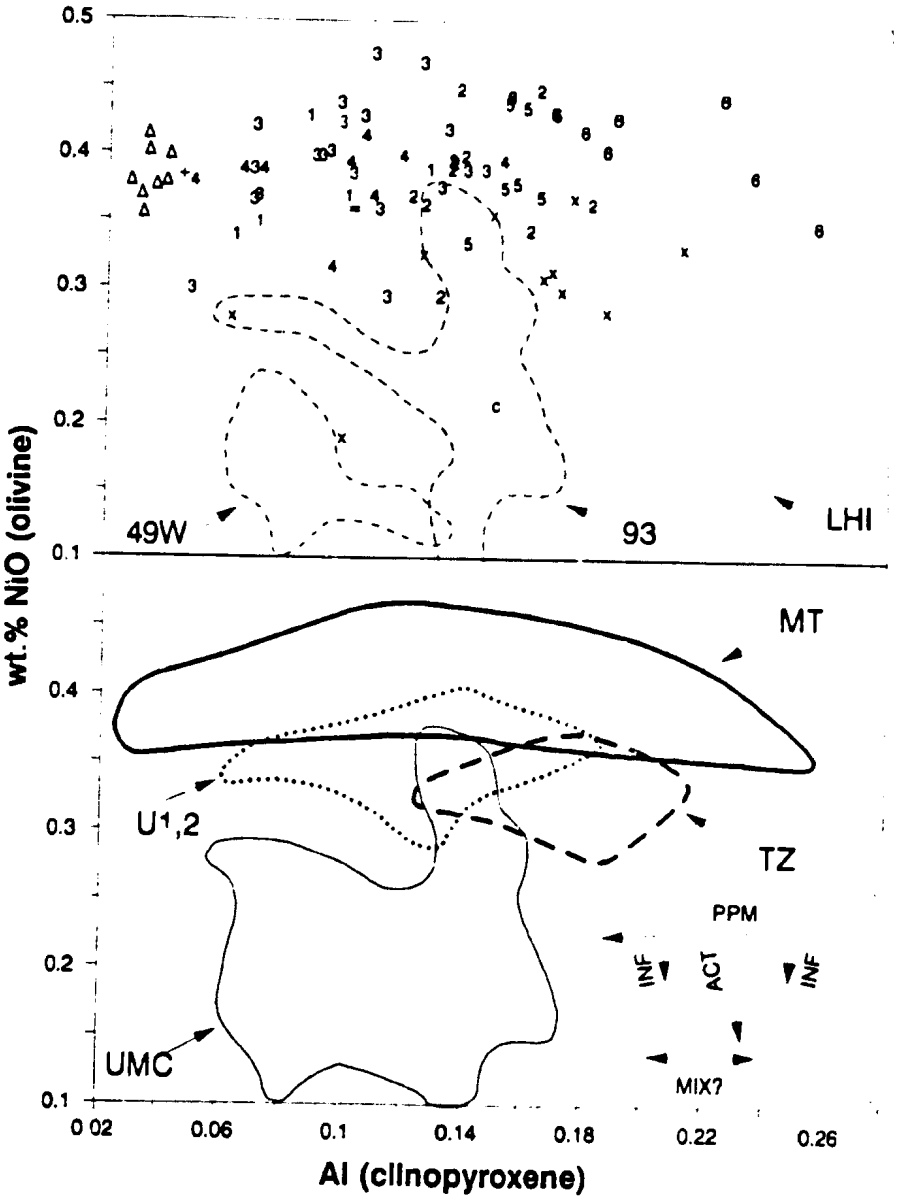

Fig. A5.7e. For legend see first page of figure.
Note that for the field 'TZ', two data points were not included as they plot in isolated positions.

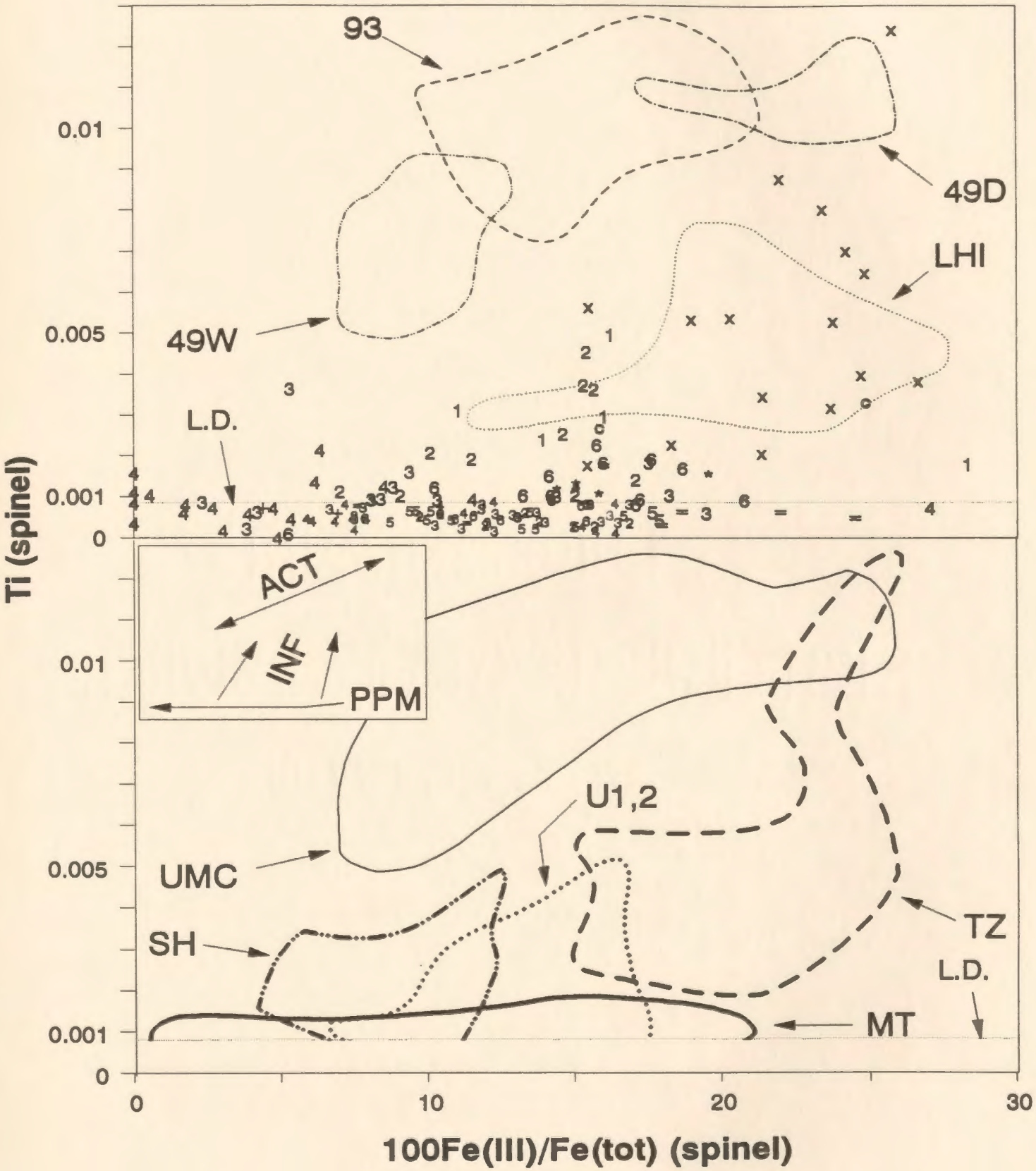

Fig. A5.7f. For legend see first page of figure.

APPENDIX B: GEOCHEMICAL METHODS AND TABLES

B.1. Whole Rock Analysis

Whole rock major element analyses were performed after acid dissolution on a Perkin Elmer atomic absorption spectrometer at Memorial University. The samples were prepared in a steel crusher followed by grinding in an agate holder. Dissolution of 0.1000g of the sample was performed with a combination of HF, H_3BO_3 and H_2O. P_2O_5 was determined by colorimetry. Loss of ignition represents the weight-loss after heating for several hours at 1000° C. In a few samples, ferrous iron was determined by titration with ammonium sulphate.

The HF-dissolution method was, however, not able to dissolve the majority of the spinel grains. This could be shown by comparing Cr_2O_3 values determined wet-chemically by AAS with values from the non-destructive X-ray fluorescence (XRF) method. Through the initiative of Steven Edwards, several samples were re-analyzed at the Newfoundland Department of Mines and Energy, Mineral Development Division, using a fusion method for dissolving the peridotites.

In the fusion method (S. Edwards, written comm.), 0.5g of lithium metaborate ($LiBO_2$) and 0.1g of sample are heated for one hour in a graphite crucible. The melt bead is transferred into a container with 25 ml of HCl (4%) and 5 ml of concentrated HF and is stirred for 1 ½ hours. at 90°C. After adding 50 ml of saturated boric acid (50g/l), the solution is heated for another 90 minutes at the same temperature. The solution is then allowed to cool, transferred to 100 ml flasks, and filled up exactly to that volume. Analyses is performed by atomic absorption spectroscopy (AAS). Matrix correction occurs with internal standards. The detection limit is 0.02 wt.%.

As can be seen from Fig. A5.1a[1], Al_2O_3 is significantly higher using the flux method compared to the acid dissolution. The correlation appears linear over the range of the Al_2O_3-values present. A best fit line for the relationship yields wt% Al_2O_3 (flux) = 1.42 wt% Al_2O_3 (acid dissolution). The determination of reference sample PCC-1 suggests that the flux data are more reliable (Fig.A5.1a, Tab. B-1). Al_2O_3-data which have not been determined with the flux method, have been recalculated using the correlation of Fig. A5.1a. The new Al_2O_3 values have been used together with Cr_2O_3 and NiO data (see below) to calculate a new sum (SUM 2, Tab. A5.1) for the major element analysis.

The elements Ni, Ca, Cr, V and Ti were determined on pressed powder pellets by X-ray florescence (XRF). A comparison of CaO determined by XRF with CaO determined by acid dissolution shows a generally good agreement (Fig. A5.1b, Tab. B-1). CaO of PCC-1 determined by AAS lies closer to the recommended value than CaO determined by XRF and is preferred.

The very low Ti-values in the region of several tens of ppm (Tab. A5.1) have been determined on a special, low-Ti calibration on the XRF. While an exact calibration of the instrument is difficult due to a lack of precisely determined reference material, background and peak-shape of Ti are free of interferences and allow an accurate peak measurement. The Ti-data should be seen mainly as *relative* abundance values (Geoff Veinott, pers. comm.).

---

1 Note that Figs. A5.1 and A5.2 are located within the figure collection of Appendix A.

B.2. Mineral Chemical Analyses

The mineral chemical data were determined with a JEOL JXA-50A electron microprobe at the Department of Earth Sciences, Memorial University. This wavelength dispersive instrument is equipped with three spectrometers. Analytical conditions were as followed: accelerating voltage 15 kV, beam current 22 nA, counting time 20 sec or 40,000 counts (whatever was reached first), beam diametre for focused analysis 1-2 micrometres, for defocused analysis approximately 20 micrometres. Data were corrected using the semi-empirical "alpha"-corrections. Calibration of the instrument was done with minerals of known composition. Care was taken to calibrate on materials whose major components closely matched those of the phases to be analyzed. Calibrations were checked numerous times before and during analysis with other minerals of known composition.

As can be seen from Tab. B-2 (see footnote on previous page), precision and accuracy are generally good for the silicates. Calcium and aluminum in orthopyroxene are, however, systematically too low compared to the recommended value of J-OPX (Tab. B-2c).

Spinels were analyzed using two different calibrations, one for aluminous spinels using reference mineral SPIN-B, the other for chromitiferous spinels using 53IN-8. As can be seen from Tab. A5.3a, analysis of aluminous spinel SPIN-B with a chromitiferous spinel calibration (and vice versa) led to very significant errors. As a result, analysis of unknown spinels with intermediate Al and Cr values yielded very different compositions depending upon which calibration was employed. In order to circumvent the problem, a correction scheme was developed. It assumes a non-linear increase of the error of a given element from the value measured for SPIN-B with a SPIN-B calibration (taken to be zero) to SPIN-B with a 53IN-8 calibration and vice versa (Fig.

A5.2). Spinel data were corrected using this scheme where necessary. Errors for spinels with intermediate compositions could be reduced though were not entirely eliminated. Ferric iron in spinel was calculated from total iron assuming spinel stoichiometry.

The limit of detection (L.D.) is considered to be three times the standard deviation of the background. It was evaluated recently for the MUN microprobe by Mengel (1987) and lies typically in the range of 0.03% wt%. Empirically, values above 0.05 wt% of an oxide became reproducible within 0.02 wt% if the analyses were repeated several times. The limit of quantification is generally considered as being 3.3 times the value of the L.D. Concentrations between 0.03 and 0.10 wt. % should thus be interpreted only qualitatively. In the diagrams of Figs. A5.6 and A5.7 values for Ti and sometimes Na are plotted even where they are below the L.D. This was done in order to demonstrate the relative abundance of samples with measureable Ti versus those without measureable Ti.

Tab. B-1 (following two pages). Whole rock major and trace element data from the analyzed samples of the Bay of Islands Complex. For details see Appendix B.1. $Fe_2O_3^t$ - total iron determined as ferric iron.

Tab. B-1

sample#	remark	SiO2	TiO2	Al2O3	Fe2O3t	MnO	MgO	CaO	Na2O	K2O	P2O5	LOI	SUM1
C863A		40.20	0.00	0.34	7.39	0.11	40.66	0.36	0.03	0.00	0.00	10.09	99.18
LH 7	CaCO3?	36.50	0.00	0.12	7.55	0.10	41.35	1.24	0.03	0.00	0.02	11.94	98.85
LH 73		36.90	0.00	0.20	7.48	0.10	41.35	0.30	0.02	0.00	0.00	13.32	99.67
LH 87		38.10	0.00	0.18	7.80	0.11	42.42	0.46	0.03	0.00	0.01	11.08	100.19
TM 58.24		38.80	0.00	0.52	7.48	0.10	42.44	0.68	0.01	0.00	0.00	8.43	98.46
TM 82.77		38.00	0.00	0.48	7.39	0.10	39.47	0.95	0.01	0.00	0.01	11.92	98.33
TM 107		36.30	0.00	0.14	7.69	0.10	41.05	0.22	0.02	0.00	0.00	13.26	98.78
TM 216		39.00	0.00	0.60	7.27	0.10	39.51	0.73	0.01	0.00	0.01	11.90	99.13
TM 233.10		36.70	0.00	0.32	7.85	0.10	41.84	0.38	0.01	0.00	0.00	11.90	99.10
TM 245		41.80	0.04	1.60	8.20	0.12	39.60	1.94	0.03	0.00	0.00	6.87	100.20
TM 290		36.30	0.00	0.30	7.82	0.11	41.87	0.50	0.02	0.01	0.00	11.82	98.75
TM 315		36.70	0.00	0.18	7.26	0.10	41.48	0.18	0.02	0.01	0.00	12.42	98.35
TM 458		35.90	0.00	0.16	7.64	0.10	41.47	0.30	0.01	0.00	0.01	13.43	99.02
TM 496		38.60	0.00	0.24	7.82	0.11	43.77	0.30	0.01	0.01	0.00	8.19	99.05
TM 509		39.40	0.00	0.88	7.58	0.11	39.12	1.68	0.02	0.01	0.02	9.72	98.54
TM 534		40.40	0.00	1.16	7.73	0.10	37.93	1.83	0.02	0.00	0.00	9.57	98.74
TM 564		39.30	0.00	0.50	7.67	0.10	39.90	0.72	0.01	0.00	0.01	10.95	99.16
TM 599		39.30	0.00	0.86	7.88	0.11	38.91	1.32	0.02	0.00	0.00	9.80	98.20
TM 613		41.40	0.00	1.36	7.97	0.10	38.52	1.73	0.03	0.00	0.00	8.44	99.55
TM 676		37.10	0.00	0.30	7.31	0.10	41.00	0.48	0.01	0.00	0.00	12.83	99.13
TM 749		38.40	0.00	0.60	7.07	0.10	40.55	0.59	0.02	0.00	0.00	11.45	98.78
TM 774		39.50	0.00	0.50	7.33	0.10	40.44	0.58	0.01	0.00	0.00	11.13	99.59
TM 827		38.50	0.00	0.90	7.72	0.10	40.11	1.11	0.01	0.00	0.00	9.73	98.18
TM 869		37.80	0.00	0.36	7.61	0.10	39.58	0.86	0.03	0.00	0.01	12.86	99.21
TM 884		40.00	0.00	0.76	7.83	0.11	40.00	1.26	0.03	0.00	0.01	9.16	99.16
TM 941		38.70	0.00	1.72	7.59	0.12	38.17	2.34	0.28	0.03	0.15	9.56	98.66
TM 966	dunite												
TM 1029.11		42.30	0.00	2.44	8.18	0.12	37.40	2.92	0.14	0.00	0.01	4.76	98.27
TM 1043.2		39.80	0.00	0.88	7.16	0.10	39.20	1.76	0.03	0.00	0.01	9.56	98.50
TM 1062		40.40	0.00	1.20	8.69	0.11	40.40	2.10	0.07	0.00	0.00	4.30	97.27
TM 1065		39.80	0.00	0.72	7.64	0.11	40.39	1.01	0.01	0.00	0.00	9.58	99.26
TM 1118		40.40	0.00	0.74	8.02	0.11	39.20	1.36	0.03	0.00	0.00	9.63	99.49
TM 1141		35.90	0.00	0.24	7.65	0.10	41.94	0.27	0.01	0.00	0.00	12.79	98.90
TM 1143		39.10	0.00	0.60	7.63	0.11	39.73	0.94	0.01	0.00	0.00	10.51	98.63
TM 1145		38.00	0.00	0.52	7.71	0.11	39.43	1.06	0.01	0.00	0.00	10.22	97.06
TM 1165.2		37.70	0.00	0.36	7.62	0.10	40.10	1.16	0.01	0.00	0.01	11.89	98.95
TM 1169	dunite	34.60	0.00	0.08	6.69	0.08	42.00	0.14	0.01	0.00	0.03	14.80	98.43
TM 1181		38.90	0.00	0.72	7.82	0.11	40.28	1.32	0.01	0.00	0.00	9.03	98.19
TM 1189.1	nxt pxt	38.50	0.00	0.33	7.70	0.10	40.45	0.64	0.02	0.00	0.00	11.74	99.48
TM 1189.2	far pxt	39.10	0.00	0.52	7.32	0.11	40.56	0.91	0.01	0.00	0.00	10.71	99.24
TM 1195		39.10	0.00	0.58	7.28	0.11	38.81	1.24	0.02	0.00	0.00	11.00	98.14
TM 1200		37.70	0.00	0.39	7.35	0.10	40.30	0.40	0.02	0.00	0.01	12.35	98.62
TM 1214		41.00	0.00	1.84	7.97	0.11	38.80	2.20	0.10	0.00	0.06	6.46	98.54
TM 1225		42.00	0.00	1.66	7.71	0.11	38.20	2.03	0.12	0.00	0.00	6.38	98.21
TM 1228.1		38.70	0.00	1.60	8.78	0.12	36.09	1.92	0.03	0.00	0.00	10.47	97.71
TM 1232		39.10	0.00	0.58	6.81	0.10	40.00	0.32	0.01	0.00	0.04	11.83	98.79
TM 1249		38.40	0.00	0.36	7.51	0.10	40.10	0.66	0.01	0.00	0.01	11.45	98.60
TM 1262		41.00	0.00	0.88	7.39	0.11	38.77	1.92	0.02	0.00	0.00	8.44	98.53
TM 1315		37.80	0.00	0.30	7.38	0.10	42.11	0.48	0.01	0.00	0.10	10.74	99.02
TM 1316	dunite	33.60	0.00	0.15	8.52	0.11	41.25	0.12	0.01	0.00	0.01	14.13	97.91
TM 1331.1		33.80	0.00	1.30	8.53	0.11	39.16	1.20	0.03	0.00	0.01	13.72	97.86
TM 1350		38.50	0.00	0.69	7.32	0.10	39.16	1.16	0.01	0.00	0.00	11.45	98.39
TM 1152.2	amph	45.70	0.28	17.90	5.16	0.09	8.35	15.50	1.25	1.08	0.01	3.68	99.00
TM 1228.2	amph	41.50	0.04	18.20	3.29	0.06	10.10	20.30	0.02	0.01	0.00	6.95	100.47
PCC1		42.70	0.00	0.45	8.05	0.12	43.95	0.56	0.01	0.00	0.00		
PCC1		41.30	0.00	0.48	8.10	0.12	42.69	0.50	0.01	0.00	0.00		
PCC1	(2)	41.90	0.00	0.64	8.16	0.12	44.48	0.53	0.01	0.00	0.01		
PCC1	(2)	41.60	0.00	0.66	8.11	0.13	43.59	0.53	0.01	0.00	0.01		
PCC-1, recommended (4)		41.67	0.013	0.67	8.25	0.12	43.43	0.52	0.027	0.007	0.002		

all elements, apart from (3), are analyzed by AAS; for further details see text
(1) includes Cr2O3, NiO and corrected Al2O3 (see text)
(2) analyzed after dissolution with flux
(3) analyzed by XRF
(4) Govindaraju (1989)

Tab. B-1 (continued)

sample#	SUM2 (1)	Fe2O3	FeO	Al2O3 (2)	Ni ppm(3)	TiO2 ppm(3)	CaO (3)	Cr ppm(3)	V ppm(3)
C863A	99.91	2.76	4.17		1967	56	0.35	2365	17
LH 7	99.47	3.27	3.86		2116	62	1.34	2479	8
LH 73	100.50	3.62	3.48		2062	52	0.35	2864	16
LH 87	100.80	3.17	4.17	0.22	1963	59	0.61	1560	5
TM 58.24	99.28	2.27	4.69		2226	51	0.8	2616	34
TM 82.77	99.06				2118	48	0.82	2545	29
TM 107	99.31	3.92	3.39		2065	45	0.32	2078	14
TM 216	100.03				2046	50	0.76	2646	38
TM 233.10	99.78	3.89	3.56		2212	44	0.46	2003	20
TM 245	101.61	2.45	5.18		1952	108	2	2628	63
TM 290	99.42	3.02	4.32		2192	48	0.57	2261	23
TM 315	98.91	3.23	3.63		2091	53	0.25	2414	4
TM 458	99.55	3.75	3.51		2177	46	0.42	1700	15
TM 496	99.79	1.87	5.36		2297	44	0.4	2524	14
TM 509	99.52				2030	64	1.65	2703	46
TM 534	99.87				1975	80	1.71	2783	58
TM 564	99.67			0.74	2110	53	0.77	289	33
TM 599	99.05			1.17	2079	66	1.22	2520	40
TM 613	100.49			1.59	2041	93	1.67	2773	62
TM 676	99.89			0.49	2158	51	0.64	2130	12
TM 749	99.59				2164	56	0.78	2270	23
TM 774	100.48				2087	69	0.73	2462	25
TM 827	99.06			1.20	2079	71	1.23	2803	44
TM 869	99.95			0.49	1995	69	0.84	2492	35
TM 884	100.09			1.06	2081	76	1.3	2461	49
TM 941	99.55			2.00	1900	231	2.76	2812	59
TM 966					8516	78	0.44	15650	71
TM 1029.11	99.49			3.05	1876	420	3.21	2739	78
TM 1043.2	99.48				2023	81	1.78	2745	47
TM 1062	98.37				2107	185	2.51	2749	62
TM 1065	100.22				2056	58	1.07	2599	37
TM 1118	100.51			1.05	2006	71	1.52	2758	58
TM 1141	99.47			0.34	2164	48	0.43	1792	15
TM 1143	99.46				2034	53	0.99	2574	43
TM 1145	97.81				2172	51	1.2	3257	49
TM 1165.2	99.75	3.36	3.83		2139	47	0.61	2796	27
TM 1169	98.89				2352	43	0.14	2001	8
TM 1181	99.21			1.17	2081	62	1.36	2572	43
TM 1189.1	100.20	3.68	3.60	0.37	2056	53	0.46	2704	30
TM 1189.2	100.32			0.93	2045	56	0.94	2580	29
TM 1195	99.06			0.94	1931	54	1.36	2865	51
TM 1200	99.35	3.78	3.21		2064	48	0.53	2605	25
TM 1214	99.98			2.64	1913	188	2.59	2750	69
TM 1225	99.51				2020	250	2.35	2601	66
TM 1228.1	99.39				2117	101	1.79	5494	90
TM 1232	99.47	3.47	3.01	0.70	2155	47	0.52	2358	20
TM 1249	99.23			0.43	2126	44	0.58	2574	28
TM 1262	99.56				1954	59	2.04	3079	53
TM 1315	99.74			0.40	2149	62	0.55	2538	14
TM 1316	99.65			1.18	1976	68	0.13	3472	19
TM 1331.1	99.10			1.98	2163	63	1.23	2799	22
TM 1350	99.27				1928	58	1.29	2958	53
TM 1152.2					141	125	17.29	546	150
TM 1228.2		0.06	3.23		338	188	19.76	1749	99
PCC1					2380	84	0.65	2867	26
PCC1		2.22	5.29		2368	88	0.64	2860	30
PCC1				0.64	2344	87	0.63	2830	26
PCC1				0.66	2263	90	0.80	2931	42
					2264	93	0.81	2944	40
PCC-1, rec		2.72	5.0		2380			2730	31

Tab. B-2a-d (following four pages). Results of multiple determinations of mineral standards on the MUN microprobe during this study. (a) Spinels; (b) clinopyroxenes; (c) orthopyroxene; (d) olivines; Fe(III) was calculated assuming spinel stoichiometry.

avg	-	average;
std	-	standard deviation;
rsd	-	relative standard deviation;
Cr#	-	100Cr/Cr+Al;
Mg#	-	100Mg/Mg+Fe^{tot};
Fe#	-	100Fe(III)/Fe^{tot};
Fe_2O_3c	-	wt.% Fe_2O_3, calculated from Fe(III) data;
FeOc	-	wt.% FeO, calculated from Fe(III) and Fe^{tot} data.

Tab. B-2a

mineral	mineral	N	TiO2	Al2O3	Cr2O3	Fe tot	MgO	MnO	NiO	V2O5	SUM
SPIN-B	avg	83	0.07	59.37	7.99	10.71	20.71	0.09	0.40	0.10	99.41
SPIN-B	std		0.01	0.49	0.14	0.27	0.25	0.02	0.06	0.02	0.74
SPIN-B	rsd		19	1	2	3	1	17	14	17	1
SPIN-B	published		0.09	59.40	8.05	10.69	20.84	0.09			99.24
53IN8	avg	110	1.34	12.81	49.23	28.10	6.13	0.26	0.08	1.34	99.01
53IN8	std		0.04	0.30	0.58	0.59	0.22	0.06	0.02	0.05	1.08
53IN8	rsd		3	2	1	2	4	22	28	4	1
53IN8	published		1.60	12.82	49.31	28.15	6.12	0.32	0.06	1.11	99.53
SPIN B with 53	avg	14	0.07	52.88	8.52	11.18	17.41	0.08	0.34	0.08	90.44
SPIN B with 53	std		0.01	1.10	0.20	0.54	0.58	0.02	0.08	0.02	1.35
SPIN B	published		0.09	59.40	8.05	10.69	20.84	0.09			99.24
53 with SPIN B	avg	8	1.32	14.41	45.65	26.42	7.34	0.27	0.11	1.29	96.80
53 with SPIN B	std		0.03	0.26	0.52	1.00	0.14	0.02	0.04	0.03	1.68
53 with SPIN B	published		1.60	12.82	49.31	28.15	6.12	0.32	0.06	1.11	99.53

mineral	mineral	N	Ti	Al	Cr	Fetot	Mg	Mn	Ni	V
SPIN-B	avg	83	0.0014	1.8005	0.1626	0.2304	0.7938	0.0019	0.0077	0.0016
SPIN-B	std		0.0003	0.0069	0.0031	0.0058	0.0046	0.0003	0.0025	0.0005
SPIN-B	rsd		19	0	2	3	1	17	32	34
SPIN-B	published		0.0017	1.8029	0.1639	0.2301	0.7994	0.0020	0.0000	0.0000
53IN8	avg	110	0.0341	0.5110	1.3174	0.7950	0.3093	0.0074	0.0018	0.0239
53IN8	std		0.0009	0.0097	0.0147	0.0123	0.0118	0.0016	0.0011	0.0120
53IN8	rsd		3	2	1	2	4	22	59	50
53IN8	published		0.0405	0.5094	1.3141	0.7932	0.3073	0.0091	0.0016	0.0247

mineral	mineral	N	Fe(III)	Fe(II)	Cr#	Mg#	Fe#	Fe2O3c	FeOc
SPIN-B	avg	83	0.0293	0.2011	8.28	79.79	12.70	1.51	9.31
SPIN-B	std		0.0059	0.0052	0.17	0.51	2.39	0.31	0.22
SPIN-B	rsd		20	3	2	1	19	20	2
SPIN-B	published		0.0297	0.2004	8.33	79.96	12.91	1.53	9.27
53IN8	avg	110	0.0317	0.7634	72.05	28.86	3.97	1.23	26.87
53IN8	std		0.0306	0.0314	0.54	1.56	3.84	1.18	1.31
53IN8	rsd		97	4	1	5	97	96	5
53IN8	published		0.0213	0.7719	72.07	28.47	2.68	0.84	27.31

Tab. B-2b

mineral		N	SiO2	TiO2	Al2O3	Cr2O3	FeO	MgO	MnO	CaO	NiO	Na2O	K2O	SUM
ACPX	avg	49	50 49	0 77	7 72	0 15	6 25	16 24	0 12	15 88	0 04	1 30	0 01	98 98
ACPX	std		0 67	0 05	0 13	0 02	0 32	0 27	0 02	0 24	0 03	0 07	0.01	1 08
ACPX	rstd		1	6	2	13	5	2	20	1	62	5	111	1
ACPX	published		50 73	0 74	7 86		6 77	16 65	0 14	15 82		1 27		99 98
WCPX	avg	58	51 75	0.47	4 94	0 60	4 01	15 77	0 08	20 81	0 06	0 84	0 00	99 33
WCPX	std		0 69	0 03	0 10	0 05	0 20	0 25	0 02	0 23	0 03	0 07	0 00	0 95
WCPX	rstd		1	7	2	9	5	2	21	1	49	9		1
WCPX	published		51 40	0 53	5.51	0 61	3 80	16 07	0 08	21 06	0 06	0.95	0 05	99 03
FCPX	avg	6	50 19	0 76	7 61	0.02	6 05	15 54	0 10	17 53	0 04	1 15	0 01	99 00
FCPX	std		0 26	0 04	0 22	0 01	0 18	0 23	0 01	0.15	0 01	0 15	0 01	0 29
FCPX	rstd		1	5	3	71	3	1	13	1	29	13	100	0
FCPX	published		49 85	0.83	7 86		6 17	15 47	0 14	17.75		1 27		99 34

mineral		N	Si	Ti	Al	Cr	Fe	Mg	Mn	Ca	Ni	Na	%en	%woll	%fs	Mg#
ACPX	avg	49	1 8491	0.0213	0 3336	0 0043	0.1914	0 8863	0 0039	0 6234	0 0012	0 0925	52 1	36 6	11 3	82 2
ACPX	std		0.0104	0.0013	0 0039	0 0006	0 0096	0 0132	0 0008	0 0090	0 0007	0 0040	0 6	0 5	0 5	0 8
ACPX	rstd		1	6	1	13	5	1	20	1	62	4	1	1	4	1
ACPX	published		1 8419	0 0202	0.3366	0.0000	0.2056	0 9010	0 0043	0.6155	0 0000	0 0894	52 3	35.7	11 9	81 4
WCPX	avg	58	1 8963	0 0129	0 2135	0 0174	0.1230	0 8611	0 0026	0 8174	0 0016	0 0598	47 8	45 4	6 8	87 5
WCPX	std		0.0083	0.0009	0.0040	0 0016	0 0062	0.0104	0 0005	0.0119	0 0008	0.0049	0 6	0 4	0.3	0 6
WCPX	rstd		0	7	2	9	5	1	21	1	49	8	1	1	5	1
WCPX	published		1 8711	0.0145	0.2366	0 0176	0 1157	0 8718	0 0025	0 8214	0 0018	0.0671	48 2	45 4	6 4	88.3
FCPX	avg	6	1 8447	0.0209	0 3300	0 0006	0.1859	0.8514	0 0032	0.6904	0.0011	0 0820	49 3	40 0	10 8	82.1
FCPX	std		0.0033	0.0011	0 0097	0.0004	0.0058	0.0116	0 0004	0.0055	0.0003	0.0105	0 4	0 1	0 4	0 7
FCPX	rstd		0	5	3	70	3	1	13	1	29	13	1	0	4	1
FCPX	published		1.8301	0.0229	0 3404	0.0000	0.1894	0.8464	0 0044	0.6982	0.0000	0 0904	48.8	40.3	10.9	81.7

Tab. B-2c

mineral		N	SiO2	TiO2	Al2O3	Cr2O3	FeO	MgO	MnO	CaO	NiO	Na2O	SUM
J-OPX	avg	106	53.83	0.09	0.87	0.71	15.32	28.86	0.45	1.29	0.02	0.02	99.47
J-OPX	std		0.75	0.02	0.06	0.05	0.51	0.32	0.05	0.10	0.02	0.01	1.17
J-OPX	rstd		1	23	7	6	3	1	12	8	114	64	1
J-OPX	published		54.09	0.16	1.23	0.75	15.22	28.79	0.49	1.52		0.13	100.38

mineral		N	Si	Ti	Al	Cr	Fe	Mg	Mn	Ca	Ni	Na	%wo	%fs	Mg#
J-OPX	avg	106	1.9594	0.0024	0.0375	0.0205	0.4665	1.4574	0.0139	0.0502	0.0004	0.0013	2.5	23.6	75.8
J-OPX	std		0.0102	0.0005	0.0024	0.0012	0.0144	0.0158	0.0016	0.0037	0.0005	0.0009	0.2	0.6	0.6
J-OPX	rstd		1	22	7	6	3	1	12	8	114	70	8	3	1
J-OPX	published		1.9514	0.0043	0.0523	0.0214	0.4592	1.4404	0.0149	0.0587	0	0.0090	3.0	23.4	75.8

Tab. B-2d

mineral		N	SiO2	Cr2O3	FeO	MgO	CaO	NiO	SUM
SWOL	avg	42	38 98	0.03	16 71	43.57	0.01	0 02	99.33
SWOL	std		0 28	0.01	0.25	0.23	0 01	0 02	0.46
SWOL	rstd		1	38	1	1	85	72	0
SWOL	published		38 95	0 02	16 62	43.58			
MOL	avg	101	39 95	0.05	11 39	48.00	0.02	0 02	99 44
MOL	std		0 29	0.01	0 33	0.38	0 01	0.01	0.61
MOL	rstd		1	25	3	1	35	80	1
MOL	published		40.24	0 07	11 53	48 08			
P140	avg	4	41.28	0.01	7 18	50 29	0.01	0 36	99.13
P140	published		40 85		7.17	51.63		0 30	

mineral		N	Si	Cr	Fe	Mg	Ca	Ni	Mg#
SWOL	avg	42	0 9936	0 0006	0 3561	1 6550	0.0003	0 0005	82 3
SWOL	std		0 0048	0.0003	0 0048	0 0072	0 0002	0 0003	0 2
SWOL	rstd		0	49	1	0	82	69	0 2
SWOL	published		0 9938	0 0004	0.3546	1.6571	0.0000	0.0000	82 4
MOL	avg	101	0 9922	0 0010	0.2366	1.7765	0 0006	0.0004	88.2
MOL	std		0 0070	0.0003	0.0063	0 0093	0 0002	0 0003	0.3
MOL	rstd		1	25	3	1	35	80	0 3
MOL	published		0 9944	0 0014	0 2383	1.7708	0 0000	0 0000	88.1
P140	avg	4	1 0079	0 0002	0 1466	1 8300	0.0003	0 0071	92.6
P140	published								

Tab. B-3 (following fifteen pages). Spinel mineral chemistry data from (a) the Table Mountain section and (b) the Lewis Hills mantle section.

Column 'rock type':

no entry - indicates a harzburgitic lithology.

Otherwise, an abbreviation is added:

amp-hz	-	amphibole-bearing harzburgite;
chrom	-	chromite seam;
cpx-du	-	clinopyroxene-bearing dunite;
du	-	dunite;
du-hz	-	dunite-harzburgite contact preserved within one sample;
lherz	-	lherzolite;
lh-band	-	lherzolite band within one sample;
nxt opxte	-	sample located next to orthopyroxenite dyke;
far opxte	-	sample located several metres away from orthopyroxenite;
ol-cpxte	-	olivine clinopyroxenite;
opxte	-	orthopyroxenite;
opx So	-	orthopyroxene-rich band in harzburgite;
pl-hz	-	plagioclase-bearing harzburgite;
pl wehrl	-	plagioclase-bearing wehrlite;
trans	-	transitional area between two lithologies in one sample;
troc	-	troctolite;
umyl	-	ultramylonite from the basal peridotite section;

Column 'unit': indicates structural unit number; CUM - from layered cumulate section.

Column 'spot': the spot-number assigned to each analyses is indicated.

Column 'comment': an (N) indicates normal Cr-Al spinel zoning, and (R) indicates reverse Cr-Al spinel zoning. Normal zoning involves an increase in Al and a decrease of Cr towards the rim of the grain. The abbreviation 'var' ("variable") indicates that repeated analyses has indicated an unusually large chemical range for the given spot or calculated average. The elements affected are listed in front of 'var'.

Column 'N': entries indicate the number of analyses per spot and number of analyses included in the average.

Tab. B-3a

rocktype	unit	sample	spot	comment	N	TiO2	Al2O3	Cr2O3	Fe tot	MgO	MnO	NiO	V2O5	SUM
umyl	6	BOB	?	rim	1	0.04	60.37	4.23	19.11	15.46	0.11	0.30	0.09	99.71
umyl	6	BOB	6	brown sp	1	0.04	41.24	25.62	16.09	15.94	0.12	0.17	0.15	99.37
umyl	6	BOB	3	incl in cpx	2	0.03	62.18	1.82	20.34	15.38	0.12	0.29	0.07	100.23
umyl	6	BOB	1	core	2	0.04	61.68	4.00	19.07	15.82	0.14	0.29	0.08	101.12
umyl	6	BOB	avg	all var	6	0.04	56.37	8.92	18.65	15.65	0.12	0.26	0.10	100.11
du	4	6c	3		1	0.10	14.12	51.73	22.43	9.92	0.29	0.02	0.35	98.96
du	4	6c	2	rim	2	0.06	13.73	49.11	27.18	8.48	0.30	0.09	0.36	99.31
du	4	6c	1	core	3	0.08	14.64	52.48	21.41	10.38	0.24	0.07	0.35	99.65
du	4	6c	1	rim	2	0.07	15.86	48.18	23.99	9.70	0.27	0.11	0.35	98.53
du	4	6c	avg	(N)	8	0.08	14.59	50.38	23.75	9.62	0.28	0.07	0.35	99.11
du	1	7.1	5		1	0.53	30.92	31.27	25.30	12.93	0.21	0.19	0.25	101.60
du	1	7.1	4	core	3	0.55	30.71	32.64	21.83	13.81	0.21	0.17	0.23	100.15
du	1	7.1	4	rim	3	0.56	30.45	32.07	23.36	13.30	0.23	0.14	0.21	100.32
du	1	7.1	3	core	1	0.60	30.36	30.93	23.82	12.63	0.21	0.08	0.30	98.93
du	1	7.1	avg	(N)	8	0.56	30.61	31.73	23.58	13.17	0.22	0.15	0.25	100.25
troc	CUM	7.3	5	rim to plag	1	1.13	24.61	36.16	26.68	11.78	0.24			100.60
troc	CUM	7.3	5	rim to ol	1	1.34	24.24	35.57	26.82	11.93	0.16			100.06
troc	CUM	7.3	3	incl in plag	2	1.38	24.47	34.66	28.32	11.43	0.29			100.55
troc	CUM	7.3	3	in ol mx	2	1.40	23.39	35.68	30.13	10.20	0.28			101.08
troc	CUM	7.3	3	rim to plag	1	1.47	23.92	34.51	28.10	11.42	0.27			99.69
troc	CUM	7.3	avg		7	1.34	24.13	35.32	28.01	11.35	0.25			100.40
pl wehrl	CUM	7.5	8		2	2.17	17.51	23.95	51.05	5.02	0.34			100.04
pl wehrl	CUM	7.5	6	rim to cpx/pl	1	2.48	15.32	24.05	54.67	3.60	0.48			100.60
pl wehrl	CUM	7.5	4		1	2.29	16.52	26.90	49.38	4.93	0.39			100.41
pl wehrl	CUM	7.5	avg		4	2.31	16.45	24.97	51.70	4.52	0.40			100.35
ol-cpxte	CUM	7.8	2	in ol	1	0.09	31.80	31.66	25.18	10.28	0.25	0.04	0.28	99.58
ol-cpxte	CUM	7.8	1	incl in cpx	3	0.15	31.59	33.00	21.17	12.86	0.14	0.18	0.25	99.34
ol-cpxte	CUM	7.8	avg		4	0.12	31.70	32.33	23.18	11.57	0.20	0.11	0.27	99.46
hz	3	194.16dl	1	core	1	0.03	20.84	47.88	21.16	11.10	0.02	0.17	0.29	101.49
hz	3	194.16dl	1	rim	1	0.02	21.58	46.98	21.31	10.94	0.07	0.07	0.29	101.26
hz	3	194.16dl	2	core	1	0.04	21.38	47.05	18.27	11.62	0.25	0.07	0.29	98.97
hz	3	194.16dl	5		1	0.00	22.31	45.21	19.46	11.30	0.15	0.10	0.29	98.82
hz	3	194.16dl	avg	hz (N)	4	0.02	21.53	46.78	20.05	11.24	0.12	0.10	0.29	100.14
du	3	194.16dr	1	core	2	0.03	19.86	47.80	19.27	11.54	0.25	0.10	0.31	99.16
du	3	194.16dr	1	rim	2	0.00	20.58	47.18	20.28	11.30	0.23	0.09	0.27	99.93
du	3	194.16dr	2		1	0.04	19.18	46.78	21.75	10.44	0.21	0.05	0.27	98.72
du	3	194.16dr	avg	du	5	0.02	19.87	47.25	20.43	11.09	0.23	0.08	0.28	99.27
du	4	26	4	core	2	0.11	10.26	58.51	20.04	9.32	0.20	0.04	0.18	98.66
du	4	26	4	rim	2	0.12	9.87	58.91	21.27	9.07	0.30	0.05	0.18	99.77
du	4	26	2	aw opx	1	0.09	10.01	58.57	21.82	9.07	0.29	0.06	0.20	100.11
du	4	26	1		2	0.12	10.31	58.02	22.22	8.55	0.21	0.05	0.21	99.69
du	4	26	avg	(R)	3	0.11	10.11	58.50	21.34	9.00	0.25	0.05	0.19	99.56
	4	49	3		1	0.00	19.66	48.95	20.14	12.02	0.17			100.94
	4	49	2		2	0.01	19.41	48.27	19.80	12.10	0.26			99.85
	4	49	avg		3	0.01	19.54	48.61	19.97	12.06	0.22			100.40
	TU	58.24	8b	rim	1	0.04	38.84	28.51	13.09	17.58	0.14			98.20
	TU	58.24	8c	rim	1	0.04	27.90	42.35	14.73	15.84	0.13			100.99
	TU	58.24	8a	core	2	0.02	27.38	42.73	15.73	15.63	0.23			101.72
	TU	58.24	6d	core	2	0.03	29.43	40.00	14.78	15.63	0.13			100.00
	TU	58.24	6c	rim	2	0.03	30.98	38.45	15.02	16.01	0.20			100.69
	TU	58.24	6b	rim	2	0.07	30.96	38.88	15.00	16.20	0.17			101.28
	TU	58.24	6a	core	2	0.04	29.10	40.45	15.73	15.58	0.19			101.09
	TU	58.24	5		1	0.06	33.62	35.03	14.23	16.52	0.16			99.62
	TU	58.24	4a	core	4	0.01	33.25	35.77	13.94	16.93	0.14			100.04
	TU	58.24	3	rim	2	0.04	33.44	35.88	13.86	16.81	0.17			100.20
	TU	58.24	avg	(N)	18	0.04	30.67	38.84	14.78	16.13	0.17			100.63
du	3	60.4b	5		2	0.13	22.95	37.77	25.38	11.12	0.22	0.16	0.39	98.12
du	3	60.4b	4		2	0.14	21.22	38.14	28.67	10.73	0.26	0.23	0.45	99.84
du	3	60.4b	avg		4	0.14	22.09	37.96	27.03	10.93	0.24	0.20	0.42	98.98
du	3	60.6e	3	rim	2	0.07	26.73	37.59	20.40	11.94	0.23	0.18	0.34	97.48
du	3	60.6e	3	core	3	0.09	27.44	38.71	18.82	12.59	0.16	0.17	0.30	98.28
du	3	60.6e	2		1	0.08	27.57	34.93	22.59	11.29	0.24	0.21	0.33	97.24
du	3	60.6e	1		1	0.08	25.49	36.86	24.01	11.04	0.25	0.17	0.45	98.35
du	3	60.6e	avg	all var	7	0.08	26.81	37.02	21.46	11.72	0.22	0.18	0.36	97.84
	3	77	3		1	0.00	37.13	31.06	17.25	14.83	0.19	0.02	0.26	100.74
	3	77	5		1	0.02	31.59	37.98	15.63	15.11	0.13	0.10	0.23	100.79
	3	77	2	core	2	0.04	32.13	36.64	15.54	14.80	0.18	0.13	0.19	99.65
	3	77	2	rim to opx	1	0.04	33.29	34.65	15.44	15.02	0.14	0.11	0.22	98.91
	3	77	avg		4	0.03	32.34	36.42	15.54	14.98	0.15	0.11	0.21	99.78
opxte	3	82.111	2	core	1	0.03	15.72	52.62	20.48	10.87	0.22			99.94

Tab. B-3a (continued)

rocktype	unit	sample	spot	comment	N	TiO2	Al2O3	Cr2O3	Fe tot	MgO	MnO	NiO	V2O5	SUM
opxte	3	82.111	avg		1	0.03	15.72	52.62	20.48	10.87	0.22			99.94
	4	107	4a		1	0.02	11.83	57.61	23.32	8.66	0.29			101.73
	4	107	3		1	0.04	10.77	57.75	23.20	7.46	0.35			99.57
	4	107	1	core	2	0.07	9.67	59.75	21.13	9.32	0.34			100.28
	4	107	1	rim	2	0.07	10.39	58.70	23.38	8.39	0.29			101.22
	4	107	avg	(N)	6	0.05	10.67	58.45	22.76	8.46	0.32			100.70
du-hz	3	128	2	core	2	0.04	23.46	44.78	18.43	12.47	0.21			99.39
du-hz	3	128	2	rim	1	0.03	23.73	43.85	18.26	12.59	0.26			98.72
du-hz	3	128	avg	du-band	3	0.04	23.60	44.32	18.35	12.53	0.24			99.06
du-hz	3	128	11		2	0.04	20.63	49.00	19.15	11.60	0.28			100.70
du-hz	3	128	avg	hz-host	2	0.04	20.63	49.00	19.15	11.60	0.28			100.70
	4	154.1	8c		1	0.04	29.54	36.30	17.97	15.01	0.21			99.57
	4	154.1	3		1	0.05	25.48	40.77	18.44	14.90	0.29			99.93
	4	154.1	1	core	2	0.02	24.96	43.16	17.67	15.15	0.20			101.16
	4	154.1	1	rim	2	0.02	27.96	39.25	17.28	15.97	0.13			100.61
	4	154.1	avg	(N)	6	0.03	26.99	40.00	17.84	15.26	0.21			100.32
	TU	205	5		1	0.00	17.32	50.65	20.05	10.30	0.24	0.10	0.45	99.11
	TU	205	4	core	2	0.00	14.35	54.47	19.46	10.35	0.27	0.02	0.40	99.32
	TU	205	4	rim	2	0.00	15.65	52.85	19.92	10.47	0.27	0.05	0.39	99.60
	TU	205	avg	(N)	5	0.00	15.77	52.66	19.81	10.37	0.26	0.06	0.41	99.34
	TU	216	5	rim	1	0.02	29.68	37.77	17.21	13.19	0.23	0.09	0.27	98.46
	TU	216	3	core	1	0.02	28.43	40.21	15.61	14.33	0.21	0.05	0.25	99.11
	TU	216	3	rim	1	0.02	29.07	39.27	16.48	13.75	0.15	0.10	0.25	99.09
	TU	216	1		1	0.02	29.87	39.13	15.92	13.88	0.20	0.11	0.24	99.37
	TU	216	avg	(N)	4	0.02	29.26	39.10	16.31	13.79	0.20	0.09	0.25	99.01
	3	229	9		1	0.00	32.02	34.27	17.40	13.73	0.16	0.12	0.28	97.98
	3	229	8	core	2	0.02	30.29	38.26	16.36	14.31	0.18	0.10	0.23	99.75
	3	229	8	rim	3	0.02	31.40	35.45	16.12	14.67	0.22	0.13	0.23	98.24
	3	229	avg	(N)	6	0.01	31.24	35.99	16.63	14.24	0.19	0.12	0.25	98.66
lherz	6	245	8	rim	1	0.05	53.34	14.14	13.80	18.89	0.11	0.32	0.15	100.80
lherz	6	245	7	rim	1	0.03	50.85	15.98	13.59	18.44	0.13	0.35	0.18	99.55
lherz	6	245	7	core	1	0.04	51.15	15.38	13.66	18.43	0.09	0.29	0.11	99.15
lherz	6	245	6		1	0.04	51.75	14.77	14.75	18.39	0.11	0.23	0.20	100.44
lherz	6	245	avg	(R)	4	0.04	51.77	15.12	13.95	18.54	0.11	0.30	0.16	99.99
lherz	6	247	6	core	1	0.04	50.97	13.57	17.04	17.20	0.07	0.34	0.12	99.35
lherz	6	247	3	core	1	0.04	50.06	16.30	13.61	18.24	0.12	0.37	0.16	98.90
lherz	6	247	1	rim	2	0.04	51.41	16.06	13.34	18.68	0.12	0.24	0.16	100.05
lherz	6	247	1	core	2	0.04	49.01	17.35	13.61	18.45	0.10	0.32	0.12	99.00
lherz	6	247	avg	(N)	6	0.04	50.36	15.82	14.40	18.14	0.10	0.32	0.14	99.33
	TU	255	6	core	1	0.03	28.41	39.79	17.28	12.91	0.14	0.12	0.23	98.91
	TU	255	5	core	1	0.03	26.59	42.33	16.75	13.09	0.25	0.05	0.31	99.40
	TU	255	4	rim	3	0.02	26.19	42.07	18.18	12.45	0.20	0.09	0.29	99.49
	TU	255	4	core	2	0.02	25.91	43.69	17.78	12.71	0.18	0.07	0.30	100.66
	TU	255	avg	(N)	7	0.03	26.78	41.97	17.50	12.79	0.19	0.08	0.28	99.62
	5	259	5	in ol mx	2	0.01	33.74	34.05	16.27	14.95	0.15	0.14	0.23	99.54
	5	259	5	between cpx?	1	0.02	31.93	35.50	17.07	14.86	0.18	0.09	0.20	99.85
	5	259	3	rim to opx	2	0.01	32.28	36.67	15.56	15.69	0.12	0.11	0.20	100.64
	5	259	3	rim to cpx	2	0.00	33.54	33.16	16.55	15.72	0.16	0.16	0.17	99.46
	5	259	3	core	2	0.02	32.36	36.23	15.41	15.86	0.18	0.09	0.18	100.33
	5	259	avg	(N)	9	0.01	32.77	35.12	16.17	15.42	0.16	0.12	0.20	99.96
du	TU	284	3	rim	1	0.09	11.61	57.60	16.05	11.45	0.20	0.05	0.23	97.28
du	TU	284	3	core	1	0.09	11.92	57.05	15.66	11.50	0.27	0.09	0.22	96.80
du	TU	284	2	core	1	0.11	11.20	57.99	16.77	10.83	0.26	0.09	0.25	97.50
du	TU	284	1	aw opx	1	0.11	12.10	58.22	15.80	11.27	0.25	0.04	0.25	98.04
du	TU	284	avg	avg (R)	4	0.10	11.71	57.72	16.07	11.26	0.25	0.07	0.24	97.41
	4	317	4	core	1	0.04	6.67	61.82	23.07	6.92	0.28	0.03	0.19	99.02
	4	317	3	rim	2	0.02	7.59	61.43	21.82	7.53	0.28	0.01	0.25	98.93
	4	317	3	core	2	0.02	7.40	62.02	20.50	7.84	0.30	0.06	0.24	98.38
	4	317	2		1	0.01	8.13	60.00	22.11	6.92	0.33	0.05	0.18	97.73
	4	317	avg	dun: ic (N)	6	0.02	7.45	61.32	21.88	7.30	0.30	0.04	0.22	98.52
cpx-du	3	406	1	core	2	0.04	12.89	56.35	19.73	10.08	0.21	0.09	0.20	99.59
cpx-du	3	406	1	rim	1	0.05	13.26	55.22	20.16	9.82	0.28	0.09	0.18	99.06
cpx-du	3	406	avg	(N)	2	0.05	13.08	55.79	19.95	9.95	0.25	0.09	0.19	99.33
cpx-du	3	456	3		1	0.01	24.49	39.05	21.49	12.04	0.18	0.19	0.50	97.95
cpx-du	3	456	2		2	0.02	25.47	38.42	21.96	12.16	0.22	0.17	0.39	98.81
cpx-du	3	456	avg		3	0.02	24.98	38.74	21.73	12.10	0.20	0.18	0.45	98.38
	3	458	5		1	0.05	20.20	47.28	19.57	10.60	0.24	0.11	0.28	98.33
	3	458	2		1	0.01	21.97	45.02	19.08	10.62	0.18	0.03	0.30	97.21
	3	458	1	core	2	0.02	20.00	47.91	19.57	10.92	0.23	0.05	0.29	98.99
	3	458	avg		4	0.03	20.72	46.74	19.41	10.71	0.22	0.06	0.29	98.17

Tab. B-3a (continued)

rocktype	unit	sample	spot	comment	N	TiO2	Al2O3	Cr2O3	Fe tot	MgO	MnO	NiO	V2O5	SUM
	3	465	6	core	2	0.05	26.24	43.35	17.46	14.15	0.24			101.49
	3	465	6	1/2 rim	1	0.04	26.50	42.59	17.39	14.61	0.21			101.34
	3	465	6	smallest grain	2	0.04	28.03	41.20	16.08	14.57	0.17			100.09
	3	465	6	rim to ol	2	0.02	27.56	41.90	17.30	14.45	0.18			101.41
	3	465	4	rim	2	0.04	30.43	37.89	17.09	14.48	0.21			100.14
	3	465	4	core	1	0.02	30.29	37.91	16.39	14.87	0.12			99.60
	3	465	3	other grain	1	0.06	30.23	35.77	18.80	14.11	0.20			99.17
	3	465	3	one grain	1	0.02	28.39	40.59	16.74	14.40	0.21			100.35
	3	465	avg	(N)	12	0.04	28.46	40.15	17.16	14.46	0.19			100.45
	6	509	9	core, all var	2	0.04	40.90	26.93	14.41	16.71	0.12	0.19	0.18	99.48
	6	509		aw opx, also mt	1	0.00	41.23	25.03	14.16	16.79	0.16	0.21	0.20	97.78
	6	509	avg		3	0.02	41.07	25.98	14.29	16.75	0.14	0.20	0.19	98.63
	6	511	4	between cpx	3	0.02	47.64	19.13	12.96	17.80	0.12	0.26	0.14	98.07
	6	511	3		1	0.04	43.66	23.41	14.23	17.01	0.13	0.16	0.14	98.78
	6	511	2	core	1	0.04	42.14	24.96	13.59	16.88	0.15	0.19	0.17	98.12
	6	511	2	rim	1	0.01	43.22	23.42	13.67	16.89	0.19	0.22	0.21	97.83
	6	511	avg	(N), all var	6	0.03	44.17	22.73	13.61	17.15	0.15	0.21	0.17	98.20
lherz	6	534	5		1	0.02	49.84	18.92	13.71	18.40	0.09	0.14	0.17	101.29
lherz	6	534	4		1	0.04	49.07	19.28	14.24	18.23	0.09	0.16	0.14	101.25
lherz	6	534	3		1	0.02	49.05	20.14	14.35	18.13	0.14	0.12	0.14	102.09
lherz	6	534	avg		3	0.03	49.32	19.45	14.10	18.25	0.11	0.14	0.15	101.54
cpx-du	3	542.1	5	large, core	2	0.05	25.71	42.40	17.24	13.10	0.14	0.16	0.23	99.03
cpx-du	3	542.1	4	same, rim	2	0.05	26.54	40.45	17.69	12.82	0.21	0.14	0.23	98.13
cpx-du	3	542.1	3	small	2	0.04	25.58	42.32	18.45	12.33	0.18	0.14	0.24	99.28
cpx-du	3	542.1	avg	(N)	6	0.05	25.94	41.72	17.79	12.75	0.18	0.15	0.23	98.81
host	3	542.2	3	same, rim	2	0.04	28.59	38.57	18.09	12.79	0.17	0.11	0.28	98.64
host	3	542.2	3	large,core	1	0.00	26.41	41.20	18.27	12.58	0.23	0.16	0.29	99.14
host	3	542.2	avg	(N), host to du	3	0.02	27.50	39.89	18.18	12.69	0.20	0.14	0.29	98.89
opx So	3	543	3	core	1	0.00	23.41	44.46	19.61	11.86	0.21	0.07	0.33	99.95
opx So	3	543	2	core	1	0.00	23.30	45.00	20.40	11.64	0.18	0.11	0.29	100.92
opx So	3	543	1	rim	1	0.02	24.66	42.82	21.88	11.71	0.24	0.09	0.36	101.78
opx So	3	543	1	core	1	0.04	23.22	45.19	19.94	12.32	0.25	0.14	0.33	101.13
opx So	3	543	avg	(N)	4	0.02	23.65	44.37	20.46	11.81	0.22	0.10	0.33	100.95
	TU	564	6	rim	2	0.05	27.14	41.30	17.42	12.41	0.21	0.09	0.26	98.88
	TU	564	6	core	3	0.04	26.64	42.07	17.23	12.24	0.19	0.10	0.24	98.75
	TU	564	avg	(N)	5	0.05	26.89	41.69	17.33	12.33	0.20	0.10	0.25	98.82
	3	574	2a		2	0.04	19.04	47.85	20.74	11.23	0.25	0.02	0.23	99.40
	3	574	1	rim	1	0.06	21.05	46.41	19.13	12.45	0.26	0.05	0.24	99.65
	3	574	1	core	2	0.03	19.80	48.46	20.48	12.02	0.26	0.10	0.23	101.38
	3	574	avg	(N)	5	0.04	19.96	47.57	20.12	11.90	0.26	0.06	0.23	100.14
	4	578.3	3	core	2	0.04	15.56	53.14	20.16	9.71	0.26	0.03	0.38	99.28
	4	578.3	3	rim	2	0.03	16.60	52.39	20.71	9.98	0.20	0.05	0.37	100.33
	4	578.3	2	core	1	0.02	17.62	50.98	19.50	10.20	0.25	0.04	0.34	98.95
	4	578.3	1		1	0.03	15.28	52.85	20.31	9.63	0.25	0.03	0.32	98.70
	4	578.3	avg	(N)	6	0.03	16.27	52.34	20.17	9.88	0.24	0.04	0.35	99.32
	3	589	2		1	0.02	21.20	46.70	19.35	11.05	0.24	0.06	0.29	98.91
	3	589	1	rim to opx	2	0.04	19.33	51.04	18.27	11.45	0.21	0.10	0.34	100.78
	3	589	1	core	1	0.05	19.58	49.18	17.57	11.43	0.18	0.08	0.29	98.36
	3	589	avg		4	0.04	20.04	48.97	18.40	11.31	0.21	0.08	0.31	99.35
	3	590.1	3	rim	1	0.02	26.96	39.94	19.45	12.21	0.21	0.08	0.26	99.13
	3	590.1	2	core	1	0.03	25.94	42.57	18.97	11.84	0.20	0.08	0.23	99.86
	3	590.1	1	core	1	0.02	26.09	41.45	18.54	12.42	0.20	0.07	0.22	99.01
	3	590.1	avg		3	0.02	26.33	41.32	18.99	12.16	0.20	0.08	0.24	99.33
	3	591	3	rim	1	0.07	31.60	37.26	16.20	14.92	0.14	0.09	0.18	100.46
	3	591	3	core	2	0.07	30.34	37.84	15.87	14.47	0.20	0.11	0.20	99.10
	3	591	2		1	0.04	34.89	34.39	16.81	14.60	0.22	0.14	0.15	101.24
	3	591	2		1	0.05	34.53	32.19	16.52	13.91	0.11	0.03	0.16	97.50
	3	591	1	core, large gr.	1	0.04	30.28	38.79	16.50	14.46	0.24	0.07	0.18	100.56
	3	591	1	small grain	1	0.04	30.32	38.09	15.03	14.91	0.17	0.24	0.19	98.99
	3	591	1	rim	1	0.08	28.75	39.80	17.23	14.22	0.15	0.13	0.20	100.56
	3	591	avg	Al,Cr var	8	0.06	31.53	36.91	16.31	14.50	0.18	0.12	0.18	99.77
	3	592	9	betw opx	1	0.05	33.16	34.18	16.98	14.88	0.19	0.12	0.20	99.76
	3	592	8	rim	2	0.01	32.57	33.70	17.95	14.18	0.20	0.14	0.23	98.98
	3	592	8	core	1	0.03	37.51	28.27	16.73	15.08	0.20	0.14	0.25	98.21
	3	592	10		2	0.02	34.25	31.88	17.63	13.91	0.17	0.17	0.24	98.27
	3	592	avg	(R)	6	0.03	34.37	32.01	17.32	14.51	0.19	0.14	0.23	98.80
lherz	2	599	4	next to opx	1	0.03	41.14	26.03	14.95	16.93	0.14	0.30	0.18	99.70
lherz	2	599	4		1	0.02	41.09	26.49	14.69	16.69	0.16	0.24	0.16	99.54
lherz	2	599	2		2	0.02	42.73	25.62	14.08	17.76	0.15	0.31	0.16	100.83
lherz	2	599	2	incl in opx	1	0.02	39.99	28.14	13.27	16.68	0.11	0.24	0.11	98.56

Tab. B-3a (continued)

rocktype	unit	sample	spot	comment	N	TiO2	Al2O3	Cr2O3	Fe tot	MgO	MnO	NiO	V2O5	SUM
lherz	2	599	1	rim	1	0.00	40.96	26.46	14.54	16.51	0.16	0.19	0.18	99.00
lherz	2	599	1	core	1	0.02	39.26	27.01	14.28	16.94	0.14	0.23	0.17	98.03
lherz	2	599	avg	(N)	7	0.02	40.86	26.63	14.30	16.92	0.14	0.25	0.16	99.28
lherz	6	613	4		1	0.01	47.92	20.28	13.24	17.54	0.14	0.25	0.19	99.57
lherz	6	613	3		1	0.00	47.98	19.91	12.88	17.78	0.05	0.29	0.20	99.09
lherz	6	613	avg		2	0.01	47.95	20.10	13.06	17.66	0.10	0.27	0.20	99.33
	4	672	3	core	1	0.02	27.27	40.65	18.00	12.56	0.17	0.04	0.30	99.01
	4	672	2		1	0.00	29.55	37.83	18.12	12.97	0.17	0.07	0.29	99.00
	4	672	1	rim	2	0.02	28.65	38.81	18.35	12.82	0.19	0.10	0.25	99.19
	4	672	1	core	2	0.03	27.29	40.81	17.89	12.55	0.22	0.06	0.29	99.14
	4	672	avg	(N)	6	0.02	28.19	39.53	18.09	12.73	0.19	0.07	0.28	99.09
	3	676	5	core	2	0.04	25.53	42.41	18.61	12.44	0.21	0.10	0.20	99.54
	3	676	5	rim	2	0.05	27.49	39.14	17.75	12.67	0.18	0.14	0.20	97.62
	3	676	3		1	0.03	28.09	38.12	19.28	11.99	0.16	0.14	0.23	98.04
	3	676	2	rim	1	0.04	27.02	39.25	19.27	13.28	0.16	0.05	0.22	99.29
	3	676	2	core	1	0.04	26.18	40.34	19.19	12.03	0.20	0.11	0.20	98.29
	3	676	avg	(N)	7	0.04	26.86	39.85	18.82	12.48	0.18	0.11	0.21	98.56
	4	701	3		1	0.04	16.58	50.13	21.54	9.82	0.27	0.07	0.36	98.81
	4	701	2	core	1	0.04	14.65	53.36	22.51	9.95	0.24	0.08	0.38	101.21
	4	701	1	rim	2	0.03	16.00	50.59	21.77	10.09	0.29	0.05	0.38	99.20
	4	701	1	core	2	0.02	14.80	53.44	20.83	10.34	0.31	0.10	0.36	100.20
	4	701	avg	(N)	6	0.03	15.51	51.88	21.66	10.05	0.28	0.08	0.37	99.86
	TU	705	3		1	0.02	25.82	42.41	18.06	11.99	0.21	0.05	0.34	98.90
	TU	705	2	core	2	0.00	24.45	44.42	17.88	12.05	0.23	0.07	0.27	99.37
	TU	705	1	core	1	0.00	25.42	43.79	18.74	12.37	0.28	0.03	0.30	100.93
	TU	705	1	rim	2	0.01	27.30	40.75	17.79	12.23	0.21	0.07	0.29	98.65
	TU	705	avg	(N)	3	0.01	25.75	42.84	18.12	12.16	0.23	0.06	0.30	99.46
	TU	719	3		1	0.00	36.82	31.24	15.97	16.07	0.20	0.06	0.25	100.61
	TU	719	2	core	1	0.02	35.28	33.02	14.79	15.79	0.19	0.08	0.22	99.39
	TU	719	1	core	2	0.01	34.22	34.13	15.61	15.67	0.19	0.11	0.20	100.14
	TU	719	1	rim to ol	1	0.02	35.37	31.27	14.61	17.32	0.20	0.11	0.21	99.11
	TU	719	avg	(N)	5	0.01	35.42	32.42	15.25	16.21	0.20	0.09	0.22	99.81
	4	723.1	3		1	0.03	30.51	37.66	16.49	13.71	0.17	0.12	0.23	98.92
	4	723.1	2	core	1	0.02	31.61	37.20	17.23	14.05	0.19	0.07	0.21	100.58
	4	723.1	1	rim	2	0.02	31.28	37.11	16.85	14.09	0.18	0.15	0.23	99.91
	4	723.1	1	core	2	0.00	29.41	39.29	16.28	13.97	0.16	0.12	0.20	99.43
	4	723.1	avg	mod strain (N)	6	0.02	30.70	37.82	16.71	13.96	0.18	0.12	0.22	99.71
	4	723.2	3	core	1	0.00	28.90	39.85	16.70	13.59	0.18	0.07	0.26	99.55
	4	723.2	2	core	1	0.03	28.40	40.53	16.90	13.86	0.17	0.13	0.21	100.23
	4	723.2	1	core	1	0.03	28.87	39.61	16.28	14.21	0.21	0.07	0.24	99.52
	4	723.2	1	rim	2	0.02	29.23	39.49	16.76	14.04	0.17	0.10	0.26	100.07
	4	723.2	avg	low strain (N)	5	0.02	28.85	39.37	16.66	13.93	0.18	0.09	0.24	99.84
	4	723.3	3	core	1	0.03	11.19	56.68	21.71	8.54	0.25	0.05	0.30	98.65
	4	723.3	2	rim to cpx	2	0.01	10.79	55.68	24.56	7.35	0.35	0.08	0.30	99.12
	4	723.3	2	core	2	0.00	11.09	55.77	23.69	8.00	0.29	0.03	0.32	99.19
	4	723.3	1	core	1	0.01	11.10	55.90	22.37	8.37	0.39	0.05	0.25	98.44
	4	723.3	1	rim	1	0.04	11.80	55.18	22.98	8.30	0.28	0.05	0.33	98.96
	4	723.3	avg	high strain (N)	7	0.02	11.19	55.82	23.06	8.11	0.31	0.05	0.30	98.87
cpx-du	3	733.2	6	core	1	0.03	17.82	47.70	26.18	9.67	0.19	0.11	0.27	101.97
cpx-du	3	733.2	3	rim	2	0.07	18.55	46.94	25.23	9.89	0.23	0.05	0.25	101.21
cpx-du	3	733.2	3	core	2	0.06	17.92	48.39	22.23	11.07	0.24	0.05	0.25	100.21
cpx-du	3	733.2	avg	(N), Fe,Mg var	5	0.05	18.10	47.68	24.55	10.21	0.22	0.07	0.26	101.13
	3	749	3	rim to ol	2	0.02	34.92	32.90	15.82	15.97	0.15	0.18	0.15	100.01
	3	749	3	core	2	0.03	34.55	33.43	15.84	16.19	0.16	0.20	0.16	100.56
	3	749	2	rim	1	0.02	35.03	32.99	15.43	15.76	0.13	0.15	0.20	99.71
	3	749	2	core	1	0.01	35.34	32.40	16.45	15.95	0.14	0.10	0.17	100.56
	3	749	1	core	2	0.03	34.50	32.68	14.81	16.24	0.18	0.20	0.16	98.80
	3	749	1	rim	2	0.04	35.18	32.83	15.49	15.84	0.18	0.18	0.16	99.90
	3	749	avg	(N)	10	0.03	34.92	32.86	15.64	15.99	0.16	0.17	0.17	99.92
	6	755	6		1	0.00	45.89	21.82	14.92	17.84	0.14	0.11	0.17	100.89
	6	755	4		1	0.04	46.63	20.94	14.67	17.54	0.04	0.12	0.18	100.16
	6	755	3	core	1	0.02	44.39	22.13	14.29	17.64	0.06	0.29	0.14	98.96
	6	755	3	rim	1	0.02	46.01	21.80	14.30	17.79	0.14	0.08	0.16	100.30
	6	755	avg	(N)	4	0.02	45.73	21.67	14.55	17.70	0.10	0.15	0.16	100.08
	5	757	4		1	0.01	40.40	26.46	15.46	15.79	0.18	0.10	0.20	98.60
	5	757	3		1	0.02	41.42	26.20	15.68	16.18	0.15	0.16	0.16	99.97
	5	757	1		1	0.03	41.13	25.60	15.20	16.02	0.17	0.11	0.16	98.42
	5	757	avg		3	0.02	40.98	26.09	15.45	16.00	0.17	0.12	0.17	99.00
	3	772.1	7	core	2	0.02	27.47	38.16	20.24	13.18	0.19	0.09	0.26	99.61
	3	772.1	7	rim	2	0.01	28.79	37.59	19.38	11.94	0.19	0.10	0.23	98.23

Tab. B-3a (continued)

rocktype	unit	sample	spot	comment	N	TiO2	Al2O3	Cr2O3	Fe tot	MgO	MnO	NiO	V2O5	SUM
	3	772.1	2	core	1	0.00	28.30	38.29	18.78	12.01	0.21	0.10	0.27	97.96
	3	772.1	avg	(N)	5	0.01	28.19	38.01	19.47	12.38	0.20	0.10	0.25	98.60
	3	774	7		1	0.08	26.40	40.27	18.87	12.06	0.16	0.11	0.20	98.15
	3	774	2		1	0.07	27.34	40.23	17.89	11.91	0.18	0.14	0.23	97.99
	3	774	1	rim	1	0.07	28.30	36.93	21.09	12.04	0.23	0.10	0.23	98.99
	3	774	1	core	2	0.06	25.68	40.81	20.75	11.66	0.23	0.09	0.22	99.50
	3	774	avg	(N)	5	0.07	26.93	39.56	19.65	11.92	0.20	0.11	0.22	98.66
du-hz	3	779S2	3		1	0.04	21.47	46.41	19.92	10.66	0.24	0.06	0.22	99.02
du-hz	3	779S2	1	core	2	0.03	19.80	47.80	19.75	10.79	0.29	0.11	0.26	98.83
du-hz	3	779S2	avg	hz host	3	0.04	20.64	47.11	19.84	10.73	0.27	0.09	0.24	98.93
du-hz	3	779S2	1	core	2	0.04	19.95	48.92	19.20	11.28	0.24	0.07	0.24	99.94
du-hz	3	779S2	1	rim	2	0.02	19.50	47.50	20.38	10.63	0.27	0.05	0.24	98.59
du-hz	3	779S2	1	rim	2	0.01	19.33	47.80	21.20	10.38	0.26	0.07	0.26	99.31
du-hz	3	779S2	avg	du	6	0.02	19.59	48.07	20.26	10.76	0.26	0.06	0.25	99.28
	3	788	5	core	2	0.02	24.74	43.19	17.98	12.36	0.17	0.03	0.23	98.72
	3	788	5	rim	1	0.02	24.91	42.91	19.06	11.86	0.20	0.05	0.30	99.31
	3	788	4	rim	1	0.04	25.23	42.30	18.45	12.27	0.16	0.05	0.23	98.73
	3	788	4	core	1	0.02	24.59	43.58	18.20	12.27	0.20	0.09	0.24	99.19
	3	788	3	core	1	0.05	25.08	42.84	18.39	12.34	0.20	0.10	0.22	99.22
	3	788	avg	(N)	6	0.03	24.91	42.96	18.42	12.22	0.19	0.06	0.24	99.03
	3	801	3	core	2	0.07	30.22	37.57	17.14	15.06	0.17			100.23
	3	801	2	core	2	0.08	28.99	40.11	15.71	15.32	0.18			100.39
	3	801	2	rim to ol	2	0.09	29.28	39.05	16.05	15.37	0.18			100.02
	3	801	2	rim to opx	2	0.09	28.20	40.86	16.45	15.13	0.18			100.91
	3	801	avg	(N)	8	0.08	29.17	39.40	16.34	15.22	0.18			100.39
	5	806	2	rim	3	0.02	38.95	29.30	14.37	16.53	0.12	0.15	0.20	99.64
	5	806	1		2	0.04	36.93	30.84	13.98	16.32	0.16	0.16	0.2*	98.64
	5	806	avg		5	0.03	37.94	30.07	14.18	16.43	0.14	0.16	0.21	99.14
	TU	808.1	3	intergrowth opx	1	0.02	35.27	32.77	15.54	15.52	0.18	0.10	0.22	99.52
	TU	808.1	2	core	1	0.04	35.03	33.22	15.32	15.73	0.16	0.16	0.15	99.81
	TU	808.1	1	rim	2	0.03	36.05	31.64	16.16	15.59	0.14	0.14	0.20	99.95
	TU	808.1	1	core	1	0.02	34.68	33.27	15.29	15.29	0.19	0.16	0.24	99.14
	TU	808.1	avg	(N)	5	0.03	35.26	32.73	15.58	15.53	0.17	0.14	0.20	99.63
	5	827	9		1	0.02	40.37	25.05	15.27	16.51	0.04	0.01	0.20	97.77
	5	827	8		1	0.02	40.34	25.03	15.38	15.93	0.16	0.19	0.22	98.77
	5	827	7	rim	3	0.03	38.47	28.18	15.43	17.00	0.18	0.00	0.19	99.48
	5	827	7	corg	3	0.02	38.84	28.33	14.68	16.56	0.16	0.23	0.20	99.02
	5	827	6	core	2	0.02	40.44	25.65	15.63	16.72	0.12	0.16	0.21	98.95
	5	827	10	core	1	0.01	39.85	26.54	14.77	16.60	0.16	0.18	0.18	98.29
	5	827	avg		11	0.02	39.72	26.46	15.44	16.55	0.14	0.18	0.20	98.71
	6	829	4		1	0.06	24.71	38.95	24.61	10.48	0.25	0.11	0.22	99.39
	6	829	3	core	2	0.09	17.95	46.07	25.75	8.88	0.28	0.10	0.28	99.40
	6	829	3	core	2	0.09	18.52	45.50	25.93	8.84	0.23	0.10	0.28	99.49
	6	829	2		1	0.05	18.13	44.25	29.39	7.67	0.26	0.06	0.29	100.10
	6	829	avg	(N), 1x excl	6	0.08	20.39	43.51	25.43	9.40	0.25	0.10	0.26	99.43
	4	835.1	6	core	1	0.07	36.00	32.89	13.45	16.36	0.11	0.18	0.16	99.22
	4	835.1	6	rim	2	0.04	36.08	32.23	14.00	15.77	0.19	0.12	0.20	98.63
	4	835.1	5	core	1	0.09	35.53	32.80	13.84	16.05	0.12	0.14	0.16	98.73
	4	835.1	10		2	0.05	39.77	28.12	12.92	16.71	0.12	0.11	0.19	97.99
	4	835.1	avg	(N)	6	0.06	36.85	31.51	13.55	16.22	0.14	0.14	0.18	98.64
	4	835.2	8	core	1	0.04	28.66	40.11	16.24	14.06	0.20	0.12	0.27	99.70
	4	835.2	8	rim	1	0.03	28.38	40.80	15.31	14.02	0.14	0.07	0.25	99.00
	4	835.2	7		1	0.03	31.56	37.20	15.48	14.74	0.21	0.10	0.30	99.62
	4	835.2	3	core	2	0.04	28.26	40.82	15.00	14.38	0.26	0.16	0.30	99.22
	4	835.2	3	rim	3	0.02	29.90	38.55	15.97	14.09	0.22	0.11	0.30	99.16
	4	835.2	avg	(N)	7	0.03	29.35	39.50	15.60	14.26	0.21	0.11	0.28	99.34
	4	835.3	4	rim	2	0.07	13.28	56.58	18.02	9.60	0.27	0.05	0.29	98.16
	4	835.3	4	core	2	0.05	11.97	57.92	18.60	9.64	0.20	0.07	0.32	98.77
	4	835.3	3		1	0.07	12.39	56.97	20.13	9.31	0.27	0.08	0.31	99.53
	4	835.3	avg	(N)	5	0.06	12.55	57.16	18.92	9.52	0.25	0.07	0.31	98.82
pl-hz	2	849	9		1	0.08	32.36	34.48	20.00	13.38	0.19	0.13	0.29	100.91
pl-hz	2	849	6		1	0.10	31.63	34.32	19.36	13.51	0.20	0.07	0.23	99.42
pl-hz	2	849	3		2	0.22	30.14	35.80	20.07	13.23	0.21	0.17	0.33	100.17
pl-hz	2	849	10		1	0.06	32.50	34.11	20.36	13.33	0.20	0.15	0.29	101.00
pl-hz	2	849	avg		5	0.12	31.66	34.68	19.95	13.36	0.20	0.13	0.29	100.38
ol-cpxte	1	860	6		2	0.23	26.25	37.73	24.02	11.18	0.25	0.07	0.33	100.06
ol-cpxte	1	860	5	rim	2	0.23	24.03	39.18	25.93	10.17	0.28	0.05	0.34	100.21
ol-cpxte	1	860	5	core	2	0.25	23.88	39.55	26.27	10.54	0.27	0.05	0.34	101.15
ol-cpxte	1	860	4	du	1	0.25	24.75	39.29	24.48	10.86	0.30	0.07	0.33	100.33
ol-cpxte	1	860	3	du	1	0.20	25.20	39.11	24.87	10.57	0.20	0.05	0.36	100.56

Tab. B-3a (continued)

rocktype	unit	sample	spot	comment	N	TiO2	Al2O3	Cr2O3	Fe tot	MgO	MnO	NiO	V2O5	SUM
ol-cpxte	1	860	avg	banded (N)	8	0.23	24.82	38.97	25.11	10.66	0.26	0.06	0.34	100.46
	1	861	5	core	2	0.20	22.94	44.13	19.49	11.99	0.14	0.17	0.30	99.36
	1	861	3	rim	2	0.11	23.97	43.16	19.30	12.00	0.23	0.12	0.30	99.19
	1	861	3	core	2	0.13	23.16	44.73	17.96	13.08	0.25	0.14	0.26	99.71
	1	861	1		1	0.10	23.99	44.02	20.04	12.45	0.27	0.16	0.32	101.35
	1	861	avg	(N)	7	0.14	23.52	44.01	19.20	12.38	0.22	0.15	0.30	99.90
lherz	1	862	6	incl in opx	1	0.28	31.76	34.55	17.82	15.11	0.23	0.26	0.35	100.36
lherz	1	862	5		1	0.21	31.21	34.18	19.66	13.25	0.20	0.20	0.40	99.31
lherz	1	862	2	core	3	0.18	29.56	35.53	20.86	12.82	0.21	0.13	0.33	99.62
lherz	1	862	avg	has pl-band	5	0.22	30.84	34.75	19.45	13.73	0.21	0.20	0.36	99.76
	2	866	5	aw opx?	1	0.08	36.06	31.43	18.36	14.53	0.17	0.06	0.24	100.93
	2	866	4	rim to cpx	2	0.08	33.43	33.39	17.15	14.46	0.20	0.15	0.16	99.02
	2	866	4	in mx	1	0.12	35.29	31.86	16.89	14.93	0.19	0.10	0.18	99.56
	2	866	4	core	1	0.10	35.40	32.11	16.89	14.91	0.21	0.13	0.23	99.98
	2	866	4	rim to ol	1	0.10	36.17	31.27	17.35	14.98	0.14	0.10	0.23	100.34
	2	866	2	aw cpx	1	0.05	35.14	31.89	15.85	14.73	0.13	0.11	0.20	98.10
	2	866	avg	(N)	7	0.09	35.25	31.99	17.08	14.76	0.17	0.11	0.21	99.66
	1	869	3		2	0.10	19.73	45.93	22.68	10.34	0.23	0.06	0.28	99.35
	1	869	2	rim	1	0.12	20.09	45.00	22.70	10.14	0.19	0.08	0.32	98.64
	1	869	1		1	0.08	19.05	45.12	24.39	9.16	0.14	0.14	0.30	98.38
	1	869	avg		4	0.10	19.62	45.35	23.26	9.98	0.19	0.09	0.30	98.79
lh-band	2	873	7	aw cpx	1	0.01	38.00	29.26	17.80	14.91	0.19	0.16	0.17	100.50
lh-band	2	873	7		1	0.02	38.13	30.16	15.54	15.68	0.14	0.14	0.18	99.99
lh-band	2	873	4	core	1	0.02	38.79	30.28	16.02	15.93	0.12	0.15	0.20	101.51
lh-band	2	873	4	other grain	1	0.04	37.44	29.32	16.48	14.71	0.18	0.10	0.20	98.47
lh-band	2	873	4	rim	1	0.02	38.33	30.36	15.20	15.77	0.15	0.14	0.17	100.14
lh-band	2	873	2	tail	1	0.02	37.43	30.25	16.59	14.86	0.11	0.14	0.20	99.60
lh-band	2	873	2	core	1	0.04	36.92	30.53	16.47	15.15	0.13	0.21	0.20	99.65
lh-band	2	873	avg	lherz band	7	0.02	37.86	30.02	16.30	15.29	0.15	0.15	0.19	99.98
du-band	2	873	1	core	2	0.03	37.12	30.68	16.68	15.14	0.16	0.16	0.19	100.16
du-band	2	873	1	rim, Al,Cr var	5	0.04	35.54	31.47	17.85	14.72	0.18	0.13	0.20	100.13
du-band	2	873	avg	bit px (R)	7	0.04	36.33	31.08	17.27	14.93	0.17	0.15	0.20	100.15
	3	881	7	aw cpx,rim	2	0.02	35.58	31.96	16.68	15.86	0.16	0.09	0.20	100.55
	3	881	3		1	0.02	34.63	32.39	18.65	14.06	0.22	0.09	0.24	100.90
	3	881	1	rim to ol	2	0.00	35.95	31.42	17.66	15.19	0.16	0.11	0.24	100.73
	3	881	1	rim to cpx	1	0.03	35.39	31.97	17.79	15.68	0.14	0.18	0.21	101.99
	3	881	1	core	2	0.02	34.92	32.14	17.02	15.27	0.17	0.21	0.20	99.95
	3	881	avg	(N)	8	0.02	35.41	32.10	17.56	15.21	0.17	0.14	0.22	100.82
	2	884	5		1	0.00	39.83	27.29	15.63	16.29	0.16	0.21	0.18	99.59
	2	884	4	small	2	0.04	39.53	26.77	15.74	16.45	0.16	0.23	0.16	99.08
	2	884	3	small	1	0.01	40.18	25.05	16.16	15.95	0.11	0.21	0.22	97.89
	2	884	avg		4	0.02	39.85	26.37	15.84	16.23	0.14	0.22	0.19	98.85
	2	886	-2		1	0.17	31.03	36.92	19.02	13.28	0.21			100.63
	2	886	-1		1	0.17	32.05	34.30	19.13	14.05	0.27			99.97
	2	886	1		1	0.16	31.57	35.69	19.45	13.88	0.26			101.01
	2	886	0		1	0.16	32.34	34.92	17.62	14.53	0.18			99.75
	2	886	avg		4	0.17	31.75	35.46	18.81	13.94	0.23			100.34
pl-hz	2	900	unmarked		1	0.05	33.02	33.07	19.89	12.41	0.16	0.20	0.26	99.06
pl-hz	2	900	3		1	0.15	30.20	35.58	20.38	12.12	0.18	0.07	0.28	98.96
pl-hz	2	900	1		1	0.08	33.59	31.79	19.52	12.98	0.15	0.13	0.26	98.50
pl-hz	2	900	avg		3	0.09	32.27	33.48	19.93	12.50	0.16	0.13	0.27	98.84
nxt opxt	3	901.1	6		2	0.07	14.51	51.11	26.18	7.47	0.27	0.03	0.29	99.93
nxt opxt	3	901.1	4	rim	2	0.08	16.53	50.75	22.65	9.52	0.19	0.07	0.33	100.12
nxt opxt	3	901.1	4	core	2	0.05	15.96	51.03	22.09	9.53	0.26	0.02	0.30	99.24
nxt opxt	3	901.1	1		1	0.04	16.74	49.61	22.26	8.83	0.24	0.03	0.31	98.06
nxt opxt	3	901.1	avg	nxt opxte (N)	7	0.06	15.94	50.63	23.30	8.84	0.24	0.04	0.31	99.34
far opxt	3	901.3	6		1	0.02	36.61	30.50	16.62	14.82	0.12			98.69
far opxt	3	901.3	4		2	0.03	37.83	29.47	17.24	14.64	0.16			99.37
far opxt	3	901.3	1	rim	1	0.00	35.36	31.39	16.30	15.56	0.16			98.77
far opxt	3	901.3	1	core	1	0.02	35.46	31.76	16.09	15.45	0.21			98.99
far opxt	3	901.3	avg	away f. dyke	5	0.02	36.32	30.78	16.56	15.12	0.16			98.96
	5	918	4	aw cpx	1	0.02	37.64	30.17	16.29	15.91	0.11	0.19	0.17	100.50
	5	918	3		1	0.00	36.91	30.74	15.89	15.32	0.14	0.16	0.25	99.91
	5	918	2	rim	2	0.02	39.39	29.06	15.70	16.33	0.16	0.11	0.19	100.96
	5	918	2	core	1	0.00	36.65	31.71	15.56	16.01	0.11	0.16	0.20	100.40
	5	918	1	core	2	0.01	36.73	31.18	15.60	16.18	0.16	0.14	0.21	100.21
	5	918	avg	(N)	7	0.01	37.46	30.57	15.81	16.05	0.14	0.15	0.20	100.40
lherz	6	922	3		1	0.05	49.68	17.87	13.99	18.15	0.16			99.90
lherz	6	922	2		1	0.04	49.73	17.57	13.77	19.06	0.11			100.28
lherz	6	922	1		2	0.05	49.73	17.88	13.68	18.61	0.13			100.08

Tab. B-3a (continued)

rocktype	unit	sample	spot	comment	N	TiO2	Al2O3	Cr2O3	Fe tot	MgO	MnO	NiO	V2O5	SUM
lherz	6	922	avg		4	0.05	49.71	17.77	13.81	18.61	0.13			100.09
lherz	6	932	9		2	0.05	55.30	13.14	11.70	19.74	0.10			100.03
lherz	6	932	7	core	2	0.06	54.40	14.45	11.06	20.43	0.10			100.50
lherz	6	932	7	rim	2	0.06	54.64	14.64	11.37	19.97	0.09			100.77
lherz	6	932	1	core	2	0.08	54.51	15.24	11.26	20.16	0.11			101.36
lherz	6	932	avg		8	0.06	54.71	14.37	11.35	20.08	0.10			100.67
amph-du	6	934.1	4		3	0.04	36.66	28.40	21.86	12.97	0.22	0.16	0.10	100.41
amph-du	6	934.1	1		2	0.02	30.45	33.40	23.27	11.69	0.32	0.10	0.11	99.36
amph-du	6	934.1	avg	Al,Cr var. S2	5	0.03	33.56	30.90	22.57	12.33	0.27	0.13	0.11	99.89
umyl	6	941		small	1	0.00	51.86	15.86	14.22	18.75	0.14	0.28	0.09	101.20
umyl	6	941	8	rim	1	0.03	46.13	21.21	14.60	18.00	0.16	0.33	0.12	100.58
umyl	6	941	8	core	1	0.00	50.55	17.41	13.41	19.01	0.16	0.30	0.10	100.94
umyl	6	941	4	incl in amph	2	0.02	39.39	27.94	16.60	16.47	0.17	0.12	0.12	100.83
umyl	6	941	11	core	1	0.01	52.11	15.00	13.97	18.55	0.08	0.33	0.10	100.15
umyl	6	941	11	rim	1	0.04	51.28	16.86	14.25	18.86	0.13	0.26	0.10	101.78
umyl	6	941	avg	all var (R)	7	0.02	48.55	19.05	14.51	18.27	0.14	0.27	0.11	100.91
du	4	959	?		2	0.07	7.74	63.00	19.66	9.13	0.34	0.03	0.28	100.25
du	4	959	3	core	2	0.07	7.09	63.85	18.63	9.46	0.22	0.05	0.25	99.62
du	4	959	3	rim	2	0.08	7.29	62.83	20.09	8.89	0.25	0.10	0.23	99.76
du	4	959	avg	has opx	6	0.07	7.37	63.23	19.46	9.16	0.27	0.06	0.25	99.88
	3	963	2		1	0.02	31.86	37.08	17.36	14.32	0.08	0.15	0.21	101.08
	3	963	1	core	1	0.04	32.11	35.75	17.14	14.77	0.11	0.05	0.24	100.21
	3	963	3		1	0.02	33.05	35.11	18.04	14.69	0.13	0.05	0.22	101.31
	3	963	avg		3	0.03	32.34	35.98	17.51	14.59	0.11	0.08	0.22	100.87
	2	1022	4	rim	1	0.06	35.32	33.69	15.38	15.31	0.16	0.14	0.20	100.26
	2	1022	4	core	2	0.06	34.78	34.43	15.13	15.53	0.16	0.16	0.19	100.44
	2	1022	2	rim	1	0.04	35.05	32.79	14.29	15.93	0.14	0.10	0.16	98.50
	2	1022	2	core	1	0.06	34.97	33.05	14.05	15.39	0.18	0.19	0.14	98.03
	2	1022	1		1	0.04	35.61	32.79	15.05	15.28	0.18	0.10	0.18	99.23
	2	1022	avg	(N)	6	0.05	35.15	33.35	14.78	15.49	0.16	0.14	0.17	99.29
lherz	6	1027	3		2	0.05	47.16	20.82	13.64	17.83	0.18			99.68
lherz	6	1027	2		2	0.05	45.96	21.81	14.11	17.98	0.15			100.06
lherz	6	1027	avg		4	0.05	46.56	21.32	13.88	17.91	0.17			99.87
lherz	6	1029.11	3		2	0.07	57.93	9.80	12.81	20.05	0.13	0.37	0.09	101.25
lherz	6	1029.11	13		2	0.07	56.72	9.95	12.62	19.06	0.07	0.41	0.12	99.02
lherz	6	1029.11	1	core	1	0.09	57.97	9.34	13.17	19.67	0.09	0.39	0.09	100.81
lherz	6	1029.11	1	rim	1	0.08	57.45	9.78	12.71	19.82	0.08	0.41	0.15	100.48
lherz	6	1029.11	avg		6	0.08	57.52	9.72	12.83	19.65	0.09	0.40	0.11	100.39
	5	1037	5	rim to opx	2	0.03	42.24	25.88	14.06	17.74	0.16	0.25	0.18	100.54
	5	1037	5	core	2	0.03	38.64	28.52	14.91	16.87	0.14	0.23	0.14	99.48
	5	1037	2		1	0.02	40.09	27.79	14.53	16.85	0.14	0.26	0.17	99.85
	5	1037	1		1	0.02	40.20	27.28	16.12	16.61	0.15	0.10	0.18	100.66
	5	1037	avg	(N)	6	0.03	40.29	27.37	14.91	17.02	0.15	0.21	0.17	100.13
	6	1043.2	4		1	0.01	46.44	22.62	13.19	17.84	0.09	0.16	0.11	100.46
	6	1043.2	4	incl in opx	1	0.00	46.91	22.70	13.27	18.48	0.14	0.25	0.15	101.90
	6	1043.2	2	rim to ?	1	0.03	43.83	26.13	13.87	17.65	0.12	0.25	0.16	102.04
	6	1043.2	2	core	2	0.05	43.26	25.77	14.17	17.82	0.17	0.24	0.14	101.62
	6	1043.2	avg		5	0.02	45.11	24.31	13.63	17.95	0.13	0.23	0.14	101.51
	5	1048	9	core	2	0.02	39.81	26.68	13.99	16.60	0.15	0.14	0.18	97.57
	5	1048	9	rim	2	0.02	41.57	27.16	14.39	16.60	0.16	0.21	0.20	100.31
	5	1048	avg		2	0.02	40.69	26.92	14.19	16.60	0.16	0.18	0.19	98.94
	5	1052	3	aw cpx, all var	2	0.04	44.02	22.16	14.95	17.25	0.11	0.15	0.16	98.84
	5	1052	2		1	0.02	45.64	21.22	15.42	17.44	0.14	0.13	0.14	100.15
	5	1052	avg		3	0.03	44.83	21.69	15.19	17.35	0.13	0.14	0.15	99.50
	6	1060	3		1	0.05	49.78	17.26	13.49	17.99	0.14	0.25	0.14	99.07
	6	1060	2		1	0.03	51.17	17.09	12.27	18.30	0.10	0.29	0.14	99.39
	6	1060	1		2	0.02	50.02	17.76	13.25	17.97	0.12	0.30	0.11	99.55
	6	1060	avg		4	0.02	50.32	17.37	13.00	18.09	0.12	0.28	0.13	99.34
lherz	6	1062	1	core	2	0.14	53.81	14.38	13.29	19.77	0.08	0.24	0.07	101.78
lherz	6	1062	2		1	0.06	53.26	14.47	13.25	19.42	0.09	0.34	0.11	101.00
lherz	6	1062	1	rim	1	0.06	54.22	13.64	13.60	19.71	0.14	0.31	0.09	101.77
lherz	6	1062	avg		4	0.09	53.76	14.16	13.38	19.63	0.10	0.30	0.09	101.52
	6	1063.1	3	core	1	0.08	28.90	35.45	21.96	11.76	0.27	0.12	0.23	98.77
	6	1063.1	3	rim	1	0.04	31.92	31.58	20.19	12.67	0.16	0.16	0.21	96.93
	6	1063.1	1		1	0.12	28.39	35.91	21.06	11.96	0.17	0.09	0.24	97.94
	6	1063.1	avg	(N) mod strain	3	0.08	29.74	34.31	21.07	12.13	0.20	0.12	0.23	97.88
	6	1063.2	3	core	2	0.08	27.61	38.06	22.83	11.24	0.24	0.08	0.23	100.37
	6	1063.2	3	rim	2	0.07	30.53	34.99	22.73	11.64	0.23	0.08	0.24	100.51
	6	1063.2	2		1	0.14	27.18	37.55	23.34	11.66	0.23	0.11	0.16	100.37
	6	1063.2	1		1	0.11	26.41	38.94	22.63	11.30	0.12	0.12	0.30	99.93

Tab. B-3a (continued)

rocktype	unit	sample	spot	comment	N	TiO2	Al2O3	Cr2O3	Fe tot	MgO	MnO	NiO	V2O5	SUM
	6	1063.2	avg	(N) high strain	6	0.10	27.93	37.39	22.88	[illegible]	0.21	0.10	0.23	100.30
lherz	6	1063.3	3	core	2	0.05	54.38	11.43	12.63	19.65	0.09	0.30	0.10	98.63
lherz	6	1063.3	3	rim	2	0.07	55.35	11.44	11.86	19.25	0.08	0.41	0.10	98.56
lherz	6	1063.3	2		1	0.02	56.13	10.78	11.64	19.58	0.10	0.33	0.09	98.67
lherz	6	1063.3	1	rim	1	0.05	55.34	11.50	12.17	18.91	0.13	0.40	0.11	98.61
lherz	6	1063.3	1	core	1	0.07	55.52	11.11	12.60	19.52	0.09	0.21	0.11	99.23
lherz	6	1063.3	avg	(N) low strain	7	0.05	55.34	11.25	12.18	19.38	0.10	0.33	0.10	98.74
	5	1065	8	incl in opx	1	0.02	40.88	26.84	14.25	17.06	0.17	0.23	0.24	99.69
	5	1065	4	core	1	0.00	38.48	28.17	14.64	16.46	0.21	0.14	0.21	98.31
	5	1065	3		2	0.00	41.14	25.71	15.18	17.13	0.16	0.16	0.21	99.69
	5	1065	avg		4	0.01	40.17	26.91	14.69	16.88	0.18	0.18	0.22	99.23
	5	1071	6	in opx	1	0.02	39.32	28.54	15.46	16.16	0.14	0.16	0.16	99.66
	5	1071	3		1	0.03	35.80	31.47	14.97	15.97	0.15	0.09	0.20	98.68
	5	1071	1		2	0.02	38.63	29.13	15.18	16.24	0.16	0.23	0.20	99.79
	5	1071	avg	all var	4	0.02	37.82	29.71	15.20	16.12	0.15	0.16	0.19	99.38
lherz	5	1079.2	6	small	1	0.02	39.71	27.50	14.36	16.03	0.21	0.16	0.19	98.18
lherz	5	1079.2	5	largest	2	0.04	39.99	27.07	14.49	16.33	0.15	0.20	0.19	98.46
lherz	5	1079.2	3	aw cpx	1	0.03	40.21	26.98	14.63	16.29	0.11	0.20	0.22	98.67
lherz	5	1079.2	avg		4	0.03	39.97	27.18	14.49	16.22	0.16	0.19	0.20	98.44
	4	1086	3	rim	2	0.02	28.81	39.55	17.63	12.39	0.20	0.07	0.33	99.00
	4	1086	3	core	2	0.01	28.57	40.25	17.48	12.38	0.20	0.02	0.30	99.21
	4	1086	2		2	0.02	30.39	36.38	18.27	12.22	0.18	0.07	0.44	97.97
	4	1086	1		2	0.02	27.47	39.90	17.29	12.72	0.20	0.12	0.30	100.02
	4	1086	avg		8	0.02	29.31	39.02	17.67	12.43	0.20	0.07	0.34	99.05
	4	1090	5	incl	1	0.07	11.76	57.25	17.87	9.82	0.24	0.07	0.25	97.33
	4	1090	5	incl	1	0.05	11.78	57.49	18.34	9.22	0.19	0.09	0.23	97.39
	4	1090	3	rim to ol	2	0.03	12.50	56.68	20.63	8.71	0.24	0.04	0.26	99.09
	4	1090	3	rim to opx	2	0.02	11.38	58.51	19.38	9.01	0.23	0.05	0.25	98.83
	4	1090	3	core	2	0.05	11.71	57.92	19.48	9.29	0.19	0.07	0.26	98.97
	4	1090	avg	(N)	8	0.04	11.83	57.57	19.14	9.21	0.22	0.06	0.25	98.32
	2	1112	6	core	1	0.06	31.62	36.68	18.08	14.67	0.22			101.33
	2	1112	6	rim	1	0.07	31.72	35.82	18.05	14.69	0.22			100.57
	2	1112	5		1	0.06	31.93	35.52	17.80	14.21	0.23			99.75
	2	1112	4		3	0.05	32.11	35.91	17.75	14.54	0.21			100.57
	2	1112	2		1	0.08	29.59	37.05	19.71	13.58	0.23			100.24
	2	1112	avg		9	0.06	31.39	36.20	18.28	14.34	0.22			100.49
	1	1118	?		1	0.05	38.41	30.14	15.30	16.20	0.21			100.31
	1	1118	9		2	0.07	26.94	38.67	20.55	12.46	0.26			98.95
	1	1118	7		1	0.07	33.89	33.14	18.33	14.00	0.22			99.65
	1	1118	7		1	0.07	31.96	35.14	17.46	14.78	0.14			99.55
	1	1118	5		1	0.02	39.10	27.60	19.37	14.04	0.21			100.34
	1	1118	3		2	0.00	34.89	32.32	18.27	14.04	0.22			99.74
	1	1118	10	near plag?	1	0.06	40.17	27.31	16.60	15.64	0.16			99.94
	1	1118	10	in mx	1	0.04	38.72	26.62	18.17	14.65	0.17			98.37
	1	1118	1		2	0.05	28.02	37.58	21.48	11.69	0.21			99.03
	1	1118	avg	all var	12	0.05	34.68	32.06	18.39	14.17	0.20			99.54
	2	1125	6	core	1	0.04	34.91	34.08	16.36	15.14	0.16	0.15	0.27	101.11
	2	1125	6	rim	2	0.03	32.64	34.86	16.82	14.54	0.19	0.14	0.23	99.45
	2	1125	4		2	0.01	35.00	32.80	16.42	15.14	0.16	0.15	0.26	99.94
	2	1125	avg	(R)	5	0.03	34.18	33.91	16.53	14.94	0.17	0.15	0.25	100.17
amp-hz	2	1136.2	7	rim	3	0.14	37.02	28.72	18.86	14.88	0.21			99.83
amp-hz	2	1136.2	7	corg	2	0.12	38.43	29.91	17.90	14.90	0.14			101.40
amp-hz	2	1136.2	5		2	0.10	37.38	30.28	18.60	14.83	0.18			101.37
amp-hz	2	1136.2	1		1	0.10	37.73	28.96	19.19	13.81	0.19			99.98
amp-hz	2	1136.2	avg	low-T SZ (R)	8	0.12	37.64	29.47	18.64	14.61	0.18			100.65
	TU	1141	8	core	1	0.04	22.35	46.76	17.51	12.83	0.21			99.70
	TU	1141	7	rim	2	0.04	21.21	47.27	17.74	12.38	0.24			98.88
	TU	1141	7	core	1	0.04	21.46	46.41	17.67	12.85	0.23			98.66
	TU	1141	6		2	0.03	22.02	45.94	18.58	12.68	0.27			99.52
	TU	1141	avg		5	0.04	21.76	46.60	17.88	12.69	0.24			99.19
	5	1143	6	core	1	0.04	36.80	32.76	14.98	15.81	0.16			100.55
	5	1143	6	rim	1	0.02	36.24	32.99	15.25	15.21	0.21			99.92
	5	1143	10	core	2	0.04	35.85	33.05	15.00	15.64	0.16			99.74
	5	1143	10	rim to ol	1	0.01	37.33	30.88	14.71	15.85	0.19			98.93
	5	1143	10	rim to opx	1	0.04	36.36	32.12	14.83	16.27	0.17			99.79
	5	1143	avg	(N)	6	0.03	36.52	32.36	14.95	15.76	0.17			99.79
	5	1145	9		1	0.00	37.25	29.77	17.41	14.59	0.17	0.20	0.30	99.69
	5	1145	5		1	0.02	34.96	33.39	16.77	14.35	0.14	0.11	0.22	99.96
	5	1145	3	rim	3	0.02	36.07	32.30	16.49	14.92	0.15	0.20	0.24	100.39
	5	1145	3	core	1	0.03	33.62	35.05	16.76	14.88	0.18	0.16	0.22	100.90

Tab. B-3a (continued)

rocktype	unit	sample	spot	comment	N	TiO2	Al2O3	Cr2O3	Fe tot	MgO	MnO	NiO	V2O5	SUM
	5	1145	avg	(N) Al,Cr var	6	0.02	35.48	32.63	16.86	14.69	0.16	0.17	0.25	100.24
umyl	UMY	1153.1	3	core	2	0.05	56.86	10.72	12.69	19.59	0.11	0.19	0.09	100.30
umyl	UMY	1153.1	2	along opx pc	2	0.03	57.20	9.46	13.03	19.82	0.14	0.38	0.08	100.14
umyl	UMY	1153.1	1	core	1	0.06	55.27	8.89	15.19	19.30	0.19	0.45	0.13	99.48
umyl	UMY	1153.1	avg		5	0.05	56.44	9.69	13.64	19.57	0.15	0.34	0.10	99.97
	TU	1165	7	rim	1	0.02	25.48	42.34	17.07	11.28	0.14	0.06	0.30	96.69
	TU	1165	7	core	2	0.02	24.44	44.91	16.51	11.78	0.21	0.06	0.29	98.22
	TU	1165	4		2	0.02	26.14	42.66	18.35	11.36	0.21	0.08	0.30	99.12
	TU	1165	2	core	2	0.00	25.11	43.84	16.82	11.98	0.12	0.09	0.26	98.22
	TU	1165	avg	(N)	7	0.02	25.29	43.44	17.19	11.60	0.17	0.07	0.29	98.06
du	TU	1169	2	core	2	0.02	8.23	61.57	17.96	9.54	0.25	0.05	0.29	97.91
du	TU	1169	1	core	2	0.04	8.79	61.48	18.62	9.53	0.29	0.05	0.26	99.06
du	TU	1169	1	rim	2	0.04	8.93	61.14	19.33	9.20	0.29	0.04	0.31	99.28
du	TU	1169	avg		6	0.03	8.65	61.40	18.64	9.42	0.28	0.05	0.29	98.75
	5	1181	?	aw opx nb	1	0.03	43.53	25.49	13.06	17.92	0.11	0.21	0.17	100.52
	5	1181	4	aw cpx	1	0.03	43.87	24.60	13.95	17.73	0.16	0.22	0.18	100.74
	5	1181	2	rim ol + cpx	4	0.02	42.23	26.44	13.97	17.57	0.16	0.20	0.20	100.79
	5	1181	2	core	2	0.04	40.95	27.44	14.36	17.57	0.17	0.18	0.19	100.90
	5	1181	avg	(N)	8	0.03	42.65	25.99	13.84	17.70	0.15	0.20	0.19	100.74
nxt opxt	3	1189.1	8	core	1	0.07	18.62	50.21	19.97	10.84	0.29			100.00
nxt opxt	3	1189.1	8	smallest grain	1	0.10	18.16	49.32	23.08	9.70	0.35			100.71
nxt opxt	3	1189.1	8	rim	2	0.07	18.14	49.89	21.06	10.41	0.28			99.85
nxt opxt	3	1189.1	4	rim	2	0.06	18.69	48.43	23.15	9.73	0.33			100.39
nxt opxt	3	1189.1	4	core	2	0.05	17.92	50.53	21.05	10.87	0.23			100.65
nxt opxt	3	1189.1	1	small grain	2	0.05	19.80	48.78	20.91	10.57	0.26			100.37
nxt opxt	3	1189.1	1	core	2	0.06	18.39	49.94	21.92	9.80	0.25			100.36
nxt opxt	3	1189.1	1	all var	5	0.07	17.69	51.21	22.48	9.39	0.34			101.18
nxt opxt	3	1189.1	avg	(R)	17	0.07	18.43	49.79	21.70	10.16	0.29			100.44
far opxt	3	1189.2	6	core	2	0.02	35.64	31.78	15.55	16.09	0.21	0.20	0.20	99.69
far opxt	3	1189.2	6	rim to cpx	2	0.03	36.93	30.68	15.28	15.76	0.21	0.16	0.18	99.23
far opxt	3	1189.2	4		2	0.04	36.98	28.82	17.32	17.08	0.21	0.16	0.19	100.80
far opxt	3	1189.2	2	aw cpx	1	0.02	41.78	23.31	16.72	16.07	0.16	0.23	0.22	98.51
far opxt	3	1189.2	avg	(N) Al,Cr var	7	0.03	37.83	28.65	16.22	16.25	0.20	0.19	0.20	99.56
du	3	1193	4		2	0.19	20.19	49.09	16.63	12.66	0.25	0.09	0.28	99.38
du	3	1193	3	core	2	0.16	19.45	50.94	14.48	13.56	0.21	0.11	0.22	99.13
du	3	1193	3	rim	2	0.17	18.68	50.93	15.29	12.69	0.23	0.13	0.25	98.37
du	3	1193	avg	(R)	6	0.17	19.44	50.32	15.47	12.97	0.23	0.11	0.25	98.96
	4	1194	7	core	1	0.11	28.55	40.01	16.82	13.10	0.18	0.10	0.21	99.08
	4	1194	5	core	1	0.10	28.45	39.88	17.05	13.62	0.24	0.13	0.14	99.61
	4	1194	5	rim	1	0.10	31.60	36.26	17.81	13.83	0.13	0.12	0.20	100.05
	4	1194	2		1	0.07	28.91	39.60	17.34	13.17	0.08	0.10	0.21	99.48
	4	1194	avg	(N)	4	0.10	29.38	38.94	17.26	13.43	0.16	0.11	0.19	99.56
	4	1195	3	core	1	0.02	28.68	38.40	17.77	12.39	0.20	0.14	0.26	97.86
	4	1195	2	core		0.02	30.53	38.58	17.18	12.73	0.14	0.14	0.26	99.58
	4	1195	2	rim	1	0.04	31.01	36.68	17.48	12.85	0.18	0.10	0.26	98.60
	4	1195	avg	(N)	3	0.03	30.07	37.89	17.48	12.66	0.17	0.13	0.26	98.68
	TU	1200	7	rim to opx	1	0.05	19.59	48.46	17.43	12.66	0.21			98.40
	TU	1200	7	rim to ol	2	0.03	19.64	49.89	17.87	12.41	0.22			100.06
	TU	1200	7	core	2	0.03	19.53	49.74	17.61	12.68	0.23			99.82
	TU	1200	2	core	1	0.05	21.21	48.32	17.43	12.80	0.21			100.02
	TU	1200	2	rim to ol	1	0.04	21.39	47.81	18.20	12.84	0.23			100.51
	TU	1200	avg		7	0.04	20.27	48.84	17.71	12.68	0.22			99.76
lherz	6	1214	3	core	2	0.04	55.48	12.68	11.97	20.32	0.01	0.32	0.11	100.93
lherz	6	1214	3	rim	2	0.08	54.84	12.69	11.86	19.13	0.16	0.36	0.07	99.19
lherz	6	1214	4	smaller	1	0.02	55.70	11.71	12.55	19.93	0.03	0.41	0.11	100.46
lherz	6	1214	?	aw cpx	1	0.02	55.92	12.23	12.03	20.37	0.17	0.38	0.14	101.26
lherz	6	1214	avg		6	0.04	55.49	12.33	12.10	19.94	0.09	0.37	0.11	100.46
amp-hz	6	1222	7		1	0.06	34.61	29.86	21.04	12.92	0.20	0.16	0.12	98.97
amp-hz	6	1222	5	1/2 rim	1	0.03	56.13	10.70	13.56	18.76	0.12	0.38	0.13	99.81
amp-hz	6	1222	3	rim	1	0.02	46.84	11.49	20.62	18.48	0.16	0.38	0.09	98.08
amp-hz	6	1222	3	core	1	0.01	54.66	12.84	12.40	19.34	0.09	0.30	0.07	99.71
amp-hz	6	1222	2		2	0.06	23.70	40.56	25.02	10.30	0.25	0.10	0.12	100.11
amp-hz	6	1222	1	rim	2	0.02	50.37	16.39	15.36	17.64	0.15	0.23	0.08	100.24
amp-hz	6	1222	1	core	2	0.02	52.59	14.15	13.42	18.86	0.13	0.34	0.10	99.61
amp-hz	6	1222	avg	sh zone. all var	10	0.03	45.56	19.43	17.35	16.61	0.16	0.27	0.10	99.50
umyl	UMY	1225	3	rim	1	0.01	51.66	14.50	16.33	19.05	0.12	0.40	0.11	102.18
umyl	UMY	1225	3	core	1	0.03	52.70	14.05	14.86	18.97	0.11	0.30	0.11	101.13
umyl	UMY	1225	2	rim	1	0.02	51.61	15.23	15.47	18.85	0.13	0.35	0.15	101.81
umyl	UMY	1225	2	core	1	0.03	51.03	15.18	15.77	18.50	0.14	0.38	0.13	101.16
umyl	UMY	1225	1	core	2	0.04	52.25	13.94	15.62	18.62	0.11	0.39	0.11	101.08

Tab. B-3a (continued)

rocktype	unit	sample	spot	comment	N	TiO2	Al2O3	Cr2O3	Fe tot	MgO	MnO	NiO	V2O5	SUM
umyl	UMY	1225	avg		6	0.03	51.85	14.58	15.61	18.80	0.12	0.36	0.12	101.47
umyl	UMY	1228.1	7	core	1	0.09	29.81	35.61	20.44	12.76	0.30			99.01
umyl	UMY	1228.1	7	rim	1	0.05	40.57	25.44	18.68	14.91	0.20			99.85
umyl	UMY	1228.1	6		1	0.09	31.09	34.71	20.65	12.48	0.21			99.23
umyl	UMY	1228.1	6	rim	1	0.07	36.07	30.32	19.44	13.63	0.21			99.74
umyl	UMY	1228.1	5?		1	0.02	58.68	8.62	12.86	19.33	0.12			99.63
umyl	UMY	1228.1	4	rim	3	0.11	37.88	27.56	19.00	14.61	0.18			99.34
umyl	UMY	1228.1	4	core	2	0.10	35.93	30.88	19.04	14.10	0.22			100.27
umyl	UMY	1228.1	3	core	2	0.13	26.33	38.66	22.46	11.83	0.25			99.66
umyl	UMY	1228.1	3	rim	2	0.11	36.07	30.36	19.29	13.98	0.19			100.00
umyl	UMY	1228.1	3	1/2 rim	1	0.12	29.65	36.84	20.84	12.67	0.21			100.33
umyl	UMY	1228.1	2		2	0.02	53.79	13.80	14.63	18.53	0.10			100.87
umyl	UMY	1228.1	avg	(N) all var	17	0.08	37.81	28.44	18.85	14.44	0.20			99.81
	3	1232	8		1	0.03	29.49	37.79	16.79	14.16	0.17			98.43
	3	1232	1	larger	1	0.04	29.67	37.82	16.16	14.62	0.10			98.41
	3	1232	1	small	1	0.05	29.56	38.15	15.02	15.21	0.16			98.15
	3	1232	avg		3	0.04	29.57	37.92	15.99	14.66	0.14			98.33
	3	1237	8	aw cpx	1	0.02	34.26	33.29	17.97	14.06	0.17	0.17	0.23	100.17
	3	1237	7?	rim to cpx	2	0.03	31.77	35.77	18.25	14.03	0.19	0.19	0.23	100.43
	3	1237	7	rim to ol	2	0.01	32.97	34.35	18.71	14.17	0.18	0.14	0.22	100.75
	3	1237	7	core	2	0.04	31.13	36.21	18.48	13.84	0.14	0.15	0.23	100.22
	3	1237	avg	(N)	7	0.03	32.53	34.91	18.35	14.02	0.17	0.16	0.23	100.39
	4	1245	7	core	1	0.03	12.27	56.84	20.10	9.53	0.28	0.07	0.32	99.44
	4	1245	6	core, Fe,Mg var	2	0.03	12.55	57.20	20.19	9.30	0.24	0.04	0.31	99.86
	4	1245	6	rim to ol	2	0.04	13.08	55.69	21.31	8.75	0.23	0.11	0.30	99.51
	4	1245	2		2	0.03	13.28	55.36	20.37	8.95	0.26	0.07	0.32	98.64
	4	1245	avg	(N)	7	0.03	12.80	56.27	20.49	9.13	0.25	0.07	0.31	99.36
	4	1249	?	small in mx	1	0.00	22.26	44.20	22.01	10.40	0.28	0.07	0.33	99.55
	4	1249	7	core	1	0.02	18.52	49.32	19.76	10.93	0.23	0.12	0.25	99.15
	4	1249	7	rim	1	0.00	19.49	47.85	19.92	10.88	0.23	0.02	0.32	98.71
	4	1249	4	core	1	0.01	19.35	49.27	20.08	10.42	0.23	0.09	0.31	99.76
	4	1249	4	rim	1	0.01	21.88	45.77	20 20	11.00	0.18	0.02	0.29	99.35
	4	1249	avg	(N)	5	0.01	20.30	47.28	20.39	10.73	0.23	0.06	0.30	99.30
	3	1251	3	rim to ol	1	0.00	33.92	33.29	15.18	15.10	0.12	0.08	0.21	97.90
	3	1251	3	core	2	0.03	34.23	33.52	15.25	15.89	0.17	0.14	0.20	99.43
	3	1251	3	rim to cpx	2	0.02	35.75	31.37	15.21	15.94	0.14	0.12	0.18	98.73
	3	1251	2		1	0.04	33.86	33.72	15 95	15.44	0.08	0.13	0.20	99.42
	3	1251	1	rim, all var	4	0.04	35.03	33.16	15.30	16.13	0.16	0.10	0.16	100.08
	3	1251	1	core	2	0.04	33.79	34.69	14.98	16.41	0.13	0.11	0.20	100.35
	3	1251	avg		12	0.03	34.43	33.29	15.31	15.82	0.13	0.11	0.19	99.32
	3	1258	4		2	0.04	25.02	42.01	18.14	13.40	0.24			98.85
	3	1258	3		2	0.04	25.48	41.65	17.71	13.41	0.16			98.45
	3	1258	2	rim	1	0.04	24.03	44.09	18.68	13.92	0.22			100.98
	3	1258	2	core	1	0.06	23.69	43.63	18.63	13.46	0.27			99.74
		1258	avg	(N) hz host	6	0.05	24.56	42.35	18.29	13.55	0.22			99.51
	3	1258	1		2	0.05	24.42	42.89	18 75	13.26	0.18			99.55
		1258	avg	du band	1	0.05	24.42	42.89	18.75	13.26	0.18			99.55
	3	1262	4	next to opx	2	0.03	38.35	28.86	16.20	16.08	0.17			99.69
	3	1262	3	incl in opx	2	0.05	35.79	32.14	16.05	15.96	0.20			100.19
	3	1262	2	incl	1	0.03	38.70	28.82	15.77	16.22	0.16			99.70
	3	1262	2		2	0.04	38.14	29.65	16.37	15.90	0.21			100.31
	3	1262	avg		7	0.04	37.75	29.87	16.10	16.04	0.19			99.97
	4	1272	2	core	1	0.01	26.18	40.16	17.81	12.43	0.20	0.14	0.21	97.14
	4	1272	1	rim to cpx	2	0.04	24.95	42.37	18.48	12.12	0.16	0.07	0.21	98.40
	4	1272	1	rim to ol	3	0.05	26.63	40.88	18.52	12.21	0.18	0.12	0.25	98.84
	4	1272	1	core	2	0.04	24.68	43.16	18.38	12.21	0.21	0.12	0.25	99.05
	4	1272	avg	(N)	8	0.04	25.61	41.64	18.30	12.24	0.19	0.11	0.23	98.36
	4	1274	6		1	0.00	28.66	38.66	19.60	11.98	0.13	0.07	0.26	99.36
	4	1274	2	core, Fe,Mg var	2	0.04	29.16	37.68	18.53	12.20	0.17	0.11	0.25	98.14
	4	1274	avg		3	0.02	28.91	38.17	19.07	12.09	0.15	0.09	0.26	98.75
	3	1292			1	0.04	35.00	33.00	16.41	14.80	0.17	0.15	0.24	99.81
	3	1292	?	rim	1	0.00	33.34	34.61	18.80	14.38	0.22	0.12	0.26	101.73
	3	1292	?	core	2	0.04	32.13	34.56	16.94	14.21	0.18	0.15	0.20	98.41
	3	1292	5	core	3	0.04	34.28	34.09	16.70	14.81	0.23	0.12	0.24	100.51
	3	1292	4	core	2	0.04	32.00	35.46	17.00	14.79	0.20	0.12	0.25	99.86
	3	1292	avg	(N)	9	0.03	33.35	34.34	17.17	14.60	0.20	0.13	0.24	100.06
	3	1295	6	rim	2	0.02	38.30	29.69	14.46	16.97	0.12	0.14	0.18	99.88
	3	1295	6	core	2	0.03	38.06	30.23	15.00	16.77	0.14	0.19	0.21	100.63
	3	1295	1	aw cpx,rim	1	0.00	38.14	30.20	14.98	16.80	0.22	0.27	0.18	100.79
	3	1295	1	aw cpx,core	1	0.02	38.36	30.14	15.52	17.01	0.14	0.17	0.20	101.56

Tab. B-3a (continued)

rocktypeunit	sample	spotcomment	N	TiO2	Al2O3	Cr2O3	Fe tot	MgO	MnO	NiO	V2O5	SUM
3	1295	avg	6	0.02	38.22	30.07	14.99	16.89	0.16	0.19	0.19	100.72
1	1315	3 core	1	0.08	13.45	50.18	26.52	9.79	0.34			100.36
1	1315	3 rim	2	0.09	13.81	49.78	26.96	9.99	0.31			100.94
1	1315	2	2	0.08	15.04	48.93	25.83	10.72	0.30			100.90
1	1315	1	2	0.05	16.84	46.53	25.79	10.48	0.21			99.90
1	1315	avg (N)	7	0.08	14.79	48.86	26.28	10.25	0.29			100.53
1	1316	5 core	1	0.20	45.31	20.93	16.18	18.22	0.19	0.23	0.16	101.42
1	1316	4	4	0.18	44.03	21.36	16.16	17.96	0.13	0.21	0.16	100.19
1	1316	3	2	0.18	44.28	21.27	16.38	17.93	0.14	0.25	0.18	100.61
1	1316	1	1	0.20	45.04	21.02	16.39	18.10	0.16	0.14	0.17	101.22
1	1316	avg	8	0.19	44.67	21.15	16.28	18.05	0.16	0.21	0.17	100.86
chrom. 1	1316.2	4 ol mx	1	0.20	51.14	13.88	15.52	18.26	0.15	0.34	0.23	99.72
chrom. 1	1316.2	4 smallest grain	1	0.18	50.16	13.51	18.30	17.21	0.11	0.30	0.21	99.98
chrom. 1	1316.2	2 away from plag	2	0.24	52.71	12.30	15.54	18.98	0.14	0.32	0.21	100.44
chrom. 1	1316.2	2 incl in plag	3	0.08	54.77	12.67	13.70	19.04	0.11	0.25	0.17	100.79
chrom. 1	1316.2	avg sp-rich du	7	0.18	52.20	13.09	15.77	18.37	0.13	0.30	0.21	100.23
chrom. 1	1316.2	1 chr seam	1	0.24	41.59	24.05	16.58	16.94	0.20	0.27	0.26	100.13
chrom. 1	1316.2	1 chr seam	2	0.27	40.94	24.08	18.04	16.85	0.13	0.26	0.27	100.84
chrom. 1	1316.2	avg chr seam	3	0.26	41.27	24.07	17.31	16.90	0.17	0.27	0.27	100.49
du 1	1321	2 near cpx	1	0.34	30.84	32.63	22.19	13.47	0.21	0.21	0.29	100.18
du 1	1321	1 large, core	2	0.36	30.62	33.29	20.68	13.54	0.21	0.19	0.26	99.15
du 1	1321	1 same, rim	2	0.38	29.28	33.74	20.79	13.82	0.22	0.21	0.27	98.71
du 1	1321	avg (R)	5	0.36	30.25	33.22	21.22	13.61	0.21	0.20	0.27	99.35
du-band 1	1324	6 core	1	0.23	15.55	49.88	24.55	9.98	0.14			100.33
du-band 1	1324	6 rim	2	0.26	15.83	49.66	25.14	9.79	0.27			100.95
du-band 1	1324	6 rim	2	0.26	15.83	49.66	25.14	9.79	0.27			100.95
du-band 1	1324	5 rim	2	0.24	16.86	48.98	23.94	10.15	0.34			100.51
du-band 1	1324	5 rim	2	0.24	16.86	48.98	23.94	10.15	0.34			100.51
du-band 1	1324	5 core	2	0.22	17.53	48.96	23.25	10.43	0.31			100.70
hz-band 1	1324	4	1	0.15	18.29	48.30	23.66	9.79	0.29			100.48
hz-band 1	1324	3 core	1	0.16	19.01	48.78	21.26	11.06	0.27			100.54
hz-band 1	1324	3 rim	1	0.15	18.79	48.22	22.08	10.94	0.23			100.41
hz-band 1	1324	1 rim	1	0.08	18.95	48.25	21.79	11.25	0.27			100.59
hz-band 1	1324	1 core	1	0.09	18.49	49.10	22.66	10.73	0.26			101.33
hz-band 1	1324	avg hz host	14	0.13	18.71	48.53	22.29	10.75	0.26			100.67
du-band 1	1324	avg (N) du-band	5	0.24	16.44	49.37	24.22	10.09	0.27			100.62
cpx-troc 1	1326	4 larger, mx	1	0.12	41.23	25.43	15.96	17.36	0.17	0.23	0.19	100.69
cpx-troc 1	1326	3 in mx	3	0.14	40.64	24.64	15.63	16.66	0.13	0.22	0.18	98.24
cpx-troc 1	1326	1 incl in plag	2	0.08	43.39	24.17	13.80	17.11	0.12	0.19	0.15	99.01
cpx-troc 1	1326	1 next to cpx	2	0.10	44.16	22.30	14.32	17.90	0.15	0.24	0.16	99.34
cpx-troc 1	1326	avg	8	0.11	42.36	24.14	14.93	17.26	0.15	0.22	0.17	99.32
pl-wehrl 2	1331.1	8	2	0.05	39.88	27.80	15.88	16.45	0.16	0.15	0.23	100.60
pl-wehrl 2	1331.1	8 rim	1	0.09	39.53	28.18	15.18	16.22	0.16	0.21	0.18	99.75
pl-wehrl 2	1331.1	6 rim	1	0.13	40.15	27.06	16.54	16.66	0.10	0.24	0.18	101.06
pl-wehrl 2	1331.1	6 core	1	0.07	40.04	27.88	15.73	16.89	0.15	0.23	0.20	101.19
pl-wehr 2	1331.1	4	1	0.09	39.59	27.97	16.27	16.19	0.14	0.20	0.25	100.70
pl-wehrl 2	1331.1	avg (N)	6	0.09	39.84	27.78	15.92	16.48	0.14	0.21	0.21	100.66
du 2	1331.2	2 large, core	2	0.31	31.42	32.79	22.36	13.44	0.16	0.21	0.21	100.90
du 2	1331.2	2 rim	3	0.34	30.91	32.05	24.62	13.00	0.19	0.15	0.22	101.48
du 2	1331.2	1 core	1	0.31	31.53	32.88	22.11	13.28	0.20	0.14	0.19	100.64
du 2	1331.2	avg	6	0.32	31.29	32.57	23.03	13.24	0.18	0.17	0.21	101.01
3	1340	6 core	1	0.04	18.99	49.27	20.23	10.73	0.22	0.11	0.32	99.91
3	1340	4 core	2	0.05	19.48	47.69	21.39	10.63	0.25	0.06	0.33	99.88
3	1340	4 rim	2	0.04	19.85	47.11	21.55	10.48	0.26	0.12	0.38	99.79
3	1340	1	3	0.03	19.28	48.51	20.28	10.55	0.32	0.07	0.35	99.39
3	1340	avg (N)	8	0.04	19.40	48.15	20.86	10.60	0.26	0.09	0.35	99.74
3	1344	4 small	3	0.00	26.92	40.90	18.50	12.36	0.14	0.14	0.24	99.20
3	1344	3 core	2	0.03	27.84	40.75	16.71	12.66	0.20	0.14	0.21	98.54
3	1344	2 rim, Cr,Al var	4	0.00	29.14	39.53	15.95	13.29	0.19	0.17	0.21	98.48
3	1344	2 core, in opx	2	0.02	28.02	40.61	16.05	13.36	0.20	0.18	0.21	98.65
3	1344	1 core	1	0.00	27.53	41.84	16.22	14.20	0.21	0.09	0.20	100.29
3	1344	avg (N)	12	0.01	27.89	40.73	16.69	13.17	0.19	0.14	0.21	99.03
3	1350	7	2	0.03	37.69	29.98	15.34	16.07	0.18	0.14	0.20	99.63
3	1350	3 in mx	1	0.03	36.17	31.39	14.77	16.25	0.19	0.20	0.25	99.25
3	1350	3 incl in opx	2	0.01	35.55	32.89	13.60	16.40	0.21	0.21	0.23	99.10
3	1350	2 incl in opx	2	0.02	36.15	32.04	14.48	16.73	0.18	0.17	0.18	99.95
3	1350	avg	7	0.02	36.39	31.58	14.55	16.36	0.19	0.18	0.22	99.48
du 1	1353	4	2	0.33	33.65	30.60	19.32	14.84	0.11	0.21	0.21	99.27
du 1	1353	3 large, core	3	0.31	34.95	30.53	19.47	15.78	0.14	0.23	0.17	101.58
du 1	1353	3 same, rim	2	0.27	35.71	27.80	19.39	15.13	0.19	0.22	0.17	98.88

Tab. B-3a (continued)

rocktype	unit	sample	spot	comment	N	TiO2	Al2O3	Cr2O3	Fe tot	MgO	MnO	NiO	V2O5	SUM
du	1	1353	2		1	0.29	34.06	30.33	19.89	14.72	0.12	0.18	0.17	99.76
du	1	1353	avg	(N)	8	0.30	34.59	29.82	19.52	15.12	0.14	0.21	0.18	99.87
pl-band	1	1360	8	core	2	0.33	34.36	31.43	18.69	14.48	0.11	0.14	0.19	99.73
pl-band	1	1360	6	core	1	0.29	34.23	30.71	18.50	14.98	0.28	0.14	0.00	99.13
pl-band	1	1360	6	rim	1	0.24	34.87	31.46	18.41	14.68	0.17	0.10	0.18	100.11
pl-band	1	1360	4	rim to ol	2	0.23	32.89	33.14	18.34	13.85	0.27	0.11	0.21	99.04
pl-band	1	1360	4	rim to plag	2	0.29	34.50	32.20	17.03	14.79	0.13	0.11	0.18	99.23
pl-band	1	1360	4	core	1	0.18	34.86	32.14	17.92	14.77	0.06	0.02	0.19	100.14
pl-band	1	1360	4	large grain	2	0.25	33.59	32.59	17.76	14.37	0.17	0.18	0.17	99.08
pl-band	1	1360	avg	(N) pl wehrl	11	0.26	34.19	31.95	18.09	14.56	0.17	0.11	0.16	99.49
du-band	1	1360	2		2	0.21	31.43	33.17	22.46	13.04	0.14	0.05	0.15	100.65
du-band	1	1360	1	small	2	0.28	31.97	33.44	21.10	13.53	0.21	0.17	0.26	100.96
du-band	1	1360	avg	cpx-du	4	0.25	31.70	33.31	21.78	13.29	0.18	0.11	0.21	100.81
umyl	6	1366.2	5		1	0.00	34.77	30.36	19.59	14.39	0.18	0.10	0.21	99.60
umyl	6	1366.2	5	incl in opx	2	0.00	40.18	28.07	17.45	14.54	0.17	0.12	0.19	100.72
umyl	6	1366.2	4		2	0.05	34.90	33.67	16.77	14.75	0.19	0.11	0.22	100.66
umyl	6	1366.2	3	Fe,Mg var	4	0.02	35.25	32.69	17.94	14.11	0.21	0.12	0.20	100.54
umyl	6	1366.2	avg	all var	9	0.02	36.28	31.20	17.94	14.45	0.19	0.11	0.21	100.38
	5	1378	5		2	0.00	39.88	27.95	14.27	16.91	0.13	0.22	0.18	99.54
	5	1378	3		2	0.02	38.94	28.83	14.52	16.61	0.13	0.16	0.18	99.39
	5	1378	avg		4	0.01	39.41	28.39	14.40	16.76	0.13	0.19	0.18	99.47
	3	1396	7	rim	2	0.04	20.02	48.96	21.70	10.85	0.25	0.05	0.31	102.18
	3	1396	7	core	2	0.03	19.59	49.87	20.62	11.22	0.22	0.05	0.31	101.91
	3	1396	5	rim	1	0.03	20.18	48.04	21.85	10.55	0.27	0.00	0.31	101.23
	3	1396	5	core	1	0.05	18.93	49.95	20.77	10.33	0.21	0.12	0.31	100.67
	3	1396	3	incl in opx	2	0.04	21.53	47.27	20.65	11.07	0.26	0.07	0.25	101.14
	3	1396	avg	(N)	8	0.04	20.05	48.82	21.12	10.80	0.24	0.06	0.30	101.43
hz-band	3	1402	10		1	0.14	16.28	52.29	21.31	9.60	0.26	0.05	0.39	100.32
hz-band	3	1402	9		1	0.16	15.50	51.68	21.32	9.54	0.29	0.07	0.30	98.86
hz-band	3	1402	avg	hz band	2	0.15	15.89	51.99	21.32	9.57	0.28	0.06	0.35	99.59
trans	3	1402	7		1	0.11	14.74	51.92	21.91	9.41	0.27	0.07	0.29	98.72
trans	3	1402	5	rim	2	0.14	13.97	53.66	21.45	9.46	0.16	0.06	0.34	99.24
trans	3	1402	5	core	2	0.11	15.17	52.95	19.37	9.88	0.21	0.07	0.35	98.11
trans	3	1402	avg	(R) trarsition	5	0.12	14.63	52.84	20.91	9.58	0.21	0.07	0.33	98.69
du	3	1402	4		1	0.14	13.93	53.51	22.13	9.32	0 33	0.14	0.32	99.72
du	3	1402	3	rim	2	0.18	14.24	52.63	23.07	9.18	0.22	0.09	0.34	99.95
du	3	1402	3	core	2	0.12	14.42	52.66	21.59	9.67	0.30	0.02	0.33	99.11
du	3	1402	2		1	0.10	15.91	51.34	21.52	9.58	0.26	0.07	0.33	99.11
du	3	1402	1		2	0.09	14.36	52.69	23.05	9.50	0.29	0.07	0.30	100.35
du	3	1402	avg	du	8	0.13	14.57	52.57	22.27	9.45	0.28	0.06	0.32	99.65
du	1	1415	3	core	2	0.18	40.71	26.07	15.75	17.54	0.18	0.26	0.20	100.89
du	1	1415	3	rim	2	0.12	40.31	26.10	17.51	17.23	0.16	0.13	0.20	101.76
du	1	1415	2		1	0.13	40.75	25.11	16.66	16.76	0.12	0.17	0.26	99.96
du	1	1415	1		1	0.19	41.24	26.09	16.91	17.41	0.14	0.19	0.18	102.35
du	1	1415	avg		6	0.16	40.75	25.84	16.71	17.24	0.15	0.19	0.21	101.24
lherz	2	1420	3		2	0.20	33.23	32.99	19.47	13.95	0.16	0.16	0.30	100.46
lherz	2	1420	2		2	0.18	32.06	34.14	20.00	13.63	0.14	0.16	0.34	100.65
lherz	2	1420	10		2	0.24	30.16	35.88	21.06	13.05	0.14	0.13	0.33	100.99
lherz	2	1420	avg		6	0.21	31.82	34.34	20.18	13.54	0.15	0.15	0.32	100.70
	2	1428	4	core	2	0.02	26.40	42.71	18.94	13.29	0.18	0.11	0.30	101.95
	2	1428	3		1	0.00	28.32	39.82	19.56	13.43	0.16	0.16	0.34	101.79
	2	1428	2		1	0.02	27.73	40.88	18.64	13.34	0.19	0.09	0.30	101.19
	2	1428	avg		4	0.01	27.48	41.14	19.05	13.35	0.18	0.12	0.31	101.64
	2	1442.1	4out		1	0.00	40.52	27.00	16.79	16.52	0.14	0.21	0.20	101.38
	2	1442.1	2		1	0.03	40.46	27.16	15.38	16.47	0.11	0.28	0.21	100.10
	2	1442.1	1		1	0.01	40.39	27.58	15.95	16.07	0.14	0.19	0.21	100.24
	2	1442.1	avg		3	0.01	40.36	27.25	16.04	16.35	0.13	0.23	0.21	100.57
cpx-du	2	1447	4	small	1	0.16	35.66	27.57	22.34	13.54	0.23	0.23	0.28	100.01
cpx-du	2	1447	5	core	3	0.19	37.85	26.58	19.19	15.62	0.16	0.30	0.20	100.09
cpx-du	2	1447	5	rim	2	0.16	38.42	25.59	19.33	15.52	0.09	0.24	0.23	99.57
cpx-du	2	1447	6	core	2	0.24	37.35	26.92	20.47	15.29	0.16	0.26	0.24	100.93
cpx-du	2	1447	avg	cpx-du	8	0.19	37.32	26.67	20.33	14.99	0.16	0.26	0.24	100.15
pl-lherz	2	1447	1		1	0.16	28.94	37.13	21.58	13.10	0.06	0.11	0.36	101.44
pl-lherz	2	1447	2		1	0.18	28.52	36.96	20.30	12.53	0.14	0.06	0.33	99.02
p -lherz	2	1447	3	near cpx	1	0.16	29.02	36.85	20.25	12.87	0.18	0.07	0.30	99.70
pl-lherz	2	1447	avg	pl lherz	3	0.17	28.83	36.98	20.71	12.83	0.13	0.08	0.33	100.05
lherz	2	1454	1	small	2	0.02	40.92	26.63	16.45	16.48	0.02	0.17	0.16	100.85
lherz	2	1454	3	near cpx	1	0.00	41.25	26.13	16.77	16.48	0.12	0.13	0.17	101.05
lherz	2	1454	8		1	0.02	41.16	26.92	16.02	16.22	0.00	0.25	0.13	100.72
lherz	2	1454	avg		4	0.01	41.11	26.56	16.41	16.39	0.05	0.18	0.15	100.87

Tab. B-3a (continued)

rocktype	unit	sample	spot	comment	N	TiO2	Al2O3	Cr2O3	Fe tot	MgO	MnO	NiO	V2O5	SUM
pl-du	2	1459	3	large, core	2	0.13	39.11	25.91	16.57	16.84	0.16	0.28	0.21	99.21
pl-du	2	1459	2	sma l	2	0.08	40.89	23.91	15.80	17.16	0.18	0.27	0.18	98.47
pl-du	2	1459	1	small	2	0.06	47.54	19.95	13.98	18.60	0.16	0.30	0.16	100.75
pl-du	2	1459	1	smallest	1	0.13	43.79	22.85	15.23	16.83	0.19	0.28	0.20	99.50
pl-du	2	1459	avg	Al,Cr var	7	0.10	42.83	23.16	15.40	17.36	0.17	0.28	0.19	99.48
	2	1462	7		1	0.04	32.79	33.91	17.14	14.24	0.22	0.15	0.20	98.69
	2	1462	5		1	0.05	32.74	34.95	16.38	14.15	0.14	0.12	0.23	98.76
	2	1462	2		2	0.05	32.02	35.14	16.80	14.00	0.20	0.11	0.20	98.52
	2	1462	avg		4	0.05	32.52	34.67	16.77	14.13	0.19	0.13	0.21	98.66
	3	1468	9		2	0.03	40.28	28.19	15.88	15.96	0.14	0.16	0.23	100.87
	3	1468	3	core	2	0.01	37.93	30.02	15.23	16.90	0.11	0.18	0.25	100.63
	3	1468	1	rim	2	0.01	39.64	29.81	14.48	16.88	0.14	0.16	0.24	101.36
	3	1468	1	core	2	0.02	38.22	30.51	14.44	16.76	0.14	0.16	0.25	100.50
	3	1468	avg	(N)	8	0.02	39.02	29.63	15.01	16.63	0.13	0.17	0.24	100.84
troct?	cum	1475	4	core	2	0.18	30.06	33.83	22.49	13.07	0.18	0.16	0.23	100.20
troct?	cum	1475	4	rim	2	0.15	29.68	33.65	22.95	12.61	0.12	0.12	0.22	99.50
troct?	cum	1475	3		1	0.15	29.76	33.40	24.26	12.79	0.19	0.16	0.22	100.93
troct?	cum	1475	?	small	1	0.12	30.35	32.25	23.14	13.08	0.13	0.07	0.27	99.41
troct?	cum	1475	avg		6	0.15	29.96	33.28	23.21	12.89	0.16	0.13	0.24	100.01
	3	1485	6	core	1	0.00	28.68	40.64	17.73	13.85	0.19	0.12	0.21	101.42
	3	1485	4	core	2	0.02	28.07	41.56	17.43	14.17	0.18	0.10	0.25	101.78
	3	1485	4	rim to cpx	1	0.00	30.61	35.58	18.14	13.99	0.17	0.09	0.25	98.83
	3	1485	4	rim to ol	1	0.01	29.78	38.84	17.20	14.51	0.14	0.15	0.26	100.89
	3	1485	avg	(N)	5	0.01	29.29	39.16	17.63	14.13	0.17	0.12	0.24	100.73
du	2	1499	2	large	2	0.41	35.87	27.29	18.36	15.00	0.18	0.19	0.23	97.53
du	2	1499	1	small	2	0.39	35.92	27.29	19.80	14.64	0.19	0.23	0.25	98.71
du	2	1499	avg		4	0.40	35.90	27.29	19.08	14.82	0.19	0.21	0.24	98.12

Tab. B-3b

lithol	sample	spot	details	N	TiO2	Al2O3	Cr2O3	Fe tot	MgO	MnO	NiO	V2O5	SUM
	LH47	1	core	2	0.10	13.81	54.23	20.40	10.02	0.32	n.d.	n.d.	98.88
	LH47	1	rim	3	0.09	13.33	55.41	21.09	9.49	0.30	n.d.	n.d.	99.71
	LH47	1		2	0.09	12.48	55.80	21.80	9.11	0.29	n.d.	n.d.	99.57
	LH47	1a		1	0.10	13.81	53.46	20.78	9.93	0.25	n.d.	n.d.	98.33
	LH47	avg	(R)	8	0.10	13.36	54.73	21.02	9.64	0.29	n.d.	n.d.	99.12
	LH47	std			0.01	0.54	0.93	0.51	0.36	0.03	n.d.	n.d.	0.56
	LH76	3	core	2	0.13	13.03	54.74	21.29	9.84	0.31	n.d.	n.d.	99.34
	LH76	3	rim	2	0.11	12.15	56.20	21.07	9.53	0.21	n.d.	n.d.	99.27
	LH76	6	core, large	1	0.13	12.77	54.27	21.55	9.99	0.32	n.d.	n.d.	99.03
	LH76	6	rim	1	0.11	11.85	56.15	21.88	9.54	0.32	n.d.	n.d.	99.85
	LH76	6		2	0.08	11.57	56.16	21.71	9.46	0.25	n.d.	n.d.	99.23
	LH76	avg	(R)	8	0.11	12.27	55.50	21.50	9.67	0.28	n.d.	n.d.	99.34
	LH76	std			0.02	0.55	0.83	0.29	0.21	0.04	n.d.	n.d.	0.27
	LH11	3	core, large	2	0.16	16.61	52.43	19.52	11.32	0.24	n.d.	n.d.	100.28
	LH11	3	rim	3	0.13	17.47	51.00	19.81	11.05	0.27	n.d.	n.d.	99.73
	LH11	6		1	0.16	17.53	51.01	19.98	10.94	0.14	n.d.	n.d.	99.76
	LH11	avg		6	0.15	17.20	51.48	19.77	11.10	0.22	n.d.	n.d.	99.92
	LH11	std			0.01	0.42	0.67	0.19	0.16	0.06	n.d.	n.d.	0.25
	LH87	5	incl in cpx	1	0.09	13.58	55.05	20.78	9.74	0.34	n.d.	n.d.	99.58
	LH87	3	incl in opx	2	0.09	14.27	53.68	19.76	9.91	0.32	n.d.	n.d.	98.03
	LH87	7	core	1	0.09	14.23	53.79	20.56	10.05	0.28	n.d.	n.d.	99.00
	LH87	7	rim	1	0.06	13.21	53.18	22.50	8.91	0.21	n.d.	n.d.	98.07
	LH87	avg		5	0.08	13.82	53.93	20.90	9.65	0.29	n.d.	n.d.	98.67
	LH87	std			0.01	0.45	0.69	1.00	0.44	0.05	n.d.	n.d.	0.65
	LH73	8	core, large	3	0.11	15.24	53.58	20.92	10.60	0.30	n.d.	n.d.	100.75
	LH73	8	rim	2	0.06	14.71	54.26	21.11	10.16	0.31	n.d.	n.d.	100.61
	LH73	6	incl in opx	2	0.06	16.38	52.76	18.91	11.00	0.28	n.d.	n.d.	99.39
	LH73	8		2	0.07	14.42	54.71	22.05	9.63	0.30	n.d.	n.d.	101.18
	LH73	avg	(R)	9	0.08	15.19	53.83	20.75	10.35	0.30	n.d.	n.d.	100.48
	LH73	std			0.02	0.75	0.74	1.14	0.51	0.01	n.d.	n.d.	0.66
chrom.	LH84	1	core	2	0.19	11.82	56.57	23.05	9.09	0.33	n.d.	n.d.	101.05
chrom.	LH84	1	rim to cpx	2	0.20	11.23	57.81	23.46	8.98	0.38	n.d.	n.d.	102.06
chrom.	LH84	1	rim to ol	2	0.20	10.86	58.00	24.38	7.96	0.36	n.d.	n.d.	101.46
chrom.	LH84	2	core	1	0.21	11.53	55.63	22.35	9.52	0.26	n.d.	n.d.	99.50
chrom.	LH84	2	rim	1	0.18	11.26	56.73	23.11	9.27	0.27	n.d.	n.d.	100.82
chrom.	LH84	3	core	2	0.17	10.30	58.29	22.79	9.22	0.33	n.d.	n.d.	101.10
chrom.	LH84	avg	(R)	10	0.19	11.17	57.17	23.14	9.01	0.32	n.d.	n.d.	101.00
chrom.	LH84	std			0.01	0.49	0.94	0.54	0.50	0.04	n.d.	n.d.	0.78
	LH12	2	core, large	2	0.16	9.52	61.52	19.68	9.44	0.31	n.d.	n.d.	100.63
	LH12	2	rim	2	0.12	10.73	58.94	21.39	9.11	0.32	n.d.	n.d.	100.61
	LH12	4		1	0.11	9.46	61.00	21.43	9.14	0.30	n.d.	n.d.	101.44
	LH12	avg	(N)	5	0.13	9.90	60.49	20.83	9.23	0.31	n.d.	n.d.	100.89
	LH12	std			0.02	0.59	1.11	0.82	0.15	0.01	n.d.	n.d.	0.39
	LH16	4	in px aggr	2	0.09	13.54	55.53	22.45	9.44	0.26	n.d.	n.d.	101.31
	LH16	5	core	2	0.13	16.09	51.52	20.64	10.97	0.28	n.d.	n.d.	99.63
	LH16	5	rim	2	0.13	14.64	55.18	21.47	10.24	0.31	n.d.	n.d.	101.97
	LH16	avg	(R)	6	0.12	14.76	54.08	21.52	10.22	0.28	n.d.	n.d.	100.97
	LH16	std			0.02	1.04	1.81	0.74	0.62	0.02	n.d.	n.d.	0.99
	LH22	3	core, large	2	0.08	13.08	56.97	20.90	9.89	0.31	n.d.	n.d.	101.23
	LH22	3	rim	1	0.06	12.96	56.98	21.11	9.15	0.33	n.d.	n.d.	100.59
	LH22	7		2	0.07	13.03	54.00	21.86	8.85	0.29	n.d.	n.d.	98.10
	LH22	avg		5	0.07	13.02	55.98	21.29	9.30	0.31	n.d.	n.d.	99.97
	LH22	std			0.01	0.05	1.40	0.41	0.44	0.02	n.d.	n.d.	1.35
	LH49	2	core	2	0.00	13.33	56.42	20.57	10.21	0.28	n.d.	n.d.	100.81
	LH49	5	incl, near cpx	2	0.03	15.98	53.80	19.03	11.48	0.28	n.d.	n.d.	100.60
	LH49	5	incl, near opx	1	0.04	15.81	54.40	19.17	11.41	0.30	n.d.	n.d.	101.13
	LH49	6		1	0.02	15.28	54.84	20.73	10.16	0.29	n.d.	n.d.	101.32
	LH49	avg		6	0.02	15.10	54.87	19.88	10.82	0.29	n.d.	n.d.	100.97
	LH49	std			0.01	1.05	0.97	0.78	0.63	0.01	n.d.	n.d.	0.28
	LH8	2	incl in opx	1	0.03	16.86	51.68	22.21	9.96	0.32	n.d.	n.d.	101.06
	LH8	5	incl in cpx	2	0.07	16.66	52.79	18.40	11.48	0.29	n.d.	n.d.	99.69
	LH8	6	core, large	2	0.07	17.16	52.74	19.26	11.36	0.25	n.d.	n.d.	100.84
	LH8	6	rim	2	0.07	18.22	51.68	19.16	11.45	0.25	n.d.	n.d.	100.83
	LH8	avg	(N)	7	0.06	17.23	52.22	19.76	11.06	0.28	n.d.	n.d.	100.61
	LH8	std			0.02	0.60	0.54	1.45	0.64	0.03	n.d.	n.d.	0.54
	LH62	3	core, large	2	0.06	18.84	50.37	18.89	11.55	0.29	0.05	0.29	100.34
	LH62	3	rim	2	0.04	20.75	47.89	18.91	11.88	0.25	0.11	0.31	100.14
	LH62	5	in opx, small	1	0.04	17.99	48.97	18.92	11.41	0.27	0.07	0.23	97.90

Tab. B-3b (continued)

lithol	sample	spotdetails	N	TiO2	Al2O3	Cr2O3	Fe tot	MgO	MnO	NiO	V2O5	SUM
	LH62	8 core	2	0.04	19.66	49.61	19.07	11.29	0.26	0.07	0.27	100.27
	LH62	8 rim to opx	1	0.03	19.30	49.85	19.39	11.27	0.23	0.04	0.28	100.39
	LH62	8 rim to ol	2	0.03	21.07	48.33	18.84	11.96	0.18	0.04	0.31	100.76
	LH62	avg (N)	10	0.04	19.60	49.17	19.00	11.56	0.25	0.06	0.28	99.97
	LH62	std		0.01	1.06	0.86	0.19	0.27	0.03	0.02	0.03	0.94
	LH67	2	2	0.09	16.34	52.07	19.86	10.27	0.29	0.09	0.30	99.31
	LH67	3	1	0.08	16.14	52.02	20.25	10.05	0.23	0.04	0.27	99.08
	LH67	4 core, large	2	0.06	14.80	54.78	19.40	10.55	0.24	0.03	0.29	100.15
	LH67	4 rim to opx	2	0.06	15.32	54.33	19.38	10.74	0.25	0.07	0.29	100.44
	LH67	4 rim to ol	2	0.07	15.18	54.13	20.04	10.12	0.32	0.04	0.25	100.15
	LH67	avg (R)	9	0.07	15.56	53.47	19.79	10.35	0.27	0.05	0.28	99.83
	LH67	std		0.01	0.59	1.18	0.35	0.26	0.03	0.02	0.02	0.53
	LH106	5 aw cpx	3	0.02	23.75	41.80	20.56	10.72	0.23	0.05	0.24	97.37
	LH106	9 aw cpx+opx	3	0.02	21.64	45.25	19.69	11.25	0.19	0.09	0.29	98.42
	LH106	1 core, aw cpx	2	0.04	21.05	47.79	17.64	11.83	0.24	0.08	0.23	98.90
	LH106	1 rim to opx	1	0.00	21.30	48.31	17.59	11.79	0.30	0.09	0.20	99.58
	LH106	avg	9	0.02	21.94	45.79	18.87	11.40	0.24	0.08	0.24	98.57
	LH106	std		0.01	1.07	2.58	1.29	0.45	0.04	0.02	0.03	0.80
du	LH106.2	2 largest	3	0.25	24.20	41.28	22.28	11.27	0.23	0.09	0.29	99.89
du	LH106.2	1 smaller	2	0.27	23.14	40.28	26.41	10.78	0.29	0.10	0.27	101.54
du	LH106.2	avg	5	0.26	23.67	40.78	24.35	11.03	0.26	0.10	0.28	100.72
du	LH106.2	std		0.01	0.53	0.50	2.06	0.24	0.03	0.01	0.01	0.83
	LH121	5 core, aw opx	2	0.03	21.87	47.33	16.97	11.98	0.21	0.16	0.25	98.80
	LH121	5 in cpx sympl	1	0.00	22.66	45.96	17.49	12.02	0.24	0.09	0.29	98.75
	LH121	6 in cpx sympl	2	0.04	20.95	47.27	20.44	10.82	0.29	0.07	0.34	100.22
	LH121	1 in cpx sympl	2	0.00	20.39	46.67	19.36	11.12	0.21	0.09	0.29	98.13
	LH121	1 aw opx	1	0.09	22.13	47.27	17.93	12.17	0.20	0.14	0.29	100.22
	LH121	avg	8	0.03	21.60	46.90	18.44	11.62	0.23	0.11	0.29	99.22
	LH121	std		0.03	0.82	0.53	1.28	0.54	0.03	0.03	0.03	0.85
	LH122	1 aw cpx, defor	2	0.02	27.05	40.91	19.33	12.33	0.27	0.09	0.27	100.27
	LH122	2 aw cpx	1	0.04	27.03	41.59	19.30	12.64	0.21	0.11	0.29	101.21
	LH122	3 aw cpx, defor	1	0.02	26.76	42.23	18.89	12.06	0.25	0.06	0.31	100.58
	LH122	avg	4	0.03	26.95	41.58	19.17	12.34	0.24	0.09	0.29	100.69
	LH122	std		0.01	0.13	0.54	0.20	0.24	0.02	0.02	0.02	0.39
	LH110	1 near opx	2	0.03	50.77	15.59	14.09	18.27	0.08	0.39	0.15	99.37
	LH110	2 near opx	3	0.06	50.16	16.25	13.59	18.62	0.13	0.33	0.17	99.31
	LH110	2	2	0.07	51.49	15.73	13.68	18.41	0.14	0.30	0.14	99.96
	LH110	3	1	0.06	50.27	15.77	14.25	17.77	0.09	0.30	0.17	98.68
	LH110	avg	8	0.06	50.67	15.84	13.90	18.27	0.11	0.33	0.16	99.33
	LH110	std		0.01	0.52	0.25	0.28	0.31	0.03	0.04	0.01	0.45
	LH112	2	1	0.04	46.70	21.39	12.55	18.24	0.12	0.15	0.03	99.22
	LH112	3 core	2	0.07	45.63	22.04	12.98	18.48	0.13	0.21	0.05	99.59
	LH112	avg	3	0.06	46.17	21.72	12.77	18.36	0.13	0.18	0.04	99.41
	LH112	std		0.01	0.53	0.32	0.22	0.12	0.01	0.03	0.01	0.18
	LH113	3	2	0.09	53.95	14.34	13.33	19.69	0.13	0.29	0.08	101.90
	LH113	2 core	2	0.08	52.51	15.29	14.43	19.63	0.13	0.23	0.07	102.37
	LH113	2 rim	2	0.06	52.95	15.38	12.99	19.53	0.11	0.27	0.11	101.40
	LH113	avg	6	0.08	53.14	15.00	13.58	19.62	0.12	0.26	0.09	101.89
	LH113	std		0.01	0.60	0.47	0.61	0.07	0.01	0.02	0.02	0.40
	LH117	1	2	0.06	44.14	22.69	14.10	17.66	0.20	0.23	0.18	99.26
	LH117	4 core	2	0.06	41.43	26.15	13.56	17.48	0.12	0.21	0.17	99.18
	LH117	4 rim	3	0.05	41.04	26.20	13.83	17.30	0.14	0.20	0.14	98.90
	LH117	3	2	0.07	42.66	24.38	13.33	17.55	0.16	0.22	0.18	98.55
	LH117	avg	9	0.06	42.32	24.86	13.71	17.50	0.16	0.22	0.17	98.97
	LH117	std		0.01	1.21	1.45	0.29	0.13	0.03	0.01	0.02	0.28
	LH119	1 core, bit opx	2	0.07	47.42	20.64	13.09	18.43	0.11	0.21	0.11	100.08
	LH119	1 rim	2	0.02	49.25	18.00	12.05	19.35	0.11	0.28	0.11	99.17
	LH119	2 core	1	0.06	49.43	18.70	12.08	19.39	0.07	0.20	0.08	100.01
	LH119	avg	5	0.05	48.70	19.11	12.41	19.06	0.10	0.23	0.10	99.75
	LH119	std		0.02	0.91	1.12	0.48	0.44	0.02	0.04	0.01	0.41

Tab. B-4 (following eighteen pages). Clinopyroxene mineral chemistry data from (a) the Table Mountain section, and (b) the Lewis Hills mantle section.

'def' - defocused beam analyses;

* - warns that the sum of the cations is unusually high in the analyzed sample. This typically was the case during defocused beam analyses. The reason for the high cation sums probably lies in minor oxidation and amphibole formation along cleavage planes and exsolution lamellae; aw - associated with; EL - exsolution lamellae;

pc - porphyroclast:

nb - neoblast;

mx - matrix.

See also comments for Tab. B-3.

Tab. B-4a

sample	spot	comment	core/rim	N	other	SiO2	TiO2	Al2O3	Cr2O3	FeO	MgO	MnO	CaO	NiO	Na2O	K2O	SUM
7 5	6B			1		51 74	0 57	3 45	0 75	6 47	16 43	0 10	20 60	0 07	0 31	0 00	100 49
7 5	6	granular		1		52 01	0 56	3 70	0 73	7 16	17 86	0 18	18 32	0 05	0 34	0 01	100 92
7 5	3	granular	rim to ol	1		50 88	0 61	3 30	0 68	5 95	15 64	0 16	21 99	0 04	0 48	0 00	99 73
7 5	3	larger cpx	core	1		50 75	0 51	3 22	0 76	6 40	16 72	0 13	20 06	0 00	0 43	0 01	98 99
7 5	1	twinned cpx	core	1		51 09	0 57	3 54	0 81	5 76	15 84	0 16	21 67	0 02	0 06	0 01	99 53
7 5	avg			5		51 29	0 56	3 44	0 75	6 35	16 50	0 15	20 53	0 04	0 32	0 01	99 93
7 5	std					0 49	0 03	0 17	0 04	0 49	0 78	0 03	1 31	0 02	0 15	0 00	0 69
7 9	2			1		50 50	0 32	4 17	0 38	6 10	15 38	0 14	22 71	0 00	0 31	0 01	100 02
7 9	1			2		51 82	0 26	4 63	0 25	6 21	15 25	0 10	22 51	0 00	0 26	0 00	101 29
7 9	avg			3		51 16	0 29	4 40	0 32	6 16	15 32	0 12	22 61	0 00	0 29	0 01	100 66
7 9	std					0 66	0 03	0 23	0 06	0 05	0 06	0 02	0 10	0 00	0 02	0 01	0 63
58 24				3		52 61	0 05	2 39	1 02	1 95	17 82	0 09	23 59	0 05			99 57
58 24	avg			3		52 61	0 05	2 39	1 02	1 95	17 82	0 09	23 59	0 05			99 57
82 107	10			1		54 61	0 00	0 48	0 18	2 09	19 02	0 04	23 92	0 04	0 02	0 01	100 41
82 107	avg			1		54 61	0 00	0 48	0 18	2 09	19 02	0 04	23 92	0 04	0 02	0 01	100 41
82 77	?	between sp		1		53 70	0 05	2 72	0 91	2 21	18 94	0 01	22 26	0 14	0 03	0 00	100 97
82 77	6	in mx		1		52 59	0 03	2 52	0 97	2 25	17 40	0 07	23 52	0 09	0 06	0 01	99 51
82 77	avg			2		53 15	0 04	2 62	0 94	2 23	18 17	0 08	22 89	0 12	0 05	0 01	100 24
82 77	std					0 56	0 01	0 10	0 03	0 02	0 77	0 03	0 63	0 03	0 02	0 01	0 73
128	6	along opx pc		1		52 10	0 00	1 90	0 77	2 10	18 80	0 11	22 62	0 04	0 02	0 01	98 47
128	10	impregn type		1		54 82	0 00	2 18	0 94	2 23	18 48	0 09	22 57	0 04	0 10	0 00	101 45
128	avg			2		53 46	0 00	2 04	0 86	2 17	18 64	0 10	22 60	0 04	0 06	0 01	99 98
128	std					1 36	0 00	0 14	0 08	0 06	0 16	0 01	0 02	0 00	0 04	0 01	1 49
229	3	aw sp		1		52 61	0 01	2 37	0 83	2 64	19 80	0 11	20 92	0 00	0 04	0 01	99 34
229	11?	impregn type		1		53 28	0 01	1 86	0 57	1 84	18 10	0 11	24 42	1 00	0 04	0 03	101 26
229	10?	impregn type		1		54 88	0 02	2 18	0 56	2 63	18 64	0 01	22 80	0 00	0 00	0 00	101 72
229	avg			3		53 59	0 01	2 14	0 65	2 37	18 85	0 08	22 71	0 33	0 03	0 01	100 77
229	std					0 95	0 00	0 21	0 12	0 37	0 71	0 05	1 43	0 47	0 02	0 01	1 03
229 2	8	aw sp		1		54 32	0 00	0 90	0 37	2 48	21 00	0 04	21 29	0 03	0 01	0 00	100 44
229 2	7	impregn type		1		54 73	0 00	1 98	0 80	2 53	18 89	0 09	22 50	0 07	0 09	0 00	101 68
229 2	0	impregn type		2		54 13	0 00	1 09	0 76	2 34	18 64	0 08	22 93	0 00	0 05	0 00	100 92
229 2	avg			4		54 39	0 00	1 62	0 64	2 45	19 51	0 07	22 24	0 03	0 05	0 00	101 01
229 2	std					0 25	0 00	0 51	0 19	0 08	1 06	0 02	0 69	0 03	0 03	0 00	0 51
255	2			1		53 02	0 01	2 59	1 08	2 27	18 09	0 09	22 03	0 05	0 15	0 02	99 40
255	1	in opx aggr		1		53 48	0 04	3 09	1 36	2 04	17 19	0 12	23 27	0 00	0 15	0 02	100 76
255	avg			2		53 25	0 03	2 84	1 2	2 16	17 64	0 11	22 65	0 03	0 15	0 02	100 08
255	std					0 23	0 02	0 25	0 14	0 11	0 45	0 02	0 62	0 03	0 00	0 00	0 68

Tab. B-4a (continued)

sample	spot	comment	xe/rim	N	other	SiO2	TiO2	Al2O3	Cr2O3	FeO	MgO	MnO	CaO	NiO	Na2O	K2O	SUM
259	3	aw sp		2		53 61	0 03	3 13	1 20	2 55	19 59	0 07	20 37	0 08	0 23	0 01	100 87
259	avg	aw sp		2		53 61	0 03	3 13	1 20	2 55	19 59	0 07	20 37	0 08	0 23	0 01	100 87
406	4			1	*, def	55 35	0 02	0 79	0 63	1 59	18 43	0 04	24 62	0 15	0 29	0 01	101 92
406	avg			1	*, def	55 35	0 02	0 79	0 63	1 59	18 43	0 04	24 62	0 15	0 29	0 01	101 92
458	7	aw sp		2		53 98	0 00	1 45	0 71	1 81	17 74	0 07	22 63	0 00	0 23	0 01	98 83
458	6	twinned? in mx		1		53 80	0 01	1 87	1 00	1 79	17 75	0 05	22 97	0 05	0 24	0 00	99 53
458	3	granular in mx		2		54 71	0 00	1 78	0 86	1 71	17 44	0 07	23 63	0 05	0 26	0 00	100 31
458	avg			5		54 16	0 00	1 63	0 86	1 77	17 64	0 06	23 08	0 03	0 24	0 00	99 49
458	std					0 39	0 00	0 18	0 12	0 04	0 14	0 01	0 42	0 02	0 01	0 00	0 69
465	7	incl in opx pc		1		52 45	0 05	2 49	1 08	1 84	17 11	0 04	23 52	0 04	0 13	0 00	98 73
465	3	incl in opx pc	rim to opx	2		52 77	0 04	2 50	0 94	2 16	17 36	0 04	22 77	0 08	0 15	0 00	98 81
465	3	incl in opx pc	rim to ol	2		53 08	0 03	2 23	0 81	1 93	17 23	0 09	23 15	0 05	0 15	0 00	98 73
465	3	in opx aggr	core	2		52 92	0 03	2 90	1 17	1 99	17 11	0 10	23 01	0 06	0 16	0 00	98 45
465	2	granular in mx		1		53 09	0 04	2 39	0 90	2 30	18 50	0 09	21 44	0 07	0 19	0 02	99 03
465	avg			8		52 86	0 04	2 50	0 98	2 04	17 46	0 07	22 78	0 06	0 16	0 00	98 95
465	std					0 23	0 01	0 22	0 13	0 17	0 53	0 03	0 71	0 02	0 02	0 01	0 27
524	2	nb		2		53 46	0 07	4 84	0 50	1 77	17 55	0 08	23 57	0 05	0 16	0 00	102 05
524	1	pc	core	12	def	52 48	0 07	6 04	0 88	2 07	18 96	0 09	20 76	0 07	0 17	0 00	101 59
524	avg			14		52 97	0 07	5 44	0 69	1 92	18 26	0 09	22 17	0 06	0 17	0 00	101 82
524	std					0 49	ERR	0 60	0 19	0 15	0 70	0 00	1 40	0 01	0 01	0 00	0 23
534	3			1		52 11	0 09	4 05	0 97	2 34	18 60	0 11	23 18	0 05	0 13	0 01	99 64
534	2		core	1		52 53	0 04	4 31	1 09	2 31	18 65	0 11	23 30	0 05	0 19	0 01	100 59
534	2		rim	1		51 99	0 06	4 14	1 02	2 51	18 64	0 13	23 26	0 08	0 15	0 00	100 00
534	avg			3		52 21	0 07	4 17	1 03	2 39	18 63	0 12	23 25	0 06	0 16	0 01	100 08
534	std					0 23	0 02	0 11	0 05	0 09	0 02	0 01	0 05	0 01	0 02	0 00	0 39
542 2	2			2		53 89	0 03	2 67	1 04	2 31	17 71	0 08	23 90	0 07	0 10	0 00	101 80
542 2	avg			2	*, def	53 89	0 03	2 67	1 04	2 31	17 71	0 08	23 90	0 07	0 10	0 00	101 80
564	4	aw sp		1		53 98	0 00	2 34	0 86	2 06	18 22	0 01	22 93	0 05	0 08	0 00	100 51
564	2	incl in opx		1		52 97	0 04	2 69	1 08	1 84	15 98	0 11	23 45	0 05	0 10	0 00	98 29
564	1	same, diff day		2		53 00	0 03	2 76	1 11	1 86	17 39	0 11	22 91	0 06	0 09	0 00	99 32
564	1	in opx aggr		1		52 62	0 04	1 99	0 61	2 62	19 02	0 07	21 23	0 09	0 05	0 01	98 55
564	1	pc	core	2	*, def	53 07	0 05	2 77	1 15	2 36	18 62	0 10	21 88	0 04	0 08	0 01	100 13
564	avg			7		53 13	0 03	2 51	0 96	2 19	17 84	0 08	22 46	0 06	0 08	0 00	99 36
564	std					0 45	0 02	0 30	0 20	0 37	1 08	0 04	0 81	0 02	0 02	0 00	0 86
574	5	granular in mx		1		54 34	0 03	1 59	0 77	2 14	19 16	0 01	22 07	0 00	0 11	0 00	100 22
574	3	impregn type	core	1		53 [illegible]	0 00	1 97	0 82	2 06	18 18	0 08	23 55	0 03	0 13	0 00	99 84
574	3	impregn type	rim	2		54 63	0 02	1 65	0 57	2 32	18 91	0 09	23 00	0 00	0 12	0 00	101 31

Tab. B-4a (continued)

sample	spot	comment	core/rim	N	other	SiO2	TiO2	Al2O3	Cr2O3	FeO	MgO	MnO	CaO	NiO	Na2O	K2O	SUM
574	2	granular in mx	core	2		53 65	0 01	2 11	0 79	1 98	19 95	0 10	22 04	0	0 16	0 01	100 81
574	2	granular in mx	rim	1		54 22	0 02	1 93	0 89	2 09	18 87	0 09	22 63	0 08	0 23	0 01	101 06
574	avg			7		53 97	0 02	1 65	0 77	2 12	19 01	0 07	22 66	0 02	0 15	0 00	100 65
574	std					0 57	0 01	0 20	0 11	0 11	0 57	0 03	0 57	0 03	0 04	0 00	0 54
592	7	impregn type		1		52 27	0 01	2 98	0 95	2 98	18 34	0 13	22 34	0 03	0 08	0 00	100 11
592	6	impregn type	rim	2	Fe var	53 76	0 00	3 06	1 11	1 98	17 80	0 10	23 21	0 03	0 09	0 00	101 14
592	6	recryst pc	core	3		50 80	0 01	3 12	1 00	2 97	20 34	0 09	19 68	0 02	0 09	0 01	98 13
592	2	impregn type		2	Al var	53 65	0 02	2 95	0 94	2 29	17 77	0 09	23 11	0 02	0 09	0 00	100 93
592	1	impregn type		2	Mg, Fe,Ca var	54 32	0 03	2 11	0 56	2 50	20 49	0 09	20 45	0 04	0 06	0 01	100 66
592	avg			10		52 96	0 01	2 84	0 91	2 54	18 95	0 10	21 76	0 03	0 08	0 00	100 19
592	std					1 27	0 01	0 37	0 19	0 39	1 22	0 02	1 44	0 01	0 01	0 00	1 09
599	4		core	1	def	53 20	0 08	4 27	1 19	2 93	17 86	0 10	21 52	0 12	0 30	0 00	101 57
599	3		core	3		51 62	0 04	4 28	1 11	2 52	16 67	0 06	21 82	0 04	0 18	0 01	98 35
599	3		rim	1		51 45	0 03	4 10	0 99	2 91	17 25	0 07	21 92	0 12	0 19	0 00	99 03
599	avg			5		52 09	0 05	4 22	1 10	2 79	17 26	0 08	21 75	0 09	0 22	0 00	99 65
599	std					0 79	0 02	0 08	0 08	0 19	0 49	0 02	0 17	0 04	0 05	0 00	1 39
613	3	nb		1		53 81	0 09	3 59	1 03	2 04	16 92	0 05	23 80	0 07	0 21	0 00	101 61
613	2	nb		1		51 76	0 10	4 19	0 98	1 98	16 40	0 11	23 35	0 05	0 25	0 01	99 18
613	1	nb nxt pc		1		52 36	0 03	4 75	1 25	3 26	19 00	0 11	18 80	0 07	0 24	0 02	99 89
613	1		rim	1		52 08	0 05	3 55	0 84	2 20	18 87	0 03	20 47	0 05	0 25	0 01	98 40
613	1	pc	core	6	def	52 37	0 07	4 92	1 25	3 31	19 26	0 09	18 89	0 13	0 20	0 01	100 50
613	1	pc	core	1	avoid EL	52 02	0 08	4 83	1 32	2 48	15 96	0 06	23 06	0 11	0 24	0 00	100 16
613	avg			11		52 40	0 07	4 31	1 11	2 55	17 74	0 08	21 40	0 08	0 23	0 01	99 96
613	std					0 66	0 02	0 57	0 17	0 55	1 34	0 03	2 09	0 03	0 02	0 01	1 01
676	4	granular in ol mx		1		53 68	0 02	2 22	0 75	2 20	17 21	0 18	24 07	0 03	0 11	0 00	100 47
676	3	granular in ol mx		1		53 79	0 02	1 93	0 55	2 31	18 04	0 06	22 99	0 05	0 09	0 00	99 83
676	avg			2		53 74	0 02	2 08	0 65	2 26	17 63	0 12	23 53	0 04	0 10	0 00	100 15
676	std					0 06	0 00	0 14	0 10	0 05	0 42	0 06	0 54	0 01	0 01	0 00	0 32
723 2	6		rim	1		53 94	0 00	2 46	1 05	2 02	17 70	0 04	22 65	0 08	0 02	0 01	99 97
723.2	6	aggr	core	1		53 69	0 01	2 19	0 88	1 86	17 33	0 07	22 84	0 04	0 02	0 01	98 94
723 2	4			1		53 51	0 00	2 69	1 00	2 28	18 22	0 07	21 45	0 11	0 06	0 02	99 41
723.2	avg			3		53 71	0 00	2 45	0 98	2 05	17 75	0 06	22 31	0 08	0 03	0 01	99 44
723 2	std					0 18	0 00	0 20	0 07	0 17	0 37	0 01	0 62	0 03	0 02	0 00	0 42
733.2	2	aw sp	near ol	1		53 54	0 05	2 39	1 00	2 67	16 79	0 05	23 77	0 08	0 31	0 00	100 65
733.2	2	s above	rim to sp	3	Al var	53 21	0 03	2 50	0 81	2 34	16 96	0 04	24 31	0 05	0 31	0 01	100 57
733 2	1	fluffy in mx		1		53 67	0 05	2 32	0 99	2 16	16 71	0 04	24 04	0 03	0 29	0 00	100 30
733 2	avg			5		53 47	0 04	2 40	0 93	2 39	16 82	0 04	24 04	0 05	0 30	0 00	100 51

Tab. B-4a (continued)

sample	spot	comment	core/rim	N	other	SiO2	TiO2	Al2O3	Cr2O3	FeO	MgO	MnO	CaO	NiO	Na2O	K2O	SUM
733 2	std					0 19	0 01	0 07	0 09	0 21	0 10	0 00	0 22	0 02	0 01	0 00	0 15
755	5	s. above	rim	1		52 12	0 08	3 01	0 75	2 04	17 63	0 03	22 28	0 12	0 16	0 02	98 24
755	5	pc, small	centre	1		51 42	0 06	3 99	1 01	2 09	16 73	0 09	22 78	0 08	0 20	0 02	98 47
755	4	blebs in opx pc		1		51 83	0 08	3 81	1 07	1 95	16 22	0 09	22 93	0 08	0 19	0 00	98 25
755	2	neoblast in mx		1		52 59	0 10	3 37	0 91	2 06	16 58	0 09	22 76	0 05	0 20	0 01	98 72
755	avg			4		51 99	0 08	3 55	0 94	2 04	16 79	0 08	22 69	0 08	0 19	0 01	98 42
755	std					0 43	0 01	0 38	0 12	0 05	0 52	0 03	0 24	0 02	0 02	0 01	0 20
757	6	blebs in opx pc		2		51 80	0 05	3 51	1 04	2 54	16 73	0 05	23 61	0 05	0 18	0 02	99 58
757	3	in opx aggr		1		51 84	0 06	3 68	1 00	2 62	16 95	0 06	22 75	0 05	0 22	0 01	99 24
757	2	neoblast		2		52 41	0 02	2 91	0 78	2 79	17 64	0 09	22 35	0 05	0 15	0 02	99 21
757	2	pc	centre	1		52 95	0 06	3 98	1 11	2 55	16 29	0 07	23 37	0 08	0 13	0 02	100 61
757	2	pc	core	3	*, def	53 22	0 07	3 78	1 22	2 99	19 20	0 04	20 41	0 08	0 15	0 01	101 17
757	avg			9		52 44	0 05	3 57	1 03	2 70	17 36	0 06	22 50	0 06	0 17	0 02	99 96
757	std					0 57	0 02	0 36	0 15	0 17	1 02	0 02	1 14	0 01	0 03	0 00	0 79
772 1	5	pc, small		2		53 37	0 03	2 86	0 97	2 21	17 57	0 07	23 61	0 04	0 09	0 00	100 82
772 1	5	pc, small		1	*, def	52 55	0 03	2 76	1 13	2 41	17 53	0 06	23 84	0 00	0 14	0 02	100 47
772 1	avg			3		52 96	0 03	2 81	1 05	2 31	17 55	0 07	23 73	0 02	0 12	0 01	100 65
774	avg	v small in mx		1		53 79	0 06	2 54	0 75	2 44	17 10	0 05	23 55	0 06	0 10	0 02	100 46
774	10	impregn type		2	Al,Cr,Ca var	53 80	0 05	1 85	0 53	2 41	18 30	0 03	22 78	0 05	0 18	0 00	99 98
774	avg			3		53 80	0 06	2 20	0 64	2 43	17 70	0 04	23 17	0 06	0 14	0 01	100 22
774	std					0 00	0 01	0 34	0 11	0 01	0 60	0 01	0 38	0 01	0 04	0 01	0 24
788	3	in opx aggr		1		53 91	0 03	2 35	1 04	1 71	17 05	0 07	23 63	0 07	0 05	0 01	99 92
788	2	twin in opx pc		1		53 50	0 02	2 47	1 02	2 29	18 06	0 10	22 38	0 05	0 16	0 02	100 07
788	2	other incl		1		53 89	0 02	2 53	1 16	1 88	17 68	0 07	22 78	0 05	0 14	0 01	100 21
788	1	around opx		1		54 46	0 00	2 16	0 99	1 89	17 28	0 04	23 47	0 05	0 07	0 01	100 42
788	avg			4		53 94	0 02	2 38	1 05	1 94	17 52	0 07	23 07	0 06	0 11	0 01	100 16
788	std					0 34	0 01	0 14	0 06	0 21	0 39	0 02	0 51	0 01	0 05	0 00	0 18
801	8	fluffy type		1		53 75	0 05	2 63	0 79	2 34	17 43	0 04	22 70	0 07	0 20	0 00	100 00
801	6	aw sp		1		54 42	0 06	2 29	0 82	1 83	17 42	0 00	24 25	0 09	0 22	0 00	101 40
801	6	impregn type		1		52 95	0 05	1 93	0 48	2 00	18 21	0 09	22 86	0 05	0 21	0 00	98 83
801	avg			3		53 71	0 05	2 28	0 70	2 06	17 69	0 04	23 27	0 07	0 21	0 00	100 08
801	std					0 60	0 00	0 29	0 15	0 21	0 37	0 04	0 70	0 02	0 01	0 00	1 05
827	9	aw sp in mx	core	3		51 18	0 04	4 06	1 22	3 39	19 81	0 13	19 51	0 05	0 18	0 01	99 56
827	9	aw sp in mx	rim	3		52 40	0 04	3 85	1 09	2 55	17 71	0 08	22 44	0 02	0 13	0 01	100 32
827	5	surr by sp		2		52 62	0 06	3 85	1 07	2 77	18 33	0 09	22 45	0 01	0 07	0 00	101 32
827	3	surr by sp	rim	1		52 41	0 08	3 93	1 07	2 82	18 36	0 08	20 69	0 00	0 10	0 00	99 54
827	3	near opx aggr	core	1		52 27	0 06	4 18	1 25	3 89	20 71	0 10	18 15	0 05	0 14	0 00	100 80

Tab. 8-4a (continued)

sample	spot	comment	core/rim	N	other	SiO2	TiO2	Al2O3	Cr2O3	FeO	MgO	MnO	CaO	NiO	Na2O	K2O	SUM
827	13			2	def	52 68	0 05	3 90	1 16	2 77	17 84	0 06	22 15	0 06	0 15	0 00	100 82
827	avg			12		52 26	0 06	3 96	1 14	3 03	18 79	0 09	20 90	0 03	0 13	0 00	100 39
827	std					0 50	0 01	0 12	0 07	0 46	1 09	0 02	1 63	0 02	0 03	0 00	0 66
835 2	6	aw opx pc	core	2		54 11	0 02	2 87	1 15	1 84	17 71	0 02	23 59	0 00	0 01	0 00	101 32
835 2	6	aw opx pc	rim	2		54 48	0 04	2 52	1 02	1 68	17 84	0 08	23 42	0 02	0 00	0 00	101 10
835 2	5	aw opx pc	rim	1		55 25	0 03	2 63	0 94	2 10	17 64	0 08	22 98	0 06	0 07	0 01	101 79
835 2	5	pc in mx	core	2		54 53	0 01	3 05	1 14	2 01	17 60	0 10	23 06	0 06	0 01	0 00	101 57
835 2	1	pc in mx	rim to ol	2		53 06	0 02	2 47	0 94	1 89	18.72	0 09	22 93	0 01	0 00	0.00	100 13
835 2	1	cpx, sheared	core	2		54 81	0 01	2 87	1 11	2 04	18 78	0 06	22 92	0 00	0 00	0 00	102 60
835 2	1			2	*, def	52 35	0 04	2 61	1 05	2 08	18 33	0 08	23 03	0 10	0 03	0 00	99 70
835 2	avg			13		54 08	0 02	2 72	1 05	1 95	18 09	0 07	23 13	0 04	0 02	0 00	101 17
835.2	std					0 95	0 01	0 20	0 08	0 14	0 48	0 02	0 24	0 04	0 02	0 00	0 91
649	1	incl in opx		3		53 91	0 06	3 57	1 16	2 67	17 64	0 07	21 41	0 05	0 44	0 00	100 98
860	8		core	3	def	53 39	0 11	2 29	0 90	3 34	17 77	0 11	22 97	0 05	0 20	0 01	101 14
860	7	neoblast		1	cpxte band	53 14	0 09	2 27	0 71	3 74	19 52	0 13	19 60	0 19	0 17	0 01	99 57
860	6	impregn type		1	wehrl band	53 69	0 09	1 96	0 75	2 87	16 96	0 11	23 30	0 00	0 20	0 00	99 93
860	4	impregn type	rim to sp	2		52 67	0 13	2 41	0 78	2 94	16 88	0 10	23 32	0 03	0 14	0 00	99 40
860	4	neoblast	centre	2	low cpx band	52 84	0 12	2 49	0 89	3 37	16 74	0 10	22 80	0 03	0 19	0 00	99 57
860	2	neoblast		1	cpxte band	53 65	0 11	2 34	0 71	3 35	17 39	0 09	22 34	0 01	0 22	0 01	100.22
860	avg			10		53 23	0 11	2 29	0 79	3 27	17 54	0 11	22 39	0 05	0.19	0 01	99 97
860	std					0 38	0 01	0 17	0 08	0 29	0 95	0 01	1 29	0 06	0 03	0 00	0 59
861	8			2		55 11	0 04	2 41	0 88	2 85	18 97	0 09	21 20	0 06	0 44	0 00	102 05
861	6			2		54 36	0 08	2 20	0 91	2 27	18 14	0 11	22 24	0 05	0 35	0 00	100 71
861	2			2		53 22	0 06	2 48	0 90	2 68	18 30	0 07	22 04	0 05	0 39	0 01	100 20
861	avg			6		54 23	0 06	2 36	0 90	2 60	18 47	0 09	21 83	0 05	0 39	0 00	100 99
861	std					0 78	0 02	0 12	0 01	0 24	0 36	0 02	0 45	0 00	0 04	0 00	0 78
862	5	impregn type	core	2		53 78	0 22	2 79	0 96	2 85	17 73	0 12	22 91	0 04	0 15	0 00	101 55
862	5	impregn type	rim to sp	2		53 43	0 20	2 95	0 84	2 71	17 98	0 08	22 32	0 00	0 28	0 00	100 79
862	10	impregn type		2		54 35	0 25	3 28	0 96	2 73	17 27	0 09	22 86	0 05	0 18	0 00	102 02
862	avg			6		53 85	0 22	3 01	0 92	2 76	17 66	0 10	22 70	0 03	0 20	0 00	101 45
862	std					0 38	0 02	0 20	0 06	0 06	0 29	0 02	0 27	0 02	0 06	0 00	0 51
866	5	impregn type		1		53 23	0 13	3 78	1 00	2 84	16 95	0 11	21 84	0 05	0 46	0 01	100 40
866	4	impregn type		1		51 89	0 09	3 71	1 03	2 93	17 14	0 07	21 78	0 00	0 47	0 01	99 12
866	2	impregn type		1		52 63	0 09	3 77	0 99	2 65	17 58	0 07	21 69	0 07	0 34	0 01	99 89
866	avg			3		52 58	0 10	3 75	1 01	2.81	17 22	0 08	21 77	0 04	0 42	0 01	99 80
866	std					0 55	0 02	0 03	0 02	0 12	0 26	0 02	0 06	0 03	0 06	ERR	0 53
869	7	impregn type		1		52 69	0 05	2 20	0 99	2 80	18 29	0 03	21 34	0 02	0 29	0 00	98 70

Tab. B-4a (continued)

sample	spot	comment	core/rim	N	other	SiO2	TiO2	Al2O3	Cr2O3	FeO	MgO	MnO	CaO	NiO	Na2O	K2O	SUM
869	6	granular in mx		1		52 82	0 06	2 00	0 83	2 95	17 53	0 04	22 77	0 03	0 32	0 00	99 35
869	4	impregn type		1		53 30	0 03	1 79	0 88	3 04	16 77	0 04	22 91	0 11	0 27	0 01	99 15
869	avg			3		52 94	0 05	2 00	0 90	2 93	17 53	0 04	22 34	0 05	0 29	0 00	99 07
869	std					0 26	0 01	0 17	0 07	0 10	0 62	0 00	0 71	0 04	0 02	0 00	0 27
873	4	impregn type		1		52 75	0 06	2 80	0 80	2 36	16 61	0 07	23 66	0 04	0 15	0 01	99 31
873	2	impregn type		2		53 36	0 04	3 68	0 98	2 64	17 45	0 07	23 12	0 05	0 21	0 01	101 61
873	avg			3		53 06	0 05	3 24	0 89	2 50	17 03	0 07	23 39	0 05	0 18	0 01	100 46
873	std					0 31	0 01	0 44	0 09	0 14	0 42	0 00	0 27	0 00	0 03	0 00	1 15
881	5	aw sp		3		53 75	0 02	2 92	1 02	2 07	17 40	0 06	23 44	0 08	0 10	0 00	100 86
881	4	in mx, has EL	core	2		53 73	0 03	3 39	1 10	1 98	17 02	0 07	23 81	0 06	0 11	0 02	101 32
881	4	in mx, has EL	rim	1		52 57	0 03	3 04	1 03	2 09	17 30	0 15	23 30	0 07	0 10	0 00	99 68
881	1	close to sp		1		54 41	0 01	2 96	1 06	2 34	18 10	0 06	22 95	0 12	0 13	0 02	102 10
881	avg			7		53 62	0 02	3 08	1 04	2 12	17 46	0 09	23 38	0 08	0 11	0 01	100 99
881	std					0 66	0 01	0 19	0 04	0 13	0 40	0 04	0 31	0 02	0 01	0 01	0 88
886	6	impregn type		1		52 84	0 20	3 14	1 11	2 33	17 42	0 09	21 61	0 00	0 59	0 00	99 33
886	5	impregn type		1		53 21	0 21	2 91	0 95	2 12	17 01	0 09	23 09	0 04	0 51	0 01	100 15
886	4	granular		2		52 63	0 18	3 30	1 07	2 64	17 67	0 11	21 46	0 03	0 65	0 00	99 74
886	avg			4		52 89	0 20	3 12	1 04	2 36	17 37	0 10	22 05	0 02	0 58	0 00	99 74
886	std					0 24	0 01	0 16	0 07	0 21	0 27	0 01	0 74	0 02	0 06	0 00	0 33
900	12	nb		1		53 50	0 11	3 26	1 23	2 61	17 34	0 12	22 59	0 05	0 39	0 00	101 20
900	10	nb		1		54 00	0 19	3 12	1 21	2 99	18 22	0 07	21 75	0 07	0 33	0 00	101 95
900	avg			2		53 75	0 15	3 19	1 22	2 80	17 78	0 10	22 17	0 06	0 36	0 00	101 58
900	std					0 25	0 04	0 07	0 01	0 19	0 44	0 03	0 42	0 01	0 03	0 00	0 37
901 1	8	in mx		1		53 46	0 02	1 15	0 97	1 96	18 19	0 06	22 46	0 10	0 27	0 00	98 64
901 1	2	in mx		2		53 95	0 01	1 37	0 89	1 98	18 25	0 10	22 36	0 09	0 32	0 00	99 32
901 1	1	near sp		2		54 80	0 02	1 46	0 88	2 76	19 04	0 09	20 73	0 03	0 26	0 01	100 18
901 1	avg			5		54 07	0 02	1 33	0 95	2 23	18 49	0 08	21 85	0 07	0 28	0 00	99 38
901 1	std					0 55	0 00	0 13	0 04	0 37	0 39	0 02	0 79	0 03	0 03	0 00	0 63
901 3	5	impregn type		2		53 19	0 02	3 23	0 98	2 24	16 80	0 07	24 12	0 04	0 06	0 01	100 74
901 3	3	impregn type	core	1		52 68	0 01	3 58	0 96	2 54	16 41	0 07	23 30	0 05	0 08	0 01	99 69
901 3	3	impregn type	rim	1		51 52	0 03	2 87	0 78	2 31	17 05	0 09	24 04	0 07	0 05	0 01	98 82
901 3	avg			4		52 46	0 02	3 23	0 90	2 36	16 75	0 08	23 82	0 05	0 06	0 01	99 75
901 3	std					0 70	0 01	0 29	0 08	0 13	0 26	0 01	0 37	0 01	0 01	0 00	0 78
922	x	ribbon grain	core	1		51 05	0 09	5 60	1 14	3 12	15 46	0 21	22 47	0 05	0 27	0 01	99 47
922	7	ribbon grain	rim	2		50 38	0 09	4 87	0 95	2 84	15 89	0 09	22 62	0 07	0 39	0 01	98 20
922	7	pc aw opx aggr	core	2		50 54	0 12	5 79	1 15	3 01	16 16	0 11	22 14	0 07	0 30	0 00	99 41
922	7	pc, large	core	2	* det	51 71	0 09	5 69	1 18	3 68	21 01	0 13	15 68	0 14	0 20	0 00	99 72

Tab. B-4a (continued)

sample	spot	comment	core/rim	N	other	SiO2	TiO2	Al2O3	Cr2O3	FeO	MgO	MnO	CaO	NiO	Na2O	K2O	SUM
922	6	nb near pc		2	Al var	51 53	0 09	5 21	1 00	2 81	15 93	0 08	22 54	0 04	0 27	0 01	99 51
922	avg			9		51 04	0 10	5 43	1 08	3 13	16 89	0 12	21 09	0 07	0 29	0 01	99 26
922	std					0 52	0 01	0 34	0 09	0 39	2 07	0 05	2 71	0 03	0 06	0 00	0 54
932	8	pc	core	2	is profile	52 45	0 18	6 81	1 19	2 20	14 93	0 09	21 25	0 02	1 32	0 00	100 44
932	8	nb		1		53 29	0 22	5 18	0 83	2 44	16 94	0 07	20 63	0 01	1 13	0 00	100 74
932	8	nb	rim	1		52 70	0 22	5 65	0 97	0 70	15 05	0 03	21 56	0 00	1 30	0 00	98 18
932	3	incl in opx		2		51 82	0 25	5 70	1 14	2 18	15 93	0 04	21 21	0 02	1 30	0 00	99 59
932	2	pc	core	1		52 30	0 21	7 03	1 22	2 04	15 39	0 05	20 50	0 03	1 26	0 01	100 04
932	2	nb		1		51 72	0 20	5 61	0 86	2 42	16 40	0 07	20 30	0 00	1 18	0 01	98 77
932	avg			8		52 38	0 21	6 00	1 04	2 00	15 77	0 06	20 91	0 01	1 25	0 00	99 63
932	std					0 53	0 02	0 68	0 16	0 60	0 73	0 02	0 46	0 01	0 07	0 00	0 90
963	6			2		52 92	0 04	2 66	0 97	2 29	17 63	0 07	23 28	0 04	0 05	0 00	99 95
963	5			1		53 58	0 00	2 16	1 14	2 31	18 74	0 13	22 57	0 05	0 08	0 00	100 76
963	avg			3		53 25	0 02	2 41	1 06	2 30	18 19	0 10	22 93	0 05	0 07	0 00	100 36
963	std					0 33	0 02	0 25	0 09	0 01	0 55	0 03	0 36	0 00	0 01	0 00	0 40
1027	8	nb next to opx		1		50 32	0 07	4 20	0 75	2 64	17 04	0 12	22 66	0 08	0 23	0 01	98 12
1027	7	flaser in opx		1		52 84	0 07	3 99	0 81	2 47	16 28	0 08	23 57	0 01	0 26	0 00	100 38
1027	4	in ol mx		1		50 63	0 05	4 69	0 92	2 47	16 02	0 11	23 86	0 08	0 34	0 03	99 20
1027	avg			3		51 26	0 06	4 29	0 83	2 53	16 45	0 10	23 36	0 06	0 28	0 01	99 23
1027	std					1 12	0 01	0 29	0 07	0 08	0 43	0 02	0 51	0 03	0 05	0 01	0 92
1029 11	14	granular		1		54 16	0 41	4 44	0 66	2 77	15 88	0 08	22 80	0 03	1 26	0 00	102 49
1029 11	12	mosaic		1		52 57	0 42	6 26	0 65	3 70	17 01	0 08	19 42	0 04	1 16	0 00	101 31
1029 11	avg			2		53 37	0 42	5 35	0 66	3 24	16 45	0 08	21 11	0 04	1 21	0 00	101 90
1029 11	std					0 79	0 01	0 91	0 01	0 46	0 57	0 00	1 69	0 00	0 05	0 00	0 59
1037	7	imprgn type		1		53 76	0 06	3 45	1 02	2 22	17 86	0 04	22 32	0 07	0 08	0 02	100 90
1037	3		rim	2		54 26	0 01	3 57	0 95	2 40	17 40	0 09	22 72	0 08	0 09	0 01	101 58
1037	3	pc	core	2		53 66	0 03	3 94	1 22	2 34	16 86	0 08	22 71	0 05	0 10	0 02	101 01
1037	avg			5		53 89	0 03	3 65	1 06	2 32	17 37	0 07	22 58	0 07	0 09	0 02	101 16
1037	std					0 26	0 02	0 21	0 11	0 07	0 41	0 02	0 19	0 01	0 01	0 00	0 30
1043 2	?	smaller pc	core	1		52 53	0 09	4 29	1 30	1 79	16 42	0 03	23 92	0 05	0 26	0 04	100 72
1043 2	4	nb, near opx rim		1		53 64	0 11	3 78	0 98	1 81	16 77	0 13	23 28	0 05	0 18	0 00	100 73
1043.2	1	pc	core	2		52 75	0 08	5 00	1 36	2 25	16 38	0 06	23 32	0 04	0 18	0 01	101 43
1043 2	1	pc	core	3	* def	52 12	0 07	4 82	1 31	3 00	19 00	0 08	19 89	0 11	0 14	0 01	100 55
1043 2	avg			7		52 76	0 09	4 47	1 24	2 21	17 14	0 08	22 60	0 06	0 19	0 02	100 86
1043 2	std					0 56	0 01	0 48	0 15	0 49	1 08	0 04	1 59	0 03	0 04	0 02	0 34
1063 3	5	incl in opx		1	def	51 56	0 36	5 91	0 95	2 29	14 98	0 07	20 68	0 07	1 26	0 01	98 14
1063 3	4	pc	core	2		51 42	0 30	6 68	1 03	2 36	14 85	0 10	20 76	0 06	1 13	0 01	98 70

Tab. B-4a (continued)

sample	spot	comment	core/rim	N	other	SiO2	TiO2	Al2O3	Cr2O3	FeO	MgO	MnO	CaO	NiO	Na2O	K2O	SUM
1063 3	4	pc	core	1	*, def	52 38	0 26	6 45	0 99	3 22	17 96	0 04	18 42	0 04	1 10	0 00	100 86
1063 3	3	nb		1		52 13	0 31	6 34	1 01	2 72	16 81	0 07	19 31	0 04	1 07	0 00	99 81
1063 3	avg			5		51 87	0 31	6 35	1 00	2 65	16 15	0 07	19 79	0 05	1.14	0 01	99.38
1063 3	std					0 40	0 04	0 28	0 03	0 37	1 30	0 02	0 98	0 01	0 07	0 01	1 05
1065	9	s above	rim	2		52 82	0 03	3 27	1 05	1 86	17 10	0 06	23 88	0 02	0 05	0 00	100 14
1065	9	aggr in ol mx	core	2		52 57	0 03	3 59	1 05	2 21	18 56	0 08	22 46	0 05	0 07	0 00	100 67
1065	1	aggr, recryst in ol	core	2		53 40	0 05	3 85	1 18	2 02	17 02	0 00	23 36	0 00	0.00	0 00	100 88
1065	avg			6		52 93	0 04	3 57	1 09	2 03	17 56	0 05	23 23	0 02	0 04	0 00	100 56
1065	std					0 35	0 01	0 24	0 06	0 14	0 71	0 03	0 59	0 02	0 03	0 00	0 31
1071	8	pc	core	1		53 16	0 05	4 28	1 36	2 73	18 85	0 10	20 23	0 00	0 07	0 01	101 16
1071	8	pc	core	2	* def	52 78	0 05	4 23	1 30	3 01	19 64	0 10	19 11	0 09	0 10	0 00	100 41
1071	7		core	1		53 80	0 05	3 86	1 30	2 20	16 97	0 07	23 32	0 07	0 12	0 01	101 77
1071	2		rim	2		53 79	0 05	3 57	1 00	2 18	17 38	0 09	22 56	0 07	0 09	0 00	100 78
1071	2	pc	core	2		53 08	0 05	4 11	1 27	2 58	17 99	0 12	21 70	0 05	0 07	0 00	101 02
1071	avg			8		53 39	0 05	4 01	1 25	2 54	18 17	0 10	21 38	0 06	0 09	0 00	101 03
1071	std					0 40	0 00	0 26	0 13	0 32	0 97	0 02	1 53	0 03	0 02	0 00	0 45
1079 2	5	impregn		1	def	51 42	0 06	3 88	1 20	2 87	17 49	0 12	22 20	0 03	0 14	0 01	99 42
1079 2	2	pc	core	2	def	51 77	0 03	3 86	1 28	2 99	18 67	0 12	19 91	0 07	0 12	0 03	98 85
1079 2	2	pc	rim	1	def	51 39	0 03	3 08	1 24	2 18	18 09	0 13	21 72	0 02	0 11	0 03	98 02
1079 2	avg			4		51 53	0 04	3 61	1 24	2 68	18 08	0 12	21 28	0 04	0 12	0 02	98 76
1079 2	std					0 17	0 01	0 37	0 03	0 36	0 48	0 00	0 99	0 02	0 01	0 01	0 57
1079 3	5	vein		2		53 13	0 00	0 13	0 02	4 41	15 31	0 26	25 14	0 01	0 03	0 00	98 44
1079 3	6	vein		1		52 46	0 00	0 12	0 02	6 20	14 31	0 18	25 32	0 00	0 01	0 03	98 63
1079 3	7	vein		1		53 30	0 07	0 08	0 01	3 93	15 38	0 36	24 87	0 04	0 02	0 00	98 06
1079 3	avg	vein		4		52 96	0 02	0 11	0 02	4 85	15 00	0 26	25 11	0 02	0 02	0 01	98 38
1079 3	std					0 36	0 03	0 02	0 00	0 98	0 49	0 08	0 18	0 02	0 01	0 01	0 24
1079 3	8	host cpxte		1		51 32	0 04	3 90	1 28	3 05	18 23	0 08	20 38	0 13	0 11	0 01	98 53
1079 3	avg	host cpxte		1		51 32	0 04	3 90	1 28	3 05	18 23	0 08	20 38	0 13	0 11	0 01	98 53
1086	6	in opx aggr		1		53 42	0 04	2 22	0 77	2 27	17 51	0 06	24 25	0 08	0 07	0 01	100 70
1086	1	next to sp		1		52 23	0 02	2 68	1 00	2 29	17 23	0 07	23 81	0 05	0 04	0 02	99 44
1086	avg			2		52 83	0 03	2 45	0 89	2 28	17 37	0 07	24 03	0 07	0 06	0 02	100 07
1086	std					0 59	0 01	0 23	0 11	0 01	0 14	0 01	0 22	0 01	0 01	0 00	0 63
1112	5	grain near sp		1		53 20	0 03	2 98	0 95	2 53	17 16	0 08	23 41	0 09	0 15	0 01	100 59
1112	12	granular		1		52 80	0 05	2 86	0 78	2 69	17 40	0 07	23 73	0 05	0 18	0 00	100 61
1112	10	next to opx		2		53 52	0 04	3 01	0 95	2 59	17 68	0 04	23 36	0 05	0 16	0 01	101 41
1112	avg			4		53 17	0 04	2 95	0 89	2 60	17 41	0 06	23 50	0 06	0 16	0 01	100 87
1112	std					0 29	0 01	0 06	0 08	0 07	0 21	0 02	0 16	0 02	0 01	0 00	0 38

Tab. B-4a (continued)

sample	spot	comment	core/rim	N	other	SiO2	TiO2	Al2O3	Cr2O3	FeO	MgO	MnO	CaO	NiO	Na2O	K2O	SUM
1118	6	impregn type		2		52 66	0 05	3 52	0 82	2 50	16 51	0 10	23 13	0 00	0 18	0 00	99 47
1118	6	s above	rim to opx	1		53 33	0 03	3 52	0 90	2 84	17 30	0 09	22 18	0 03	0 29	0 02	100 53
1118	6	s. above	rim to sp	1		53 73	0 06	3 23	0 98	2 54	17 57	0 09	22 62	0 00	0 33	0 00	101 15
1118	2	impregn type		1		55 00	0 05	2 34	0 88	2 50	17 61	0 07	22 40	0 02	0 28	0 01	101 16
1118	avg			5		53 68	0 05	3 15	0 90	2 60	17 25	0 09	22 58	0 01	0 27	0 01	100 58
1118	std					0 85	0 01	0 48	0 06	0 14	0 44	0 01	0 35	0 01	0 06	0 01	0 69
1141		in ol mx		1		54 29	0 04	2 19	1 17	1 89	17 07	0 09	22 59	0 03	0 53	0 01	99 90
1141	2	in ol mx		1		55 02	0 02	2 36	1 13	2 21	18 11	0 09	21 56	0 04	0 42	0 00	100 96
1141	1	aw opx pc		2		54 30	0 03	2 12	1 16	1 77	17 64	0 07	22 50	0 01	0 47	0 00	100 07
1141	avg			4		54 54	0 03	2 22	1 15	1 96	17 61	0 08	22 22	0 03	0 47	0 00	100 31
1141	std					0 34	0 01	0 10	0 02	0 19	0 43	0 01	0 47	0 01	0 04	0 00	0 46
1143	3	pc	half rim	1		53 66	0 02	2 97	0 88	1 70	16 77	0 06	23 96	0 03	0 04	0 01	100 10
1143	3	pc	core	1		52 29	0 04	3 88	1 24	2 24	17 42	0 14	21 40	0 07	0 04	0 00	98 76
1143	2	pc	rim	2		53 67	0 03	3 37	1 00	1 95	17 31	0 10	23 05	0 00	0 07	0 00	100 55
1143	2	pc	core	2		53 13	0 03	4 02	1 25	2 35	17 18	0 07	22 70	0 03	0 11	0 00	100 87
1143	avg			6		53 19	0 03	3 56	1 09	2 06	17 17	0 09	22 78	0 03	0 07	0 00	100 07
1143	1std					0 56	0 01	0 42	0 16	0 25	0 25	0 03	0 92	0 02	0 03	0 00	0 80
1145	8	impregn type		1		54 05	0 04	2 71	0 98	1 99	17 28	0 05	23 83	0 11	0 07	0 01	101 12
1145	7	pc, bit amph	rim	1	core=amph	51 64	0 00	3 42	1 14	2 66	18 59	0 09	21 21	0 06	0 06	0 00	98 88
1145	7	pc	core	4	def	53 26	0 03	3 63	1 27	2 96	19 29	0 11	20 54	0 13	0 05	0 00	101 27
1145	1	large pc	core	2		52 91	0 03	3 77	1 31	2 18	16 45	0 07	23 39	0 05	0 05	0 01	100 22
1145	1	large pc	rim to ol	2		53 59	0 03	2 80	0 95	2 03	17 08	0 09	23 57	0 09	0 08	0 00	100 31
1145	avg			10		53 09	0 03	3 27	1 13	2 36	17 74	0 08	22 51	0 09	0 06	0 00	100 36
1145	std					0 82	0 01	0 43	0 15	0 38	1 04	0 02	1 36	0 03	0 01	0 00	0 85
1165	3		core	2		54 22	0 02	2 26	1 04	1 91	17 91	0 10	23 15	0 07	0 12	0 00	100 80
1165	avg			2		54 22	0 02	2 26	1 04	1 91	17 91	0 10	23 15	0 07	0 12	0 00	100 80
1181	4	aw sp		3	all var	53 36	0 03	3 85	1 08	2 32	17 86	0 08	23 08	0 00	0 12	0 01	101 75
1181	3	pc	core	3	all var	50 64	0 03	4 05	1 16	3 38	19 82	0 09	20 09	0 04	0 11	0 00	99 41
1181	3	pc	rim	4		53 31	0 04	4 34	1 19	2 60	17 88	0 07	22 59	0 00	0 15	0 00	102 17
1181	13	nb	rim	2		52 60	0 04	4 11	1 12	2 52	17 28	0 09	23 01	0 02	0 10	0 01	100 90
1181	13	nb	core	3	Ca,Fe,Mg var	52 18	0 05	4 33	1 21	3 07	18 63	0 12	20 93	0 05	0 11	0 00	100 68
1181	13	nb	rim	1		54 22	0 05	2 20	0 47	2 20	18 57	0 08	23 44	0 05	0 08	0 01	101 37
1181	11	impregn type		2		52 84	0 05	4 24	1 04	2 67	17 11	0 10	21 80	0 04	0 09	0 01	99 99
1181	avg			16		52 74	0 04	3 87	1 04	2 68	18 16	0 09	22 13	0 03	0 11	0 01	100 90
1181	std					1 05	0 01	0 70	0 24	0 38	0 86	0 02	1 15	0 02	0 02	0 00	0 90
1189.1	14	rim around opx		1		53 90	0 03	1 86	1 00	2 71	19 85	0 06	21 32	0 09	0 22	0 01	100 85
1189 1	13	impregn type		1		54 20	0 03	1 52	0 90	2 53	18 45	0 06	21 62	0 06	0 16	0 00	99 53

Tab. B-4a (continued)

sample	spot	comment	core/rim	N	other	SiO2	TiO2	Al2O3	Cr2O3	FeO	MgO	MnO	CaO	NiO	Na2O	K2O	SUM
1189.1	11	fussy in mx		1		54.31	0.02	1.81	1.00	2.35	19.65	0.05	22.07	0.01	0.30	0.01	101.58
1189.1	avg			3	near opxte	54.14	0.03	1.73	0.97	2.53	19.25	0.06	21.67	0.05	0.23	0.01	100.65
1189.1	std					0.17	0.00	0.15	0.05	0.15	0.57	0.00	0.31	0.03	0.06	0.00	0.85
1189.2	6	aw sp		3		52.97	0.03	3.31	1.09	2.13	17.96	0.07	22.86	0.02	0.13	0.00	100.57
1189.2	3	loose cpx aggr		2		53.05	0.03	3.53	1.08	2.07	17.16	0.08	23.30	0.03	0.18	0.00	100.51
1189.2	2	impregn type		2		53.71	0.05	2.53	0.89	2.06	17.64	0.06	24.10	0.00	0.13	0.00	101.17
1189.2	avg			7	far opxte	53.24	0.04	3.12	1.02	2.09	17.59	0.07	23.42	0.02	0.15	0.00	100.75
1189.2	std					0.33	0.01	0.43	0.09	0.03	0.33	0.01	0.51	0.01	0.02	0.00	0.30
1194	6	cpx aggr		1		53.69	0.10	1.91	0.70	1.87	17.86	0.09	22.94	0.06	0.09	0.02	99.33
1195	7	in mx	core	2		52.98	0.01	2.90	0.91	2.32	17.68	0.04	23.97	0.09	0.08	0.00	100.98
1195	7	in mx	rim	1		54.33	0.00	2.74	0.79	2.39	17.71	0.12	23.70	0.03	0.10	0.02	101.93
1195	6	small, in mx		1		52.79	0.03	2.68	0.78	2.51	17.77	0.05	23.40	0.07	0.09	0.01	100.18
1195	avg			5		53.37	0.01	2.77	0.83	2.41	17.72	0.07	23.69	0.06	0.09	0.01	101.03
1195	std					0.69	0.01	0.09	0.06	0.08	0.04	0.04	0.23	0.02	0.01	0.01	0.72
1200	4	aw sp		1		54.20	0.00	1.77	1.05	1.84	17.80	0.04	21.75	0.00	0.34	0.00	98.79
1200	3	impregn type		1		54.03	0.00	1.61	0.94	1.59	17.86	0.05	23.16	0.05	0.27	0.00	99.56
1200	2	in opx aggr		1		53.66	0.00	1.63	0.99	1.93	18.00	0.10	23.21	0.07	0.35	0.01	99.95
1200	avg			3		53.96	0.00	1.67	0.99	1.79	17.89	0.06	22.71	0.04	0.32	0.00	99.43
1200	std					0.23	0.00	0.07	0.04	0.14	0.08	0.03	0.68	0.03	0.04	0.00	0.48
1228.1	8	pc near contact	core	1		54.27	0.08	2.46	0.28	2.85	16.52	0.13	24.14	0.05	0.18	0.01	100.97
1228.1	8	pc near contact	rim to ol	1		52.07	0.06	2.41	0.24	3.02	19.13	0.09	22.16	0.05	0.10	0.00	99.33
1228.1	5	pc near contact	rim	3		54.78	0.07	1.70	0.23	2.69	18.09	0.07	23.20	0.05	0.11	0.01	101.00
1228.1	5	granular, small	core	2		52.88	0.05	2.87	0.42	2.88	16.96	0.09	23.92	0.04	0.18	0.01	100.30
1228.1	10	granular	core	1		53.97	0.05	2.69	0.33	2.73	16.68	0.06	23.68	0.04	0.18	0.01	100.62
1228.1	10	granular	rim	1		54.30	0.11	2.20	0.24	2.74	17.57	0.06	23.92	0.06	0.11	0.00	101.31
1228.1	avg			9		53.71	0.07	2.39	0.29	2.82	17.53	0.08	23.50	0.05	0.14	0.01	100.59
1228.1	std					0.94	0.02	0.37	0.07	0.11	0.88	0.02	0.67	0.01	0.04	0.00	0.65
1228.2	3		core	2		51.75	0.12	5.46	0.65	2.74	15.52	0.11	22.43	0.05	0.33	0.01	99.16
1228.3	6	pc	core	1		51.11	0.06	5.09	0.42	3.81	15.72	0.13	23.22	0.00	0.20	0.02	99.78
1228.3	6	pc	rim to ol	1		51.86	0.11	5.38	0.20	3.87	15.02	0.07	23.45	0.05	0.16	0.02	100.19
1228.3	3?	mosaic		1		52.33	0.11	4.34	0.15	3.94	15.77	0.04	23.68	0.00	0.16	0.00	100.52
1228.3	14	mosaic	next to gt	1	plag band	54.74	0.07	4.57	0.14	3.82	16.03	0.06	22.68	0.01	0.27	0.00	100.39
1228.3	1	mosaic		1		55.01	0.01	2.17	0.07	3.68	17.38	0.09	20.64	0.04	1.02	0.02	100.13
1228.3	avg			7		52.61	0.07	4.31	0.20	3.82	15.98	0.08	22.73	0.02	0.36	0.01	100.20
1228.3	std					1.32	0.04	1.13	0.12	0.09	0.77	0.03	1.10	0.02	0.33	0.01	0.25
1232	8	cpx aw sp		3		53.54	0.01	1.69	0.54	1.78	17.98	0.05	23.28	0.02	0.04	0.00	98.93
1232	6	near opx aggr	rim	2	c-r same	54.06	0.03	2.35	0.80	1.76	17.68	0.04	23.79	0.01	0.07	0.00	100.59

Tab. B-4a (continued)

sample	spot	comment	core/rim	N	other	SiO2	TiO2	Al2O3	Cr2O3	FeO	MgO	MnO	CaO	NiO	Na2O	K2O	SUM
1232	4	impregn type		1		54 02	0 01	2 46	0 63	2 00	20 74	0 09	18 45	0 00	0 09	0 00	98 49
1232	3	in opx aggr		2		54 02	0 00	2 58	0 81	1 80	17 36	0 07	23 45	0 04	0 05	0 00	100 18
1232	avg			8		53 91	0 01	2 27	0 70	1 84	18 44	0 06	22 24	0 02	0 06	0 00	99 55
1232	std					0 21	0 01	0 34	0 11	0 10	1 35	0 02	2 20	0 01	0 02	0 00	0 86
1237	9	impregn type		2		52 84	0 03	2 48	0 91	1 98	17 60	0 09	23 57	0 08	0 09	0 02	99 69
1237	8	aw sp		1		53 05	0 03	2 30	0 83	1 98	17 31	0 06	23 02	0 07	0 09	0 01	98 75
1237	3	impregn type		1		53 48	0 00	2 89	1 01	2 09	16 95	0 04	23 74	0 04	0 09	0 01	100 34
1237	avg			4		53 12	0 02	2 56	0 92	2 02	17 29	0 06	23 44	0 06	0 09	0 01	99 59
1237	std					0 27	0 01	0 25	0 07	0 05	0 27	0 02	0 31	0 02	ERR	0 00	0 65
1245	4	impregn type		1		56 36	0 02	1 19	1 03	1 70	17 68	0 06	22 97	0 05	0 47	0 02	101 55
1245	3	near opx		2		55 95	0 02	1 14	0 97	1 77	17 94	0 09	22 58	0 04	0 50	0 01	101 01
1245	avg			3		56 16	0 02	1 17	1 00	1 74	17 81	0 08	22 78	0 05	0 49	0 02	101 28
1245	std					0 20	0 00	0 02	0 03	0 03	0 13	0 01	0 19	0 00	0 02	0 00	0 27
1249	2	impregn type		1		54 45	0 00	1 52	0 69	1 81	18 26	0 04	23 88	0 12	0 06	0 00	100 83
1249	1	impregn type		2		54 55	0 00	1 56	0 73	2 04	18 19	0 10	23 52	0 03	0 04	0 01	100 77
1249	avg			3		54 50	0 00	1 54	0 71	1 93	18 23	0 07	23 70	0 08	0 05	0 01	100 80
1249	std					0 05	0 00	0 02	0 02	0 12	0 03	0 03	0 18	0 05	0 01	0 01	0 03
1258	7	in opx aggr		1		53 34	0 05	2 24	0 86	2 65	17 72	0 08	23 37	0 00	0 18	0 01	100 50
1258	6	incl A in opx		1		53 89	0 02	1 74	0 77	2 10	17 22	0 05	23 84	0 04	0 16	0 00	99 83
1258	6	incl D in opx		1		53 88	0 00	2 41	0 96	2 57	17 91	0 04	22 66	0 03	0 20	0 00	100 66
1258	4	next to sp		1		53 57	0 04	2 07	0 85	2 08	17 51	0 03	23 27	0 10	0 14	0 00	99 66
1258	avg			4		53 67	0 03	2 12	0 86	2 35	17 59	0 05	23 29	0 04	0 17	0 00	100 16
1258	std					0 23	0 02	0 25	0 07	0 26	0 26	0 02	0 42	0 04	0 02	0 00	0 43
1262	7	cpx aggr	rim	2		53 16	0 02	2 66	0 73	2 27	17 59	0 06	23 66	0 06	0 17	0 01	100 39
1262	7	cpx aggr	core	2		53 07	0 03	3 87	1 06	2 45	16 78	0 09	23 61	0 03	0 15	0 00	101 14
1262	7	cpx aggr	core	2	*, def	53 70	0 03	3 56	1 19	2 57	17 45	0 05	22 97	0 02	0 14	0 00	101 68
1262	5	incl A in opx		1		53 39	0 03	3 55	1 02	3 11	18 32	0 07	21 06	0 03	0 17	0 02	100 77
1262	5	incl B in opx		1		52 16	0 02	3 39	1 04	2 42	16 83	0 06	23 11	0 07	0 14	0 00	99 24
1262	5	incl C in opx		1		52 13	0 03	3 98	1 06	2 57	16 91	0 05	23 39	0 02	0 16	0 00	100 30
1262	2	aw sp		1		52 46	0 05	2 86	0 92	3 60	18 91	0 12	21 46	0 02	0 05	0 01	100 46
1262	avg			10		52 87	0 03	3 41	1 00	2 71	17 54	0 07	22 75	0 04	0 14	0 01	100 57
1262	std					0 57	0 01	0 45	0 13	0 44	0 75	0 02	0 98	0 02	0 04	0 01	0 71
1274.1	3	trails	core	2		54 07	0 02	2 56	0 95	2 05	17 61	0 06	23 52	0 09	0 02	0 00	100 95
1274.1	2	granular		2		54 11	0 00	2 17	0 72	1 82	17 64	0 04	23 64	0 06	0 00	0 00	100 20
1274.1	avg			4		54 09	0 01	2 37	0 84	1 94	17 63	0 05	23 58	0 08	0 01	0 00	100 58
1274 1	std					0 02	0 01	0 19	0 11	0 11	0 02	0 01	0 06	0 01	0 01	0 00	0 37
1292	1			2		53 40	0 04	2 65	1 02	2 34	18 13	0 04	23 04	0 07	0 19	0 00	100 92

Tab. B-4a (continued)

sample	spot	comment	core/rim	N	other	SiO2	TiO2	Al2O3	Cr2O3	FeO	MgO	MnO	CaO	NiO	Na2O	K2O	SUM
1292	avg			2		53 40	0 04	2 65	1 02	2 34	18 13	0 04	23 04	0 07	0 19	0 00	100 92
1295	5		core	2		53 05	0 05	3 49	1 24	2 02	17 35	0 06	23 40	0 04	0 22	0 00	100 92
1295	5		core	1	def	51 84	0 03	3 77	1 13	3 16	18 14	0 11	20 78	0 12	0 16	0 02	99 06
1295	5		rim	2		54 28	0 05	2 62	0 90	1 84	17 22	0 08	24 20	0 05	0 12	0 00	101 36
1295	3		core	2		53 45	0 06	3 68	1 04	2 36	18 54	0 09	20 54	0 07	0 18	0 00	100 01
1295	1	rimmed by sp		2		54 81	0 07	2 24	0 88	1 84	17 53	0 08	23 05	0 05	0 18	0 01	100 74
1295	avg			9		53 45	0 05	3 16	1 04	2 24	17 76	0 08	22 39	0 07	0 17	0 01	100 42
1295	std					1 09	0 01	0 61	0 14	0 50	0 50	0 02	1 47	0 03	0 03	0 01	0 81
1315	8	impregn type		1		51 73	0 05	1 60	0 69	2 76	18 52	0 04	22 20	0 08	0 16	0 01	97 84
1315	6	impregn type		1		53 71	0 03	1 65	0 68	2 50	17 83	0 09	23 11	0 08	0 18	0 01	99 87
1315	avg			2		52 [illegible]	0 04	1 63	0 69	2 63	18 18	0 07	22 66	0 08	0 17	0 01	98 86
1315	std					0 99	0 01	0 03	0 00	0 13	0 34	0 02	0 45	0 00	0 01	0 00	1 01
1316 2	6			2		50 58	0 68	4 28	0 44	2 94	15 78	0 05	24 16	0 05	0 21	0 00	99 1[illegible]
1316 2	avg			2		50 58	0 68	4 28	0 44	2 94	15 78	0 05	24 16	0 05	0 21	0 00	99 17
1321	2			3		53 08	0 26	1 43	0 45	1 83	16 89	0 04	25 44	0 03	0 12	0 05	99 62
1321	avg			3		53 08	0 26	1 43	0 45	1 83	16 89	0 04	25 44	0 03	0 12	0 05	99 62
1324	4	near sp		1		53 70	0 09	1 46	0 68	2 46	17 84	0 04	22 84	0 08	0 26	0 00	99 45
1324	avg	near sp		1		53 70	0 09	1 46	0 68	2 46	17 84	0 04	22 84	0 08	0 26	0 00	99 45
1326	4			1		52 29	0 25	3 76	0 86	2 39	15 87	0 06	22 81	0 09	0 38	0 00	98 76
1326		rim on plag		2	Na var	51 42	0 25	3 99	0 89	2 51	15 87	0 06	23 20	0 03	0 39	0 02	98 63
1326	avg			3		51 86	0 25	3 88	0 88	2 45	15 87	0 06	23 01	0 06	0 39	0 01	98 70
1326	std					0 43	0 00	0 12	0 01	0 06	0 00	0 00	0 19	0 03	0 00	0 01	0 06
1331 1	8	near sp, pl		3	Fe var	52 02	0 15	4 31	1 16	3 45	16 63	0 11	21 89	0 07	0 41	0 01	100 21
1331 1	5			1		53 16	0 12	4 00	1 32	2 01	16 11	0 11	23 04	0 08	0 62	0 01	100 58
1331 1	3		rim	2		53 21	0 20	3 93	1 21	2 29	16 53	0 06	23 02	0 07	0 40	0 00	100 92
1331 1	3	large	core	2		52 89	0 17	4 25	1 30	2 25	16 42	0 06	22 93	0 09	0 67	0 00	101 03
1331 1	spot	large	core	1	*, def	52 71	0 16	4 07	1 21	2 33	16 21	0 07	23 21	0 07	0 48	0 01	100 53
1331 1	avg			9		52 80	0 16	4 11	1 24	2 47	16 38	0 08	22 82	0 08	0 52	0 01	100 65
1331 1	std					0 43	0 03	0 15	0 06	0 50	0 19	0 02	0 47	0 01	0 11	0 00	0 29
1331 2	6	mx		2	*	53 79	0 28	2 59	0 64	2 46	16 49	0 01	24 36	0 07	0 34	0 00	101 03
1331 2	5	mx		1	*	52 84	0 21	3 27	0 76	2 41	16 09	0 04	24 40	0 00	0 36	0 00	100 38
1331 2	avg			3		53 32	0 25	2 93	0 70	2 44	16 29	0 03	24 38	0 04	0 35	0 00	100 71
1331 2	std					0 47	0 03	0 34	0 06	0 02	0 20	0 02	0 02	0 03	0 01	0 00	0 [illegible]2
1340	6	near sp		1	*	55 43	0 01	1 48	0 83	1 99	18 11	0 04	23 73	0 07	0 18	0 02	101 89
1340	3	in opx		2		54 74	0 02	1 81	0 89	1 95	17 96	0 06	23 17	0 02	0 23	0 00	100 85
1340	avg			3		55 09	0 02	1 65	0 66	1 97	18 04	0 05	23 45	0 05	0 21	0 01	101 37
1340	std					0 35	0 00	0 16	0 03	0 02	0 07	0 01	0 28	0 02	0 02	0 01	0 52

Tab. B-4a (continued)

sample	spot	comment	core/rim	N	other	SiO2	TiO2	Al2O3	Cr2O3	FeO	MgO	MnO	CaO	NiO	Na2O	K2O	SUM
1344	3			2		53 48	0 02	2 55	1 11	2 08	17 40	0 04	22 38	0 00	0 18	0 01	99 25
1344	2	incl in opx		3	Fe var	53 41	0 03	2 36	1 02	2 10	17 57	0 10	22 98	0 07	0 18	0 00	99 82
1344	avg			5		53 45	0 03	2 46	1 07	2 09	17 49	0 07	22 68	0 04	0 18	0 01	99 54
1344	std					0 03	0 00	0 09	0 04	0 01	0 08	0 03	0 30	0 03	0 00	0 01	0 29
1350	8		core	1	opx EL excl	52 98	0 05	3 89	1 30	2 16	17 46	0 09	21 77	0 07	0 06	0 01	99 84
1350	8		rim	1		51 77	0 03	3 14	1 06	2 17	17 94	0 06	22 02	0 07	0 06	0 01	98 33
1350	6	pc	core	10	"defocused"	52 51	0 04	3 77	1 38	2 67	17 85	0 10	21 60	0 05	0 08	0 00	100 05
1350		aw opx aggr	rim	2		52 80	0 05	3 55	1 23	2 55	17 83	0 09	21 06	0 11	0 09	0 02	99 38
1350	avg			14		52 52	0 04	3 59	1 24	2 39	17 77	0 09	21 61	0 08	0 07	0 01	99 40
1350	std					0 46	0 01	0 29	0 12	0 23	0 18	0 01	0 35	0 02	0 01	0 01	0 66
1360	8			2	du band	52 47	0 26	2 85	1 00	2 27	16 99	0 02	23 87	0 08	0 33	0 01	100 15
1360	5		core	2	pl wehrl band	51 76	0 36	3 97	1 21	2 33	16 92	0 07	22 48	0 00	0 52	0 01	99 63
1360	5		rim	1	pl wehrl band	53 85	0 26	2 98	1 00	2 24	16 81	0 02	23 42	0 02	0 43	0 01	101 04
1360	3			1	transition	52 04	0 25	3 64	1 16	2 02	16 81	0 04	22 81	0 01	0 40	0 01	99 19
1360	avg			3	du band	52 47	0 26	2 85	1 00	2 27	16 99	0 02	23 87	0 08	0 33	0 01	100 15
1360	avg			4	pl wehrl band	52 81	0 31	3 48	1 11	2 29	16 87	0 05	22 95	0 01	0 48	0 01	100 54
1366 2	3	next to sp		2		54 21	0 04	2 36	0 73	1 80	17 25	0 04	23 02	0 08	0.56	0 00	100 09
1366 2	3	within sp trail		3		54 63	0 07	1 64	0 57	1 86	17 47	0 01	23 32	0 04	0 48	0 01	100 10
1366 2	1	between sp, opx		2		54 71	0 03	2 30	0 73	2 02	17 38	0 07	22 95	0 05	0 62	0 00	100 86
1366 2	avg			7		54 52	0 05	2.10	0 68	1 89	17.37	0 04	23 10	0 06	0.55	0 00	100 35
1366 2	std					0 22	0.02	0 33	0 08	0.09	0 09	0 02	0.16	0 02	0 06	0 00	0 36
1378	6	aw opx aggr		2		52 27	0 05	3 86	1 30	2 07	17 07	0 07	23 54	0 07	0 27	0 01	100 58
1378	5	aw sp		1		52 59	0 06	3 47	1 27	2 53	18 37	0 11	21.37	0.09	0.27	0.01	100 14
1378	3	aw sp		1		52 93	0 02	3 62	1.18	2 08	17 88	0 04	22.76	0.07	0 28	0 00	100 86
1378	1	larger	core	2		52 89	0.03	4 01	1.44	2.13	17 10	0 09	22 46	0.09	0 26	0 02	100 52
1378	1		core	1	*, def	53 05	0 04	4 09	1 33	2 34	18 56	0 04	21.24	0.07	0 16	0.02	100 94
1378	1		rim	2		53 40	0.05	3 47	1 15	1 88	17 66	0 07	23 45	0 04	0 26	0 01	101 44
1378	avg			9		52 86	0 04	3 75	1.28	2.17	17 77	0 07	22 47	0 07	0 25	0 01	100 75
1378	std					0 35	0.01	0 25	0 10	0 21	0.57	0.03	0 90	0 02	0.04	0.01	0 40
1396	9	in opx aggr		1		55 64	0 04	1 58	0 83	2 37	18 48	0 11	22 01	0 17	0 20	0 01	101.44
1396	10			2		54 19	0 05	1.66	0 96	2 19	18 06	0 06	22 51	0 11	0 13	0 01	99 93
1396	avg			3		54 92	0.05	1 62	0 90	2 28	18 27	0 09	22 26	0.14	0 17	0 01	100 69
1396	std					0 72	0 00	0.04	0 06	0 09	0 21	0 02	0.25	0 03	0 04	0.00	0 75
1402	2	small		2		55 54	0.05	1.16	0.70	2 29	18 33	0 07	23 84	0 05	0 38	0 01	102 42
1402	avg			2		55 54	0 05	1.16	0.70	2.29	18 33	0 07	23.84	0.05	0.38	0 01	102 42
1415	1	aw sp		3		52 89	0 26	3 65	0 93	2 18	16.64	0.04	23 90	0 09	0 35	0 01	100 94
1415	1	aw sp		1		52 11	0 30	3 45	0.79	2.29	16 72	0 06	23.69	0.12	0 29	0.01	99 83

Tab. B-4a (continued)

sample	spot	comment	core/rim	N	other	SiO2	TiO2	Al2O3	Cr2O3	FeO	MgO	MnO	CaO	NiO	Na2O	K2O	SUM
1415	avg			4		52 50	0.28	3 55	0 86	2 24	16.68	0 05	23 80	0.11	0.32	0 01	100.39
1415	std					0 39	0 02	0 10	0 07	0 05	0 04	0 01	0.10	0 02	0 03	0 00	0 55
1420	6			2		53 93	0 22	3 22	0 97	2 50	17 70	0 11	22 38	0 09	0 33	0 01	101.46
1420	5			1		53 98	0 23	3 12	1 08	2 82	18 04	0 09	21 89	0 13	0.19	0 02	101 59
1420	3			2		53 56	0 23	3 36	0 93	2 53	17.77	0.12	22 60	0 11	0 30	0 00	101 51
1420	2	in plag layer		1		52 71	0 22	3 20	1 10	2 73	17.36	0 04	22.05	0 00	0.30	0 00	99 71
1420	avg			6		53.55	0 23	3 23	1 02	2 65	17 72	0 09	22 23	0 08	0 28	0 01	101 07
1420	std					0 51	0 00	0 09	0 07	0.13	0 24	0 03	0.28	0 05	0 05	0 01	0 79
1428	5			2		53 37	0 02	2 23	0 96	2 04	18.21	0 07	23.15	0 08	0 17	0 00	100 30
1428	5		core	4	def	52 22	0 04	2 19	0 90	2 79	18 91	0 07	21 93	0 04	0 17	0 00	99 26
1428	4	"dirty"		1		54 71	0.03	2 44	1 11	2 32	18 39	0 07	22 23	0 05	0 21	0 00	101 56
1428	3			1		53 71	0.00	2 44	0 95	2 19	17 53	0 11	23 17	0 07	0 21	0 00	100 38
1428	avg			8		53 50	0 02	2 33	0 98	2 34	18 26	0 08	22 62	0 06	0 19	0 00	100 38
1428	std					0 89	0 01	0 12	0 08	0 28	0 49	0 02	0 55	0 02	0 02	0 00	0 81
1442	7	impregn type		2		53 35	0 08	3 83	1 06	2 64	17 62	0 08	21 42	0 05	0 25	0 01	100 39
1442	4			2		52 00	0 07	3 83	1 09	2 91	17 80	0 09	21 20	0 12	0 30	0 02	99 43
1442	1	aw sp trail		2		53 70	0 05	3 73	1 04	2 75	17 80	0 04	21 73	0 11	0 22	0 00	101 17
1442	avg			6		53 02	0 07	3 80	1 06	2 77	17 74	0 07	21 45	0 09	0 26	0 01	100 33
1442	std					0 73	0 01	0 05	0 02	0 11	0 08	0 02	0 22	0 03	0 03	0 01	0 71
1447	6	core		2	du band	52 40	0 26	4 01	0 97	2 70	16 00	0 06	22 25	0 03	0 19	0 00	98 87
1447	4	near sp		1	du band	51 15	0 29	3 49	0 84	2 45	16 65	0 07	24 14	0 00	0 18	0.00	99.26
1447	4			3	du band, def	51 96	0 26	4 07	0 96	2 89	16 66	0 04	23 36	0 09	0 22	0 00	100 51
1447	4	away from sp		2	du band	51 64	0 26	3 74	0 92	2 59	16 55	0 09	23.09	0 07	0 20	0 00	99 15
1447	8	smaller		1	pl lherz band	51 56	0 14	3 06	1 09	2 96	17 20	0 04	22 39	0 11	0 30	0 00	98 85
1447	3		core	4	pl lherz band	52 38	0 16	3 09	1 09	3 19	17 81	0 09	21 30	0 09	0 27	0 01	99 48
1447	3		rim to opx	2	pl lherz band	52 54	0 10	2 73	0 96	2 72	17 59	0 09	22 26	0 11	0 24	0 00	99 34
1447	3	large	core	3	pl lherz band	52 67	0 15	3 20	1 11	2 86	17 04	0 13	22 16	0 08	0 31	0 00	99 71
1447	avg			10	pl lherz band	52 29	0 14	3 02	1 06	2 93	17 41	0 09	22 03	0 10	0 28	0 00	99 35
1447	avg			8	du band	51 79	0 27	3 83	0 92	2 66	16 47	0 07	23 21	0 05	0 20	0 00	99 45
1447	std				du band	0 46	0 01	0 23	0 05	0 16	0 27	0 02	0 68	0 03	0 01	0 00	0 63
1447	std				pl lherz band	0 47	0 05	0 33	0 08	0 21	0 44	0 03	0 57	0 02	0 04	0 00	0 29
1454	6		core	3		52 74	0 08	3 59	0 94	2 65	17 57	0 04	21 10	0 04	0 22	0 00	98 97
1454	2			2		51 90	0 07	4 05	1 07	2 64	18 12	0 09	21 91	0 14	0 28	0 00	100 27
1454	avg			5		52 32	0 08	3 82	1 01	2 65	17 85	0 07	21 51	0 09	0 25	0 00	99 62
1454	std					0 42	0 00	0 23	0 06	0 01	0 27	0 02	0 40	0 05	0 03	0 00	0 65
1459	2	near plag		1		50 04	0 26	4 28	0 92	2 62	15 54	0 04	24 15	0 00	0 46	0 00	98 31
1459	1	interstitial		1		49 31	0 26	5 02	0 86	2 54	15 29	0 12	23 56	0 00	0 27	0 03	97 26

Tab. B-4a (continued)

sample	spot	comment	core/rim	N	other	SiO2	TiO2	Al2O3	Cr2O3	FeO	MgO	MnO	CaO	NiO	Na2O	K2O	SUM
1459	1			1		50 80	0 21	5 13	0 91	2 15	15 03	0 04	24 66	0 01	0 38	0.05	99 37
1459	avg			3		50 05	0 24	4 81	0 90	2 44	15 29	0 07	24 12	0 00	0.37	0 03	98 31
1459	std					0 61	0 02	0.38	0 03	0 21	0 21	0 04	0 45	0.00	0 08	0.02	0 86
1462	5	next to sp		1	*, def	54 08	0 07	2 83	1 01	2 46	17 94	0 08	22 66	0.03	0 23	0 01	101 40
1462	5	away from sp		1	*, def	53 62	0.05	3 07	1.00	2.39	18 16	0.04	21.79	0.12	0.27	0 00	100 51
1462	5		core	1	def	53 38	0 06	2 81	1 05	2 50	17.20	0 09	23.39	0.00	0.21	0.01	100 70
1462	avg			3		53 69	0 06	2 90	1 02	2 45	17 77	0 07	22 61	0 05	0 2a	0 01	100 87
1462	std					0 29	0 01	0 12	0 02	0 05	0.41	0 02	0 65	0 05	0.02	0.00	0.38
1468	5		core	1	def	51.85	0 05	3 62	1 27	2 45	19 81	0 09	20 15	0.13	0.07	0.00	99 49
1468	1			6		53 52	0 06	3 04	1 09	2.15	17 46	0 09	22 65	0 05	0.23	0 01	100.35
1468	10	near opx		2		53 02	0 06	2 36	0 68	2 14	17 70	0 07	23 41	0.05	0.07	0 01	99 57
1468	3	aw spinel		2		52 87	0 03	2 60	0 77	2 09	17 70	0 06	22 97	0 07	0 12	0 01	99 29
1468	avg			11		52 82	0 05	2 91	0 95	2 21	18 17	0.08	22 29	0.08	0 12	0 01	99 68
1468	std					0 61	0 01	0 48	0 24	0 14	0 95	0 01	1 27	0 03	0 07	0 00	0 40
1485	6	aw sp		3		54 43	0 05	2 38	0 93	2 06	17.71	0 05	23 46	0 12	0 08	0 00	101 27
1485	3	aw opx aggr		2		54 39	0 05	2 59	1 05	2 12	17 89	0 12	22 64	0 08	0 09	0 01	101 03
1485	avg			5		54 41	0 05	2 49	0 99	2 09	17 80	0 09	23 05	0 10	0 09	0 01	101 15
1485	std					0 02	0 00	0 10	0 06	0 03	0 09	0 03	0.41	0 02	0.00	0 01	0 12
1499	1			2		52 23	0 43	4 02	0 93	2 99	16 36	0 07	23 23	0 05	0 20	0 02	100 53
1499	4			2		51 29	0 52	3 96	0 86	2 54	16 11	0 07	24 38	0 06	0 39	0 00	100 18
1499	avg			4		51 76	0 48	3 99	0 90	2 77	16 24	0 07	23 81	0 06	0 30	0 01	100 36
1499	std					0 47	0 04	0 03	0 03	0 [illegible]	0 13	0.00	0.58	0 01	0 09	0 01	0 17

Tab. B-4b

sample	spot	comment	core/rim	N	other	SiO2	TiO2	Al2O3	Cr2O3	FeO	MgO	MnO	CaO	NiO	Na2O	K2O	SUM
lh 73	5	nb		4	no zoning	54 55	0 01	0 85	0 61	1 79	18 47	0 07	23 84	0 01	0 10	0.00	100 30
lh 73	avg	nb		4	no zoning	54 55	0 01	0.85	0.61	1 79	18 47	0 07	23 84	0 01	0 10	0 00	100.30
lh 47	2	in opx aggr.		2		54 02	0 02	0.53	0 31	1.41	18 09	0 08	23 87	0 02	0 08	0 00	98 43
lh 47	6	nb in mx		2		53 52	0 02	0 82	0 64	1 76	18 21	0 05	22 45	0 05	0 24	0 00	97 76
lh 47	2	in opx aggr		1		54.78	0.01	0 91	0 55	1 73	17 61	0 01	23 71	0 02	0.16	0 00	99 52
lh 47	9	next to opx pc		2		54 89	0 03	0 65	0 50	1 57	17.82	0 04	23 92	0 05	0 14	0 00	98 61
lh 47	avg			7		54 35	0.02	0.75	0 52	1 65	18 04	0 06	23 56	0 03	0.14	0 00	99 12
lh 47	std					0 51	0.01	0.14	0 12	0.14	0 30	0 02	0 56	0 02	0 06	0 00	0.91
lh 11	2	granular in mx		2		54 71	0 05	0 93	0 59	1 79	17 93	0 04	23 55	0 05	0 14	0.01	99 79
lh 11	6	near opx,sp		2		54.46	0.05	0.87	0 58	1 75	17 87	0 04	23.79	0 03	0 24	0 01	99 49
lh 11	1	in opx aggr.	core	1		53 86	0.04	0.81	0 53	1 49	17.60	0 05	23.50	0 03	0 13	0 00	98 04
lh 11	1	in opx aggr.	rim	1		55 54	0 04	0.51	0 43	1.35	17 48	0 08	23 57	0 05	0 09	0 00	99 14
lh 11	2	close to opx		1		54.89	0 02	0 74	0 52	1 55	17 61	0 11	23 17	0 00	0 14	0 00	98.75
lh 11	6	in opx aggr		2	ev zoned	53.32	0 05	0.77	0 63	1 65	17 81	0 02	23.16	0 03	0.18	0 00	97 62
lh 11	avg			9		54 46	0 04	0.77	0.55	1 60	17.68	0 06	23 46	0.03	0 15	0 00	98 81
lh 11	std					0 72	0.01	0.13	0 06	0.15	0.15	0.03	0 23	0 02	0.05	0 00	0.77
lh 87	4	cpx aggr aw opx		1		55 18	0.03	0 80	0 48	2.01	18.68	0 09	21 86	0 08	0 20	0 01	99 42
lh 87	5	cpx aggr	core	2		52.93	0.03	0 65	0.50	1.95	17 39	0 08	24 28	0 08	0 21	0.01	98 11
lh 87	5		rim to am	3	Na,Cr,Al var	54.13	0.02	0.69	0.47	1.75	17.86	0.08	23.39	0 05	0 17	0 00	98 61
lh 87	5	cpx aggr	core	2	rerun	54 35	0.02	0 71	0.47	1.87	17 55	0.04	23 92	0 03	0.18	0 00	99 14
lh 87	5	cpx aggr	rim	2	rerun	53.77	0 03	0.70	0 58	1 72	17.95	0 06	24 03	0 00	0.18	0 00	99 02
lh 87	5			2		54 04	0.02	0 81	0.42	2 05	18 27	0.06	22.89	0 07	0 40	0 02	99 05
lh 87	6	small, in mx		1		54 42	0 04	0.81	0.50	1 92	17 80	0 07	23 33	0 07	0 06	0 00	99 02
lh 87	avg			13		54 12	0.03	0.74	0 49	1 90	17.93	0.07	23 39	0 05	0 20	0 01	98 91
lh 87	std					0.63	0 01	0.06	0 04	0 12	0 40	0.02	0.76	0 03	0 09	0.01	0 39
lh 22	8	in opx aggr.		1		55 02	0 02	0.93	0.59	1 89	18.25	0.09	24.07	0 04	0.12	0 00	101.02
lh 22	9	small, in mx		1		54.16	0 03	0.84	0 64	2 14	19 32	0.08	22.60	0 05	0.14	0 00	100.00
lh 22	avg			2		54 59	0.03	0.89	0 62	2 02	18 79	0.09	23 34	0 05	0.13	0 00	100 51
lh 22	std					0 43	0 00	0.04	0.02	0.12	0 53	0 00	0.73	0.00	0.01	0 00	0 51
lh 8	3	nb aggr		2		54 00	0.01	0 80	0 47	1.59	18.09	0.06	24 52	0 03	0 11	0 01	99 69
lh 8	5	nb trail		1		54.45	0.00	1.05	0.56	2 16	19 59	0.07	21 94	0.08	0.21	0 01	100 12
lh 8	avg			3		54 23	0 01	0.93	0 52	1 88	18.84	0.07	23.23	0.06	0 16	0 01	99 91
lh 8	std					0.23	0 01	0.12	0 05	0.28	0 75	0.01	1 29	0 03	0.05	0.00	0.21
lh 76	1	in mx		1		54 05	0 03	0 79	0 57	1 77	17 55	0 12	21 00	0 02	0 12	0 02	99 04
lh 76	2	in opx aggr		2		54 43	0.03	0.77	0 57	1.86	17.97	0.06	22.84	0 08	0 21	0 00	98 82
lh 76	avg			3		54 24	0 03	0 78	0 57	1 82	17 76	0 09	23 42	0 05	0 17	0 01	98 93
lh 76	std					0 19	0 00	0.01	0.00	0.04	0.21	0.03	0 58	0.03	0.04	0.01	0 11

Tab. B-4b (continued)

sample	spot	comment	core/rim	N	other	SiO2	TiO2	Al2O3	Cr2O3	FeO	MgO	MnO	CaO	NiO	Na2O	K2O	SUM
lh 49	1	cpx aggr	core	2		53 95	0.01	0 89	0.54	1 70	18 45	0 05	23 81	0 04	0 10	0 00	99 54
lh 49	1	cpx aggr	rim	2	all var	55 77	0 01	1 02	0 58	1 99	19 78	0 04	21 64	0 02	0.16	0 00	101 01
lh 49	3	near opx aggr	core	1		54 48	0 01	1 00	0 61	2.16	19 45	0 06	21 83	0.11	0.14	0 01	99 86
lh 49	3	near opx aggr	rim	1		54 37	0 02	0 94	0 52	1 84	18 77	0 07	23 31	0 03	0.11	0 00	99 98
lh 49	4	in mx		1		55 39	0 03	1.17	0 61	1 96	18 69	0 09	22 80	0.10	0.16	0 00	101.00
lh 49	5	in opx aw sp	rim to sp	1		54 74	0 00	0 58	0.30	1.52	18.37	0 07	24 55	0.07	0.09	0 01	100 30
lh 49	5	in opx aw sp	rim to opx	1		54 92	0 01	0 75	0 43	1 64	18 39	0 05	23 31	0 05	0 13	0 00	99 68
lh 49	avg			9		54 80	0 01	0 91	0.51	1.83	18 84	0 06	23 04	0 06	0.13	0 00	100 20
lh 49	std					0.58	0.01	0.18	0 10	0 21	0 52	0 02	0 96	0.03	0 03	0 00	0 56
lh 67	5	in opx aggr	rim to opx	1		55.41	0.03	0 71	0 43	1 63	17 63	0 04	24.20	0 04	0.14	0 00	100 26
lh 67	5	sheared in opx		1		54 87	0 03	0 55	0 57	1.46	17 64	0 06	23 98	0 02	0.15	0 01	99 34
lh 67	6	aw opx aggr	core	2		54 62	0 02	0 54	0.39	1 55	17 68	0 03	24 48	0 05	0 09	0 01	99 46
lh 67	6	aw opx aggr	rim	1		54 61	0 02	0 52	0 50	1.52	7 86	0 10	24 59	0 07	0 09	0 00	99 88
lh 67	7	fussy in mx		1		54 46	0 00	0 86	0.49	2 16	19.03	0 04	22 14	0 03	0.11	0 00	99 32
lh 67	1	in opx aggr		1		52 92	0 00	0 66	0 51	1 54	17 65	0 07	24 56	0 01	0 16	0 00	98 08
lh 67	avg			7		54 48	0 02	0 64	0 48	1 64	17 92	0 06	23 99	0 04	0 12	0 00	99 39
lh 67	std					0 76	0 01	0 12	0 06	0 24	0 50	0 02	0 86	0 02	0 03	0 00	0 67
lh 62	5	in opx aggr		1		55 46	0 01	1 01	0 59	1 64	18 32	0 00	24 13	0 05	0 14	0 01	101 36
lh 62	1	in opx aggr	core	1	has incl	53 52	0 04	0 88	0 43	1 78	18 43	0 06	24 70	0 10	0 14	0 00	100 08
lh 62	1	in opx aggr	rim	1		54 75	0 04	0 98	0 42	1 66	17 77	0 07	23 90	0 03	0 12	0 00	99 74
lh 62	avg			3		54 58	0 03	0 96	0 48	1 69	18 17	0 04	24 24	0 06	0 13	0 00	100 39
lh 62	std					0 80	0 01	0 06	0 08	0 06	0 29	0 03	0 34	0 03	0 01	0 00	0 70
lh 16	1	granular in mx		2	Cr var	54 94	0 00	0 73	0 42	1 98	18 21	0 06	23 67	0 01	0 25	0 00	100 27
lh 16	avg	granular in mx		2	Cr var	54 94	0 00	0 73	0 42	1 98	18 21	0 06	23 67	0 01	0 25	0 00	100 27
lh 84	1	rim around sp		1	chromit !	56 29	0 03	0 40	0 46	1 o	18 34	0 04	24 33	0 05	0 16	0 00	101 86
lh 84	5	in mx		1		54 68	0 03	0 80	0 59	2 11	17 63	0 06	23 60	0 05	0 22	0 00	99 77
lh 84	3			2		55 99	0 02	0 24	0 21	1 44	18 52	0 04	24 44	0 04	0 11	0 00	101 05
lh 84	avg			4		55 48	0 02	0 54	0 42	1 82	18 18	0 05	24 01	0 04	0 19	0 00	100 74
lh 84	std					0 68	0 01	0 23	0 14	0 25	0 33	0 01	0 38	0 02	0 05	0 00	0 79
LH 106 2	1			3	Cr,Al var	54 89	0 11	1 30	0 53	1 69	17 82	0 03	24 84	0 02	0 32	0 01	101 56
LH 106 2	5	next to opx		3	all var	53 97	0 01	1 11	0 39	2 48	23 62	0 10	17 38	0 00	0 04	0 03	99 13
LH 106 2	avg			6	all var	54 43	0 06	1 21	0 46	2 09	20 72	0 07	21 11	0 01	0 18	0 02	100 35
LH 106 2	std					0 46	0 05	0 10	0 07	0 39	2 90	0 04	3 73	0 01	0 14	0 01	1 22
LH 121	3	rimming opx		1		53 39	0 02	0 75	0 31	1 78	17 65	0 07	23 59	0 05	0 06	0 00	97 67
LH 121	6	in sympl		1	pure??	53 60	0 02	1 70	1 95	3 40	24 41	0 11	15 26	0 08	0 00	0 00	100 53
LH 121	6	in sympl		1		55 07	0 03	1 07	0 50	1 62	18 28	0 10	24 52	0 09	0 13	0 04	101 45
LH 121	avg	biased, as var		3		55 07	0 03	1 07	0 50	1 62	18 28	0 10	24 52	0 09	0 13	0 04	101 45

Tab. B-4b (continued)

sample	spot	comment	core/rim	N	other	SiO2	TiO2	Al2O3	Cr2O3	FeO	MgO	MnO	CaO	NiO	Na2O	K2O	SUM
LH 122	5	sympl with sp		3	Cr,Al var	53.92	0.03	1.04	0.42	1.57	17.96	0.03	24.57	0.07	0.04	0.01	99.66
LH 122	1	sympl with sp		1		52.42	0.03	1.41	1.07	1.91	18.20	0.04	23.79	0.07	0.09	0.00	99.03
LH 122	3	sympl with sp		1		54.05	0.01	0.69	0.18	2.63	19.77	0.15	23.36	0.09	0.05	0.02	100.00
LH 122	avg			5		53.46	0.02	1.05	0.56	2.04	18.64	0.07	23.57	0.08	0.06	0.01	99.56
LH 122	std					0.74	0.01	0.29	0.38	0.44	0.80	0.05	0.92	0.01	0.02	0.01	0.40

Tab. B-5 (following seven pages). Orthopyroxene mineral chemistry data from the Table Mountain and Lewis Hills massifs. For legend see Tabs. B-3, B-4.

Tab. B-5

sample	spot	detail	N	SiO2	TiO2	Al2O3	Cr2O3	FeO	MgO	MnO	CaO	NiO	Na2O	SUM
LH 11	4	core, pc, def	1	57 83	0 00	1.04	0.41	5.87	34.11	0 14	0 56	0 11	0 01	100 08
LH 11	2	core, pc, bit def	2	57 04	0 03	1 03	0 31	5 76	34 20	0 13	0 58	0 05	0.03	99.16
LH 11	1	nb, large, def	1	57 11	0 01	0.98	0 41	5 76	34.18	0 11	0 56	0 11	0.03	99 26
LH 11	avg		4	57.33	0 01	1.02	0 38	5 80	34.16	0 13	0 57	0 09	0.02	99 50
LH 11	std			0 36	0 01	0 03	0.05	0 05	0.04	0 01	0 01	0.03	0 01	0.41
LH 117	6	core, pc def	2	55 32	0.05	3.51	0.73	5.90	33 42	0 09	0.75	0.14	0.02	99 93
LH 117	6	rim, def	2	55 34	0.05	3.20	0.60	5.66	33.50	0.08	0 83	0.09	0.03	99 38
LH 117	5	near cpx, def	1	53.66	0.05	2.86	0 41	6 00	33.76	0.12	0 61	0.13	0.05	97.65
LH 117	avg		5	54.77	0.05	3.19	0.58	5.85	33.56	0.10	0.73	0.12	0.03	98.99
LH 117	std			0.79		0 27	0 13	0 14	0.15	0.02	0.09	0 02	0.01	0 97
LH 16	4	def	1	58 41	0 03	0 76	0 38	5 42	35 66	0.13	0 63	0 15	0.00	101.57
LH 16	3	core, nb, def	3	57 24	0 00	0 86	0.34	5.35	35.55	0 14	0.57	0 11	0 04	100 20
LH 16	avg		4	57.83	0.02	0.81	0.36	5.39	35.61	0 14	0.60	0 13	0.02	100.89
LH 16	std			0 58	0.02	0.05	0.02	0.03	0 05	0 00	0.03	0 02	0.02	0 68
LH 62	10	core, def	2	56 62	0.00	1.13	0.38	5.85	34 86	0.11	0 85	0.10	0.03	99 93
LH 62	10	rim, def	2	57 55	0 02	0 75	0 24	5 44	35 48	0 13	0 40	0.09	0 00	100 10
LH 62	10	nb, def	1	56 91	0 03	1.17	0.40	5 68	34.82	0 05	0 86	0 05	0.02	99.99
LH 62	avg		5	57.03	0.02	1.02	0.34	5.66	35 05	0.10	0 70	0.08	0.02	100 01
LH 62	std			0 39	0.01	0.19	0.07	0.17	0.30	0 03	0 21	0.02	0 01	0 07
LH 67	6	rim, def	1	57 69	0.00	0.96	0.35	5.55	35 53	0.14	0.86	0.12	0 05	101.25
LH 67	5	rim, def	1	57 28	0.00	0 80	0.36	5 73	35.34	0.16	0.69	0 06	0.04	100.46
LH 67	5	core, def	2	57 52	0.03	0 85	0 33	5 45	35.16	0 11	0.69	0.11	0.02	100.27
LH 67	3	nb	1	58.60	0.00	0.73	0 34	5.44	34.98	0.13	0 72	0 05	0.04	101.03
LH 67	avg		5	57.77	0.01	0.84	0 35	5 54	35 25	0 14	0 74	0 09	0 04	100.75
LH 67	std			0.50	0 01	0.08	0.01	0.12	0.20	0.02	0.07	0.03	0.01	0.40
LH 73	4	nb	2	58.17	0 00	0 97	0.38	5.46	34.36	0 15	0 88	0.07		100.44
LH 73	4	pc, blebs avoided	3	57.33	0 03	1.13	0.42	5.49	34 91	0.15	0.52	0.10		100 08
LH 73	1	pc, blebs avoided	3	57.16	0 01	1 09	0.40	5.53	34 57	0.14	0.48	0 0:		99 43
LH 73	1	nb	1	57.48	0 00	0 95	0.39	5.47	34 73	0.14	0 91	0 08		100 15
LH 73	avg		9	57.54	0 01	1.04	0.40	5.49	34 64	0 15	0.70	0.08	0 00	100 02
LH 73	std			0 38	0.01	0 08	0 01	0 03	0 20	0 00	0 20	0 02	0.00	0.37
LH 76	7	rim, nb, def	1	57.12	0 00	0 63	0.36	5 60	34 56	0 11	0 96	0 15	0.02	99 51
LH 76	5	rim, def	1	57.46	0 04	0 50	0.13	5 55	36 23	0 14	0 36	0.08	0.00	100 49
LH 76	5	core, pc, def	1	56.78	0 00	0.63	0.31	5 01	34 58	0.11	0 90	0 07	0 02	98.41
LH 76	avg		3	57 12	0 01	0.59	0 27	5 39	35.12	0.12	0.74	0.10	0 01	99.47
LH 76	std			0.28	0.02	0.06	0 10	0.27	0 78	0.01	0 27	0.04	0.01	0.85
LH 8	7	core, pc, def	2	57 38	0.00	1 07	0 48	6.18	35 13	0.13	0 36	0.08	0.02	100 83
LH 8	7	rim, def	1	57.64	0 02	1.03	0.41	5.70	35 04	0 09	0.31	0.12	0 00	100.36
LH 8	2	nb, def	2	57.38	0 00	1.07	0.39	5.54	34 85	0.16	0.67	0.08	0 00	100 14
LH 8	avg		5	57.47	0.01	1.08	0.43	5.81	35 01	0.13	0.45	0.09	0.01	100.44
LH 8	std			0.12	0 01	0.02	0.04	0.27	0.12	0.03	0.16	0.02	0 01	0.29
LH 87	2	core, pc, def	1	57 14	0 08	0 86	0 35	5.76	34 88	0 13	0.95	0 12	0.00	100.27
LH 87	1	core, def	2	57 28	0.04	0 89	0 33	5.45	34.59	0.16	0 93	0.08	0.02	99.77
LH 87	1	rim, def	1	57.80	0 00	0.33	0.08	5.33	35 21	0 11	0.30	0 13	0 00	99 29
LH 87	avg		4	57.41	0.04	0.69	0.25	5.51	34 89	0 13	0.73	0 11	0.01	99.78
LH 87	std			0 28	0.03	0.26	0.12	0.18	0 25	0 02	0.30	0.02	0 01	0.40
58 24	2	nb-aggr	2	56 43	0.04	2.61	0.83	5.10	34.55	0.09	0.69	0.05		100.39
58 24	1	rim	2	56.56	0 03	1.73	0 51	5 16	34 96	0.13	0.47	0 11		99.66
58 24	1	core, pc	2	54 83	0 05	2.57	0.89	5.05	34 09	0.14	0.73	0 10		98.45
58 24	avg		6	55.94	0.04	2.30	0 74	5.10	34 53	0.12	0 63	0.09		99.50
58 24	std			0.79	0 01	0 41	0.17	0.04	0.36	0.02	0.11	0.03		0.80
49	2	nb around pc	2	57 57	0.00	1.18	0.27	5.51	35.44	0.13	0.51	0.10	0.01	100.72
49	1a	core, pc	2	56 76	0.00	1.68	0 68	5.44	35.00	0.14	0.82	0.10	0.00	100 62
49	avg		4	57.17	0.00	1.43	0.48	5.48	35.22	0.14	0.67	0.10	0.01	100.67
49	std			0 40	0 00	0 25	0.21	0.03	0 22	0.00	0.15	0.00	0 01	0.05
111	3	rim to cpx, pc	2	57 05	0 01	1.66	0.43	5.68	35 28	0 16	0.63	0.11	0.04	101.05
111	4	core, pc	2	56.16	0 00	1 05	0.49	5.64	34.74	0 13	1.36	0.10	0.03	99.70
111	avg		4	56 61	0.01	1 36	0 46	5.66	35 01	0.15	1.00	0.11	0.04	100.38
111	std			0 45	0 01	0 30	0.03	0.02	0 27	0.01	0.36	0.00	0 00	0.68

Tab. B-5 (continued)

sample	spot	details	N	SiO2	TiO2	Al2O3	Cr2O3	FeO	MgO	MnO	CaO	NiO	Na2O	SUM
317	6	core, pc, def	2	57.31	0 00	0 41	0 27	5 57	35 30	0 13	0 92	0 13	0 01	100 05
317	5	def	1	57 90	0 02	0 27	0 16	4 98	36 17	0 08	0 46	0 10	0 02	100 16
317	2	def	1	57 50	0 00	0 38	0 27	5 74	35 48	0 13	0 97	0 12	0 01	100 60
317	avg		4	57 57	0 01	0 35	0 23	5 43	35 65	0 11	0 78	0 12	0 01	100 27
317	std			0 25	0 01	0 06	0 05	0 33	0 37	0 02	0 23	0 01	0 00	0 24
485	9	core, pc, def	3	55 18	0 03	2 45	0 85	5 43	33 50	0 11	1 37	0 12	0 00	99 04
485	9	rim, def	2	55 52	0 02	2 17	0.69	5 62	33 76	0 11	1 09	0 09	0 00	99 07
485	3	near cpx, def	2	55.75	0 03	2 17	0 58	5 61	33 30	0 11	1 09	0 09	0 00	98 73
485	avg		7	55 48	0 03	2 26	0 71	5 55	33.52	0 11	1 18	0 10	0 00	98 95
485	std			0 23	0 00	0 13	0 11	0 09	0.19	0 00	0 13	0 01	0 00	0 15
534		core, nb, def	1	53 71	0 01	3 95	0.79	6 11	31.77	0.15	1 96	0 10	0 01	98 56
534		rim, def	1	54 52	0 02	3 77	0 61	6 72	32.79	0 19	1 09	0 13	0 01	99 85
534	avg		2	54 12	0 02	3 86	0 70	6 42	32 28	0.17	1 53	0.12	0 01	99 21
534	std			0.41	0 00	0 09	0 09	0 30	0 51	0 02	0 43	0 02	0 00	0 64
564	2	blebs avoided,def	3	56 92	0 02	2 55	0 00	5 53	33 42	0 12	1 46	0 09	0 04	100 95
564	1	nb, def	3	56 30	0 03	2 24	0 63	5 93	34 13	0 14	1 25	0.11	0 00	100 76
564	avg		6	56 61	0 03	2 40	0 72	5.73	33 78	0 13	1 36	0 10	0 02	100 86
564	std			0 31	0 00	0 15	0 08	0 20	0 35	0 01	0 10	0 01	0 02	0 09
575	3	core, pc, def	1	54 00	0 03	2 91	0 66	6 61	33 13	0 14	1 43	0 10	0 03	99 04
575	avg		1	54 00	0 03	2 91	0 66	6 61	33 13	0 14	1 43	0 10	0 03	99 04
676	1	core, pc	1	57 05	0 03	2 39	0 83	5 36	32 80	0 16	0 93	0 13	0 00	99 68
676	1	rim	1	56 78	0 01	1 77	0 55	5 71	33 52	0 08	0 68	0 06	0 01	99 17
676	avg		5	56 92	0 02	2 08	0 69	5 54	33 16	0 12	0 81	0 10	0 01	99 43
676	std			0 14	0 01	0 31	0 14	0 18	0 36	0 04	0 12	0 04	0 01	0 25
755	7	nb, def	2	55 67	0 03	2 34	0 34	6 41	33 74	0 14	0 54	0 06	0 00	99 27
755	7	core, pc, def	2	54 18	0 03	3 76	0 74	6 25	32 76	0 14	1 14	0 10	0 03	99 13
755	4	core, pc, def	2	53 79	0 02	3 96	0 82	6 14	32 54	0 17	0 61	0 12	0 03	98 20
755	avg		6	54 55	0 03	3 35	0 63	6 27	33 01	0 15	0 76	0 09	0 02	98 87
755	std			0 81	0 00	0 72	0 21	0 11	0 52	0 01	0 27	0 02	0 01	0 47
757	2	nb, def	1	56 35	0 05	2 81	0 57	6 74	34 02	0 09	0 78	0 10	0 06	101 57
757	2	core, pc, def	2	56 37	0 01	3 20	0 75	6 38	32 82	0 16	1 38	0 14	0 02	101 23
757	avg		3	56 36	0 03	3 01	0 66	6 56	33 42	0 13	1 08	0 12	0 04	101 40
757	std			0 01	0 02	0 19	0 09	0 18	0 60	0 04	0 30	0 02	0 02	0 17
774	6	near core, nb,def	1	54 83	0 03	2 27	0 75	5 67	33 06	0 14	1 24	0.12	0 05	98 16
774	4	core, pc, def	2	54 59	0 02	2 43	0 82	5 82	33 02	0 14	1 40	0 08	0 02	98 34
774	4	rim, def	1	54 96	0 05	2 37	0 78	5 64	33 48	0 13	1 56	0 16	0 03	99 16
774	avg		4	54 79	0 03	2 36	0 78	5 71	33 19	0 14	1 40	0 12	0 03	98 55
774	std			0.15	0.01	0.07	0 03	0 08	0 21	0 00	0 13	0 03	0 01	0 44
788	6	core, pc, def	2	56 26	0 04	2 14	0.75	5 50	33 93	0 13	1 24	0 09	0 00	100 08
788	6	rim, def	2	55.89	0 03	2 03	0.70	5 67	33 93	0 16	1 19	0 08	0 02	99 70
788	2	nb, def	1	56 55	0 04	2.15	0 77	5 71	33 71	0 13	1 12	0 09	0 04	100 31
788	avg		5	56 23	0.04	2 11	0.74	5 63	33 86	0 14	1 18	0 09	0 02	100 03
788	std			0 27	0.00	0 05	0 03	0 09	0 10	0 01	0 05	0 00	0 02	0 25
801	2	nb, def	1	55 80	0.01	2 42	0.85	5 67	33 22	0 17	1 29	0 13	0 00	99 56
801	1	core, pc, def	2	55.12	0 01	2 56	0 84	5 29	32 71	0 09	2 04	0 15	0 06	98 87
801	1	rim, def	1	55 26	0 03	2 57	0 82	5 59	32 74	0 11	1 64	0 07	0 00	98 83
801	avg		4	55 39	0 02	2 52	0 84	5 52	32 89	0 12	1 66	0 12	0 02	99 09
801	std			0 29	0 01	0 07	0 01	0 16	0 23	0 03	0 31	0 03	0 03	0 34
827	2	rim, def	1	55 88	0 03	3 52	0.73	5 82	32 26	0.16	1 41	0 11		99 92
827	2	core, pc, def	1	53 84	0 02	3 88	0 68	5.75	31 63	0 11	2 34	0 12		98 57
827	11	near core, pc,def	2	55 39	0 03	3 46	0 77	5 79	32 27	0 11	1 59	0 12		99 53
827	11	nb, def	2	55 18	0 02	2 63	0 46	5 94	32 86	0 10	0 95	0 08		98 22
827	avg		6	55 07	0 03	3 37	0 71	5 83	32 26	0 12	1 57	0 11		99 06
827	std			0 76	0 00	0 46	0.15	0 07	0 43	0 02	0 50	0 02		0 69
829	1	core, pc, def	1	54 75	0 02	3 33	0 93	5 92	33 25	0 12	0.77	0 08	0.05	99 22
829	1	rim, foc	1	56 95	0 06	2 42	0 55	6 25	33 77	0 10	0 41	0 08	0 00	100 59
829	avg		2	55 85	0 04	2 88	0.74	6 09	33 51	0 11	0 59	0 08	0 03	99 91
829	std			1.10	0.02	0 45	0.19	0 17	0 26	0 01	0 18	0 00	0 03	0 68
849	2	nb, def	1	55 62	0.09	2 20	0 64	6 27	33 36	0 14	1 25	0 08	0 04	99 69

Tab. B-5 (continued)

sample	spot	details	N	SiO2	TiO2	Al2O3	Cr2O3	FeO	MgO	MnO	CaO	NiO	Na2O	SUM
849	1		1	55 17	0 03	2 60	0 55	5 91	33 01	0 13	0 86	0 05	0 04	98 39
849	1	pc	2	55 04	0 03	2 98	0 69	6 09	32 73	0 11	1 31	0 13	0 02	99 43
849	avg		4	55 28	0 05	2 59	0 63	6 20	33 03	0 13	1 14	0 09	0 03	99 17
849	std			0 25	0 03	0 32	0 06	0 19	0 26	0 01	0 20	0 03	0 01	0 56
861	7	rim, pc, def	1	55 74	0 07	1 77	0 50	5 79	33 57	0 11	1 19	0 13	0 04	98 91
861	10	rim, def	1	55 97	0 06	1 82	0 58	5 76	33 90	0 18	1 28	0 09	0 05	99 69
861	10	core pc, def	2	56 29	0 04	1 84	0 61	5 68	33 72	0 07	1 47	0 11	0 04	99 87
861	avg		4	56 00	0 06	1 81	0 56	5 74	33 73	0 12	1 31	0 11	0 04	99 49
861	std			0 23	0 01	0 03	0 05	0 05	0 13	0 05	0 12	0 02	0 00	0 42
862	8		2	55 85	0 11	2 63	0 58	6 40	32 50	0 15	1 15	0 07		99 44
862	6	rim	2	55 85	0 11	2 38	0 58	6 32	32 77	0 14	1 02	0 07		99 24
862	6	core pc	3	56 24	0 09	2 53	0 66	6 34	32 53	0 14	1 24	0 06		99 85
862	avg		7	55 98	0 10	2 51	0 61	6 35	32 60	0 14	1 14	0 07		99 51
862	std			0 18	0 01	0 10	0 04	0 03	0 12	0 00	0 09	0 00		0 25
866	6	nb, def	1	55 79	0 03	2 74	0 67	6 52	33 53	0 11	1 27	0 11	0 01	100 78
866	1	rim, def	1	56 03	0 04	2 79	0 62	6 07	34 04	0 10	0 96	0 15	0 01	100 81
866	1	core, pc, def	2	55 15	0 04	2 88	0 70	6 36	33 61	0 12	1 43	0 09	0 00	100 38
866	avg		4	55 66	0 04	2 80	0 66	6 32	33 73	0 11	1 22	0 12	0 01	100 66
866	std			0 37	0 00	0 06	0 03	0 19	0 22	0 01	0 20	0 02	0 00	0 20
869		rim, def	1	57 69	0 01	1 46	0 55	6 30	33 84	0 13	1 30	0 06	0 04	101 38
869		nb, def	1	56 97	0 03	1 60	0 55	5 85	33 87	0 07	1 46	0 08	0 02	100 50
869		core, def	2	56 75	0 04	1 70	0 61	6 25	33 89	0 13	1 54	0 13	0 01	101 05
869	avg		4	57 14	0 03	1 59	0 57	6 13	33 87	0 11	1 43	0 09	0 02	100 98
869	std			0 40	0 01	0 10	0 03	0 20	0 02	0 03	0 10	0 03	0 01	0 36
873	8	pc, def, du-band	1	56 80	0 04	3 16	0 70	6 57	33 03	0 11	1 34	0 12	0 00	101 87
873	5	core, pc, def	1	56 27	0 00	3 07	0 75	6 30	34 10	0 14	1 27	0 12	0 02	102 04
873	avg		2	56 54	0 02	3 12	0 73	6 44	33 57	0 13	1 31	0 12	0 01	101 86
873	std			0 26	0 02	0 04	0 03	0 13	0 53	0 02	0 03	0 00	0 01	0 08
881	6	nb, def	1	56 45	0 00	3 00	0 73	5 85	33 67	0 11	1 51	0 13	0 00	101 45
881	2	core, pc, def	2	56 16	0 01	2 89	0 78	6 04	33 87	0 15	1 38	0 09	0 00	101 37
881	2	rim, def	1	56 54	0 00	2 87	0 75	6 36	34 04	0 10	0 98	0 08	0 00	101 72
881		core, nb, def	1	55 52	0 00	3 13	0 74	6 12	33 68	0 11	1 27	0 12	0 05	100 74
881	avg		5	56 17	0 00	2 97	0 75	6 09	33 82	0 12	1 29	0 11	0 01	101 32
881	std			0 40	0 00	0 10	0 02	0 18	0 15	0 02	0 20	0 02	0 02	0 36
886	8	rim, def	1	56 30	0 07	2 53	0 73	6 31	33 17	0 16	1 32	0 09	0 05	100 73
886	8	core, pc, def	1	55 00	0 11	2 47	0 67	6 00	33 23	0 11	0 98	0 08	0 00	98 65
886	2	pc, def	2	56 32	0 05	2 59	0 69	6 23	33 86	0 14	0 91	0 10	0 05	100 94
886	avg		4	55 87	0 08	2 53	0 70	6 18	33 42	0 14	1 07	0 09	0 03	100 11
886	std			0 62	0 02	0 05	0 02	0 13	0 31	0 02	0 18	0 01	0 02	1 03
900	8	def	1	55 44	0 03	2 46	0 61	6 37	32 79	0 09	1 35	0 11	0 00	99 25
900	7	def	1	54 82	0 05	2 18	0 69	6 21	33 02	0 16	1 35	0 14	0 02	98 64
900	avg		2	55 13	0 04	2 32	0 65	6 29	32 91	0 13	1 35	0 13	0 01	98 95
900	std			0 31	0 01	0 14	0 04	0 08	0 11	0 04	ERR	0 02	0 01	0 30
901.1	7	nb, def	1	57.79	0.00	1.19	0.60	5.71	33.34	0.04	1.63	0 02	0.00	100.52
901 1	3	core, nb-aggr,def	2	57 67	0 03	1 18	0 57	6 34	33 66	0 09	1 35	0 09	0 02	101 00
901.1	3	rim, def	1	58.30	0.01	1.29	0.55	6.13	33 93	0 14	1 53	0 08	0.02	101 98
901.1	avg		4	57.92	0.01	1.22	0.57	6.06	33.64	0.09	1.50	0.06	0.01	101.10
901 1	std			0 27	0.01	0.05	0.02	0.26	0.24	0.04	0.12	0 03	0.01	0.68
901 3	4	nb aggr, def	1	56.00	0.03	2.98	0.71	6.02	32.75	0.08	1.33	0.14	0.00	100.04
901 3	2	core, pc, def	2	55.65	0.02	2 99	0.80	6.09	32 74	0.11	1 78	0 09	0.00	100.27
901 3	2	rim, def	1	55.18	0 00	3.00	0.72	6.40	33.12	0.15	1.25	0.11	0.00	99.93
901 3	avg		4	55.61	0 02	2 99	0.74	6.17	32.87	0 11	1.45	0.11	0.00	100.08
901 3	std			0.34	0 01	0.01	0.04	0.17	0.18	0 03	0.23	0 02	0.00	0.14
918	5	core, pc, def	3	54.60	0.03	3 06	0.80	5.71	32.49	0.09	1.84	0 11	0.00	98.73
918	avg		1	54.60	0.03	3.06	0 80	5 71	32.49	0 09	1.84	0.11	0.00	98.73
922	5	nb, def	1	56.22	0 03	3.81	0.55	6 38	33 43	0 16	0 97	0.19	0.02	101.76
922	5	core, pc, def	2	55 89	0 05	4.66	0.83	6.16	32.11	0.12	2.11	0.14	0.05	102.12
922	4	rim, def	1	55 44	0.05	4.65	0.80	6.47	33 01	0.10	1.41	0.08	0.00	102.01
922	4	core, pc, def	2	54.75	0 08	5.15	1 00	5 93	31 32	0 09	2.81	0.09	0.05	101.27

Tab. 3-5 (continued)

sample	spot	details	N	SiO2	TiO2	Al2O3	Cr2O3	FeO	MgO	MnO	CaO	NiO	Na2O	SUM
922	avg		10	55 58	0 05	4 57	0 80	6 24	32 47	0 12	1 83	0 13	0 03	101 79
922	std			0 55	0 02	0 48	0 16	0 21	0 82	0 03	0 70	0 04	0 02	0 33
932	?	rim, def	3	53 76	0 07	4 93	0 66	5 96	31 18	0 13	1 99	0 06	0 14	98 88
932	?	core, pc, def	2	52 57	0 08	6 10	0 89	6 31	31 41	0 12	1 70	0 13	0 12	99 43
932	3	core, pc, def	3	53 48	0 09	5 75	0 75	5 53	30 41	0 16	2 42	0 14	0 14	98 87
932	avg		8	53 27	0 08	5 59	0 77	5 93	31 00	0 14	2 04	0 11	0 13	99 06
932	std			0 51	0 01	0 49	0 09	0 32	0 43	0 02	0 30	0 04	0 01	0 26
941		nb	1	55 62	0 01	1 73	0 24	6 21	37 13	0 09	0 16	0 05		101 24
941		nb	1	56 52	0 03	2 57	0 39	6 13	33 69	0 13	0 39	0 07		99 92
941		pc, Al var 3-7%	3	53 95	0 04	5 43	0 83	6 40	32 93	0 12	0 49	0 09		100 28
941	avg		5	55 36	0 03	3 24	0 49	6 25	34 58	0 11	0 35	0 07		100 48
941	std			1 06	0 01	1 58	0 25	0 11	1 83	0 02	0 14	0 02		0 56
1027	9	core, pc, def	2	54 42	0 03	4 47	0 88	6 44	31 80	0 13	2 03	0 04	0 02	100 26
1027	6	core, pc, def	2	54 64	0 03	4 84	1 00	6 29	31 63	0 16	2 21	0 01	0 02	100 83
1027	6	rim, def	1	54 08	0 06	4 41	0 82	6 17	31 49	0 05	1 61	0 13	0 03	98 85
1027	avg		5	54 38	0 04	4 57	0 90	6 30	31 64	0 11	1 95	0 06	0 02	99 98
1027	std			0 23	0 01	0 19	0 07	0 11	0 13	0 05	0 25	0 05	0 00	0 83
1029 11	7	core, pc, def	1	55 16	0 14	5 32	0 46	6 56	32 02	0 14	0 78	0 09		100 67
1029 11	7	rim, def	2	55 62	0 13	4 56	0 39	6 81	32 95	0 14	0 63	0 06		101 29
1029 11	6	def	1	53 55	0 18	6 35	0 81	6 19	30 45	0 16	2 12	0 10		99 41
1029 11	6	def	1	53 92	0 14	6 26	0 58	6 66	30 03	0 06	1 70	0 14		100 39
1029 11	6		1	54 09	0 16	6 04	0 57	6 41	30 41	0 10	1 61	0 07		99 46
1029 11	6	rim, pc, def	1	54 21	0 14	5 40	0 44	6 70	32 20	0 07	0 82	0 10		100 08
1029.11	6	rim, def	1	53 84	0 14	5 23	0 53	6 84	31 53	0 18	0 92	0 11		99 32
1029 11	6	def	1	52 95	0 20	6 16	0 63	6 45	29 78	0 16	2 44	0 10		98 87
1029 11	6	core, def	1	54 00	0 18	6 14	0 55	6 77	30 68	0 17	1 66	0 05		100 20
1029 11	6	def	1	53 68	0 14	6 12	0 62	6 64	30 41	0 12	1 64	0 11		99 48
1029 11	6		1	54 06	0 18	6 07	0 61	6 50	30 62	0 15	1 82	0 08		100 09
1029 11	5	core, def	2	53 72	0 19	5 73	0 55	6 28	30 91	0 09	1 61	0 07		99 15
1029 11	5	rim, def	2	53 98	0 14	4 95	0 37	6 79	32 07	0 14	0 65	0 05		99 14
1029.11	4	core, pc, def	4	53 13	0 14	5 56	0 53	6 74	31 26	0 17	1 68	0 08		99 9
1029 11	avg		20	53 99	0 16	5 69	0 53	6 60	31 16	0 13	1 43	0 09		99 77
1029 11	std			0 67	0 02	0 51	0 08	0 20	0 85	0 04	0 55	0 02		0 67
1043 2	7	near sp, def	1	55 07	0 00	3 27	0 55	6 10	33 38	0 09	0 90	0 09	0 00	99 93
1043 2	5	core, pc, def	5	53 83	0 05	4 10	0 85	5 76	32 01	0 11	2 63	0 09	0 02	99 45
1043.2	5	rim, def	2	54 73	0 03	3 81	0 69	5 85	33 01	0 09	1 48	0 07	0 00	99 76
1043 2	4	near cpx, def	1	54 83	0 00	3 57	0 69	5 81	32 96	0 05	1 29	0 07	0 02	99 29
1043 2	avg		9	54 62	0 02	3 69	0 70	5 88	32 96	0 09	1 58	0 08	0 01	99 61
1043.2	std			0 47	0 02	0 31	0 11	0 13	0 65	0 02	0 64	0 01	0 01	0 25
1065	7	rim, def	1	55 18	0 00	3 36	0 89	4 00	32 32	0 18	1 87	0 14		97 94
1065	7	core, pc, def	3	53 75	0 01	3 50	0 84	6 55	31 88	0 09	1 73	0 07		98 42
1065	6	rim, def	3	55 23	0 01	2 91	0 66	5 78	32 84	0 11	1 25	0 08		98 87
1065	6	core, pc, def	2	55 19	0 01	3 58	0 88	5 35	32 00	0 13	2 36	0 34		99 84
1065	10	nb, def	3	56 08	0 02	3 02	0 77	5 67	33 39	0 10	1 09	0 10		100 24
1065	avg		12	55 09	0 01	3 27	0 81	5 47	32 49	0 12	1 56	0 15		99 06
1065	std			0 75	0 01	0 26	0 09	0 83	0 56	0 03	0 45	0 10		0 86
1071	4	core, pc, def	2	55 57	0 02	3 36	0 83	5 65	32 39	0 14	2 24	0 11	0 01	100 32
1071	4	rim, def	2	55 10	0 03	3 23	0 70	5 92	32 70	0 11	1 49	0 09	0 05	99 72
1071	4	nb, def	1	55 17	0 03	3 37	0 69	5 97	33 22	0 17	1 30	0 03	0 04	99 99
1071	avg		5	55 38	0 03	3 32	0 74	5 85	32 77	0 14	1 68	0 08	0 03	100 01
1071	std			0 16	0 00	0 06	0 06	0 14	0 34	0 02	0 41	0 03	0 02	0 25
1079.2	spot	core, pc, def	1	55 05	0 04	3 09	0 84	6 02	32 19	0 11	2 00	0 11	0 01	99 51
1079 2	avg		1	55 05	0 04	3 09	0 84	6 02	32 19	0 11	2 00	0 11	0 01	99 51
1086	9	nb	2	57 06	0 02	2 36	0 62	6 18	33 14	0 15	1 38	0 06	0 04	101 01
1086	8	pc, def	2	54 43	0 01	2 48	0 73	5 89	32 47	0 14	1 47	0 08	0 00	97 70
1086	avg		3	55 75	0 02	2 42	0 68	6 04	32 81	0 15	1 43	0 07	0 02	99 36
1086	std			1 31	0 00	0 06	0 05	0 14	0 34	0 00	0 04	0 01	0 02	1 66
1090	5	core, pc, def	2	56 50	0 00	0 77	0 48	5 26	33 67	0 12	0 90	0 11	0 02	97 83
1090	5	rim	1	57 30	0 03	0 77	0 26	5 13	33 47	0 11	0 47	0 10	0 03	97 67

Tab. B-5 (continued)

sample	spot	details	N	SiO2	TiO2	Al2O3	Cr2O3	FeO	MgO	MnO	CaO	NiO	Na2O	SUM
1090	3	def	2	56 45	0 00	0.75	0 54	5 29	33 54	0 07	0 93	0 07	0 05	97 69
1090	avg		5	56 75	0 01	0 76	0 43	5 23	33 56	0 10	0 77	0 09	0 03	97 73
1090	std			0 39	0 01	0 01	0 12	0 07	0 08	0.02	0 21	0 02	0 01	0 07
1112	13	rim, def	1	56 17	0 05	2 15	0 62	6 15	33 87	0 11	1 09	0 00	0 00	100 21
1112	13	core, pc, def	2	55 38	0 05	2 26	0 69	5 94	32 91	0 13	2 16	0 05	0 03	99 60
1112		def	1	56 78	0 05	2 38	0 64	5 84	33.12	0 09	1 43	0.00	0 00	100 33
1112	avg		4	56 11	0 05	2 26	0 65	5 98	33 30	0 11	1 56	0 02	0.01	100 05
1112	std			0 57	ERR	0 09	0 03	0 13	0 41	0.02	0 45	0 02	0.01	0 32
1118	5	def	1	55 76	0 00	3.14	0 61	6 24	33 21	0 13	1 46	0 15	0 01	100 71
1118	11	core, pc, def	3	56 28	0 01	2 92	0 66	5.77	33 03	0 12	1 29	0 12	0 04	100.24
1118	avg		4	56 02	0 01	3 03	0 64	6.01	33.12	0 13	1 38	0 14	0.03	100 48
1118	std			0 26	0 01	0 11	0.02	0.23	0 09	0 01	0 09	0 01	0 02	0.24
1136 2	4	core, pc, def	3	52 32	0 06	3.35	0 70	6 26	34.06	0 11	0 64	0 09	0 05	98 64
1136 2	4	rim, def	1	54 09	0 06	3 04	0 59	7 23	32 58	0 14	0 60	0 08	0.07	98 48
1136 2	avg		4	53 71	0 06	3 20	0 65	6.75	33 32	0 13	0 62	0 09	0 06	98 56
1136 2	std			0 38	0 00	0.15	0 05	0 48	0 74	0 02	0 02	0 00	0 01	0 08
1141	10	rim	3	55 97	0 04	1 91	0 77	5 53	33.16	0.14	1 58	0.12	0 05	99 27
1141	10	core, def	2	55 24	0 00	2 04	0 88	5 50	32 56	0 11	1 90	0 05	0 04	98 32
1141	avg		5	55 61	0 02	1 98	0 83	5 52	32 86	0 13	1.74	0 09	0.05	98 80
1141	std			0 36	0 02	0 06	0 05	0 01	0 30	0 02	0 16	0 03	0 00	0 47
1143	13	core, pc, def	2	55 75	0 02	3 09	0 84	5 84	32 60	0 15	1.97	0 13	0 00	100 39
1143	avg		1	55.75	0 02	3 09	0 84	5 84	32 60	0 15	1 97	0 13	0 00	100 39
1145	3	nb, def	1	55 29	0 03	2 88	0 61	6 35	32 74	0.13	0 91	0 03	0 01	98 98
1145	2	core, pc, def	3	55 72	0 01	3 07	0 87	6 04	32 09	0 13	2 26	0.14	0 04	100 37
1145	2	rim, def	3	55 99	0 01	2 71	0 63	6 04	32 96	0 13	1 04	0 12	0 04	99 67
1145	avg		10	55 67	0.02	2 89	0 70	6 14	32.60	0 13	1 40	0.10	0 03	99 67
1145	std			0 29	0 01	0 15	0 12	0.15	0 37	ERR	0 61	0.05	0.01	0 57
1181	1	core, pc, def	2	55 42	0 01	3.67	0 87	6 22	31.94	0.08	2 32	0.14	0.01	100 68
1181	1	rim, def	2	55 56	0 05	3 57	0 72	6 30	32 39	0 11	1.52	0 06	0 00	100 28
1181	14	core, pc, def	1	55 07	0 03	4 02	0 96	5 99	31 81	0 14	2 20	0 00	0 00	100 22
1181	1	core, nb, def	1	55 06	0 01	3 86	0 86	5.84	32 36	0 17	1 67	0 07	0 02	99 92
1181	avg		6	55 28	0 03	3 78	0 85	6.09	32 13	0.13	1 93	0 07	0 01	100.28
1181	std			0 22	0 02	0.17	0.09	0.18	0 25	0.03	0.34	0.05	0 01	0.27
1189 1	5	nb, def	1	56 77	0.00	1 47	0 60	5 99	34 32	0.14	0 64	0 05		99 98
1189 1	11	rim, pc, def	2	57 26	0 01	1 39	0 58	5 38	34 02	0 11	1 24	0 10		100.09
1189 1	1	rim def	2	57 30	0 03	1.42	0 64	5 61	33.04	0 07	1 03	0.11		99.25
1189 1	1	co , pc, def	1	57.62	0 01	1 48	0 59	5.65	33 81	0 14	2.08	0.09		101.47
1189 1	avg		6	57 24	0 01	1.44	0 60	5 66	33 80	0 12	1.25	0 09		100.20
1189 1	std			0 30	0 01	0.04	0 02	0 22	0 47	0.03	0 53	0.02		0 80
1189 2	5			55.75	0 01	2.83	0 74	5.55	32.45	0 12	1.65	0 07		99.17
1189 2	3	nb	1	55 42	0 01	2 98	0 68	5 69	33 29	0 10	1.17	0 14		99.48
1189 2	0	core, pc	3	54 73	0 02	3 02	0 77	5 36	32 75	0 14	1.58	0 11		98.48
1189 2	avg	variable	4	55 30	0 01	2 94	0 73	5 53	32.83	0.12	1.47	0.11		99.04
1189 2	std			0 42	0 00	0 08	0 04	0 14	0 35	0 02	0.21	0 03		0 42
1194	2	core, def	1	56 37	0.04	2 68	0 89	5.75	33 90	0 14	0 83	0.07	0.04	100.71
1194	2	rim, def	1	56 73	0 04	2.22	0.60	5 88	33 78	0 10	0 68	0.11		100.14
1194	2	nb, def	1	57 14	0 07	2 29	0 69	5 64	33 65	0 09	1.02	0.13	0.02	100.74
1194	2	core, def	1	55 95	0 08	2.79	0.98	5 18	32 02	0 15	3.27	0.03	0 05	100.50
1194	avg		4	56 55	0 08	2 50	0.79	5.61	33 34	0.12	1.45	0 09	0 04	100.52
1194	std			0 44	0 02	0.24	0.15	0.26	0 77	0.03	1.06	0.04	0.01	0.24
1195	4	nb, def	1	56 00	0 00	2 36	0.69	5.84	33.75	0.09	1 02	0.12	0.00	99.87
1195	2	core, def	3	55 36	0 00	2 49	0.75	5.91	32 91	0 14	1 88	0.12	0 02	99.58
1195	2	rim, def	1	56 02	0 00	2.16	0 59	6.18	34.68	0.13	0.62	0.13	0.07	100.58
1195	avg		5	55 79	0 00	2.34	0.68	5 98	33.78	0.12	1.17	0.12	0.03	100 01
1195	std			0 31	0 00	0.14	0.07	0.15	0.72	0 02	0.53	0.00	0.03	0.42
1200	8	rim, def	1	56 58	0 01	1.58	0.69	5.33	33.39	0.08	0.60	0.13	0.00	98.39
1200	8	core, pc, def	2	56 94	0 00	1.45	0.66	5.45	33 03	0.14	1.80	0.15	0.04	99.66
1200		core, pc, def	2	56 48	0 01	1 54	0 65	5 49	33 47	0 16	1.55	0.12	0.05	99.52
1200	avg		5	56.67	0 01	1.52	0.67	5.42	33 30	0.13	1.32	0.13	0.03	99.19

Tab. B-5 (continued)

sample	spot	details	N	SiO2	TiO2	Al2O3	Cr2O3	FeO	MgO	MnO	CaO	NiO	Na2O	SUM
1200	std			0 20	0 00	0 05	0 02	0 07	0 19	0 03	0 52	0 01	0 02	0 57
1222	5	nb	1	57 55	0 00	2 29	0 19	7 02	33 57	0 06	0 45	0 07	0 05	101 25
1222	5	rim, pc	1	56 75	0 06	3 46	0 39	6 92	33 66	0 17	0 34	0 08	0 03	101 86
1222	5	core, pc, def	3	53 66	0 08	5 50	0 70	6 19	31 11	0 12	2 27	0 12	0 10	99 85
1222	avg		5	55 99	0 05	3 75	0 43	6 71	32 78	0 12	1 02	0 09	0 06	100 99
1222	std			1 68	0 03	1 33	0 21	0 37	1 18	0 04	0 89	0 02	0 03	0 84
1228 1	9		1	56 31	0 04	3 21	0 22	7 00	32 17	0 11	0 55	0 11	0 00	99 72
1228 1	8		1	55 99	0 03	3 03	0 26	7 45	32 87	0 13	0 50	0 11	0 02	100 39
1228 1	avg		2	56 15	0 04	3 12	0 24	7 23	32 52	0 12	0 53	0 11	0 01	100 06
1228 1	std			0 16	0 00	0 09	0 02	0 22	0 35	0 01	0 03	ERR	0 01	0 33
1228 3	2	core	4	55 30	0 00	4 21	0 07	9 83	31 14	0 20	0 61	0 09	0 02	101 47
1228 3	2	rim	2	56 23	0 02	4 20	0 05	10 48	31 05	0 18	0 42	0 01	0 00	102 64
1228 3	18	near cpx	1	52 77	0 05	3 56	0.07	10 68	31 17	0 21	0 42	0 03	0 19	99 15
1228 3	avg		7	54.77	0 02	3 99	0.06	10 33	31 12	0 20	0 48	0 04	0 07	101 09
1228 3	std			1.46	0 02	0.30	0.01	0.36	0 05	0 01	0 09	0 03	0 09	1 45
1232	5	core, pc, def	1	55.72	0 00	2 68	0 84	5 42	32 72	0 13	1 66	0 14	0 02	99 33
1232	5	rim, def	1	57 26	0 01	2 29	0 63	5 41	33 96	0 13	0 69	0 06	0 04	100 48
1232	10	def	1	56 70	0 00	2 36	0 70	5 49	34 32	0 14	0 58	0 07	0 02	100 38
1232	avg		3	56 56	0 00	2 44	0 72	5 44	33 67	0 13	0 98	0 09	0 03	100 06
1232	std			0 64	0 00	0 17	0 09	0 04	0 69	0 00	0 49	0 04	0 01	0 52
1237	5	core, pc, def	2	55 65	0 02	2 82	0 75	5 99	33 33	0 13	1 41	0 06	0 04	100 20
1237	11	nb, def	2	56 87	0 00	2 37	0 52	5 94	33 89	0 14	0 95	0 12	0 00	100 80
1237	1	core	1	56 27	0 01	2 82	0 83	5 79	33 08	0 14	1 61	0 13	0 04	100 72
1237	avg		5	56 26	0 01	2 67	0 70	5 91	33 43	0 14	1.32	0 10	0 03	100 57
1237	std			0 50	0 01	0 21	0 13	0 08	0 34	0 00	0 28	0 03	0 02	0 27
1245	8	rim, nb, def	2	57 58	0 00	0 92	0 52	5 29	34 93	0 11	1 03	0.08	0.04	100.50
1245	5	def	2	58 61	0 01	0 95	0 52	5 70	34 68	0 15	0.76	0 10	0 01	101 49
1245	avg		4	58 10	0 01	0 94	0 52	5 50	34 81	0 13	0 90	0 09	0 03	101 00
1245	std			0 52	0 01	0 01	0 00	0 20	0 12	0 02	0 14	0 01	0 02	0 49
1249	5	core, pc, def	1	55.95	0.03	1.42	0 66	5 84	34 19	0 10	1 33	0 01	0.06	99 59
1249	3	rim, def	1	57 57	0 03	1 50	0 50	5 87	34 59	0 05	0 56	0 13	0 00	100 90
1249	3	core, pc, def	2	55 72	0 01	1.57	0 61	5 96	33 10	0 09	1 89	0 08	0 02	99 05
1249	avg		4	56 41	0 02	1 50	0 59	5 89	33 96	0 08	1 28	0 07	0 03	99 85
1249	std			0 82	0 01	0 06	0 07	0 05	0 63	0 02	0 50	0 05	0 02	0 78
1262	8	core, pc, def	3	54 86	0 02	3 11	0 74	6 26	32 97	0 13	1 59	0 08	0 00	99 76
1262	4	nb, def	1	55 72	0 03	2.96	0 63	6.77	33 24	0.13	1 13	0.08	0 02	100 71
1262	2	core, nb, def	3	55 45	0 01	2 94	0 72	6 05	32 46	0 14	1 67	0.12	0.03	99 59
1262	avg		7	55 34	0.02	3 00	0.70	6.36	32 89	0 13	1 46	0 09	0 02	100 02
1262	std			0 38	0.01	0.08	0.05	0 30	0 32	0 00	0 24	0.02	0 01	0 49
1272	3	core, pc, def	2	55.65	0 01	2.20	0 80	5.65	31.90	0 11	2.13	0 12	0 00	98 66
1272	2	nb, def	2	56.40	0.00	1.48	0.41	5 90	34.08	0 11	0.62	0.08	0 02	99 10
1272	2	core, pc, def	2	55.38	0.00	2 13	0 64	5 76	33 05	0 09	1.52	0 08	0.02	98 67
1272	avg		6	55 81	0.00	1.94	0 62	5.77	33 04	0.10	1 42	0 09	0 01	98 81
1272	std			0.43	0 00	0 32	0.16	0.10	0 85	0.01	0 62	0 02	0 01	0 21
1274.1	7	core, pc, def	2	56 04	0 00	2.57	0.79	5 81	33 41	0.13	1 41	0 11	0 01	100 28
1274.1	7	rim, def	1	56.71	0 00	2 20	0.57	6 22	34 38	0 12	0 62	0.09	0 02	100 93
1274.1	1	rim, def	2	57 46	0.03	2.16	0.59	5 95	34.16	0.14	0 60	0 03	0 02	101 14
1274.1	1	core, def	2	56.17	0.00	2 52	0 72	5.70	33.46	0 11	1 50	0 09	0 02	100 29
1274 1	avg		7	56 60	0 01	2 36	0 67	5 92	33 85	0 13	1 03	0 08	0.02	100 66
1274 1	std			0 56	0 01	0.18	0 09	0.19	0 43	0 01	0 42	0 03	0 00	0 38
1315	5	rim, def	2	57.98	0.03	1.46	0.48	5 92	33.67	0.09	1.11	0.08	0.02	100.84
1315	5	core, pc, def	2	57.52	0.01	1 32	0.56	5.73	33 57	0 16	1 54	0 06	0.01	100 48
1315	2	nb, def	1	57.90	0.01	1.29	0.43	5 66	34 77	0.17	1.06	0.06	0.04	101 39
1315	avg		5	57 80	0 02	1 36	0.49	5.77	34 00	0 14	1 24	0 07	0 02	100 90
1315	std			0.20	0.01	0.07	0 05	0.11	0 54	0.04	0 22	0.01	0.01	0 37
1324	2	def	4	56 45	0 00	1.47	0 57	6.40	33 11	0 14	1 30	0 05	0 00	99 49
1324	avg		1	56 45	0.00	1.47	0 57	6.40	33 11	0 14	1 30	0 05	0 00	99 49
1340	5	core, pc, def	1	56 27	0.00	1.55	0.61	5 66	32.70	0 09	2.08	0 06	0 05	99 07
1340	5	rim, pc, def	1	55 68	0 02	1.45	0 55	5 82	33 57	0 05	1 16	0 11	0.00	98 41

Tab. B-5 (continued)

sample	spot	details	N	SiO2	TiO2	Al2O3	Cr2O3	FeO	MgO	MnO	CaO	NiO	Na2O	SUM
1340	3	def	2	55 76	0 03	1 46	0 60	5 59	32 31	0 11	2 16	0 03	0 06	98 11
1340	avg		9	55 90	0.02	1 49	0 59	5 69	32 86	0 08	1 80	0 07	0 04	98 53
1340	std			0 26	0 01	0 04	0 03	0 10	0 53	0 02	0 45	0 03	0 03	0 40
1378	8	nb, def	1	56 08	0 02	3 40	0.73	5.65	33 95	0 11	1 50	0 11	0.00	101 55
1378	4	rim, def	3	56 10	0 03	3 62	0 89	5 47	33 53	0 07	1 51	0 14	0 07	101 43
1378	4	core, pc, def	3	55 48	0 01	3.46	0 89	5 26	32 85	0 11	2 35	0.07	0 05	100 53
1378	avg		7	55 89	0 02	3.49	0 84	5 46	33 44	0.10	1 79	0 11	0.04	101 17
1378	std			0 29	0 01	0 09	0.08	0.16	0 45	0.02	0 40	0.03	0 03	0 46
1396	8	rim, def	2	56 40	0.02	1.45	0.59	5 49	34 36	0.12	1.18	0.11	0.00	99 72
1396	8	core, def	1	56 43	0 03	1 65	0.72	5 67	34.05	0.11	1 53	0 13	0 02	100 34
1396	1	nb, def	2	56 12	0 03	1 53	0 51	5.66	34 42	0.09	1 07	0.07	0 06	99 56
1396	avg		5	56 32	0 03	1 54	0.61	5 61	34.28	0 11	1.26	0 10	0 03	99 87
1396	std			0 14	0 00	0.08	0 09	0 08	0 16	0.01	0 20	0 02	0 02	0.34
1420	7	def	1	55.05	0 11	2.55	0 50	6 08	32.83	0 08	1 27	0 09	0.02	98 58
1420	5	no plag, nb, def	1	55 12	0 09	2.32	0 52	6.20	33 42	0.12	0.85	0 08	0.04	98.76
1420	1	plag-bear., def	2	54 91	0 09	2 28	0 62	6 28	32 78	0 09	1.19	0 09	0 02	98 35
1420	avg		4	55 03	0.10	2 38	0 55	6 19	33 01	0 10	1.10	0.09	0 03	98 56
1420	std			0.09	0 01	0.12	0.05	0.08	0 29	0 02	0 18	0 00	0.01	0 17
1447	8	core, pc, def	2	56.20	0 06	2 46	0.64	5 82	33.06	0 15	1.45	0.11	0 07	100 02
1447	8	rim, def	1	56.14	0 05	2 22	0.61	6.55	33 51	0.16	1.36	0.03	0 04	100.67
1447	10	nb, def	2	55 91	0 05	2 20	0 55	6 38	33.42	0 20	1.35	0.12	0 03	100 21
1447	avg		5	56 08	0 05	2.29	0.60	6 25	33 33	0.17	1 39	0 09	0 05	100 30
1447	std			0 12	0.00	0 12	0.04	0.31	0.19	0.02	0.04	0.04	0 02	0.27
1454	7	core, pc, def	6	55 71	0 03	3.15	0.64	6 13	32.65	0 08	1 51	0.10	0.00	100.00
1454	7	rim, def	1	56 23	0 05	3 05	0.61	6 23	33 21	0.08	1 25	0 22	0.00	100 93
1454	4	next cpx, def	1	55 26	0 03	3.20	0 67	6 42	33 70	0 10	1 25	0 16	0.02	100 81
1454	3	near cpx, def	1	55 73	0 04	3 29	0.63	6 43	32 93	0.10	1.24	0.05	0 03	100 47
1454	avg		9	55 73	0 04	3.17	0 64	6 30	33.12	0 09	1.31	0 13	0 01	100 55
1454	std			0 34	0 01	0 09	0.02	0 13	0 39	0.01	0.11	0.06	0 01	0 38
1468	7	aw sp, def	2	54.51	0 03	2.95	0.63	5 67	32 97	0 09	1 22	0 09	0 04	98 20
1468	4	core, pc def	2	54 27	0 04	2 39	0 58	5.90	32 69	0 14	1 13	0 08	0 00	98 02
1468	2	core, pc, def	3	54 80	0 03	3.20	0 88	5 81	32 24	0 08	2.24	0.11	0.01	99 40
1468	2	nb, def	2	55 46	0 03	2.39	0 43	6 24	33 87	0 17	0.85	0.12	0 04	99 60
1468	avg		9	54 76	0 03	2 86	0.63	5 91	32 94	0.12	1 44	0.10	0.02	98 81
1468	std			0.45	0 00	0 29	0.16	0.21	0 60	0 04	0.51	0.02	0 02	0.70
1485	6	near cpx, def	1	55 40	0 00	2.38	0 61	5 40	32 84	0 06	1 24	0 08	0 04	98.05
1485	5	core, pc, def	3	55 63	0 01	2 52	0 83	5.56	32 88	0 13	2.14	0 14	0.01	99 85
1485	5	rim, def	2	55 32	0.01	2 32	0 68	5 68	33 36	0 10	1 55	0 12	0.00	99 14
1485	2	nb, def	2	55.25	0.00	2 48	0 66	6 07	33 33	0.13	1.30	0 06	0 02	99 30
1485	avg		8	55.40	0.01	2 43	0.70	5.68	33.10	0 11	1.56	0.10	0 02	99.09
1485	std			0.14	0.01	0.08	0 08	0.25	0.24	0.03	0.36	0.03	0 01	0 65

Tab. B-6 (following seven pages). Olivine mineral chemistry data from the Table Mountain and Lewis Hills massifs. For legend see Tabs. B-3, B-4.

Tab. B-6

sample	min	details	N	SiO2	Cr2O3	FeO	MgO	CaO	NiO	SUM
LH8	7		2	41.98	0.03	8.87	51.12	0.00	0.40	102.40
LH8	8		2	41.71	0.00	8.96	50.50	0.01	0.36	101.54
LH8	avg		4	41.85	0.02	8.92	50.81	0.01	0.38	101.97
LH11		mx	1	39.85	0.02	8.89	49.25	0.02	0.43	98.46
LH11	1	incl in opx	1	40.81	0.00	7.68	48.36	0.04	0.40	97.29
LH11	avg		2	40.33	0.01	8.29	48.81	0.03	0.42	97.88
LH16	5		2	40.47	0.00	8.27	50.52	0.01	0.38	99.65
LH16	6		2	40.23	0.01	8.43	50.03	0.00	0.38	99.08
LH16	avg		4	40.35	0.01	8.35	50.28	0.01	0.37	99.36
LH47	1	ol incl in opx	1	40.32	0.04	7.84	49.65	0.02	0.49	98.36
LH62	10		2	40.64	0.10	8.76	50.07	0.02	0.38	99.97
LH62	11		2	39.92	0.01	9.00	49.52	0.02	0.42	98.89
LH62	avg		5	40.28	0.06	8.88	49.80	0.02	0.40	99.43
LH67	3		2	39.64	0.01	9.30	50.78	0.01	0.39	100.13
LH67	4		2	40.44	0.00	8.67	48.13	0.00	0.38	97.62
LH67	avg		4	40.04	0.01	8.99	49.46	0.00	0.38	98.68
LH73	1		2	41.26	0.00	8.05	50.30	0.02	0.27	99.90
LH73	1	corrodes opx	1	41.49	0.01	8.16	50.40	0.00	0.40	100.46
LH73	3	incl in opx	1	41.39	0.00	8.05	50.82	0.02	0.46	100.74
LH73	avg		4	41.38	0.00	8.09	50.51	0.01	0.38	100.37
LH76	1	mx	1	40.61	0.00	8.11	48.73	0.02	0.43	97.90
LH76	1	mx	2	40.45	0.01	8.82	49.47	0.00	0.38	99.13
LH76	5	incl in opx	1	39.99	0.02	8.14	49.68	0.02	0.40	98.25
LH76	7	mx	2	40.34	0.00	9.21	50.52	0.01	0.40	100.48
LH76	avg		6	40.35	0.01	8.57	49.60	0.01	0.40	98.94
LH87	1	incl in opx	4	40.82	0.00	8.19	49.90	0.01	0.39	99.31
LH87	1	mx	1	40.27	0.02	8.80	49.43	0.02	0.40	98.94
LH87	2	incl in opx	2	40.93	0.02	8.02	49.61	0.01	0.39	98.98
LH87	2		2	39.82	0.00	8.66	49.37	0.01	0.33	98.19
LH87	7	mx	1	40.79	0.03	9.35	50.18	0.00	0.27	100.62
LH87	avg		10	40.53	0.01	8.60	49.70	0.01	0.36	99.21
LH106 2	3		2	40.39	0.02	8.93	48.45	0.01	0.29	98.09
LH106 2	4		2	40.81	0.00	9.37	48.27	0.04	0.34	98.83
LH106 2	avg		4	40.60	0.01	9.15	48.36	0.03	0.32	98.46
LH117	1	mx	4	40.25	0.00	8.77	49.95	0.02	0.42	99.41
LH117	1	near sp	1	40.56	0.00	8.96	49.59	0.02	0.47	99.60
LH117	5	near cpx	2	40.55	0.00	8.15	50.20	0.00	0.44	99.34
LH117	avg		7	40.15	0.00	8.63	49.91	0.01	0.44	99.45
LH121	7		1	40.80	0.00	8.55	49.43	0.00	0.46	99.24
LH121	8		2	41.26	0.00	8.76	50.41	0.01	0.31	100.75
LH121	avg		3	41.03	0.00	8.66	49.92	0.01	0.39	100.00
7.1	6		2	41.07	0.00	10.19	48.13	0.04	0.27	99.70
7.1	7		1	40.11	0.00	10.13	47.70	0.14	0.36	98.44
7.1	avg		3	40.59	0.00	10.16	47.92	0.09	0.32	99.07
7.3	1		2	39.97	0.01	12.37	47.77	0.04	0.29	100.45
7.3	6		3	40.57	0.00	11.74	47.94	0.04	0.32	100.61
7.3	avg		5	40.27	0.01	12.06	47.86	0.04	0.31	100.53
7.5	1		2	38.96	0.00	15.43	44.50	0.02	0.19	99.10
7.5	9	mx	2	39.07	0.00	17.01	45.23	0.05	0.24	101.60
7.5	avg		4	39.02	0.00	16.22	44.87	0.04	0.22	100.35
7.8	2		3	41.03	0.01	11.42	47.90	0.04	0.21	100.61
7.8	3		1	40.27	0.05	11.28	47.18	0.04	0.17	98.99
7.8	avg		4	40.65	0.03	11.35	47.54	0.04	0.19	99.80
26	6		2	41.25	0.02	8.27	51.43	0.06	0.41	101.44
26	7		2	41.38	0.00	8.11	50.82	0.04	0.39	100.74
26	avg		4	41.32	0.01	8.19	51.13	0.05	0.40	101.09
229	4	mx	1	40.04	0.03	8.87	49.39	0.02	0.45	98.80
229	9	mx	2	41.35	0.00	8.59	50.07	0.02	0.35	100.38
229	avg		3	40.70	0.02	8.73	49.73	0.02	0.40	99.59

Tab. B-6 (continued)

sample	min	details	N	SiO2	Cr2O3	FeO	MgO	CaO	NiO	SUM
229 2	4	mx	2	40 36	0 00	8 50	48 66	0 04	0 39	97 95
229 2	avg		2	40 36	0.00	8 50	48 66	0 04	0 39	97 95
317			2	40 47	0 02	8 02	50 90	0 01	0 36	99 78
317	1		2	40 41	0 02	8.30	50 52	0 00	0 38	99 63
317	avg		3	40 44	0 02	8 16	50 71	0 01	0 37	99.71
456	5		2	40 71	0.00	8 84	48.54	0.17	0.36	98 62
456	6		2	40 22	0.01	9 04	48 66	0 18	0 38	98 49
456	avg		4	40.47	0.01	8.94	48.60	0 18	0.37	98 56
458	2	mx	2	40 76	0.00	8 33	50 03	0.04	0 35	99 51
458	5		3	40 87	0.00	8.10	49 84	0 02	0 39	99 22
458	avg		5	40 82	0 00	8 22	49 94	0 03	0 37	99 37
465		mx	2	39 75	0.00	8 80	49.92	0 00	0 50	98 97
465	3	in opx aggr	2	40 00	0 00	8 83	50.50	0 02	0 39	99.74
465	6	near sp	2	40 72	0 05	7 41	50.58	0 01	0 54	99.31
465	avg		6	40.16	0.02	8 35	50.33	0 01	0 48	99 34
534	3		1	40.52	0 02	9 89	48 83	0 02	0 42	99 50
534	6	mx	2	40.60	0 02	10 12	49 45	0 01	0 42	100 62
534	avg		3	40 56	0.02	9 91	49 14	0 02	0 42	100 06
542.1	2	mx	3	41.26	0 00	8 47	49 55	0 02	0 32	99 82
542 1	4		1	41.05	0 00	8 30	49 27	0 04	0 36	99 02
542 1	avg		4	41 16	0.00	8 39	49 41	0 03	0 34	99 32
542 2	2		1	40 68	0 02	8 70	49.64	0.00	0 25	99 29
542 2	5	mx	3	41 23	0.00	8 80	49 53	0 01	0 34	99 91
542 2	avg		4	40.96	0 01	8.75	49 59	0 01	0 30	99 60
564	1		2	39 56	0 03	8 54	49 80	0 05	0 43	98 41
564	5		2	40 72	0 02	9 16	50 73	0 02	0 31	100 96
564	avg		4	40 14	0 03	8 85	50 27	0 04	0 37	99 69
592	1	core of below	2	41 20	0 00	8 68	49 07	0 04	0 38	99 37
592	1	near cpx impregn	2	40 85	0 00	8 79	49 91	0 02	0 36	99 93
592	avg		4	41 03	0 00	8 74	49 49	0 03	0 37	99 65
599	6		2	40.45	0 00	9 38	49 11	0 02	0 38	99.34
599	7		2	41 08	0 03	9 22	48 23	0 02	0 35	98 93
599	avg		4	40 77	0.02	9 30	48 67	0 02	0 37	99 14
676	3		2	40 65	0 00	8 29	49 76	0 00	0 40	99 10
676	avg		2	40.65	0 00	8 29	49.76	0 00	0 40	99.10
733 2	4	mx	2	40.90	0 00	9 85	49 93	0 14	0 33	101 15
733 2	6	near sp	2	40 44	0 00	9 81	49 23	0 11	0 35	99 94
733 2	avg		4	40 67	0 00	9 83	49 58	0 13	0 34	100 55
755			2	40 30	0 01	9 21	49 85	0 01	0 40	99 78
755	7		3	40 58	0 04	9 20	49 82	0 04	0 49	100 17
755	avg		5	40 44	0 03	9 21	49 84	0 03	0 45	99 98
757	3		3	40 23	0 00	9 55	49 74	0 02	0 42	99 96
757	7	mx	2	40.77	0 02	9 94	49 46	0 04	0 46	100 69
757	avg		5	40 50	0 01	9 75	49 60	0 03	0 44	100 33
774	4	incl in opx	1	39 42	0 02	9 00	49 21	0 02	0 42	98 09
774	6	mx	2	39.48	0 00	9 05	49 33	0.02	0 35	98 23
774	11	mx	2	40.02	0.00	9.14	49 63	0 02	0 44	99 25
774	avg		5	39 64	0 01	9 06	49 39	0 02	0 40	98 52
788	2		4	40 24	0 00	8 67	50 77	0 02	0 40	100 10
788	2		3	41.15	0 01	8 46	49 25	0 02	0 38	99 27
788	6		2	41.09	0 00	8 28	50 48	0 02	0 38	100 25
788	avg		9	40 83	0 00	8 47	50 17	0 02	0 39	99 87
801	2		4	40 64	0 01	7.72	49 95	0 02	0 46	98 80
801	3	near sp	2	40 51	0 01	8 19	50 81	0 02	0 39	99 93
801	avg		6	40 58	0 01	7 96	50 38	0.02	0 43	99 37
827	1		3	40 57	0.01	9 01	49 04	0 04	0 45	99 12
827	5	near sp	1	41 37	0 00	8 92	49 31	0 04	0 43	100 07
827	12	incl in opx	2	40 87	0 04	8 83	49 20	0 04	0 42	99 40
827	avg		6	40 94	0 02	8 92	49 18	0 04	0 43	99 53

Tab. B-6 (continued)

sample	min	details	N	SiO2	Cr2O3	FeO	MgO	CaO	NiO	SUM
829	2		2	39.93	0.00	8.93	50.31	0.01	0.36	99.54
829	3	mx	2	40.52	0.01	8.64	50.00	0.01	0.38	99.56
829	avg		4	40.23	0.01	8.79	50.16	0.01	0.37	99.55
849	2	near opx	2	39.61	0.00	10.22	49.14	0.02	0.42	99.41
849	12	mx	2	39.61	0.02	10.05	48.93	0.04	0.40	99.05
849	avg		4	39.61	0.01	10.14	49.04	0.03	0.41	99.23
860	1a		2	39.55	0.00	12.24	47.45	0.04	0.24	99.52
860	4		2	39.73	0.02	12.65	47.60	0.04	0.14	100.18
860	avg		4	39.64	0.01	12.45	47.53	0.04	0.19	99.85
861		near sp	4	39.75	0.01	8.29	49.49	0.04	0.39	97.97
861	2	near cpx	2	40.41	0.00	8.74	49.61	0.04	0.30	99.10
861	4	mx, rerun later	3	40.18	0.04	8.79	49.05	0.05	0.32	98.43
861	4	mx	3	40.41	0.00	8.53	49.50	0.05	0.47	98.96
861	avg		12	40.19	0.01	8.59	49.41	0.05	0.37	98.62
862	2	near sp	2	39.78	0.00	9.25	48.54	0.02	0.40	97.99
862	3	mx	2	39.85	0.03	9.61	48.21	0.02	0.39	98.11
862	4	near cpx+sp	2	40.02	0.00	10.10	49.20	0.04	0.38	99.74
862	avg		6	39.88	0.01	9.65	48.65	0.03	0.39	98.61
866	1	mx	2	39.84	0.00	9.75	50.18	0.02	0.34	100.13
866	7	mx	2	40.22	0.01	9.68	49.71	0.04	0.35	100.01
866	avg		4	40.03	0.01	9.72	49.95	0.03	0.35	100.07
869	7		2	40.58	0.00	8.86	50.14	0.02	0.43	100.03
869	avg		2	40.58	0.00	8.86	50.14	0.02	0.43	100.03
873	1		3	40.82	0.00	8.74	50.83	0.02	0.41	100.82
873	3		2	40.32	0.02	8.94	51.05	0.02	0.38	100.73
873	avg	du-band	5	40.57	0.01	8.84	50.94	0.02	0.40	100.78
873	2	near sp	3	40.07	0.00	8.79	50.73	0.02	0.38	99.99
873	7		4	40.65	0.01	8.78	50.72	0.02	0.42	100.60
873	avg	lherz band	7	40.36	0.01	8.79	50.73	0.02	0.40	100.30
881	1	mx	2	40.75	0.02	8.47	50.86	0.02	0.40	100.52
881	2	incl ?	1	40.68	0.03	8.53	51.25	0.02	0.35	100.86
881	3	mx	3	40.99	0.00	8.85	50.90	0.01	0.38	101.13
881	avg		6	40.81	0.02	8.62	51.00	0.02	0.38	100.84
884	3		3	41.39	0.01	9.18	49.60	0.04	0.40	100.62
884	5		2	41.26	0.02	9.27	49.89	0.04	0.39	100.87
884	avg		5	41.33	0.02	9.23	49.75	0.04	0.40	100.75
886	2		2	39.47	0.03	9.26	49.60	0.04	0.36	98.76
886	8		2	39.72	0.02	9.38	49.73	0.02	0.42	99.29
886	avg		4	39.60	0.03	9.32	49.67	0.03	0.39	99.03
900	2		2	39.74	0.00	9.80	49.59	0.04	0.40	99.57
900	9		2	40.29	0.02	9.59	49.77	0.04	0.39	100.10
900	avg		4	40.02	0.01	9.70	49.68	0.04	0.40	99.84
901.1	1		2	39.89	0.02	9.64	50.11	0.01	0.35	100.02
901.1	6		2	40.57	0.02	9.61	49.93	0.04	0.43	100.60
901.1	avg		4	40.23	0.02	9.63	50.02	0.03	0.39	100.31
901.3	?		3	40.04	0.00	9.11	49.68	0.02	0.39	99.24
901.3	7	mx	2	40.53	0.01	9.48	49.60	0.02	0.39	100.03
901.3	avg		5	40.29	0.01	9.30	49.64	0.02	0.39	99.64
918	1	aw sp-cpx	2	39.85	0.01	8.89	49.44	0.02	0.43	98.64
918	2	aw sp-cpx	2	41.18	0.00	9.39	50.40	0.03	0.46	101.46
918	7	mx	3	40.73	0.01	9.31	49.74	0.04	0.41	100.24
918	avg		7	40.59	0.01	9.20	49.86	0.03	0.43	100.11
922	3		2	40.59	0.04	9.00	50.11	0.00	0.38	100.12
922	5	incl in opx	1	40.66	0.02	9.04	50.16	0.02	0.43	100.33
922	8	pc	2	40.95	0.02	9.58	49.85	0.04	0.35	100.77
922	avg		5	40.73	0.03	9.20	50.04	0.02	0.39	100.41
932	3		3	40.90	0.01	9.88	49.47	0.04	0.35	100.65
932	7		1	40.94	0.05	9.96	50.20	0.02	0.35	101.52
932	avg		4	40.92	0.03	9.92	49.84	0.03	0.35	101.09

Tab. B-6 (continued)

sample	min	details	N	SiO2	Cr2O3	FeO	MgO	CaO	NiO	SUM
941	9		2	40.76	0.00	9.21	49.45	0.02	0.34	99.78
941	12		2	41.06	0.01	9.05	50.22	0.01	0.41	100.76
941	avg		4	40.91	0.01	9.13	49.84	0.02	0.38	100.27
959	4		2	40.71	0.00	7.75	50.94	0.04	0.36	99.80
959	5		1	41.09	0.05	7.27	50.27	0.07	0.32	99.07
959	avg		3	40.90	0.03	7.51	50.61	0.06	0.34	99.44
1027	2		3	40.66	0.01	9.38	50.16	0.02	0.43	100.66
1027	3		4	41.15	0.00	9.05	49.94	0.02	0.38	100.54
1027	avg		7	40.91	0.01	9.22	50.05	0.02	0.41	100.60
1029.11		incl in opx	1	40.50	0.02	10.30	49.84	0.02	0.49	101.17
1029.11	16	mx, nb	2	41.40	0.02	10.39	50.04	0.01	0.40	102.26
1029.11	avg		3	40.95	0.02	10.35	49.94	0.02	0.45	101.72
1043.2	3	mx	2	41.08	0.01	9.06	50.00	0.04	0.43	100.62
1043.2	7	near opx	2	41.08	0.01	8.98	50.22	0.00	0.43	100.72
1043.2	avg		4	41.08	0.01	9.02	50.11	0.02	0.43	100.67
1063.2	3		2	41.03	0.00	9.15	48.88	0.00	0.40	99.46
1063.2	3	nb	2	41.83	0.03	9.35	48.88	0.01	0.34	100.44
1063.2	avg		4	41.43	0.02	9.25	48.88	0.01	0.37	99.95
1065	2	mx	2	40.90	0.01	8.85	49.95	0.04	0.38	100.13
1065	6	incursion	1	41.22	0.04	9.03	50.54	0.01	0.38	101.22
1065	11		2	41.31	0.00	9.24	49.59	0.02	0.43	100.59
1065	avg		6	41.14	0.02	9.04	50.03	0.02	0.40	100.65
1071	4		1	40.19	0.03	8.49	49.36	0.02	0.43	98.52
1071	1		2	40.30	0.00	9.18	49.98	0.02	0.47	99.95
1071	1		2	41.36	0.02	9.59	50.88	0.02	0.42	102.29
1071	5		3	40.86	0.02	8.75	49.83	0.04	0.41	99.91
1071	5	mx	1	41.05	0.02	9.75	50.95	0.04	0.43	102.24
1071	avg		9	40.75	0.02	9.15	50.20	0.03	0.43	100.58
1079.2	1		3	40.68	0.03	9.20	49.02	0.04	0.36	99.33
1079.2	4		3	39.87	0.03	9.06	48.24	0.03	0.40	97.63
1079.2	avg		6	40.28	0.03	9.13	48.63	0.04	0.38	98.48
1086	8		2	40.52	0.02	9.04	50.06	0.00	0.38	100.02
1086	10	mx	2	40.25	0.00	9.49	50.18	0.04	0.45	100.41
1086	avg		4	40.39	0.01	9.27	50.12	0.02	0.42	100.22
1090	3		2	40.79	0.00	8.97	49.83	0.02	0.35	99.96
1090	7	mx	2	40.41	0.02	9.21	49.95	0.02	0.39	100.00
1090	avg		4	40.60	0.01	9.09	49.89	0.02	0.37	99.98
1112	2		3	40.38	0.01	9.49	49.95	0.02	0.38	100.23
1112	7		2	41.03	0.04	9.18	48.99	0.03	0.37	99.64
1112	13		2	40.89	0.02	9.24	49.79	0.01	0.34	100.29
1112	avg		7	40.77	0.02	9.30	49.58	0.02	0.36	100.05
1118	5		2	40.24	0.03	9.70	49.45	0.04	0.41	99.87
1118	11		1	40.82	0.00	9.97	48.88	0.04	0.35	100.06
1118	12	mx	2	40.43	0.03	9.92	50.03	0.02	0.43	100.86
1118	avg		5	40.50	0.02	9.86	49.45	0.03	0.40	100.26
1136.2	1		3	41.18	0.00	8.98	50.64	0.02	0.40	101.22
1136.2	4		2	40.53	0.00	8.59	50.55	0.01	0.39	100.07
1136.2	avg		5	40.86	0.00	8.79	50.60	0.02	0.40	100.65
1141	2		2	40.39	0.00	8.77	49.68	0.04	0.43	99.31
1141	7		1	39.98	0.04	8.82	49.64	0.02	0.23	98.73
1141	11		1	40.43	0.02	9.00	49.67	0.02	0.29	99.43
1141	avg		4	40.27	0.02	8.86	49.66	0.03	0.32	99.16
1143	12	near opx	2	41.10	0.03	8.98	49.78	0.04	0.33	100.26
1143	13	mx, rim	2	40.07	0.02	9.22	49.78	0.03	0.40	99.52
1143	13	mx, core	2	40.36	0.01	8.95	49.35	0.02	0.40	99.09
1143	avg		6	40.51	0.02	9.05	49.64	0.03	0.38	99.62
1145	3		1	41.58	0.00	10.15	50.32	0.04	0.35	102.44
1145	4		2	40.60	0.02	10.13	49.74	0.00	0.32	100.81
1145	avg		3	41.09	0.01	10.14	50.03	0.02	0.34	101.63

Tab. B-6 (continued)

sample	min	details	N	SiO2	Cr2O3	FeO	MgO	CaO	NiO	SUM
1169	3		1	41.44	0.00	7.44	50.97	0.05	0.36	100.26
1169	4		3	40.80	0.03	7.39	49.93	0.05	0.38	98.58
1169	avg		4	41.12	0.02	7.42	50.45	0.05	0.37	99.42
1181	7		3	40.74	0.02	8.90	49.30	0.04	0.38	99.38
1181	11		1	40.88	0.00	9.09	49.83	0.02	0.38	100.20
1181	15	rerun	3	40.82	0.01	9.25	49.57	0.04	0.35	100.04
1181	avg		7	40.81	0.01	9.08	49.57	0.03	0.37	99.87
1189.1		mx	2	40.10	0.00	8.62	49.48	0.04	0.38	98.62
1189.1	7	mx	2	41.46	0.01	8.85	49.77	0.03	0.44	100.56
1189.1	avg		4	40.78	0.01	8.74	49.63	0.04	0.41	99.59
1189.2	7		2	40.85	0.00	8.41	50.18	0.04	0.46	99.94
1189.2	11		2	40.54	0.00	8.41	49.51	0.04	0.38	98.88
1189.2	avg		4	40.70	0.00	8.41	49.85	0.04	0.42	99.41
1193	5		3	41.49	0.01	5.62	51.32	0.12	0.54	99.10
1193	6		1	40.94	0.04	5.76	51.14	0.10	0.50	98.48
1193	avg		4	41.22	0.03	5.69	51.25	0.11	0.52	98.79
1194	5		2	41.03	0.00	8.07	50.19	0.02	0.41	99.72
1194	8	mx	2	40.81	0.00	8.26	50.34	0.02	0.39	99.82
1194	avg		4	40.92	0.00	8.17	50.27	0.02	0.40	99.77
1195	1	mx	2	40.78	0.00	9.02	49.79	0.01	0.40	100.00
1195	4	mx	2	40.52	0.00	9.25	50.03	0.01	0.40	100.21
1195	avg		[illegible]	40.65	0.00	9.14	49.91	0.01	0.40	100.11
1200			1	40.56	0.03	9.22	49.89	0.02	0.38	100.10
1200	4		1	39.68	0.00	9.29	49.32	0.04	0.40	98.73
1200	avg		2	40.12	0.02	9.26	49.61	0.03	0.39	99.42
1214	8		3	40.29	0.00	9.65	48.64	0.02	0.39	98.99
1214	9		9	40.27	0.00	9.66	49.09	0.01	0.24	99.27
1214	avg		12	40.28	0.00	9.66	48.87	0.02	0.32	99.13
1222	2	amph rich band	3	40.29	0.01	9.35	49.03	0.01	0.27	98.96
1222	5	low strain	2	39.93	0.00	9.88	48.60	0.00	0.41	98.82
1222	8	high strain	1	39.76	0.00	9.88	48.81	0.02	0.29	98.76
1222	avg		6	39.99	0.00	9.70	48.81	0.01	0.32	98.85
1228.1			1	40.39	0.00	11.00	48.20	0.02	0.36	99.97
1228.1	avg		1	40.39	0.00	11.00	48.20	0.02	0.36	99.97
1232	6	mx	3	40.56	0.02	7.96	50.01	0.02	0.45	99.02
1232	9	mx	2	40.06	0.00	8.28	49.82	0.02	0.43	98.61
1232	avg		5	40.31	0.01	8.12	49.92	0.02	0.44	98.82
1237	2	mx	2	40.63	0.01	9.72	49.98	0.02	0.36	100.72
1237	11		2	40.79	0.01	9.53	50.30	0.01	0.36	101.00
1237	avg		4	40.71	0.01	9.63	50.14	0.02	0.36	100.86
1245	1		2	40.69	0.00	8.09	49.46	0.04	0.41	98.69
1245	1		1	40.61	0.00	7.67	50.05	0.02	0.35	98.70
1245	avg		3	40.65	0.00	7.88	49.76	0.03	0.38	98.70
1249	5		3	40.21	0.00	8.11	50.15	0.00	0.40	99.17
1249	8	mx	2	40.94	0.02	8.10	49.46	0.01	0.38	99.61
1249	avg		5	40.58	0.01	8.61	49.81	0.01	0.39	99.39
1258	8		3	40.38	0.03	8.89	49.75	0.04	0.38	99.47
1258	9		1	40.91	0.01	8.69	49.67	0.04	0.38	99.70
1258	avg		4	40.65	0.02	8.79	49.71	0.04	0.38	99.59
1262	4		3	40.62	0.02	9.20	49.22	0.01	0.39	99.46
1262	4		2	41.13	0.00	9.84	50.17	0.01	0.38	101.53
1262	5		2	40.46	0.00	9.29	49.41	0.02	0.40	99.58
1262	avg		[illegible]	40.74	0.01	9.44	49.60	0.01	0.39	100.19
1272	1	near large sp	2	40.85	0.04	8.07	50.19	0.02	0.42	99.59
1272	1	mx	2	40.32	0.00	8.66	49.85	0.01	0.40	99.24
1272	avg		4	40.59	0.02	8.37	50.02	0.02	0.41	99.42
1274.1	1		2	41.45	0.01	9.23	50.98	0.01	0.36	102.04
1274.1	2		2	41.86	0.00	9.46	50.78	0.00	0.43	102.53
1274.1	avg		4	41.66	0.01	9.35	50.88	0.01	0.40	102.29

Tab. B-6 (continued)

sample	min	details	N	SiO2	Cr2O3	FeO	MgO	CaO	NiO	SUM
1315	2		2	41 38	0 00	8 74	51 11	0 01	0 35	101 59
1315	5		2	40 80	0 00	8 66	50 88	0 02	0 35	100 71
1315	avg		4	41 09	0 00	8 70	51 00	0 02	0 35	101 15
1316	6		1	40 52	0.00	9 47	48 84	0 15	0 29	99 27
1316	7	rim	2	40 24	0 02	9.45	48 96	0 18	0 35	99 20
1316	7	core	2	40 46	0.00	9 37	48 67	0 20	0 36	99 06
1316	8		2	40.78	0 02	9 36	48.70	0.13	0 29	99 28
1316	avg		7	40.50	0.01	9 41	48 79	0 17	0 32	99 20
1316.2	4		2	40 45	0.01	10 82	47 33	0.11	0 25	98 97
1316 2	5		2	40.05	0 00	11 27	47.43	0 10	0 32	99 17
1316 2	avg		4	40 25	0 01	11.05	47 38	0 11	0 29	99 07
1321	5		3	40 65	0 00	9 71	48 56	0 17	0 28	99 37
1321	avg		3	40 65	0 00	9 71	48 56	0 17	0 28	99 37
1324	2		2	41 23	0 00	9 97	49 83	0 02	0 34	101 39
1324	4		3	40 43	0 00	9 66	49 59	0 02	0 34	100 04
1324	avg		5	40 83	0 00	9 82	49 71	0 02	0 34	100 72
1326	5	next to plag	2	40 84	0 00	9 96	48 43	0 06	0 31	99 66
1326	6		4	40 84	0 00	9 87	48 55	0 08	0 32	99 66
1326	avg		6	40 84	0 00	9 92	48 52	0 07	0.32	99 66
1331 1	1	mx	2	39 91	0 00	10 29	49 12	0 08	0 30	99 70
1331.1	2	near sp	2	40 97	0 00	10 00	49 44	0 08	0.43	100 92
1331.1	avg		4	40 44	0.00	10 15	49 28	0 08	0 37	100 31
1331 2	2		2	40 29	0 05	11 58	47 82	0 15	0 36	100 25
1331 2	3		3	39 75	0 02	11 30	47 24	0 19	0 28	98 78
1331 2	7	mx	3	39.73	0 01	11.82	47 32	0 17	0 34	99 39
1331 2	avg		8	39 92	0 03	11 57	47.46	0.17	0 33	99 47
1340	1	mx	2	40 54	0 01	9 22	49 65	0 02	0 36	99 80
1340	1	near sp	2	40 40	0 00	8 97	50 24	0 02	0 49	100 12
1340	3	rer.in later	3	41 42	0 00	8 84	49 55	0 02	0 40	100 23
1340	3		2	40 65	0 02	8 99	49 46	0 02	0 44	99 58
1340	avg		9	40 75	0 01	9 01	49 73	0 02	0 42	99 93
1360	3	near du So	2	40 69	0 00	9 91	49 08	0 04	0 36	100 08
1360	5	near cpx, lherz	2	40 80	0 03	9 98	49 52	0 04	0 33	100 70
1360	6	mx, in lherz band	2	40 26	0 00	10 05	49 13	0 04	0 38	99 86
1360	avg		6	40 58	0 01	9 98	49 24	0 04	0 36	100 21
1378		mx	1	41 28	0 00	8 58	50 46	0 02	0 40	100 74
1378	2	mx	4	40 68	0 00	8 40	50 99	0 04	0 46	100 57
1378	3	in cpx/sp sympl	3	40 36	0 00	7 99	50 56	0 01	0 45	99 37
1378	avg		5	40 77	0 00	8 32	50 67	0 02	0 44	100 23
1396	1	near opx	2	41.22	0 00	8 34	50 67	0 00	0 40	100 63
1396	1	mx	1	40 60	0 04	8 57	50 05	0 04	0 43	99.73
1398	5		2	40 84	0 00	8 63	50 32	0 04	0 27	100 10
1396	avg		5	40 89	0 01	8 51	50 35	0 03	0 37	100 15
1402	14	hz-layer	2	40 30	0 04	9 04	48 92	0 02	0 30	98 62
1402	15	transition	2	40 44	0 02	9 32	49 07	0 09	0 30	99 24
1402	avg		4	40 37	0 03	9 18	49 00	0 06	0 30	98 93
1420	1		2	40 07	0 00	9 45	49 42	0 04	0 40	99 38
1420	2	So with plag	3	40 07	0 04	9 53	49.06	0 02	0 48	99 20
1420	5		2	40 00	0 00	9 40	49 52	0 02	0 50	99 44
1420	7	mx	3	40 14	0 00	9 11	49 15	0 02	0 42	98 84
1420	avg		10	40.07	0 01	9 37	49 29	0 03	0 45	99 22
1447	1	pl wehrl So	2	41 64	0 04	10 16	49 80	0 04	0 23	101 91
1447	3	pl wehrl So	2	41.08	0 02	10 27	50 18	0 05	0 36	101 96
1447	avg		4	41 36	0 03	10 22	49 99	0 05	0 30	101 94
1447	4	cpx du	2	40 81	0 02	10 16	50 17	0 08	0 29	101 53
1447	7	cpx du	2	40 82	0 00	9 64	49	0 11	0 33	100 45
1447	avg		4	40 82	0 01	9 90	49 86	0 10	0 31	100 99
1454		mx	2	41 35	0 00	9 89	50 30	0 04	0 36	101 94
1454	3	mx	2	40 88	0 00	9 31	49 68	0 02	0 47	100 36

Tab. B-6 (continued)

sample	min	details	N	SiO2	Cr2O3	FeO	MgO	CaO	NiO	SUM
1454	3	near cpx	1	40.49	0.03	9.36	50.59	0.04	0.52	101.03
1454	avg		5	40.91	0.01	9.52	50.19	0.03	0.45	101.11
1459			2	40.68	0.02	9.27	48.09	0.17	0.38	98.61
1459			2	40.70	0.04	9.15	48.08	0.16	0.32	98.45
1459	4		3	40.36	0.01	9.58	48.68	0.18	0.31	99.12
1459	5		3	40.75	0.02	9.11	48.39	0.22	0.32	98.81
1459	avg		10	40.62	0.02	9.28	48.31	0.18	0.33	98.75
1468	6	mx	2	40.21	0.00	8.84	49.85	0.02	0.42	99.34
1468	7	near sp	1	40.63	0.05	7.94	50.18	0.02	0.50	99.32
1468	7	mx	1	40.14	0.00	8.96	49.08	0.02	0.49	98.69
1468	avg		4	40.33	0.02	8.58	49.70	0.02	0.47	99.12
1485	6	betw px|sp	2	40.85	0.02	8.26	50.02	0.01	0.38	99.54
1485	7	mx	3	40.59	0.02	8.65	49.93	0.04	0.48	99.77
1485	avg		5	40.72	0.02	8.46	50.01	0.03	0.43	99.66
1499	1		2	39.66	0.04	11.24	47.88	0.14	0.31	99.27
1499	4		4	40.86	0.04	10.86	47.72	0.14	0.29	99.91
1499	avg		6	40.26	0.04	11.05	47.80	0.14	0.30	99.59

Tab. B-7 (following two pages). Mineral chemical analyses of amphiboles from the Table Mountain and Lewis Hills massifs. Data for garnets and plagioclase are listed as well. For legend see Tabs. B-3, B-4.

Tab. B-7

sample	spot	details	N	SiO2	TiO2	Al2O3	Cr2O3	FeO	MgO	MnO	CaO	NiO	Na2O	K2O	SUM
LH 11	1		1	54 18	0 10	3 34	0 81	1 93	22 75	0 02	12 69	0.11	0 57	0 00	96 50
LH 12	1		2	48 55	0 21	8 28	2 21	2 32	20 33	0 06	12 10	0 11	2 40	0 15	96 72
LH 12	3	needles	1	48 02	0 17	8 65	2 30	2 48	19 93	0 06	11 99	0 07	2 53	0 12	96 32
LH 12	7		1	47 98	0 27	8 00	2 32	2 30	20 04	0 06	12 37	0 08	2 34	0 16	95 92
LH 47	1	incl	1	53 43	0 01	3 46	1 09	2 04	23 05	0 06	12 05	0 05	0 41	0 01	95 66
LH 49	1	rim, core cpx?	1	55 82	0 00	3 89	0 61	1 98	21 52	0 04	13 72	0 15	0 86	0 07	98 66
LH 73	6	blebs in opx	3	54 67	0 05	4 32	1 28	1 86	22 13	0 05	12 56	0 07	0 61	0 03	97 63
LH 76	4	needles	1	56 93	0 03	1 02	0 07	3 32	24 27	0 14	10 25	0 05	0 33	0 01	96 42
LH 87	5	alt of opx?	1	53 29	0 10	4 18	1 11	2 30	21 50	0 10	12 33	0 15	0 71	0 02	95 79
LH 87	5	between cpx	1	55 14	0 06	2 62	0 65	2 41	22 46	0 04	12 80	0 11	0 65	0 04	97 18
LH 87	5	incl B	1	52 04	0 07	4 53	0 90	2 45	21 62	0 06	12 75	0 14	1 06	0 14	95 76
LH 113	1	low alterat	1	47 75	0 20	5 62	1 10	3 35	18 02	0 09	20 11	0 00	0 35	0 01	96 60
LH 113	1	med alterat	1	47 18	0 21	5 12	1 13	4 11	18 60	0 12	18 77	0 11	0 27	0.00	95 62
LH 113	1	high alterat	1	46 40	0 17	4 46	0 99	5 67	21 57	0 15	16.05	0 11	0 26	0 01	95 84
BMD 12	1	rim on plag	1	43.55	0 57	14 50	0 98	2 88	17.83	0 05	12 39	0 02	3 62	0 00	96 39
BMD 12	4	rim on plag	2	43 17	0 63	14 59	0 86	2 99	18.31	0 05	12 76	0 03	2 86	0 03	96 28
934 1	2		2	48 29	0 21	10 13	1 11	3 77	20 18	0 03	12 16	0 13	1 90	0 33	98 24
934 1		sp–intergrowth	2	47 60	0 19	11 22	1 30	3 88	19 65	0 04	12 36	0 09	2 09	0 35	98 77
934 1	1	close to sp	1	47 53	0 17	10 61	1 58	3 64	18 90	0 03	13 07	0 22	2 21	0 23	98 19
941	1		2	44 19	0 56	12 32	1 99	3 82	18 26	0 07	10 78	0 03	3 51	0 86	96 39
941	2	pc, core	2	44 03	0 19	13 15	1 81	4 43	18.35	0 11	9 98	0 03	3.28	0 50	95.86
941	2	pc, rim	2	44 59	0 21	13 10	1 56	3 60	17.86	0 06	11.12	0 02	3 54	0.43	96 09
941	3	pc, core	1	44 93	0 23	13 01	1 55	3 78	18 56	0 11	10 90	0 08	3 74	0 54	97 43
941	4	pc, core	1	44 63	0 19	13 34	2 09	3 93	17 73	0.09	10 77	0 06	3 82	0 42	97 07
941	6	pseudo–phlog	1	43.37	1 72	13 71	0 91	4 69	17 74	0 10	10 55	0 05	3 48	0 19	96 51
1029.11	11	needles	1	58 30	0 09	0.73	0 1[illegible]	3 07	24 24	0 07	12 24	0 02	0 35	0 01	99 23
1118	4A		2	54 62	0 05	3 57	1 36	2.77	21.64	0 07	12 57	0 05	0 69	0 02	97 41
1136 2	3	needles	1	46 97	0 16	9 54	1.19	3 19	20.23	0 04	12 15	0 08	1 95	0 02	95 82
1143	4		1	52.48	0 02	3 88	1 12	4 38	24 59	0 08	11 62	0 06	0 11	0.00	98 34
1145	7	alt cpx?	2	54.08	0.00	3 63	1 20	3 77	23 89	0 11	13 43	0 08	0 04	0 00	100 23
1222	4	aggreg	2	47.70	0 20	11 25	1 41	3 37	19 16	0 06	12 38	0 17	1 63	0 27	97 60
1222	6		1	47 20	0 18	10 97	1 41	3 61	19 17	0 04	11 79	0 07	1 83	0 23	96 50
1222	9		1	45 06	0 19	10 08	1 25	4.19	17 42	0 05	15 64	0 11	1 50	0 23	95 72
1228.1	10	next to cpx	2	45 52	0.40	12 37	0 91	4.16	18 08	0 06	12 42	0 09	2.14	0 29	96 44
1228 2	1	amphibolite	1	45 36	0 67	13 65	0.37	5.89	16 63	0 07	11 95	0 09	2 18	0 11	96 97
1228 2	5	amphibolite	1	52 99	0 03	5 23	0.30	6 70	19 22	0 20	11 46	0 05	0 75	0 04	96 97
1228.3	9	outside sympl	1	45 31	0 10	14 90	0 05	7 48	17 43	0 13	10 77	0 00	2 13	0 05	98 35

Tab. B-7 (continued)

sample	spot	details	N	SiO2	TiO2	Al2O3	Cr2O3	FeO	MgO	MnO	CaO	NiO	Na2O	K2O	SUM
1228 3	9	adj. sympl	1	45 53	0 13	14 22	0 13	7 45	16 78	0.08	12 30	0 01	2 38	0 02	99 03
1228 3	10	pc, core	1	44 69	0 17	14 83	0 29	6 46	17 09	0 12	11 89	2 00	2 61	0 04	100 19
1228 3	15	pc, core	2	44 31	0 13	15 65	0 13	5 65	16 71	0 03	12 04	0 08	2 43	0 05	97 21
1228 3	1		1	46 34	0 19	13 80	0 15	6 55	17 36	0 08	12 23	0 00	2 22	0 07	98 99
1428	1	alt. near vein	2	52 32	0 06	5 31	1 29	2 46	21 73	0 09	12 20	0 16	1 23	0 16	97 01
1459	2	rims plag	1	41 45	0 21	15 97	0 14	3 78	16 66	0 04	13 33	0 12	3 11	0 42	95 23
82 111	3	opxte	1	50 50	0 07	8 66	1 54	2 73	20 42	0 07	12 30	0 18	1 36	0 43	98 26
82 111	6	opxte	2	48 25	0 05	10 46	1 91	2 72	19 51	0 04	12 27	0 15	1 43	0 65	97 44
82 111		opxte	1	54 57	0 05	4 56	0 65	2 38	22 02	0 07	12 48	0 09	0 42	0 07	97 36
GARNET															
1228 3	9	core	1	43 30	0 01	22 89	0 09	12 16	18 38	0 26	6 13	0 05	0 04	0 01	103 32
1228 3	9	half rim:	1	42 78	0 00	22 33	0 13	12 02	18 07	0 25	6 05	0 05	0 00	0 01	101 69
1228 3	9	rim to sympl	1	43 52	0 03	22 95	0 10	11 73	17 79	0 37	6 33	0 00	0 00	0 00	102 82
PLAGIO	CLASE														
900	10	An=85 7	1	48 16	0	32 35	n d	0 09	0	0 03	17 65	n d	1 63	0 03	99 94
1331 1	1	An=86 2	3	47 38	0 03	34 55	n d	0 04	0 05	0	17 11	n d	1 52	0 01	100 69

Tab. B-8 (following thirteen pages). Selected and recalculated mineral chemistry data from the Table Mountain and Lewis Hills mantle sections. The samples represent the total range of mineral chemistries encountered in this investigation. (a) Spinel; (b) clinopyroxene; (c) orthopyroxene; (d) olivine; (e) amphibole.

Tab. B-8a

ref #	1	2	3	4	5	6	7	8	9	10	11	12
sample	TM862	TM1315	TM1321	TM1360	TM1360	TM849	TM886	TM1420	TM 873	TM1454	TM1331 2	TM1232
rocktype	lherz	hz	du	pl-wehrl	cpx-du	pl-hz	hz	lherz	hz	lherz	du	hz
remark	pl-band			banded	banded	pl-band						
unit	1	1	1	1	1	2	2	2	2	2	2	3
TiO2	0.18	0.08	0.36	0.3?	0.21	0.10	0.17	0.18	0.04	0.02	0.31	0 04
Al2O3	29.56	13 45	30.62	34.36	31.43	31.63	32.05	32.06	36.92	41.16	31.42	29.67
Cr2O3	35.53	50.18	33.29	31.43	33.17	34.32	34.30	34.14	30.53	26.92	32.79	37.82
Fe tot	20.86	26.52	20.68	18.69	22.46	19.36	19 13	20.00	16.47	16.02	22.36	16.16
MgO	12.82	9.79	13.54	14.48	13.04	13.51	14.05	13.63	15.15	16.22	13.44	14.62
MnO	0.21	0.34	0.21	0.11	0.14	0 20	0 27	0.14	0.13	0.00	0.16	0.10
NiO	0.13	n.d.	0.19	0.14	0.05	0.07	n.d.	0.16	0.21	0.25	0.21	n.d.
V2O5	0.33	n.d.	0.26	0.19	0.15	0.23	n.d.	0.34	0.20	0.13	0.21	n.d.
SUM	99.62	100.36	99.15	99.73	100.65	99.42	99.97	100 65	99.65	100.72	100.90	98.41
Fe2O3calc	3.78	7.91	4.75	3.32	5.29	3.20	3.89	3.35	2.39	2.22	5.74	2.53
FeOcalc	17.22	18.74	16.12	15.52	17.36	16.30	15.41	16.79	14 32	13.92	16.83	13.76
Ti	0 0041	0.0019	0.0081	0.0072	0.0046	0.0022	0 0038	0.0040	0.0009	0.0004	0 0068	0.0009
Al	1.0442	0.5135	1.0759	1.1782	1.0908	1 1055	1.1092	1.1070	1.2575	1 3520	1.0856	1.0463
Cr	0.8419	1.2849	0.7846	0.7229	0.7722	0 8045	0.7963	0.7907	0 6974	0.5931	0.7599	0.8946
Fetot	0.5226	0.7180	0.5153	0.4545	0.5528	0.4799	0.4695	0.4898	0.3978	0.3732	0.5479	0.4041
Mg	0.5723	0.4723	0.6012	0.6275	0.5719	0.5967	0.6145	0.5948	0.6520	0.6733	0.5868	0.6516
Mn	0 0053	0.0093	0.0053	0.0027	0.0035	0.0050	0.0067	0 0035	0.0032	0.0000	0 0040	0.0025
Ni	0.0031	n.d.	0.0046	0.0033	0.0012	0 0017	n.d.	0.0038	0.0049	0.0056	0 0049	n.d.
V	0.0065	n.d.	0.0051	0 0037	0.0029	0 0045	n d.	0.0066	0 0038	0.0024	0 0041	n.d.
Fe(III)calc	0 0862	0.1977	0 1081	0 0735	0.1190	0.0720	0.0870	0 0746	0.0520	0.0469	0.1287	0 0573
Fe(II)calc	0.4363	0.5203	0.4072	0.3810	0.4339	0.4078	0.3825	0.4151	0.3457	0.3263	0.4192	0 3468
Cr#	45	71	42	38	41	42	42	42	35	30	41	46
Mg#	57	48	60	62	57	59	62	59	65	67	58	65
Fe#	17	28	21	16	22	15	19	15	13	13	23	14

Tab. B-8a (continued)

ref #	13	14	15	16	17	18	19	20	21	22	23	24
sample	TM1340	TM676	TM733.2	TM60.6e	TM1193	TM1249	TM1245	TM672	TM26	TM959	TM564	TM1169
rocktype	hz	hz	du	du	du	hz	hz	hz	du	du	hz	du
remark												
unit	3	3	3	3	3	4	4	4	4	4	TU	TU
TiO2	0.04	0.04	0.06	0.09	0.16	0.01	0.03	0.03	0.11	0.07	0.04	0.04
Al2O3	18.99	25.53	17.92	27.44	19.45	19.35	12.55	27.29	10.26	7.09	26.64	8.79
Cr2O3	49.27	42.41	48.39	38.71	50.94	49.27	57.20	40.81	58.51	63.85	42.07	61.48
Fe tot	20.23	18.61	22.23	18.82	14.48	20.08	20.19	17.89	20.04	18.63	17.23	18.62
MgO	10.73	12.44	11.07	12.59	13.56	10.42	9.30	12.55	9.32	9.46	12.24	9.53
MnO	0.22	0.21	0.24	0.16	0.21	0.23	0.24	0.22	0.20	0.22	0.19	0.29
NiO	0.11	0.10	0.05	0.17	0.11	0.09	0.04	0.06	0.04	0.05	0.10	0.05
V2O5	0.32	0.20	0.25	0.30	0.22	0.31	0.31	0.29	0.18	0.25	0.24	0.26
SUM	99.91	99.54	100.21	98.28	99.13	99.76	99.86	99.14	98.66	99.62	98.75	99.06
Fe2O3calc	1.50	1.77	4.33	2.16	0.20	0.85	0.17	0.84	0.95	0.00	0.00	0.00
FeOcalc	18.78	16.91	18.03	16.75	14.29	19.26	20.02	17.08	19.11	18.80	17.28	18.70
Ti	0.0010	0.0009	0.0014	0.0021	0.0038	0.0002	0.0007	0.0007	0.0028	0.0018	0.0009	0.0010
Al	0.7087	0.9200	0.6677	0.9904	0.7162	0.7237	0.4866	0.9794	0.4059	0.2819	0.9639	0.3484
Cr	1.2334	1.0251	1.2093	0.9371	1.2581	1.2360	1.4875	0.9824	1.5525	1.7026	1.0210	1.6345
Fetot	0.5354	0.4756	0.5874	0.4817	0.3781	0.5326	0.5551	0.4553	0.5622	0.5253	0.4421	0.5234
Mg	0.5061	0.5665	0.5212	0.5743	0.6310	0.4925	0.4557	0.5692	0.4659	0.4753	0.5597	0.4774
Mn	0.0059	0.0054	0.0064	0.0041	0.0056	0.0062	0.0067	0.0057	0.0057	0.0063	0.0049	0.0083
Ni	0.0028	0.0025	0.0013	0.0042	0.0028	0.0023	0.0011	0.0015	0.0011	0.0014	0.0025	0.0014
V	0.0067	0.0040	0.0052	0.0061	0.0045	0.0065	0.0067	0.0058	0.0040	0.0056	0.0049	0.0058
Fe(III)calc	0.0359	0.0410	0.1045	0.0501	0.0046	0.0203	0.0043	0.0193	0.0241	0.0000	0.0000	0.0000
Fe(II)calc	0.4996	0.4346	0.4829	0.4316	0.3735	0.5123	0.5508	0.4360	0.5381	0.5300	0.4435	0.5256
Cr#	64	53	64	49	64	63	75	50	79	86	51	82
Mg#	50	57	52	57	63	49	45	57	46	47	56	48
Fe#	7	9	18	10	1	4	1	4	4	0	0	0

Tab B-8a (continued)

ref #	25	26	27	28	29	30	31	32	33	34	35	36
sample	TM827	TM1181	TM613	TM932	TM922	TM941	TM934.1	TM1447	TM1447	TM1324	TM1324	TM1324
rocktype	hz	hz	lherz	lherz	lherz	amph-hz	amph-du	cpx-du	pl-lherz	du,rim	du,core	hz
remark						umyl	sh-zone	banded	banded	banded	banded	banded
unit	5	5	6	6	6	6	6	2	2	1	1	1
TiO2	0.02	0.04	0.01	0.06	0.05	0.00	0.02	0 19	0.18	0.24	0.22	0 16
Al2O3	38.84	40.95	47.92	54.40	49.68	50.55	30.45	37.85	28.52	16.86	17.53	19.01
Cr2O3	28.33	27.44	20.28	14.45	17 87	17.41	33.40	26.58	36.96	48.98	48.96	48.78
Fe tot	14.68	14.36	13.24	11.06	13.99	13.41	23 27	19.19	20.30	23 94	23.25	21.26
MgO	16.56	17.57	17.54	20.43	18.15	19.01	11.69	15.62	12.53	10.15	10.43	11.06
MnO	0.16	0.17	0.14	0.10	0.16	0.16	0.32	0.16	0.14	0.34	0.31	0.27
NiO	0.23	0.18	0.25	n.d.	n.d.	0.30	0.10	0.30	0.06	n.d.	n.d.	n.d.
V2O5	0.20	0.19	0.19	n.d.	n.d.	0.10	0 11	0.20	0.33	n.d.	n.d.	n.d.
SUM	99.02	100.90	99.57	100.50	99.90	100.94	99.36	100.09	99.02	100.51	100.70	100.54
Fe2O3calc	2.36	2.62	0.71	1.68	2.21	2.64	5.05	5.34	2.94	5.02	4.56	3.29
FeOcalc	12.46	11.89	12.57	9.50	12.00	10 94	16.38	14.09	17.47	19.04	18.82	18.09
Ti	0 0004	0.0008	0.0002	0.0012	0.0010	0.0000	0.0005	0.0041	0.0041	0.0057	0.0052	0.0038
Al	1.3008	1.3336	1.5382	1.6676	1.5837	1.5774	1.0810	1.2676	1.0188	0.6329	0 6541	0.7034
Cr	0.6364	0.5994	0.4366	0.2971	0.3820	0.3644	0.7954	0 5971	0 8856	1.2333	1.2253	1.2106
Fetot	0 3487	0.3316	0.3014	0.2404	0 3162	0 2968	0.5859	0 4558	0.5143	0.6373	0.6152	0 5579
Mg	0.7009	0.7231	0.7115	0.7915	0.7310	0.7497	0.5245	0 6611	0.5656	0.4815	0.4918	0.5172
Mn	0.0038	0.0040	0.0032	0.0022	0.0037	0.0036	0.0082	0.0038	0 0036	0.0092	0.0083	0.0072
Ni	0.0053	0.0040	0.0055	n.d	n.d.	0.0064	0.0024	0.0069	0.0015	n.d.	n.d.	n d
V	0.0038	0.0035	0.0034	n.d.	n.d.	0.0017	0.0022	0 0038	0.0066	n.d.	n d	n d.
Fe(III)calc	0.0507	0.0550	0.0146	0.0329	0.0450	0.0529	0.1161	0 1160	0.0676	0.1223	0.1101	0.0784
Fe(II)calc	0.2979	0.2767	0.2868	0.2075	0.2712	0.2438	0.4698	0.3398	0.4466	0.5151	0.5051	0.4794
Cr#	33	31	22	15	19	19	42	32	47	66	65	63
Mg#	70	72	71	79	72	75	53	66	56	48	49	52
Fe#	15	17	5	14	14	18	20	25	13	19	18	14

Tab. B-8a (continued)

ref #	37	38	39	40	41	42
sample	TM1189.1	TM1189.1	TM1189.2	TM1189.2	LH 62	LH 87
rocktype	hz, core	hz, rim	hz, core	hz, rim	hz	hz
remark	near opxt	near opxt	far opxt	far opxt		
unit	3	3	3	3	SH	SH
TiO2	0.06	0.07	0 02	0.03	0.06	0.09
Al2O3	18.39	17.69	35.64	36.93	18.84	14.23
Cr2O3	49 94	51.21	31.78	30.68	50.37	53.79
Fe tot	21.92	22.48	15.55	15.28	18 89	20 56
MgO	9 80	9.39	16 09	15.76	11.55	10 05
MnO	0.25	0.34	0.21	0.21	0.29	0.28
NiO	n.d.	n.d.	0.20	0.16	0.05	0 00
V2O5	n.d.	n.d.	0.20	0.18	0.29	0 00
SUM	100.36	101.18	99.69	99.23	100.34	99.00
Fe2O3calc	2.17	2.02	2.85	1.94	1.90	2.40
FeOcalc	19.82	20.52	12.86	13 45	17.18	18 40
Ti	0 0014	0.0017	0.0004	0.0006	0.0014	0.0022
Al	0.6893	0.6622	1.2050	1.2499	0.7004	0 5526
Cr	1.2556	1.2859	0.7207	0.6965	1.2557	1.4008
Fetot	0.5827	0 5968	0.3729	0.3667	0 4979	0.5661
Mg	0 4642	0.4442	0.6875	0.6741	0.5425	0.4931
Mn	0.0067	0.0091	0.0051	0.0051	0.0077	0.0078
Ni	n.d.	n.d.	0.0046	0 0037	0.0013	0.0000
V	n.d.	n.d.	0.0038	0.0034	0.0060	0.0000
Fe(III)calc	0.0522	0.0485	0.0621	0.0421	0.0451	0 0595
Fe(II)calc	0.5305	0.5483	0.3108	0.3246	0.4528	0.5066
Cr#	65	66	37	36	64	71
Mg#	47	45	69	67	54	49
Fe#	9	8	17	11	9	10

Tab. B-8b

ref #	1	2	3	4	5	6	7	8	9	10	11	12	13
sample	TM862	TM1315	TM1321	TM1360	TM1360	TM849	TM886	TM1420	TM873	TM1454	TM1232	TM1232	TM1340
lithol.	lherz	hz	du	pl-wehrl	cpx-du	pl-hz	hz	lherz	hz	lherz	hz	hz	hz
remark				banded	banded	pl band					with sp	granular	
unit	1	1	1	1	1	2	2	2	2	2	3	3	3
SiO2	53.43	53.71	53.08	51.76	52.47	53.91	52.84	52.71	52.75	51.90	53.54	54.06	54.74
TiO2	0.20	0.03	0.26	0.36	0.26	0.06	0.20	0.22	0.06	0.07	0.01	0.03	0.02
Al2O3	2.95	1.65	1.43	3.97	2.85	3.57	3.14	3.20	2.80	4.05	1.69	2.35	1.81
Cr2O3	0.84	0.68	0.45	1.21	1.00	1.16	1.11	1.10	0.80	1.07	0.54	0.80	0.89
FeO	2.71	2.50	1.83	2.53	2.27	2.67	2.33	2.73	2.36	2.64	1.78	1.76	1.95
MgO	17.98	17.83	16.89	16.92	16.99	17.64	17.42	17.36	16.61	18.12	17.98	17.68	17.96
MnO	0.08	0.09	0.04	0.07	0.02	0.07	0.09	0.04	0.07	0.09	0.05	0.04	0.06
CaO	22.32	23.11	25.44	22.48	23.87	21.41	21.61	22.05	23.66	21.91	23.28	23.79	23.17
NiO	0.00	0.08	0.03	0.00	0.08	0.05	0.00	0.00	0.04	0.14	0.02	0.01	0.02
Na2O	0.28	0.18	0.12	0.52	0.33	0.44	0.59	0.30	0.15	0.28	0.04	0.07	0.23
K2O	0.00	0.01	0.05	0.01	0.01	0.00	0.00	0.00	0.01	0.00	0.00	0.00	0.00
SUM	100.79	99.87	99.62	99.63	100.15	100.98	99.33	99.71	99.31	100.27	98.93	100.59	100.85
Si	1.9232	1.9538	1.9445	1.8898	1.9108	1.9301	1.9266	1.9188	1.9321	1.8817	1.9582	1.9459	1.9634
Ti	0.0054	0.0008	0.0072	0.0099	0.0071	0.0016	0.0055	0.0060	0.0017	0.0019	0.0003	0.0008	0.0005
Al	0.1252	0.0708	0.0618	0.1710	0.1224	0.1508	0.1350	0.1374	0.1210	0.1732	0.0729	0.0998	0.0766
Cr	0.0239	0.0196	0.0130	0.0349	0.0288	0.0329	0.0320	0.0317	0.0232	0.0307	0.0156	0.0228	0.0253
Fe	0.0816	0.0761	0.0561	0.0711	0.0691	0.0799	0.0710	0.0831	0.0723	0.0801	0.0544	0.0530	0.0585
Mg	0.9645	0.9666	0.9221	0.9206	0.9221	0.9412	0.9466	0.9418	0.9067	0.9791	0.9800	0.9484	0.9601
Mn	0.0024	0.0028	0.0012	0.0022	0.0006	0.0021	0.0028	0.0012	0.0022	0.0028	0.0015	0.0012	0.0018
Ca	0.8608	0.9008	0.9986	0.8794	0.9314	0.8213	0.8442	0.8601	0.9286	0.8512	0.9123	0.9175	0.8905
Ni	0.0000	0.0023	0.0009	0.0000	0.0023	0.0014	0.0000	0.0000	0.0012	0.0041	0.0006	0.0003	0.0006
Na	0.0195	0.0127	0.0085	0.0368	0.0233	0.0305	0.0417	0.0212	0.0107	0.0197	0.0028	0.0049	0.0160
K	0.0000	0.0005	0.0023	0.0005	0.0005	0.0000	0.0000	0.0000	0.0005	0.0000	0.0000	0.0000	0.0000
Mg#	92.2	92.7	94.3	92.8	93.0	92.2	93.0	91.9	92.6	92.4	94.7	94.7	94.3
%en	50.6	49.7	46.6	49.2	48.0	51.1	50.8	50.0	47.5	51.3	50.3	49.4	50.3
%woll	45.1	46.3	50.5	47.0	48.4	44.6	45.3	45.6	48.7	44.6	46.9	47.8	46.6
%fs	4.3	3.9	2.8	3.8	3.6	4.3	3.8	4.4	3.8	4.2	2.8	2.8	3.1

Tab. B-8b (continued)

ref #	14	15	16	17	18	19	20	21	22	23	24	25	26
sample	TM1331.2	TM676	TM733.2	TM1249	TM1245	TM564	TM827	TM1181	TM613	TM932	TM922	TM1447	TM1447
lithol.	du	hz	du	hz	hz	hz	hz	hz	lherz	lherz	lherz	cpx-du	pl-lherz
remark												banded	banded
unit	2	3	3	4	4	TU	5	5	6	6	6	2	2
SiO2	52.84	53.79	53.54	54.45	55.95	53.07	52.27	52.18	52.37	52.45	50.54	52.40	52.38
TiO2	0.21	0.02	0.05	0.00	0.02	0.05	0.06	0.05	0.07	0.18	0.12	0.26	0.16
Al2O3	3.27	1.93	2.39	1.52	1.14	2.77	4.18	4.33	4.92	6.81	5.79	4.01	3.09
Cr2O3	0.76	0.55	1.00	0.69	0.97	1.15	1.25	1.21	1.25	1.19	1.15	0.97	1.09
FeO	2.41	2.31	2.67	1.81	1.77	2.36	3.89	3.07	3.31	2.20	3.01	2.70	3.19
MgO	16.09	18.04	16.79	18.26	17.94	18.62	20.71	18.63	19.26	14.93	16.18	16.00	17.81
MnO	0.04	0.06	0.05	0.04	0.03	0.10	0.10	0.12	0.09	0.09	0.11	0.06	0.09
CaO	24.40	22.90	23.77	23.88	22.58	21.88	18.15	20.93	18.89	21.25	22.14	22.25	21.30
NiO	0.00	0.05	0.08	0.12	0.04	0.04	0.05	0.05	0.13	0.02	0.07	0.03	0.09
Na2O	0.36	0.09	0.31	0.06	0.50	0.08	0.14	0.11	0.20	1.32	0.30	0.19	0.27
K2O	0.00	0.00	0.00	0.00	0.01	0.01	0.00	0.00	0.01	0.00	0.00	0.00	0.01
SUM	100.38	99.83	100.65	100.83	101.01	100.13	100.80	100.68	100.50	100.44	99.41	98.87	99.48
Si	1.9191	1.9524	1.9387	1.9573	1.9969	1.9200	1.8742	1.8800	1.8802	1.8860	1.8529	1.9213	1.9139
Ti	0.0057	0.0005	0.0014	0.0000	0.0005	0.0014	0.0016	0.0014	0.0019	0.0049	0.0033	0.0072	0.0044
Al	0.1401	0.0826	0.1021	0.0644	0.0480	0.1182	0.1768	0.1840	0.2083	0.2888	0.2504	0.1734	0.1332
Cr	0.0218	0.0158	0.0286	0.0196	0.0274	0.0329	0.0355	0.0345	0.0355	0.0338	0.0333	0.0281	0.0315
Fe	0.0732	0.0701	0.0809	0.0544	0.0528	0.0714	0.1167	0.0925	0.0994	0.0662	0.0923	0.0828	0.0975
Mg	0.8709	0.9759	0.9061	0.9783	0.9543	1.0039	1.1067	1.0003	1.0305	0.8001	0.8840	0.8743	0.9698
Mn	0.0012	0.0018	0.0015	0.0012	0.0027	0.0031	0.0030	0.0037	0.0027	0.0027	0.0034	0.0019	0.0028
Ca	0.9496	0.8941	0.9223	0.9198	0.8635	0.8482	0.6973	0.6080	0.7267	0.8188	0.8697	0.8742	0.8339
Ni	0.0000	0.0015	0.0023	0.0035	0.0011	0.0012	0.0014	0.0014	0.0038	0.0006	0.0021	0.0009	0.0026
Na	0.0254	0.0063	0.0218	0.0042	0.0346	0.0056	0.0097	0.0077	0.0139	0.0920	0.0213	0.0135	0.0191
K	0.0000	0.0000	0.0000	0.0000	0.0005	0.0005	0.0000	0.0000	0.0005	0.0000	0.0000	0.0000	0.0005
Mg#	92.2	93.3	91.8	94.7	94.8	93.4	90.5	91.5	91.2	92.4	90.5	91.3	90.9
%en	46.0	50.3	47.5	50.1	51.0	52.2	57.6	52.6	55.5	47.5	47.9	47.7	51.0
%woll	50.1	46.1	48.3	47.1	46.2	44.1	36.3	42.5	39.1	48.6	47.1	47.7	43.9
%fs	3.9	3.6	4.2	2.8	2.8	3.7	6.1	4.9	5.4	3.9	5.0	4.5	5.1

Tab. B-8b (continued)

ref #	27	28	29	30	31
sample	TM1324	TM1189.1	TM1189.2	LH 62	LH87
lithol.	hz	hz	hz	hz	hz
remark	banded	near opxt	far opxt		
unit	1	3	3	SH	SH
SiO2	53.70	54 20	52.97	53.52	55.18
TiO2	0.09	0.03	0 03	0.04	0.03
Al2O3	1.46	1.52	3.31	0.88	0.80
Cr2O3	0.68	0.90	1.09	0 43	0.48
FeO	2.46	2.53	2.13	1.78	2.01
MgO	17.84	18.45	17.96	18.43	18.68
MnO	0.04	0.06	0.07	0.06	0.09
CaO	22.84	21.62	22.86	24.70	21.86
NiO	0.08	0.06	0.02	0.10	0.08
Na2O	0.26	0.16	0.13	0.14	0.20
K2O	0.00	0.00	0.00	0.00	0.01
SUM	99.45	99.53	100.57	100.08	99.42
Si	1.9600	1.9681	1.9103	1.9479	1.9984
Ti	0.0025	0.0008	0.0008	0.0011	0.0008
Al	0.0629	0.0651	0.1408	0.0378	0.0342
Cr	0 0196	0.0259	0.0311	0.0124	0.0138
Fe	0.0751	0.0768	0.0642	0.0542	0 0609
Mg	0.9704	0.9985	0.9653	0.9997	1.0082
Mn	0.0012	0.0018	0.0021	0.0018	0.0028
Ca	0.8932	0.8412	0.8834	0.9633	0.8483
Ni	0.0023	0.0018	0.0006	0.0029	0.0023
Na	0.0184	0.0113	0 0091	0.0099	0.0140
K	0.0000	0.0000	0.0000	0.0000	0.0005
Mg#	92.8	92.9	93.8	94.9	94.3
%en	50.1	52.1	50.5	49 6	52.6
%woll	46.1	43.9	46.2	47 8	44.2
%fs	3.9	4 0	3.4	2.7	3.2

Tab. B-8c

ref #	1	2	3	4	5	6	7	8	9	10	11	12	13
sample	TM862	TM1315	TM849	TM886	TM1420	TM873	TM1454	TM1232	TM1340	TM676	TM1249	TM1245	TM564
lithol.	lherz	hz	pl-hz	hz	lherz	hz	lherz	hz	hz	hz	hz	hz	hz
remark			pl-band										
unit	1	1	2	2	2	2	2	3	3	3	4	4	TU
SiO2	56.24	57.52	55.04	55.00	55.12	56.80	55.71	55.72	56.27	57.05	55.95	57.58	56.92
TiO2	0.09	0.01	0.03	0.11	0.09	0.04	0.03	0.00	0.00	0.03	0.03	0.00	0.02
Al2O3	2.53	1.32	2.98	2.47	2.32	3.16	3.15	2.68	1.55	2.39	1.42	0.92	2.55
Cr2O3	0.66	0.56	0.69	0.67	0.52	0.70	0.64	0.84	0.61	0.83	0.66	0.52	0.80
FeO	6.34	5.73	6.39	6.00	6.20	6.57	6.13	5.42	5.66	5.36	5.84	5.29	5.53
MgO	32.53	33.57	32.73	33.23	33.42	33.03	32.[illegible]	32.72	32.70	32.80	34.19	34.93	33.42
MnO	0.14	0.16	0.11	0.11	0.12	0.11	0.08	0.13	0.09	0.16	0.10	0.11	0.12
CaO	1.24	1.54	1.31	0.98	0.85	1.34	1.51	1.66	2.08	0.93	1.33	1.03	1.46
NiO	0.08	0.06	0.13	0.08	0.08	0.12	0.10	0.14	0.06	0.13	0.01	0.08	0.09
Na2O	n.d.	0.01	0.02	0.00	0.04	0.00	0.00	0.02	0.05	0.00	0.06	0.04	0.04
SUM	99.85	100.48	99.43	98.65	98.76	101.87	100.00	99.33	99.07	99.68	99.59	100.50	100.95
Si	1.9486	1.9753	1.9205	1.9290	1.9318	1.9317	1.9283	1.9382	1.9644	1.9677	1.9444	1.9721	1.9456
Ti	0.0023	0.0003	0.0008	0.0029	0.0024	0.0010	0.0008	0.0000	0.0000	0.0008	0.0008	0.0000	0.0005
Al	0.1034	0.0535	0.1226	0.1022	0.0959	0.1268	0.1286	0.1100	0.0638	0.0972	0.0582	0.0372	0.1028
Cr	0.0181	0.0152	0.0190	0.0186	0.0144	0.0188	0.0175	0.0231	0.0168	0.0226	0.0181	0.0141	0.0216
Fe	0.1837	0.1646	0.1865	0.1760	0.1817	0.1869	0.1774	0.1577	0.1652	0.1546	0.1697	0.1515	0.1581
Mg	1.6798	1.7181	1.7020	1.7369	1.7455	1.6741	1.6842	1.6962	1.7013	1.6860	1.7707	1.7829	1.7024
Mn	0.0041	0.0047	0.0033	0.0033	0.0036	0.0032	0.0023	0.0038	0.0027	0.0047	0.0029	0.0032	0.0035
Ca	0.0460	0.0567	0.0490	0.0368	0.0319	0.0488	0.0560	0.0619	0.0778	0.0344	0.0495	0.0378	0.0535
Ni	0.0022	0.0017	0.0036	0.0023	0.0023	0.0033	0.0028	0.0039	0.0017	0.0036	0.0003	0.0022	0.0025
Na	n.d.	0.0007	0.0014	0.0000	0.0027	0.0000	0.0000	0.0013	0.0034	0.0000	0.0040	0.0027	0.0027
Mg#	90.1	91.3	90.1	90.8	90.6	90.0	90.5	91.5	91.1	91.6	91.3	92.2	91.5
%en	88.0	88.6	87.8	89.1	89.1	87.7	87.8	88.5	87.5	89.9	89.0	90.4	88.9
%woll	2.4	2.9	2.5	1.9	1.6	2.6	2.9	3.2	4.0	1.8	2.5	1.9	2.8
%fs	9.6	8.5	9.6	9.0	9.3	9.8	9.3	8.2	8.5	8.2	8.5	7.7	8.3

Tab. B-8c (continued)

ref #	14	15	16	17	18	19	20	21	22	23	24
sample	TM827	TM1181	TM932	TM922	TM941	TM1447	TM1324	TM1189.1	TM1189.2	LH 62	LH 87
lithol.	hz	hz	lherz	lherz	amph-hz	pl-lherz	hz	hz	hz	hz	hz
remark					umyl	banded	banded	near opxt	far opxt		
unit	5	5	6	6	UMY	2	1	3	3	SH	SH
SiO2	55.39	55.06	52.57	54.75	53.95	56.20	56.45	57.30	55.42	56.62	57.14
TiO2	0.03	0.01	0.08	0.08	0.04	0.06	0.00	0.03	0.01	0.00	0.08
Al2O3	3.46	3.86	6.10	5.15	5.43	2.46	1.47	1.42	2.98	1.13	0.86
Cr2O3	0.77	0.86	0.89	1.00	0.83	0.64	0.57	0.64	0.68	0.38	0.35
FeO	5.79	5.84	6.31	5.93	6.40	5.82	6.40	5.61	5.69	5.85	5.76
MgO	32.27	32.36	31.41	31.32	32.93	33.06	33.11	33.04	33.29	34.86	34.88
MnO	0.11	0.17	0.12	0.09	0.12	0.15	0.14	0.07	0.10	0.11	0.13
CaO	1.59	1.67	1.70	2.81	0.49	1.45	1.30	1.03	1.17	0.85	0.95
NiO	0.12	0.07	0.13	0.09	0.09	0.11	0.05	0.11	0.14	0.10	0.12
Na2O	n.d.	0.02	0.12	0.05	n.d.	0.07	0.00	n.d.	n.d.	0.03	0.00
SUM	99.53	99.92	99.43	101.27	100.28	100.02	99.49	99.25	99.48	99.93	100.27
Si	1.9245	1.9085	1.8409	1.8797	1.8638	1.9427	1.9643	1.9861	1.9248	1.9564	1.9663
Ti	0.0008	0.0003	0.0021	0.0021	0.0010	0.0016	0.0000	0.0008	0.0003	0.0000	0.0021
Al	0.1418	0.1578	0.2520	0.2086	0.2213	0.1003	0.0603	0.0581	0.1221	0.0461	0.0349
Cr	0.0212	0.0236	0.0247	0.0272	0.0227	0.0175	0.0157	0.0175	0.0187	0.0104	0.0095
Fe	0.1682	0.1693	0.1848	0.1703	0.1849	0.1683	0.1863	0.1626	0.1653	0.1690	0.1658
Mg	1.6710	1.6716	1.6393	1.6026	1.6955	1.7031	1.7171	1.7068	1.7231	1.7951	1.7888
Mn	0.0032	0.0050	0.0036	0.0026	0.0035	0.0044	0.0041	0.0021	0.0029	0.0032	0.0038
Ca	0.0592	0.0620	0.0638	0.1034	0.0181	0.0537	0.0485	0.0383	0.0435	0.0315	0.0350
Ni	0.0034	0.0020	0.0037	0.0025	0.0025	0.0031	0.0014	0.0031	0.0039	0.0028	0.0033
Na	n.d.	0.0013	0.0081	0.0033	n.d.	0.0047	0.0000	n.d.	n.d.	0.0020	0.0000
Mg#	90.9	90.8	89.9	90.4	90.2	91.0	90.2	91.3	91.2	91.4	91.5
%en	88.0	87.8	86.8	85.4	89.3	88.5	88.0	89.5	89.2	90.0	89.9
%woll	3.1	3.3	3.4	5.5	1.0	2.8	2.5	2.0	2.3	1.6	1.8
%fs	8.9	8.9	9.8	9.1	9.7	8.7	9.5	8.5	8.6	8.5	8.3

Tab. B-8d

ref #	1	2	3	4	5	6	7	8	9	10	11	12	13
sample	TM862	TM1315	TM1321	TM1360	TM849	TM886	TM1420	TM873	TM1454	TM1331.2	TM1232	TM1340	TM676
rocktype	pl-lherz	hz	du	pl-wehrl	pl-hz	hz	lherz	hz	lherz	du	hz	hz	hz
remark													
unit	1	1	1	1	2	2	2	2	2	2	3	3	3
SiO2	40.02	40.80	40.65	40.26	39.61	39.72	40.07	40.07	40.88	40.29	40.56	40.40	40.65
Cr2O3	0.00	0.00	0.00	0.00	0.02	0.02	0.00	0.00	0.00	0.05	0.02	0.00	0.00
FeO	10.10	8.66	9.71	10.05	10.05	9.38	9.45	8.79	9.31	11.58	7.96	8.97	8.29
MgO	49.20	50.88	48.56	49.13	48.93	49.73	49.42	50.73	49.68	47.82	50.01	50.24	49.76
CaO	0.04	0.02	0.17	0.04	0.04	0.02	0.04	0.02	0.02	0.15	0.02	0.02	0.00
NiO	0.38	0.35	0.28	0.38	0.40	0.42	0.40	0.38	0.47	0.36	0.45	0.49	0.40
SUM	99.74	100.71	99.37	99.86	99.05	99.29	99.38	99.99	100.36	100.25	99.02	100.12	99.10
Si	0.9872	0.9893	1.0025	0.9911	0.9845	0.9821	0.9890	0.9808	0.9972	0.9946	0.9971	0.9878	0.9993
Cr	0.0000	0.0000	0.0000	0.0000	0.0004	0.0004	0.0000	0.0000	0.0000	0.0010	0.0004	0.0000	0.0000
Fe	0.2084	0.1756	0.2003	0.2069	0.2089	0.1940	0.1951	0.1799	0.1899	0.2391	0.1637	0.1834	0.1704
Mg	1.8087	1.8385	1.7847	1.8024	1.8125	1.8324	1.8179	1.8505	1.8060	1.7592	1.8322	1.8308	1.8230
Ca	0.0011	0.0005	0.0045	0.0011	0.0011	0.0005	0.0011	0.0005	0.0005	0.0040	0.0005	0.0005	0.0000
Ni	0.0075	0.0068	0.0056	0.0075	0.0080	0.0084	0.0079	0.0075	0.0092	0.0071	0.0089	0.0096	0.0079
Fo(ol)	89.7	91.3	89.9	89.7	89.7	90.4	90.3	91.1	90.5	88.0	91.8	90.9	91.5

Tab. B-8d (continued)

ref #	14	15	16	17	18	19	20	21	22	23	24	25	26
sample	TM733 2	TM1193	TM1249	TM1245	TM26	TM959	TM564	TM1169	TM827	TM1181	TM932	TM922	TM941
rocktype	du	du	hz	hz	du	du	hz	du	hz	hz	lherz	lherz	amph-hz
remark													u-myl
unit	3	3	4	4	4	4	TU	TU	5	5	6	6	6
SiO2	40.44	41 49	40.21	40.69	41.38	40.71	40 72	41.44	40 57	40 88	40.90	40.59	40.76
Cr2O3	0.00	0.01	0.00	0.00	0.00	0.00	0.02	0.00	0.01	0 00	0.0.	0 04	0.00
FeO	9.81	5.62	8.41	8.09	8.11	7.75	9.16	7 44	9.01	9.09	9.68	9.00	9.21
MgO	49.23	51.32	50.15	49.46	50.82	50.94	50.73	50.97	49.04	49.83	49.47	50.11	49.45
CaO	0.11	0.12	0.00	0.04	0.04	0.04	0.02	0.05	0.04	0.02	0.04	0.00	0 02
NiO	0.35	0.54	0.40	0.41	0.39	0.36	0.31	0 36	0.45	0.38	0.35	0 38	0 34
SUM	99.94	99.10	99.17	98.69	100.74	99.80	100.96	100.26	99.12	100 20	100.65	100.12	99.78
Si	0.9933	1.0074	0.9897	1.0033	0.9993	0.9920	0.9872	1 0021	1.0006	0.9974	0.9968	0.9916	0.9989
Cr	0.0000	0.0002	0.0000	0.0000	0.0000	0.0000	0.0004	0.0000	0.0002	0.0000	0.0002	0.0008	0.0000
Fe	0.2015	0.1141	0.1731	0.1668	0.1638	0.1579	0.1857	0.1505	0 1859	0 1855	0.2014	0 1839	0.1666
Mg	1 8021	1.8571	1.8396	1.8175	1.8290	1.8499	1.8328	1 8370	1.8026	1.8118	1.7968	1.8244	1.8061
Ca	0.0029	0.0031	0.0000	0.0011	0.0010	0.0010	0.0005	0.0013	0.0011	0.0005	0.0010	0.0000	0.0005
Ni	0.0069	0.0105	0.0079	0.0081	0.0076	0.0071	0.0060	0.0070	0 0089	0.0075	0.0069	0.0075	0.0067
Fo(ol)	89.9	94.2	91.4	91.6	91.8	92.1	90.8	92.4	90.7	90.7	89.9	90.7	90.5

Tab. B-8d (continued)

ref #	27	28	29	30	31	32	33
sample	TM1447	TM1447	TM1324	TM1189.1	TM1189.2	LH62	LH87
rocktype	cpx du	pl-lherz	hz	hz	hz	hz	hz
remark	banded	banded		near opxt	far opxt		
unit	6	2	1	3	3	SH	SH
SiO2	40.82	41.64	40.43	41.46	40.85	40.64	40.27
Cr2O3	0.00	0.04	0.00	0.01	0.00	0.10	0.02
FeO	9.64	10.16	9.66	8.85	8.41	8.76	8.80
MgO	49.55	49.80	49.59	49.77	50.18	50.07	49.43
CaO	0.11	0.04	0.02	0.03	0.04	0.02	0.02
NiO	0.33	0.23	0.34	0.44	0.46	0.38	0.40
SUM	100.45	101.91	100.04	100.56	99.94	99.97	98.94
Si	0.9960	1.0017	0.9913	1.0057	0.9968	0.9932	0.9947
Cr	0.0000	0.0008	0.0000	0.0002	0.0000	0.0019	0.0004
Fe	0.1967	0.2044	0.1981	0.1795	0.1716	0.1790	0.1818
Mg	1.8019	1.7855	1.8121	1.7993	1.8248	1.8237	1.8197
Ca	0.0029	0.0010	0.0005	0.0008	0.0010	0.0005	0.0005
Ni	0.0065	0.0045	0.0067	0.0086	0.0090	0.0075	0.0079
Fo(ol)	90.2	89.7	90.1	90.9	91.4	91.1	90.9

Tab. B-8e

ref #	1	2	3	4	5	6	7	8	9	10
sample	TM1459	TM1118	TM1136.2	TM1222	TM934.1	TM941	TM941	TM1228.3	LH 73	LH 87
lithol.	pl-du	hz	hz	lherz	amph-du	amph-hz	amph-hz	lherz	hz	hz
remark			sh. zone	sh. zone	sh. zone	umyl	umyl	umyl		
unit	2	2	2	6	6	6	6	6	SH	SH
amph-na	parg	trem	ed-hbl	mag-hbl	ed-hbl	parg-hbl	parg	parg-hbl	trem	trem
SiO2	41.45	54.62	46.97	47.7	47.53	44.63	43.37	44.31	54.67	55.14
TiO2	0.21	0.05	0.46	0.2	0.17	0.19	1.72	0.13	0.05	0.06
Al2O3	15.97	3.57	9.54	11.25	10.61	13.34	13.71	15.65	4.32	2.82
Cr2O3	0.14	1.36	1.19	1.41	1.58	2.09	0.91	0.13	1.28	0.65
FeO	3.78	2.77	3.19	3.37	3.64	3.93	4.09	5.65	1.86	2.41
MgO	16.66	21.64	20.23	19.16	18.9	17.73	17.74	16.71	22.13	22.46
MnO	0.04	0.07	0.04	0.06	0.03	0.09	0.1	0.03	0.05	0.04
CaO	13.33	12.57	12.15	12.38	13.07	10.77	10.55	12.04	12.56	12.8
NiO	0.12	0.05	0.08	0.17	0.22	0.06	0.05	0.08	0.07	0.11
Na2O	3.11	0.69	1.95	1.63	2.21	3.82	3.48	2.43	0.61	0.65
K2O	0.42	0.02	0.02	0.27	0.23	0.42	0.19	0.05	0.03	0.04
SUM	95.23	97.41	95.82	97.6	98.19	97.07	96.51	97.21	97.63	97.18
Si	6.0603	7.5652	6.7204	6.6959	6.6797	6.3773	6.2369	6.3045	7.5170	7.6348
Ti	0.0231	0.0052	0.0495	0.0211	0.0180	0.0204	0.1860	0.0139	0.0052	0.0062
Al	2.7541	0.5832	1.6100	1.8627	1.7588	2.2484	2.3255	2.6264	0.7006	0.4606
Cr	0.0162	0.1490	0.1347	0.1566	0.1756	0.2362	0.1035	0.0146	0.1392	0.0712
Fe	0.4622	0.3209	0.3817	0.3956	0.4278	0.4697	0.5641	0.6723	0.2139	0.2791
Mg	3.6302	4.4669	4.3137	4.0084	3.9585	3.7757	3.8020	3.5433	4.5348	4.6347
Mn	0.0050	0.0082	0.0048	0.0071	0.0036	0.0109	0.0122	0.0036	0.0058	0.0047
Ca	2.0883	1.8655	1.8627	1.8621	1.9681	1.6490	1.6257	1.8356	1.8504	1.8991
Ni	0.0141	0.0056	0.0092	0.0192	0.0249	0.0069	0.0058	0.0092	0.0077	0.0123
Na	0.8817	0.1853	0.5410	0.4437	0.6022	1.0584	0.9704	0.6704	0.1626	0.1745
K	0.0783	0.0035	0.0037	0.0484	0.0412	0.0766	0.0349	0.0091	0.0053	0.0071
Mg#	88.7	93.3	91.9	91.0	90.2	88.9	87.1	84.1	95.5	94.3

Tab. B-9 (following seven pages). Average compositions of phase chemistry in the Bay of Islands Ophiolite. The data are averaged for each structural unit. For each unit, orthopyroxene-bearing and orthopyroxene-free assemblages are separated. Data for ultramafic cumulates are taken from Komor et al. (1985a). (a) Spinel, for legend of Cr#, Mg#, and Fe#, see Tab. B-2; (b) clinopyroxene; (c) orthopyroxene; (d) olivine.

Tab. B-9a

UNIT	LITHOLOGY	N	#SPOT	#ANAL		TiO2	Al2O3	Cr2O3	Fe tot	MgO	MnO	NiO	V2O5	SUM	Ti	Al
ULTRAMAFIC CUMULATES	DUNITE+ WEHRL/CPXTE	30			avg	0.35	27.11	36.53	23.89	10.50	0.31	n.d.	0.48	99.21	0.0082	0.9771
					std	0.07	7.26	6.83	2.44	1.32	0.05	n.d.	0.08	0.66	0.0019	0.2238
UNITS 1,2	MASSIVE DU, WEHRLITE	12	37	91	avg	0.25	38.03	27.08	18.47	15.68	0.17	0.20	0.21	100.08	0.0054	1.2673
					std	0.13	6.21	5.51	2.83	1.84	0.03	0.05	0.03	0.83	0.0029	0.1624
UNIT 1	OPX-BEARING PERIDOTITE	5	18	35	avg	0.12	24.69	41.01	21.31	12.08	0.22	0.09	0.19	99.70	0.0027	0.8840
					std	0.06	7.25	6.46	3.00	1.75	0.04	0.08	0.16	0.56	0.0013	0.2277
UNIT 1	OPX-FREE PERIDOTITE	2	6	13	avg	0.23	20.63	44.17	24.67	10.38	0.26	0.03	0.17	100.54	0.0055	0.7586
					std	0.00	4.19	5.20	0.45	0.29	0.00	0.03	0.17	0.08	0.0002	0.1406
UNIT 2	HARZBURGITE-LHERZOLITE	15	47	78	avg	0.07	34.89	32.37	17.51	14.72	0.17	0.13	0.18	100.03	0.0015	1.1874
					std	0.06	4.05	4.14	1.83	1.27	0.04	0.08	0.10	0.85	0.0013	0.1133
UNIT 2	OPX-FREE PERIDOTITE	2	5	15	avg	0.11	36.83	28.87	18.80	14.96	0.17	0.20	0.22	100.15	0.0024	1.2430
					std	0.08	0.49	2.21	1.53	0.03	0.01	0.06	0.02	0.00	0.0016	0.0134
UNIT 3	HARZBURGITE	32	89	212	avg	0.03	29.98	37.78	17.51	13.93	0.18	0.10	0.20	98.71	0.0007	1.0441
					std	0.02	5.82	5.96	1.79	1.85	0.03	0.06	0.09	5.92	0.0004	0.1698
UNIT 3	DUNITE	12	25	56	avg	0.07	21.04	45.36	20.67	11.48	0.23	0.10	0.25	99.19	0.0016	0.7761
					std	0.05	4.20	5.70	2.96	1.21	0.03	0.06	0.13	0.76	0.0012	0.1418
UNIT 4	HARZBURGITE	18	47	102	avg	0.03	22.94	45.31	18.61	11.90	0.21	0.07	0.23	99.32	0.0008	0.8291
					std	0.02	7.79	8.19	2.13	2.17	0.04	0.04	0.11	0.67	0.0005	0.2521
UNIT 4	DUNITE	4	11	27	avg	0.07	9.88	58.36	21.61	8.77	0.27	0.06	0.25	99.27	0.0018	0.3889
					std	0.03	2.93	4.90	1.53	0.88	0.02	0.01	0.06	0.51	0.0008	0.1080
TU	HARZBURGITE	12	34	75	avg	0.02	27.77	40.67	16.84	13.60	0.20	0.07	0.20	99.38	0.0005	0.9786
					std	0.01	6.63	7.00	1.48	2.00	0.03	0.05	0.13	0.60	0.0003	0.1971
TU	DUNITE	2	5	10	avg	0.07	10.18	59.56	17.35	10.34	0.26	0.06	0.26	98.08	0.0017	0.4018
					std	0.03	1.53	1.84	1.28	0.92	0.02	0.01	0.02	0.67	0.0008	0.0575
UNIT 5	HARZBURGITE	13	37	74	avg	0.02	39.01	28.63	15.13	16.30	0.15	0.15	0.18	99.57	0.0005	1.3012
					std	0.01	3.03	3.42	0.82	0.76	0.01	0.05	0.06	0.68	0.0001	0.0834
UNIT 6	LHERZOLITE	16	43	76	avg	0.04	49.93	17.72	13.38	18.46	0.11	0.22	0.12	99.98	0.0008	1.5751
					std	0.02	4.52	4.63	0.88	0.97	0.02	0.12	0.06	0.99	0.0004	0.1072
UNIT 6	ULTRAMYL	6	21	50	avg	0.04	47.88	18.64	16.53	16.86	0.15	0.22	0.10	100.44	0.0008	1.5242
					std	0.02	8.14	8.61	2.05	2.09	0.03	0.13	0.06	0.58	0.0005	0.2065
SPRINGERS HILL	HARZBURGITE	13	35		avg	0.09	14.48	54.38	20.70	10.15	0.28	0.01	0.04	100.13	0.0023	0.5501
					std	0.04	2.54	2.64	1.03	0.78	0.03	0.02	0.10	0.74	0.0011	0.0682

Tab. B-9a (continued)

UNIT	LITHOLOGY	Cr	Fetot	Mg	Mn	Ni	V	Fe(III)	Fe(II)	Cr#	Mg#	Fe#	Fe2O3c	FeOc
ULTRAMAFIC	DUNITE+	0.8968	0.6180	0.4806	0.0080	n.d.	0.0097	0.0773	0.5406	48.1	47.1	12.0	3.25	20.71
CUMULATES	WEHRL/CPXTE	0.1895	0.0817	0.0435	0.0015	n.d.	0.0017	0.0453	0.0456	11.0	4.4	4.9	1.75	1.14
UNITS 1,2	MASSIVE DU.	0.6126	0.4409	0.6612	0.0040	0.0046	0.0039	0.0974	0.3435	32.7	65.8	21.9	4.47	14.21
	WEHRLITE	0.1410	0.0810	0.0560	0.0007	0.0011	0.0007	0.0270	0.0592	7.8	5.8	3.4	1.12	1.96
UNIT 1	OPX-BEARING	1.0018	0.5500	0.5497	0.0058	0.0021	0.0039	0.0972	0.4528	53.3	54.8	16.9	4.09	17.35
	PERIDOTITE	0.1931	0.0973	0.0592	0.0011	0.0019	0.0032	0.0522	0.0591	11.3	5.9	6.0	2.03	1.56
UNIT 1	OPX-FREE	1.0958	0.6454	0.4837	0.0070	0.0007	0.0035	0.1243	0.5211	59.1	48.1	19.3	5.19	19.60
	PERIDOTITE	0.1488	0.0002	0.0045	0.0002	0.0007	0.0035	0.0018	0.0017	7.6	0.2	0.3	0.02	0.43
UNIT 2	HARZBURGITE	0.7425	0.4242	0.6337	0.0041	0.0030	0.0035	0.0565	0.3678	38.5	63.3	13.3	2.57	15.06
	LHERZOLITE	0.1087	0.0511	0.0421	0.0011	0.0017	0.0020	0.0146	0.0445	5.7	4.3	3.0	0.66	1.54
UNIT 2	OPX-FREE	0.6538	0.4499	0.6382	0.0040	0.0046	0.0041	0.0862	0.3637	34.4	63.7	18.7	3.95	15.02
	PERIDOTITE	0.0517	0.0355	0.0004	0.0001	0.0013	0.0004	0.0338	0.0016	2.0	0.1	6.0	1.55	0.04
UNIT 3	HARZBURGITE	0.8934	0.4367	0.6142	0.0047	0.0024	0.0040	0.0493	0.3873	46.1	61.3	11.6	2.20	15.41
		0.1726	0.0588	0.0615	0.0010	0.0013	0.0019	0.0155	0.0635	8.8	6.3	4.1	0.71	2.01
UNIT 3	DUNITE	1.1293	0.5432	0.5361	0.0060	0.0025	0.0052	0.0758	0.4674	59.2	53.4	13.2	3.17	17.59
		0.1636	0.0807	0.0474	0.0009	0.0016	0.0028	0.0514	0.0492	7.8	4.8	7.2	2.13	1.54
UNIT 4	HARZBURGITE	1.1241	0.4863	0.5476	0.0056	0.0018	0.0048	0.0309	0.4554	57.5	54.6	6.4	1.32	17.34
		0.2539	0.0736	0.0767	0.0014	0.0010	0.0024	0.0319	0.0776	12.9	7.7	6.6	1.37	2.28
UNIT 4	DUNITE	1.5508	0.6059	0.4378	0.0078	0.0015	0.0056	0.0400	0.5659	79.8	43.6	6.3	1.59	20.05
		0.1540	0.0387	0.0366	0.0006	0.0003	0.0013	0.0427	0.0346	6.2	3.6	6.6	1.72	0.92
TU	HARZBURGITE	0.9763	0.4262	0.6075	0.0052	0.0017	0.0041	0.0319	0.3943	49.9	60.7	8.0	1.42	15.49
		0.2029	0.0538	0.0657	0.0009	0.0012	0.0026	0.0243	0.0681	10.3	6.7	6.4	1.09	2.17
TU	DUNITE	1.5790	0.4866	0.5162	0.0074	0.0015	0.0058	-0.0015	0.4881	79.7	51.4	-0.3	-0.06	17.41
		0.0602	0.0395	0.0422	0.0005	0.0003	0.0006	0.0028	0.0423	2.9	4.2	0.6	0.11	1.39
UNIT 5	HARZBURGITE	0.6422	0.3584	0.6874	0.0036	0.0034	0.0033	0.0457	0.3127	33.0	68.7	12.8	2.13	13.12
		0.0851	0.02..	0.0230	0.0003	0.0011	0.0011	0.0116	0.0235	4.4	2.3	3.1	0.55	0.83
UNIT 6	LHERZOLITE	0.3778	0.3003	0.7367	0.0026	0.0047	0.0021	0.0394	0.2609	19.3	73.8	13.1	1.94	11.56
		0.1069	0.0248	0.0216	0.0005	0.0026	0.0011	0.0113	0.0227	5.5	2.2	3.5	0.56	0.77
UNIT 6	ULTRAMYL.	0.4079	0.3770	0.6799	0.0035	0.0048	0.0019	0.0607	0.3163	21.1	68.3	16.7	2.95	13.75
		0.2042	0.0582	0.0619	0.0008	0.0027	0.0011	0.0148	0.0637	10.6	6.3	5.2	0.74	2.40
SPRINGERS	HARZBURGITE	1.3907	0.5598	0.4882	0.0077	0.0002	0.0009	0.0519	0.5079	71.7	49.0	9.2	2.11	18.66
HILL		0.0868	0.0352	0.0296	0.0008	0.0005	0.0021	0.0148	0.0282	4.5	2.9	2.3	0.59	0.76

Tab. B-9b

UNIT	LITHOLOGY	N	#spots		SiO2	TiO2	Al2O3	Cr2O3	FeO	MgO	MnO	CaO	NiO	Na2O	SUM	Si
ULTRA[illegible]	DUNITE+	48		avg	53.13	0.04	1.92	0.67	2.89	17.81	0.12	23.29	0.00	0.15	99.95	1.9359
CUMUL[illegible]	WEHRL/CPXTE			std	0.45	0.02	0.37	0.13	0.33	0.26	0.02	0.26	0.00	0.01	0.40	0.0098
UNITS 1,2	MASSIVE DUNITE	9	17	avg	52.12	0.32	3.53	0.85	2.41	16.33	0.05	23.83	0.05	0.34	99.84	1.9036
				std	1.02	0.14	0.90	0.24	0.29	0.53	0.02	0.75	0.03	0.11	0.80	0.0239
UNIT 1	OPX-BEARING	4	10	avg	53.44	0.09	2.25	0.85	2.73	17.96	0.07	22.38	0.05	0.26	100.09	1.9386
	PERIDOTITE			std	0.63	0.08	0.51	0.10	0.13	0.38	0.02	0.35	0.02	0.09	1.14	0.0070
UNIT 1	OPX-FREE	1	5	avg	53.23	0.11	2.29	0.79	3.27	17.54	0.11	22.39	0.05	0.19	99.97	1.9380
	PERIDOTITE			std	0.00	0.00	0.00	0.00	0.00	0.00	0.00	0.00	0.00	0.00	0.00	0.0000
UNIT 2	HARZBURGITE	10	25	avg	53.12	0.10	3.27	1.02	2.60	17.59	0.08	22.28	0.06	0.30	100.41	1.9196
				std	0.58	0.07	0.51	0.09	0.16	0.32	0.01	0.55	0.03	0.12	0.65	0.0117
UNIT 2	DUNITE+	1	2	avg	51.79	0.27	3.83	0.92	2.66	16.47	0.07	23.21	0.05	0.20	99.45	1.8975
	WEHRLITE			std	0.00	0.00	0.00	0.00	0.00	0.00	0.00	0.00	0.00	0.00	0.00	0.0000
UNIT 3	HARZBURGITE	29	76	avg	53.53	0.03	2.53	0.91	2.23	17.92	0.07	22.84	0.07	0.13	100.27	1.9354
				std	0.64	0.02	0.58	0.15	0.23	0.58	0.02	0.60	0.06	0.06	0.58	0.0173
UNIT 3	DUNITE	2	3	avg	54.41	0.03	1.60	0.78	1.99	17.63	0.04	24.33	0.10	0.30	101.21	1.9544
				std	0.94	0.01	0.81	0.15	0.40	0.81	0.00	0.29	0.05	0.01	0.71	0.0166
UNIT 4	HARZBURGITE	8	17	avg	54.17	0.01	1.99	0.81	2.05	17.95	0.06	23.39	0.06	0.10	100.60	1.9512
				std	0.93	0.01	0.78	0.26	0.20	0.47	0.01	0.56	0.02	0.15	0.58	0.0244
TU	HARZBURGITE	7	16	avg	53.52	0.03	2.49	1.07	2.00	17.75	0.08	22.86	0.04	0.17	100.02	1.9385
				std	0.67	0.01	0.55	0.09	0.13	0.13	0.02	0.44	0.02	0.16	0.53	0.0192
UNIT 5	HARZBURGITE	9	25	avg	52.90	0.04	3.63	1.13	2.55	18.05	0.09	21.83	0.05	0.12	100.39	1.9090
				std	0.70	0.01	0.28	0.08	0.26	0.73	0.02	0.81	0.02	0.05	0.70	0.0131
UNIT 6	LHERZOLITE	10	27	avg	52.23	0.15	4.93	0.96	2.46	16.83	0.09	21.84	0.06	0.51	100.05	1.8912
				std	0.69	0.12	0.86	0.18	0.43	0.70	0.02	1.10	0.02	0.45	1.09	0.0128
UNIT 6	ULTRAMYL.	3	8	avg	53.61	0.06	2.93	0.39	2.85	16.96	0.07	23.11	0.04	0.35	100.38	1.9396
				std	0.78	0.01	0.98	0.21	0.79	0.69	0.02	0.31	0.02	0.17	0.16	0.0213
SPRINGERS	HARZBURGITE	12		avg	54.57	0.02	0.79	0.52	1.80	18.24	0.06	23.60	0.04	0.16	99.79	1.9797
HILL				std	0.35	0.01	0.12	0.06	0.13	0.39	0.01	0.34	0.02	0.04	0.68	0.0087

1 from Komor et al. (1985)

Tab. B-9b (continued)

UNIT	LITHOLOGY	Ti	Al	Cr	Fe	Mg	Mn	Ca	Ni	Na	%en	%wol	%fs	Mg#
ULTRAMAFIC	DUNITE+	0.0011	0.0826	0.0192	0.0881	0.9672	0.0036	0.9092	0.0000	0.0104	49.2	46.3	4.5	91.7
CUMULATES[1]	WEHRL/CPXTE	0.0004	0.0159	0.0038	0.0103	0.0119	0.0006	0.0110	0.0000	0.0008	0.6	0.5	0.5	0.9
UNITS 1,2	MASSIVE DUNITE	0.0087	0.1522	0.0244	0.0737	0.8886	0.0016	0.9330	0.0015	0.0238	46.9	49.2	3.9	92.3
		0.0040	0.0395	0.0069	0.0089	0.0232	0.0006	0.0329	0.0009	0.0077	1.1	1.0	0.5	1.0
UNIT 1	OPX-BEARING PERIDOTITE	0.0025	0.0960	0.0244	0.0829	0.9711	0.0022	0.8702	0.0016	0.0186	50.5	45.2	4.3	92.1
		0.0020	0.0207	0.0026	0.0044	0.0219	0.0007	0.0202	0.0005	0.0060	0.9	0.7	0.2	0.5
UNIT 1	OPX-FREE PERIDOTITE	0.0030	0.0985	0.0228	0.0995	0.9519	0.0033	0.8734	0.0015	0.0132	49.5	45.4	5.2	90.5
		0.0000	0.0000	0.0000	0.0000	0.0000	0.0000	0.0000	0.0000	0.0000	0.0	0.0	0.0	0.0
UNIT 2	HARZBURGITE	0.0026	0.1393	0.0291	0.0787	0.9472	0.0025	0.8626	0.0017	0.0209	50.2	45.7	4.2	92.3
		0.0018	0.0223	0.0025	0.0050	0.0162	0.0003	0.0192	0.0007	0.0085	0.7	0.7	0.3	0.5
UNIT 2	DUNITE+ WEHRLITE	0.0074	0.1654	0.0267	0.0814	0.8991	0.0020	0.9112	0.0014	0.0140	47.5	48.2	4.3	91.7
		0.0000	0.0000	0.0000	0.0000	0.0000	0.0000	0.0000	0.0000	0.0000	0.0	0.0	0.0	0.0
UNIT 3	HARZBURGITE	0.0008	0.1080	0.0261	0.0674	0.9655	0.0022	0.8849	0.0019	0.0090	50.3	46.1	3.5	93.5
		0.0005	0.0251	0.0045	0.0069	0.0287	0.0006	0.0241	0.0017	0.0042	1.2	1.3	0.4	0.6
UNIT 3	DUNITE	0.0009	0.0680	0.0222	0.0599	0.9432	0.0013	0.9364	0.0029	0.0207	48.6	48.3	3.1	94.0
		0.0003	0.0348	0.0045	0.0125	0.0348	0.0001	0.0030	0.0014	0.0006	1.2	0.5	0.7	1.4
UNIT 4	HARZBURGITE	0.0003	0.0847	0.0230	0.0617	0.9637	0.0019	0.9030	0.0017	0.0066	50.0	46.8	3.2	94.0
		0.0003	0.0333	0.0073	0.0063	0.0252	0.0003	0.0240	0.0005	0.0103	0.9	0.7	0.3	0.6
TU	HARZBURGITE	0.0008	0.1066	0.0306	0.0605	0.9583	0.0025	0.8873	0.0012	0.0118	50.3	46.5	3.2	94.1
		0.0004	0.0232	0.0024	0.0040	0.0108	0.0006	0.0188	0.0005	0.0110	0.5	0.5	0.2	0.4
UNIT 5	HARZBURGITE	0.0011	0.1543	0.0323	0.0769	0.9706	0.0026	0.8440	0.0016	0.0082	51.3	44.6	4.1	92.7
		0.0003	0.0118	0.0023	0.0081	0.0376	0.0005	0.0328	0.0006	0.0035	1.7	1.9	0.4	0.6
UNIT 6	LHERZOLITE	0.0040	0.2106	0.0275	0.0746	0.9080	0.0026	0.8475	0.0017	0.0357	49.6	46.3	4.1	92.4
		0.0031	0.0358	0.0051	0.0130	0.0345	0.0006	0.0463	0.0006	0.0317	1.3	1.5	0.8	1.3
UNIT 6	ULTRAMYL.	0.0017	0.1253	0.0111	0.0862	0.9144	0.0021	0.8960	0.0012	0.0247	48.2	47.2	4.5	91.4
		0.0003	0.0424	0.0059	0.0242	0.0344	0.0006	0.0104	0.0005	0.0117	1.4	0.2	1.3	2.5
SPRINGERS HILL	HARZBURGITE	0.0005	0.0338	0.0148	0.0546	0.9859	0.0020	0.9174	0.0012	0.0110	50.4	46.9	2.8	94.8
		0.0003	0.0050	0.0018	0.0037	0.0175	0.0004	0.0133	0.0005	0.0027	0.7	0.8	0.2	0.3

[1] from Komor et al. (1985)

Tab. B-9c

UNIT	LITHOLOGY	N	#SPOTS		SiO2	TiO2	Al2O3	Cr2O3	FeO	MgO	MnO	CaO	NiO	Na2O	SUM	Si
UNIT 1	OPX-BEARING HARZBURGITE	4	8	AVG	56.73	0.05	1.82	0.56	6.00	33.55	0.13	1.28	0.09	0.02	100.22	1.9561
				STD	0.78	0.03	0.43	0.04	0.25	0.56	0.01	0.11	0.02	0.02	0.72	0.0117
UNIT 2	HARZBURGITE + LHERZOLITE	8	16	AVG	55.60	0.05	2.64	0.64	6.18	33.21	0.12	1.27	0.10	0.02	99.82	1.9235
				STD	0.39	0.03	0.31	0.04	0.12	0.25	0.02	0.15	0.04	0.01	0.76	0.0069
UNIT 3	HARZBURGITE	17	35	AVG	55.54	0.02	2.52	0.70	5.86	33.28	0.12	1.31	0.10	0.02	99.47	1.9317
				STD	0.84	0.01	0.49	0.06	0.39	0.41	0.01	0.29	0.01	0.01	0.77	0.0167
UNIT 4	HARZBURGITE	9	18	AVG	56.55	0.01	1.80	0.60	5.71	33.82	0.12	1.12	0.09	0.02	99.84	1.9546
				STD	0.71	0.02	0.63	0.11	0.26	0.74	0.02	0.28	0.02	0.01	1.00	0.0188
TU	HARZBURGITE	5	10	AVG	55.98	0.02	2.29	0.75	5.45	33.39	0.12	1.34	0.11	0.02	99.48	1.9426
				STD	0.60	0.01	0.58	0.06	0.20	0.72	0.00	0.39	0.02	0.02	0.72	0.0156
UNIT 5	HARZBURGITE	8	12	AVG	55.39	0.03	3.20	0.77	6.00	32.56	0.12	1.68	0.10	0.02	99.88	1.9218
				STD	0.50	0.01	0.26	0.07	0.25	0.39	0.02	0.30	0.02	0.02	0.78	0.0063
UNIT 6	LHERZOLITE	7	16	AVG	54.36	0.06	4.47	0.72	6.23	32.07	0.13	1.59	0.10	0.03	99.75	1.8907
				STD	0.65	0.05	0.84	0.11	0.23	0.76	0.03	0.40	0.02	0.04	0.91	0.0133
UNIT 6	ULTRAMYL.	3	6	AVG	55.43	0.03	3.45	0.26	7.93	32.74	0.14	0.45	0.07	0.03	100.54	1.9175
				STD	0.57	0.00	0.38	0.17	1.74	1.42	0.04	0.08	0.03	0.03	0.42	0.0178
SPRINGERS HILL	HARZBURGITE	8	18	AVG	57.43	0.02	0.88	0.35	5.57	34.97	0.13	0.65	0.10	0.02	100.11	1.9745
				STD	0.26	0.01	0.17	0.06	0.16	0.40	0.01	0.10	0.02	0.01	0.50	0.0054

Tab. B-9c (continued)

UNIT	LITHOLOGY	Ti	Al	Cr	Fe	Mg	Mn	Ca	Ni	Na	%en	%wo!l	%fs	Mg#
UNIT 1	OPX-BEARING	0.0013	0.0740	0.0152	0.1730	1.7241	0.0037	0.0473	0.0024	0.0015	88.7	2.4	8.9	90.9
	HARZBURGITE	0.0009	0.0181	0.0012	0.0078	0.0213	0.0004	0.0039	0.0005	0.0010	0.4	0.2	0.5	0.5
UNIT 2	HARZBURGITE+	0.0013	0.1079	0.0175	0.1794	1.7172	0.0034	0.0471	0.0028	0.0014	88.3	2.4	9.2	90.5
	LHERZOLITE	0.0007	0.0122	0.0010	0.0040	0.0108	0.0004	0.0056	0.0010	0.0007	0.2	0.3	0.2	0.2
UNIT 3	HARZBURGITE	0.0006	0.1032	0.0193	0.1706	1.7252	0.0036	0.0489	0.0028	0.0014	88.7	2.5	8.8	91.0
		0.0004	0.0202	0.0017	0.0118	0.0186	0.0004	0.0108	0.0003	0.0010	0.7	0.6	0.6	0.6
UNIT 4	HARZBURGITE	0.0004	0.0733	0.0165	0.1651	1.7420	0.0034	0.0417	0.0025	0.0015	89.4	2.1	8.5	91.3
		0.0004	0.0256	0.0029	0.0077	0.0281	0.0005	0.0106	0.0004	0.0006	0.9	0.6	0.4	0.5
TU	HARZBURGITE	0.0005	0.0939	0.0206	0.1581	1.7267	0.0037	0.0499	0.0031	0.0013	89.2	2.6	8.2	91.6
		0.0003	0.0238	0.0017	0.0057	0.0296	0.0001	0.0148	0.0007	0.0012	1.1	0.8	0.3	0.4
UNIT 5	HARZBURGITE	0.0007	0.1310	0.0211	0.1742	1.6832	0.0036	0.0626	0.0029	0.0010	87.7	3.3	9.1	90.6
		0.0002	0.0108	0.0020	0.0063	0.0142	0.0005	0.0113	0.0005	0.0010	0.4	0.6	0.3	0.3
UNIT 6	LHERZOLITE	0.0015	0.1836	0.0197	0.1813	1.6628	0.0038	0.0591	0.0027	0.0022	87.4	3.1	9.5	90.2
		0.0012	0.0346	0.0030	0.0069	0.0401	0.0008	0.0147	0.0006	0.0029	0.9	0.8	0.4	0.4
UNIT 6	ULTRAMYL.	0.0007	0.1409	0.0072	0.2298	1.6878	0.0042	0.0168	0.0021	0.0018	87.2	0.9	11.9	88.0
		0.0001	0.0162	0.0047	0.0514	0.0659	0.0011	0.0029	0.0008	0.0021	2.8	0.2	2.7	2.7
SPRINGERS HILL	HARZBURGITE	0.0004	0.0357	0.0094	0.1602	1.7915	0.0037	0.0240	0.0026	0.0010	90.7	1.2	8.1	91.8
		0.0003	0.0067	0.0015	0.0047	0.0158	0.0004	0.0037	0.0005	0.0007	0.2	0.2	0.3	0.3

Tab. B-9d

sample	Unit	N	#spots		SiO2	Cr2O3	FeO	MgO	CaO	NiO	SUM	Si	Cr	Fe	Mg	Ca	Ni	Fo(ol)
ULTRAMAFIC CUMULATES*	DUNITE + WEHRLITE	54		AVG	40.26	n.d.	11.71	47.31	0 04	0.18	99.49	1.0003	n.d.	0.2434	1.7514	0.0010	0.0036	87.8
				STD	0.35	n.d.	1.30	1.07	0.08	0.03	0.56	0.0039	n.d.	0.0283	0.0293	0.0021	0.0006	1.4
UNITS 1,2	MASSIVE DUNITE	10	23	AVG	40.47	0.01	10.23	48.33	0.12	0 32	99.47	0.9997	0 0002	0.2113	1.7793	0.0032	0.0064	89 4
				STD	0.25	0 01	0.72	0.64	0.05	0.03	0.47	0.0051	0.0003	0.0155	0.0149	0.0013	0.0005	0.8
UNIT 1	DUNITE/WEHRL.	1	2	AVG	39.64	0 01	12.45	47.53	0 04	0.19	99 85	0 9865	0.0002	0.2590	1.7627	0.0011	0.0038	87.2
UNIT 1	OPX - BEARING PERIDOTITE	5	12	AVG	40 45	0.01	9.13	49 73	0 03	0.39	99 75	0 9926	0.0002	0 1875	1 8187	0.0007	0.0076	90.7
				STD	0.40	0 01	0.52	0.79	0 01	0.03	0 99	0 0013	0.0001	0.0116	0.0118	0.0003	0.0005	0.6
UNIT 2	DUNITE + WEHRLITE	2	4	AVG	40.69	0.01	9.37	50 40	0.06	0.35	100.88	0 9883	0.0002	0 1903	1.8243	0.0015	0.0069	90.6
				STD	0 12	0.00	0.53	0.54	0.04	0.04	0.11	0 0036	0.0000	0.0109	0 0183	0.0010	0.0008	0 6
UNIT 2	HARZBURGITE + LHERZOLITE	10	23	AVG	40.39	0 01	9.44	49 64	0 03	0.40	99.91	0.9911	0.0002	0.1937	1.8152	0.0007	0.0078	90.4
				STD	0 57	0.01	0 34	0 52	0 01	0.03	0.71	0 0080	0.0001	0.0080	0.0135	0.0002	0.0006	0 4
UNIT 3	HARZBURGITE	20	40	AVG	40.58	0.01	8.66	49.87	0 02	0 40	99 55	0 9953	0.0002	0.1776	1.8230	0.0006	0.0080	91.1
				STD	0 31	0 01	0.43	0 46	0.01	0 03	0.67	0.0049	0 0001	0.0087	0.0109	0.0003	0.0007	0.4
UNIT 3	DUNITE	5	10	AVG	40.75	0 01	8 27	49 94	0.08	0.38	99.44	0.9984	0.0002	0.1696	1.8235	0.0022	0.0075	91 5
				STD	0 30	0 01	1.40	0.93	0 07	0 08	0 71	0.0064	0.0002	0.0289	0.0259	0.0018	0.0015	1 4
UNIT 4	HARZBURGITE	8	14	AVG	40.75	0 01	8.73	50.08	0 02	0.40	99.98	0 9953	0.0001	0 1783	1 8228	0.0004	0.0078	91.1
				STD	0.37	0.01	0 52	0.34	0 01	0 01	0.98	0.0038	0 0001	0.0098	0.0052	0.0002	0.0003	0.5
UNIT 4	DUNITE	2	4	AVG	41.11	0 02	7 85	50 87	0 05	0 37	100 26	0.9968	x003	0.1592	1.8382	0 0014	0.0072	92.0
				STD	0 21	0 01	0.34	0.26	0 00	0 03	0.83	0.0016	0.0001	0.0058	0.0029	0.0001	0.0005	0.3
TU	HARZBURGITE	4	10	AVG	40 42	0 02	9 00	49 89	0.03	0 37	99 73	0 9914	0 0004	0.1847	1.8239	0.0008	0 0073	90.8
				STD	0 42	0.00	0 16	0 27	0 00	0 03	0.56	0 0050	0 0001	0.0036	0 0102	0.0001	0.0006	0.2
TU	DUNITE	1	2	AVG	41.12	0.02	7.42	50 45	0.05	0 37	99.42	1.0029	0.0003	0.1513	1.8339	0 0013	0 0073	92 4
UNIT 5	HARZBURGITE + LHERZOLITE	9	22	AVG	40 63	0 01	9 24	49 65	0.03	0 40	99 97	0 9949	0 0003	0 1893	1 8119	0 0007	0 0078	90.5
				STD	0 27	0 01	0 40	0.47	0.01	0 04	0 82	0.0049	0.0001	0.0074	0.0113	0.0002	0.0007	0.4
UNIT 6	LHERZOLITE	9	18	AVG	40 81	0 02	9 52	49 63	0 02	0.40	100 40	0 9959	0 0003	0 1944	1 8051	0 0005	0 0078	90 3
				STD	0 33	0 01	0 42	0 49	0 01	0 04	0 70	0 0061	0 0002	0 0086	0 0120	0 0002	0 0008	0 4
UNIT 6	ULTRAMYL	2	3	AVG	40 65	0 00	10 07	49 02	0 02	0 37	100 12	0 9970	0 0000	0 2066	1 7916	0 0005	0 0072	89 7
				STD	0 26	0 00	0 94	0.82	0 00	0.01	0 15	0 0005	0 0000	0 0204	0 0193	0 0001	0 0001	1.0
SPRINGERS HILL	HARZBURGITE	8		AVG	40 64	0 01	8 58	49 87	0 01	0 39	99 48	0 9965	0 0003	0 1761	1 8225	0 0003	0 0076	91 2
				STD	0 59	0 02	0 31	0 60	0 01	0 07	1 15	0 0051	0 0003	0 0064	0 0085	0 0002	0 0004	0 3

*from Komor et al (1985)

PLATES

All illustrations in the plates are from localities on the eastern limb of the synform at Table Mountain, unless specified otherwise.

PLATE 1

(a) Transition zone of the Table Mountain massif, looking north. Boundary of massive dunite with harzburgite is located in valley. Layered ultramafic cumulates can be seen in foreground and on top of hill on left side.

(b) Chromite seam and diffuse chromite bands in massive dunites of unit 1.

(c) Central dunite band (D) cross-cutting wehrlitic banding (W). A transitional area (T) is symmetrically developed around the dunite band and is depleted in clinopyroxene. Note discontinuous chromite stringer parallel to banding. Top part of massive dunites, unit 2, western limb.

(d) Harzburgite-dunite banding in transition from harzburgite to massive dunites. Unit 1/2 boundary.

(e) Discrete bands of clinopyroxene in harzburgite intersected (?) by lherzolite. Unit 1/2 boundary.

(f) Well developed orthopyroxenitic and websteritic banding near unit 2/3 contact.

(g) Repetitive, subtle banding marked by slight variation of orthopyroxene to olivine ratio in harzburgite. Unit 3.

(h) Patchy distribution of dunite in orthopyroxene-poor harzburgite. Unit 3.

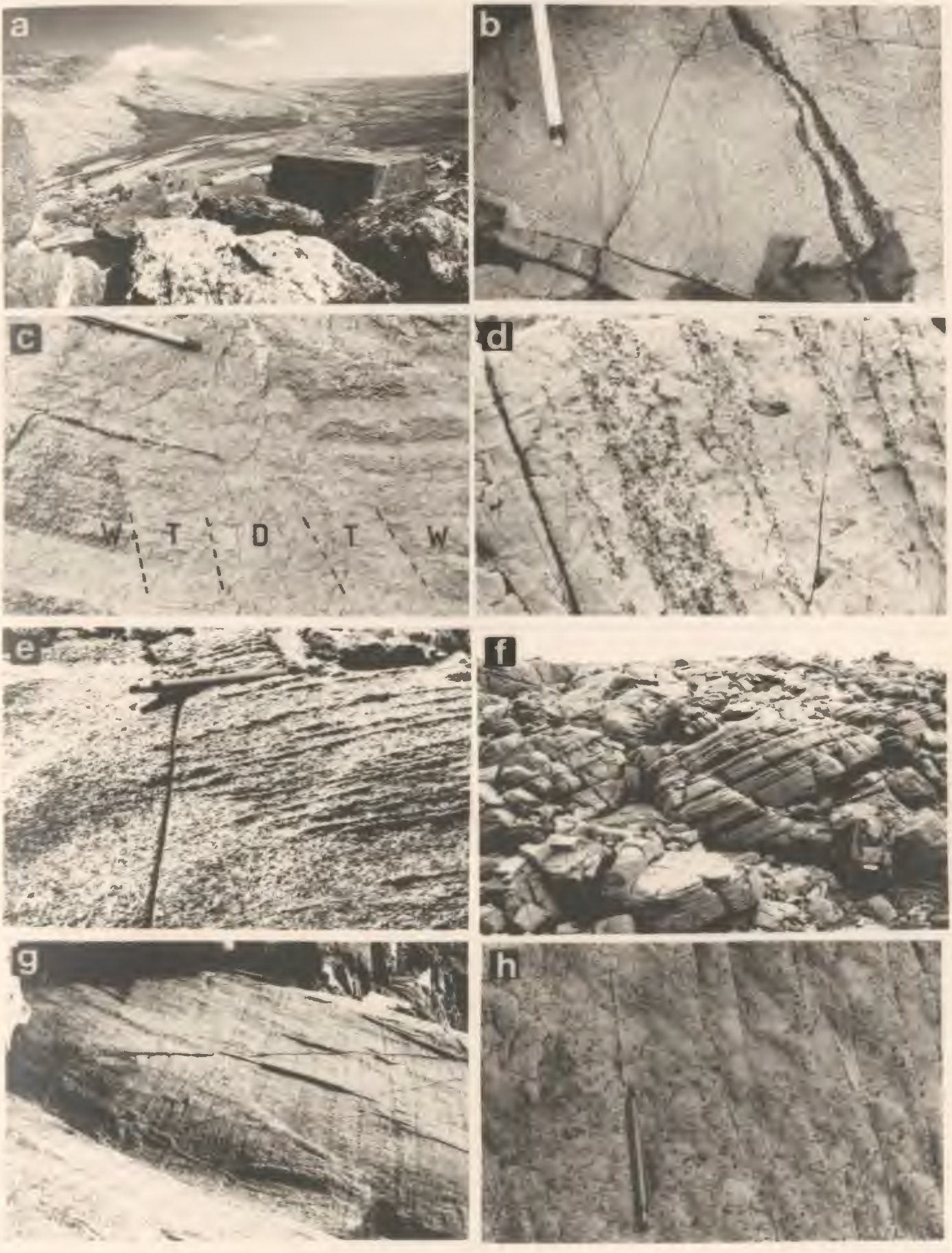
a
b
c
W T D T W
d
e
f
g
h

PLATE 2

(a) Vertically oriented banding showing different intensities of buckling depending on the olivine-pyroxene ratio in the banding. Foliation trace (not visible) is horizontal at high angle to banding. Unit 5.

(b) Mylonitic harzburgite of unit 4. Dark stringer with high relief represents highly recrystallized orthopyroxenitic banding. Note knobby appearance caused by unserpentinized patches of recrystallized olivine which weather out with positive relief.

(c) Orthopyroxene-rich harzburgite or lherzolite with poorly developed shape fabric of pyroxenes. Foliation-trace is parallel to websteritic banding seen in lower part of photo.

(d) Orthopyroxene-ribbon mylonite of unit 6. Dark attenuated lenses represent orthopyroxene-ribbon grains. Knobby appearance is due to unserpentinized, recrystallized patches of olivine (as in Pl. 2b).

(e) Slight folding ("flexure") of banding and foliation along orthopyroxenite dyke located in a grove running from upper left to lower right. Dyke weathers more rapidly than harzburgite and has therefore highly negative relief. Lower part of unit 2.

(f) S-type folds of orthopyroxenitic banding (marked by arrow with F) developed adjacent to orthopyroxenitic dykes. Unit 3, looking northwest.

(g) Open folding of orthopyroxenitic banding with variably oriented axial planes (A.P.). Lower part of unit 3.

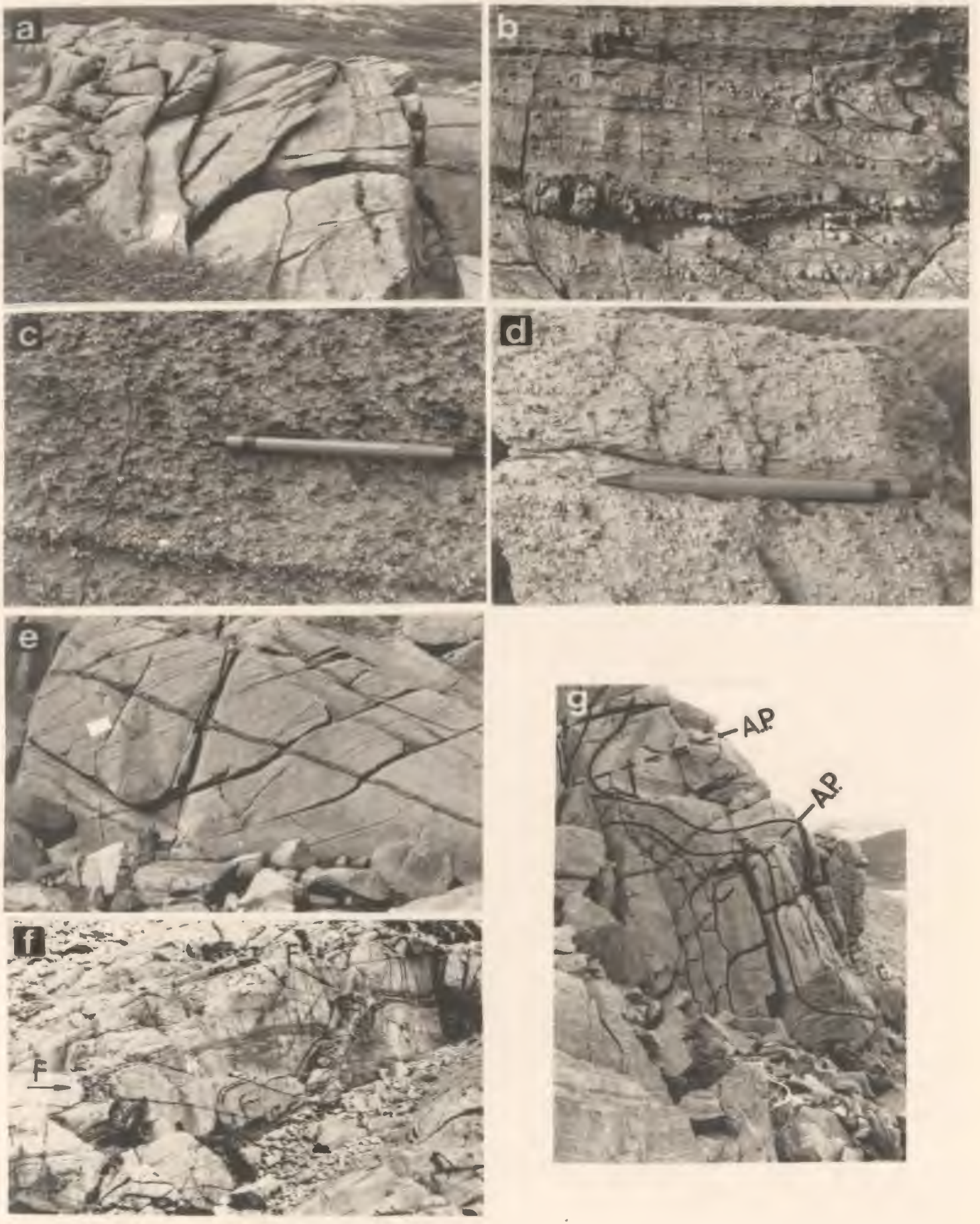
a
b
c
d
e
f
F
F
g
A.P.
A.P.

PLATE 3

(a) S-type fold of orthopyroxenitic banding developed adjacent to boudinaged, olivine orthopyroxenite dyke. The banding contains isoclinal folds which appear to have a Z-asymmetry. Hammer for scale. Lower part of unit 3, looking southwest.

(b) Hook-shaped Z-folds of orthopyroxenitic banding, indicating polyphase deformation. Lower part of unit 3, looking west.

(c) Open folds of orthopyroxenitic banding in TU. Banding is cut and preferentially resorbed by dunite-band. Notebook for scale.

(d) Isoclinal fold of orthopyroxenitic banding in TU. Banding is itself isoclinally folded. The early isoclinal folds have highly attenuated limbs or are rootless.

(e) Orthopyroxenitic to websteritic banding which is buckled but probably has also been affected by an early period of boudinage. Unit 5, pen for scale.

(f) Asymmetric folding affecting orthopyroxenitic banding of unit 5. The shape fabric within these peridotites is L > S. Foliation as determined by bleaching in the laboratory is at high angle to the banding. Looking southeast; pen for scale.

(g) Open folding at right side of picture (south) developing into tight folding at left near a shear zone in the lower left of the picture. Progressive attenuation of fold hinge of banding is probably associated with rotation of fold axis. Fold axis is oriented normal to plane of photo at right (plunging gently to west) but nearly parallel to it at left. Attentuation of fold hinge has been used to infer the sense of shear in the shear zone. A.P. designates axial plane. Unit 3, looking west. Backpack for scale is located to the right of centre of picture.

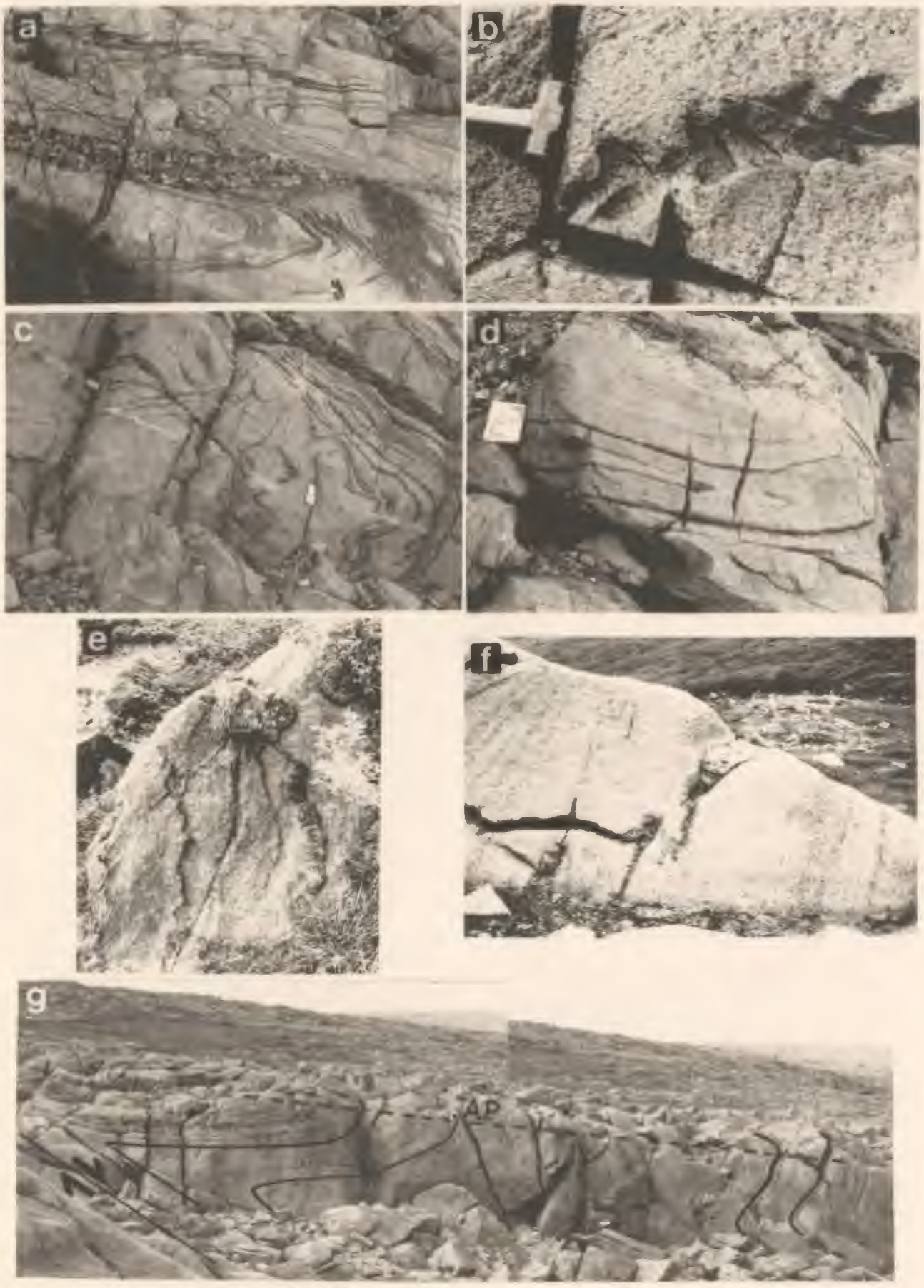
a
b
c
d
e
f
g
AP

PLATE 4

(a) Deflection of an early, strong foliation within unit 6 by anastamozing, typically amphibole-bearing, high strain zones.

(b) Well developed, small-scale shear zone with apparent sinistral sense of shear. Unit 6.

(c) Pegmatitic dyke showing huge single crystal of amphibole. Unit 3, western limb.

(d) Comb-textured, undeformed orthopyroxenite within harzburgites of unit 2, western limb.

(e) En-échelon arrangement of orthopyroxenite dykes intersecting more diffuse lithological banding. Tips of dykes preserve delicate finger-like morphologies which are poorly visible in reproduction. Upper part of unit 3.

(f) Y-shaped branch of an orthopyroxenite dyke. Pen for scale is located above branch-point. Unit 2.

(g) Orthopyroxenite (opx) intersecting wehrlitic banding (cpx) within unit 3. Note dunitic reaction zone around the dyke. Pen for scale is located in fracture in the reaction zone.

(h) Dyke plane containing chocolate-tablet type, orthopyroxenitic boudins. Compass for scale in lower part of picture (very bright). Unit 3.


a
b
c
d
e
f
g
opx
cpx
h

PLATE 5

(a) Highly attenuated boudin of orthopyroxenite dyke. Asymmetric "wings" indicate sinistral shear. Unit 4. Pen for scale lies on top of boudin.

(b) Olivine orthopyroxenite dyke with enrichment of orthopyroxene near dyke margin. Pen is parallel to foliation trace of host harzburgite. Base of unit 4.

(c) Clinopyroxenitic dyke with well developed dunite margin in clinopyroxene-bearing harzburgite. Top of unit 2.

(d) Mutually intersecting dunite bands in harzburgite resulting in a dunite-network. Width of picture is 4 m. Unit 2.

(e) Dunite band reacting preferentially with websteritic banding in harzburgite and transforming websterite into dunite. Unit 5.

(f) Dunite band parallel to foliation within lherzolite of unit 2. Along strike of the dunite band, enrichment of clinopyroxene occurs, transforming dunite into wehrlite.

(g) Dunite cutting across and partially resorbing well developed orthopyroxenitic banding in harzburgite. Unit 3. Hammer for scale.

(h) Contact between dunite pod (at right, with large spinel grains) and harzburgite host. The contact area (marked by arrow) is depleted in orthopyroxene. Unit 3.

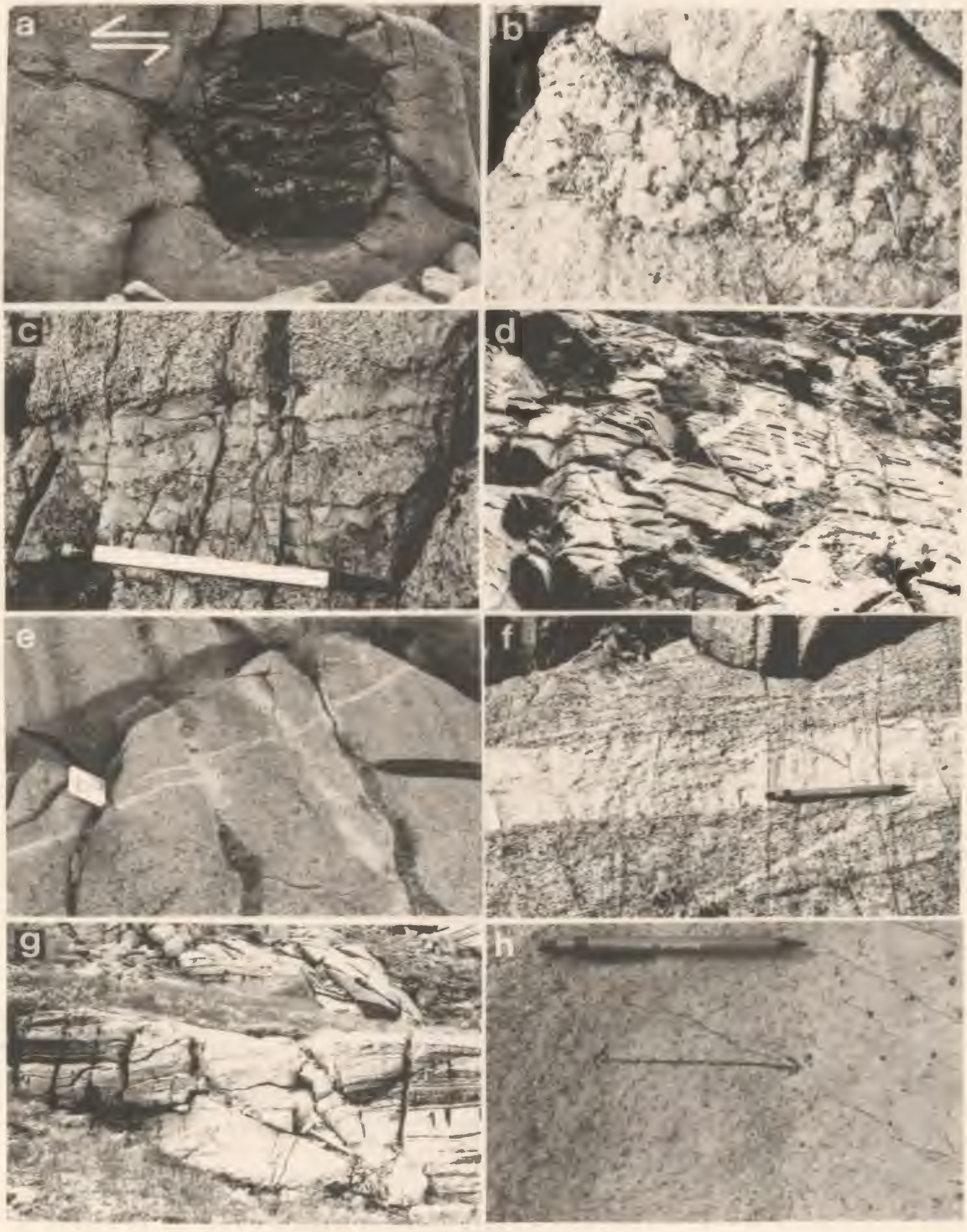
a
b
c
d
e
f
g
h

PLATE 6 (COLOUR)

(a) Intrafolial folds of clinopyroxenitic bands within unit 2. Fold axes are parallel to stretching lineation (indicated by pen).

(b) Intersection of two dunite bands. The steeply oriented band contains clinopyroxenitic dykes. The horizontal band (parallel to the pen) preserves a clinopyroxenitic tension gash at the right side of the picture. The gash intersects the dunite - lherzolite boundary. Unit 2; pen parallel to foliation.

(c) Boundary between a wehrlite band (bottom) and lherzolite or harzburgite. The boundary is marked by enrichment in clinopyroxene. Unit 2, western limb.

(d) Harzburgite with E-W oriented foliation trace. Orthopyroxene grains have their long axis normal to the foliation trace but their cleavage is parallel to it. An origin by pull-apart of formerly large orthopyroxene grains is very likely. TM 747; unit 3; long side of photo is 4.2 mm.

(e) Highly erratic morphology of orthopyroxene in the olivine matrix of a harzburgite. An origin by corrosion is likely. Olivine petrofabric work of the same sample (Fig. 3.9c) indicates a strong lattice fabric which suggests synkinematic corrosion; TM 1232; unit 3; long side of photo 1.7 mm.

(f) Fine grained, equigranular microstructure of a mylonitic harzburgite. Note large spinel grain in upper left, porphyroclastic orthopyroxene grain in upper right, and unserpentinized patch of olivine matrix in lower right. The latter one represents one of the bright yellow knobs visible in hand specimens (cf. Pl. 2b); TM 578.3; unit 4; long side of photo 4.2 mm.

(g) Shard-like opx grains which have their cleavage trace oriented at high angle to the E-W running foliation trace; unit 4; TM 578.3; long side of photo 0.7 mm.

(h) Interstitial clinopyroxene (high relief) within largely serpentinized olivine matrix. In lower left, spinel is intergrown with serpentinized orthopyroxene. An origin by melt-impregnation is suggested for clinopyroxene; TM 1071; unit 5; long side of photo 1.7 mm.

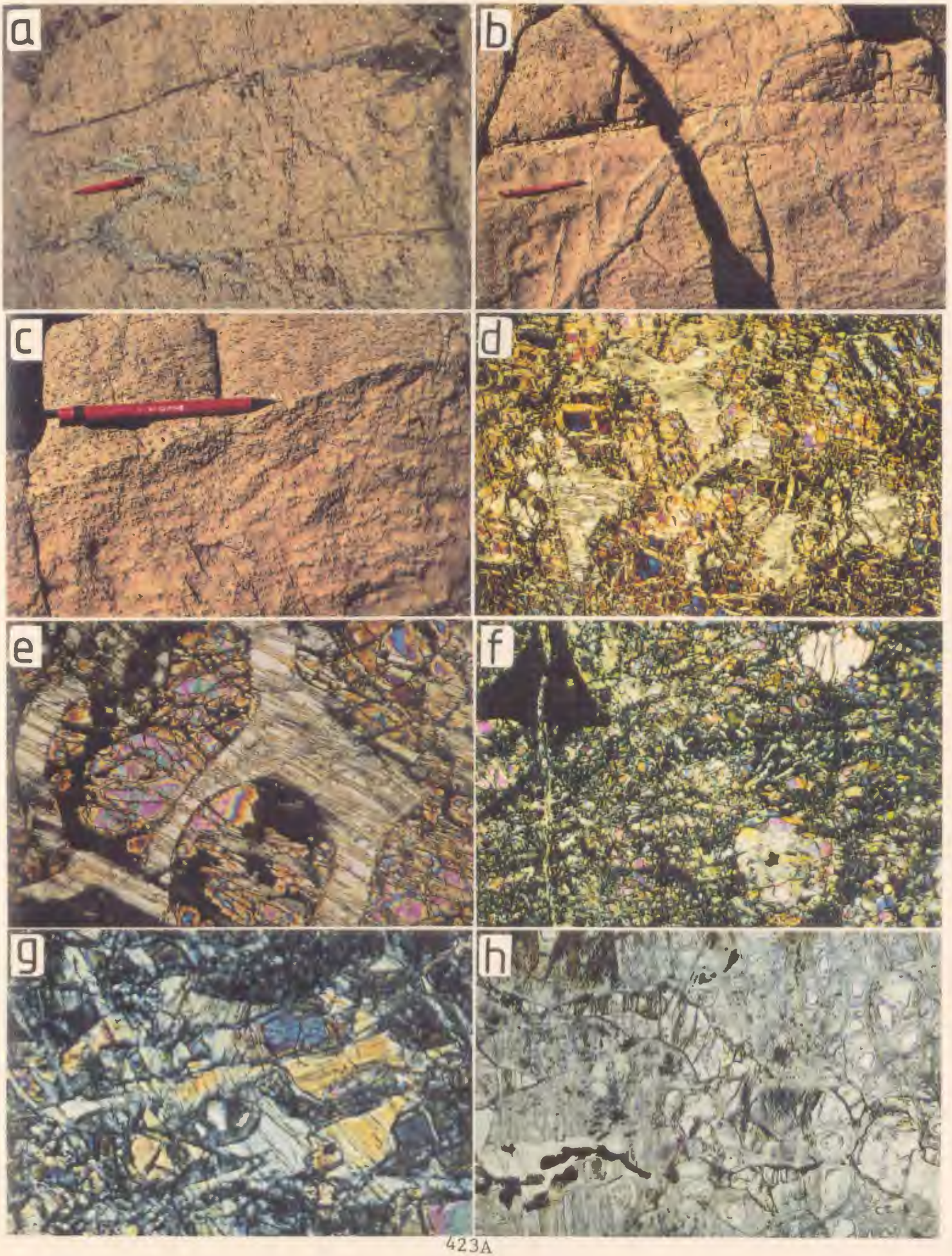
a
b
c
d
e
f
g
h

PLATE 7 (COLOUR)

(a) Thin band ("film") of clinopyroxene between serpentinized olivine matrix, suggesting an origin by melt-impregnation; TM 827; unit 5; long side of photo 0.7 mm.

(b) Simple growth twin of clinopyroxene associated with spinel grain; TM 626; unit 6; long side of photo 0.7 mm.

(c) Simple growth twin of clinopyroxene (upper left) closely associated with spinel. The Spinel-clinopyroxene symplectite is located at margin of large orthopyroxene aggregate; TM 1378; harzburgite sliver within metamorphic sole; long side of photo 1.7 mm.

(d) Interstitial clinopyroxene grains (high relief) in partially serpentinized olivine matrix, located at left side of an orthopyroxene porphyroclast (part of which is seen at right side of picture). Clinopyroxene could represent accumulation of melt in pressure shadow of orthopyroxene grain; foliation trace E-W; TM 922; unit 6; long side of photo 1.7 mm.

(e) Equigranular olivine matrix, oriented obliquely to the E-W running foliation trace. At bottom, an orthopyroxene ribbon grain is visible.; TM 1056; unit 6; long side of photo 3.3 mm.

(f) Equigranular olivine matrix containing large spinel grain (black) and clinopyroxene ribbon grain with extensive orthopyroxene exsolution lamellae (upper right); TM 1063.3; unit 6; long side of photo 4.2 mm.

(g) Orthopyroxene ribbon grain within olivine matrix. Note that olivine matrix contains abundant spinel grains whereas orthopyroxene grain is free of spinel; TM 922; unit 6; long side of photo 11 mm.

(h) Tabular equigranular microstructure in an ultramylonite located directly above the metamorphic sole. Note the presence of amphibole grains (e.g. at top right of central area of photo, difficult to see in reproduction); TM 1225; unit 6, long side of photo 4.2 mm.

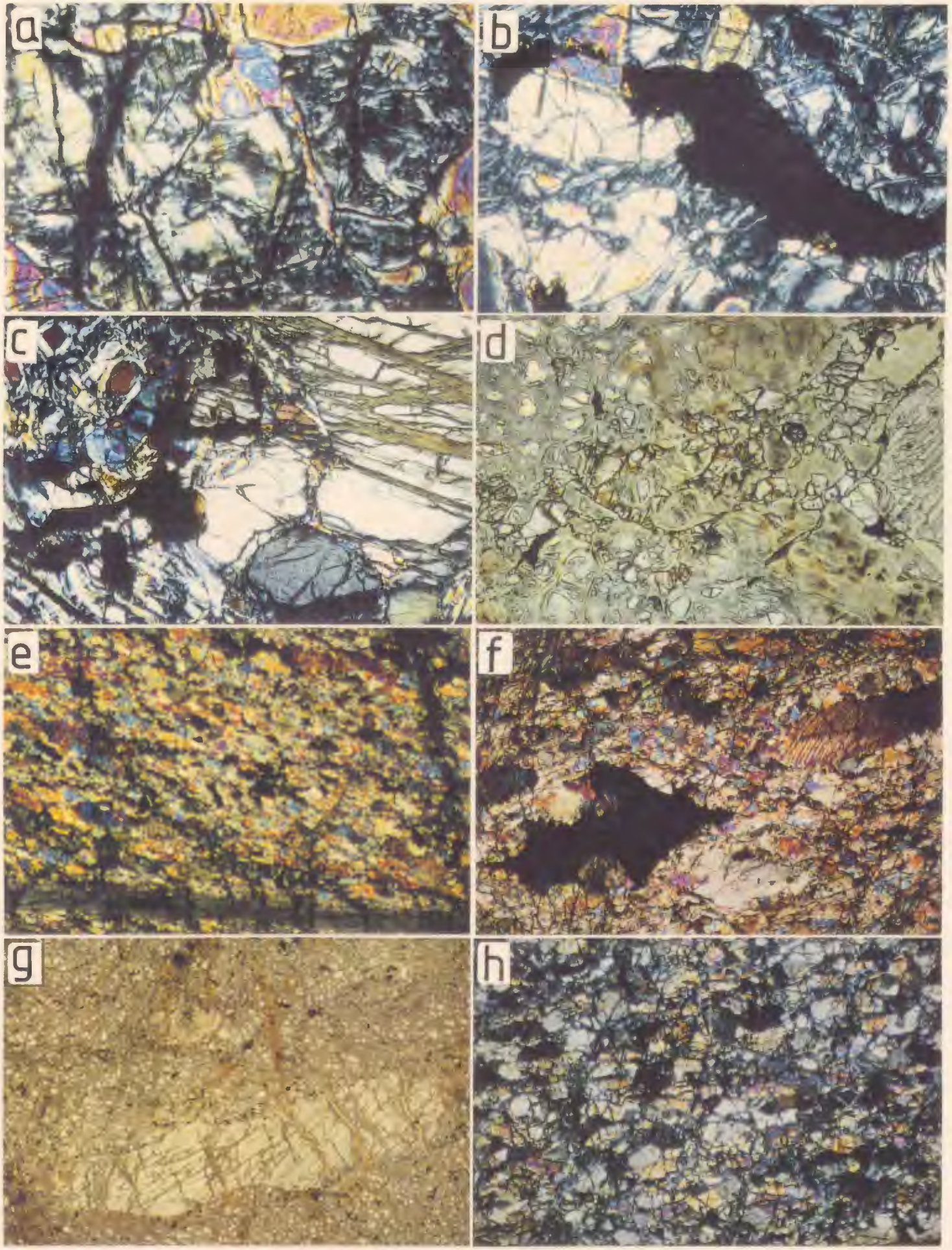
a
b
c
d
e
f
g
h

PLATE 8 (COLOUR)

(a) Symplectic intergrowth of clinopyroxene and spinel in serpentinized olivine matrix. Note the irregular outline of the symplectite grains and a growth twin of clinopyroxene in top part of clinopyroxene/spinel intergrowth with white interference colour. Harzburgite sample LH 122 from basal part of ophiolite in the eastern Lewis Hills; long side of photo 4.2 mm.

(b) Clinopyroxene growth twin in clinopyroxenitic band within harzburgite. Orientation of band is parallel to foliation; TM 1463; unit 2; western limb; long side of photo 4.2 mm.

(c,d) Orthopyroxene aggregate in plane polarized light (c) and crossed polars (d). The aggregate contains spinel exsolutions of uniform orientation. The orientation of the exsolutions does not change across the boundaries of the orthopyroxene neoblasts. TM 1447; unit 2; long side of photos 1.7 mm.

(e) Olivine-amphibole banding in late shear zone within lherzolites of unit 6; TM 934.1, long side of photo 4.2 mm.

(f) Contoured geochemical map of 100 Cr/Cr+Al ratio in spinels within the Table Mountain massif.

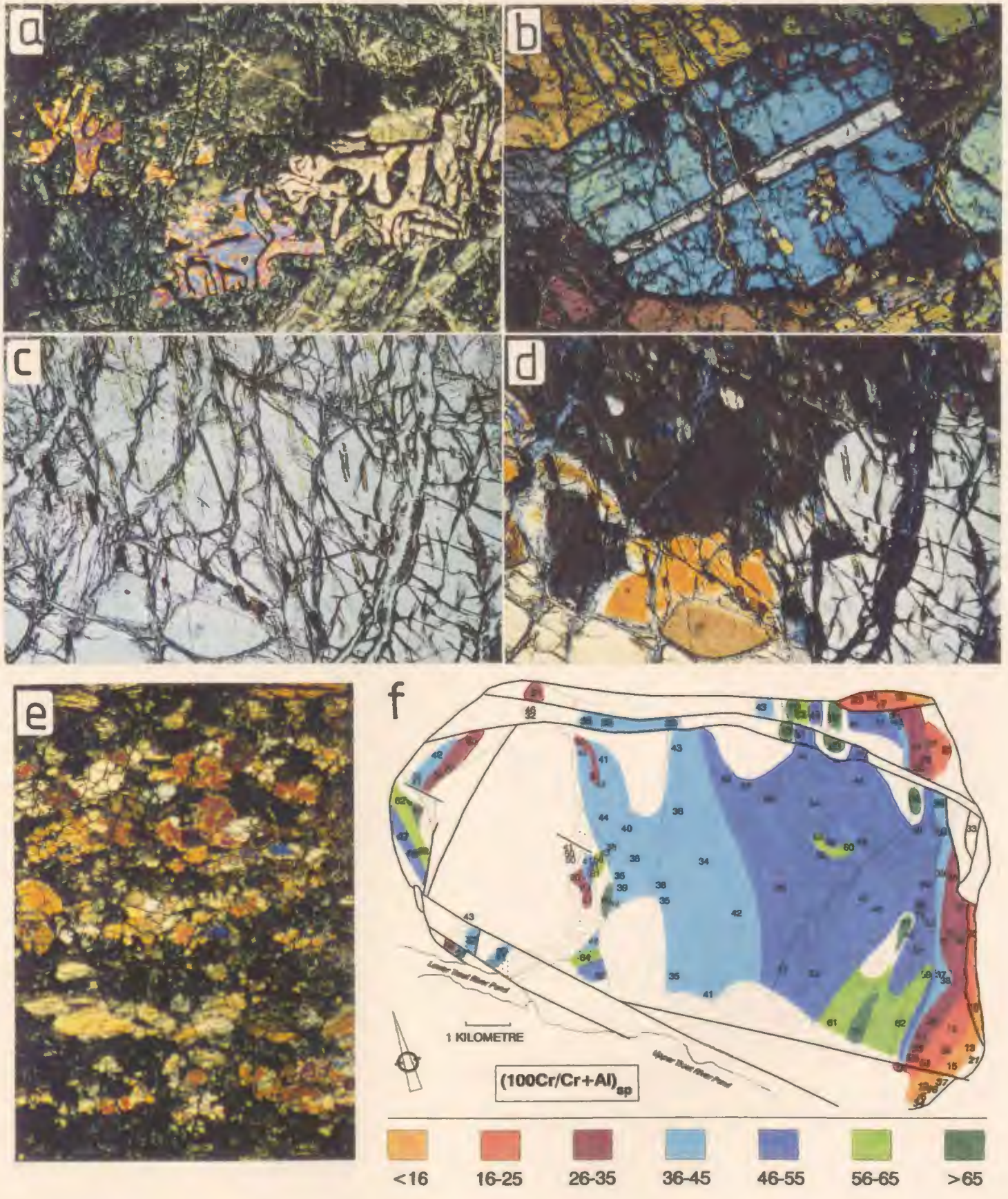
a
b
c
d
e
f
1 KILOMETRE
(100Cr/Cr+Al)sp
<16
16-25
26-35
36-45
46-55
56-65
>65

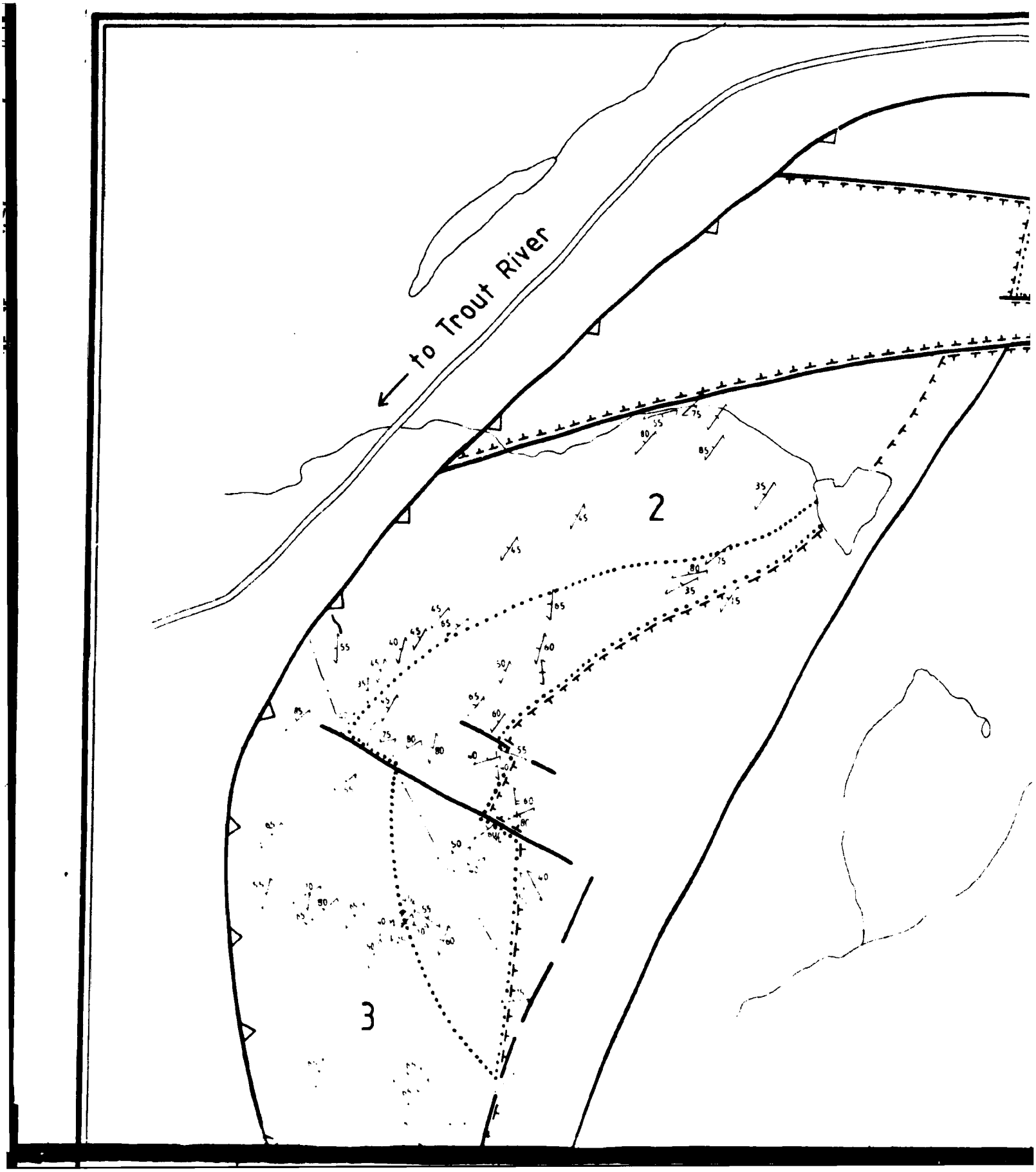
to Trout River
2
3

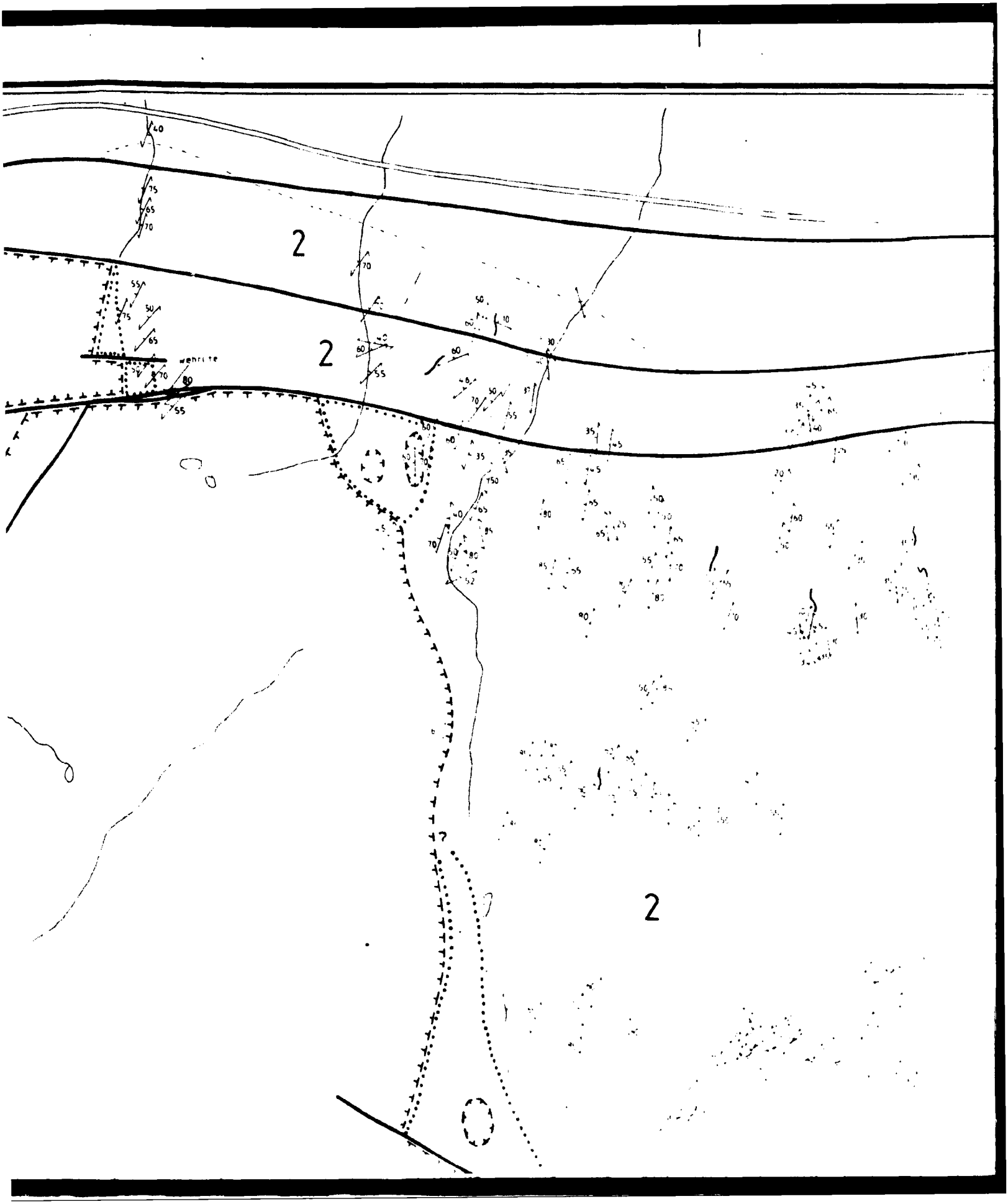
1
2
2
2
Penrith

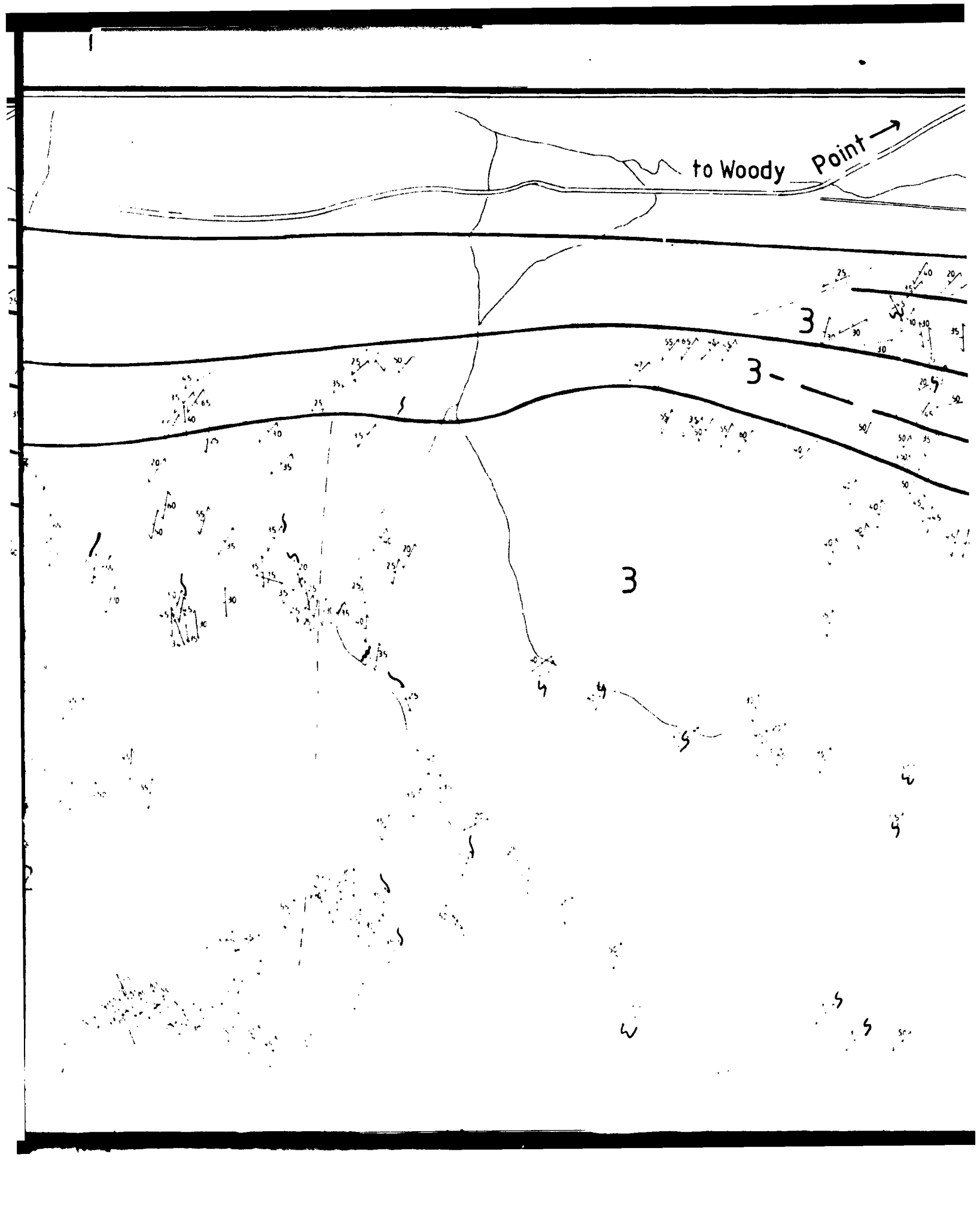
to Woody Point
3
3
3

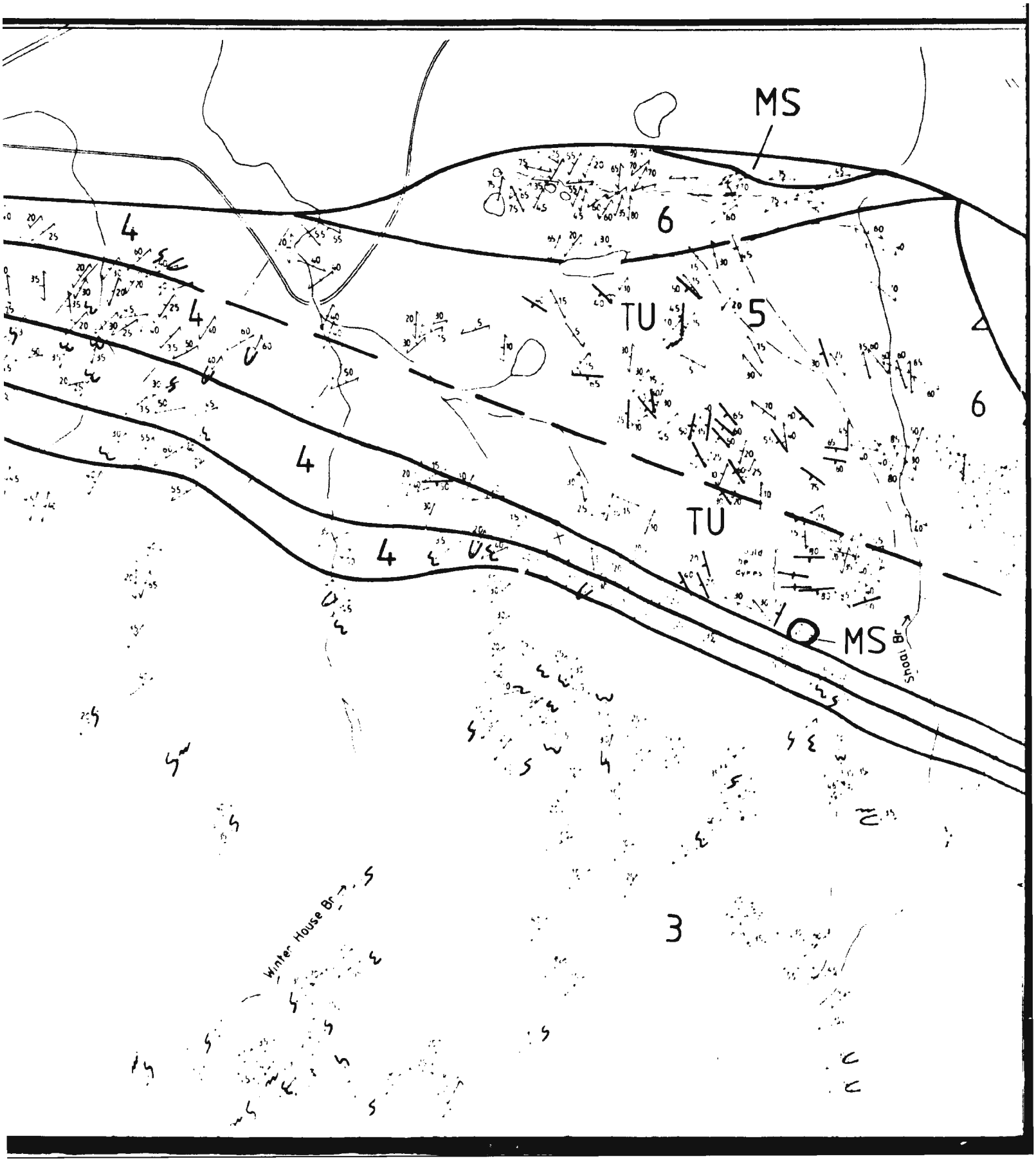
MS
6
4
4
TU
5
6
4
TU
4
MS
Shoal Br
3
Winter House Br

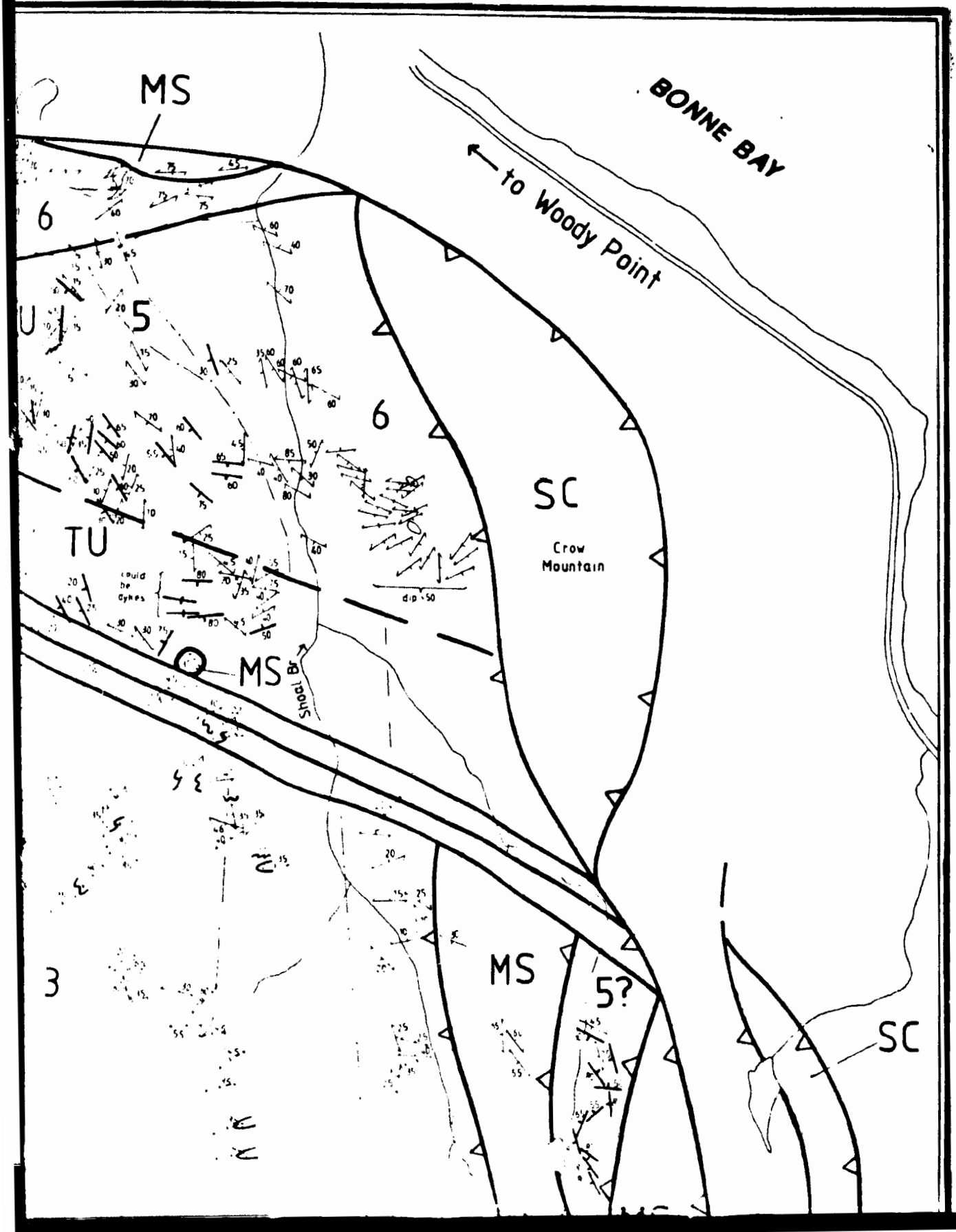
MS
BONNE BAY
← to Woody Point
6
U
5
6
SC
Crow
Mountain
TU
could be dykes
dip 50
MS
Shoal Br
3
MS
5?
SC

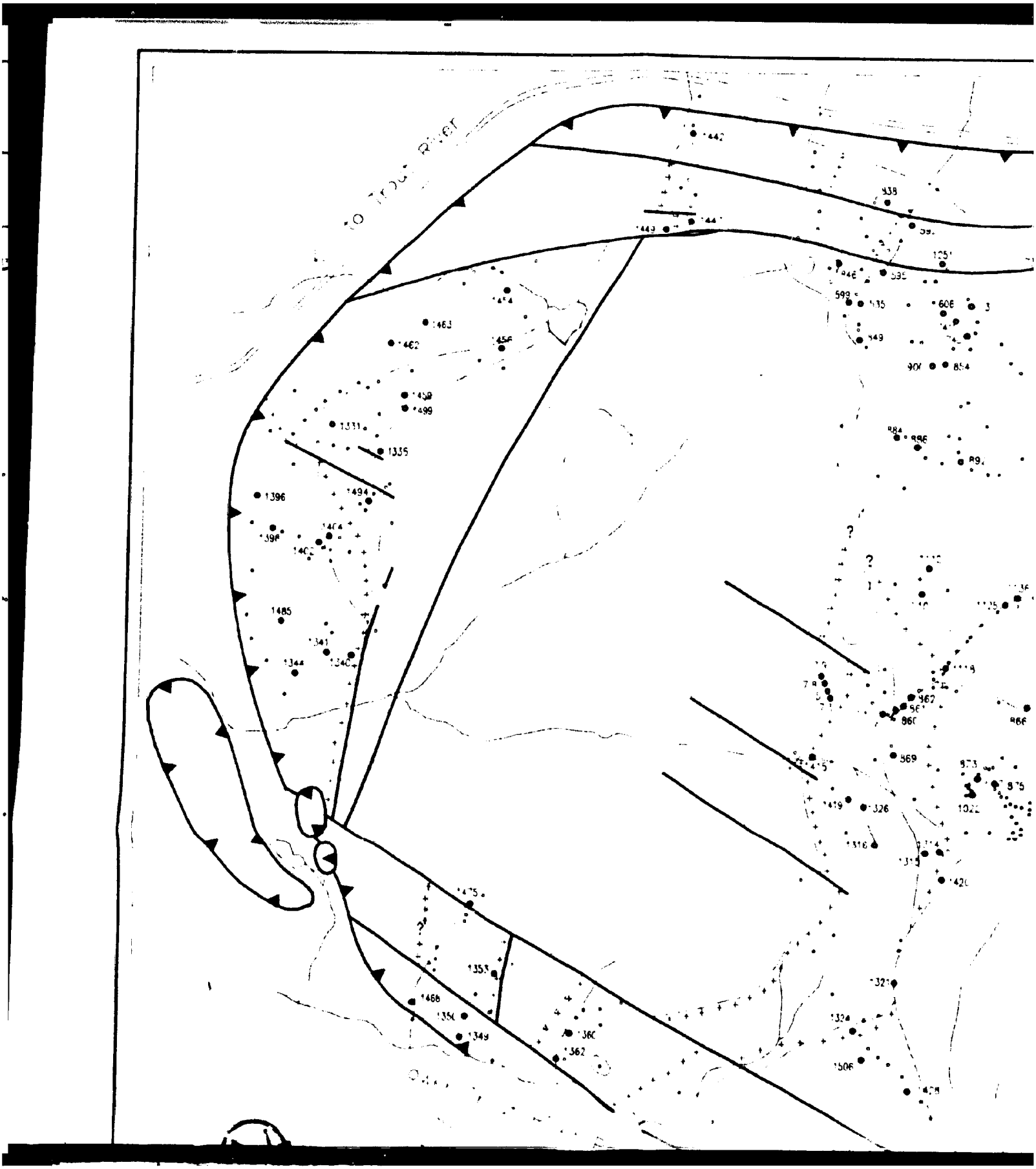
TO TOCE RIVER
442
938
443
444
1251
446
535
599
535
606
549
854
1463
462
456
459
499
1331
1335
1396
1494
1404
1402
1485
341
1344
1340
862
869
326
1475
1353
1468
1350
1349
360
362
1321
1324
1506
1428

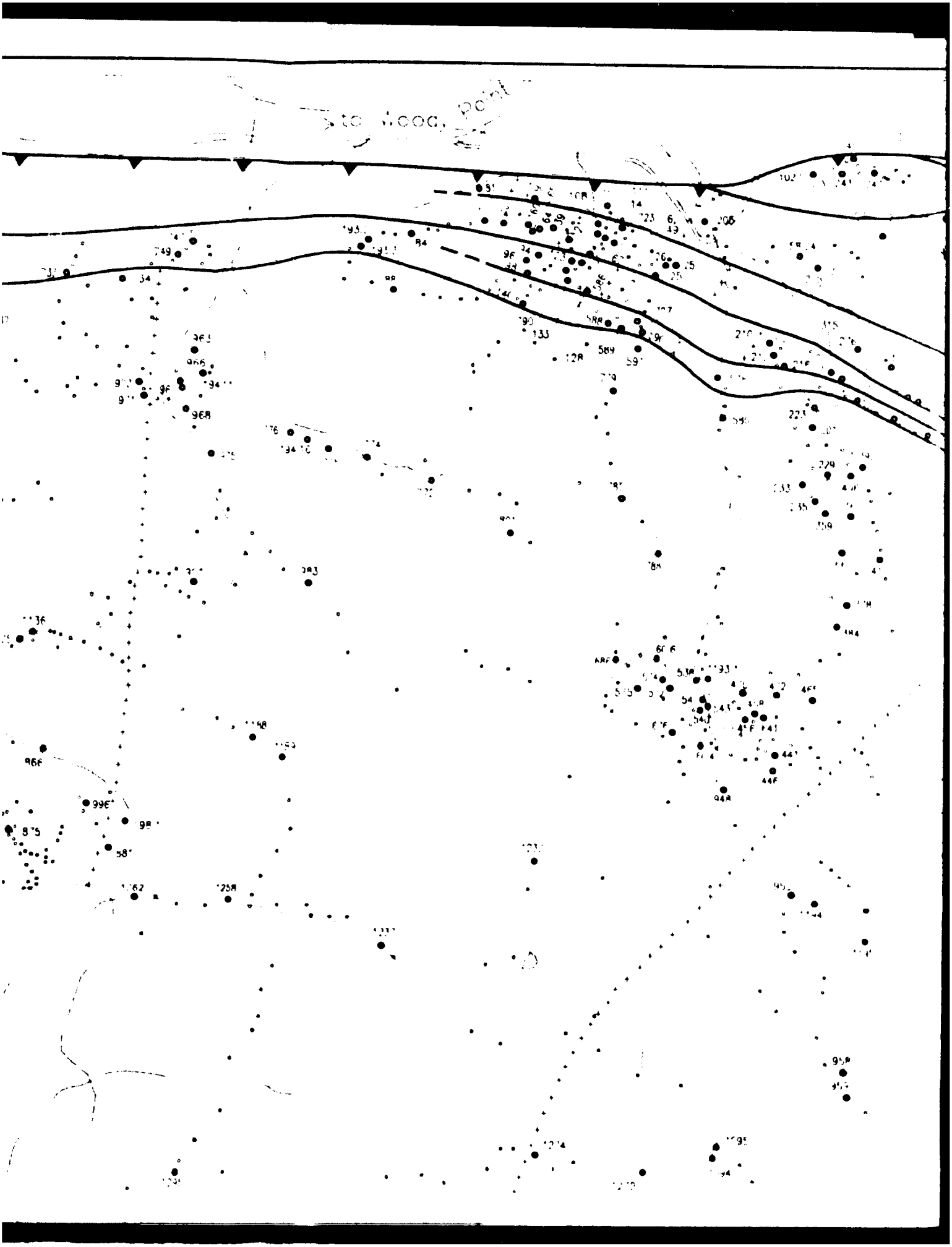

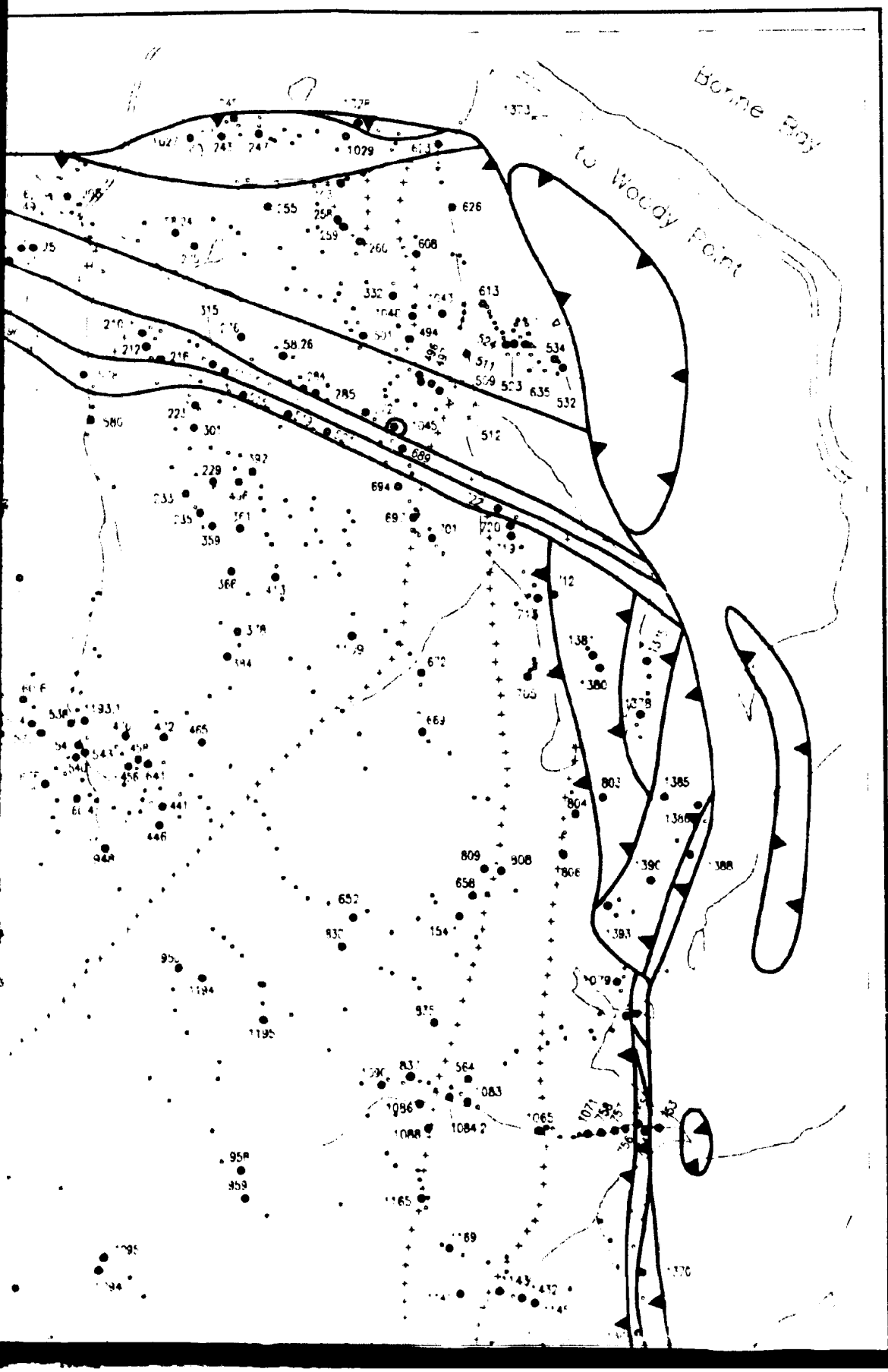
Borne Bay
to Woody Point

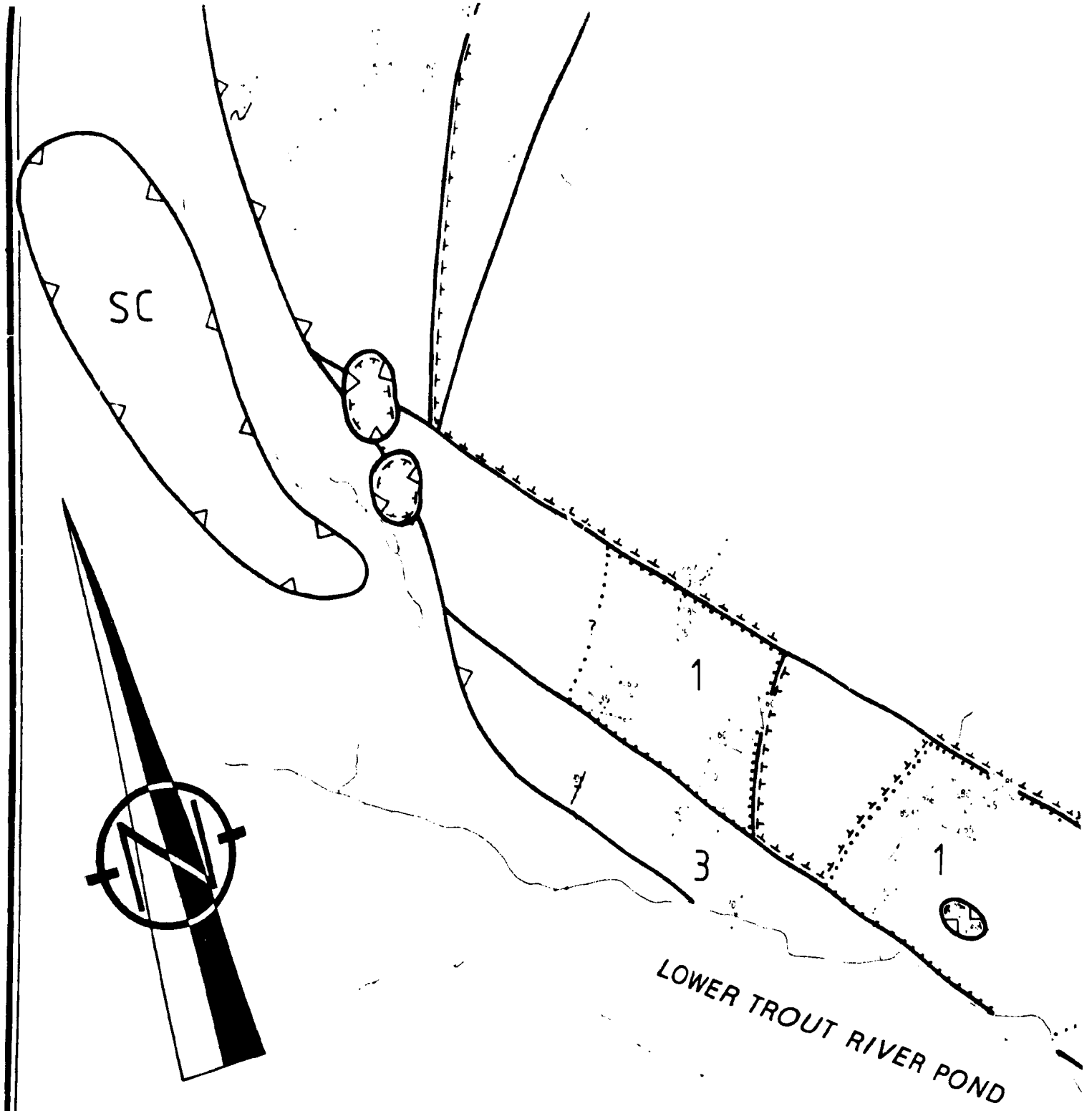

TABLE MOUNTAIN MANTLE SECTION

foliation, lithological banding, and fold style

structural units in ultramafic rocks

foliation with dip, vertical, f

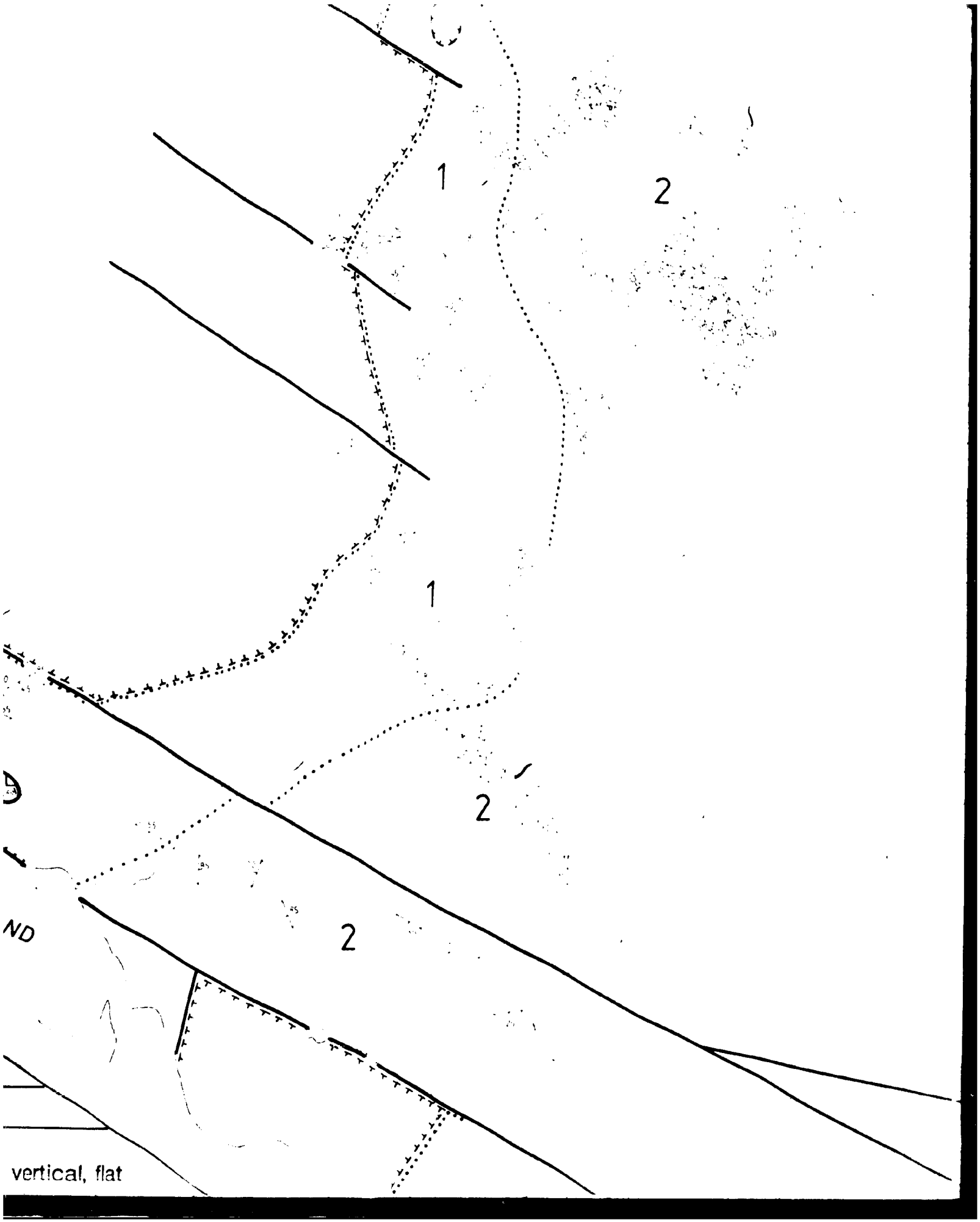
1
2
1
2
2
ND
vertical, flat

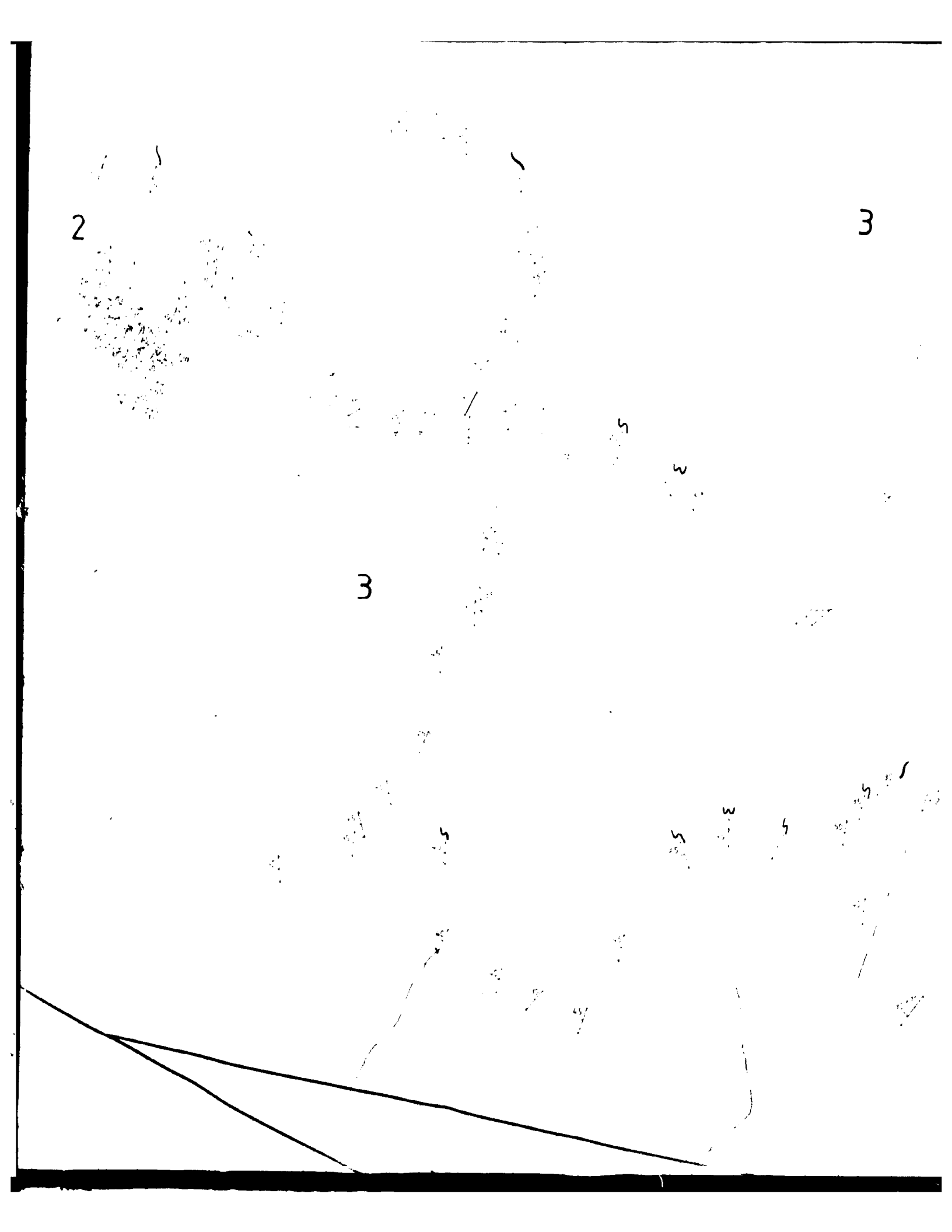
2
3
3

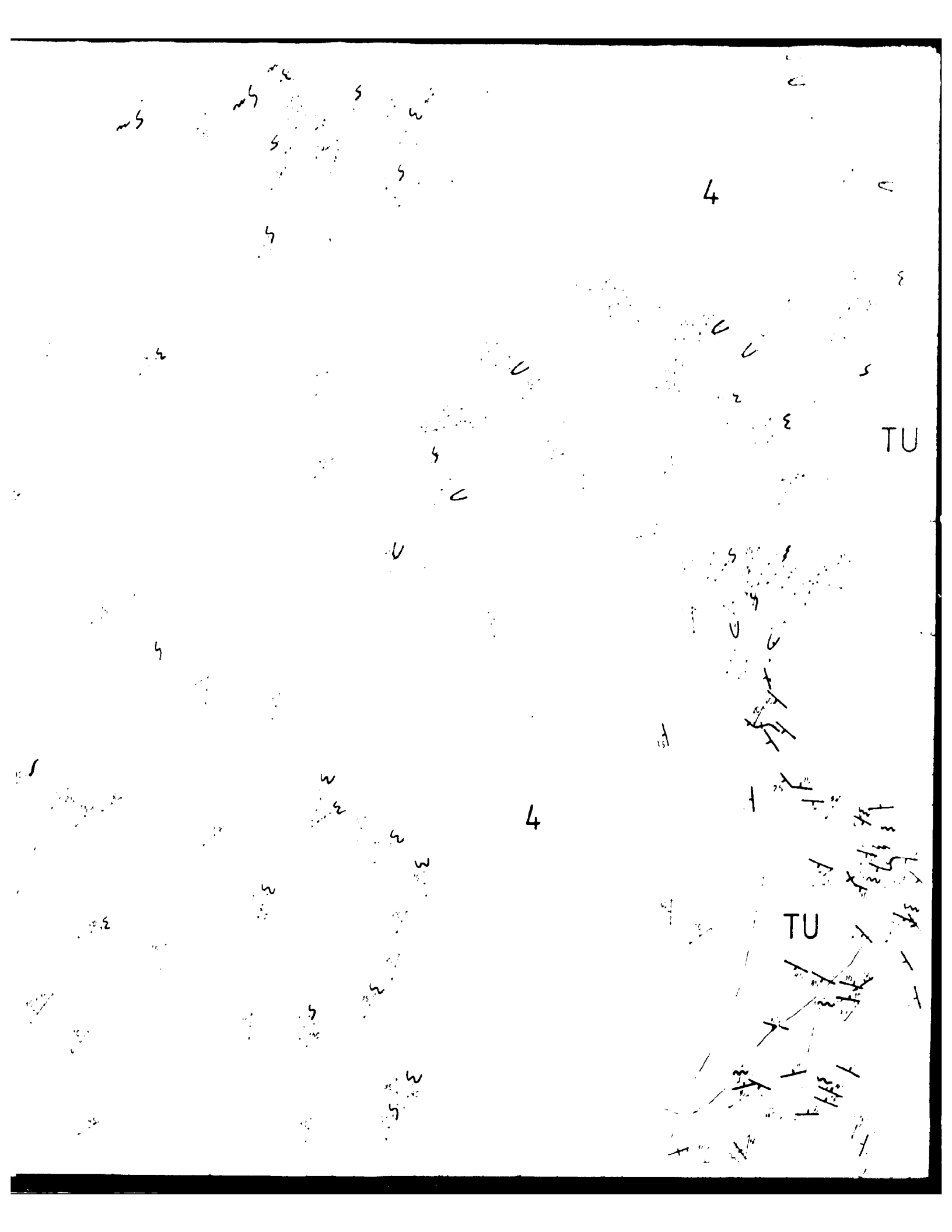
4
TU
4
TU

MS
4
5
6?
TU
2
MS
SC
6
5
TU
MS

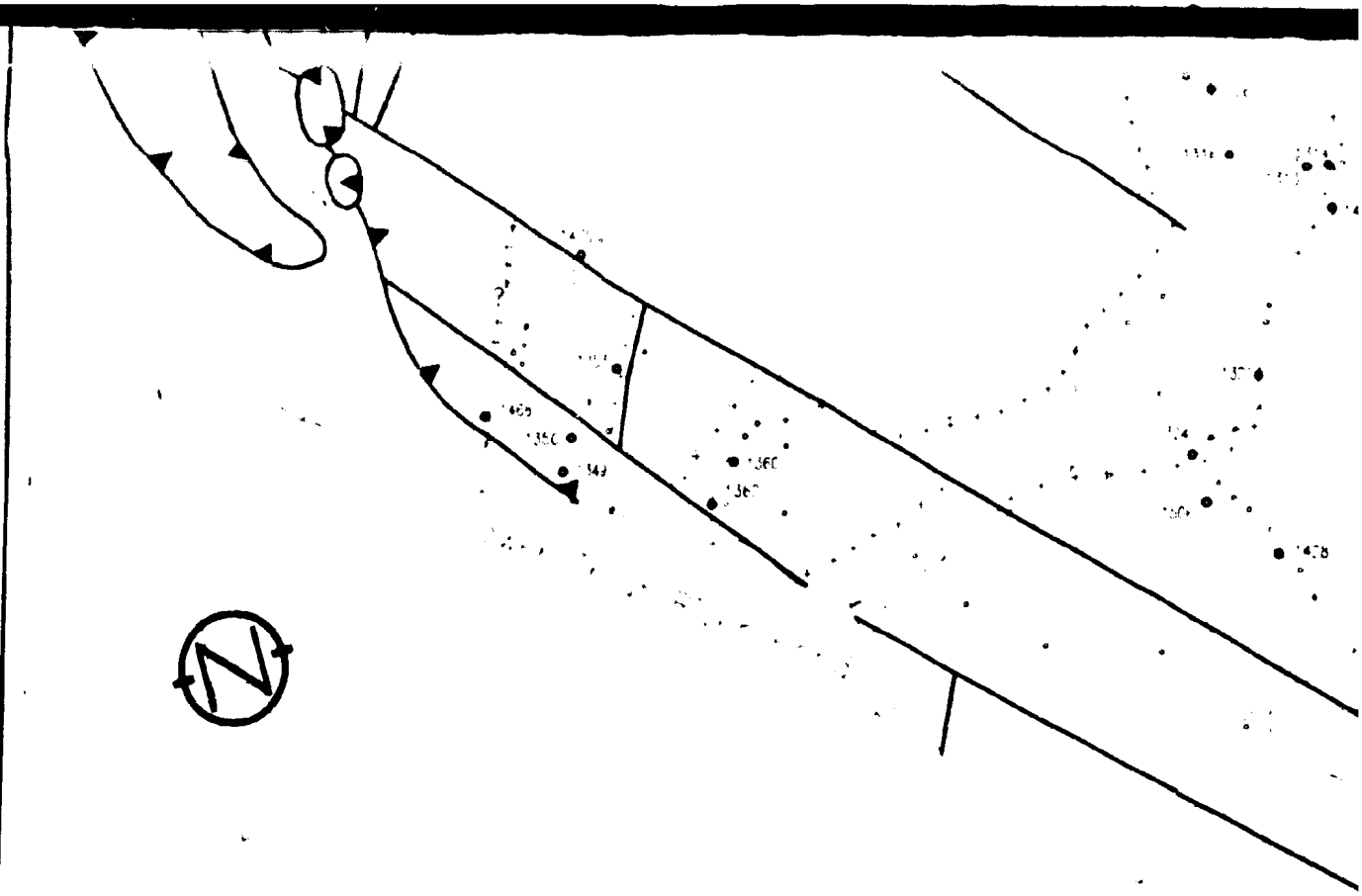

TABLE MOUNTAIN MASSIF

Sample and Station Location Map

- station location, no station number indicated

•1483 station and sample location, with station number

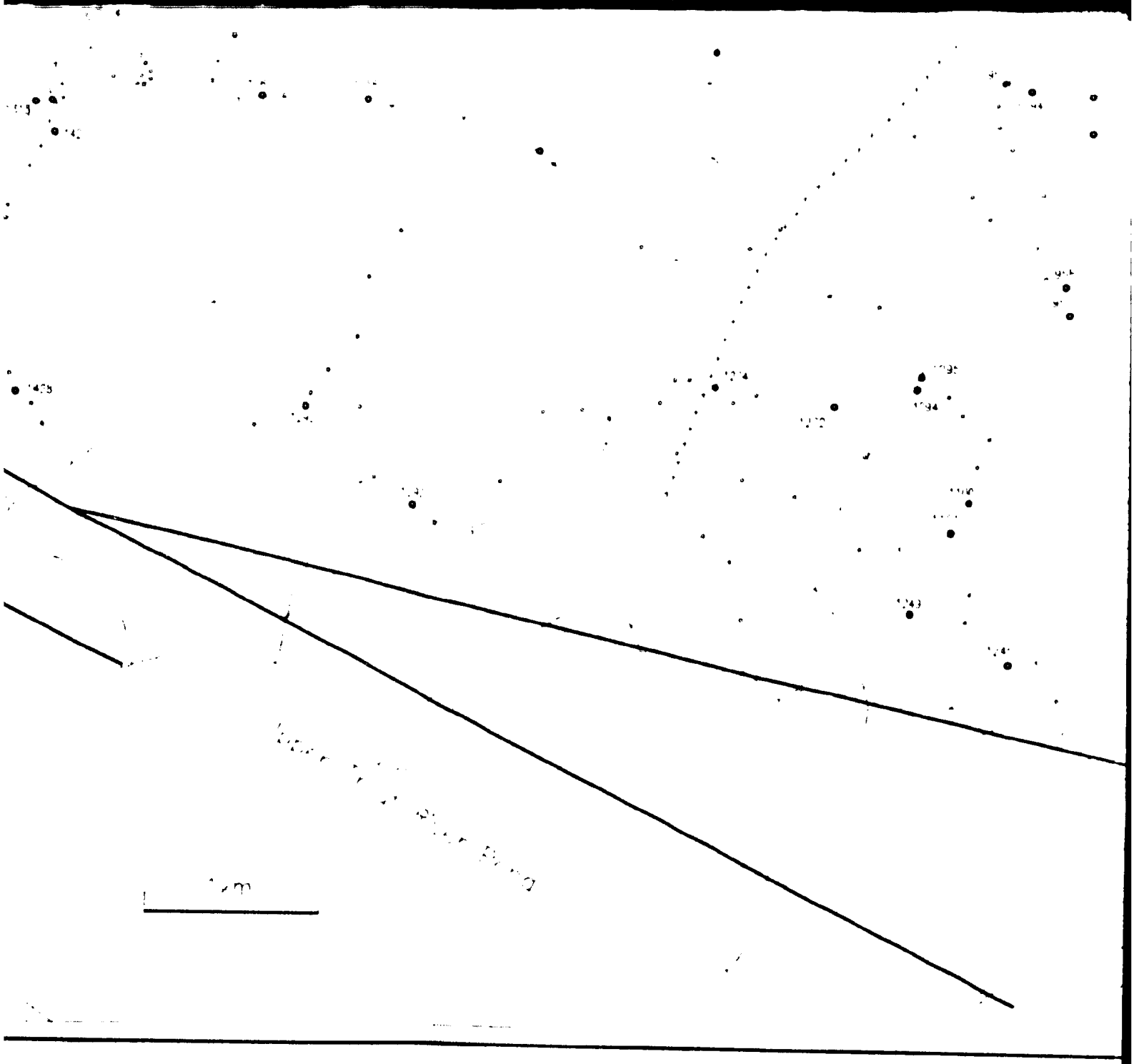

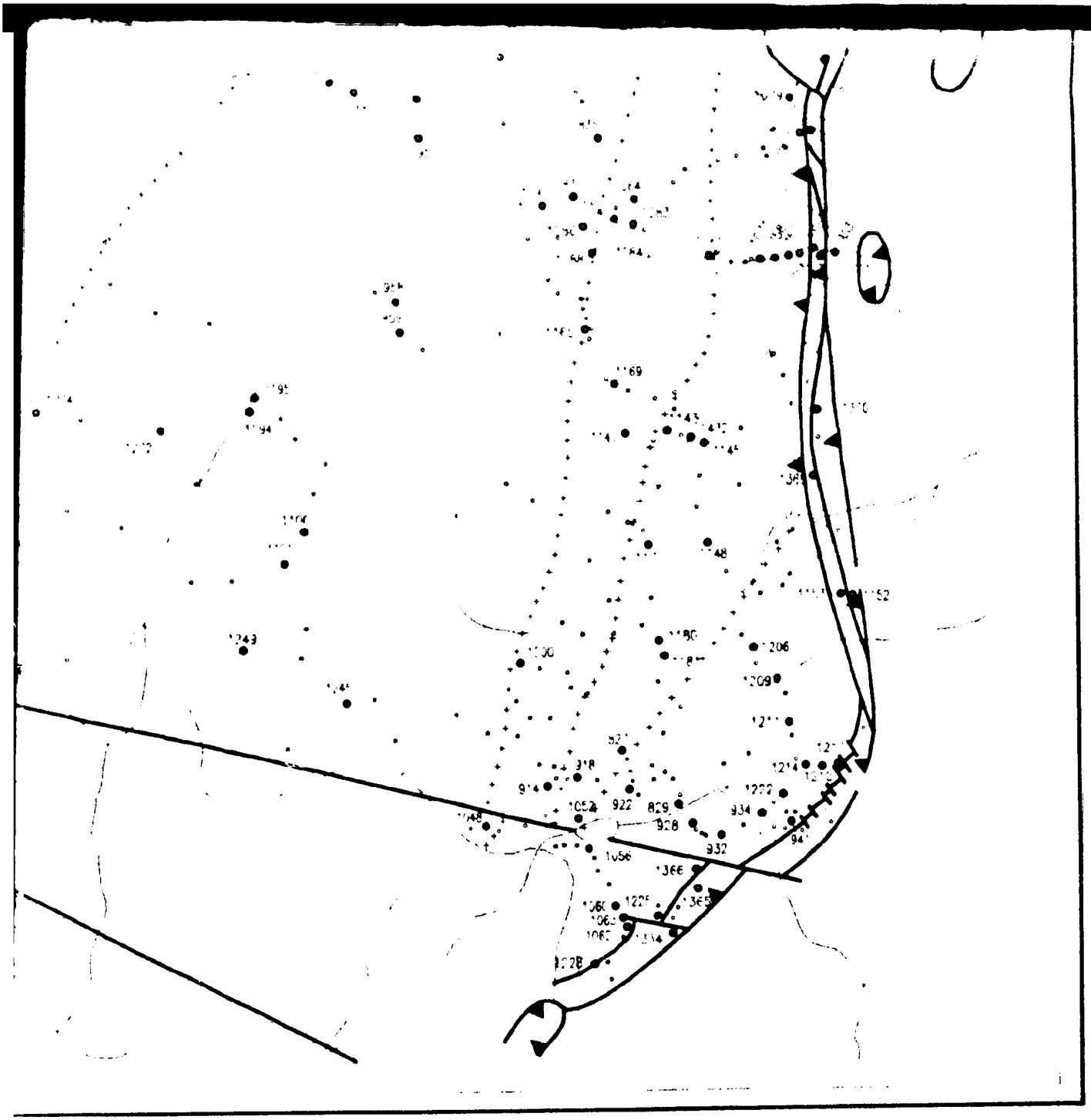

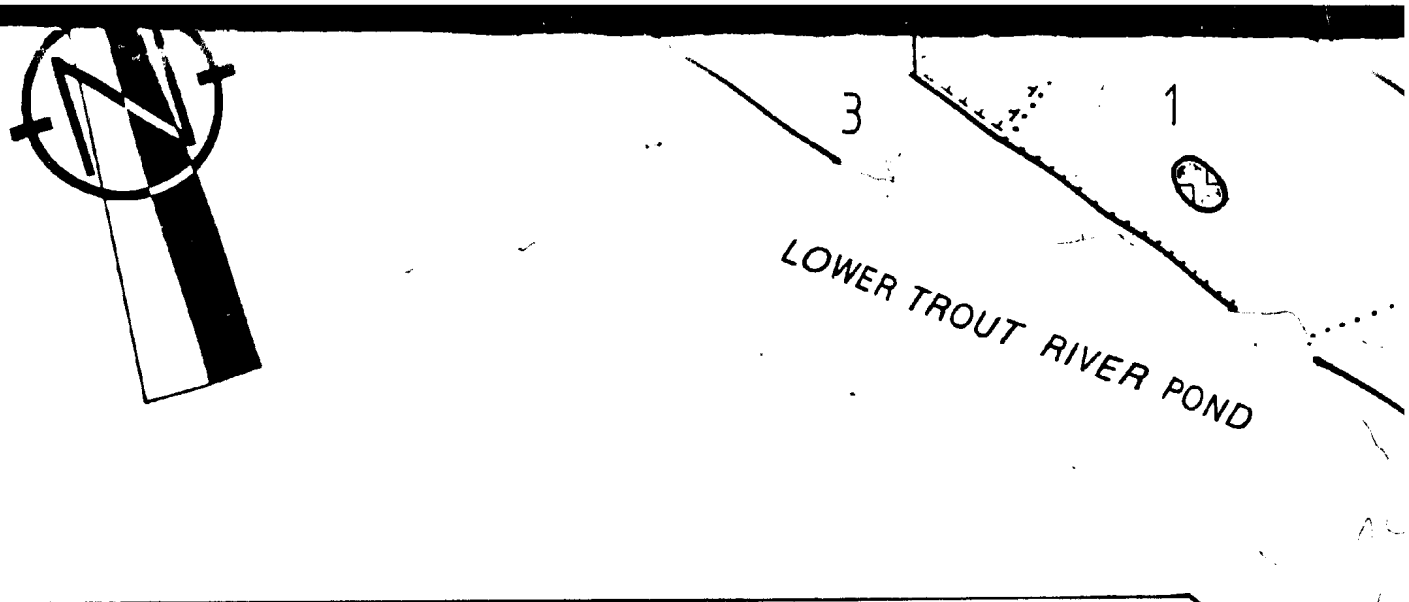

TABLE MOUNTAIN MANTLE SECTION

foliation, lithological banding, and fold style

1,2,..6,TU — structural units in ultramafic rocks (harzburgite, lherzolite, dunite)

structural unit boundary in ultramafic rocks

massive dunite with minor (plagioclase–) wehrlite

massive gabbro and layered cumulates

MS — metamorphic sole and associated rocks (amphibolite, greenschist)

SC — Skinner Cove Formation

high angle fault, determined

~ , assumed

low angle fault, ductile

low angle fault, brittle

foliation with dip, vertical, flat lying

foliation in shear zone, relative deformation

shear zone, relative later defor

lithological banding where regi foliation or where foliation we

fold style of lithological bandir

S–flexure

S–,Z–asymmetric

M–style (open)

isoclinal

parasitic folds to lithological ba

~

ultramylonite

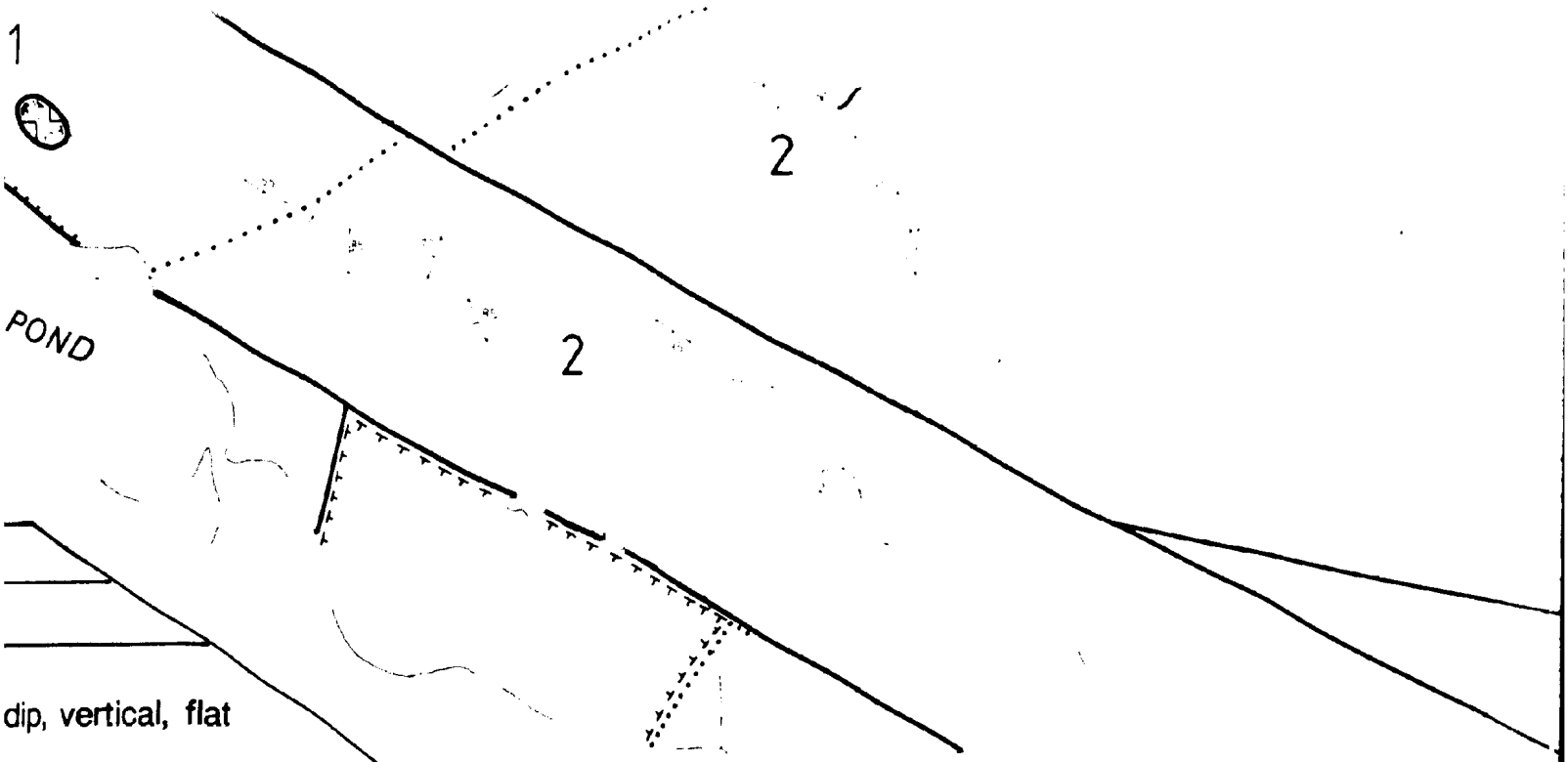

dip, vertical, flat

ear zone, relative later

elative later deformation
nding where regionally oblique to
where foliation weak (unit 5 and TU)
ithological banding, down plunge view:

imetric
pen)

to lithological banding, S,Z,or M asymmetry
, asymmetry undetermined

UPPE

0

Geolo

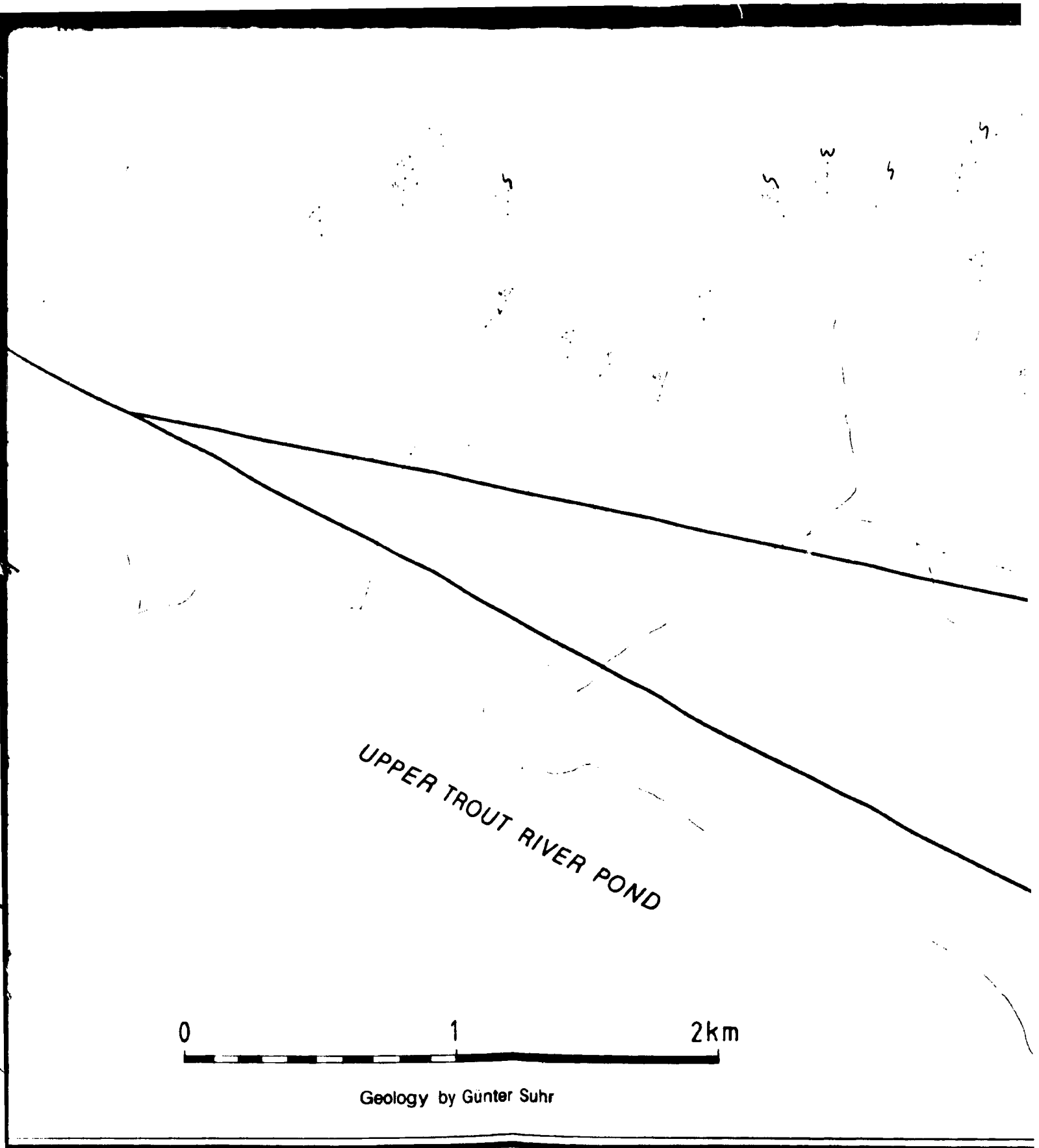

Geology by Günter Suhr

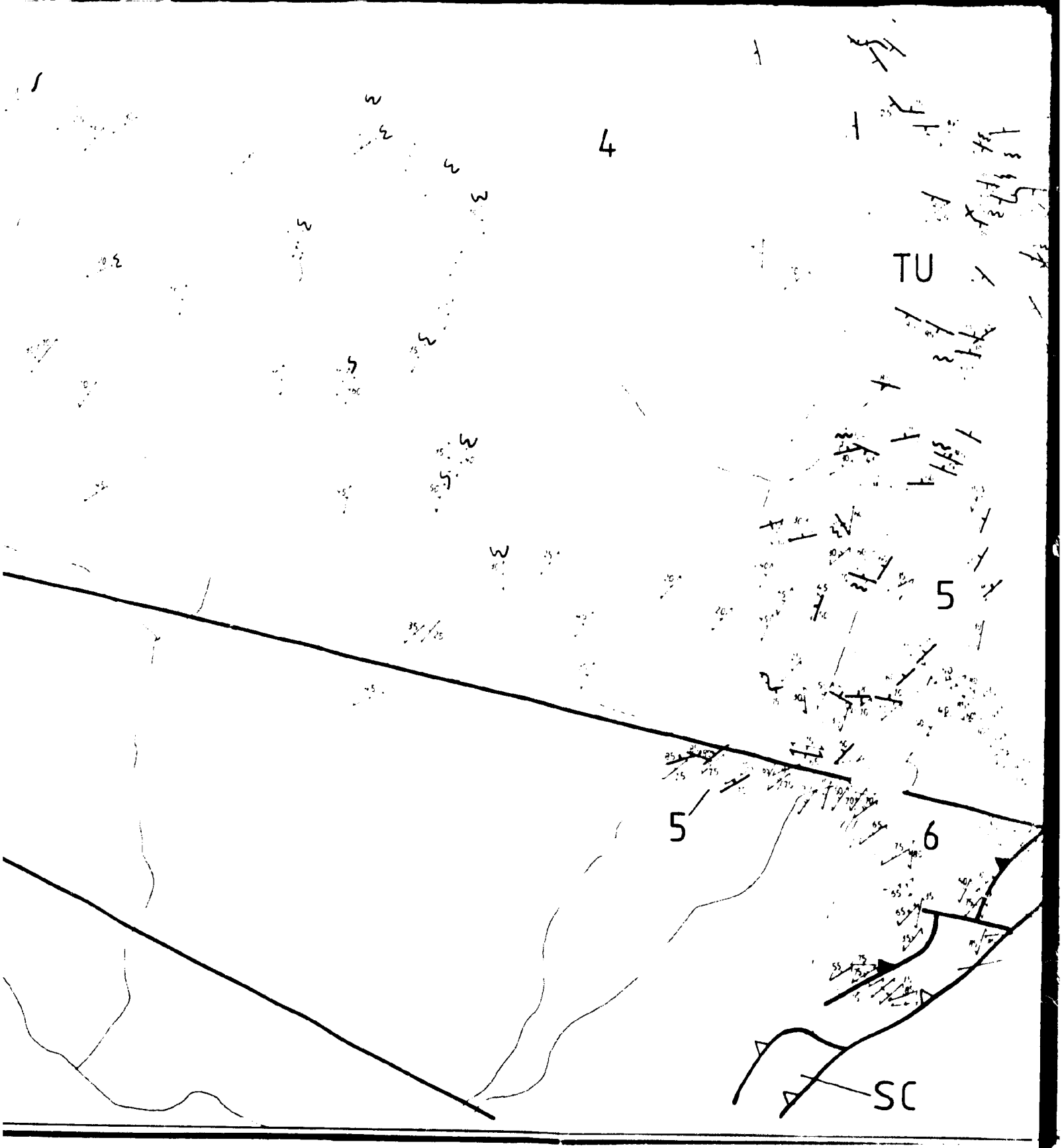
4
TU
5
5
6
SC

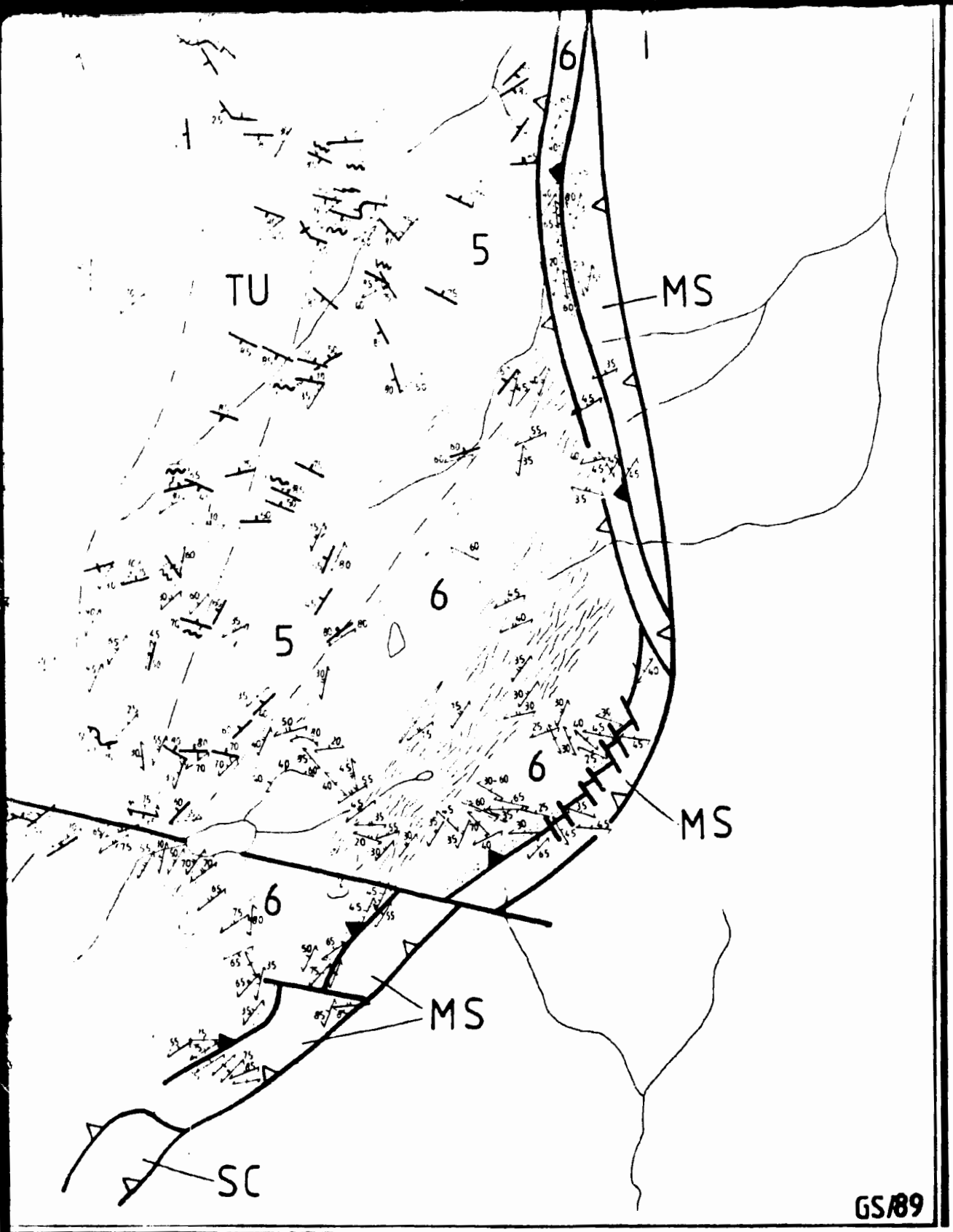
6
1
TU
5
MS
5
6
6
MS
6
MS
SC
GSA89

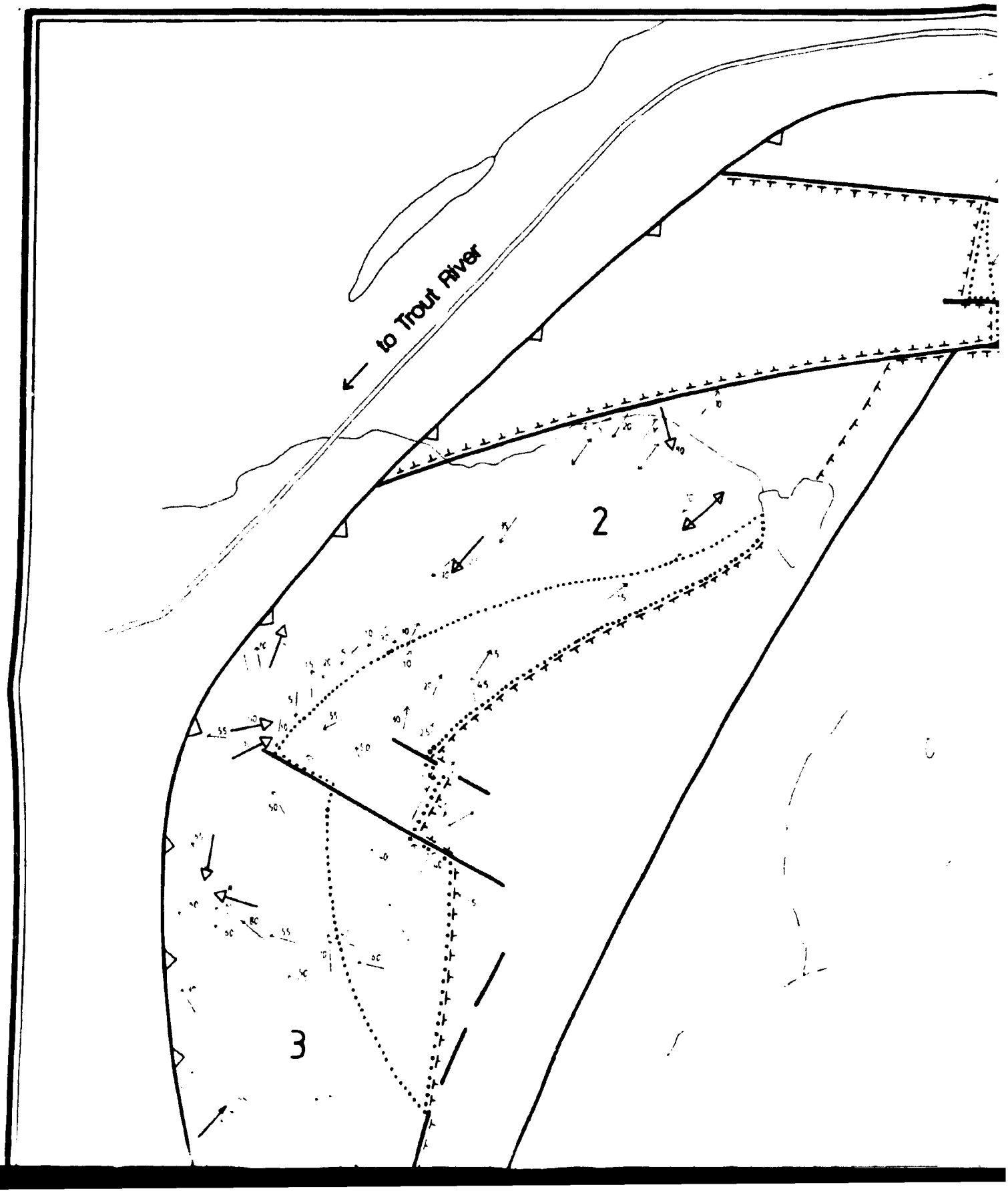
to Trout River
2
3

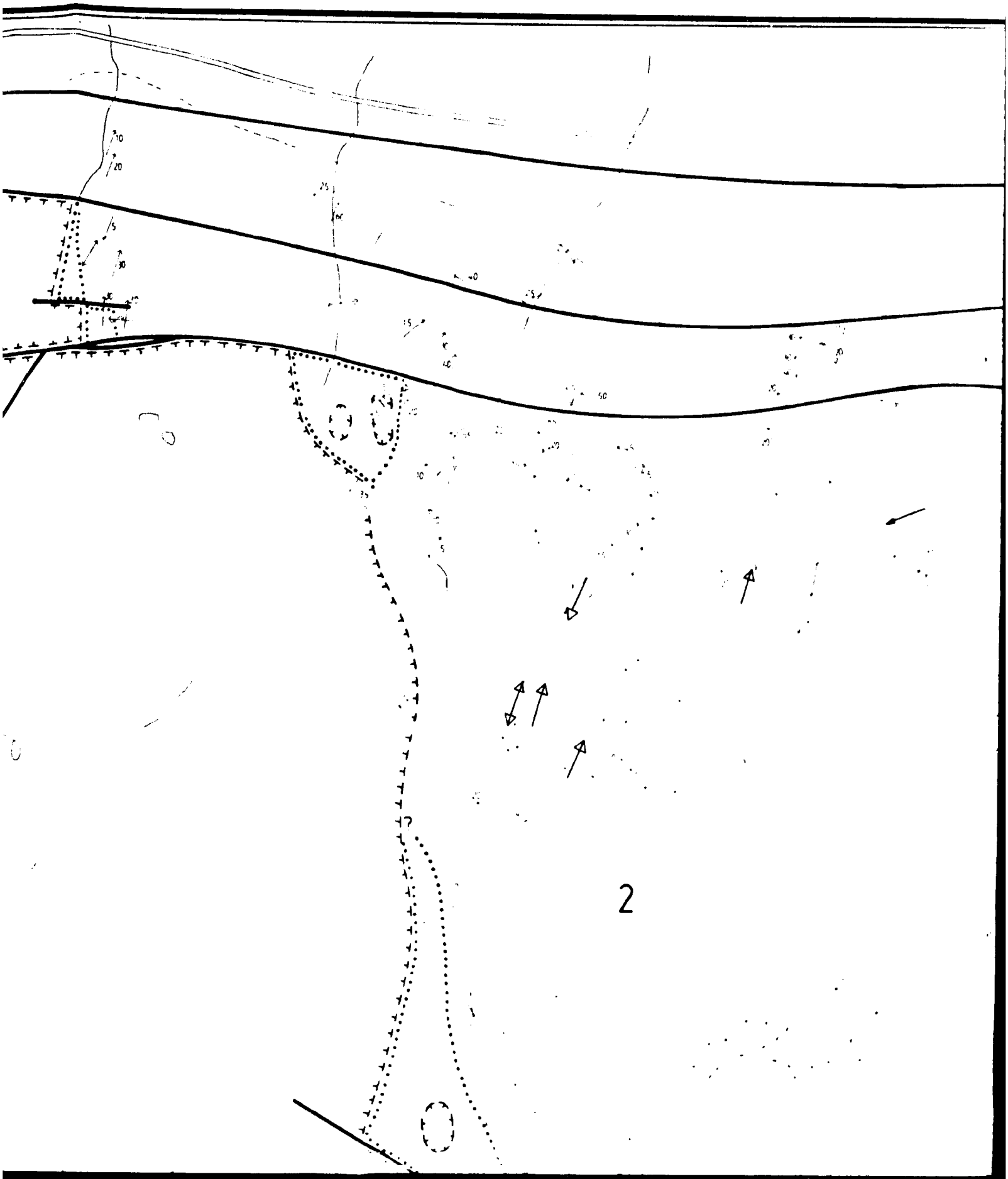
N
2

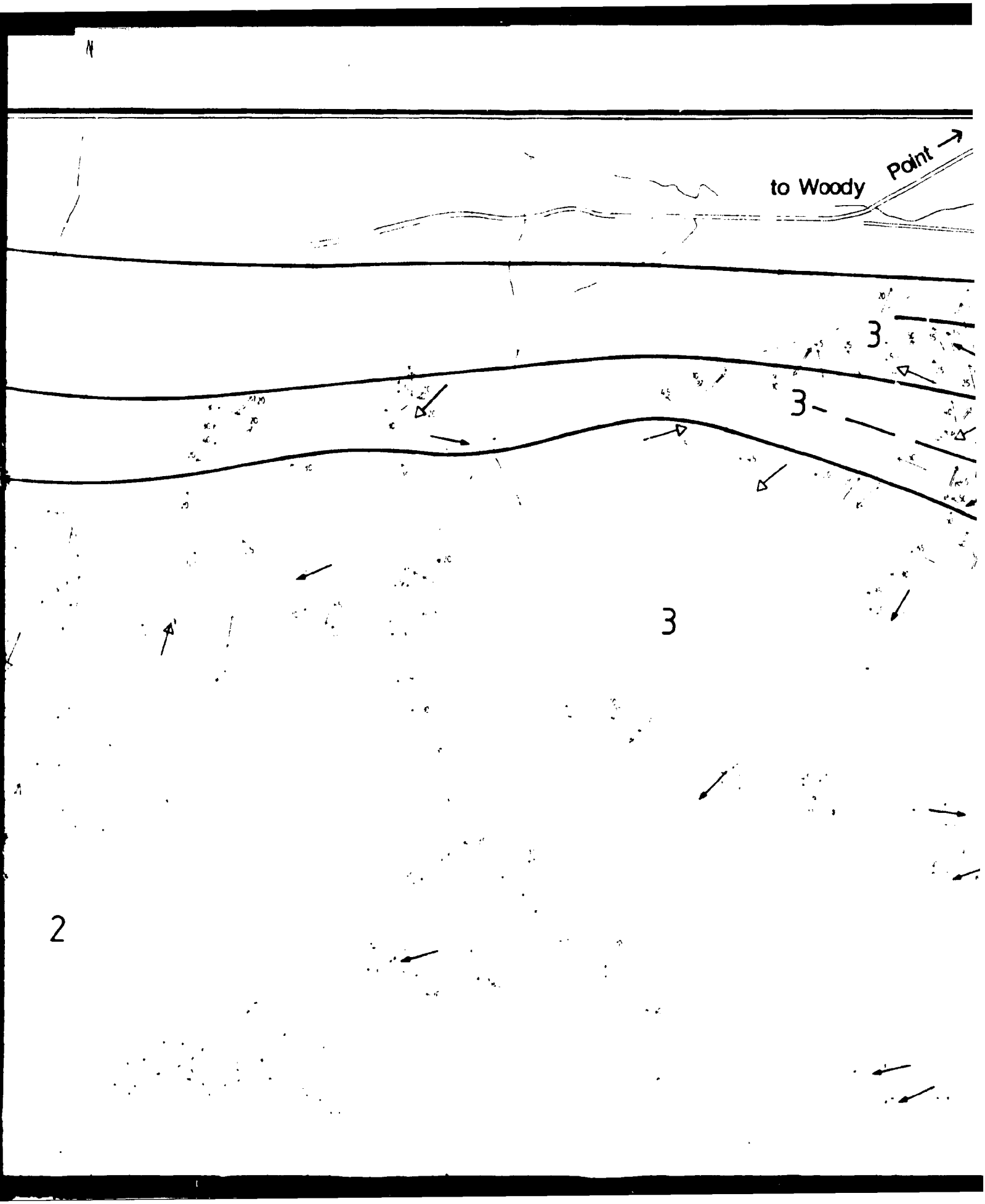
N
to Woody Point
3
3
3
2

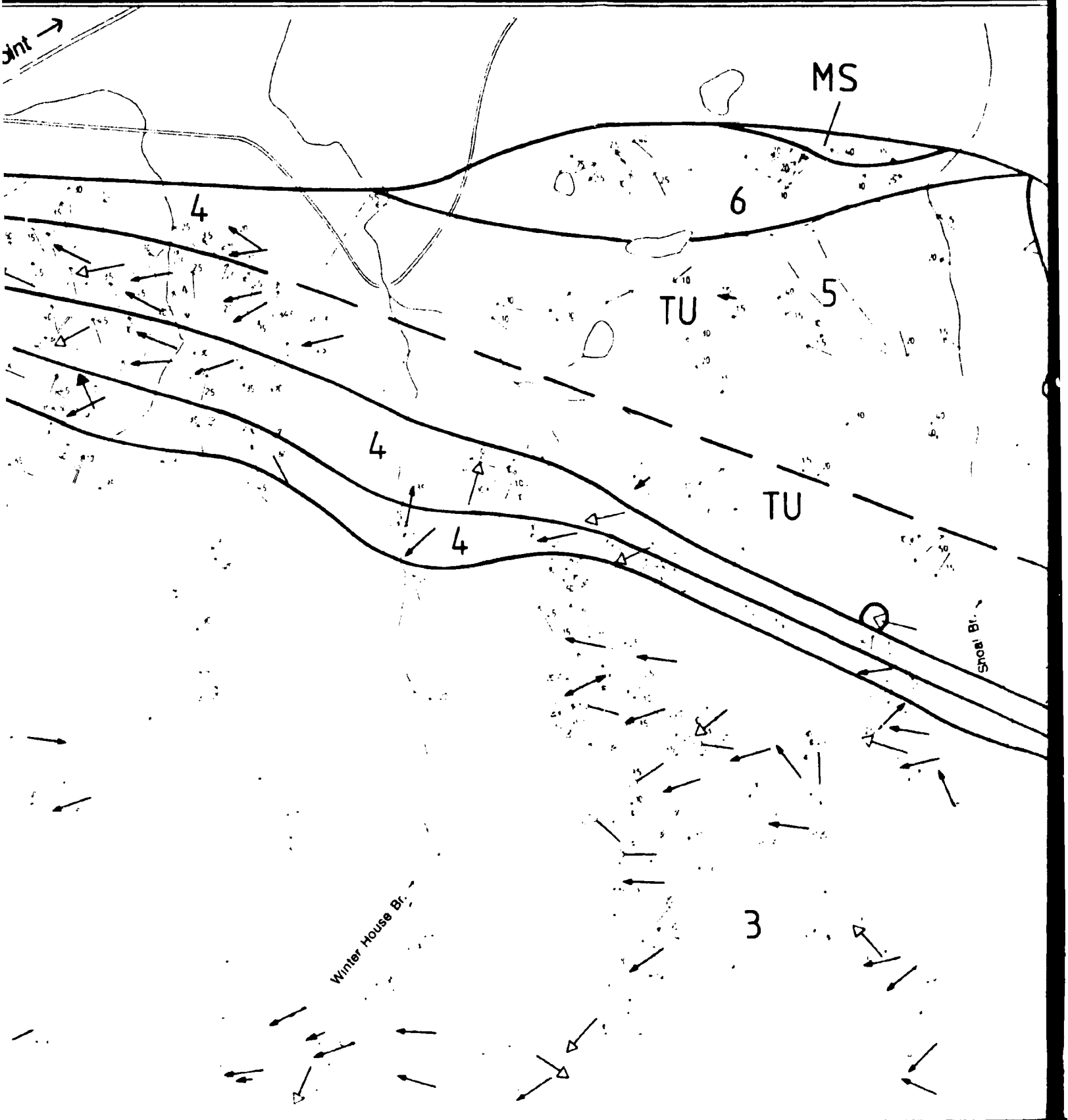
MS
6
4
TU
5
4
TU
4
Shoal Br.
Winter House Br.
3

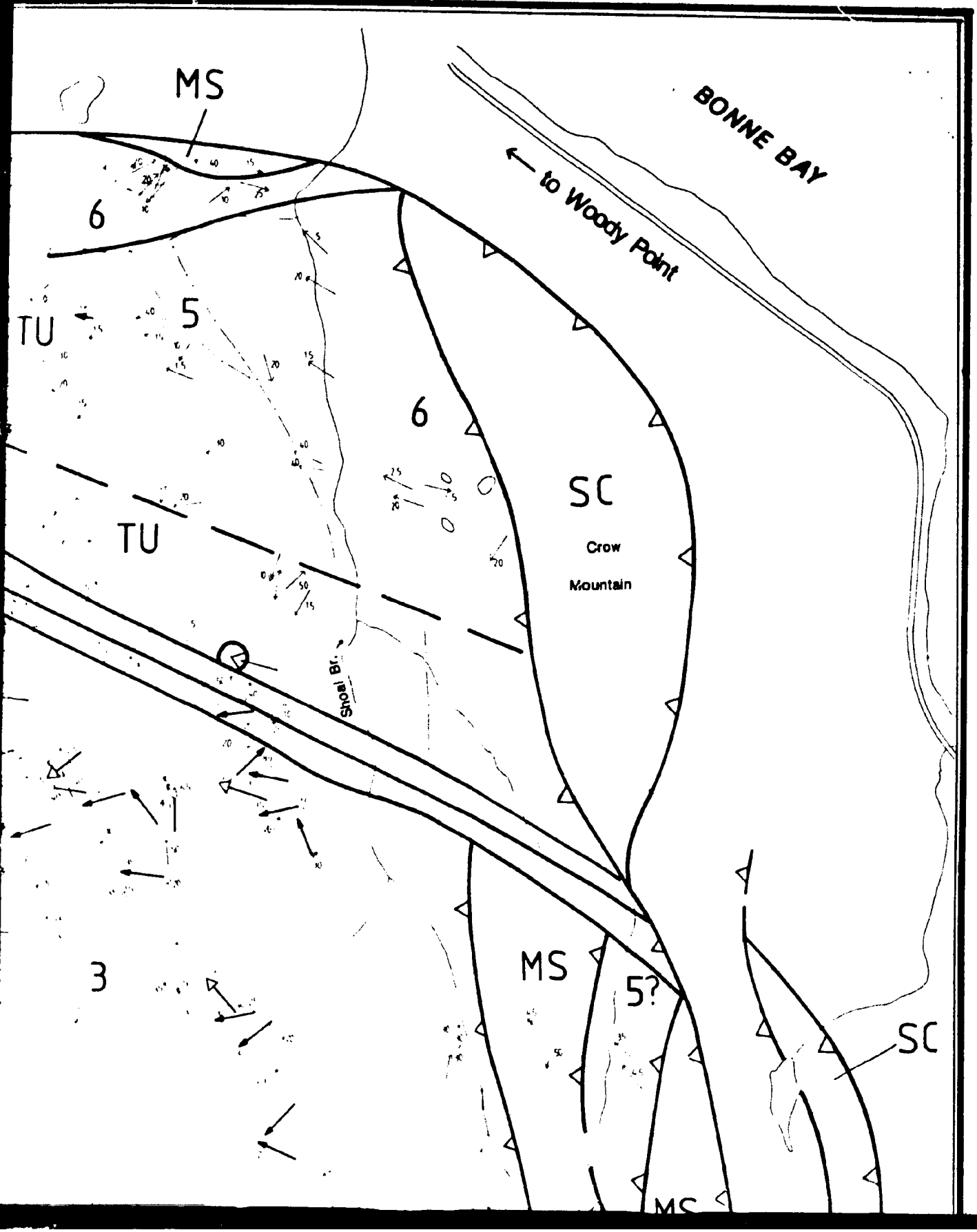
MS
BONNE BAY
← to Woody Point
6
TU
5
6
SC
Crow
Mountain
TU
Shoal Br.
3
MS
5?
SC
MS

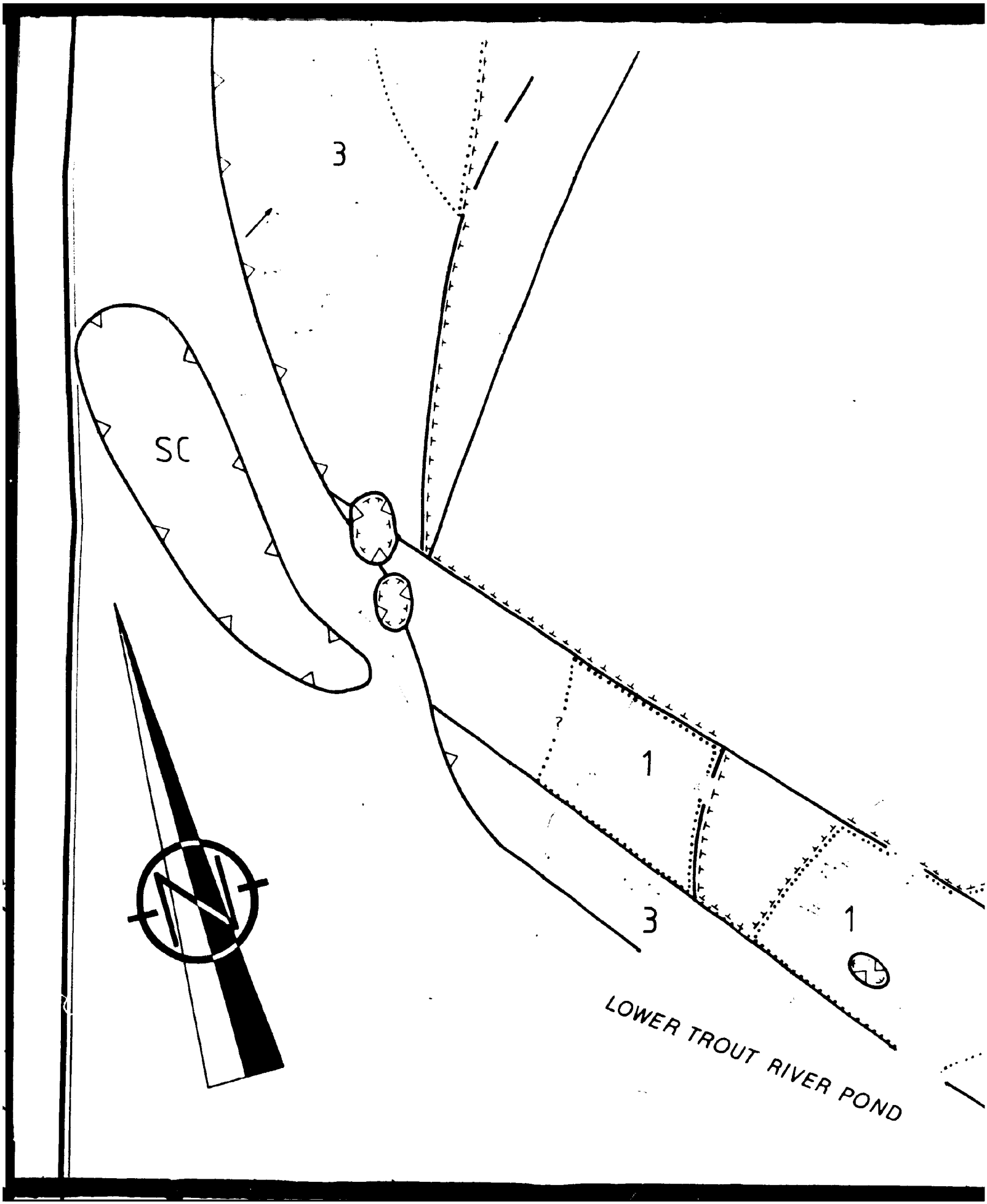
3
SC
1
3
1
N
LOWER TROUT RIVER POND

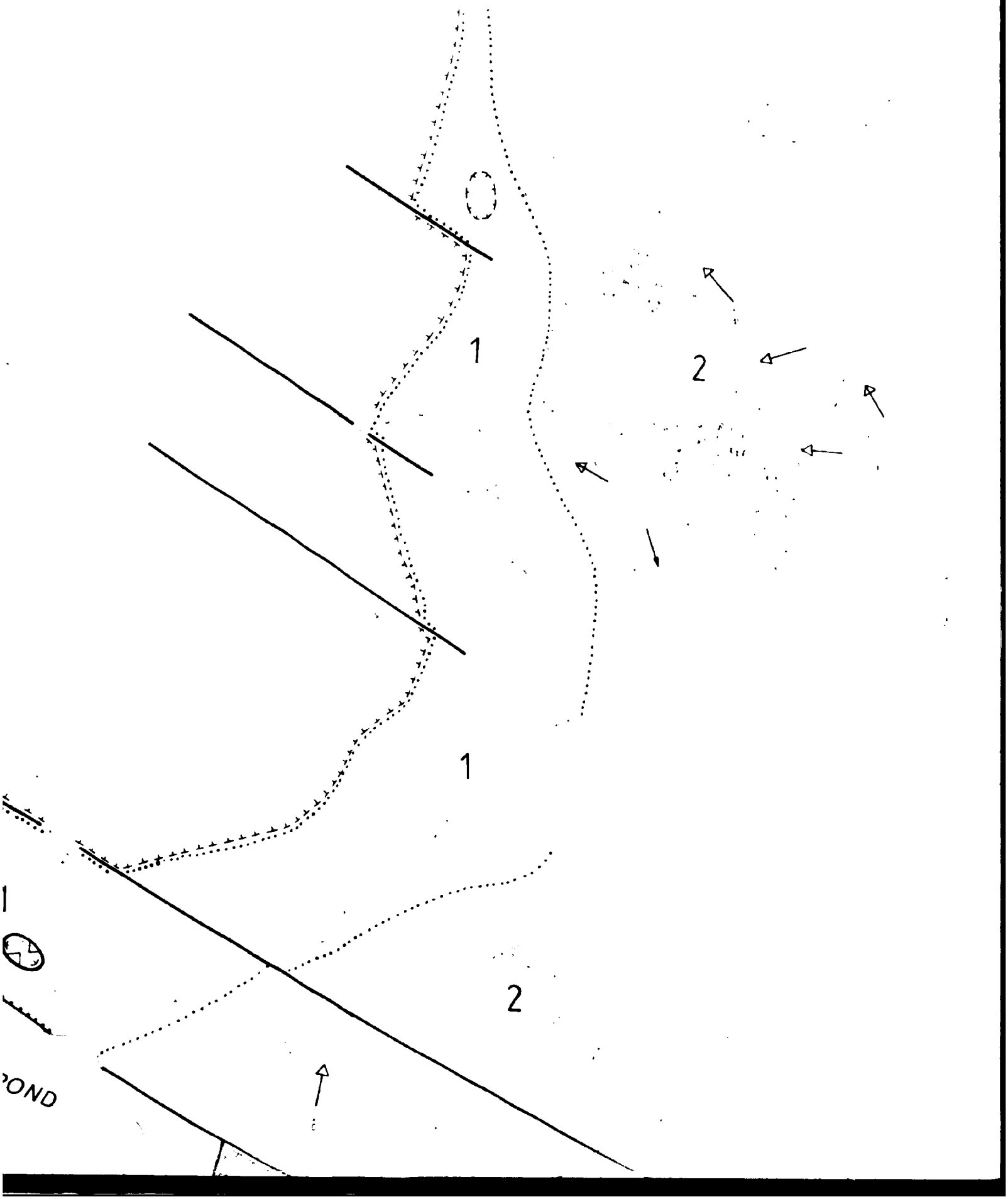
1
2
1
2
POND


2
3
3

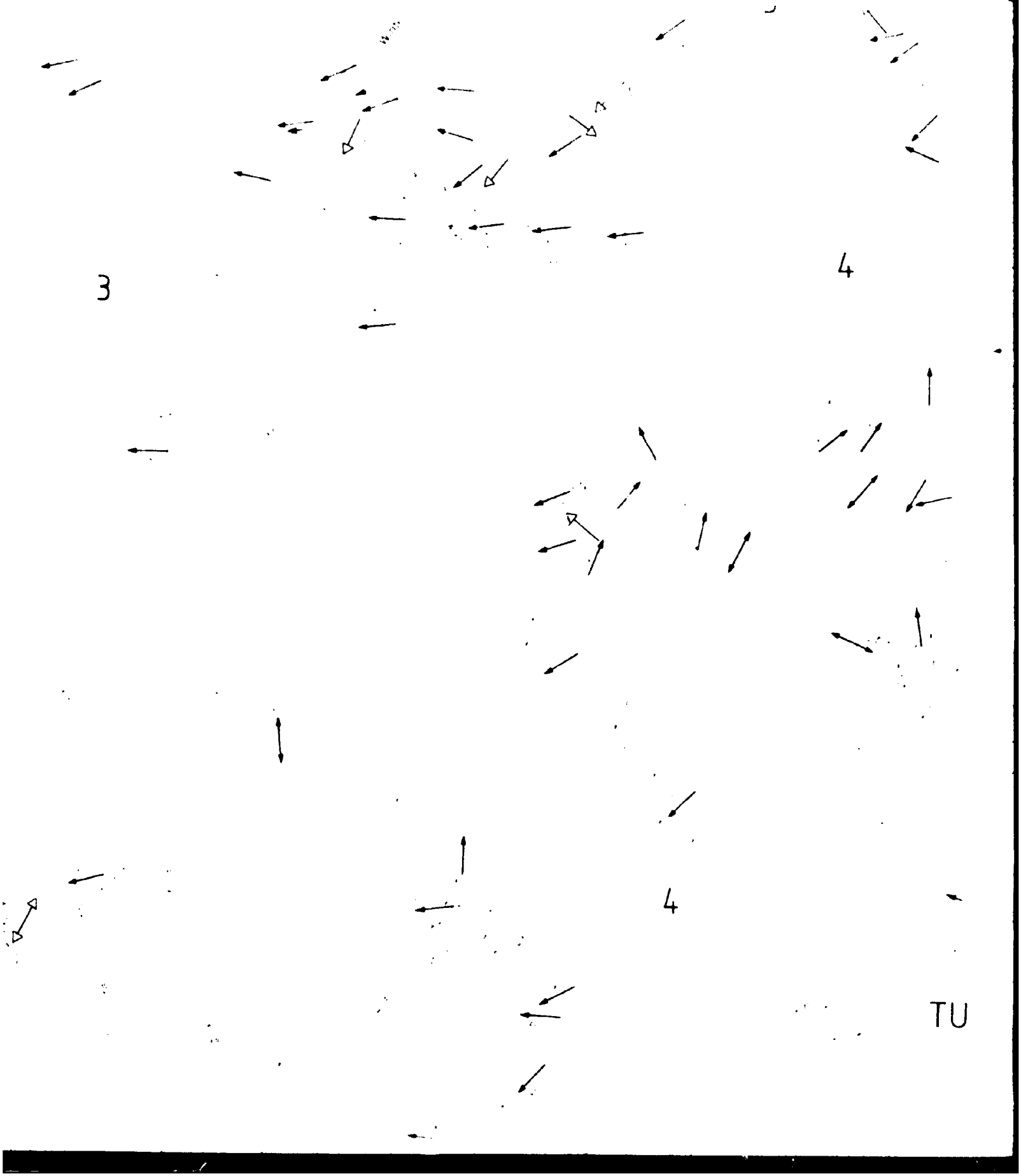
3
4
4
TU

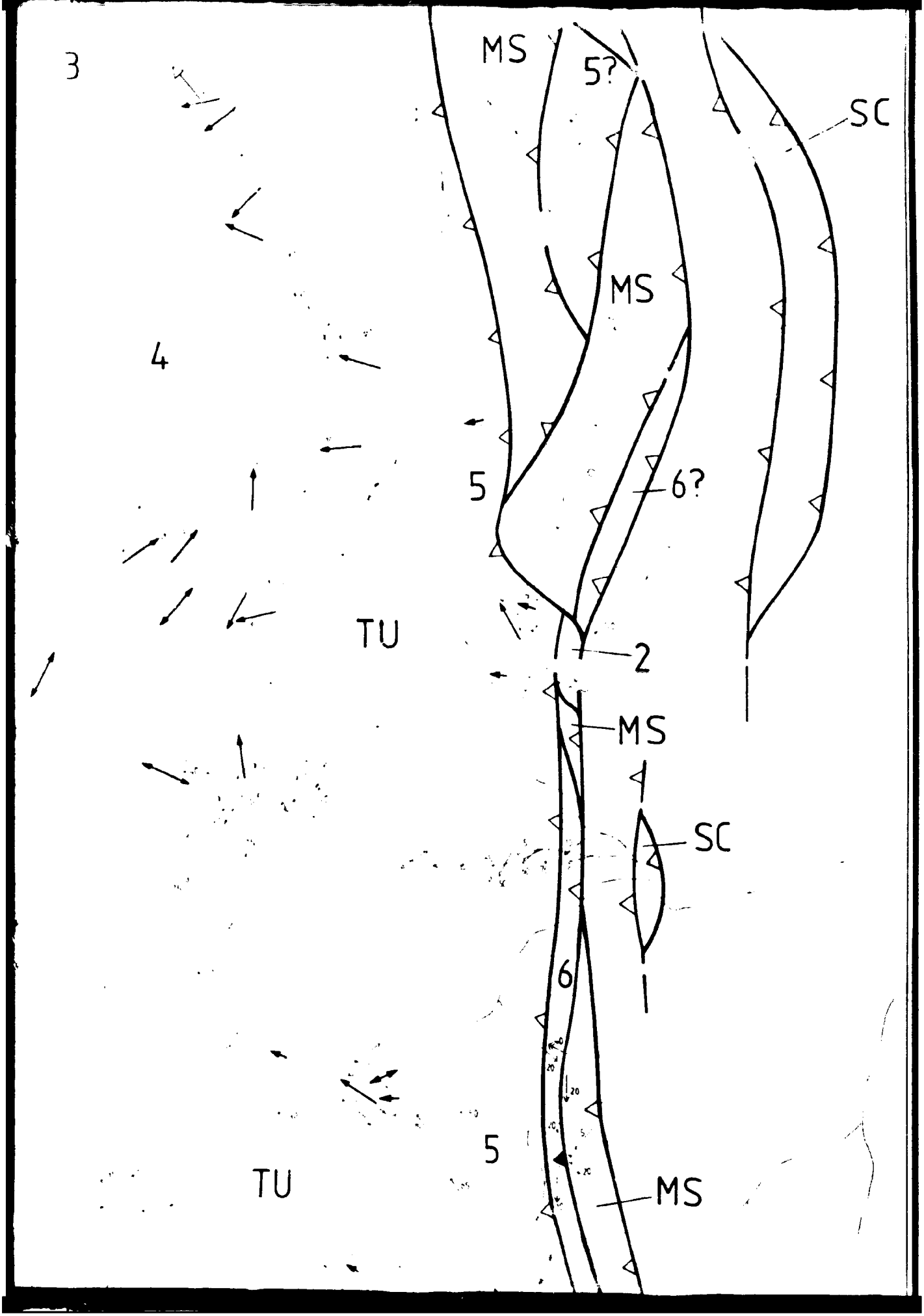
3
MS
5?
SC
MS
4
5
6?
TU
2
MS
SC
6
5
TU
MS

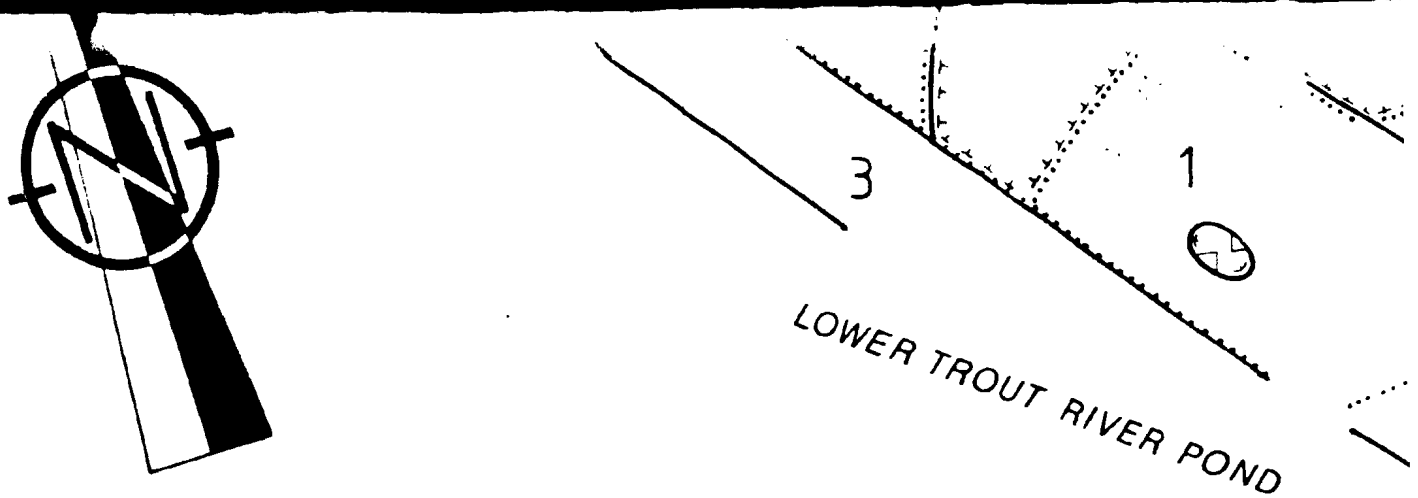

TABLE MOUNTAIN MANTLE SECTION

mineral lineations, boudin elongtions, and fold axes

1,2,...6,TU	structural units in ultramafic rocks (harzburgite, lherzolite, dunite)
	structural unit boundary in ultramafic rocks
	massive dunite with minor (plagioclase–) wehrlite
	massive gabbro and layered cumulates
MS	metamorphic sole and associated rocks (amphibolite, greenschist)
SC	Skinner Cove Formation
	high angle fault, determined
	~ , assumed
	low angle fault, ductile
	low angle fault, brittle
	mineral lineation with plun flat lying, vertical
	mineral lineation in shear z later deformation
	boudin elongation
	fold axis of lithological bar
	fold axis of banding in she
	fold axis of parasitic fold
	fold axis of orthopyroxenite
	fold axis of clinopyroxenite
	shear zone, relative later de ultramylonite

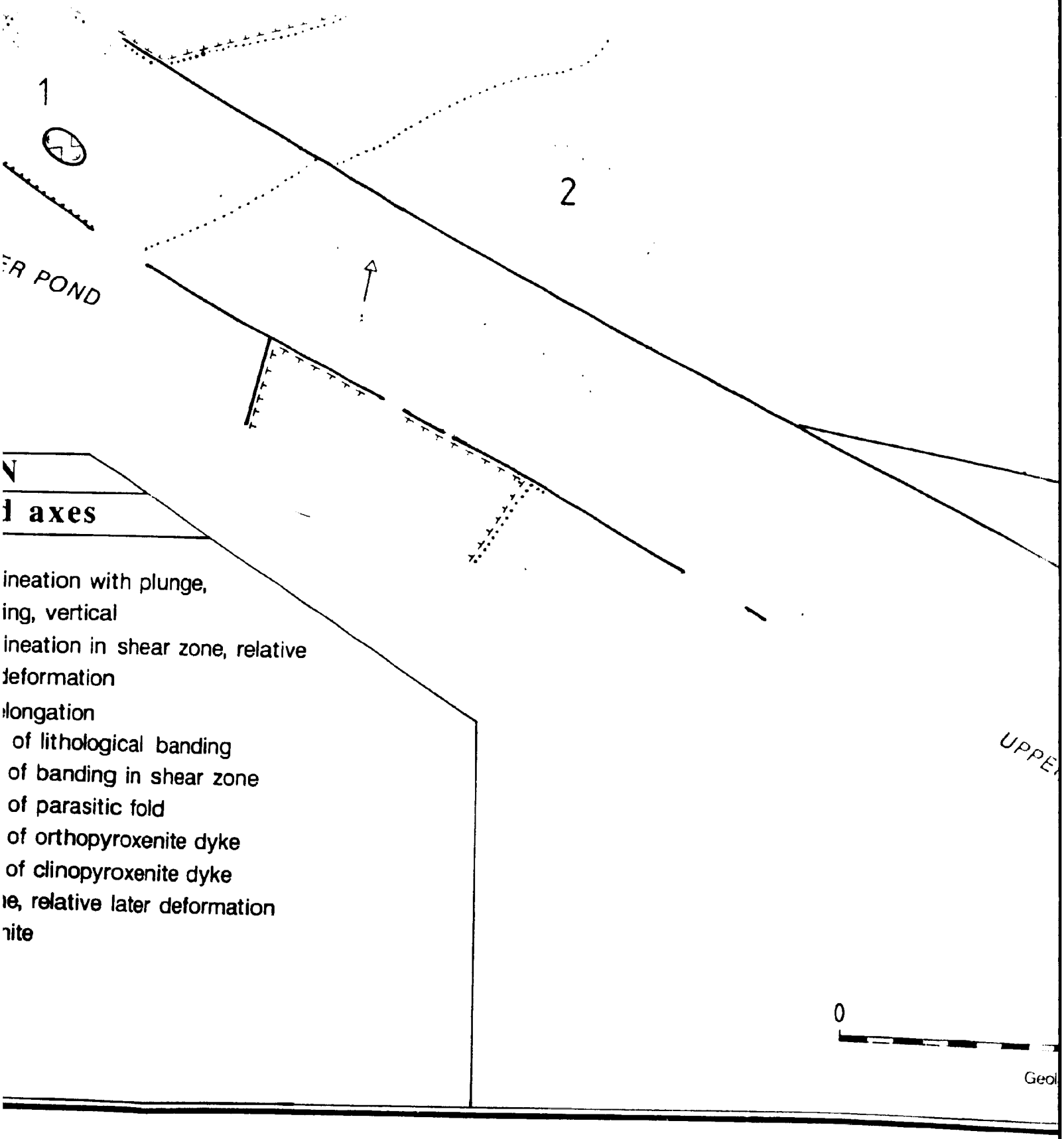
1
2
ER POND
N
l axes
ineation with plunge,
ing, vertical
ineation in shear zone, relative
deformation
longation
of lithological banding
of banding in shear zone
of parasitic fold
of orthopyroxenite dyke
of clinopyroxenite dyke
ne, relative later deformation
nite
UPPE
0
Geol

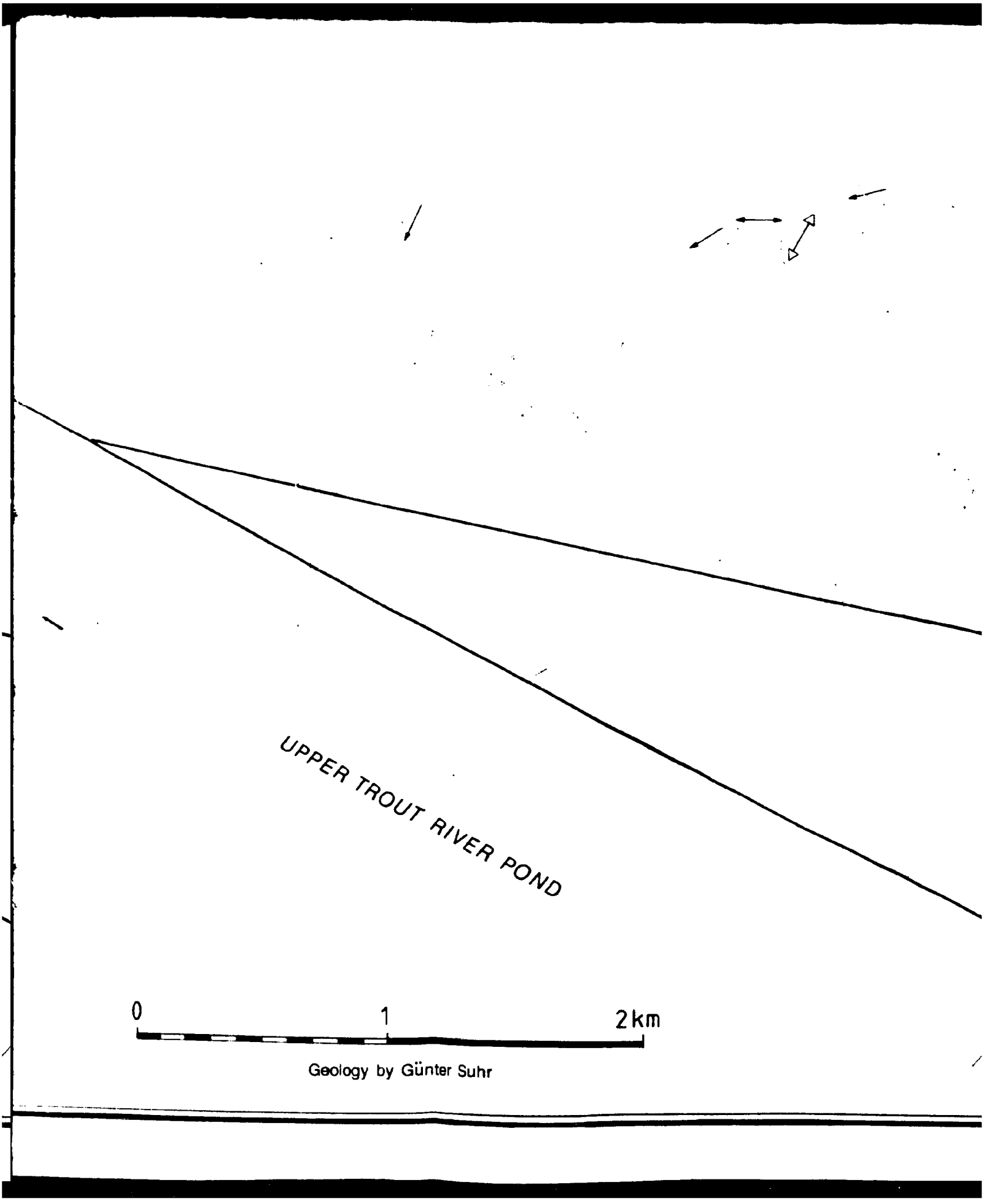

Geology by Günter Suhr

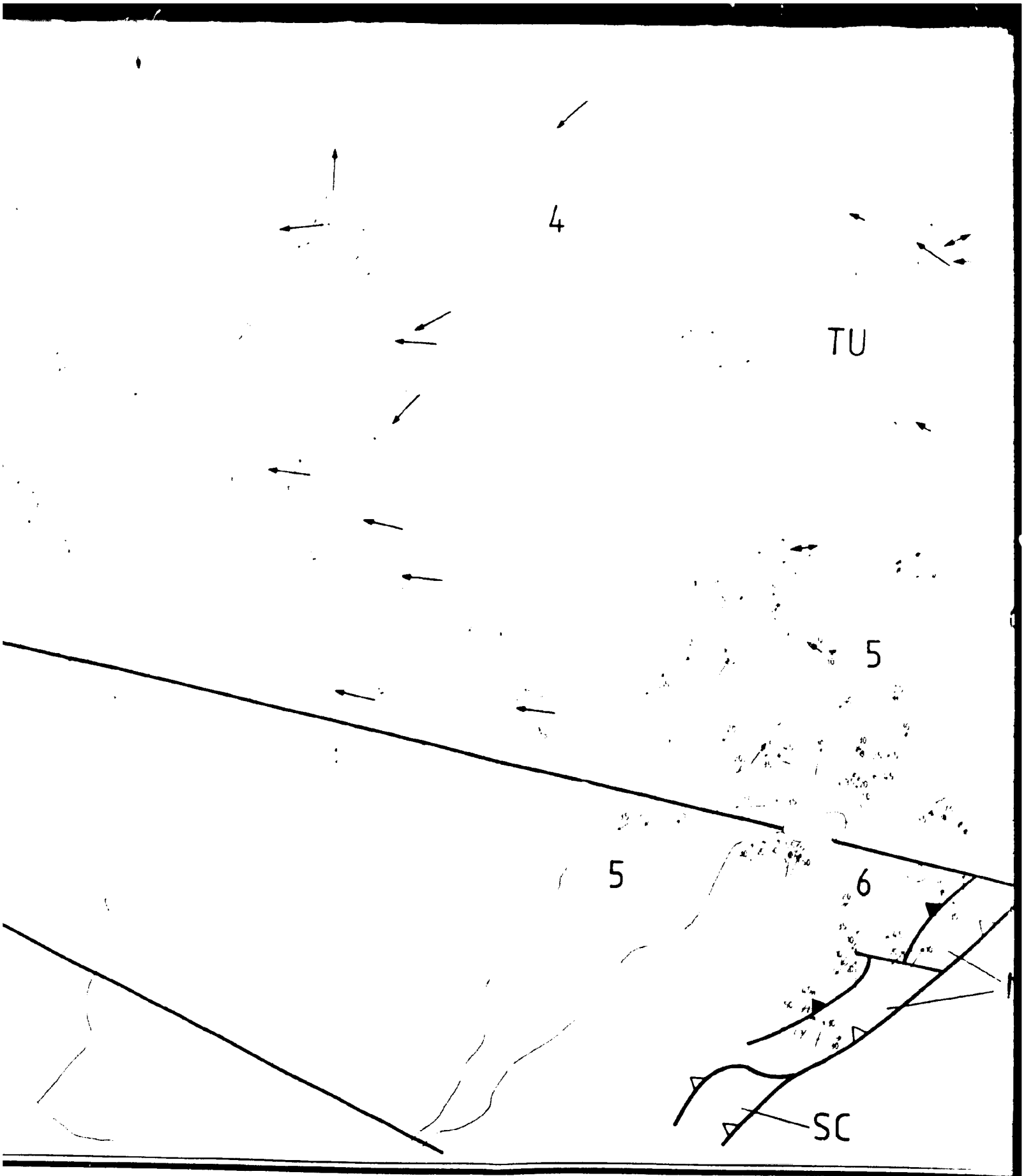
4
TU
5
5
6
SC

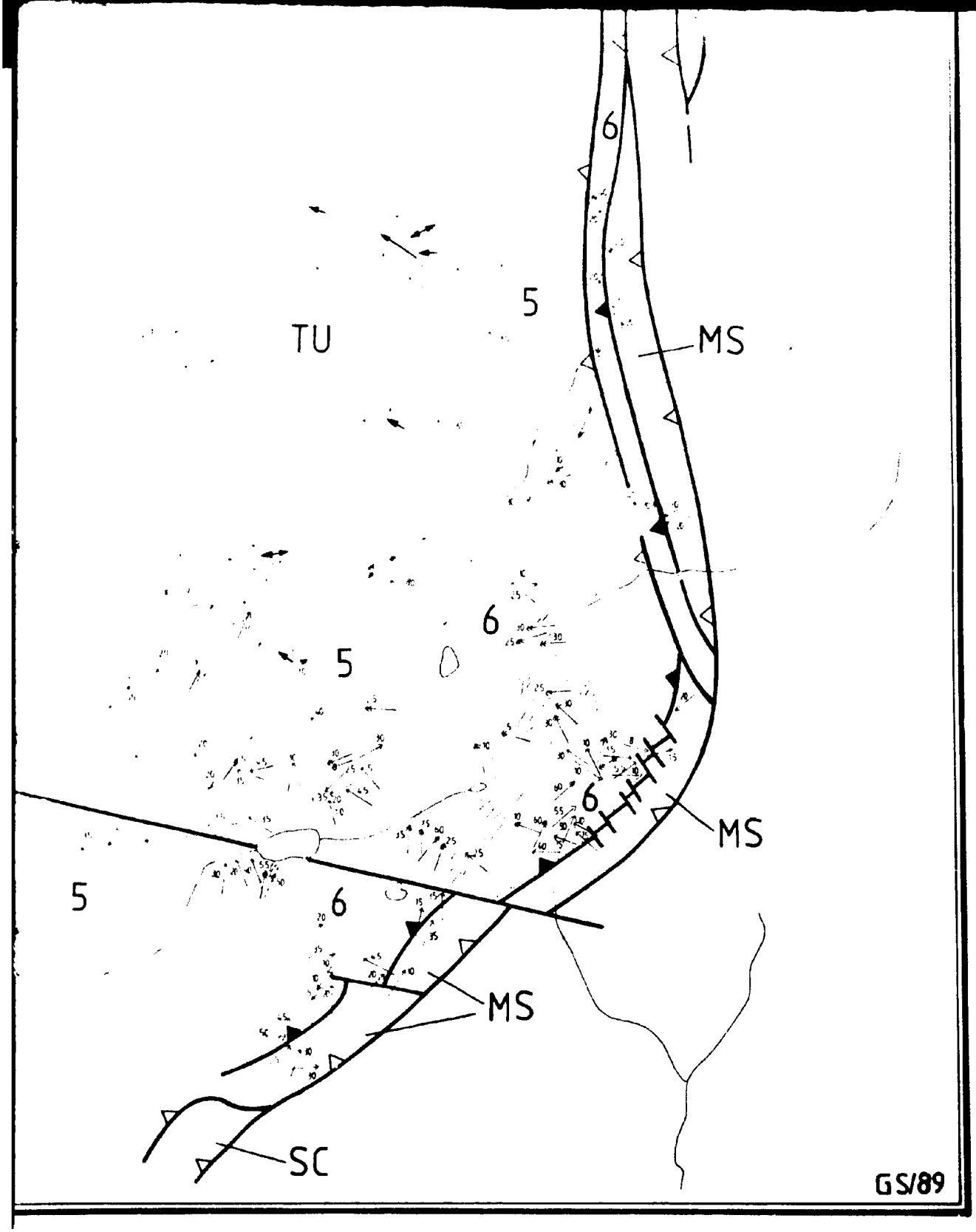
6
5
TU
MS
6
5
6
MS
5
6
MS
SC
GS/89